UNIVERSITÀ DEGLI STUDI DI SALERNO
Dipartimento di Ingegneria Civile

Dottorato di Ricerca
in
Rischio e sostenibilità
nei sistemi dell'ingegneria civile, edile ed ambientale

XXXIV (2018-2021)

Seismic behaviour of steel structures equipped with traditional and innovative beam-to-column connections

Sabatino Di Benedetto

Il Tutor
Prof. Gianvittorio Rizzano

Il Coordinatore
Prof. Fernando Fraternali

Il Co-Tutor
Prof. Massimo Latour

RINGRAZIAMENTI

Al termine di questo percorso desidero ringraziare il prof. Gianvittorio Rizzano, il prof. Massimo Latour ed il prof. Vincenzo Piluso per l'opportunità che mi hanno offerto di partecipare alle attività di ricerca discusse nella presente tesi. Non mi hanno mai fatto mancare il loro aiuto fornendo sempre preziosi consigli ed indicazioni.
Ringrazio anche i dottorandi ed i tesisti con cui ho condiviso le giornate in "aula dottorandi": Giovanni, Bonaventura, Adamo, Luigi, Simona, Alessandro, Elena, Annarosa, Alberico, Roberto, Rosa, Raffaele, Narinder, Maria, Francesco.
Ringrazio l'ing. Francesco Perri e l'ing. Ciro Esposito per il loro indispensabile lavoro nelle attività di laboratorio.
Ringrazio il prof. Bursi, il prof. Tondini, il prof. Bonelli, il prof. Broccardo, Fabrizio, Giulia, Roberto, Chiara, Luca ed Osman per l'accoglienza ed i suggerimenti forniti nei pochi mesi di studio trascorsi presso l'Università di Trento.
Ringrazio il prof. Fabio Freddi e Ludovica Pieroni dell'University College of London per la possibilità di collaborare con loro in un'attività di ricerca che esula dalla presente tesi.
Un ringraziamento particolare è rivolto al prof. Massimo Latour ed all'ing. Antonella Bianca Francavilla per essere sempre stati presenti in questi anni offrendomi costantemente il loro supporto con pazienza ed entusiasmo.
Un ringraziamento, infine, alla mia famiglia per avermi supportato in questi anni.

CONTENTS

ABSTRACT

One of the most common ways to conceive seismic-resistant steel structures is by adopting the Moment Resisting Frames (MRFs). This approach ensures that the building withstands the seismic event through the development of plastic hinges at the beam ends, beam-to-column connections or column bases. The most widespread design philosophy relies on the strong-column strong-connection weak-beam approach, which ensures the development of plastic hinges only at the beam ends and first-floor column bases. Nevertheless, this approach implicitly accepts the development of structural damages during a severe seismic event to dissipate the input energy. This is a negative aspect because it affects the reparability and functionality of buildings.
For this reason, in the last decades, as an alternative to this classic design strategy relying on full-strength joints, a new design philosophy based on the use of partial-strength beam-to-column connections was developed. This method relies on the strong-column weak-connection strong-beam approach so that the dissipation of the seismic input energy occurs only in well-defined nodal components, which can be easily substituted at the end of the earthquake. In such a way, structural resilience is also achieved.
Several traditional and innovative solutions have been proposed and investigated within this framework. These beam-to-column joints have been widely studied based on experimental tests, numerical simulations, and theoretical formulations deriving from adequately defined analytical models. In particular, the experimental tests and the corresponding simulations have regarded beam-to-column sub-assemblies under monotonic or cyclic loading histories. In such a way, the basic information related to the analysed joints' stiffness, resistance, ductility and energy dissipation capacity could be easily derived. Instead, very few tests on large-scale steel structures subjected to seismic inputs have been performed.
In this framework, a relevant research programme has been planned at the University of Salerno. It aims at assessing the dynamic behaviour of different beam-to-column connections over the seismic response of large-scale structures. In particular, a significant part of this investigation relates to performing pseudo-dynamic tests on a mock-up building equipped with different traditional and innovative joints: the Reduced Beam Section (RBS or dog-bone) connection; the FREE from DAMage (FREEDAM) joint; the double-split dissipative T-stub (or X-shaped) connection.
The configurations mentioned above represent joints connecting double-tee beam and column profiles, reflecting possible American and European applications. However, since there is widespread use in Japan of tubular columns, configurations connecting hollow sections and double-tee profiles should not remain unexplored. Under this perspective, this thesis also focuses on the static characterisation of joints connecting circular-hollow-section (CHS) columns and through-all double-tee beams by adopting the component method approach. At the moment, the most common way of conceiving such a kind of joint consists of simply welding the beam to the external surface of the column or using collar plates or composite solutions. However, these alternatives do not ensure relevant mechanical properties and simply structural detailing of the connections. Instead, the recent technological advancements introduced the possibility of using 3D Laser-Cutting for manufacturing the joint mentioned above, whose peculiarity is that the beam can intersect the column, enhancing the mechanical properties but with simple nodal detailing. Therefore, the need to study this connection's behaviour through the component method approach relies on the possibility of employing this joint together with other solutions (i.e. RBS, …).

However, because of the incompatibility between the profiles of the columns, the seismic response of this connection cannot be investigated through the same mock-up building used to perform the pseudo-dynamic tests. For this reason, at the end of this thesis, a preliminary and brief introduction to the hybrid simulations with dynamic substructuring technique is reported.
For the sake of clarity, the thesis is divided into six chapters.
Chapter 1 focuses on a brief introduction to the traditional steel frames and beam-to-column joints. In particular, attention is paid to the four connection typologies investigated in the following chapters, and the objectives of the thesis are reported.
Chapter 2 deals with the static characterisation of the Reduced Beam Section (RBS) joint and circular hollow section to through-all double-tee beam connections. In particular, concerning the dog-bone solution, the basic experimental, numerical and analytical activities carried out in the past years at the University of Salerno are reported. Instead, due to the novelty induced by the 3D Laser Cutting Technology, most of Chapter 2 relates to the study of the static behaviour of CHS through I-beam joints. The investigation is based on experimental tests, numerical simulations and analytical formulations concerning the whole beam-to-column sub-assembly and its components. In particular, the components are adequately identified, and formulations to provide their stiffness, strength and cyclic behaviour are reported and implemented through an OpenSees code.
In **Chapter 3**, the basic information related to two innovative partial-strength beam-to-column connections is reported. In particular, the analysed joints consist of the FREE from DAMage (FREEDAM) connection, which is endowed with friction devices, and a joint characterised by dissipative T-stubs which connect the beam flanges to the column flange. The peculiarity of this solution is that the flange of the T-stub is suitably weakened by an hourglass-shaped cut in the zone between the flange-to-stem attachment and the bolts.
In **Chapter 4**, three experimental campaigns concerning pseudo-dynamic tests on a large-scale steel structure equipped with RBS, FREEDAM and X-shaped T-stub connections are discussed. All the experimental data are complemented with numerical simulations developed through SeismoStruct, OpenSees or Abaqus software. In this case, the tested mock-up has been conceived to be demountable so that the connections could be substituted in an effortless and fast way. However, since the columns of the tested structure consist of double-tee profiles, it is clear that no pseudo-dynamic tests could be performed concerning the CHS to through-all I-beam connection.
For this reason, **Chapter 5** is devoted to a brief introduction to the hybrid simulation with dynamic substructuring technique. Such a tool represents a fascinating solution to assess the seismic behaviour of devices when they are part of a more complex structure. This strategy allows the experimental assessment of the considered device while the whole building can be numerically simulated. For such a reason, this approach represents the first step for future developments of this work consisting in evaluating the dynamic response of CHS to through-all I-beam joints through the hybrid simulation with dynamic substructuring technique.
Finally, in **Chapter 6**, the main conclusions are reported.
The topics addressed in this thesis must be framed within broader research projects begun at the University of Salerno a few years ago. Consequently, the author's contribution constitutes only a tiny part of these researches. Therefore, to better place the issues addressed in this thesis in more general fields of study, the following chapters are composed of both the main outcomes of the research projects and the author's personal contributions. In particular, the personal contributions will be summarized at the end of each chapter. For clarity, Table 1 summarizes the topics for which the author’s contribution can be found. These contributions are discussed in much more detail than the bibliographic studies and the results of the previous projects.

Table 1 – Contribution to the thesis

Section or *topic*	**Contribution**
• **Chapter 1**	Bibliographic studies
Study about beam-to-column sub-assemblies	
• **Chapter 2**	
• RBS connection	Results of previous research projects
• CHS to through-all I-beam connection	Personal contribution
• **Chapter 3**	
• FREEDAM and dissipative X-shaped T-stub connections	Results of previous research projects
Study about beam-to-column connections as part of a large-scale structure subjected to dynamic loading	
• **Chapter 4**	
• Pseudo-dynamic tests and numerical simulations	Personal contribution
• **Chapter 5**	
• Hybrid testing method with substructuring technique	Bibliographic studies

CHAPTER 1 - Introduction

1.1 Seismic behaviour of Moment-Resisting Frames (MRFs)

A Moment Resisting Frame (MRF) is a seismic-resistant system capable of supporting relevant horizontal loads through the bending of its members. MRFs ensure stiffness and strength through the flexural resistance that the structural members (i.e. beams, columns and connections) are able to provide. In a perimetral layout, MRFs are located along the building edges, while all the other frames are designed to sustain only gravity loads; for this reason, their beam-to-column joints and column bases are pinned, exhibiting minor flexural stiffness and strength. Consequently, in the hypothesis of rigid decks and during a seismic event, the equivalent horizontal actions induced by the global mass of the building can be considered ideally distributed only among the MRFs (Figure 1.1).

Figure 1.1 – Steel Moment Resisting Frames (MRFs)

Alternative solutions such as eccentrically braced frames (EBFs), concentrically braced frames (CBFs) or shear walls are also widely adopted. Nevertheless, even though the braced and shear walls systems generally allow obtaining stiffer configurations resulting in structures less prone to second-order effects and complying with the serviceability limit states more easily compared to MRFs, the braces and the walls could provide limits from an architectural or functional point of view.

MRFs can be designed to exhibit fully elastic or dissipative behaviour. In the first case, the structural members of the frame are designed consistently with the maximum design actions and, therefore, no structural damages or yielded structural elements should be observed at the end of the event. This strategy is able to preserve human life and the serviceability limit states, but it generates a relevant oversizing of the structural elements. Furthermore, the structural response is supposed to be so rigid that the expected floor accelerations can be incompatible with the building's functionality.

Instead, the dissipative strategy assumes that the structure can withstand the earthquake effects by dissipating the seismic input energy through the activation of well-defined dissipative fuses. Even though the location of these elements is strictly dependent on the assumed design philosophy, generally, they are located at beam ends, column bases and beam-to-column joints.

The traditional design approach applies the capacity design criterion according to the strong-column strong-joint weak-beam philosophy. This strategy relies on the plastic engagement of beams at their ends to dissipate the input energy in case of rare seismic events, while the adoption of full-strength joints and the application of beam-column hierarchy criteria prevent, respectively,

the plastic engagement of the connections and panel zones and the yielding of the columns. Alternatively, it is possible to apply another approach based on the strong-column weak-joint strong-beam philosophy. It assumes partial-strength beam-to-column connections and allows energy dissipation through the plastic engagement of well-defined joint components while the column and the beam end behave elastically.
As highlighted by Astaneh-Als in [1], different typologies of MRFs can be individuated in practice. The classification is based on the following information: the three-dimensional layout of the frames; the connections' typology (riveted, bolted, welded); the ductility class (Low, Medium, High); the stiffness of the joints (pinned, semi-rigid or rigid); selection of the dissipative zone (beam end, panel zone, connection, column).
Concerning the spatial distribution, MRFs can be classified into the following categories: space frames, perimeter frames, perimeter frames with only a few MRFs, planar frames and hybrid systems.
In a structure with space frames (Figure 1.2), all the frames withstand vertical and horizontal loads resulting in an ineffective solution. On the other hand, a perimeter framed building (Figure 1.2) is characterized by frames located only along the perimeter, while the inner frames have a pendular behaviour and sustain only the gravity loads. Such a solution is more effective and cheaper than the previous one, primarily because of the lower number of rigid connections belonging to MRFs.

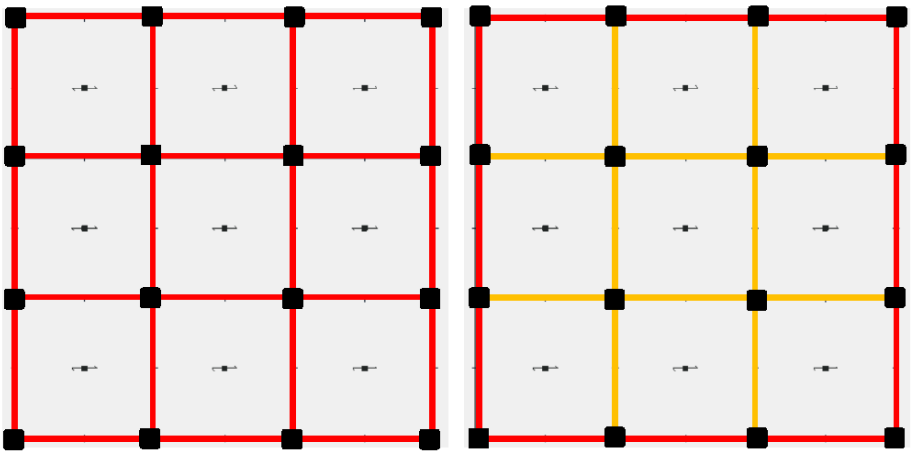

Figure 1.2 – Space (left) and perimeter (right) MRFs - MRFs are highlighted in red and pendular frames in yellow

In some cases, especially with the adoption of double-tee columns, only a few bays of the perimeter may be part of MRFs, further reducing the number of continuous joints (Figure 1.3). Furthermore, sometimes different seismic-resistant strategies can be adopted along with the main directions of the building. For example, this happens in the case of planar frames (different systems in the two directions, as reported in Figure 1.3) and hybrid systems (combination of two systems in the same direction), where the solution with MRFs can be coupled with other strategies (e.g. EBFs, CBFs).

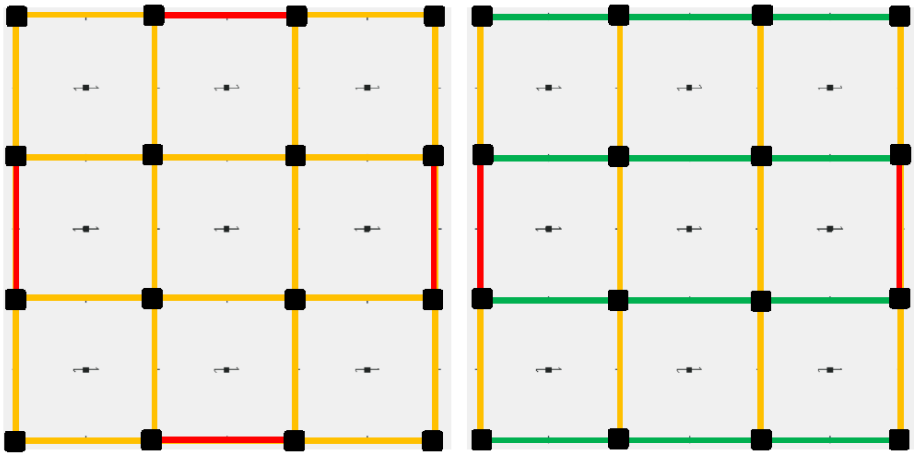

Figure 1.3 – Perimeter frames with a few MRFs (left) and planar frames (right) - MRFs are highlighted in red, pendular frames in yellow and other structural systems in green

1.2 Type of joints used in MRFs

Another way to classify the MRFs depends on the connection between beams and columns, which could be riveted, bolted or welded (Figure 1.4).

Figure 1.4 – Rivetted (left), bolted (centre) and welded (right) connections

In the first decades of the previous century, the riveted solution was the most exploited since the rivets enabled the connections to withstand both shear and tension loads. However, afterwards, High Strength Bolts represented an excellent alternative to the rivets thanks to the friction mechanism developed between the two clamped surfaces. These solutions allowed to speed up the construction times thanks to mechanical fasteners to join steel members. Nevertheless, starting from the 1950s, the welding technique started being exploited; it allows connecting beams and columns by melting the two parts and adding filler material. The first applications were limited to shear connections, but then the welding technique was also applied in the case of full-strength beam-to-column connections. Nevertheless, during the unfortunately famous earthquakes of Kobe (1995) [2] and Northridge (1994) [3], many welded beam-to-column connections belonging to MRFs exhibited brittle fracture (Figure 1.5).

Figure 1.5 – Damaged connections after the seismic event of Northridge

In fact, the unexpected failure of welds occurred both in several perimeter MRFs, typically used in the USA, and in space MRFs typically adopted in Japan. Such unsatisfactory behaviour was found in the welding techniques used at the time, which proved to be inadequate and characterized by low ductility [4].

1.3 Joint classification

The stiffness and strength of the joints influence the overall dynamic structural behaviour of MRFs, affecting the design at the Serviceability Limit States (SLS) and Ultimate Limit States (ULS). Unlike concrete structures, where the connections can be considered rigid so that no relative rotations among the connected members are allowed, in the case of steel structures, this solution represents an extreme behaviour of joints. The other and opposite extremal configuration comprises the flexible joint, which allows relative rotations among the members converging in the node. In the case of rigid connections, the frames can be considered continuous, while in the second solution, they are pinned.

The classification of the joints depends on their rotational stiffness, strength and ductility. In particular, referring to the stiffness classification, three categories can be defined:

- nominally pinned connections that are able to transfer only shear and axial force since they allow the relative rotation among the members converging in the node without the development of bending moments; as a consequence, the initial stiffness is negligible;
- rigid connections that are able to transfer not only shear and axial actions but also bending moments since the relative rotation among the members of the joint is significantly limited;
- semi-rigid connections exhibit an intermediate behaviour between the two previously described solutions.

Concerning the classification in terms of flexural strength of the connections, three categories can be considered:

- full-strength joints, which are designed to have higher resistance than the connected members so that plastic hinges can develop only at the beam or the column ends;
- partial-strength joints, which are designed to have lower resistance than the connected members ($0.25M_{beam,pl,Rd} < M_{joint,Rd} < M_{beam,pl,Rd}$) and for this reason, they are characterized by dissipative components which are damaged or activated during a seismic event;
- nominally pinned joints, whose design resistance is much lower than the ones of the connected members ($M_{joint,Rd} < 0.25M_{beam,pl,Rd}$).

Finally, the last classification concerns the plastic rotation supply of the joints, which are divided into:

- full-ductility connections, whose plastic rotation supply is equal to or higher than that of the connected members;
- partial-ductility connections, whose plastic rotation supply is lower than the connected members.

According to this classification, in the case of elastic analyses, only the rotational stiffness can affect the overall structural behaviour, and the connections can be considered pinned, semi-rigid or rigid. Instead, the stiffness and flexural strength must be considered if an elastic-plastic analysis is performed. Finally, in the case of a rigid-plastic analysis, only the bending resistance plays a relevant role, and for this reason, the joints can be classified as full-strength, partial-strength or pinned.
A summary of the joint classification is reported in Table 1.1.

Table 1.1 – Joint classification

Method of global analysis	**Classification of the joint**		
Elastic	Nominally pinned	Rigid	Semi-rigid Semi-rigid and partial-strength
Elastic-plastic	Nominally pinned	Rigid and full-strength	Semi-rigid and full-strength Rigid and partial-strength
Rigid-plastic	Nominally pinned	Full-strength	Partial-strength
Type of joint model	**Simple**	**Continuous**	**Semi-continuous**

1.4 Frame classification

The frame classification is strictly related to the joints' stiffness, strength, and ductility that are part of the seismic-resistant structures.
According to Eurocode 3 [5], the frames can be classified into sway and non-sway:

- a non-sway frame is characterized by such small values of lateral displacements that it is possible to consider negligible the internal actions induced by the deformability of the frame;
- a sway frame is affected by relevant internal actions induced by its high lateral deformability.

Eurocode 3 points out that a frame can be considered non-sway if the following inequalities are satisfied:

- $\alpha_{cr} = \frac{F_{cr}}{F_{Ed}} > 10$ for elastic analysis;
- $\alpha_{cr} = \frac{F_{cr}}{F_{Ed}} > 15$ for plastic analysis.

Where α_{cr} is the multiplier of the design loading to cause the global elastic instability, F_{cr} is the elastic critical buckling load for global instability on the initial elastic stiffness, and F_{Ed} is the design loading.
Another classification involves the braced and unbraced frames, which differ in the presence or absence of specific stiffening elements able to reduce the lateral displacements by at least 80%.
Concerning the characteristics of a joint, three different frames can be defined:

- simple, if the connections can be considered as nominally pinned and so they do not transfer flexural actions to the columns but allow the free rotation of the connected beams;
- continuous, when the joints are rigid and, for this reason, over-resistant for the beams;
- semi-continuous if the connections are semi-rigid and exhibit an intermediate response between the last two categories; in this case, the behaviour of the joint should be appropriately modelled.

As it is clear, the last classification is strictly related to the rotational stiffness of the joints. However, in order to have a more precise boundary among the rigid, semi-rigid and nominally pinned connections, the Eurocode 3 Part 1-8 [6] suggests the following parameters for their categorization: $S_b = \frac{EI_b}{L_b}$ and $S_c = \frac{EI_c}{L_c}$.

In particular, S_b and S_c are the flexural stiffness of the beam and the column, E is the modulus of elasticity, I_b and I_c are the inertia modulus of the beam and the column, L_b and L_c are lengths of the beam and the column. Eurocode 3 states that a connection is rigid if its stiffness does not decrease the Euler buckling load of the structure with full-rigid attachments by more than 5%. Figure 1.6 provides detailed information.

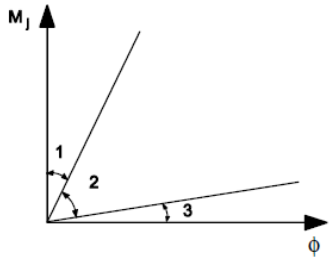

Zone 1: rigid, if $S_{j,ini} \geq k_b EI_b / L_b$

where
$k_b = 8$ for frames where the bracing system reduces the horizontal displacement by at least 80 %
$k_b = 25$ for other frames, provided that in every storey $K_b/K_c \geq 0{,}1$ *)

Zone 2: semi-rigid

All joints in zone 2 should be classified as semi-rigid. Joints in zones 1 or 3 may optionally also be treated as semi-rigid.

Zone 3: nominally pinned, if $S_{j,ini} \leq 0{,}5\ EI_b / L_b$

*) For frames where $K_b/K_c < 0{,}1$ the joints should be classified as semi-rigid.

Key:

K_b	is	the mean value of I_b/L_b for all the beams at the top of that storey;
K_c	is	the mean value of I_c/L_c for all the columns in that storey;
I_b	is	the second moment of area of a beam;
I_c	is	the second moment of area of a column;
L_b	is	the span of a beam (centre-to-centre of columns);
L_c	is	the storey height of a column.

Figure 1.6 – Classification of the connections concerning their stiffness

Finally, also the ductility gives additional data useful for the frame classification. Similarly to the ductility definition at the local level of the material or the member sections, the global ductility of MRFs can be assessed as the ratio between the ultimate and the elastic top sway displacements. According to the requirements proposed by the Eurocodes, three ductility classes have been defined, differentiating for the rotational capacity of the beam-to-column connections and the column bases (Table 1.2).

Table 1.2 – Classification of the structures about their ductility

EUROCODE 8	
Ductility Class	**Minimum Rotational Capacity (mrad)**
Ductility Class Low (DCL)	-
Ductility Class Medium (DCM)	25
Ductility Class High (DCH)	35

1.5 Traditional and innovative steel beam-to-column connections

The best strategy to design seismic-resistant steel structures is to increase their energy dissipation capacity by developing a relevant number of dissipative fuses characterized by wide and stable hysteresis loops adequately designed according to the first principle of the capacity design accounting for the maximum actions deriving from the design phase. Instead, the non-dissipative zones must behave elastically and, for this reason, according to the second principle of the capacity design, they are designed considering the maximum actions that the yielded and strain-hardened dissipative fuses are able to transfer. This principle assures, in most cases, the prevention of both brittle crises and the development of storey mechanisms. However, the storey mechanisms represent the worst approach through which the structure withstands a seismic event because they induce the plastic engagement of the top and base ends of the columns belonging to the same storey. Furthermore, it is well-known that, due to the relevant axial loads sustained by vertical elements, the developed plastic hinges are characterized by low ductility and energy dissipation capacity. For this reason, all the codes establish that the structures have to be designed to promote a global type collapse mechanism, which consists of developing plastic hinges located only at the beam ends, or the joints, and at the first-floor column bases.

The above-depicted situation shows that the beam-to-column connections play a relevant role in the overall structural behaviour. In particular, for many decades, there has been deep exploitation of full-strength welded or bolted beam-to-column joints. However, during the unfortunately famous earthquakes of Northridge (1994) [3] and Kobe (1995) [2], many welded beam-to-column connections belonging to MRFs exhibited brittle fracture. In fact, unexpected failure of welds occurred both in several perimeter MRFs, typically used in the USA, and in space MRFs typically adopted in Japan. The reasons for such unsatisfactory behaviour were found in the welding techniques used at the time, which demonstrated to be inadequate and characterized by low ductility [4] but also to the reason that the design criteria adopted did not assure the right overstrength to the complete development of the beam plastic rotation capacity. To solve these issues, in the earthquake aftermath, two strategies were proposed. The first one was based on strengthening the welding details. The second one was based on the concept of weakening the beam ends into areas located sufficiently far from the column [4, 7]. This weakening approach, called Reduced Beam Section (RBS) or dog-bone [7-13] (Figure 1.7), allows concentrating the damage in specific regions and overall enhancing the seismic performance. Such an improvement is mainly related to reducing stress concentrations in the welds and increasing the local ductility.

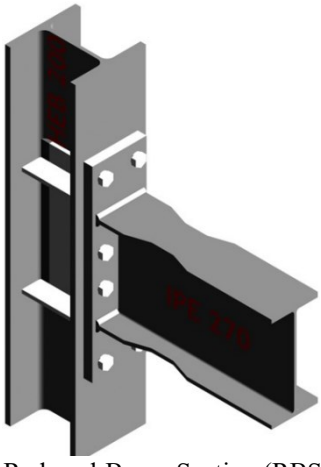

Figure 1.7 – Reduced-Beam-Section (RBS) connection

As an alternative to this design philosophy, the use of partial-strength beam-to-column joints has emerged in the last decades. Partial strength joints can lead to a high ductility and energy

dissipation capacity, provided that their geometry is designed applying capacity design principles at the level of the single components [14-17]. The weakest joint component can be initially selected and designed to provide the required ductility and energy dissipation supply within this framework. In contrast, all the other joint components, including the beam end, must be designed with appropriate over-strength to account for the strain hardening and random material variability exhibited by the weakest joint component [17-20]. This approach has been applied in the last decades in many experimental activities worldwide, showing that traditional connections (e.g. extended end-plate, double split-tee) can assure high ductility supply when properly designed [21-31].

The double split T-stub joint represents an excellent example of such a strategy. This connection typology is characterized by using a couple of T-stubs to connect the beam flanges to the column. The T-stubs, if properly designed, can act as seismic dampers with levels of ductility and energy dissipation capacity that can be easily calibrated in the design phase. With this approach, the upper and lower flanges of the beam ends are bolted to the stems of T elements which are bolted to the flange of the column. In such a way, according to the component method approach, the bending moment at the beam end can be ideally schematized as opposite horizontal forces, respectively stressing the T-stubs in tension and compression.

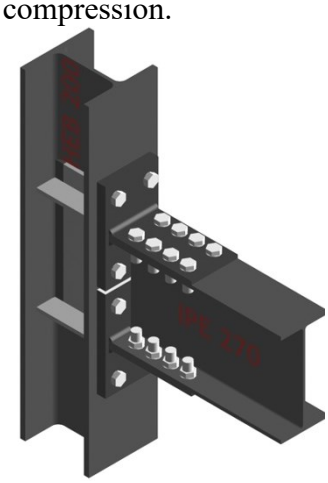

Figure 1.8 – Traditional T-stub connection

Many studies have been carried out on the classic T-stub connection (Figure 1.8); in particular, also a component method approach has been proposed by Zoetemeijer [32] starting from the knowledge of the single component (T-stub) and thoroughly investigated by many other authors [15, 33-34]. For instance, Bezerra [33] carried out a parametric study to observe the effects of the thickness of the flange on the contact stress distribution between the flange and the rigid base, the prying actions, and the shear stresses of the bolts. Bravo [34], through many cyclic tests, observed that the failure modes and limit states that control the behaviour of the built-up T-stubs are the same that govern the hot-rolled T-stub behaviour. Wang [35] studied the cyclic behaviour of T-stubs connected to hollow section columns using T-head Square-neck One-side Bolted connections (TSOBCs). Wang-Dong-Liu [36] proposed three different T-stub fuses (Figure 1.9) with a damage-controllable and earthquake-resistant structure. In particular, their approach is based on the adoption of Low-Yield Point (LYP) T-stubs to increase the free-deformation length of the stem. In this way, the protection of the primary frame members is achieved without excessively reducing the strength of the connection.

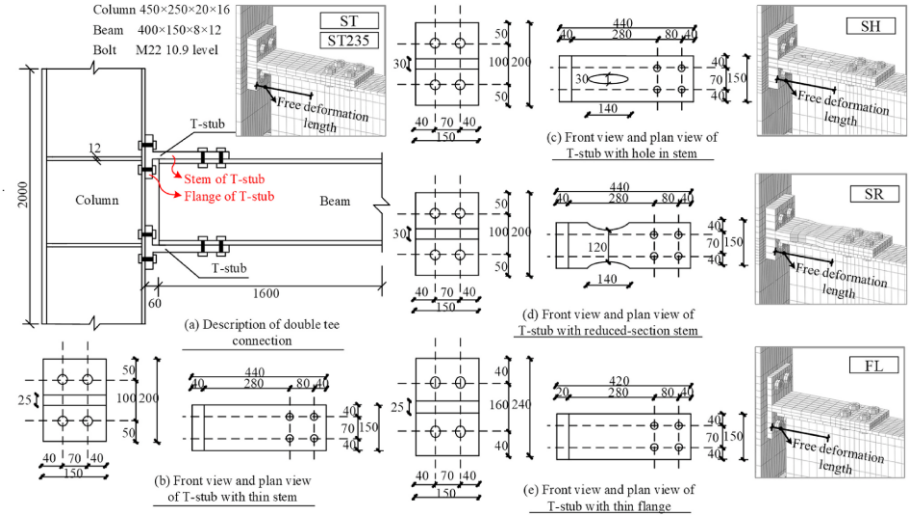

Figure 1.9 – Solutions studied by [36]

Furthermore, the free deformation of the stem can be increased by adequately designing a hole or a reduced section in the stem. A similar method has also been proposed by Irvani [37]. According to the traditional approach, the T-stubs effectively dissipate the seismic input energy only if they are subjected to tensile forces; to have the additional load-bearing capacity, stiffness and ductility, Zhu [38] proposed a new solution consisting in adding supplementary plates in-between the T-stub and the column so that the T-stub can also work in compression. This approach makes it possible to adopt the classic T-stub at the upper flange-to-column attachment and this innovative solution at the lower flange. In fact, in this way, the upper T-stub acts as a centre of rotation, while the lower T-stub effectively allows the rotation of the connection.

The previous cases ensure the energy dissipation capacity properly weakening the stem of the T-stubs; however, there are also other proposed solutions weakening the flange of the T-element. For instance, Bayat [39] proposed a beam-to-column connection with T-shaped slit dampers. In this case, the author adequately weakened the flange of the T-stubs with holes to fix the zone to be yielded. Furthermore, he demonstrated that this solution could provide more energy dissipation capacity and stiffness and ensure fast reparability.

Considering a similar approach, Latour and Rizzano [40-42] have proposed another kind of connection characterized by X-shaped T-stubs (Figure 1.10).

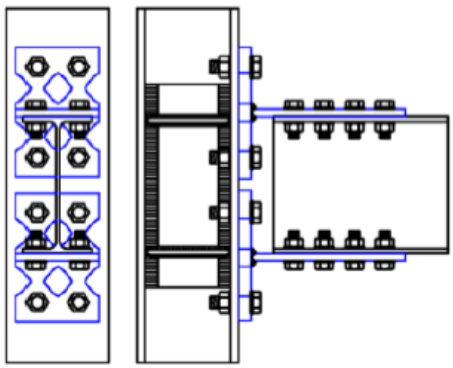

Figure 1.10 – Connection with dissipative T-stubs

This connection typology differs from the traditional one because the flange of the T-element is properly cut thanks to an hourglass shape similar to the bending moment that arises in the plate part between the stem and the bolts. Therefore, it is possible to ensure a uniform yielding of this part. At the University of Salerno, many research studies have been carried out on this innovative connection since experimental, numerical and analytical works have been performed. An analytical model has been proposed by Latour and Rizzano [40-42] to design the effective hourglass shape of the joint, and it has been validated against experimental results characterized by cyclic tests on a beam-to-column sub-assembly [17].
Another solution consists in endowing steel beam-to-column connections with friction dampers, usually bolted at the lower beam flange. These connections can provide high local ductility and energy dissipation capacity provided that the damper stroke is appropriately selected and the damper components are designed through the application of capacity design principles at the global and local level [14-15, 17, 19]. Significant examples of such connections are represented by the Sliding Hinge Joint (SHJ) [43-49], developed by the research group of the University of Auckland, and the FREEDAM joints (Figure 1.11) recently developed within a European project [50-54].
In these connections, a friction damper is located at the beam bottom flange to control the joint resistance by appropriately regulating the tightening torque of pre-loadable high strength bolts and the joint ductility by adequately designing the length of the slotted holes. Moreover, the high initial stiffness, independent of the preload applied to the bolts, and the constant flexural resistance achieved at the slippage force allow to numerically model the moment-rotation hysteretic behaviour with a rigid perfectly plastic law.

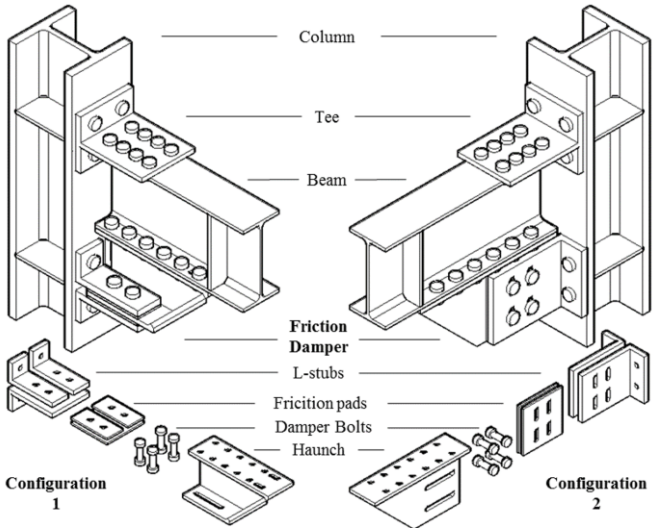

Figure 1.11 – Two possible configurations of the FREEDAM joint

As well as the previous references, double-tee profiles for the structural members of steel moment-resisting frames (MRFs) are widespread in Europe and the USA. This extensive use is due to reliable formulations able to accurately predict the mechanical behaviour of I- or H-shape members and the possibility of adopting a wide range of easy-to-construct beam-to-column connections.
Nevertheless, while in Europe and the USA, I- or H- shapes are more common, hollow sections are more widespread in Japan due to the benefits deriving from equal inertia. This difference depends mainly on a technical reason. While in Europe and the USA, perimetral frames are more

common, space frames are more widely used in Japan. In space frames, the symmetry of the tubular sections allows for better exploitation of the characteristics of these profiles, which are mainly subjected to biaxial bending in this particular scheme. In many cases, due to the circular symmetry, circular hollow section (CHS) members are preferred in the design practice due to the following features: (i) the high values of the radius of gyration, due to the ideal material distribution; (ii) the absence of a weak axis, which characterizes, instead, the double-tee profiles; (iii) the low surface area, compared to the double-tee profiles, with the benefit of reducing paintings, fire and corrosion protection costs; (iv) the lower drag coefficients affecting wind forces; (v) the possibility of reducing the cost of transportation and assembly of the members; (vi) the higher aesthetical aspect. This cross-section typology has been investigated, starting from 1924 when Greene [55] experimentally studied the axial compression capacity of CHS profiles. Afterwards, these efforts were carried on by Bouwkamp [56], Marzullo and Ostapenko [57], Chen and Ross [58], Elchalakani, Zhao and Grzebieta [59], Ma, Chan and Young [60], Xiong, Xiong and Liew [61], Meng and Gardner [62], as is well reported by Meng et al. [63] Instead, the mechanical flexural behaviour was studied by Korol and Hubonda [64], Willhoit Jr. and Mervin [65] and Sherman [66]. At the same time, the combined compression and bending actions have been investigated by Prion and Birkemoe [67], O'Shea and Bridge [68], Pan [69], Nseir [70], Ma [71], Pournara et al. [72] and Meng and Gardner [62].
Despite the benefits highlighted before, one of the main drawbacks limiting the use of these profiles is related to the complexity of the connections, especially between circular hollow section columns and double-tee beams. Different solutions have been investigated to solve this issue, as has already been reported in [73, 74]. Nevertheless, a recently studied alternative consists of conceiving a connection with a beam that passes through the tubular column (Figure 1.12).

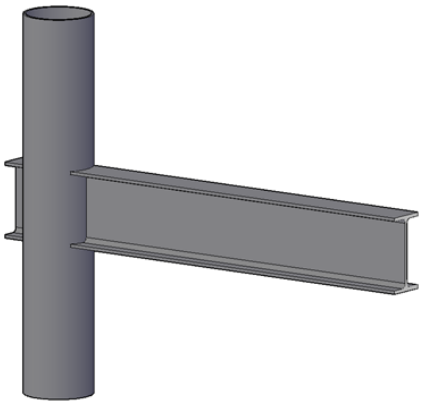

Figure 1.12 – CHS to though-all I-beam connection

Such a solution has only been recently introduced thanks to the adoption of 3D-laser cutting technology (3D-LCT) in civil engineering. The importance of this solution is justified by the efforts devoted to this topic by Voth [75, 76] and Kanyilmaz [77, 78].
Furthermore, the characterization of the behaviour of such a kind of connection can allow combining it with other traditional or innovative design approaches. For instance, as shown in Figure 1.13, the RBS strategy can be applied to the connection between a CHS column and a through-beam. However, this solution can be exploited only once the connection between the tubular section and the I-beam has been adequately defined. This design philosophy allows conceiving dissipative connections also characterized by tubular columns.

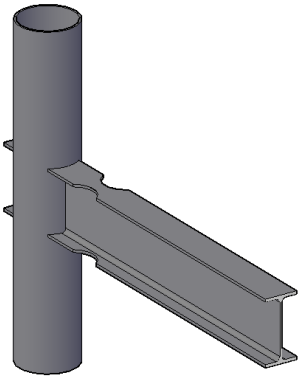

Figure 1.13 – Application of the RBS strategy to a connection with a tubular column

1.6 Objective of the Thesis

The literature review depicted in the previous paragraph proves that many research efforts are devoted to characterising the behaviour of many different kinds of steel beam-to-column connections. In most cases, these studies have focused on assessing the static response of traditional and innovative joints connecting the classic double-tee shaped profiles through the development of extensive experimental, numerical and analytical activities.

However, due to the recent technological innovations, many other fields of study have been explored in the last decades.

In particular, the main objectives of the present thesis are the following.

1) In the framework of the investigation of the static behaviour of full-strength beam-to-column connections, the recent use of the 3D Laser Cutting Technology (3D-LCT) allowed conceiving a new kind of steel joint whose peculiarity consists in the coupling of a circular hollow section profile column and a double-tee section beam. In particular, the adopted innovative technology enables a precise column cut according to the beam's shape so that the double-tee profile can be inserted into the tubular member and then welded. This solution appears more effective than the classic approach based on simply welding the I-beam to the external surface of the hollow profile. In fact, the traditional strategy is easy to manufacture, but the mechanical properties (stiffness, resistance and ductility) of the obtained connection are inadequate for intensive use in MRFs. Instead, the solution characterized by the intersection of the structural members represents an interesting alternative. However, similarly to the currently most exploited double-tee to double-tee connections, also this joint needs investigation to characterize its behaviour both at a global level and especially at its single nodal components. In fact, a full investigation of the single components constituting the joint can let the combination of mixed solution. For instance, using the RBS strategy in structures characterized by circular hollow section columns can also represent a desirable solution. However, as already pointed out, a preliminary characterization of the behaviour of the CHS to the through-all I-beam joint is necessary. In this view and in the framework of the component method approach, experimental and numerical activities have been carried out at the University of Salerno to contribute to filling this knowledge gap.

2) There is currently a great wealth of research on the behaviour of both traditional and innovative joint typologies. Nevertheless, while many tests of sub-assemblies of beam-to-column joints are now available, the impact of the local behaviour of such connections on the overall response of frames under seismic loading conditions has rarely been experimentally analysed. The consequences consist of uncertainties in the validity range of modelling approaches commonly

adopted for non-linear time-history analyses. In fact, numerical models are commonly adopted, but the analyst is not aware of the limitations concerning their application because of the limited availability of full-scale experimental data [79-81]. Obviously, such a lack is due to the practical limitations arising from limited resources, availability of full-scale test equipment and the significant efforts needed to carry out campaigns on full-scale specimens of frames.
For this reason, the second aim of this work consists in presenting the results of an experimental program carried out at the STRENGTH (STRuctural ENGineering Test Hall) Laboratory of the University of Salerno. The planned testing activity regards the seismic simulation of a large-scale two-storey steel building employing the pseudo-dynamic method. In particular, MRFs equipped with traditional and innovative beam-to-column connections have been tested by the pseudo-dynamic method considering a sequence of earthquake events. Furthermore, the work aims to compare the seismic behaviour of similar steel frames, designed according to capacity design principles, whose only difference is the adopted connection typology. The whole experimental program regards the investigation of five different connection typologies, all designed to provide a rotation capacity higher than the minimum required by Eurocode 8 for Ductility Class High (DCH). However, in this work, only three typologies have been studied, as follows:

- MRF-RBS: in this case, the structural scheme to be tested is an MRF equipped with RBSs;
- MRF-FREEDAM: it is an MRF with partial-strength joints equipped with friction dampers; the connection is characterised by the application of damping devices at the level of the bottom beam flange;
- MRF-DST-X: this specimen is constituted by MRFs equipped with partial-strength DST joints with hourglass dissipative T-stubs, which are appropriately weakened to maximize the energy dissipation capacity.

The results of the experimental work are reported in detail with a focus on the global and local structural responses. These results have been complemented with numerical works carried out by SeismoStruct [82], OpenSees [83] and Abaqus [84]. Finally, the accuracy of the adopted models is assessed, underlining the main issues encountered.
Finally, since the mock-up used to perform the three mentioned experimental campaigns is characterized by double-tee columns, the seismic behaviour of CHS to through-all I-beam connections cannot be studied by performing pseudo-dynamic tests. Therefore, an alternative approach consists in carrying out hybrid tests with the dynamic substructuring technique to examine the seismic behaviour of a physical beam-to-column sub-assembly as part of a more complex numerical structure.

1.7 Personal contribution

Chapter 1 represents the introduction to this thesis. Consequently, it mainly comprises bibliographic studies to frame the present work in a more general research field.

1.8 References

1. Astaneh-Asl: “Seismic Design of Bolted Steel Moment-Resisting Frames”. July, 1995.
2. NIST Special Publication 901, “The January 17, 1995 Hyogoken-Nanbu (Kobe) Earthquake”, July 1996.
3. Kaufmann EJ. Fisher JW DiJulio RM, Gross JL, “Failure analysis of welded steel moment frames damaged in the Northridge earthquake. In (2nd edn)”, NISTIR 5944, National Institute of Standards and Technology, Gaithersburg, MD, 1997.

4. SAC, 2000b, "Recommended Seismic Evaluation and Upgrade Criteria for Existing Welded Steel Moment-Frame Buildings", prepared by the SAC Joint Venture for the Federal Emergency Management Agency, Report No. FEMA-351, Washington, D. C.
5. CEN: "Eurocode 3: Design of Steel Structures – Part 1-1: General rules and rules for buildings", EN 1993-1-1, 2005.
6. CEN [2005]: EN 1993-1-8 Eurocode 3: Design of Steel Structures. Part 1-8: Design of Joints, CEN, European Committee for Standardization, 2005.
7. Plumier, A., "New Idea for Safe Structures in Seismic Zones", Proc., Symposium of Mixed Structures Including New Materials, pp. 431-436, IABSE, Brussels, Belgium, 1990.
8. Moore, K.S., Malley, J.O., Engelhardt, M.D., "Design of reduced Beam Section (RBS) Moment Frame Connections", AISC Structural Steel Educational Council, Moraga, CA, 1999.
9. Iwankiw, R. N. and Carter, C. J., "The Dogbone: A New Idea to Chew On", Modern Steel Construct., Vol. 36. No.4, pp. 18-23, AISC, Chicago IL, 1996.
10. Chen, S. J., Yeh, C. H. and Chu, J. M., "Ductile Steel Beam-Column Connections for Seismic Resistance", J. Struct. Engrg., Vol. 122, No. 11, pp. 1292-1299, ASCE, 1996.
11. FEMA 351, (2000): "Recommended Seismic Evaluation and Upgrade Criteria for Existing Welded Steel Moment-Frame Buildings", Federal Emergency Management Agency, Washington.
12. Montuori, R., Piluso, V., "Plastic Design of Steel Frames with Dog-Bone Beam-to-Column Joints", Third International Conference on Behaviour of Steel Structures in Seismic Areas, STESSA 200, 21-24 August, Montreal, 2000.
13. ANSI/AISC, "Prequalified Connections for Special and Intermediate Steel Moment Frames for Seismic Applications", 2016.
14. Steenhuis, M & Jaspart, J.-P & Gomes, Fernando & Leino, T., "Application of the component method to steel joints", Proceeding of the Control of the Semi-Rigid Behaviour of Civil Engineering Structural Connections Conference, 1998.
15. Faella, C., Piluso, V., Rizzano, G., "Structural Steel Semirigid Connections", CRC Press, Boca Raton, FL, 2000.
16. Swanson, J., Leon, R.T., "Bolted Steel Connections: Tests on T-stub Components", ASCE, Journal of Structural Engineering, Vol.126, No.1, pp.50-56, 2000.
17. Iannone, F., Latour, M., Piluso, V. and Rizzano, G., "Experimental Analysis of Bolted Steel Beam-to-Column Connections: Component Identification," J. Earthq. Eng., vol. 15, no. 2, pp. 214–244, 2011.
18. da Silva, L. S., Rebelo L., Mota, C., "Extension of the component method to end-plate beam-to-column steel joints subjected to seismic loading," Trends Civ. Struct. Eng. Comput. Comput. Sci., vol. 22, pp. 149–167, 2009.
19. Latour, M., Piluso, V., Rizzano, G., "Experimental analysis of beam-to-column joints equipped with sprayed aluminium friction dampers" Journal of Constructional Steel Research, 146, pp. 33-48, 2018a.
20. Francavilla, A.B., Latour, M., Piluso, V., Rizzano, G., "Design of full-strength full-ductility extended end-plate beam-to-column joints", Journal of Constructional Steel Research, 148, pp. 77-96, 2018.
21. Elnashai, A. S. and Elghazouli, A. Y., "Seismic behaviour of semi-rigid steel frames," J. Constr. Steel Res., vol. 29, no. 1–3, pp. 149–174, 1994.
22. Nogueiro, P., Da Silva, L. S., Bento, R., and Simões, R., "Experimental behaviour of standardized European end-plate beam-to-column steel joints under arbitrary cyclic loading," in

International Colloquium on Stability and Ductility of Steel Structures, SDSS 2006, 2006, no. February 2015, pp. 951–960.
23. Latour, M., Piluso, V., Rizzano G., "Experimental Behaviour of Friction T-stub Joints under Cyclic Loads", Steel Construction, Volume 6, Issue 1, pages 11–18, 2013.
24. Augusto, H., Simões da Silva, L., Rebelo, C., and Castro, J. M., "Cyclic behaviour characterization of web panel components in bolted end-plate steel joints", J. Constr. Steel Res., vol. 133, pp. 310–333, Jun. 2017.
25. Latour, M., Piluso, V. and Rizzano, G., "Cyclic modeling of bolted beam-to-column connections: Component approach," J. Earthq. Eng., vol. 15, no. 4, 2011.
26. Rassati, G. A., Leon, R. T. and Noè, S., "Component Modeling of Partially Restrained Composite Joints under Cyclic and Dynamic Loading," J. Struct. Eng., vol. 130, no. 2, pp. 343–351, 2004.
27. Girão Coelho, A. M., Bijlaard, F. S. K., Simões da Silva, L., "Experimental assessment of the ductility of extended end plate connections," Eng. Struct., 2004.
28. Montuori R., Nastri E., Piluso V., Troisi M., "Influence of connection typology on seismic response of MR-Frames with and without 'set-backs'", Earthquake Engineering & Structural Dynamics, 2017.
29. Castro J. M., Elghazouli A. Y., Izzudin B. A., "Modelling of the panel zone in steel and composite moment frames", Engineering Structures. 2005;27:129-144.
30. Dubina D, Montreau N, Stratau A, Grecea D, Zaharia R., "Testing program to evaluate behavior of dual steel connections under monotonic and cyclic loading.", Paper presented at: Proceedings of the 5th European Conference on Steel and Composite Structures, 2008; Graz, Austria.
31. Francavilla, A.B., Latour, M., Piluso, V., Rizzano, G., "Bolted T-stubs: A refined model for flange and bolt fracture modes", Steel and Composite Structures, 20 (2), pp. 267-293, 2016.
32. Zoetemeijer, P., "A design method for the tension side of statically loaded bolted beam-to-column connections", Heron, Delft University, Vol. 20, n° 1, 1974.
33. Bezerra, L. M., Bonilla, J., Silva, W. A., Matias, W. T., Experimental and numerical studies of bolted T-stub steel connection with different flange thicknesses connected to a rigid base, Engineering Structures, Volume 218, 110770, ISSN 0141-0296, https://doi.org/10.1016/j.engstruct.2020.110770, 2020.
34. Bravo, M. A., Herrera, R. A., Performance under cyclic load of built-up T-stubs for Double T moment connections, Journal of Constructional Steel Research, Volume 103, Pages 117-130, ISSN 0143-974X, https://doi.org/10.1016/j.jcsr.2014.08.005, 2014.
35. Wang, P., Sun, L., Xia, C., Gu, H., Liu, Y., Liu, M., Liu, F., Cyclic behavior of T-stub connection to hollow section steel column using TSOBs, Journal of Constructional Steel Research, Volume 185, 106874, ISSN 0143-974X, https://doi.org/10.1016/j.jcsr.2021.106874., 2021.
36. Wang, M., Dong, K., Liu, M., Damage control mechanism and seismic performance of a steel moment connection with replaceable low-yield-point steel double T-stub fuses, Thin-Walled Structures, Volume 157, 107143, ISSN 0263-8231, https://doi.org/10.1016/j.tws.2020.107143, 2020.
37. Irvani, M., Ezati, H., Khafajeh, R., Kalat Jaari, V. R., Numerically study on the seismic response of partially restrained moment connection with structural fuse T-stub for European sections, Structures, Volume 35, Pages 82-105, ISSN 2352-0124, https://doi.org/10.1016/j.istruc.2021.10.078, 2022.
38. Zhu, X., Wu, Z., Study on New Bolted T-Stub Connection with Inserted Plates under Axial and Cyclic Loads, Appl. Sci., 10, 2631. https://doi.org/10.3390/app10072631, 2020.

39. Bayat, K., Shekastehband, B., Seismic performance of beam to column connections with T-shaped slit dampers, Thin-Walled Structures, Volume 141, Pages 28-46, ISSN 0263-8231, https://doi.org/10.1016/j.tws.2019.04.010, 2019.
40. Latour, M., Rizzano, G., Latour, M., Rizzano, G., Utimate Behaviour of Dissipative Tstub Connections, STESSA Conference, 2009.
41. Latour, M., Rizzano, G., Experimental Analysis and Design of X-Shaped T-stub Joints, 2011.
42. Latour, M., Rizzano, G., Design of X-shaped double split tee joints accounting for moment–shear interaction, Journal of Constructional Steel Research. 104. 10.1016/j.jcsr.2014.10.015, 2015.
43. Pall, A. S.; Marsh, C.; Fazio P., *Limited Slip Bolted Joints for Large Panel Structures*, Proceedings, Symposium on Behavior of Building Systems and Building Components, Nashville, USA, 1979.
44. Marsh, C.; Pall, A. S., *Friction Devices to Control Seismic Response*, Proceedings Second ASCF/EMD Specialty Conference on Dynamic Response of Structures, Atlanta, U.S.A., January, pp. 809-818, 1981.
45. Pall, A. C.; Marsh, C., *Response of Friction Damped Braced Frames*, Journal of Structural Division, ASCE, Vol. 108, No. ST6, June, pp. 1313-1323, 1982.
46. Grigorian, C. E., and Popov, E. P., *Energy dissipation with slotted bolted connections*, Berkley, California, Earthquake Engineering Research Centre, 1994.
47. Butterworth, J. W.; Clifton, G. C., *Performance of Hierarchical Friction Dissipating Joints in Moment Resisting Steel Frames*, 12 World Conference on Earthquake Engineering, Paper N. 718, 2000.
48. MacRae, G. A.; Clifton, G. C., *New Technology Applications, Recent Developments and Research Directions for Seismic Steel Structures in New Zeland*, Asian Conference on Earthquake Engineering, Bangkok, Thailand, December 2010.
49. MacRae, G. A.; Clifton, G. C., *Low Damage Design of Steel Structures*, Steel Innovations, Workshop, Christchurch, 21-22 February 2013.
50. Latour, M.; Piluso V.; Rizzano G., *Free from damage beam-to-column joints: Testing and design of DST connections with friction pads*, Engineering Structures. 85:219-233, 2015.
51. Piluso, V., *Smart Connections for Seismic-Resistant Frames: a Brief Overview*, Costruzioni Metalliche, Vol. 3, 2018.
52. Latour, M., D'Aniello, M., Zimbru, M., Rizzano, G., Piluso, V., Landolfo, R., *Removable friction dampers for low-damage steel beam-to-column joints*, Soil Dynamics and Earthquake Engineering, 115, pp. 66-81, 2018.
53. Latour, M.; Rizzano, G., Santiago, A.; Simões da Silva, L., *Experimental response of a low-yielding, self-centering, rocking column base joint with friction dampers*, Soil Dynamics and Earthquake Engineering, 116, pp. 580-592, 2019.
54. Nastri, E.; D'Aniello, M.; Zimbru, M.; Streppone, S.; Landolfo, R.; Montuori, R.; Piluso, V., *Seismic response of steel Moment Resisting Frames equipped with friction beam-to-column joints*, Soil Dynamics and Earthquake Engineering. 119. 144-157. 10.1016/j.soildyn., 2019.
55. Greene, T. Strength of steel tubing under combined column and transverse loading, including tests of columns and beams. In Technologic Papers of the Bureau of Standards; National Bureau of Standards: Washington, DC, USA, 1924.

56. Bouwkamp, J. Buckling and Post-Buckling Strength of Circular Tubular Sections. In Proceedings of the Offshore Technology Conference, Houston, TX, USA, 5–8 May 1975; pp. 583–592.
57. Marzullo, M.A.; Ostapenko, A. Tests on Two High-Strength Short Tubular Columns; Laboratory Report No. 406.10; Fritz Engineering Laboratory, Lehigh University: Bethlehem, PA, USA, 1977.
58. Chen, W.F.; Ross, D.A. Test of fabricated tubular columns. J. Struct. Div. 1977, 103, 619–614.
59. Elchalakani, M.; Zhao, X.-L.; Grzebieta, R. Tests on concrete filled double-skin (CHS outer and SHS inner) composite short columns under axial compression. Thin Walled Struct. 2002, 40, 415–441, doi:10.1016/s0263-8231(02)00009-5.
60. Ma, J.-L.; Chan, T.-M.; Young, B. Experimental Investigation on Stub-Column Behavior of Cold-Formed High-Strength Steel Tubular Sections. J. Struct. Eng. 2016, 142, 04015174, doi:10.1061/(asce)st.1943-541x.0001456.
61. Xiong, M.-X.; Xiong, D.-X.; Liew, J.R. Axial performance of short concrete filled steel tubes with high- and ultra-high- strength materials. Eng. Struct. 2017, 136, 494–510, doi:10.1016/j.engstruct.2017.01.037.
62. Meng, X.; Gardner, L. Cross-sectional behaviour of cold-formed high strength steel CHS under combined axial compression and bending. In Proceedings of the 8th International Conference on Thin-Walled Structures, Lisbon, Portugal, 24–27 July 2018.
63. Meng, X.; Gardner, L.; Sadowski, A.J.; Rotter, J.M. Elasto-plastic behaviour and design of semi-compact circular hollow sections. Thin Walled Struct. 2020, 148, 106486, doi:10.1016/j.tws.2019.106486.
64. Korol, R.M.; Hudoba, J. Plastic behavior of hollow structural sections. J. Struct. Div. 1972, 98, 1007–1023.
65. Wilhoit, J.C., Jr.; Merwin, J.E. Critical Plastic Buckling Parameter for Tubing in Bending under Axial Tension. In Proceedings of the Offshore Technology Conference, Houston, TX, USA, 29 April–2 May.
66. Sherman, D.R. Test of circular steel tubes in bending. J. Struct. Div. 1976, 102, 2181–2195.
67. Prion, H.G.L.; Birkemoe, P.C. Beam?Column Behavior of Fabricated Steel Tubular Members. J. Struct. Eng. 1992, 118, 1213–1232, doi:10.1061/(asce)0733-9445(1992)118:5(1213).
68. O'Shea, M.D.; Bridge, R.Q. Local buckling of thin-walled circular steel sections with or without internal restraint. J. Constr. Steel Res. 1997, 41, 137–157, doi:10.1016/s0143-974x(97)80891-7.
69. Pan, H.M. Research on Ultimate Bearing Capacity of Large-Sized Thin-Walled Steel Tubes. Ph.D. Thesis, Tongji University, Shanghai, China, 2004.
70. Nseir, J. Development of a New Design Method for the Cross-Section Capacity of Steel Hollow Sections. Ph.D. Thesis, University of Liège, Liège, Belgium, 2015.
71. Ma, J. Behaviour and Design of Cold-Formed High Strength Steel Tubular Members; The University of Hong Kong Libraries: Pok Fu Lam, Hong Kong, 2017.
72. Pournara, A.E.; Karamanos, S.A.; Mecozzi, E.; Lucci, A. Structural resistance of high-strength steel CHS members. J. Constr. Steel Res. 2017, 128, 152–165, doi:10.1016/j.jcsr.2016.08.003.
73. Di Benedetto, S.; Latour, M.; Rizzano, G. Chord failure resistance of 3D cut welded connections with CHS columns and through I-BEAMS. Thin Walled Struct. 2020, 154, 106821, doi:10.1016/j.tws.2020.106821.

74. Di Benedetto, S.; Latour, M.; Rizzano, G. Assessment of the stiffness of 3D cut welded connections with CHS columns and through I-BEAMS. Structures 2020, 27, 247–258, doi:10.1016/j.istruc.2020.05.043.
75. Voth, A.; Packer, J.A. Branch Plate-to-Circular Hollow Structural Section Connections. I: Experimental Investigation and Finite-Element Modeling. J. Struct. Eng. 2012, 138, 995-1006.
76. Voth, A. Branch Plate-to-Circular Hollow Structural Section Connections. Ph.D. Thesis, TSpace, University of Toronto, ON, Canada, 2010.
77. Kanyilmaz, A.; Castiglioni, C.A.; Brambilla, G.; Gjoka, K.; Galazzi, A.; Raso, S.; Valli, A.; Brugnolli, M.; Hojda, R. 03.33: Experimental assessment of tolerances for the fabrication of laser-cut steel joints. ce/papers 2017, 1, 776–785, doi:10.1002/cepa.117.
78. Kanyilmaz, A. The problematic nature of steel hollow section joint fabrication, and a remedy using laser cutting technology: A review of research, applications, opportunities. Eng. Struct. 2019, 183, 1027–1048, doi:10.1016/j.engstruct.2018.12.080.
79. Magonette, Georges & Pegon, Pierre & Buchet, Philippe, “Advanced Testing Techniques at the ELSA-JRC Reaction Wall”, 1998.
80. Molina, F. J., Buchet, Ph., Magonette, G. E., Negro, P., “Bidirectional pseudodynamic techinique for testing a three-storey reinforced concrete building”, Proc. Of 13th World Conference on Earthquake Engineering, Vancouver, Paper N., 75, 2004.
81. Tsai, K., Weng, Y., Lin S. L., “Pseudo-dynamic test of a full-scale CFT/BRB frame”, 13th World Conference on Earthquake Engineering, Vancouver, August 1-6, 2004, Paper No. 750.
82. SeismoSoft (2016). “SeismoStruct 2016 – A computer program for static and dynamic analysis of framed structures”.
83. McKenna, F., *OpenSees: A Framework for Earthquake Engineering Simulation*, Computing in Science and Engineering 13, 58-66, 2011.
84. Abaqus, *Analysis user’s manual version 6.17*, Abaqus Inc., 2017.

CHAPTER 2 – Innovative beam-to-column connections

This chapter discusses the flexural behaviour of two beam-to-column connections: the Reduced Beam Section (RBS) joint and the Circular-Hollow-Section (CHS) to through-all I-beam connection. These joints represent innovative nodal configurations which have been conceived in different periods: the RBS strategy after the seismic event of Northridge (1994), while the second configuration only in the last decade since its manufacturing requires the exploitation of the 3D Laser-Cutting-Technology (3D-LCT), which is quite a novelty in the field of Civil Engineering.

2.1 The component method approach

Steel structures are more prone than concrete buildings to be affected by the behaviour of their connections. This relevant role is justified by the several efforts devoted to their stiffness and strength characterization within the framework of the component method approach [1-5]. This strategy consists in modelling the monotonic moment-rotation law of connections starting from the characterization of individual joint components in terms of stiffness and resistance. This approach has mainly been exploited to investigate connections between double-tee section profiles, assessing the response of partial-strength and/or semi-rigid connections, often referred to as semi-continuous joints. In particular, different joint components have been experimentally, numerically and analytically investigated. For instance, to model welded and bolted joints, many works focused on the study of the panel zone [6-8], the end-plates [6, 7, 9] and the T-stubs [10-12]. After these studies, in 1992, the component method was first reported in the ENV (European Norm Voluntary) version of EC3 (into annex J) [13] and, subsequently, in 2005 in Eurocode 3 part 1.8 [14].

Moreover, the Eurocode 3 provides many design formulations to assess the strength and stiffness of the following components: column web panel in shear; column web panel in transverse tension; column web in transverse compression; column flange in bending; end-plate in bending; flange cleat in bending; beam flange and web in compression; beam web in tension; bolts in shear; bolts in tension; plates in bearing; welds; haunched beam.

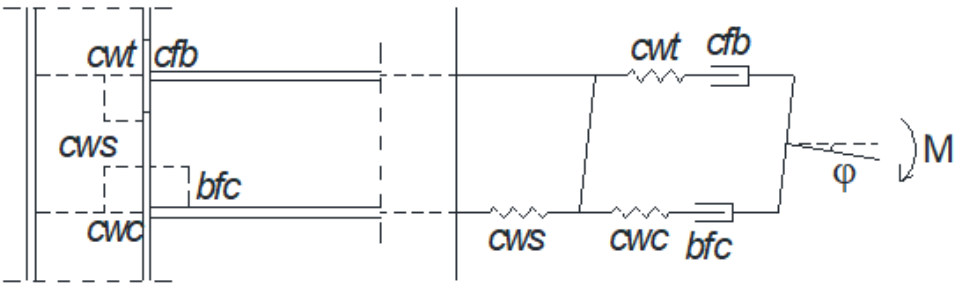

Figure 2.1 – Components belonging to the connection

For instance, in Figure 2.1 the main components of a welded connection with double-tee profiles as beam and column are reported:

1. the column web in shear (*cws*);
2. the column web in compression (*cwc*);
3. the column web in tension (*cwt*);
4. the column flange in bending (*cfb*);

5. the web and the flange of the beam in compression (*bfc*).

In particular, the column web in shear, compression and tension represent elements that directly affect the rotational stiffness and strength. Instead, the column flange in bending and the web and the flange of the beam in compression can affect only the flexural strength of the joint. Since the component method approach requires defining a force-displacement law for each joint component, an elastic-plastic relationship is assumed for *cws*, *cwc*, *cwt*, while a rigid-plastic behaviour is assigned *cfb* and *bfc* (Figure 2.2).

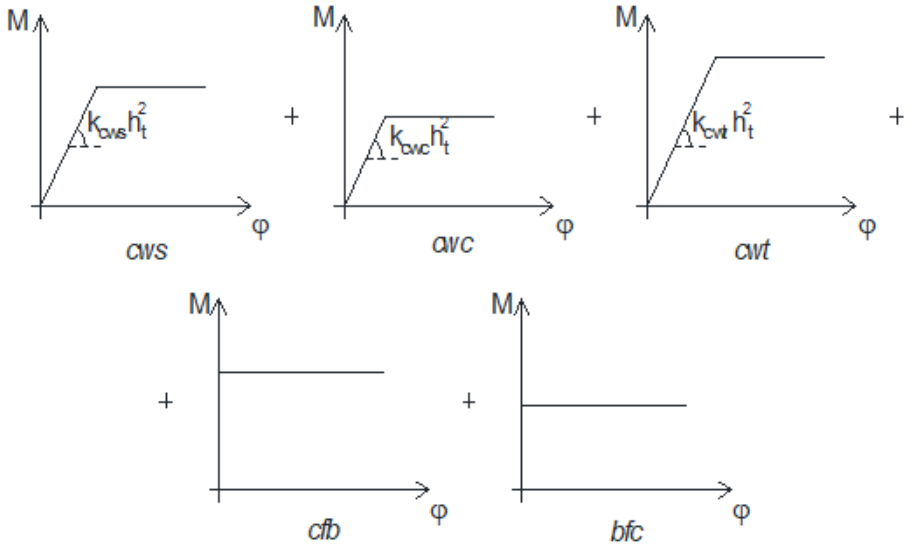

Figure 2.2 – Constitutive laws of the connections

According to the above schematization, the rotational stiffness of the connection is assessed as $k_\varphi = E\frac{h_t^2}{\frac{1}{k_{cws}}+\frac{1}{k_{cwc}}+\frac{1}{k_{cwt}}}$, where E is the modulus of elasticity, h_t is the distance between the flanges of the beam, while k_{cws}, k_{cwc} and k_{cwt} represent, respectively, the stiffness of the components *cws*, *cwc* and *cwt*. Instead, the flexural strength of the joint is related to the weakest among the abovementioned components:

$$M_{j,Rd} = min\{F_{cws}; F_{cwc}; F_{cwt}; F_{cfb}; F_{bfc}\} \cdot h_t \qquad (2.1)$$

The Eurocode [14] provides detailed formulations for the above application and more complex cases (e.g. bolted connections with end-plates or angle flange cleats …).

2.2 Full-strength joints

The strong-column strong-connection weak-beam philosophy is the most common and exploited design approach. It ensures the plasticization of the beam ends that can provide sufficient ductility to have also wide and stable hysteresis loops.

According to the first principle of capacity design, the dissipative element (the beam) is appropriately designed with the maximum design actions. Instead, the yielding of the column and the connection are prevented by applying the second principle of the capacity design, which requires the design of the non-dissipative elements with the actions that the yielded and hardened dissipative components are able to transmit. In particular, Eurocode 8 [15] requires that the joint design resistance ($M_{j,Rd}$) should be higher than the plastic moment of the connected beam ($M_{b,Rd}$)

amplified by the coefficient 1.1 to account for the effects of the material strain-hardening, and the overstrength coefficient γ_{ov} to consider the random variability of the steel yield strength:

$$M_{j,Rd} > 1.1 \cdot \gamma_{ov} \cdot M_{b,Rd} \quad (2.2)$$

This design approach should avoid damage to structural elements not conceived to dissipate the seismic input energy. Nevertheless, in some cases, the adopted design criteria cannot require the needed overstrength to fully exploit the plastic rotation capacity of the beam. For example, such an occurrence happened during the seismic events of Kobe and Northridge and caused the brittle collapse of many welded beam-to-column connections. In fact, the beam overstrength depends on the slenderness of its flanges which can affect the behavioural class of the beam section (i.e. ductile, compact, semi-compact and slender).

2.3 Reduced-Beam-Section connection (RBS)

Two strategies can be followed to avoid the brittle collapse in the connection or the column: the first one is based on strengthening these non-dissipative parts; the second one is based on the weakening of the beam end. This last approach is known as Reduced Beam Section (RBS) or dog-bone [16-21], and it fosters the damage by cutting the beam flanges in well-defined regions located sufficiently far from the columns to reduce the stresses in the welds.

This connection typology has been widely studied, and its design rules are also part of the AISC provisions [21]. Moreover, the rising interest in the cyclic behaviour of traditional and innovative joints led, in the past years, the researchers of the University of Salerno to investigate the response of RBS connections. Nevertheless, it is worth underlining that the RBS connections investigated are different from those prequalified according to AISC provisions [21]. In fact, in the prequalified RBS connections, the trimming of the beam flanges according to the classical dog-bone shape is essentially conceived as a strategy to prevent the brittle failure of the welds between the beam and column flanges. Therefore, AISC prequalified RBS connection is a welded connection. Conversely, the RBS connections analysed at the University of Salerno are extended end-plate connections whose possible low ductility failure modes are prevented by adopting the RBS strategy. However, the design rules applied for dimensioning the RBSs are the same suggested by AISC because the influence of the moment gradient along the beam length is not affected by the typology of the elements used for connecting the beam flanges to the column flange.

Experimental, numerical and analytical activities have characterized this study.

2.3.1 Experimental activity

The experimental activity performed a cyclic test on a beam-to-column sub-assembly at the STRENGTH Laboratory of the University of Salerno according to the set-up reported in Figure 2.3 and Figure 2.4.

Figure 2.3 – Specimen before the test (Latour Thesis [22])

In particular, the specimen is characterized by a HEB200 column profile and an IPE270 beam with lengths equal, respectively, to 2.00 m and 1.56 m.
The proposed configuration has been conceived to be representative of the behaviour of a connection belonging to a realistic frame (Figure 2.5). However, to ensure compatibility with laboratory equipment, the proposed configuration has been rotated 90° (Figure 2.4). In this way, two horizontal actuators have been bolted to the column and beam ends to apply the axial load in the column and the displacement history to the top end of the cantilever beam. The column ends are constrained with a hinge and a roller bolted to the laboratory's rigid steel base. This basement is anchored to the strong laboratory floor through high strength dywidag bars. Instead, the actuators are connected to a rigid steel reaction wall constituted by a steel braced frame. Furthermore, the lateral-torsional buckling of the beam is prevented through the adoption of a horizontal frame.

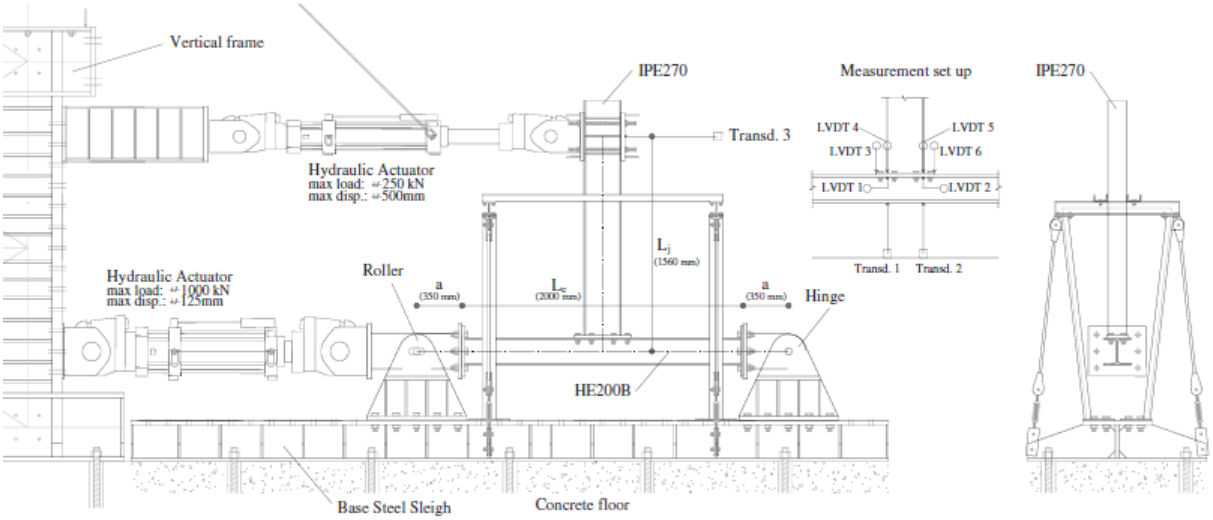

Figure 2.4 – Experimental test set-up

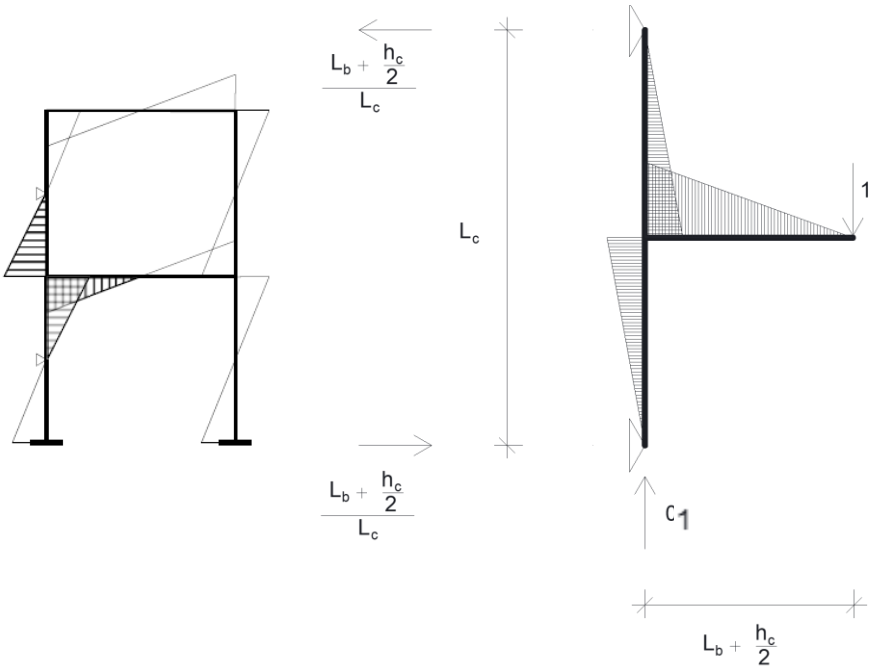

Figure 2.5 – Reference scheme

Two MTS243 hydraulic actuators have been used. In particular, the actuator connected to the column has a load capacity of ± 1000 kN, and it was set in force control to impose a constant axial compression load equal to 650 kN, which corresponds to 30% of the column squash load. Instead, the actuator connected to the beam end has a load capacity of ± 250 kN and a piston stroke equal to ± 500 mm, and it applied a displacement history complying with AISC provisions [23] to ensure a drift angle history reported in Figure 2.6.

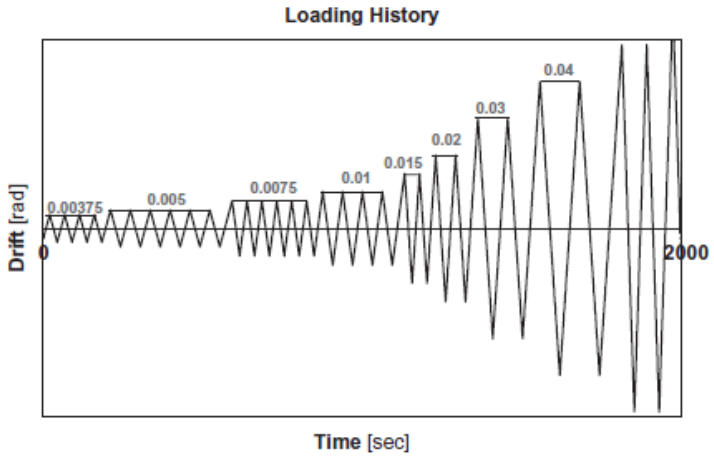

Figure 2.6 – Loading history

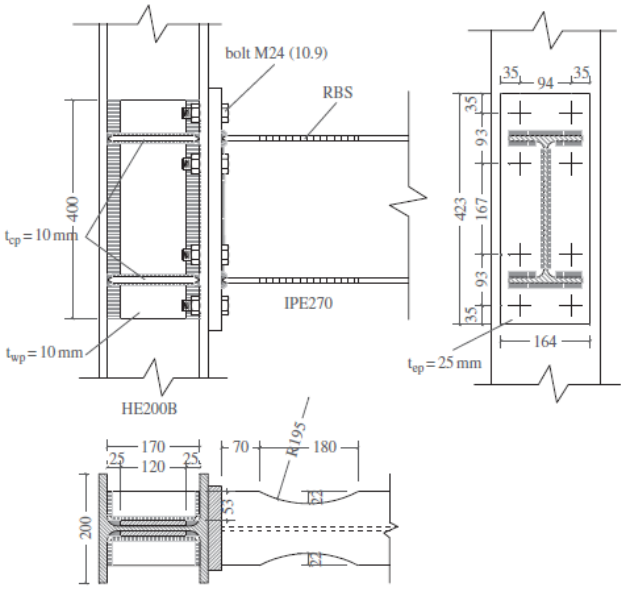

Figure 2.7 – Geometry of the RBS connection

The geometry of the RBS is shown in Figure 2.7; it is possible to observe that the centre of the reduced section is 160 mm far from the end-plate, and the maximum reduction of the beam flanges is equal to 44 mm. The end-plate has a thickness equal to 25 mm, and it is bolted to the column flange through M24 class 10.9 bolts. Additional stiffness and continuity plates have been used to prevent the yielding of the panel zone.

Many transducers, inclinometers and strain-gauges have been used to monitor the specimen's response, as shown in Figure 2.8, Figure 2.9 and Figure 2.10. In particular, these devices have been employed to assess the engagement in the plastic range of the analysed connection. The LVDTs allow monitoring of the local deformations at the top and bottom ends of the end-plate and the flanges to end-plate attachments. In addition, two inclinometers have been applied: one on the web flange of the beam in correspondence with the reduced section of the flanges; the second in the centre of the column web panel.

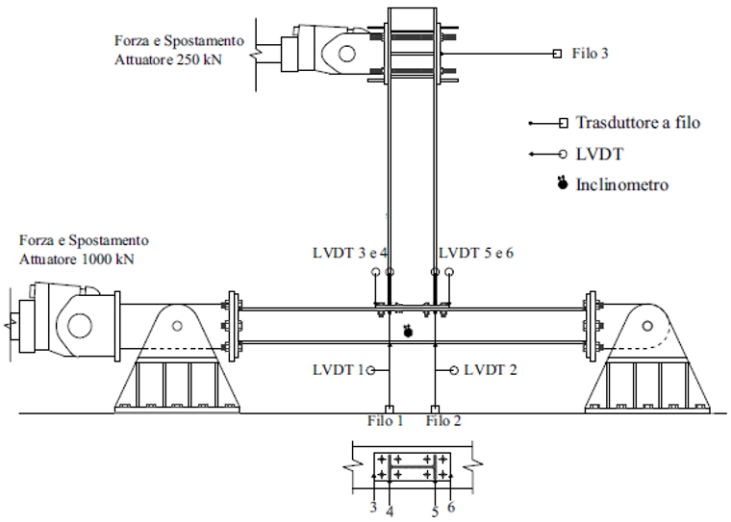

Figure 2.8 – Layout of the instruments

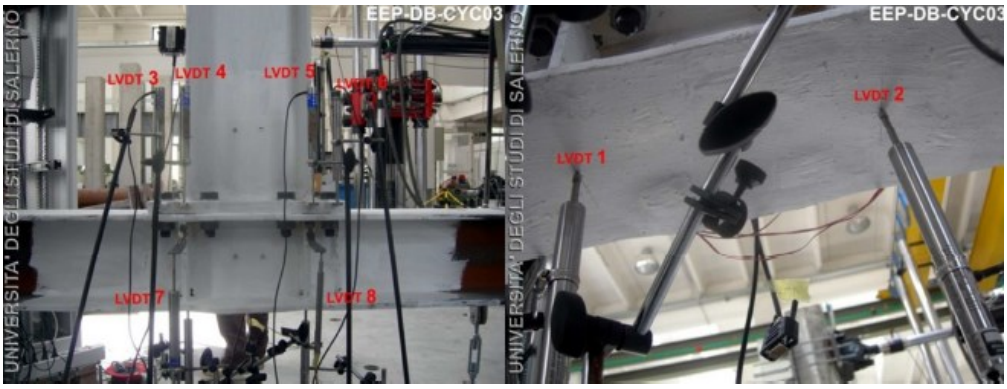

Figure 2.9 – Transducers (Latour Thesis [22])

In Figure 2.10, it is shown that a strain-gauges has been applied at the centres of the RBS, which are the zones where plasticization is expected. It is well-known that strain-gauges can measure only elastic strains; however, this choice has been adopted to assess the strains arising in the reduced sections until their plasticization occurs. In fact, when the yielding limit was achieved, the results provided by the strain-gauges were no longer acceptable.

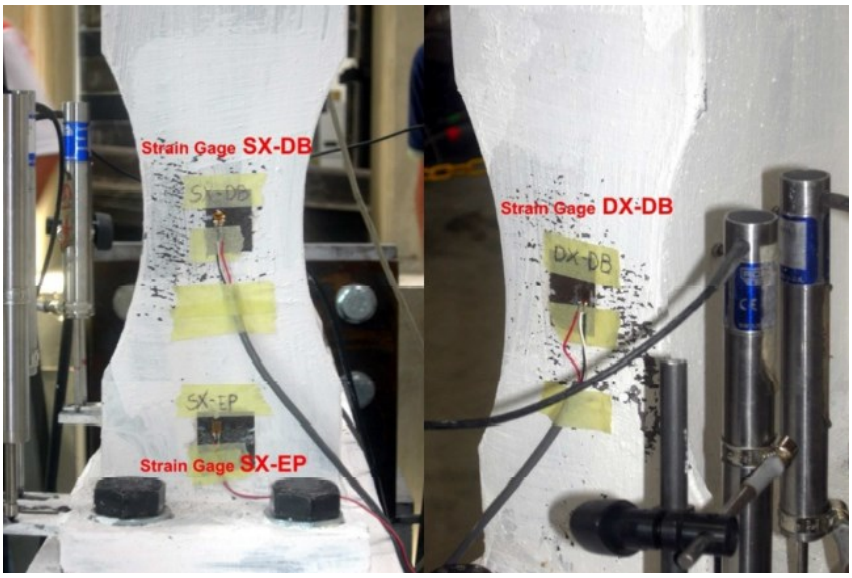

Figure 2.10 – Strain-gauges (Latour Thesis [22])

The applied displacement and the reaction forces have been recorded through the LVDT and the load cell of the actuator connected to the beam end. These parameters have been used to assess the moment-rotation hysteretic curve of the analysed connection. However, since the aim of the work consisted in assessing the behaviour of the connection alone, the recorded displacements were adequately corrected by subtracting the elastic part due to the beam and column flexural deformability according to the following formulation:

$$\delta_j = \delta_{actuator} - \frac{FL_b^3}{3EI_b} - \frac{FL_cL_b^2}{12EI_c}\left[\left(\frac{L_c}{L_c+2a}\right)^2 + \frac{6a}{L_c+2a}\right] \quad (2.3)$$

In the previous formulation $\delta_{actuator}$ is the displacement applied by the actuator, F is the corresponding reaction force, E is the modulus of elasticity, L_c and L_b are the lengths of the column

and the beam, I_c and I_b represent the inertia of the column and the beam, a is the length of the rigid parts due to the steel hinges.
Starting from the knowledge of δ_j and F, the moment and rotation have been calculated as:

$$\varphi_j = \frac{\delta_j}{L_j} \quad (2.4)$$

$$M_j = FL_j \quad (2.5)$$

In particular, L_j is the distance between the centre of the reduced section and the actuator connected to the beam end.
The RBS strategy is representative of a full-strength beam-to-column joint conceived to avoid the yielding of the components belonging to the connection but to foster the plasticization of the beam end. At the end of the cyclic test, the buckling of the flanges and the web was observed (Figure 2.11).

Figure 2.11 – Buckling of the flange and the web (Latour Thesis [22])

In Figure 2.12, the moment-rotation curve of the tested RBS is reported. The cycles are wide and stable ensuring high energy dissipation capacity and significant plastic rotation supply.

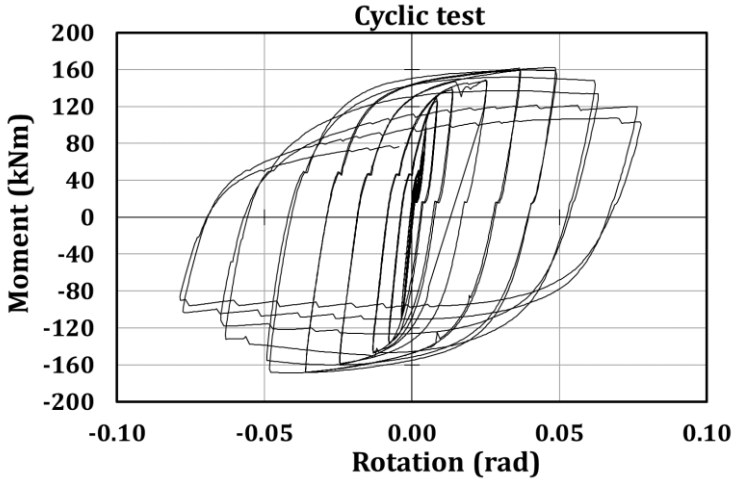

Figure 2.12 – Moment-rotation hysteretic curve of the connection

2.3.2 Numerical activity

The tested beam-to-column sub-assembly was numerically modelled using Abaqus's Finite Element (FE) software [24]. The aim was to validate the numerical model against the experimental results to provide guidelines for modelling RBS connections with different geometric properties. The specimens' geometries have been defined by extruding the cross-sections along the longitudinal direction (Figure 2.13, Figure 2.14 and Figure 2.15).

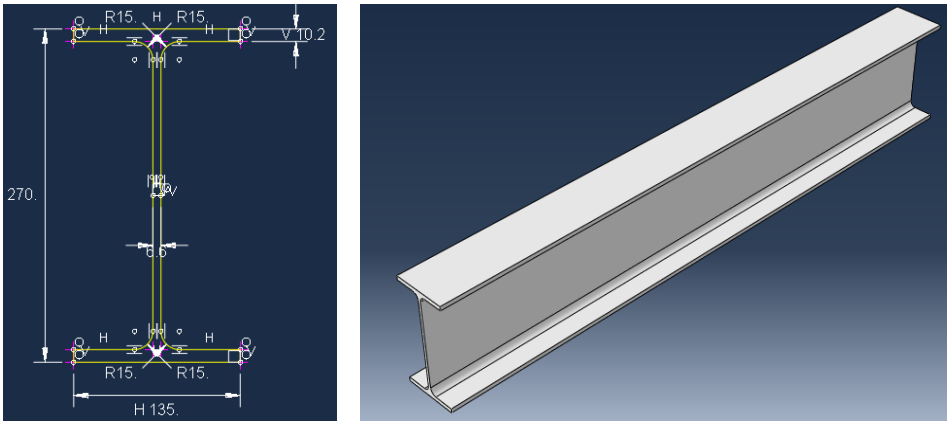

Figure 2.13 – Beam element

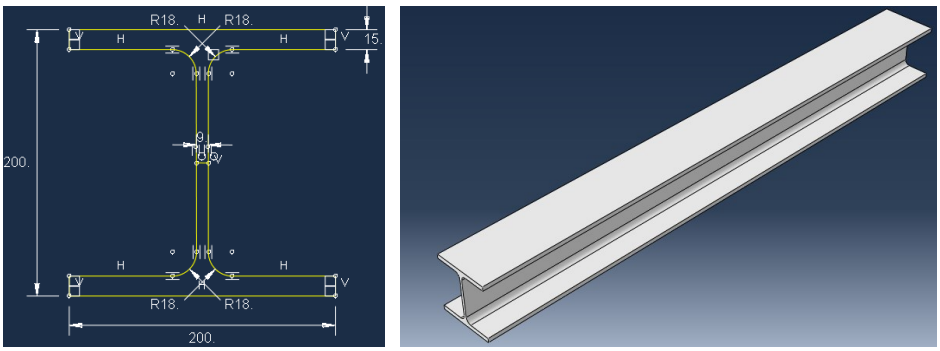

Figure 2.14 – Column element

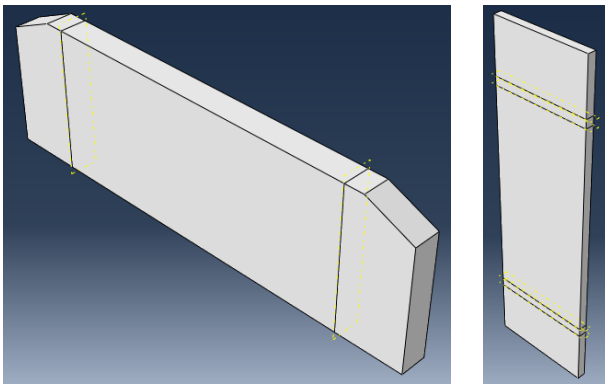

Figure 2.15 – Continuity and stiffening plates

Thanks to the cut-extrusion command, the reduced section has been created at the beam end (Figure 2.16). Furthermore, the bolt holes have been generated on the column flanges and the end-plate (Figure 2.17).

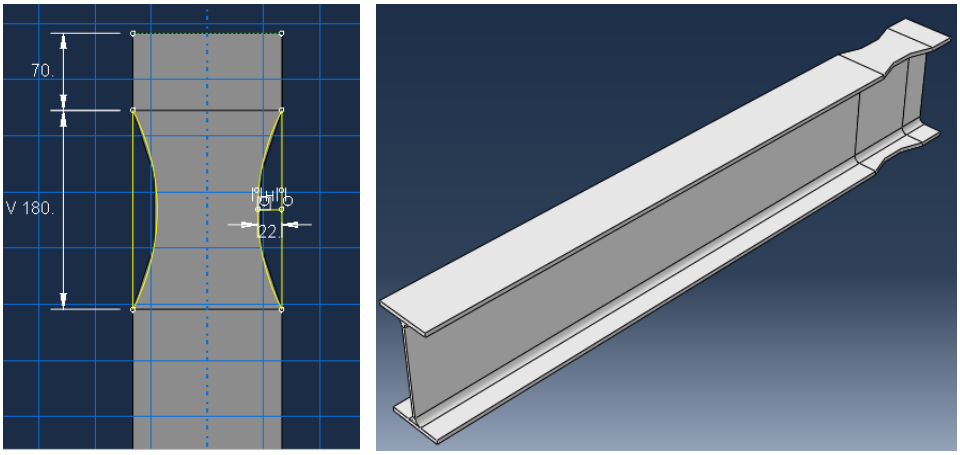

Figure 2.16 – Cutting of the beam flanges

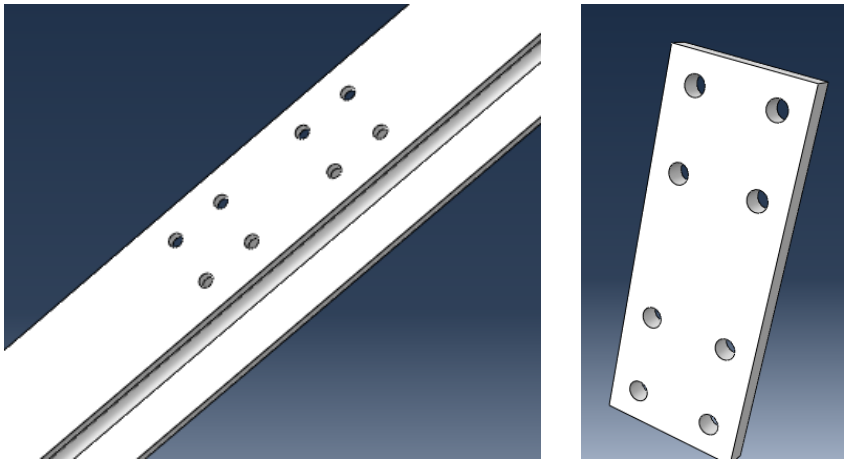

Figure 2.17 – Creation of the bolt holes in the column (left) and the end-plate (right)

Finally, the bolt was created through a 360° revolution of its half section (Figure 2.18).

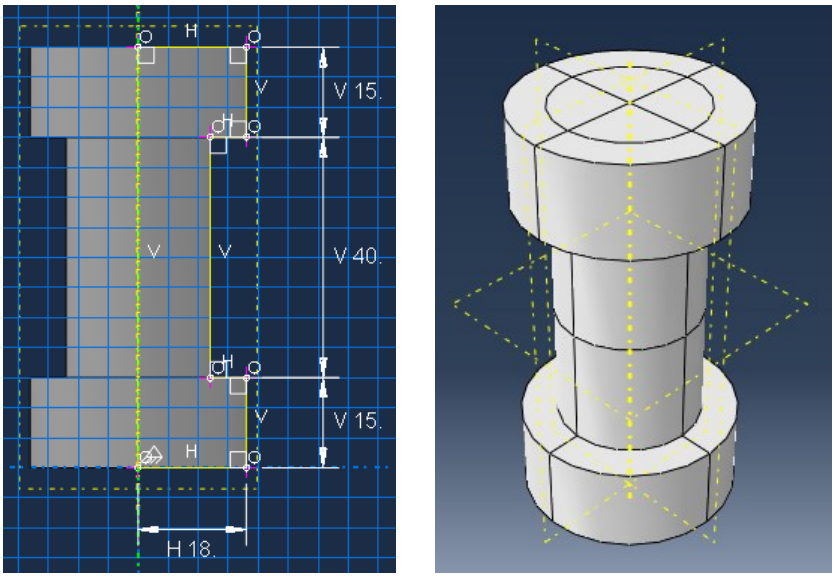

Figure 2.18 – Creation of the bolt

All the elements have been adequately partitioned to assure the correct contact between all the members.

The material properties of the beam, the column and the plates comply with the quadrilinear true stress-true strain law proposed by Faella et al. [6] (Figure 2.19), assuming the S355 steel grade for all the elements except for the beam, which is characterized by S275 steel grade. Instead, a trilinear model (Figure 2.19) has been applied to the bolts. This law depends on the yield and ultimate nominal strength of the bolt class, and the strain corresponding to the ultimate resistance and the ultimate strain have been evaluated through the formulations $\varepsilon_m = A_r[\%]$ and $\varepsilon_m = \ln\left(\frac{1}{1-Z}\right)$, where A_r is the elongation at fracture, Z is the necking ratio given by the ratio between the original cross-sectional area and the minimum cross-sectional area after fractures.

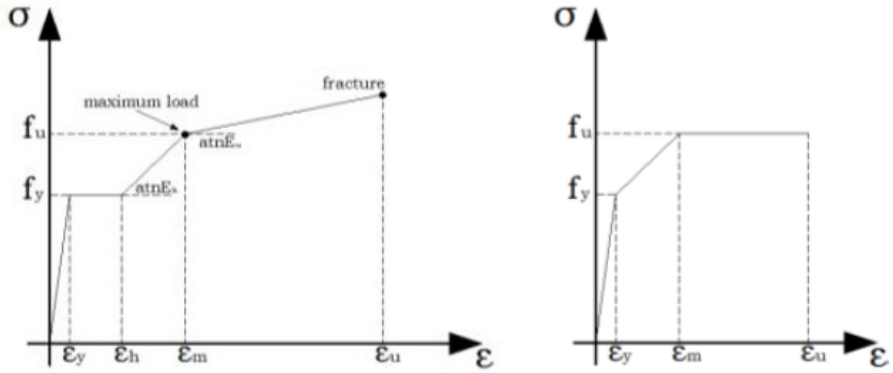

Figure 2.19 – Material constitutive laws for plates and profiles (left) and bolts (right)

In particular, for the S275 material applied to the beam, a combined cyclic hardening strategy has been adopted with the input parameters reported in Table 2.1.

Table 2.1 – Parameters for the combined hardening of steel adopted for the beam

Yield stress at zero plastic strain	Kinematic Hard parameter C1	Gamma 1	Kinematic Hard parameter C2	Gamma 2
324.09	17707	207.18	1526.2	6.22

Equivalent stress	Q-infinity	Hardening parameter b
324.09	228.2	0.11

The model has been assembled defining the interactions among the elements through surface-to-surface contacts. In particular, the interactions have been defined between: the end-plate and the column flange; the bolt head and the end-plate; the bolt shank and the plate hole; the bolt shank and the column flange hole; the end-plate and the beam end. The "hard contact" has been applied in the normal direction, while a friction coefficient equal to 0.2 has been used for the tangential direction.

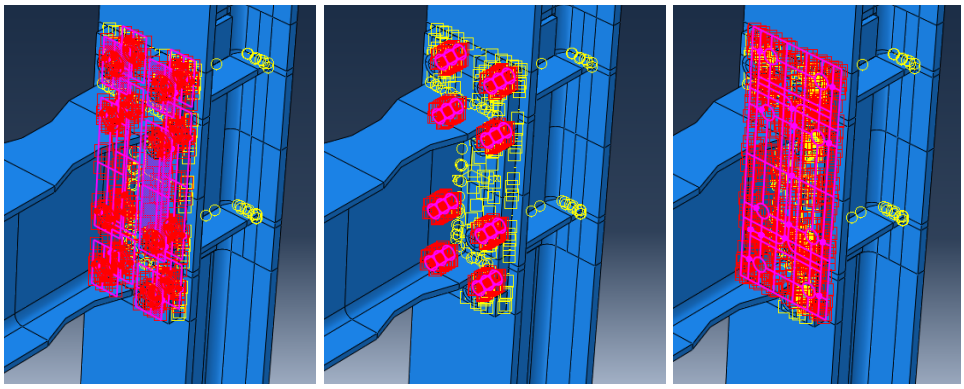

Figure 2.20 – Definition of the contacts: end-plate/column flange (left); bolt head/end-plate (centre); end-plate/beam end (right)

It is worth highlighting that the welds have not been explicitly modelled, but they are taken into account through "Tie" constraints defined along the contact surfaces.

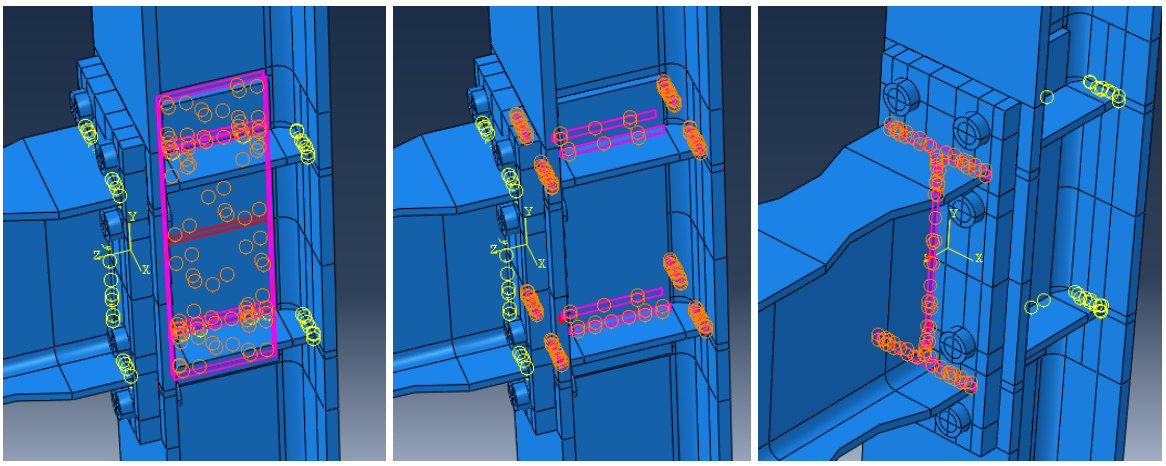

Figure 2.21 – Definition of the Tie constraints

The hinge and the roller are modelled using external reference points that are rigidly connected to the ends of the column through the coupling tool and properly constrained by suppressing the corresponding degrees of freedom (Figure 2.22).

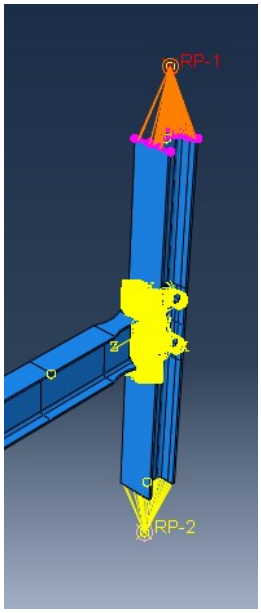

Figure 2.22 – Coupling constraints

The beam has been laterally restrained, 1380 mm far from the column face, to model the effect of the out-of-plane restraint. In order to validate the model against the experimental results, the FE simulation has been performed under cyclic loading conditions applying the same displacement histories employed to the specimen (Figure 2.23).

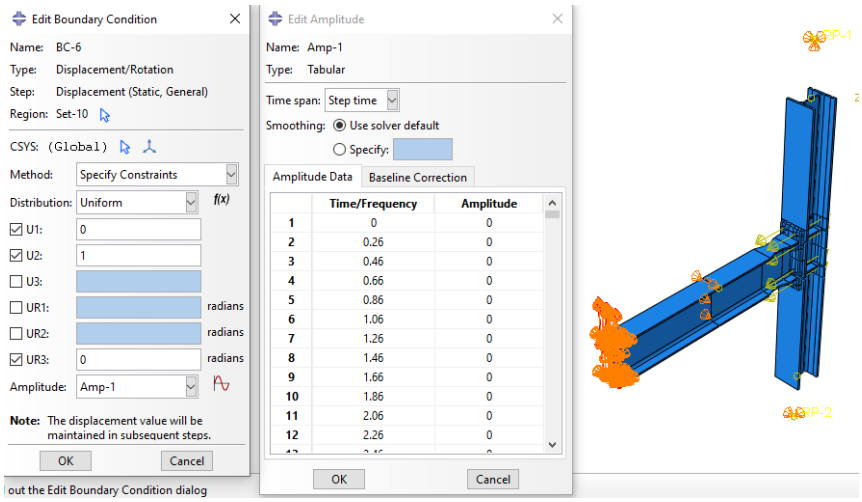

Figure 2.23 – Loading

The parts have been meshed adopting C3D8-type (8-node linear brick) elements. At least two elements have been adopted in the thickness of the flanges of the double-tee profiles. The mesh elements have a size of about 10 mm in the connection area and 50 mm in the remaining parts of the model (Figure 2.24).

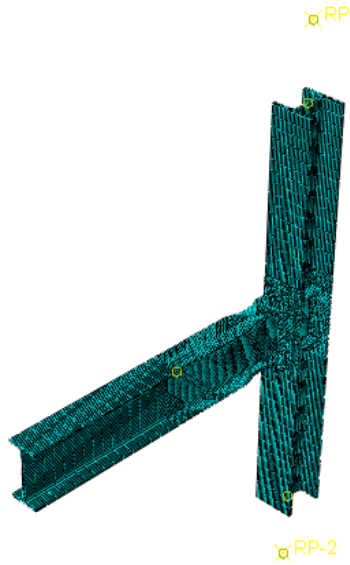

Figure 2.24 – Mesh of the FE model

Imperfections have been included in the model considering the construction tolerances provided by EN10034 [25], adopting the modelling approach proposed by the Eurocode 3 part 1.5 [26]. Therefore, linear buckling analyses were initially performed to identify the relevant buckling modes. Subsequently, the initial geometry has been distorted according to the selected buckling shapes, considering the corresponding values of the associated initial imperfections (2% of the flange width for the bow twist of the flanges of the beam). The imperfections have been implemented considering 80% of the maximum fabrication tolerance, as suggested by Eurocode 3 part 1.5 [26].
The relevant buckling modes are reported in Figure 2.25.

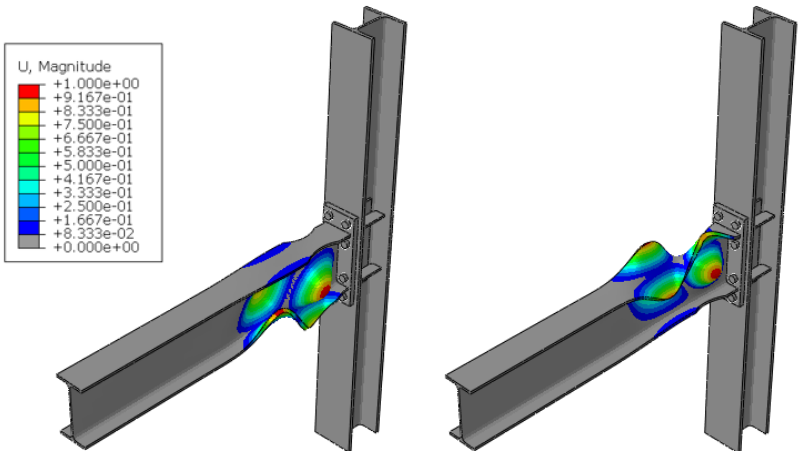

Figure 2.25 – First (left) and second (right) buckling modes

The applied imperfections have been assessed with the following formulations:

$$k^{n-th\ mode} = \frac{0.8 \cdot 0.02 \cdot b_f}{2 \cdot \delta_f} \qquad (2.6)$$

$$k^{1st\ and\ 2nd\ mode} = \frac{0.8 \cdot 0.02 \cdot 135}{2} = 1.08\ mm \qquad (2.7)$$

In particular, b_f is the width of the beam flange and δ_f is the sum of the beam flange top displacements in the buckled configuration.

The developed numerical model has been subjected to the same loading history experienced by the tested specimen.

Since the analysed joint belongs to the full-strength beam-to-column connections, it is expected to develop plastic deformations only in the weakened section, while all the other nodal components show an elastic behaviour.

The expectations have been fulfilled, as shown in Figure 2.26, where the Von Mises stresses are reported.

The FE model has shown the concentration of plastic deformations in the reduced section (Figure 2.27, Figure 2.28 and Figure 2.29), resulting in buckling phenomena in the web and the flange in compression.

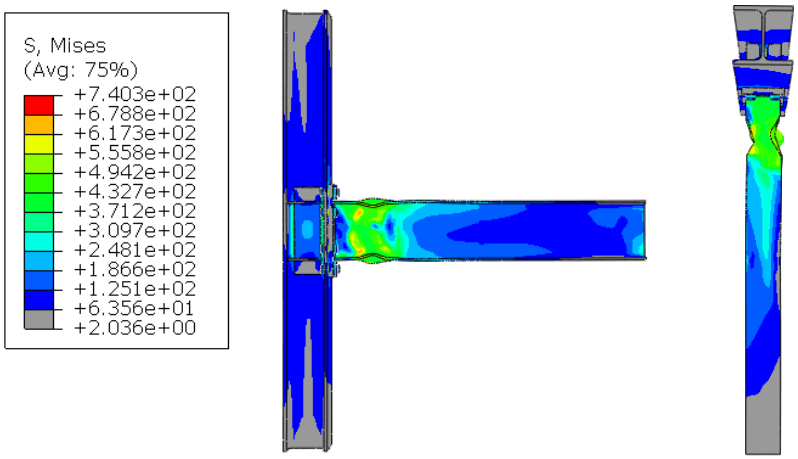

Figure 2.26 – Von Mises stresses at the end of the test

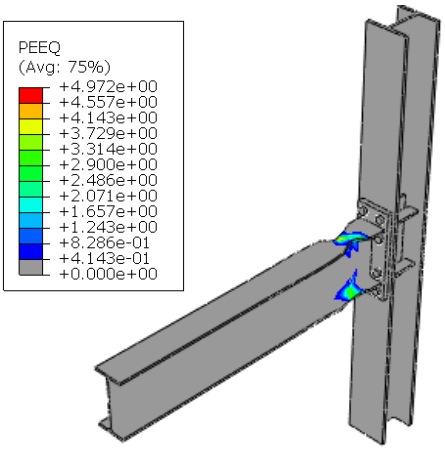

Figure 2.27 – Plastic deformations at the end of the test

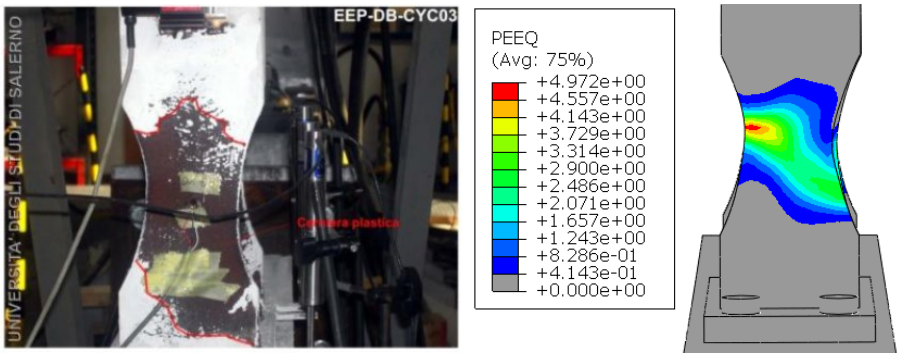

Figure 2.28 – Deformed configuration of the RBS at the end of the experimental test (left) and numerical simulation (right)

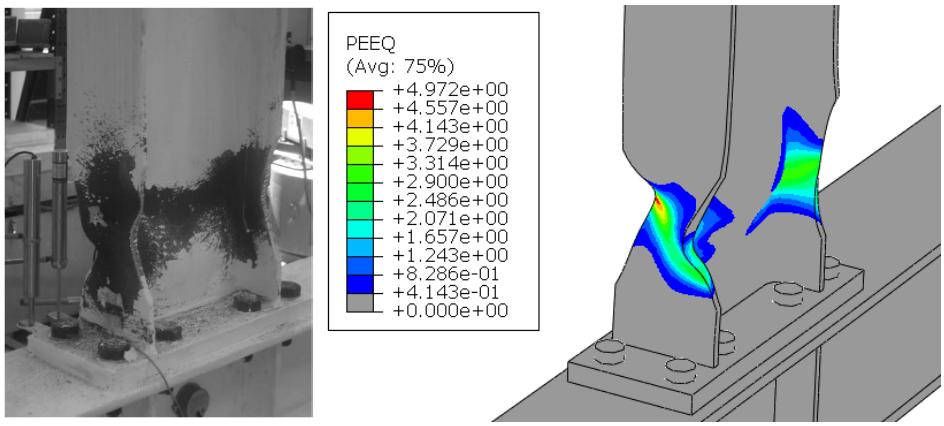

Figure 2.29 – Buckling of the flange and the web

The results in terms of moment-rotation hysteretic curves are reported in Figure 2.30. It is possible to observe that the numerical model can predict both the flexural stiffness and the resistance of the connection with high accuracy. Furthermore, the combined kinematic hardening adoption allows a good assessment of the strength degradation as it is observed referring to the cycles characterized by rotations higher than 50 mrad. The only limit of the proposed numerical solution regards the

loading and unloading branches predicted with relevant approximations, especially near the collapse of the joint.

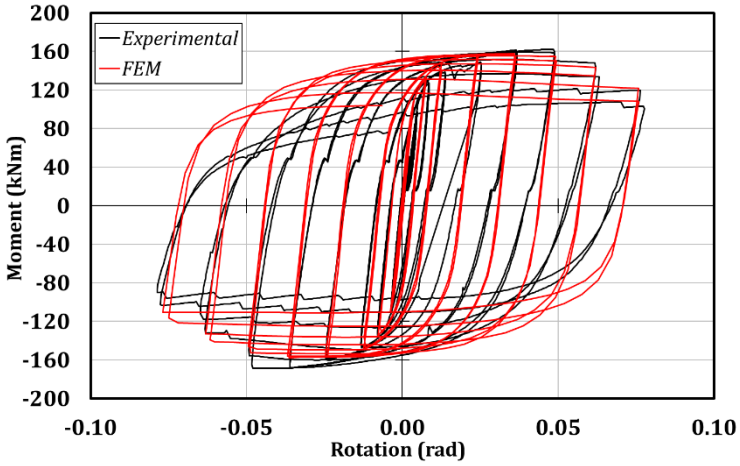

Figure 2.30 – Comparison between the experimental and FE results in terms of moment-rotation hysteretic curves

In Figure 2.30, it is possible to observe some discontinuities of the experimental moment-rotation curve. These discontinuities are caused by local minor and negligible slidings due to the clearance of the bolted connections, which compose the experimental layout (connection between the swivel and the reaction frame, supports bolted to the rigid floor)

2.3.3 Analytical model

The research activities led many researchers to propose a design procedure for the RBS joint [27-29]. The main aim of this connection typology is to weaken the beam so that the nodal components and the column can exhibit elastic behaviour.

The RBS joint consists of a reduction of the beam flanges and, for this reason, the main parameters to be designed are (Figure 2.31):

- the distance of the reduced beam section from the column flange (***a***);
- the length of the weakened zone (***b***);
- the reduction of the flange width (***c***).

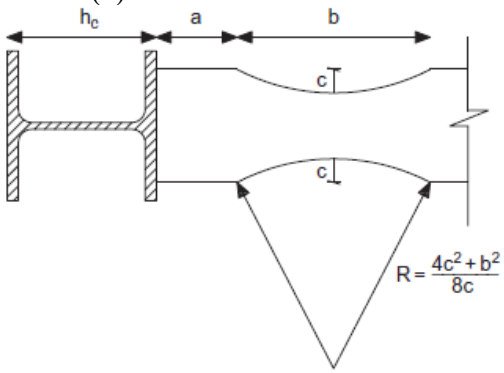

Figure 2.31 – Buckling of the flange and the web

The first two parameters should assume reduced values to minimize the moment due to the distance between the plastic hinge and the column and can be chosen arbitrarily based on the geometry of the connection to be designed as long as the following reference ranges are fulfilled:

$$0.5b_f \leq a \leq 0.75b_f$$
$$0.65d_f \leq b \leq 0.85d_f \quad (2.8)$$

b_f and d_f represent, respectively, the width of the beam flange and the beam depth.
Parameter c controls the maximum moment of the reduced section and, therefore, the maximum moment at the face of the column. This value must be limited to obtain a column face moment between 85% and 100% of the plastic moment of the beam cross-section. Furthermore, it should result that $c \leq 0{,}25b_f$.
In the design phase, it is possible to set the parameters a and b, while c is assessed through an iterative procedure starting from its upper bound of $0.25b_f$.
The bending moment at the centre of the reduced section is assessed as:

$$M_{pl,RBS} = W_{pl,RBS} f_y = \left[W_{pl,b} - 2ct_{bf}\left(d_b - t_{bf}\right)\right] f_y \quad (2.9)$$

Where $W_{pl,RBS}$ is the plastic modulus of the reduced section, $W_{pl,b}$ is the plastic modulus of the beam, t_{bf} is the thickness of the beam flange, d_b is the beam depth and f_y is the yield stress of the material.
The components belonging to the connection should remain elastic, and thus they are designed considering the dissipative zone yielded and hardened:

$$M_{RBS,E} = \gamma_{ov,rm}\gamma_{ov,sh}\gamma_{M0} W_{pl,RBS} f_y \quad (2.10)$$

γ_{M0} is a partial safety factor, while $\gamma_{ov,rm}$ and $\gamma_{ov,sh}$ are overstrength factors to account for the random material variability and strain-hardening.
Starting from the knowledge of $M_{RBS,E}$, it is necessary to calculate the bending moment at the column face to design the end-plate and the shear panel to have an elastic behaviour. For this reason, the shear force at the RBS centreline is assessed as:

$$V_{RBS,E} = \frac{M_{RBS,E}}{\left(L_b - a - \frac{b}{2}\right)} \quad (2.11)$$

Where L_b is the length of the beam.
Neglecting the thickness of the end-plate, the moment at the column face is calculated as:

$$M_c = M_{RBS,E} + V_{RBS,E}\left(a + \frac{b}{2}\right) \quad (2.12)$$

Iteratively modifying the parameter c, it is necessary to fulfil the following requirement:

$$\frac{M_c}{M_{pl,b}} \epsilon [0{,}85 \div 1] \quad (2.13)$$

Where $M_{pl,b} = W_{pl,b} \cdot 1{,}13 f_{yk}$.
Following the FEMA 267A regulations [30], the shear panel must be designed to withstand a shear action at least equal to 80% of that corresponding to the maximum bending moment acting on the face of the column:

$$\frac{V_{R,sp}}{V_{S,sp}} = \frac{V_{R,sp}}{\frac{0{,}8\sum M_c}{d_b - t_{bf}}} > 1 \quad (2.14)$$

It is also necessary to design a proper end-plate that is not the weak element but is dimensioned starting from the moment at the face of the column. The minimum thickness of the end plate to ensure a type-1 mechanism is assessed as:

$$t_{ep,min} = max\left\{\sqrt{\frac{M_c m}{2b_{eff} f_y\left(d_b - t_{bf}\right)}}; \sqrt{\frac{4B_{Rd} mn}{b_{eff} f_y (m + 2n)}}\right\} \quad (2.15)$$

This procedure is applied to design the prequalified RBS connection [21], which is a welded joint connecting steel profiles belonging to the American catalogues. However, the same procedure can be exploited if the RBS strategy is adopted in the case of flush-end plate connections characterised by double-tee profiles belonging to the European catalogues (IPE, HEA, HEB, …). In fact, this is the case of the beam-to-column sub-assembly tested and discussed in paragraph 2.3.1, whose end-plate has been designed to be elastic so that the reduced section was the weak element experiencing the engagement in the plastic range.

2.4 Circular-Hollow-Section (CHS) to through-all double-tee beam connection

The design approaches reported in the previous paragraphs have shown that while much information is given in EC3 part 1.8 for beam-to-column joints of structures made with double-tee profiles, very few rules are currently available for connections made with tubular members. Nevertheless, many research works contributed not to leave this topic unexplored over the years. The first works were proposed by Jaspart and Weynand [31-33] about connections between rectangular hollow section columns and/or open section beams. The interest in this topic is also confirmed by the research made by Park and Wang [34], who have developed a solution to compute the rotational stiffness of I-section beams to Rectangular Hollow Section (RHS) columns, connected employing conventional bolted end-plates, also relying on the research by France and Buick Davison [35, 36]. The novelty of the work by Park and Wang allowed enlarging the range of applicability of the design equations suggested by Jaspart et al. [33]. Moreover, many other aspects have been investigated; among these, it is worth highlighting: the effects of the fillet welds on connections among tubular profiles [37, 38]; the stiffness of blind-bolted connections to concrete-filled tubes using modified Hollo-bolt [39].

In order to make the traditional approaches reported in the previous paragraphs available in the case of structures with tubular profiles, this section is devoted to investigating the flexural behaviour of the connection between circular hollow section columns and through-all double-tee beams.

The typical way of conceiving full-strength steel beam-to-column connections consists in applying the hierarchy criteria to prevent any plasticization in the joint and in the column, promoting only the plastic engagement of beams to provide more ductility and energy dissipation capacity. Referring to the analysed connection typology, the plastic strengths provided by the connected members are well-known, while the only uncertainty regards the connection itself.

In this framework, the investigation of the behaviour of the single components belonging to such a kind of connection represents an interesting and innovative topic to explore.

For such a reason, experimental, numerical and analytical studies have been carried out selecting the joint members to foster the plastic engagement in the connection rather than in the beam. In particular, the joint is expected to collapse due to the tube's failure induced by the shear and the localized tension/compression forces under the beam flanges.

Such a kind of joint can be manufactured thanks to the adoption of the 3D-Laser Cutting Technology (LCT). This solution is gaining wide acceptance in many countries as it allows to solve some of the complexities arising in several applicative fields [40-44]. The success of this technology derives from the possibility of manufacturing a mass production with high accuracy. However, to date, 3D-LCT has not been fully exploited in civil engineering because the cost of large-scale structural components is still an issue that limits its extensive use. Nevertheless, this technology is also widespread in civil engineering for complex geometries. In fact, in some specific cases, such as for steel beam-to-column connections between circular hollow section

(CHS) columns and I-section beams, 3D-LCT provides significant practical advantages. However, the connection between CHS columns and I-beams is challenging due to the limited access for bolting. These connections, to date, have been realized in different ways: i) by simply welding the I-beams to the external surface of the tubular profile [14, 45, 46]; ii) by welding the flanges of the beam to additional plates which interrupt the continuity of the column [47]; iii) adopting external collar plates [48-51] welded or bolted to the tubular section; iv) by bolting tapered cover plates to diaphragm plates [52, 53]; v) adopting NiTi shape memory alloy and steel tendons connected to external diaphragms to ensure the self-recentring in case of seismic events [54]; vi) filling the chord with concrete or grout [55-57] and welding the beam to the external surface of the CHS; vii) filling the chord with concrete or grout and connecting the beam and the column by means of end-plates fixed to the column with transversal ribs [58]. The first solution is straightforward to manufacture, but the obtained connections exhibit low stiffness and resistance, suitable only for pinned or semi-continuous frames [59]. Higher bending moments can be withstood from the second to the fifth solution, but the realization of complex special elements [60, 61] is required.
Conversely, the last two solutions provide high stiffness and resistance but require pouring concrete on-site, slowing the construction process [62, 63]. Another interesting solution is represented by H-beam to SHS-column cast modular panel zone joints [64, 65]. This connection has not required the 3D-LCT; nevertheless, the possibility of conceiving cast joints between CHS and I-beams with the 3D-LCT could be a very attractive alternative.
The drawbacks of these joint typologies can be improved through 3D-LCT, which allows the I-section to cross the column before welding the two elements. Recent research is examining this solution to promote the use of I-beam to circular hollow section connections by simplifying the constructive phases thanks to the 3D Laser Cutting Technology [66]. In particular, the attention of recent works has focused mainly on technological aspects [60], while novel design tools are still needed to characterize the behaviour of these joints. The work hereinafter presented aims to fill the knowledge gap related to the mechanical behaviour of single-way connections realized employing CHS columns and through I-beams. To this scope, experimental work and a theoretical approach supported by parametric FE analyses are presented.
Even though, till now, not many studies have dealt with connections between CHS columns and through I-beams in bending, many researchers have focused their attention on the analysis of connections between tubular profiles and transverse or longitudinal branch plates welded to the external surface of the CHS [67-71]. For this typology, the first theoretical model was proposed by Togo in 1967 [67] and, subsequently, based on this model, other researchers have proposed design equations for the prediction of the flexural resistance of connections made with I-section profiles welded to the external surface of the hollow sections [14, 62, 72-74]. Recent research has also focused on connections with through-all plates [59, 63, 75], but the case of CHS columns with through I-beams is still an open issue.
Within this framework, at the STRENGTH (STRuctural ENGineering Test Hall) laboratory of the University of Salerno, a research activity dealing with the study of the flexural behaviour of one-way steel beam-to-column connections between CHS columns and through-all I-beams has begun. The research activity contemplates experimental, numerical and theoretical studies to analyse the stiffness and the resistance of these connections according to the component method approach. The experimental campaign performed tests on beam-to-column sub-assemblies made by welding CHS columns and through-all plates or I-section profiles. The experimental results have been used to calibrate and validate a finite element model of the tested connections, which has been exploited to perform a parametric analysis by varying a wide range of geometrical properties. The parametric

analyses have been used to propose strength and stiffness design equations within the framework of the component method.

2.4.1 Experimental activity

2.4.1.1 Column to through-all beam

The first phase of the experimental activity carried out at the STRENGTH laboratory of the University of Salerno consisted of performing two tests applying a monotonic and cyclic loading history on two specimens with the same members. In this section, the information needed to provide complete knowledge about the geometrical and mechanical properties of the specimens is briefly reported.

The same steel members characterized both the specimens: i) circular hollow section columns (CHS) with a diameter equal to 219.1 mm, the thickness of 6 mm and length equal to 2000 mm; ii) I-section beams consisting of IPE240 profiles with length equal to 2000 mm (Figure 2.32). To allow the I-section profiles to cross the columns without obstructions, the two sides of the tubular profiles have been cut with a tolerance of 4 mm around the imprint of the IPE 240 shape, according to the suggestions proposed by Kanyilmaz et al. [60, 61] (Figure 2.32). Even though the lengths of the steel members were fixed to be suitable for the testing rig, without any purpose of considering the specimens as belonging to a reference structure, however, it is possible to note that the adopted lengths are not too far from the standard sizes of inter-storey heights and beam spans of typical buildings. In any case, the length of the profiles may affect only the ratio between the shear and bending actions acting in the joint components, whose effects, in any case, can be considered through the methodologies suggested by the component method.

The welds have been adequately sized to provide higher strength than the connected members. They consist of single-sided full-penetration butt welds with a leg throat equal to 11 mm (Figure 2.32). It is worth underlying that the edges of the cut tubular profile have been chamfered with an angle equal to 30°. The Metal Inert Gas (MIG) welding, a subtype of the Gas Metal Arc Welding (GMAW) technique, has been adopted, complying with EN 4063-131 provision [76]. The MIG wire electrode has been chosen in such a way to provide higher strength than the welded base metal elements.

The material properties of the steel members have been defined by tension coupon tests obtained by the base metal of the sub-assembly experiencing the monotonic test. The results, in terms of stress-strain laws and yielding stress (f_y), are reported in Figure 2.33 and Figure 2.34. The yielding stresses have been assessed complying with Eurocode 3 part 1.4 [77] provision, and the obtained values concerning the beam and the column are equal to *368.4 MPa* and *346.6 MPa*, respectively. The nominal steel grade of the profiles was S355JR.

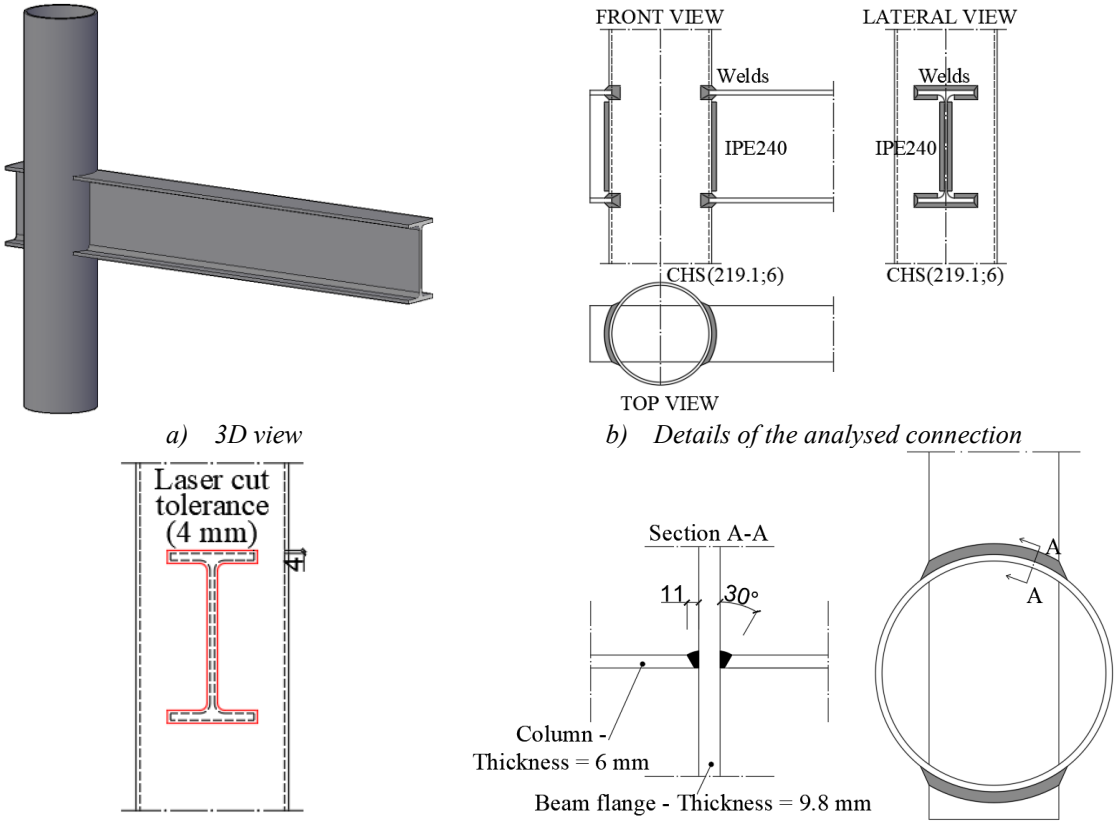

a) 3D view *b) Details of the analysed connection*

c) Tolerances *d) Welding detail*

Figure 2.32 – Analysed connection

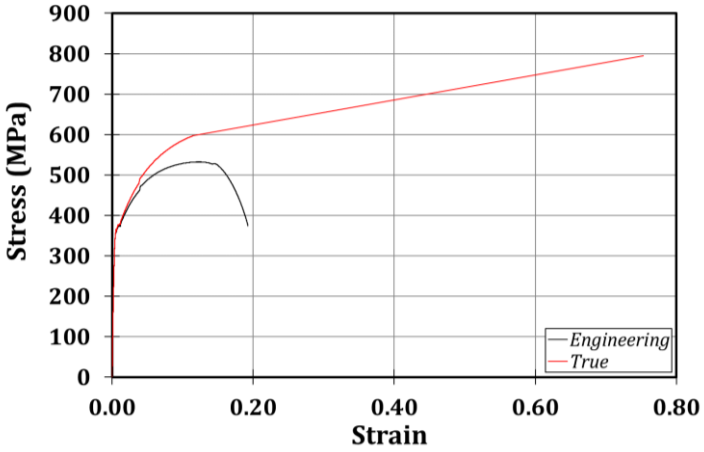

Monotonic test: stress-strain laws. f_y=368,4 MPa

Monotonic test: photos. f_y=368,4 MPa

Figure 2.33 – Results of the coupon test (IPE 240 flange)

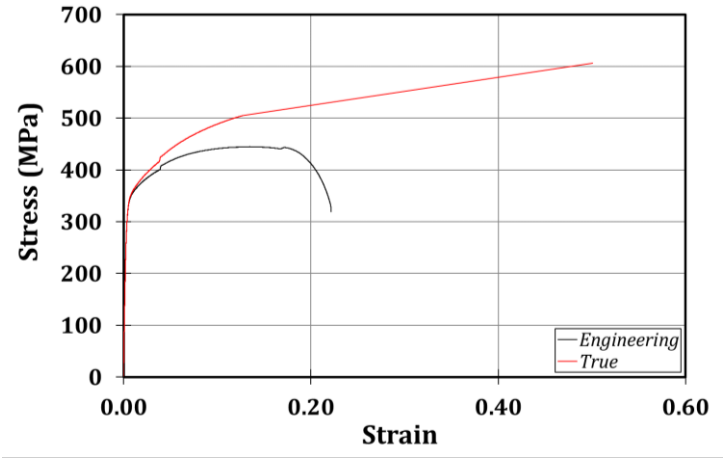

Monotonic test: stress-strain laws. f_y=346,6 MPa

Monotonic test: photos. f_y=346,6 MPa

Figure 2.34 – Results of the coupon test (Column)

The testing rig has been conceived in such a way to apply the force at the beam end employing a horizontal actuator MTS 243 (load capacity of ±250 kN and a piston stroke of ±500 mm), which is fixed to a rigid steel reaction frame constrained at its base to the strong laboratory floor (Figure 2.35). The column has been placed horizontally in the test layout, restraining its ends thanks to a roller and a steel hinge connected to a steel base. Moreover, undesired lateral-torsional buckling phenomena of the beam have been prevented by using an additional horizontal frame (Figure 2.35 and Figure 2.36).

In both the tests, the controlled point is the beam section located at a distance equal to 1560 mm from the column centreline, as shown in Figure 2.35. The cyclic displacement history at increasing amplitudes, adopted for the cyclic test, has been defined according to AISC 341-16 [23], while the monotonic test applied an increasing displacement at a 4 mm/min rate.

Starting from the knowledge of the displacements ($d_{actuator}$) and the forces ($F_{actuator}$) applied and recorded, respectively, by the actuator, it has been possible to assess the bending moments and the rotations exhibited by the connections multiplying $F_{actuator}$ or dividing $d_{actuator}$, respectively, with the distance between the centreline of the column and the axis of the actuator, which has been labelled as $L_{ref.}$ in Eqs. 2.16-2.17.

$$M = F_{actuator} L_{ref.} \quad (2.16)$$

$$\varphi = \frac{d_{actuator}}{L_{ref.}} \quad (2.17)$$

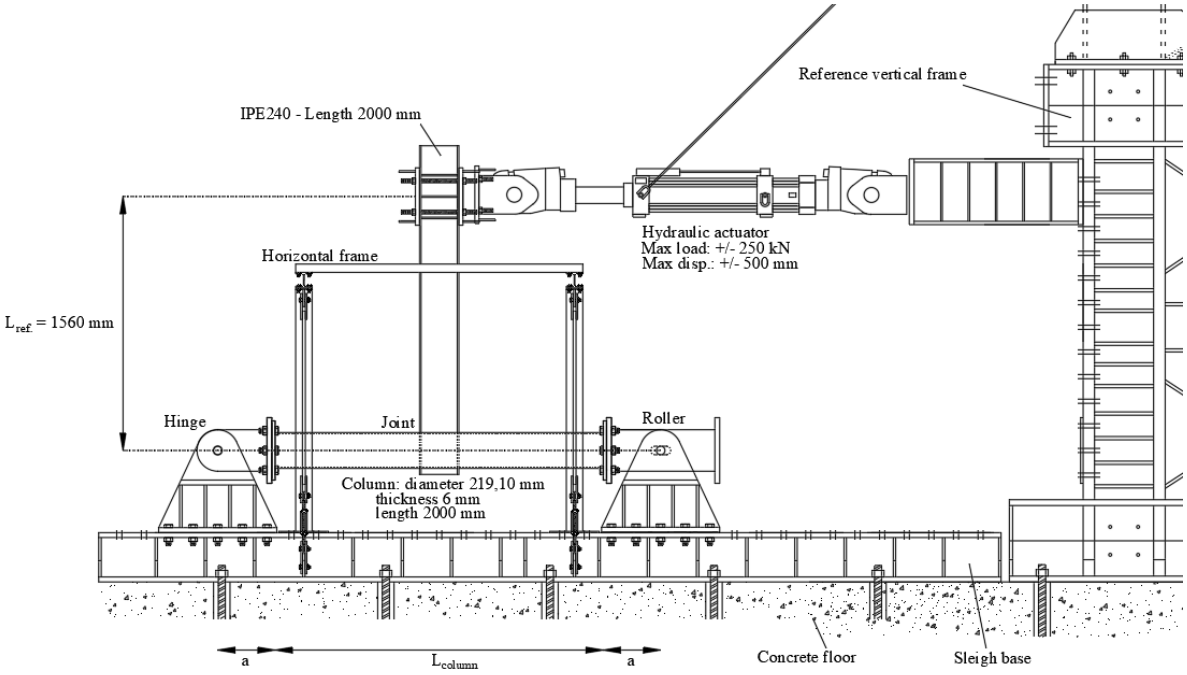

Figure 2.35 – Experimental set-up (schematic drawing)

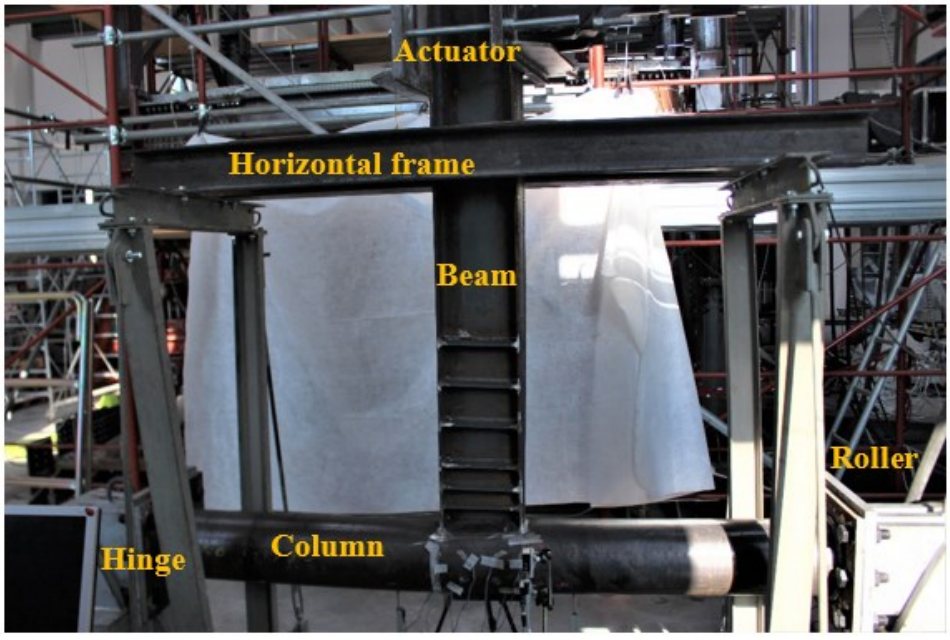

Figure 2.36 – Experimental set-up (photo)

The layout of the monotonic test has been improved using strain-gauges and linear displacement transducers (LDT). In particular, 16 strain-gauges have been employed on the tubular external

surface close to the panel zone of the connection according to a diagonal pattern (from D01 to D04 on one side and from D05 to D08 on the other side of the specimen) and along with the circumferential directions in the zone close to the beam flanges (from C01 to C04 on one side and from C05 to C08 on the other one). Instead, two LDTs (LDT01 and LDT02) have been located along the longitudinal direction of the column (Figure 2.37).
A brief discussion about the experimental results is herein reported. Both the specimens collapsed due to the achievement of the chord failure strength: the beams did not show any visible damage, while the crises happened because of the tubes' transverse crushing of the tubes induced by the large displacements in correspondence of the flanges the beams (Figure 2.38). The collapses occurred because of the spread of uniform failure patterns that embedded the tubes' circumferential area close to welds (Figure 2.38). In particular, the higher shear forces applied locally by the through-all I-section profile activated local buckling phenomena in the column at the beam-column attachments.
The plastic flexural resistance of both the specimens has been derived complying with Eurocode 3 part 1.8 [14] provisions: it has been assessed intersecting the moment-rotation curve with a straight line passing through the intersection point of the axes and characterized by a halved angular coefficient compared to the elastic branch of the moment-rotation curve.

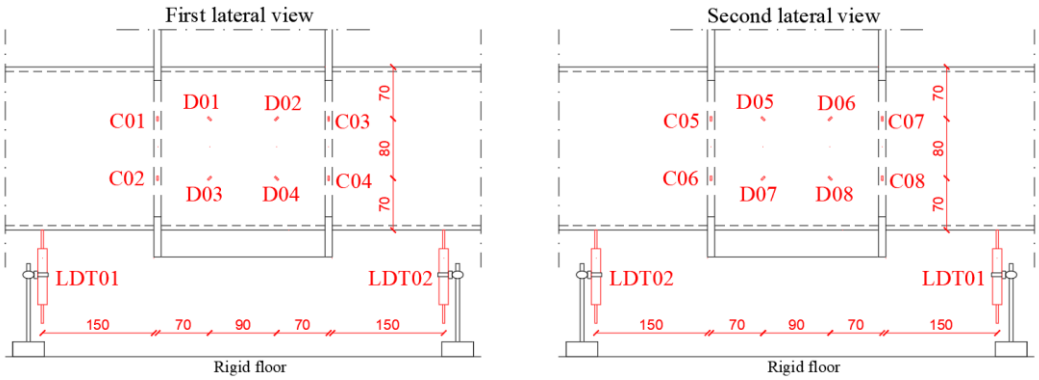

a) Pattern of strain-gauges and LDTs: first lateral view (left) and second lateral view (right)

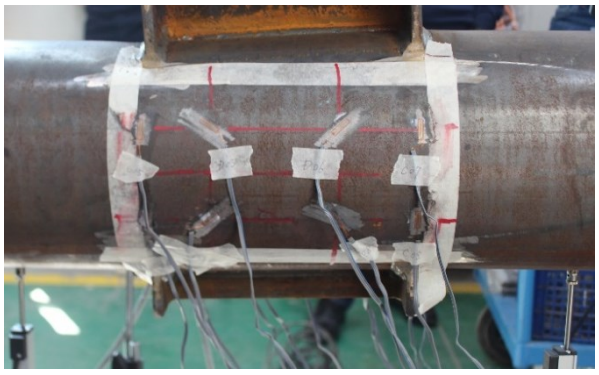

b) Experimental arrangement

Figure 2.37 - Arrangement of strain-gauges and transducers

In Table 2.2, the stiffness and the resistance observed at the end of the tests are shown: the resistance in both cases is about 150 kNm, while the stiffness varies between 6993 and 8256 kNm/rad.

Table 2.2 - Comparison of the experimental results

	Resistance (kNm)	Stiffness (kNm/rad)
Monotonic test	150	8256
Cyclic test	151	6993
Scatters (%)	1	- 15

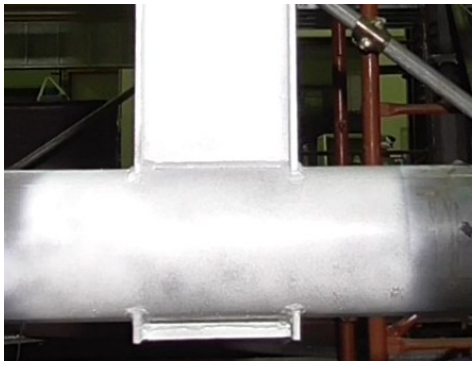

Specimen at the beginning of the cyclic test

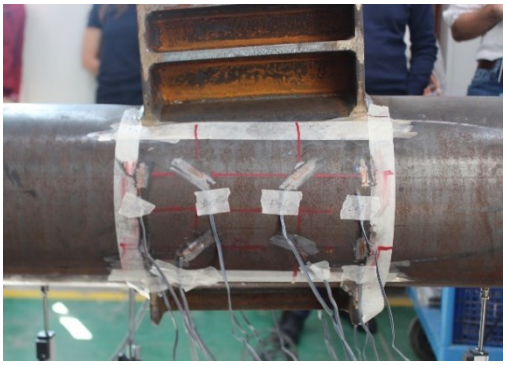

Specimen at the beginning of the monotonic test

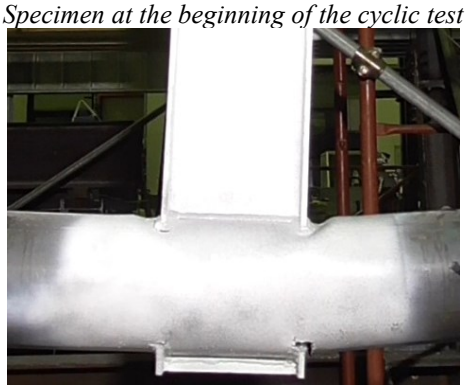

Specimen at the end of the cyclic test

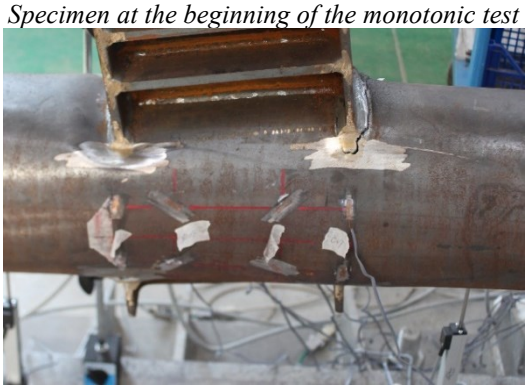

Specimen at the end of the monotonic test

Failure mode of the specimen under cyclic loading

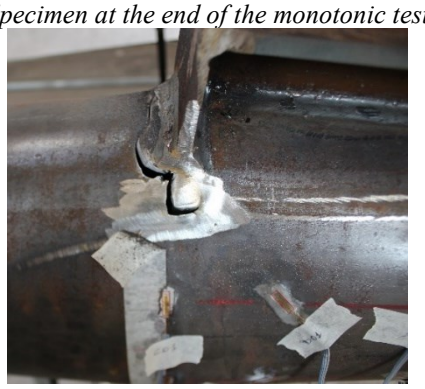

Failure mode of the specimen under monotonic loading

Figure 2.38 - Experimental tests: cyclic test (left column) and monotonic test (right column)

Starting from the knowledge of the flexural resistance exhibited by the analysed connection and considering that the plastic flexural strengths of the beam and the column are equal to 124 kNm, and 74 kNm, respectively, it is possible to classify the connection as a full-strength joint according

to Eurocode 3 part 1.8 [14]. Conversely, considering seismic provisions, the connection must be classified as a partial-strength joint according to Eurocode 8 part 1.1 [78].
The classification of the joint in terms of stiffness can be performed only after detracting the contributions due to the elastic deformation of the connected members, according to Eq. 2.18 and the scheme reported in Figure 2.39.

$$\varphi = \varphi_{exp.} - \frac{FL_{ref.}^2}{3EI_b} - \frac{2}{3}\frac{FL_{ref.}}{EI_c}\frac{\left(a + \frac{L_c}{2} - \frac{h_b}{2}\right)^3 - a^3}{(L_c + 2a)^2} - \frac{2FL_{ref.}}{(L_c + 2a)^2}\frac{\chi}{GA_{CHS}}\left(\frac{L_c}{2} - \frac{h_b}{2}\right) \quad (2.18)$$

where φ is the plastic rotation of the connection, $\varphi_{exp.}$ is the rotation assessed according to Eq. 2.17, F is the force applied by the actuator to impose the desired displacement, $L_{ref.}$ is the vertical distance between the intersection of the steel members and the actuator, E is the modulus of elasticity, I_b and I_c are the second area moments of the beam and the column, respectively, L_c is the length of the column, a is the length of the rigid elements at the end of the column, G is the shear modulus, A_{CHS} is the area of the column cross-section, χ is the shear factor (it is equal to 2 in the case of a circular hollow section) and h_b is the height of the beam.

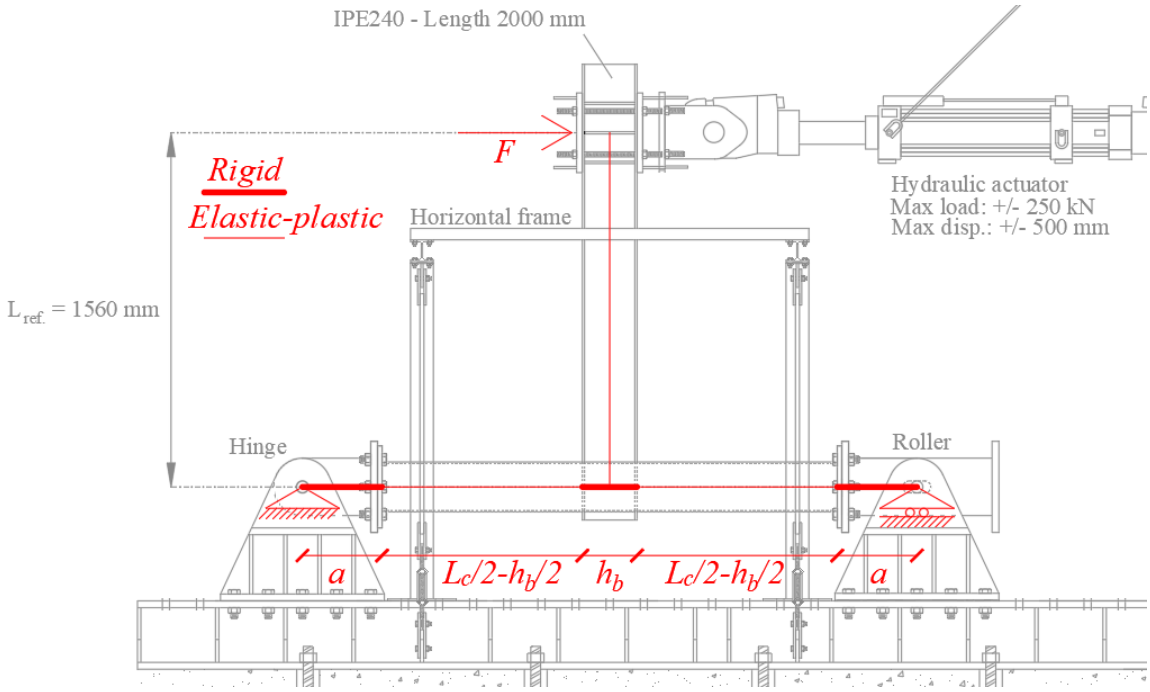

Figure 2.39 - Reference scheme adopted to detract the elastic deformations ascribed to the beam and the column

The initial plastic stiffness of the monotonically loaded specimen is 59.9 kNm/mrad. Therefore, according to the classification criteria provided by the Eurocode 3 part 1.8 [14], even in the conservative hypotheses that the specimens belong to a moment-resisting-frame characterized by an inter-storey height equal to 2 m and a span length equal to 3.12 m, it is possible to state that the joint with the through I-beam is rigid.

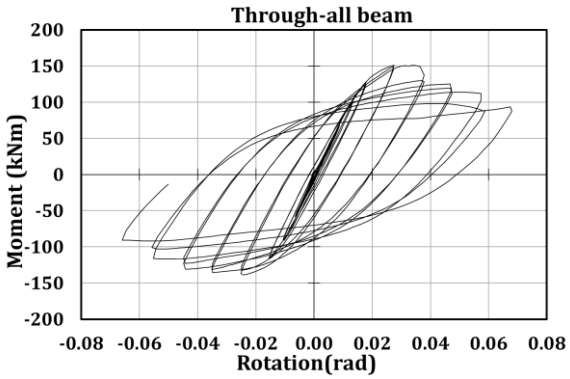

Moment-rotation curve (cyclic test)

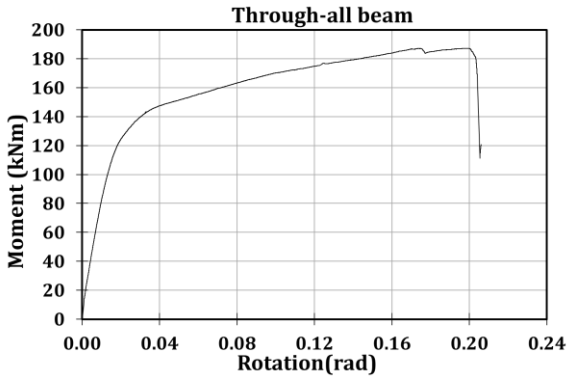

Moment-rotation curve (monotonic test)

Figure 2.40 - Experimental tests: cyclic test (left) and monotonic test (right)

Another relevant remark regards the high dissipation of energy provided by the specimen subjected to the cyclic test (Figure 2.40) before attaining local buckling at a rotation of about 40 mrad. Finally, in Figure 2.38, it is possible to note that the beam belonging to the specimen experiencing the monotonic loading is composed of additional plates welded to the beam flanges and web. This detail has been adequately conceived to prevent the beam flanges' local buckling and force the connection's plastic engagement since the plastic zone's very high rotations and strain-hardening were expected.

2.4.1.2 Column to through-all plate

Considering that the crises of the above-described tests on the beam-to-column sub-assemblies occurred because of the transverse crushing of the tubes induced by the large displacements in correspondence of the flanges of the beams, the attention has also been focused on the investigation of the behaviour of columns to through-all plates connections. This solution appears to represent the response of the flange to column attachment.

In particular, three monotonic and three cyclic tests have been executed on specimens of joints with CHS profiles and through-all plates (Figure 2.41). The different geometries characterising the specimens are reported in Table 2.3. The width of the plates has been appropriately selected to be ideally representative of the flange plate of double-tee profiles of a CHS to through-all beam connection (IPE200, IPE300 and IPE330 for the three specimens, respectively).

Similarly to the case of the beam-to-column sub-assembly, the welds have been realised with single-sided full-penetration butt weld details, chamfered with an angle equal to 30°, with the Metal Inert Gas (MIG) welding technique [76]. The material properties have been defined through coupon tests, whose results are reported in Figure 2.42. The members have been cut considering a tolerance of 2 mm of the passing-through holes (Figure 2.43) to ensure that the plates could pass through the CHS tube during construction.

Table 2.3 – Geometrical properties of the tested specimens

	Circular hollow section			Through-all plate		
Specimen	External diameter (mm)	Thickness (mm)	Length (mm)	Width (mm)	Thickness (mm)	Length (mm)
1	168.0	6.0	450.0	100.0	30.0	350.0
2	219.1	5.0	500.0	150.0	20.0	350.0
3	273.0	6.0	500.0	160.0	20.0	400.0

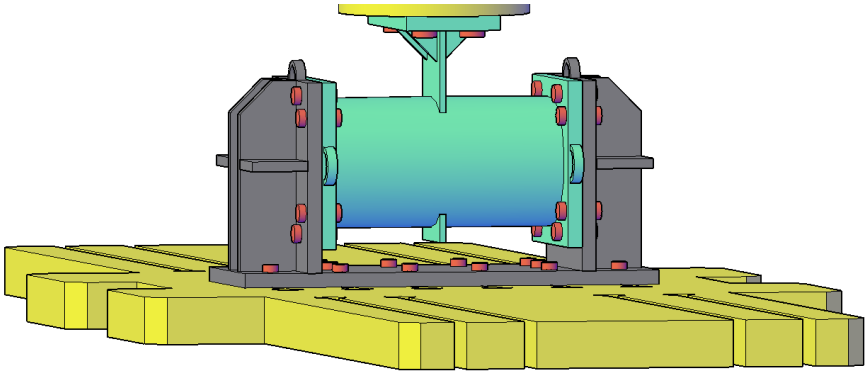

Figure 2.41 – 3D configuration of the studied connection

The testing rig has been realised to apply a force at the upper end of the plate employing a vertical actuator (load capacity of 2000 kN in tension and 3000 kN in compression) fixed to a rigid steel reaction frame constrained at its base to the strong laboratory floor (Figure 2.43).
The CHS tube has been placed horizontally (Figure 2.44). The tube ends have been restrained to steel supports conceived to fix all the degrees of freedom. The supports are bolted to the rigid base of the testing machine according to the layout reported in Figure 2.43 and Figure 2.44. The monotonic tests consisted in applying an increasing downward displacement at a quasi-static rate of 0.5 mm/min up to 10 mm of vertical displacement, 1 mm/min from 10 mm to 20 mm, and 2 mm/min for displacements larger than 20 mm. Instead, the adopted cyclic displacement histories have been characterized by increasing amplitudes up to failure complying with AISC 341–16 [23]. They are reported in TTable 2.4.

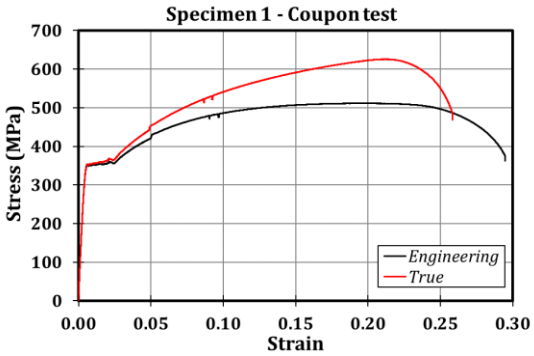

a) 168x6 mm CHS tube length of 450 mm

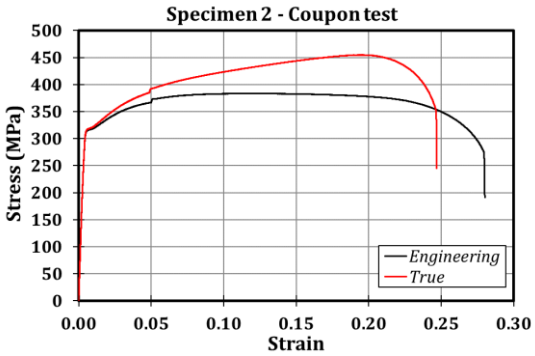

b) 219.1x5 mm CHS tube length of 500 mm

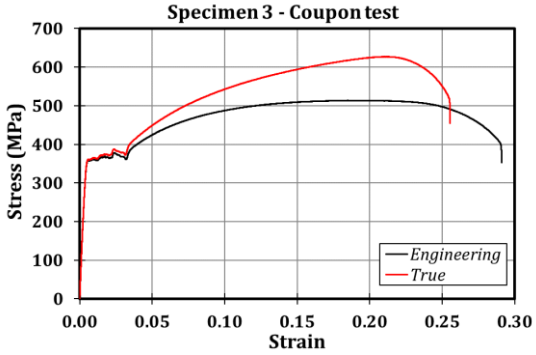

c) 273x6 mm CHS tube length of 500 mm

Figure 2.42 – Results of the coupon tests

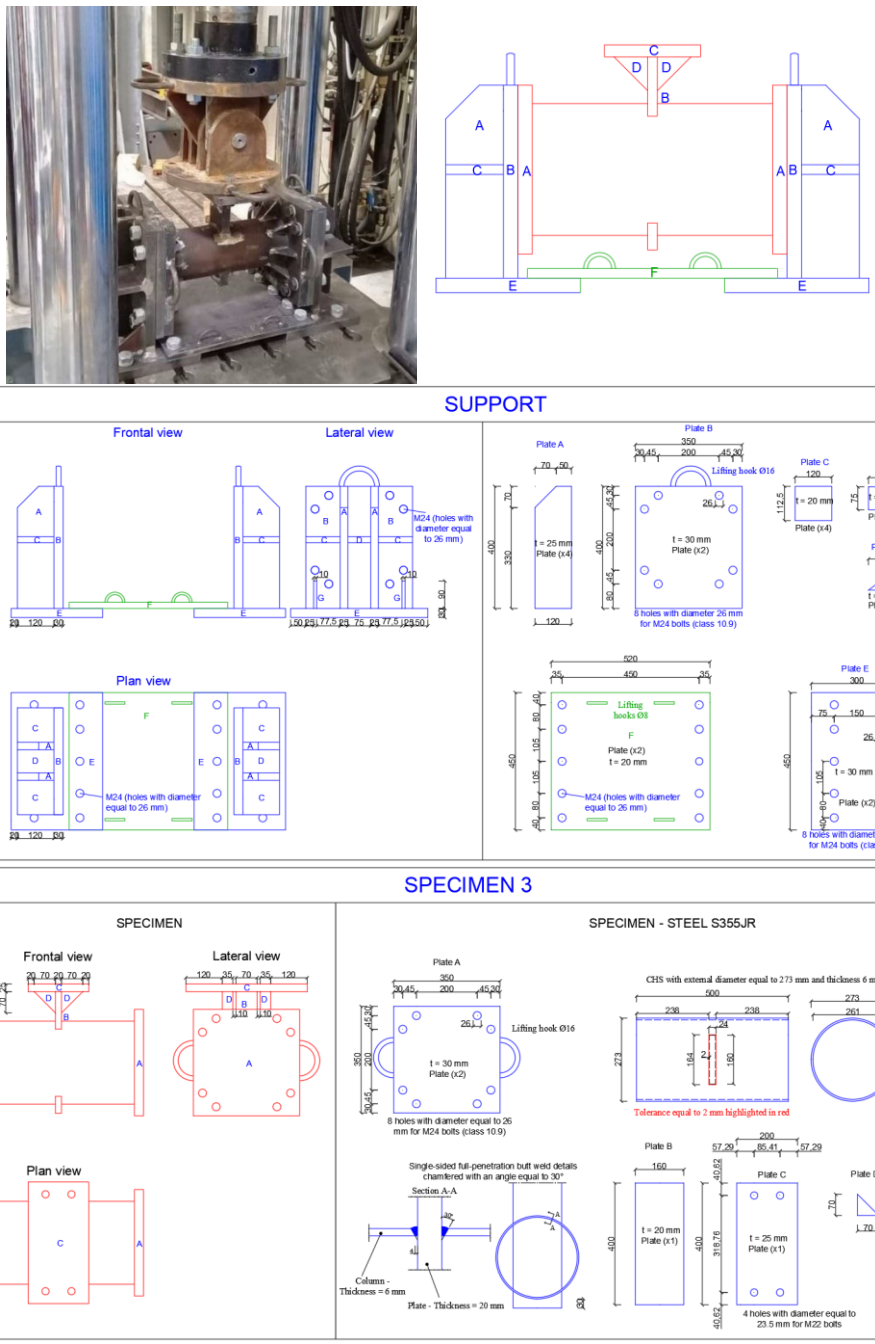

Figure 2.43 – Test layout

Table 2.4 – Cyclic loading histories

	Test 1		Test 2		Test 3	
n. cycles	Amplitude (mm)	Velocity (mm/s)	Amplitude (mm)	Velocity (mm/s)	Amplitude (mm)	Velocity (mm/s)
6	0.75	0.05	1.125	0.05	1.2	0.05
6	1	0.07	1.5	0.07	1.6	0.07
6	1.5	0.1	2.25	0.1	2.4	0.1
4	2	0.13	3	0.13	3.2	0.13
2	3	0.20	4.5	0.20	4.8	0.20
2	4	0.27	6	0.27	6.4	0.27
2	6	0.40	9	0.40	9.6	0.40
2	8	0.53	12	0.53	12.8	0.53
2	10	0.67	15	0.67	16	0.67
2	12	0.80	-	-	-	-
2	14	0.93	-	-	-	-

The specimens have been equipped with 5 LVDTs to monitor the deflection at the mid-point and potential displacements of the supports to check their full rigidity during the tests.

Figure 2.44 – Experimental set-up

All the specimens collapsed because of the transverse crushing of the tube, showing the typical deformation depicted in Figure 2.45, Figure 2.46, Figure 2.47. Specifically, in all the specimens, it was observed that a characteristic inner/outer bowing of the CHS tube occurred in the tube zone

close to the moving plate. Conversely, the failure typically arose due to the tearing of the tube at large deformations.

Figure 2.45 – Failure mode of Test 1: monotonic (left) and cyclic (right) loading

Figure 2.46 – Failure mode of Test 2: monotonic (left) and cyclic (right) loading

Figure 2.47 – Failure mode of Test 3: monotonic (left) and cyclic (right) loading

Figure 2.48 shows the force-displacement curves and the deformed configuration of the specimens at the end of the monotonic tests. In the case of monotonic tests, the maximum resistance of the connections is equal to 518 kN, 491 kN and 608 kN, respectively, and 515 kN, 462 kN and 565 kN in the case of cyclic tests. In all the cases, the maximum strength capacity has been achieved for displacements lower than 5 mm, highlighting the high stiffness of this component but the relatively low deformation capacity at the achievement of the peak strength. After achieving the peak strength, all the specimens showed a rather long softening branch, in the case of monotonic loading, with a progressive drop of resistance basically due to the residual resistance offered by the local crushing of the upper part of the tube and the local tearing of the lower part of the tube.

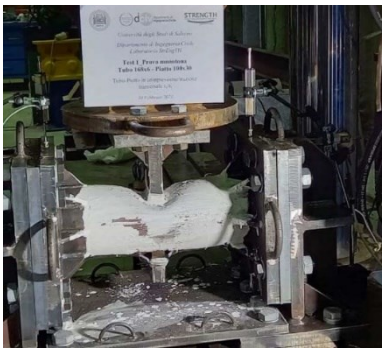

a) Specimen 1 (monotonic test)

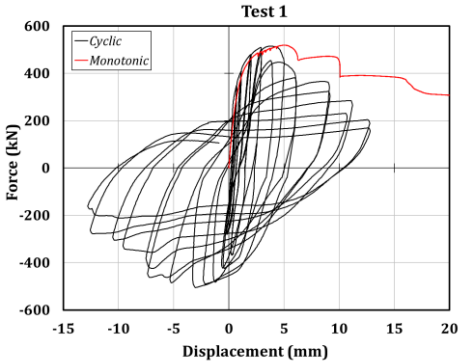

b) Force-displacement curves (test 1)

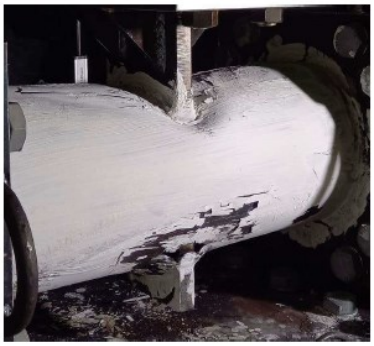

c) Specimen 2 (monotonic test)

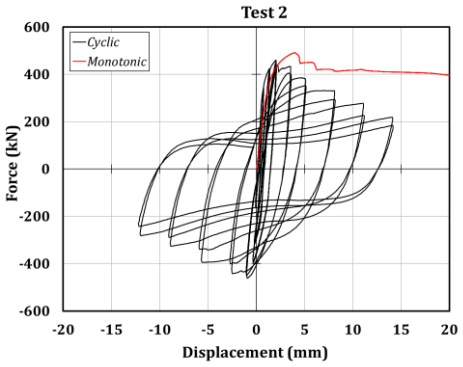

d) Force-displacement curves (test 2)

e) Specimen 3 (monotonic test)

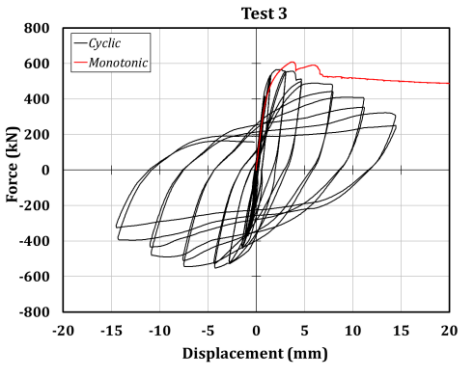

f) Force-displacement curves (test 3)

Figure 2.48 – Force-displacements curves

2.4.2 Numerical activity

2.4.2.1 Column to through-all beam

In order to extend the experimental results to a wide range of other cases, a FE model has been developed with ABAQUS software [24] and validated against the experimental results.

The profiles have been modelled by extruding the cross-sections of the considered tubular and I-section profiles along the longitudinal direction, while the welds have not been modelled explicitly since the beam and the column have been connected along the contact zone through tie constraints.

An adequate partition pattern has been conceived to guarantee the correct contact between the members. The mechanical properties of the profiles have been defined, referring to an elastic-plastic behaviour, with a modulus of elasticity of 210000 MPa, a Poisson's ratio equal to 0.30 and modelling the plastic branch according to an isotropic hardening. The stress-strain curve representative of the material has been defined according to an equivalent quadri-linear shape [6] based on the coupon test results. In order to account for the spread of damage throughout the tests, the parameters related to the damage evolution (Table 2.5) have been specified according to the works proposed by Faralli [79] and Pavlovic et al. [80] for the S355JR steel grade.

Table 2.5 – Damage evolution parameters adopted in the FE model

Fracture Strain	Stress Triaxiality
0.194	0.00
0.229	0.33
0.155	0.43
0.113	0.50
0.126	0.58

Consistently with these research studies, the equivalent plastic displacement at fracture, $\overline{u}_f^{pl}$, has been assessed according to Eq. 2.19.

$$\overline{u}_f^{pl} = \lambda_S \lambda_E L_E \left(\varepsilon_f^{pl} - \varepsilon_n^{pl}\right) = 4.8 \tag{2.19}$$

where λ_S is a parameter equal to 0.928 according to [79] for the current minimum mesh size of the elements, λ_E depends on the steel grade (for S355JR steel it is equal to 2.1), L_E is the minimum mesh size, ε_f^{pl} is the true plastic strain at failure and ε_n^{pl} is the true plastic strain at the onset of necking. C3D8-type (8-node linear brick) elements have been used to mesh the members. Specifically, the elements in the connection area have a mesh size equal to 10 mm, while the remaining parts have a 15 mm mesh size (Figure 2.49). At least two elements have been embedded in the thickness of the flanges and the columns.

Aiming at modelling the hinge and the roller of the experimental layout, reference points, restrained by suppressing the corresponding degrees of freedom and rigidly connected to the ends of the column through the coupling tool, have been defined. Instead, the effect of the horizontal frame, which prevents the beam lateral buckling, has been modelled by laterally restraining the beam at 1380 mm from the column face. The loading at the beam ends of the specimens involved the same displacement histories (cyclic and monotonic) to which the real-scale specimens were subjected (Figure 2.50).

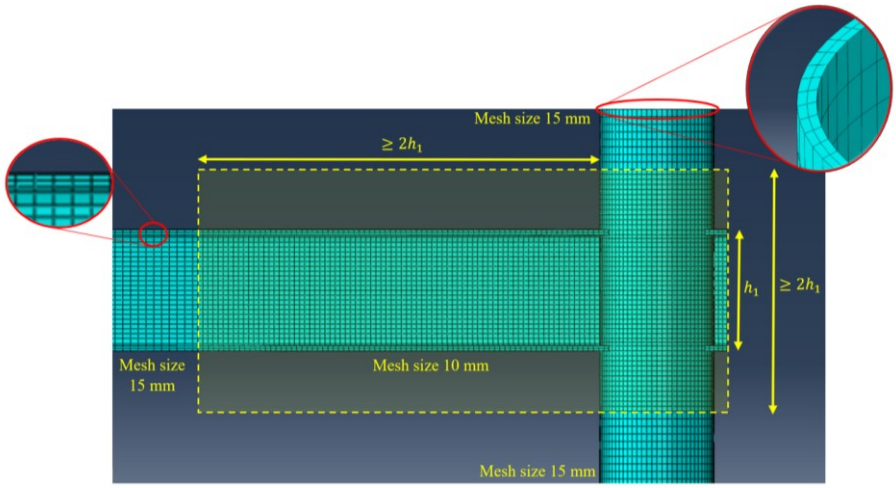

Figure 2.49 – FE model and mesh size selection

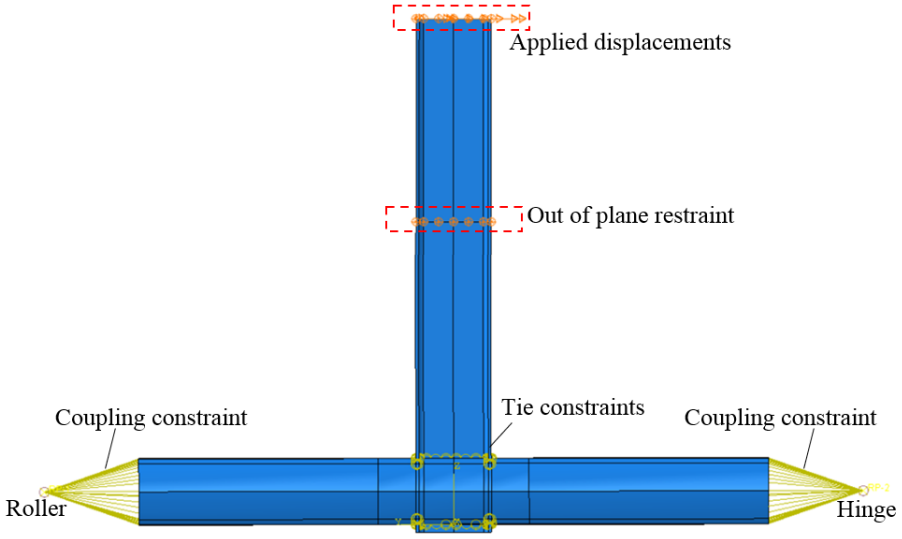

Figure 2.50 – FE model: constraints

According to Eurocode 3 part 1.5 [26] and the construction tolerances provided by EN10034 [25], imperfections have been considered in the numerical model. For this reason, preliminary buckling analyses (Figure 2.51), aimed at identifying the relevant buckling modes, have been performed. The buckling modes have adequately been amplified by the values of the initial imperfections (3% of the nominal internal diameter for the out-of-roundness tolerance, referring to CHS, and 2% of the flange width for the bow twist of the flanges of the beam). Among the elastic buckling shapes, only the imperfections related to the beam flanges' local buckling and the beam-tube attachments, which promote the local buckling of the column, have been considered. According to Eurocode 3 part 1.5 [26], the imperfections have been implemented considering the 80% of the maximum fabrication tolerance.

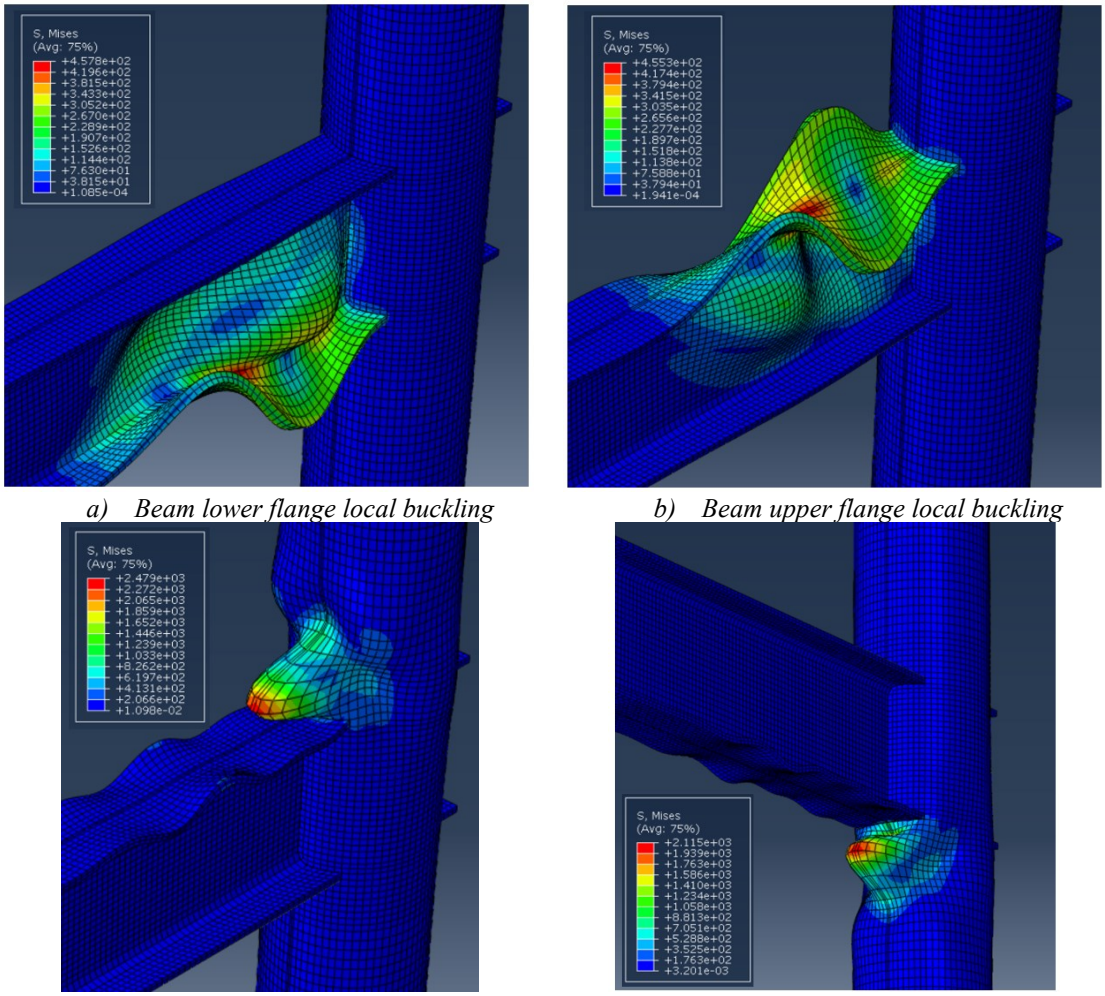

a) Beam lower flange local buckling *b) Beam upper flange local buckling*

c) Column local buckling (mode 1) *d) Column local buckling (mode 2)*

Figure 2.51 – Considered buckling modes

After the description of the main features regarding the FE model of the tested specimens, in this section, the results concerning the numerical simulations will be reported and compared to the experimental results.

The numerical models have been run adopting the static solver, and they have proved to be consistent with the experimental observations since the failure modes of the specimens have been caught in a very accurate way, as is clear from the moment-rotation hysteretic curves shown in Figure 2.52 and Figure 2.53. In fact, the onset of buckling phenomena is correctly predicted, corroborating the accuracy of the procedure adopted to introduce the geometrical imperfections in the model. In Table 2.6, the main results are summarized: the observed scatters between FE outcomes and experimental tests are very low for both resistance and stiffness. The numerical model can predict the resistance induced by the monotonic loading history with scatters of about 1%, while higher discrepancies affect the specimen under cyclic loading (maximum 8%). The same statements can be reported referring to the initial stiffness since it is underestimated by about 1% in the monotonic test while referring to the cyclic test; the result provided by the FE model is about 12% higher than the experimental counterpart.

Table 2.6 – Comparison of the experimental and FEM results in terms of stiffness and resistance

CHS to through I-beam						
	Stiffness (kNm/rad)			Resistance (kNm)		
Test	Exp.	FEM	FEM/Exp.	Exp.	FEM	FEM/Exp.
Monotonic	8256	8202	0.99	150	150	1.00
Cyclic	6993	7861	1.12	151	164	1.08

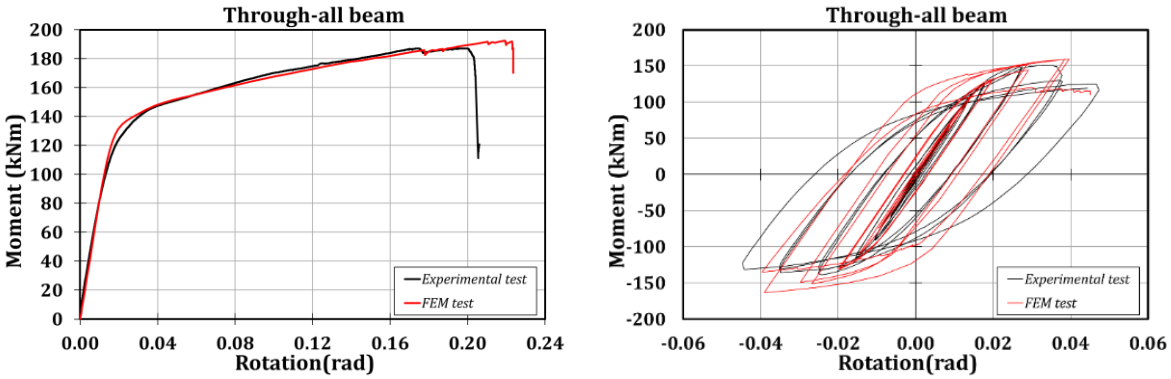

Monotonic test *Cyclic test*

Figure 2.52 – Experimental versus FE results

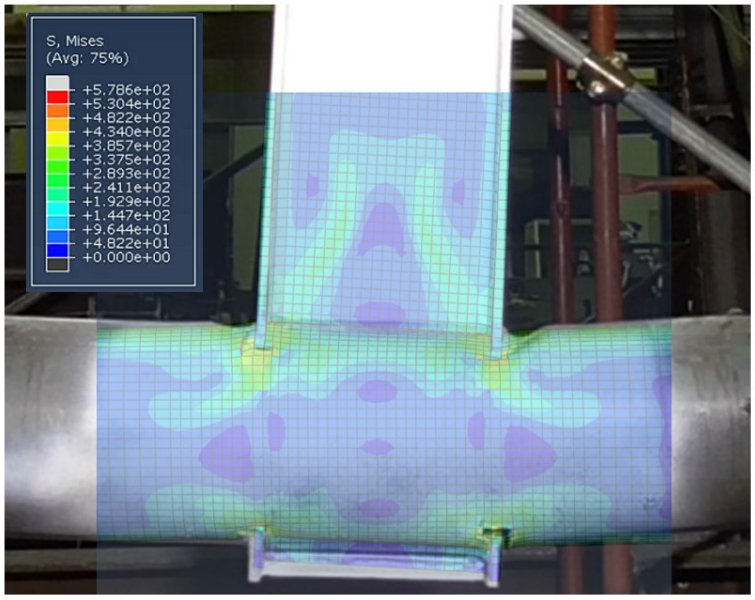

Figure 2.53 – Overlap of FE and experimental results for the cyclic test

2.4.2.2 Column to through-all plate

This paragraph shows the main features of FE models of the tested specimens developed with the software Abaqus [24]. The geometric characteristics of the specimens have been appropriately modelled through the extrusion and cut tools of the CAE Abaqus interface. Geometrically the specimens have been faithfully modelled, reflecting the actual shapes of the three CHS to through-all plate joints. The only exception is represented by the welds, which have been simplified with zero-thickness tie contacts between the plate and the tubular profile. The mechanical properties of

the model parts have been based on the materials coupon tests. Simplistically, the stress-strain laws of the materials have been modelled through an equivalent quadrilinear true-stress true-strain curve, as proposed by Faella et al. [6]. The assumed Young's modulus has been equal to 210 GPa, with a Poisson's ratio equal to 0.3. In the FE software, the specimens have been modelled together with the rigid floor of the testing rig and the supports, as shown in Figure 2.54.
All the degrees of freedom of the rigid basement have been fixed, while contacts have been imposed between the base of the supports and the basement. For all the contacts, a "hard" normal behaviour and a penalty with a friction coefficient equal to 0.3 have been assumed for the tangential response. The same assumption has been made for the interactions between the bolts' heads/nuts/shand and plate surfaces/holes. Tie contacts have been employed to model not only the welds between the through-plate and the CHS profile but also the welds among the plates of the fixed supports. A ductile damage rule has been assumed to account for the damage of the materials, considering an evolution law with an equivalent plastic displacement at fracture equal to 4.8 mm. C3D8-type (8-node linear brick) elements with mesh size equal to 5 mm have been used to mesh all the members (Figure 2.55). This type of element is more appropriate to model also potential local buckling phenomena. At least two elements within the thickness of the tube have been employed for all the models.

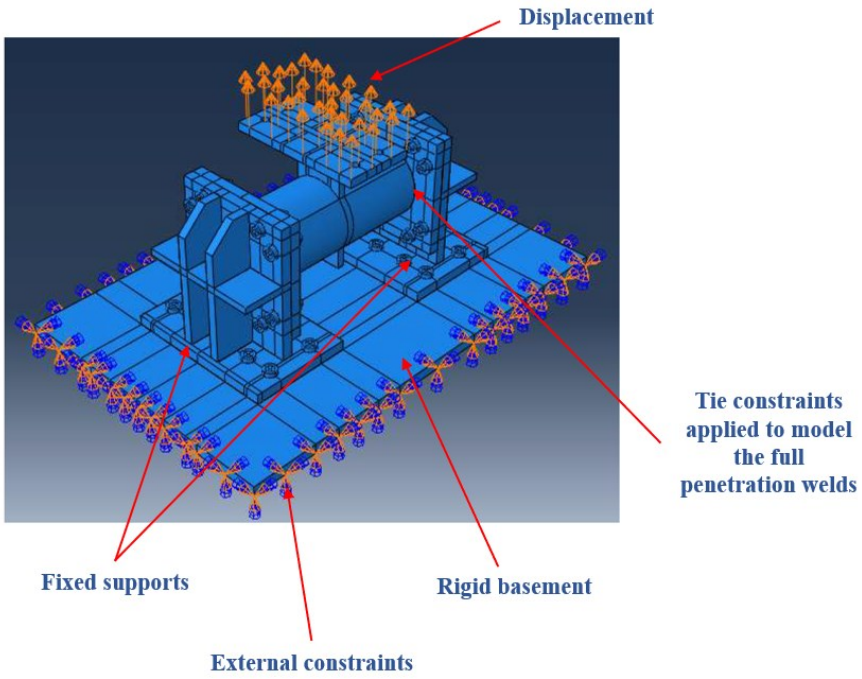

Figure 2.54 – FE model

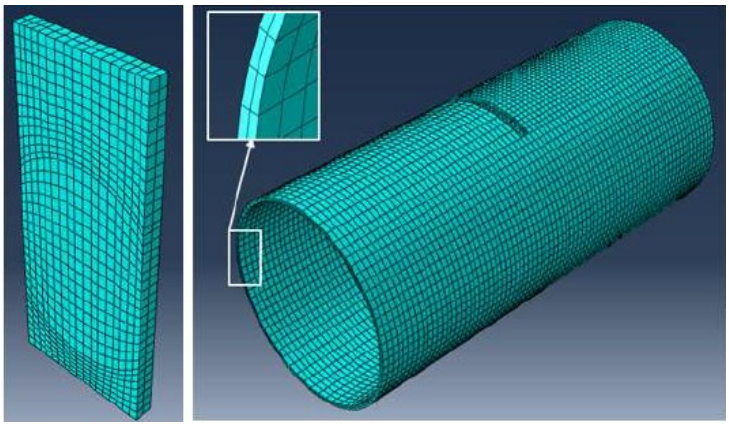

Figure 2.55 – Mesh of the FE model

The numerical model has been validated against the experimental results by applying at the end of the plate the same monotonic displacement histories of the tests. Furthermore, at the end of the simulations, carried out by adopting a static solver, it was possible to observe the consistency of the failure modes exhibited by the FE models with the experimental observations (Figure 2.56, Figure 2.57) and the satisfactory prediction of the force-displacement curves, as shown in Figure 2.59.

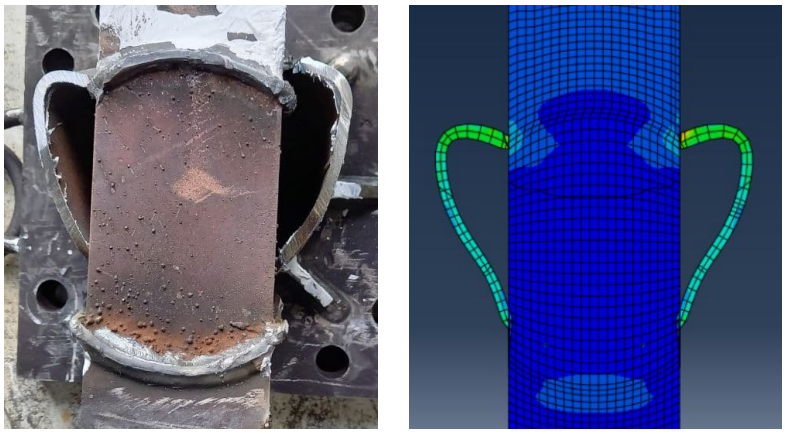

Figure 2.56 – Deformed configuration of the tube (numerical model referred to the first tested specimen)

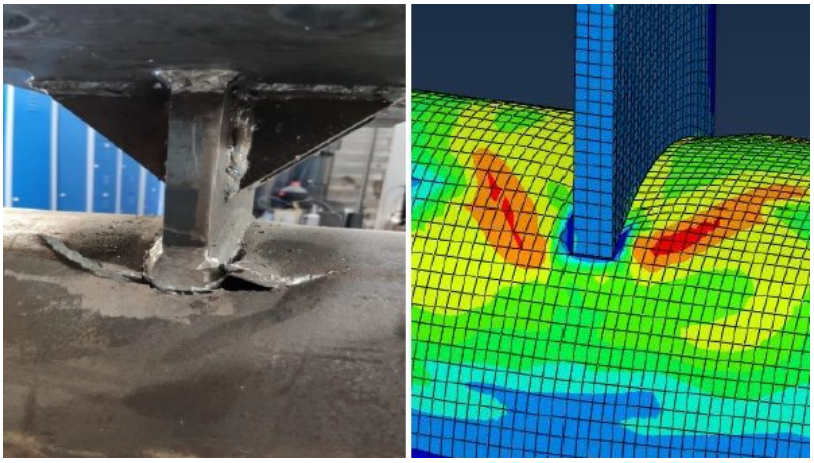

Figure 2.57 – Deformed configuration of the tube (numerical model referred to the first tested specimen)

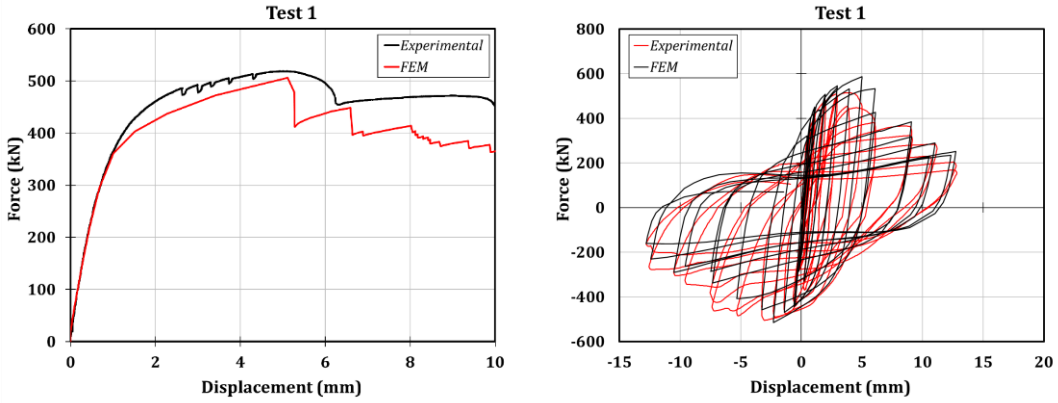

a) Force-displacement curves (test 1): monotonic (left) and cyclic (right)

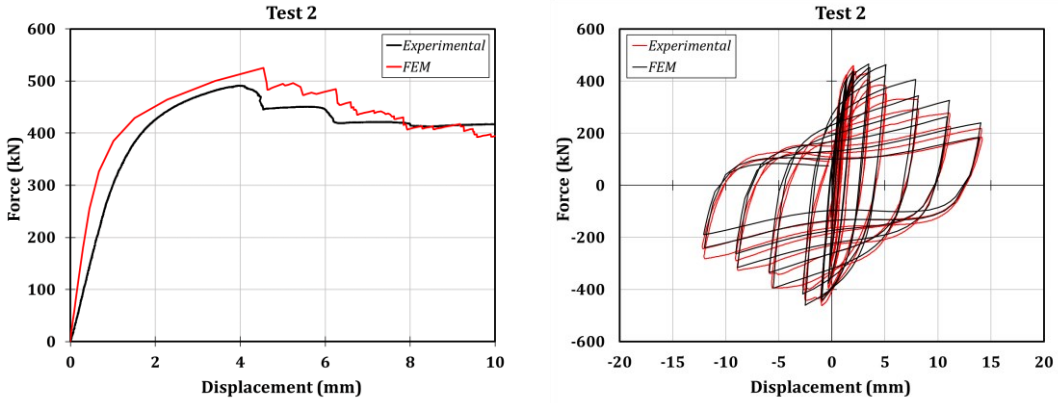

b) Force-displacement curves (test 2) : monotonic (left) and cyclic (right)

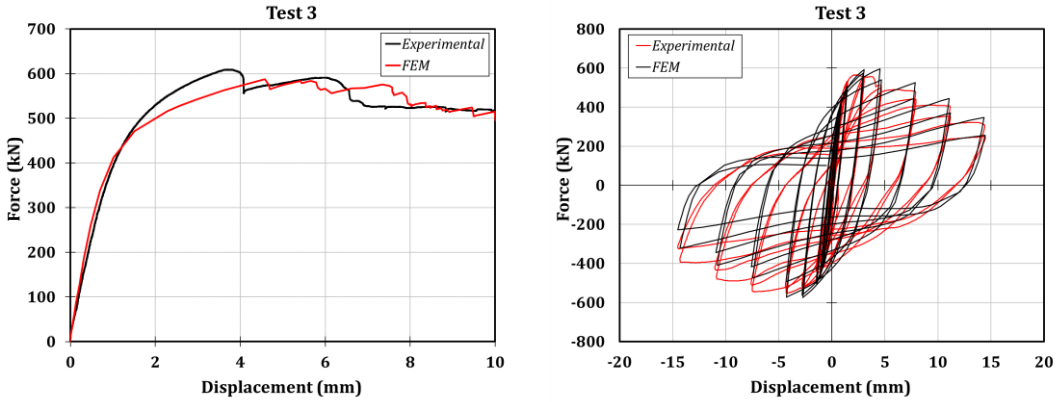

Force-displacement curves (test 3) : monotonic (left) and cyclic (right)

Figure 2.58 – Experimental versus FE results

2.4.3 Parametric analysis

2.4.3.1 Column to through-all beam

The validation of the FE models has represented a fundamental preliminary phase since it has allowed performing a parametric study consisting of simulations on 30 beam-to-column connections avoiding executing other experimental tests. In addition, the members of the connections have been adequately selected so that the column is weaker than the connected beam

and to vary in a wide range of the geometrical parameters that can affect the connection's behaviour.

Table 2.7 – Parametric analysis (CHS/I-beam connection)

Test	Column (diameter/ thickness)	Beam IPE	β	γ	η	Resistance (kNm)	Stiffness (kNm/mrad)
1	193,7/6	240	0.62	16.14	1.24	140.01	53.12
2	219,1/4	300	0.68	27.39	1.37	150.84	60.18
3	219,1/6	240	0.55	18.26	1.10	148.18	59.90
4	219,1/6	270	0.62	18.26	1.23	188.79	73.72
5	219,1/6	300	0.68	18.26	1.37	218.92	88.07
6	219,1/6	330	0.73	18.26	1.51	234.23	97.56
7	244,5/8	330	0.65	15.28	1.35	317.89	125.91
8	244,5/8	360	0.70	15.28	1.47	372.01	142.04
9	273/5	300	0.55	27.30	1.10	216.31	72.70
10	273/5	330	0.59	27.30	1.21	274.61	85.43
11	273/5	360	0.62	27.30	1.32	275.42	100.72
12	273/8	400	0.66	17.06	1.47	463.59	180.07
13	323,9/5	330	0.49	32.39	1.02	271.71	86.77
14	323,9/5	360	0.52	32.39	1.11	308.97	98.72
15	323,9/5	400	0.56	32.39	1.23	361.20	120.75
16	323,9/6,3	360	0.52	25.71	1.11	362.01	118.79
17	323,9/6,3	400	0.56	25.71	1.23	425.42	144.78
18	323,9/6,3	450	0.59	25.71	1.39	494.98	180.23
19	355,6/6	400	0.51	29.63	1.12	428.38	138.37
20	355,6/6	450	0.53	29.63	1.27	502.11	169.51
21	355,6/6	500	0.56	29.63	1.41	576.99	211.91
22	355,6/6	550	0.59	29.63	1.55	634.26	246.81
23	355,6/6	600	0.62	29.63	1.69	688.23	293.74
24	406,4/6	450	0.47	33.87	1.11	535.27	171.25
25	406,4/6	500	0.49	33.87	1.23	620.95	206.50
26	406,4/6	550	0.52	33.87	1.35	711.24	248.71
27	406,6/6	600	0.54	33.87	1.48	801.12	296.91
28	406,4/10	500	0.49	20.32	1.23	841.17	327.89
29	406,4/10	550	0.52	20.32	1.35	1022.88	412.97
30	406,4/10	600	0.54	20.32	1.48	1189.30	468.46

The selection has been based on the parameters introduced in the existing available strength formulations [59, 63], namely: $\beta = b_1/d_0$, $\gamma = d_0/(2t_0)$ and $\eta = h_1/d_0$ (where b_1 is the beam width, d_0 is the CHS diameter, t_0 is the thickness of the column and h_1 is the beam height). β varies between 0.47 and 0.70, γ between 15.28 and 33.87, while η between 1.02 and 1.55. The selected cases are reported in Table 2.7. The beams have been modelled with a length equal to 7.5 times the beam height to simulate the case of the span/depth ratio equal to 15. To perform many numerical simulations and assess both the stiffness and the flexural resistance of the analysed connections, the numerical models have been monotonically loaded with increasing displacements to the end of the beam up to the crisis of the connections. It is worth highlighting that no axial forces have been applied to the columns instead.

The primary outcomes of these analyses consist of moment-rotation curves (see Annex A) of the connections, which have been used to assess the joints' plastic initial stiffness. The main results of the FE study are reported in Table 2.7.

2.4.3.2 Column to through-all plate

According to the same approach reported in the previous paragraph, also referring to the connection between the tubular profile and the though plate, a systematic parametric analysis has been performed.

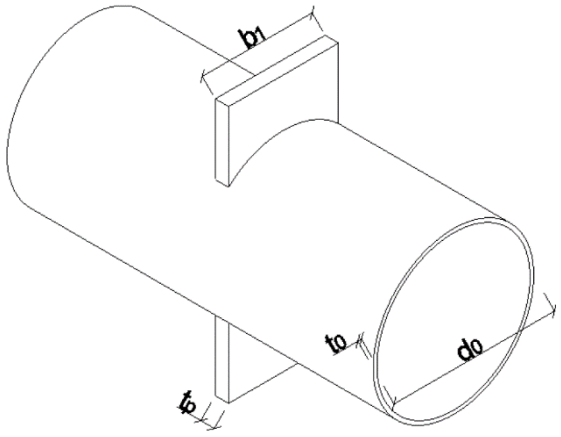

Figure 2.59 – Geometric parameters of the specimen

The objective is to investigate the broadest possible range of geometries, considering the variation of the non-dimensional parameters affecting the response of the joints, namely: i) τ, defined as the ratio between the plate and tube thicknesses (t_p and t_0); ii) β, defined as the ratio between the plate width (b_1) and tube diameter (d_0); iii) γ, defined as the ratio between the tube diameter and twice the tube thickness (Figure 2.59). The study shows that these are the main parameters affecting these joints' responses in terms of stiffness and resistance.

The analysis has concerned 61 connections, varying the parameters in the following ranges:

$$2 < \tau = \frac{t_p}{t_0} < 8.75$$
$$0.43 < \beta = \frac{b_1}{d_0} < 0.74 \quad (2.20)$$
$$15.65 < \gamma = \frac{d_0}{2t_0} < 32.33$$

All the simulations have been carried out considering an S355JR steel grade. Static analyses with a displacement-control approach have been performed, pushing the plate up to the crisis of the connection. The parametric study results are summarised in Table 2.8, where the cases investigated are reported and the plastic strength and initial stiffness values. The plastic strength of the CHS to through-all plate component has been defined, according to the rule suggested by EC3 part 1.5 [26], by evaluating the force corresponding to the achievement of plastic deformation of the material equal to 0.05. Conversely, the stiffness has been evaluated as the initial tangent value, clearing the tube's elastic flexural and shear deformability.

Table 2.8 – Parametric analysis (CHS/plate connection)

Test	d_0 [mm]	t_0 [mm]	b_1 [mm]	t_p [mm]	β	γ	τ	$F_{pl,joint}$ (kN)	k_{joint} (kN/mm)
1	193.7	6	120	20	0.62	16.14	3.33	645	1437
2	193.7	6	120	22.5	0.62	16.14	3.75	667	1587
3	193.7	6	120	25	0.62	16.14	4.17	694	1802
4	193.7	6	120	30	0.62	16.14	5	732	2159
5	193.7	6	120	35	0.62	16.14	5.83	773	2693
6	219.1	4	150	15	0.68	27.39	3.75	458	1149
7	219.1	4	150	20	0.68	27.39	5	490	1444
8	219.1	4	150	25	0.68	27.39	6.25	518	1800
9	219.1	4	150	30	0.68	27.39	7.5	546	2228
10	219.1	4	150	35	0.68	27.39	8.75	573	2882
11	244.5	8	160	25	0.65	15.28	3.13	1113	2287
12	244.5	8	160	30	0.65	15.28	3.75	1162	2704
13	244.5	8	160	32.5	0.65	15.28	4.06	1186	2930
14	244.5	8	160	35	0.65	15.28	4.38	1209	3216
15	244.5	8	160	40	0.65	15.28	5	1262	3767
16	406.4	10	200	20	0.49	20.32	2	1162	892
17	406.4	10	200	25	0.49	20.32	2.5	1228	948
18	406.4	10	200	30	0.49	20.32	3	1294	1001
19	406.4	10	200	35	0.49	20.32	3.5	1346	1084
20	193.7	6	105	25	0.54	16.14	4.17	619	1226
21	193.7	6	110	25	0.57	16.14	4.17	642	1418
22	193.7	6	115	25	0.59	16.14	4.17	674	1640
23	193.7	6	120	25	0.62	16.14	4.17	694	1802
24	193.7	6	125	25	0.65	16.14	4.17	736	2016
25	193.7	6	130	25	0.67	16.14	4.17	762	2281
26	219.1	4	120	25	0.55	27.39	6.25	397	819
27	219.1	4	130	25	0.59	27.39	6.25	432	1021
28	219.1	4	140	25	0.64	27.39	6.25	479	1370
29	219.1	4	150	25	0.68	27.39	6.25	518	1800
30	219.1	4	160	25	0.73	27.39	6.25	570	2493
31	244.5	8	140	25	0.57	15.28	3.13	970	1574
32	244.5	8	150	25	0.61	15.28	3.13	1035	1858
33	244.5	8	160	25	0.65	15.28	3.13	1113	2287
34	244.5	8	170	25	0.7	15.28	3.13	1202	2736
35	244.5	8	180	25	0.74	15.28	3.13	1289	3380
36	406.4	10	180	25	0.44	20.32	2.5	1117	760
37	406.4	10	190	25	0.47	20.32	2.5	1171	842
38	406.4	10	200	25	0.49	20.32	2.5	1228	948
39	406.4	10	210	25	0.52	20.32	2.5	1299	1053
40	406.4	10	220	25	0.54	20.32	2.5	1351	1196
41	219.1	4	120	20	0.55	27.39	5	377	691
42	219.1	4.5	120	22.5	0.55	24.34	5	445	826
43	219.1	5	120	25	0.55	21.91	5	513	997
44	219.1	5.5	120	27.5	0.55	19.92	5	587	1162
45	219.1	6	120	30	0.55	18.26	5	665	1343
46	219.1	6.5	120	32.5	0.55	16.85	5	748	1541
47	219.1	7	120	35	0.55	15.65	5	844	1831
48	273	4.5	170	18	0.62	30.33	4	514	860
49	273	5	170	20	0.62	27.3	4	592	1008
50	273	5.5	170	22	0.62	24.82	4	673	1170
51	273	6	170	24	0.62	22.75	4	771	1368
52	273	6.5	170	26	0.62	21	4	869	1571
53	273	7	170	28	0.62	19.5	4	962	1788

54	273	7.5	170	30	0.62	18.2	4	1062	2003
55	355.6	5.5	160	16.5	0.45	32.33	3	484	354
56	355.6	6	160	18	0.45	29.63	3	544	405
57	355.6	6.5	160	19.5	0.45	27.35	3	609	457
58	355.6	7	160	21	0.45	25.4	3	683	510
59	355.6	7.5	160	22.5	0.45	23.71	3	749	570
60	355.6	8	160	24	0.45	22.23	3	824	634
61	355.6	8.5	160	25.5	0.45	20.92	3	905	698

The outcomes of the simulations are relatively easy to interpret. In fact, for each of the selected parameters, both the joints' resistance and stiffness vary accordingly. As it is easy to observe both from Figure 2.60, a correlation has been observed between the stiffness/resistance of the joints and the parameters τ, β and γ. This can be easily understood by representing, for groups of homogeneous data, the joint resistance ($F_{pl,joint}$) divided by $f_y t_0^2$ *vs* the geometrical parameters τ, β and γ, individually. Similarly, representing the initial stiffness (S_{joint}) divided by Ed_0 *vs* the geometrical parameters τ, β and γ allows highlighting the dependence between the joint stiffness and the non-dimensional parameters. As shown in the next section, the resistance of this joint depends on the product of power functions of τ, β and γ, multiplied by $f_y t_0^2$ and the joint stiffness depends on the product of power functions of the significant parameters (τ, β and γ), multiplied by Ed_0. Therefore, representing the data in such a way allows highlighting the influence of the single parameters over $F_{joint}/f_y t_0^2$ and S_{joint}/Ed_0 allowing to understand the significance of the non-dimensional parameters over the joint strength, which is more relevant as soon as the exponent of the power function is higher.

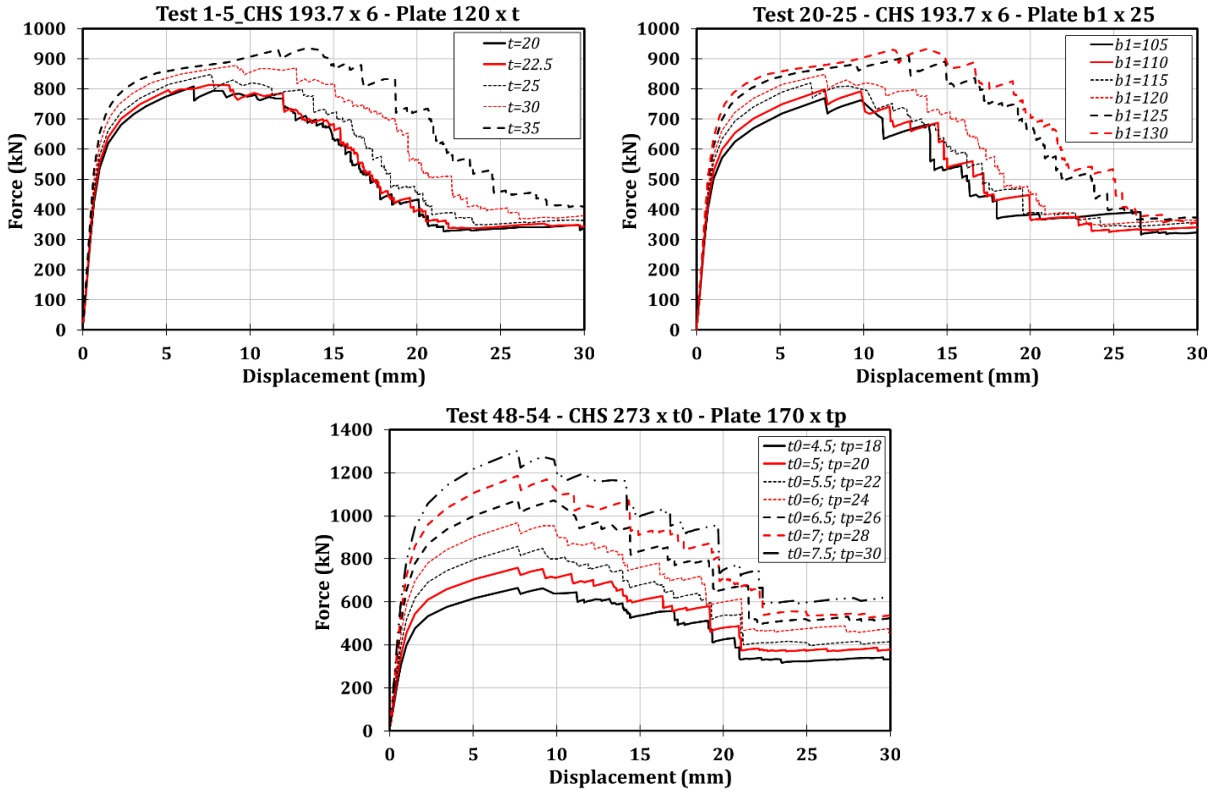

Figure 2.60 – Results of the parametric analysis

Specifically, the data of the parametric study show that $F_{joint}/f_y t_0^2$ and S_{joint}/Ed_0 increase when τ increases, according to a power-law with an exponent equal to about 0.3 and 1.12, respectively, as shown, for some of the cases, in Figure 2.61. This result is obvious considering that a τ increase corresponds to a relative increase of the plate thickness for the tube thickness.

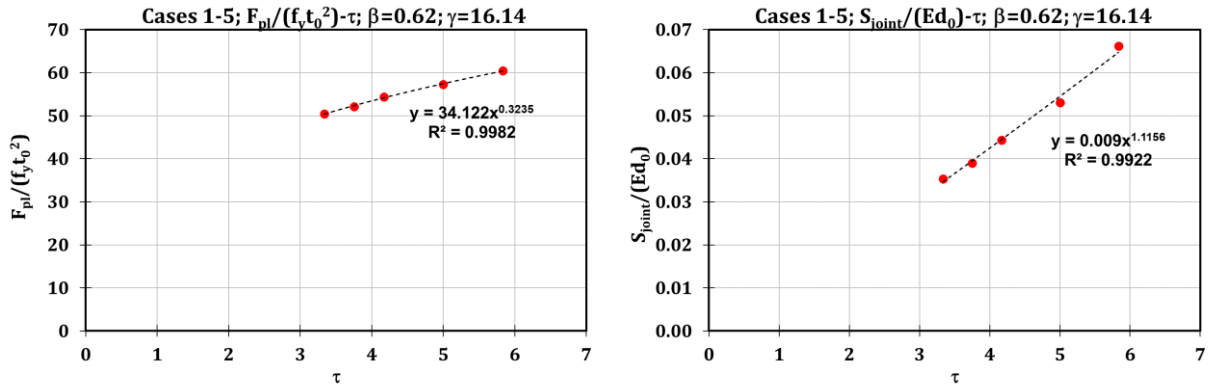

Figure 2.61 – Cases 1-5: $F_{pl}/(f_y t_0^2)$-τ (up) and $S_{joint}/(Ed_0)$-τ (down) laws when β=0.62 and γ=16.14

A similar trend can be observed considering β. In fact, when the plate width increases relatively to the tube diameter, the strength increases almost linearly. In this case, in the range of investigated data, when the results expressed in terms of $F_{joint}/f_y t_0^2$ and S_{joint}/Ed_0 are represented versus β, the regression with a power-law shows exponent of the functions equal to about 1 and 2.25, respectively, for all the considered cases (Figure 2.62).

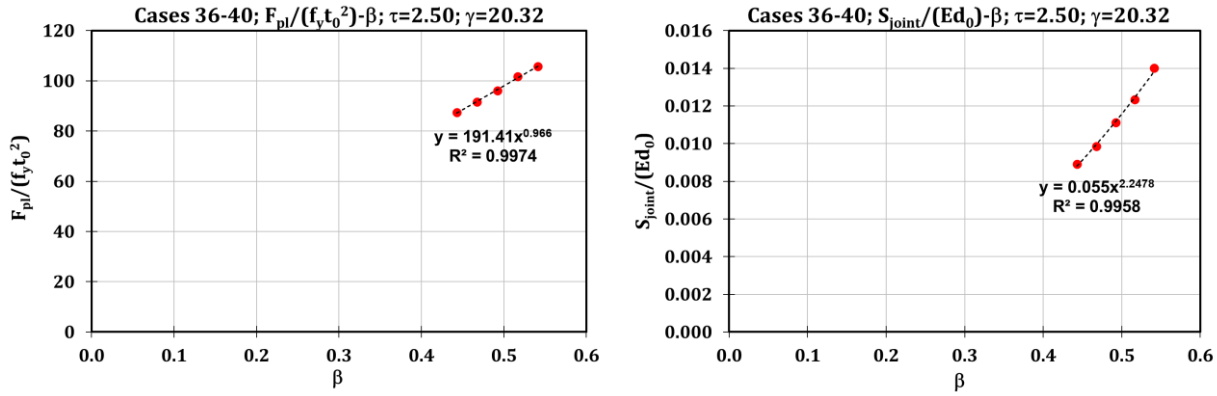

Figure 2.62 – Cases 36-40: $F_{pl}/(f_y t_0^2)$-β (up) and $S_{joint}/(Ed_0)$-β (down) laws when β=2.50 and γ =20.32

Finally, for what regards γ, $F_{joint}/f_y t_0^2$ and S_{joint}/Ed_0 increase and decrease, respectively, as soon as the non-dimensional parameter increases. In fact, if the data are represented for a group of cases with the same values of β and τ, it can be observed that $F_{joint}/f_y t_0^2$ increases according to a power-law with an exponent equal to about 0.6, while S_{joint}/Ed_0 decreases according to a power-law with an exponent equal to about -1.56 (Figure 2.63).

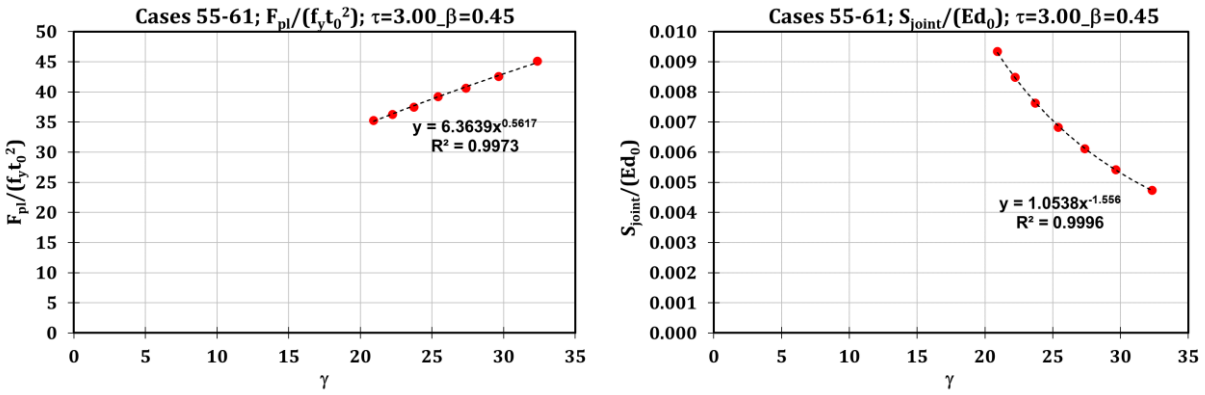

Figure 2.63 – Cases 55-61: $F_{pl}/(f_y t_0^2)$-γ (up) and $S_{joint}/(Ed_0)$-γ (down) laws when τ=3.00 and β =0.45

The main results are consistent with the data obtained from the parametric study. Overall, the parametric study concludes that the geometric parameters investigated are significant because they all affect the plastic strength and stiffness of the simulated specimens, particularly with a stronger correlation of the data to β (power equal to 1) and relatively weaker for γ and τ, referring to the strength.

2.4.4 Theoretical formulations

This section is devoted to developing the component method approach for the flexural characterization of the analysed connection typology.

This methodology allows obtaining the overall joint response starting from the mechanical behaviour of elementary components, which affect the strength and/or the deformability of the connection. The component method entails three conceptual steps [6, 14]: i) individuation of the single sources of strength and deformability of the connection (namely the joint components) based on experimental evidence, engineering judgement and FE modelling; ii) mechanical modelling of the single components in terms of strength and stiffness; iii) assembly of a mechanical spring model representative of the connection behaviour to get the overall stiffness and strength of the joint, starting from the response of the individual components.

In the case of joints with CHS columns and through-all members, the overall behaviour can be broken down into the following sources of deformability and resistance (Figure 2.64 and Figure 2.65):

- "*passing-through plate transversally welded to the column in tension/compression*" (*pct/pcc*): representing the response of the beam flange plates (in tension/compression) at the attachment with the column;
- "*CHS tube under localised transverse tension/compression*" (*ttt/ttc*): which accounts for the possible local failure of the tube due to the rigid rotation of the beam;
- "*CHS column in shear*" (*cs*): representing the part of the column subjected to localised shear forces transferred by the beam in the joint area;
- "*Beam web in shear*" (*bws*): representing the beam web subjected to localised shear forces transferred by the beam in the joint area.

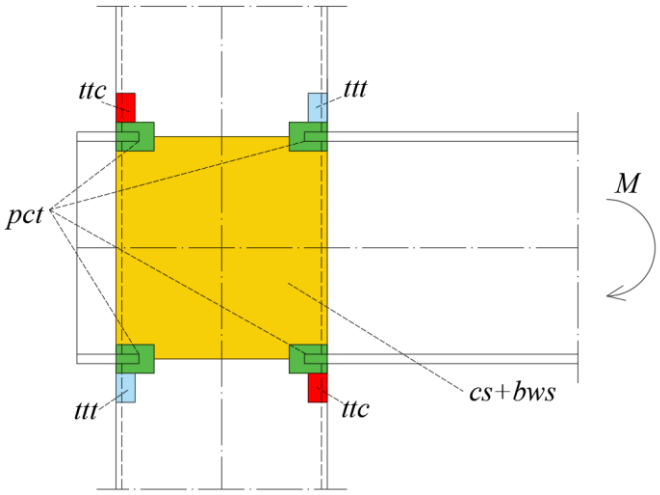

Figure 2.64 – Individuation of the joint components according to the component method philosophy

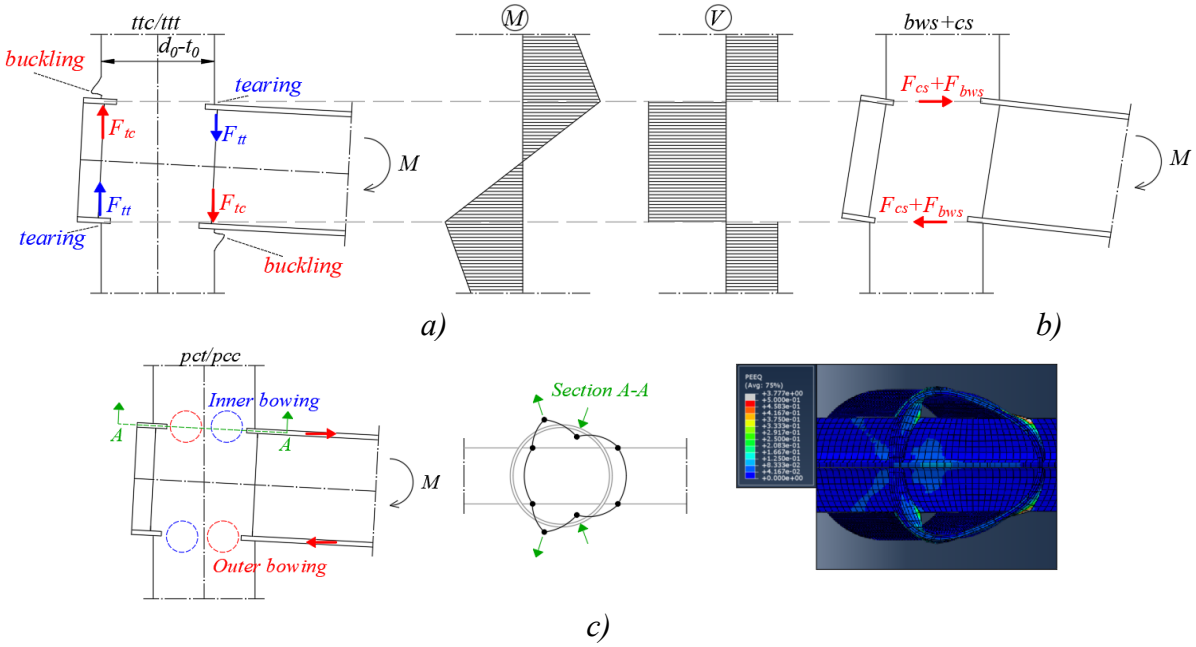

Figure 2.65 – Idealisation of the failure mode of the single components

The stiffness and strength of the third and fourth components (*cs* and *bws*) can be directly modelled by extending the equations available in EC3 part 1.8 [14], accounting for specific values of the shear area and shear factors. Conversely, the first and second components (*pct/pcc, ttt/ttc*), whose response is strongly affected by the local behaviour of the CHS tube, deserve to be separately modelled to account for their specificities.

2.4.4.1 Passing-through plate transversally welded to the column in tension/compression (pct/pcc)

2.4.4.1.1 Strength

Eurocode 3 part 1.8 [14] provides a formulation to predict the ultimate resistance of connections with beams welded on the outer face of the hollow section profile. This equation derives from the

model proposed by Togo [67] for externally welded branch plates and provides the flexural resistance of the connection by multiplying the axial strength in tension/compression of the branch plate by the beam height. However, the original study of Togo [67] cannot be easily extended to the case of through-all I-beams because the failure mode, as also shown from the experiments, is different. On this topic, Voth [59, 63] has carried out recent research to fill this knowledge gap. In particular, referring to experimental, numerical and theoretical studies, Voth [59, 63] has proposed a formulation to predict the chord failure resistance of connections with through-all plates, expressed as the addition of two terms, namely the resistance of the branch plate in tension, plus the strength of the branch plate in compression (Figure 2.66):

$$N_y = [2.46(1 + 3\beta^2)\gamma^{0,35} + 2.2(1 + 2.5\beta^2)\gamma^{0,55}]f_y t_0^2 \quad (2.21)$$

This relationship, as already shown by Voth [59, 63], in the case of through-all branch plates, provides results that are conservative underestimating, on average, the 21% connection strength.

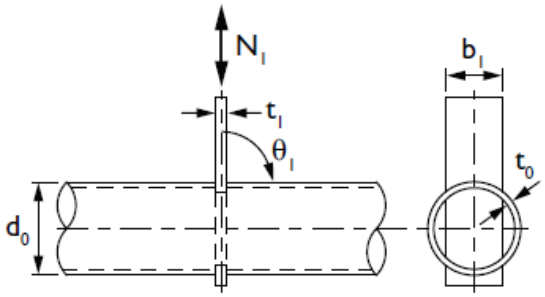

Figure 2.66 – Connection with through-all plate

Adopting the same approach proposed by EC3 part 1.8 [14] for joints with beams welded externally to the columns (extension of the formulation for transverse plates to beams), the equation proposed by Voth [59, 63] has been applied to the considered connections, by multiplying the resistance of the transverse plate joint (Eq. 2.21) by the beam depth:

$$M_{y,} = N_y h_1 \quad (2.22)$$

The resistance derived in this way has been compared with the parametric study results, evaluating the accuracy of this formulation. The comparison between the analytical and the numerical results shows that this equation significantly underestimates the resistance of the connections leading to an average ratio between FEM and predicted values equal to 0.55 with a coefficient of variation equal to 0.24 (Figure 2.67).

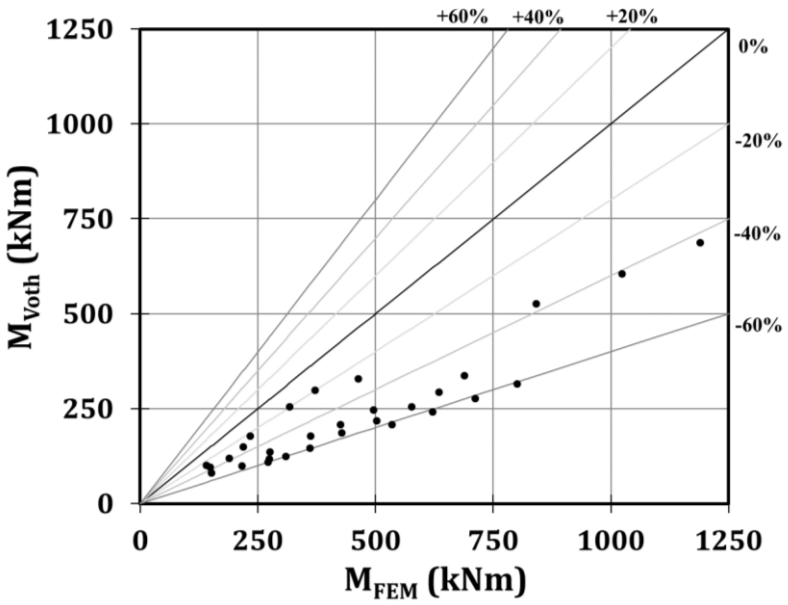

Figure 2.67 – Comparison of the results provided by the Voth and the FE models

The low mean value given in Table 2.9 does not imply that Voth's formulation is inaccurate; instead, it indicates that the current approach adopted by the Eurocode 3 part 1.8, consisting in assessing the flexural resistance by multiplying the axial strength of through plates by the distance between the flanges, is too conservative. This formulation proposed by Voth is currently implemented in the final draft of the new version of Eurocode 3 part 1.8 in the same way it has been applied before. Moreover, it is worth highlighting the difference, in terms of disclosed failure modes, between the Voth model and the FE models above described: while the model proposed by Voth refers to a connection between circular hollow section and through-all plate without experiencing bending, instead, referring to the present work, it is clear that bending moments have a relevant effect since the analysed connection is characterized by an I-section beam. In particular, it is expected that the connection can provide higher resistance, as the experimental and numerical activities have proved.

Table 2.9 – Parametric analysis and comparison with the Voth model [63]

Test	Column (diameter/thickness)	Beam	M (kNm) FEM	M (kNm) Voth	Voth/FEM
1	193,7/6	IPE240	140.01	104.39	0.75
2	219,1/4	IPE300	150.84	82.70	0.55
3	219,1/6	IPE240	148.18	98.31	0.66
4	219,1/6	IPE270	188.79	123.72	0.66
5	219,1/6	IPE300	218.92	153.77	0.70
6	219,1/6	IPE330	234.23	182.15	0.78
7	244,5/8	IPE330	317.89	263.36	0.83
8	244,5/8	IPE360	372.01	307.15	0.83
9	273/5	IPE300	216.31	103.44	0.48
10	273/5	IPE330	274.61	120.80	0.44
11	273/5	IPE360	275.42	139.93	0.51
12	273/8	IPE400	463.59	338.83	0.73
13	323,9/5	IPE330	271.71	112.81	0.42
14	323,9/5	IPE360	308.97	129.34	0.42
15	323,9/5	IPE400	361.20	151.10	0.42
16	323,9/6,3	IPE360	362.01	184.04	0.51
17	323,9/6,3	IPE400	425.42	215.02	0.51
18	323,9/6,3	IPE450	494.98	254.41	0.51
19	355,6/6	IPE400	428.38	192.50	0.45
20	355,6/6	IPE450	502.11	226.63	0.45
21	355,6/6	IPE500	576.99	263.61	0.46
22	355,6/6	IPE550	634.26	303.61	0.48
23	355,6/6	IPE600	688.23	346.81	0.50
24	406,4/6	IPE450	535.27	216.94	0.41
25	406,4/6	IPE500	620.95	250.66	0.40
26	406,4/6	IPE550	711.24	286.84	0.40
27	406,6/6	IPE600	801.12	325.64	0.41
28	406,4/10	IPE500	841.17	546.78	0.65
29	406,4/10	IPE550	1022.88	625.78	0.61
30	406,4/10	IPE600	1189.30	710.49	0.60
		Mean =			**0.55**
		Standard deviation =			**0.13**
		Coefficient of variation =			**0.24**

An analytical model based on the extension of the ring model by Togo [67] is presented, and, subsequently, simple design equations are proposed and validated against the FE results.
The flexural resistance of connections with CHS column externally welded to I-beams derives from the so-called ring model, which was initially proposed by Togo [67] but has been appropriately modified by [68-74] up to the current formulation suggested by EC3 part 1.8 [14]. The ring model deals with the study of a circular hollow section loaded with the axial forces transferred from the plate, and it is a bi-dimensional idealization of the problem which, in general, would be governed, at the achievement of the failure load, by the development of a three-dimensional pattern of yield lines.

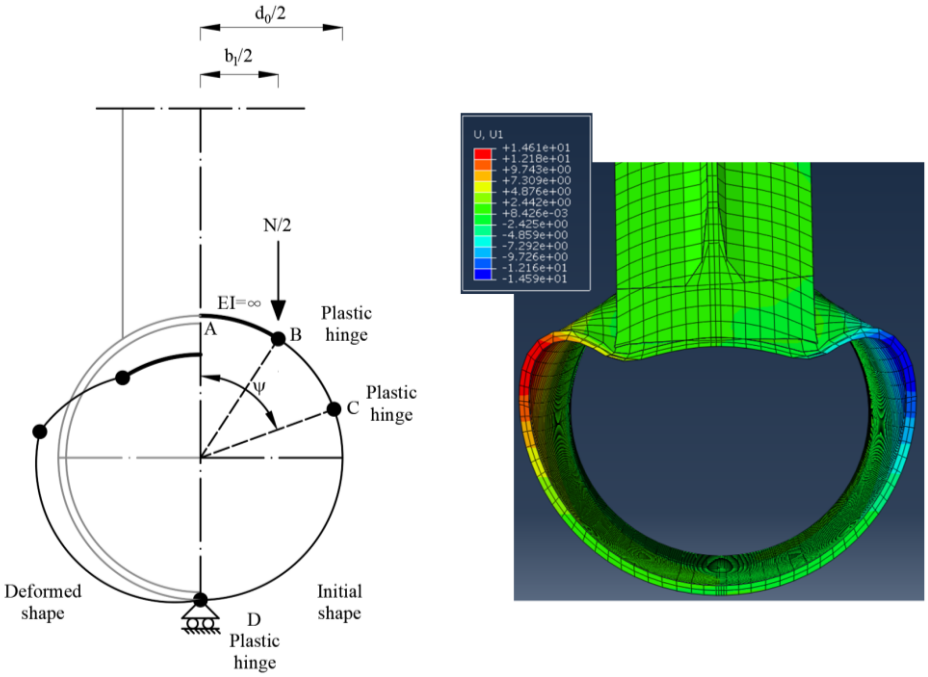

a) Distribution of plastic hinges according to Togo (1967)

b) Deformed shape of the tube (FE results)

Figure 2.68 – Ring model (Togo, 1967) and deformation of the tube (FE results)

As given in Figure 2.68, the scheme considered in the ring model proposed by Togo refers to half-tube externally constrained at point D with a roller and loaded by the branch plate at the connection saddle points with force equal to *N/2*. In this model, a plastic mechanism develops with the formation of two hinges on each side of the tube, but while hinge *B* is fixed at the connection saddle point, the location of hinge *C*, expressed by the ψ angle, is unknown. Therefore, in the Togo model, the position of hinge *C* is defined equating the external work provided by the force *N/2* and the internal work done by the plastic hinges, minimizing the energy dissipated for the given distribution of plastic hinges.

While Togo [67] developed this model neglecting the interaction among axial force (*A*), shear force (*V*) and bending moment (*M*), conversely, [68-74] updated the model accounting for *M-V-A* interaction, obtaining the following equation:

$$\frac{Nd_0}{t_0^2 f_{y,0} B_e} = \frac{4}{1-\beta+\sqrt{(1-\beta)^2+\frac{2-\beta^2}{\gamma^2}}} \tag{2.22}$$

B_e represents the equivalent width of the ring for which the energy dissipated by the actual yield line pattern is equal to the energy dissipated by the simplified bi-dimensional model. The effective length of the ring (B_e) has been calibrated by [63] based on the results of experimental tests and FE simulations, suggesting the following function:

$$B_e = R_1 \gamma^{R_2\beta - R_3\beta^2} \tag{2.23}$$

where R_1, R_2 and R_3 are regression coefficients. Based on the studies of [68-74], a simplified equation (Eq. 2.23) leads to the design equation, which is currently suggested by EC3 part 1.8 [14]:

$$N = (4 + 20\beta^2) f_y t_0^2 \frac{k_p}{\gamma_{M5}} \quad (2.24)$$

where k_p is a coefficient accounting for the influence of the axial force in the column, while γ_{M5} is a partial safety factor. More recently, Makino and Kurobane [45, 46] have proposed a recalibration of Eq. 2.24, introducing an additional exponential function, γ^c. The revised formulation is:

$$N = 2{,}2 C_f f_{y0} t_0^2 (1 + 6{,}8\beta^2) \gamma^{0,2}\, Q_f / \gamma_{M5} \quad (2.25)$$

where Q_f accounts for the axial load in the column and C_f depends on steel grade and it is equal to 1 for S355 steel grade. Eq. 2.25 is very similar to Eq. 2.21, proposed by Voth for through-all branch plates [59, 63]. Nevertheless, as previously shown, when extended to the case of beam-to-column joints with the CHS column and through I-beam, this equation cannot provide sufficient accuracy and needs to be modified appropriately.

For this reason, a new analytical model is proposed (Figure 2.69 and Figure 2.70). The model extends the original approach of Togo [67] to connections with through-all plates. The particularity of the model is due to the failure mechanism, which is varied to consider that, in the case of through-all plates, the two sides of the CHS column are mutually connected by the plate. Under this assumption, the formation of the failure mechanism requires the development of at least four plastic hinges on each side of the tube. This kinematic condition, which is necessary to develop a failure mechanism, is confirmed by the results of the FE analyses, which show that at the attainment of the failure load, consistently with this plastic hinge pattern, the distortion of the tube in the upper side is outwards, while in the lower side is inwards (Figure 2.69). Therefore, with the new given pattern of plastic hinges, the ring model proposed by Togo [67] can be updated appropriately to through-all plate connections, following the same steps. Therefore, the unknown angle (ψ), which defines the location of plastic hinges *C* and *D* can be found by equating the work done by the external forces *N/4,* which are located at the connection saddle points *B* and *E*, and the internal work done by the four plastic hinges.

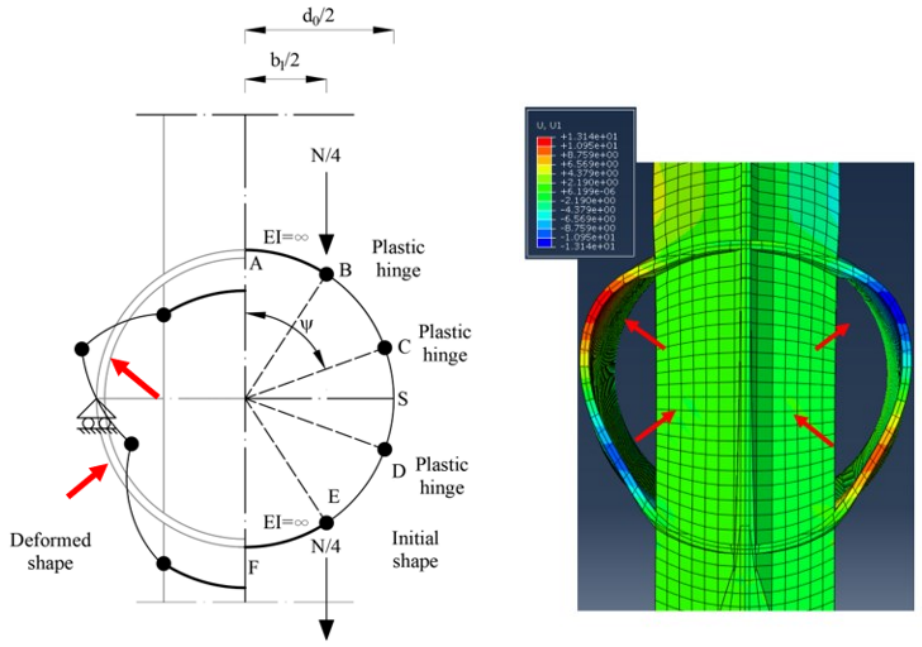

a) Assumed distribution of the plastic hinges

b) Deformed shape of the tube (FE results)

Figure 2.69 – Distribution of the plastic hinges

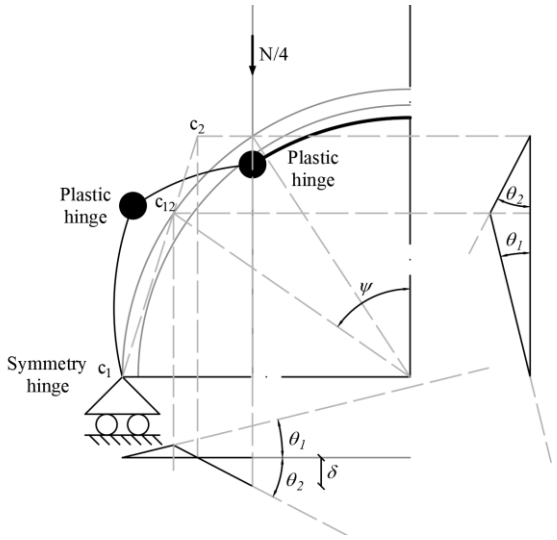

Figure 2.70 – Calculation of the plastic hinge rotations for an assigned displacement

In the mechanical model reported in Figure 2.70, for simplicity, reference is made to a quarter of the tube, properly exploiting symmetry conditions. Under these assumptions, the work done by the external force applied at the connection saddle point, for an assigned value of the plate displacement (δ), is equal to $(N\delta)/4$ and the work done by the plastic hinges depends on the rotations ϑ_1 and ϑ_2, which can be defined starting from kinematic conditions. Considering the scheme given in Figure 2.70, the internal and external works can be equated as follows:

$$\frac{N}{4}\delta = M_{pl,12}(\vartheta_1 + \vartheta_2) + M_{pl,2}\vartheta_2 \tag{2.26}$$

where $M_{pl,12}$ and $M_{pl,2}$ are the bending moments of the plastic hinges and ϑ_1, ϑ_2 and δ are three kinematic parameters that can be expressed as a function of angle ψ, β and R, which is the external radius of the tubular section:

$$\vartheta_1 = \frac{1}{R(1-\sin\psi)} \qquad \vartheta_2 = \frac{2}{R\dfrac{\sqrt{1-\beta^2}-\cos\psi}{\tan\left(\frac{\pi}{4}+\frac{\psi}{2}\right)}} \tag{2.27}$$

$$\delta = \frac{R\sin\psi - \dfrac{b_f}{2} - R\dfrac{\sqrt{1-\beta^2}-\cos\psi}{\tan\left(\frac{\pi}{4}+\frac{\psi}{2}\right)}}{R\dfrac{\sqrt{1-\beta^2}-\cos\psi}{\tan\left(\frac{\pi}{4}+\frac{\psi}{2}\right)}} \tag{2.28}$$

$M_{pl,12}$ and $M_{pl,2}$, in general, depend on the interaction between axial force (A), shear force (V), and bending moment (M) and, in this regard, different assumptions could be made. The level of accuracy of the solution has been tested, considering alternatively the adoption of a linear or square M-A interaction domain combined with a linear M-V domain highlighting that, in practical cases, the adoption of an interaction domain is not particularly beneficial. Therefore, without losing accuracy, the simplest solution can be derived by neglecting the influence of the interaction, assuming that $M_{pl,12} = M_{pl,2} = f_y \frac{t_0^2}{4} B_e$:

$$\frac{N}{4}\delta = f_y \frac{t_0^2}{4} B_e(\vartheta_1 + 2\vartheta_2) \tag{2.29}$$

where B_e is the effective width of the ring, which has to be calibrated based on experimental and FEM data. Therefore, the following solution can be found:

$$\frac{Nd_0}{t_0^2 f_{y,0} B_e} = \frac{\dfrac{2}{1-\sin\psi} + 4\dfrac{1}{\dfrac{\sqrt{1-\beta^2}-\cos\psi}{\tan\left(\frac{\pi}{4}+\frac{\psi}{2}\right)}}}{\sin\psi - \beta - \dfrac{\sqrt{1-\beta^2}-\cos\psi}{\tan\left(\frac{\pi}{4}+\frac{\psi}{2}\right)}} = g(\beta,\psi) \tag{2.30}$$

It is clear from Eq. 2.30 that finding the minimum value of the collapse load (N_y) means minimizing the right-hand side of the equation. Nevertheless, the function $g(\beta,\psi)$ is complex, and it is not easy to minimize in a closed form. Therefore, in this work, to obtain the value of the collapse load N_y, the function $g(\beta,\psi)$ has been minimized by adopting a numerical procedure. In particular, a user routine able to find an assigned value of β^* the corresponding angle ψ^*, by minimizing function $g(\beta,\psi)$, has been developed in Mathematica 5.1 [81]. Therefore, some cases have been generated by varying the variable β^* in the range of 0.45-0.70. From the obtained results, it has been verified that, for usual geometries, the angle individuating the position of the plastic hinge (ψ^*) varies only in a small range ($64° < \psi^* < 71°$). This limited variation of ψ^* allows to write the collapse load only as a function of β:

$$N_y = f_y \frac{t_0^2}{d_0} B_e k(\beta) \quad (2.31)$$

$$k(\beta) = \frac{c_1}{1-\beta^{c_2}} \quad (2.32)$$

where c_1 and c_2 are regression coefficients equal to 5.98 and 0.52 (R^2 equal to 0.99). Eq. 2.32 can be specialized to the case of through-all I-beam adopting the same approach proposed by the EC3 part 1.8 [14], namely by multiplying the resistance of the through-all branch plate by the beam depth (h_1):

$$M_y = f_y \frac{t_0^2}{d_0} B_e \frac{5.98}{1-\beta^{0.52}} h_1 \quad (2.33)$$

The value of the effective length B_e, which depends mainly on the three-dimensional pattern of yield lines, has been assessed by adopting the same approach suggested by [63], namely by performing a regression analysis of the experimental and FE data, expressing B_e as a function of β and γ:

$$F_{pl,joint} = \frac{5.98}{1-\beta^{0.52}} \frac{B_e}{d_0} f_y t_0^2 \quad (2.34)$$

where B_e is an effective length whose value depends mainly on the three-dimensional yield lines pattern. It can be numerically assessed by performing a regression study of the available FE data, expressing B_e/d_0 as a function of the significant non-dimensional parameters τ, β and γ:

$$\frac{B_e}{d_0} = c_1 \beta^{c_2} \gamma^{c_3} \tau^{c_4} \quad (2.35)$$

Based on this formulation, starting from the parametric analysis results, a regression study has been carried out calibrating the unknown coefficients as follows: c1=0.24, c2=-0.41, c3=0.43, c_4=0.47, which provides a coefficient of variation equal to 0.05. Consequently, the final design formula can be written as:

$$F_{pl,joint} = 0.24 \beta^{-0.41} \gamma^{0.43} \tau^{0.47} \frac{5.98}{1-\beta^{0.52}} f_y t_0^2 \quad (2.36)$$

The accuracy of the proposed equation is reported in Figure 2.71. The average ratio between the FE/analytical prediction is equal to 0.98, with a coefficient of variation equal to about 5%, proving a high accuracy of the formulation in a wide range of the investigated parameters and many cases. In order to show the high accuracy of the formula, it is also compared with the accuracy of the equation proposed by Voth, applicable to the connection typology considered above, which provides a mean accuracy equal to 0.68, with a CoV equal to 0.17.

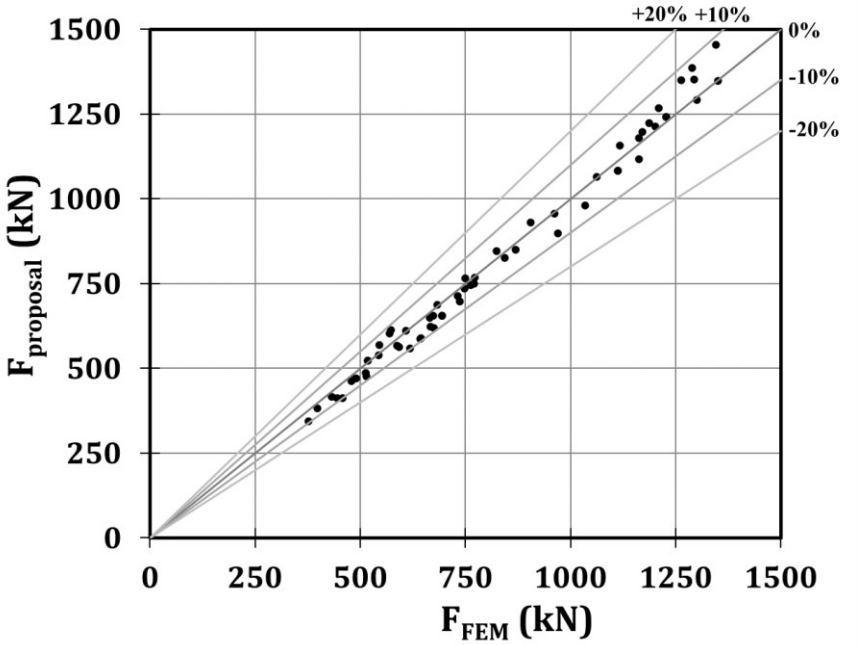

Figure 2.71 – Comparison of the strength provided by the proposed formulation and the FE models

It is worth highlighting that the experimental tests and the numerical simulations have been carried out without axial loads in the column. Nevertheless, the influence of the axial force could be considered through the extra parameter, Q_f, proposed by Eurocode 3 part 1.8. However, the influence of such a factor on the strength of the analysed beam-to-column connections is limited in typical design cases.

2.4.4.1.2 Stiffness

In order to develop a formulation for the calculation of the stiffness of the analysed component, first of all, a closed-form solution of the 2D scheme described in Figure 2.72 has been identified: guided supports have been considered at the plate to column attachments, while an external roller has been placed at the middle of the studied arch (Figure 2.73). This scheme is analogous to that considered for strength prediction. Furthermore, since the scheme is hyperstatic, the virtual work principle is adopted to assess the reactions at the restrains.

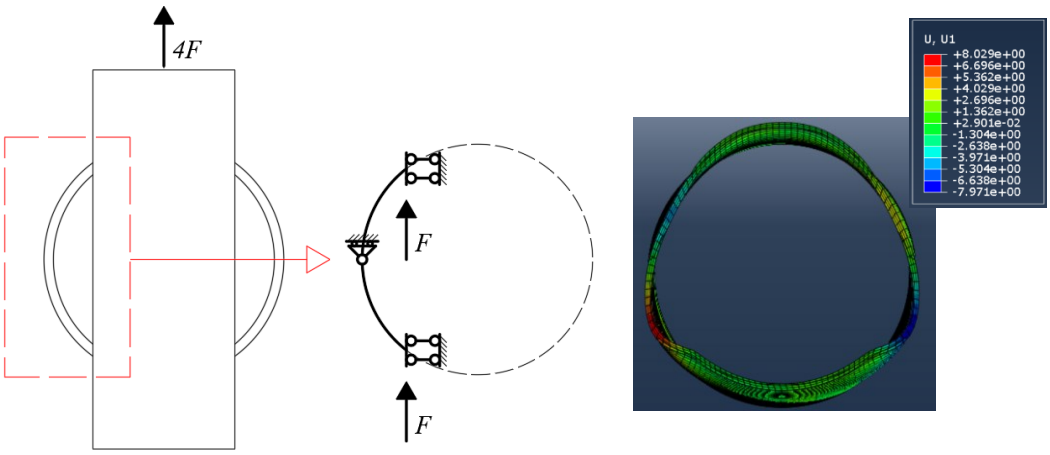

Figure 2.72 – Simplified scheme to assess the stiffness of the analysed component and corresponding FE model

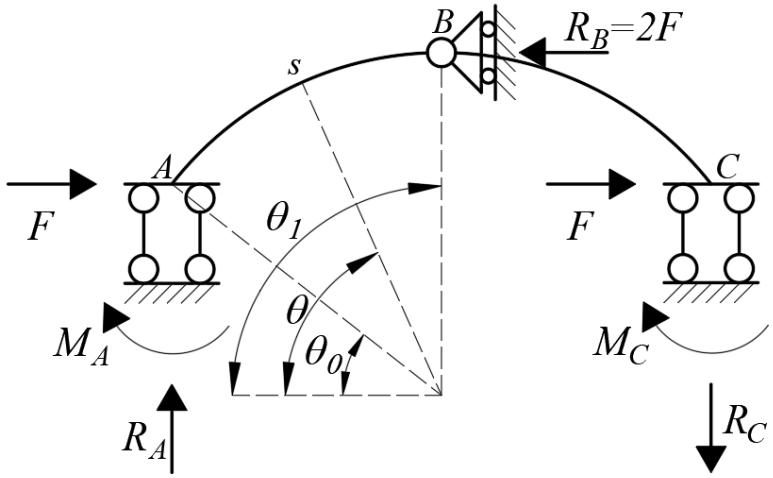

Figure 2.73 – A 2D scheme to assess the stiffness of the analysed component

Once the reactions are known, it is possible to define the deformability of the tube thanks to Clapeyron's theorem, namely:

$$1 \cdot \delta_A = \int_C M^s \, \theta^s \, dz + \int_C T^s \, \gamma^s \, dz + \int_C N^s \, \varepsilon^s \, dz \qquad (2.37)$$

$$\delta_A = \frac{d_0}{2\,E\,I}\int_{\vartheta_0}^{\vartheta_1} [X - F\frac{d_0}{2}(\sin\vartheta - \sin\vartheta_0) + R_A\frac{d_0}{2}(\cos\vartheta_0 - \cos\vartheta)]^2 d\vartheta + \frac{d_0\,\chi}{2\,G\,A}\int_{\vartheta_0}^{\vartheta_1} [F\frac{(1-\sin\vartheta_0)}{\cos\vartheta_0}\sin\vartheta - F\cos\vartheta]^2 d\vartheta + \frac{d_0}{2\,E\,A}\int_{\vartheta_0}^{\vartheta_1} [-F\frac{(1-\sin\vartheta_0)}{\cos\vartheta_0}\cos\vartheta - F\sin\vartheta]^2 d\vartheta$$

Solving the integral Eq. 2.37, it is possible to obtain the displacement induced by a unitary force so that the stiffness k_{2D} of the component can be expressed as:

$$k_{2D} = 4\frac{F}{\delta_A} \tag{2.38}$$

The closed-form is too complex for practical application (see Annex A) and, therefore, a simplified equivalent formulation has been derived. It was verified that a formulation that can interpret rather faithfully the analytical results deriving from the resolution of Eq. 2.37 can be written in the following form:

$$k_{2D} = E\frac{c_2\gamma^{c_3}}{\beta^{c_1} - 1} \tag{2.39}$$

where k_{2D} is the stiffness of a tube with unitary width, and c_1, c_2 and c_3 are regression parameters calibrated on the closed-form solution of the previous equation (see Annex A). Eq. 2.39 returns an accurate prediction of the stiffness of the 2D scheme previously described for any geometry, with regression coefficients equal to c_1=-2.61, c_2=259.49, c_3=-2.87 (with R^2=1).

Similarly to the strength model, the final equation for the stiffness prediction has been defined by evaluating an appropriate value of the effective width for stiffness calculation as a function of the three non-dimensional parameters β, γ, τ:

$$k_{3D} = EB_{eff,st}\frac{c_2\gamma^{c_3}}{\beta^{c_1} - 1} \tag{2.40}$$

$$\frac{B_{eff,st}}{d_0} = c_4\beta^{c_5}\gamma^{c_6}\tau^{c_7} \tag{2.41}$$

A regression study of the numerical data has been performed in order to evaluate $B_{eff,st}$. It has allowed identifying the values of the regression coefficients: c_4=0.037, c_5=-1.17, c_6=0.45, c_7=1.31, leading to the final formula for the stiffness prediction of connections with through-all plates and CHS tubes loaded in tension/compression:

$$k_{3D} = Ed_0c_4 \cdot \beta^{c_5} \cdot \gamma^{c_6} \cdot \tau^{c_7}\frac{c_2\gamma^{c_3}}{\beta^{c_1} - 1} \tag{2.42}$$

Referring to Figure 2.74, it is possible to highlight that the proposed formulation can predict the stiffness of CHS to through-plate connections with satisfactory accuracy; in fact, the mean value of the FE/predicted ratio is equal to 1.00, with a standard deviation and a coefficient of variation both equal to about 0.18.

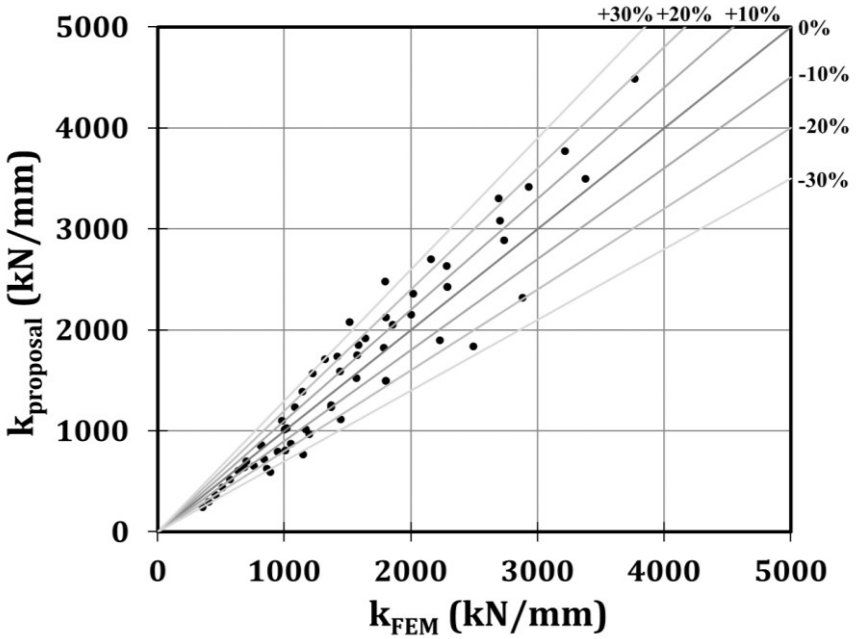

Figure 2.74 – Comparison of the stiffness provided by the proposed formulation and the FE models

2.4.4.2.3 Cyclic behaviour

In order to define the cyclic behaviour of the analysed component, 44 of the 61 models numerically investigated through the adoption of monotonic loading have been exploited to perform cyclic analyses (Table 2.10).

The simulations have been exploited to calibrate the parameters of the *hysteretic uniaxialmaterial* belonging to the OpenSees [82] library through the MultiCal tool [83]. The employed tool relies on adopting Genetic-Algorithms to minimize the scatters between the reference force-displacement curves and those derived by using the *hysteretic* material. This calibration is based on a multi-objective optimization that uses the concepts of mutation and crossover and random variability to generate populations that, step by step, allow the optimal configuration of the parameters. For clarity, the parameters of the hysteretic model are reported in Table 2.11 and Figure 2.75.

Table 2.10 – Parametric analysis: cyclic simulations

Test	d_0 (mm)	t_0 (mm)	b_1 (mm)	t_p (mm)	β	γ	τ
1	193.7	6	120	20	0.62	16.14	3.33
2	193.7	6	120	22.5	0.62	16.14	3.75
3	193.7	6	120	25	0.62	16.14	4.17
4	193.7	6	120	30	0.62	16.14	5.00
5	193.7	6	120	35	0.62	16.14	5.83
6	219.1	4	150	15	0.68	27.39	3.75
7	219.1	4	150	20	0.68	27.39	5.00
8	219.1	4	150	25	0.68	27.39	6.25
9	219.1	4	150	30	0.68	27.39	7.50
10	219.1	4	150	35	0.68	27.39	8.75
11	244.5	8	160	25	0.65	15.28	3.13
12	244.5	8	160	30	0.65	15.28	3.75
13	244.5	8	160	32.5	0.65	15.28	4.06
14	244.5	8	160	35	0.65	15.28	4.38
15	244.5	8	160	40	0.65	15.28	5.00
16	406.4	10	200	20	0.49	20.32	2.00
17	406.4	10	200	25	0.49	20.32	2.50
18	406.4	10	200	35	0.49	20.32	3.50
19	193.7	6	105	25	0.54	16.14	4.17
20	193.7	6	110	25	0.57	16.14	4.17
21	193.7	6	115	25	0.59	16.14	4.17
22	193.7	6	120	25	0.62	16.14	4.17
23	193.7	6	125	25	0.65	16.14	4.17
24	193.7	6	130	25	0.67	16.14	4.17
25	219.1	4	120	25	0.55	27.39	6.25
26	219.1	4	130	25	0.59	27.39	6.25
27	219.1	4	140	25	0.64	27.39	6.25
28	219.1	4	150	25	0.68	27.39	6.25
29	219.1	4	160	25	0.73	27.39	6.25
30	244.5	8	140	25	0.57	15.28	3.13
31	244.5	8	150	25	0.61	15.28	3.13
32	244.5	8	160	25	0.65	15.28	3.13
33	244.5	8	170	25	0.70	15.28	3.13
34	244.5	8	180	25	0.74	15.28	3.13
35	406.4	10	180	25	0.44	20.32	2.50
36	406.4	10	190	25	0.47	20.32	2.50
37	406.4	10	200	25	0.49	20.32	2.50
38	406.4	10	210	25	0.52	20.32	2.50
39	406.4	10	220	25	0.54	20.32	2.50
40	219.1	4	120	20	0.55	27.39	5.00
41	219.1	4.5	120	22.5	0.55	24.34	5.00
42	219.1	5	120	25	0.55	21.91	5.00
43	219.1	5.5	120	27.5	0.55	19.92	5.00
44	219.1	6.5	120	32.5	0.55	16.85	5.00

Table 2.11 – Parameters of the hysteretic model

Parameters	
s1p and *e1p*	force and displacement at 1st point of the envelope in the positive direction
s2p and *e2p*	force and displacement at 2nd point of the envelope in the positive direction
s3p and *e3p*	force and displacement at 3rd point of the envelope in the positive direction
s1n and *e1n*	force and displacement at 1st point of the envelope in the negative direction
s2n and *e2n*	force and displacement at 2nd point of the envelope in the negative direction
s3n and *e3n*	force and displacement at 3rd point of the envelope in the negative direction
pinchx	pinching factor for deformation during reloading
pinchy	pinching factor for force during reloading
damage1	damage due to ductility
damage2	damage due to energy
beta	power used to determine the degraded unloading stiffness based on ductility

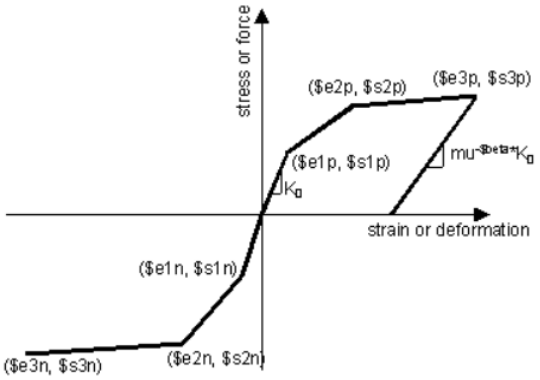

Figure 2.75 – Hysteretic uniaxialmaterial (by OpenSeesWiki)

In particular, it is worth highlighting that a symmetric behaviour of the hysteretic model has been assumed to reduce the parameters to be calibrated (*s1n=-s1p*, *e1n=-e1p*, etc.). Furthermore, *s1p* and *e1p* have been defined as reported in Eq. 2.43 and Eq. 2.44.

$$s1p = F_{pcc/pct} = 0.24\beta^{-0.41}\gamma^{0.43}\tau^{0.47}\frac{5.98}{1-\beta^{0.52}}f_y t_0^2 \tag{2.43}$$

$$e1p = \frac{\frac{2}{3}s1p}{k_{pcc/pct}} \tag{2.44}$$

In Eq. 2.43 and Eq. 2.44, f_y is the material yield strength, $F_{c/t}$ and $k_{c/t}$ are the strength and stiffness of the analysed component assessed through the studies concerning the monotonic behaviour of the joint.
Instead, *damage1* and *beta* have been assumed equal to 0, while *e2p* and *e3p* have been fixed equal to the maximum displacement of the FE simulations.
The accuracy of the following approach is highlighted in Figure 2.76.

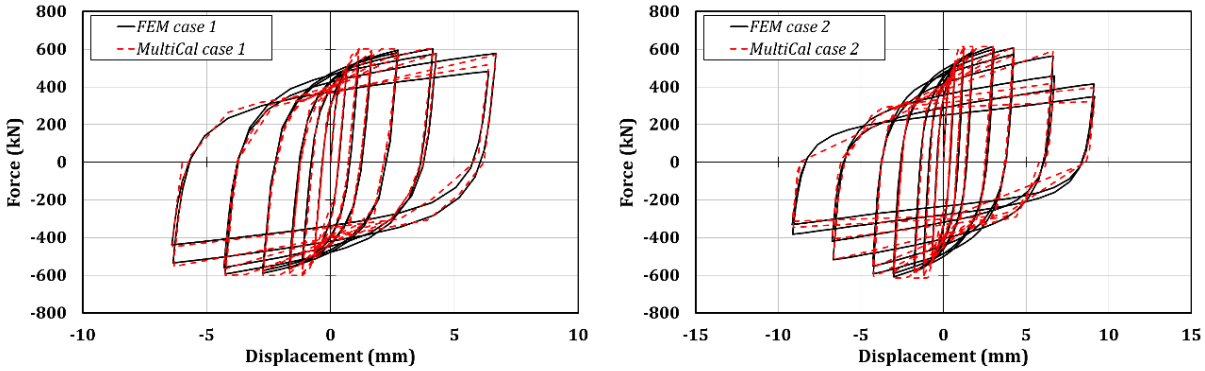

Figure 2.76 – Calibration of the hysteretic model referred to the cases 1 and 2 through MultiCal

The parametric analysis results have allowed defining formulations to predict the following parameters: *s2p=s3p, e2p, e3p, pinchx, pinchy*, and *damage2*. The regression analyses led to Eqs. 2.45-2.50.

$$s2p = s1p \cdot \beta^{-0.068}\gamma^{0.214}\tau^{-0.06} \quad (2.45)$$

$$e2p = e1p \cdot (3.6 \cdot \beta - 0.014 \cdot \gamma + 1.05 \cdot \tau) \quad (2.46)$$

$$e3p = e1p \cdot (50.5 \cdot \beta - 1.24 \cdot \gamma + 4.88 \cdot \tau) \quad (2.47)$$

$$pinchx = 0.094 \cdot \beta + 0.005 \cdot \gamma - 0.01 \cdot \tau \quad (2.48)$$

$$pinchy = \beta^{0.177}\gamma^{-0.206}\tau^{0.058} \quad (2.49)$$

$$damage2 = \beta^{1.25}\gamma^{-0.36}\tau^{-0.524} \quad (2.50)$$

2.4.4.2 CHS tube under localised transverse compression (ttc)

This component was introduced after observing the results of the experimental tests.

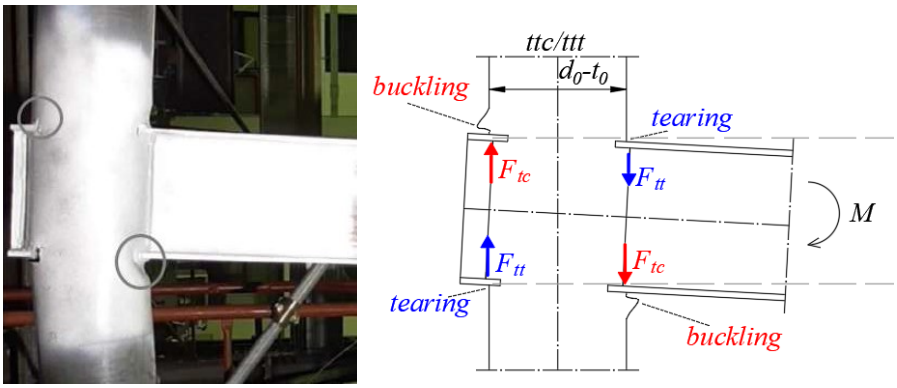

Figure 2.77 – Crisis of the tube under localised transverse compression

In particular, the experimental outcomes have highlighted that the column parts close to the flange-to-column attachment experience buckling or tearing phenomena if they are respectively loaded in compression or tension. For this reason, the introduction of the components labelled as *ttc* and *ttt* has been justified. In order to study these components, a parametric analysis has been carried out through the adoption of numerical models developed in Abaqus. 31 simulations have been performed on a CHS to through-all plate connection by applying displacements along the plate

face in the direction of the longitudinal axis of the column, as reported in Figure 2.78. The analysed cases have adequately been selected to investigate a range of geometric properties varying between 0.44 and 0.72 for the parameter β and 13.69 and 39.51 for the parameter γ.

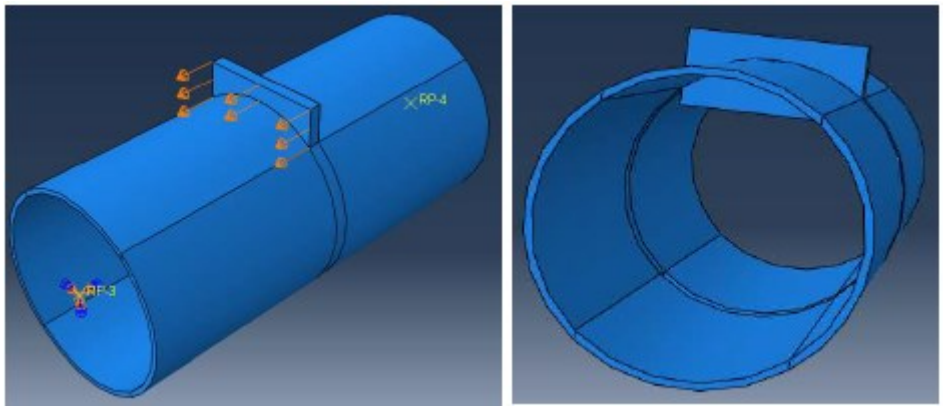

Figure 2.78 – Detail of the loaded part of the connection

The buckling analysis has been performed to apply the imperfections proposed by the Eurocode (Figure 2.79).

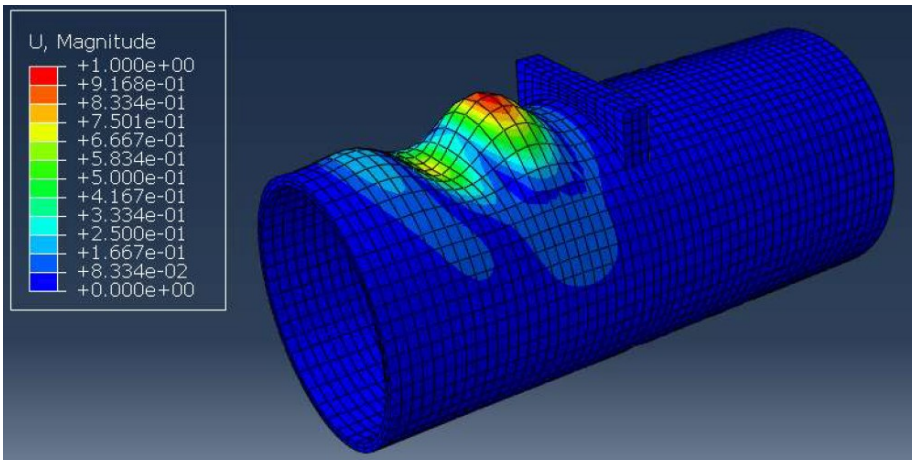

Figure 2.79 – Considered buckling mode

2.4.4.2.1 Strength

With the same approach used for the previous numerical simulations, in this case, the resistance of each analysed case has been assessed at the attainment of a plastic deformation equal to 0.05. The results are reported in Table 2.12.

Table 2.12 – Strength (component *ttc*)

Test	d_0 (mm)	t_0 (mm)	b_1 (mm)	β	γ	F_{FEM} (kN)
1	193.7	6	110	0.57	16.14	383.94
2	193.7	6	120	0.62	16.14	412.43
3	193.7	6	130	0.67	16.14	444.30
4	193.7	6	140	0.72	16.14	475.57
5	219.1	4	120	0.55	27.39	268.08
6	219.1	4	130	0.59	27.39	292.99
7	219.1	4	140	0.64	27.39	308.86
8	219.1	4	150	0.68	27.39	328.90
9	244.5	8	140	0.57	15.28	617.60
10	244.5	8	150	0.61	15.28	654.46
11	244.5	8	160	0.65	15.28	694.07
12	244.5	8	170	0.70	15.28	738.24
13	406.4	10	180	0.44	20.32	925.50
14	406.4	10	190	0.47	20.32	964.56
15	406.4	10	200	0.49	20.32	1008.38
16	406.4	10	210	0.52	20.32	1049.22
17	219.1	4	120	0.55	27.39	278.75
18	219.1	5	120	0.55	21.91	348.85
19	219.1	6	120	0.55	18.26	403.65
20	219.1	7	120	0.55	15.65	493.07
21	219.1	8	120	0.55	13.69	565.01
22	273	4.5	170	0.62	30.33	402.51
23	273	5.5	170	0.62	24.82	492.90
24	273	6.5	170	0.62	21.00	586.83
25	273	7.5	170	0.62	18.20	679.07
26	273	8.5	170	0.62	16.06	772.04
27	355.6	4.5	160	0.45	39.51	378.53
28	355.6	5.5	160	0.45	32.33	456.11
29	355.6	6.5	160	0.45	27.35	549.72
30	355.6	7.5	160	0.45	23.71	635.93
31	355.6	8.5	160	0.45	20.92	722.64

The graphs reported in the corresponding annex highlight that the strength of this component depends on β according to an exponential law with an exponent varying between 0.56 and 0.80, while referring to γ the exponent varies between -1,11 and -1.16. For this reason, a regression analysis has been performed considering the dimensionless parameters $F_{max}/(b_1 t_0 f_y)$, β and γ. The following equation has been obtained:

$$F_{ttc} = \beta^{0.46} \gamma^{0.2} b_1 t_0 f_y \tag{2.51}$$

The obtained equation is accurate, as is reported in Table 2.13.

Table 2.13 – Strength (component *ttc*): validation

Test	F_{FEM} (kN)	F_{prev} (kN)	Prev/FEM
1	385.31	312.21	0.81
2	411.31	354.43	0.86
3	440.21	398.30	0.90
4	467.74	443.74	0.95
5	260.37	247.76	0.95
6	275.81	278.42	1.01
7	292.57	310.19	1.06
8	306.81	343.01	1.12
9	613.14	526.13	0.86
10	644.69	581.80	0.90
11	676.77	639.20	0.94
12	712.10	698.26	0.98
13	793.38	795.03	1.00
14	816.17	860.23	1.05
15	842.91	927.02	1.10
16	864.04	995.36	1.15
17	241.89	247.76	1.02
18	308.92	296.42	0.96
19	372.72	343.20	0.92
20	451.36	388.46	0.86
21	522.80	432.46	0.83
22	365.44	427.25	1.17
23	458.08	502.02	1.10
24	554.22	574.15	1.04
25	651.41	644.13	0.99
26	750.39	712.29	0.95
27	297.91	364.99	1.23
28	374.59	428.86	1.14
29	453.79	490.48	1.08
30	538.53	550.26	1.02
31	624.60	608.49	0.97
	Mean		1.00
	Standard deviation		0.104
	Coefficient of variation		0.104

2.4.4.2.2 Stiffness

For each of the previously 31 cases, the stiffness has been assessed at the attainment of the $2F_{ttc}/3$. A regression analysis has been carried out considering the dimensionless parameters $k_{FEM}/(b_1 E)$, β and γ, obtaining Eq. 2.52. In Table 2.14, the accuracy of the derived equation is proven. In fact, the coefficient of variation of the predicting results against the FE outcomes is about 14%.

$$k_{ttc} = b_1 E \beta^{0.22} \gamma^{-0.8} \quad (2.52)$$

Table 2.14 – Stiffness (component *ttc*): validation of the stiffness formulation

Test	k_{FEM} [N/mm]	k_{prev} [N/mm]	Prev/FEM
1	2669973	2176253	0.82
2	2836234	2420718	0.85
3	3040961	2669784	0.88
4	3278204	2923173	0.89
5	1521235	1539651	1.01
6	1609283	1698065	1.06
7	1703291	1859228	1.09
8	1769345	2022986	1.14
9	3383171	2899806	0.86
10	3560892	3155217	0.89
11	3757766	3414466	0.91
12	4015597	3677363	0.92
13	2909890	2799625	0.96
14	2931171	2991089	1.02
15	2944675	3184819	1.08
16	2907151	3380727	1.16
17	2192166	1539651	0.70
18	1872032	1842133	0.98
19	2168739	2132891	0.98
20	2859602	2414249	0.84
21	3371274	2687802	0.80
22	1617685	2067695	1.28
23	2076532	2429628	1.17
24	2568008	2778803	1.08
25	3070647	3117552	1.02
26	3588121	3447527	0.96
27	1103192	1463307	1.33
28	1399880	1719447	1.23
29	1736309	1966558	1.13
30	2130192	2206290	1.04
31	2529651	2439813	0.96
		Mean	1.00
		Standard deviation	0.144
		Coefficient of variation	0.144

2.4.4.3 CHS tube under localised transverse tension (ttt)

2.4.4.3.1 Strength

The same approach adopted for *ttc* has also been applied for the tension component (Table 2.15): *ttt*.

$$F_{ttt} = \beta^{0.12}\gamma^{0.16}b_1 t_0 f_y \quad (2.53)$$

Table 2.15 – Strength (component *ttt*): validation

Test	F_{FEM} (kN)	F_{prev} (kN)	Prev/FEM
1	383.94	343.97	0.90
2	412.43	379.18	0.92
3	444.30	414.76	0.93
4	475.57	450.66	0.95
5	268.08	271.42	1.01
6	292.99	296.88	1.01
7	308.86	322.58	1.04
8	328.90	348.50	1.06
9	617.60	579.10	0.94
10	654.46	625.64	0.96
11	694.07	672.55	0.97
12	738.24	719.81	0.98
13	925.50	945.15	1.02
14	964.56	1004.17	1.04
15	1008.38	1063.57	1.05
16	1049.22	1123.32	1.07
17	278.75	271.42	0.97
18	348.85	327.19	0.94
19	403.65	381.16	0.94
20	493.07	433.69	0.88
21	565.01	485.00	0.86
22	402.51	446.66	1.11
23	492.90	528.40	1.07
24	586.83	607.74	1.04
25	679.07	685.12	1.01
26	772.04	760.84	0.99
27	378.53	422.01	1.11
28	456.11	499.24	1.09
29	549.72	574.20	1.04
30	635.93	647.31	1.02
31	722.64	718.85	0.99
	Mean		1.00
	Standard deviation		0.066
	Coefficient of variation		0.066

2.4.4.3.2 Stiffness

The stiffness of the CHS tube under the localised transverse tension component has assumed equal to the stiffness of the *ttc* component.

2.4.4.4 CHS column in shear (cs)

This component can be modelled through an elastic-plastic behaviour which can be characterized only by the definition of the stiffness and strength parameters. The strength and stiffness formulations referred to the circular hollow section in shear have been directly obtained by Eurocode 3.

2.4.4.4.1 Strength

In particular, resistance is defined as:

$$F_{cs} = \frac{0.9 A_{vc} f_y}{\sqrt{3}\beta_v} \tag{2.54}$$

where A_{vc} is the shear area of the tubular profile ($A_{vc} = 2A/\pi$), f_y is the yield stress and β_v depends on the type of connection and is equal to $\beta_v = 1 - \frac{h_b - t_f}{L_c}$.

2.4.4.4.2 Stiffness

According to Eurocode 3, the stiffness of this component is equal to:

$$k_{cs} = \frac{\chi A_{vc} G}{(h_b - t_f)\beta_v} \tag{2.55}$$

2.4.4.5 Beam web in shear (bws)

The same approach adopted for the column in shear has been applied to the beam web in shear.

2.4.4.5.1 Strength

In this case:

$$F_{bws} = \frac{0.9 A_{vb} f_y}{\sqrt{3}\beta_v} \tag{2.56}$$

where A_{vb} is the shear area of the beam web ($A_{vb} = d_0 t_{bw}$).

2.4.4.5.2 Stiffness

According to Eurocode 3, the stiffness of this component is equal to:

$$k_{bws} = \frac{\chi A_{vb} G}{(h_b - t_f)\beta_v} \tag{2.57}$$

2.4.4.6 Component method approach

The components analysed in the previous sections have been used to develop a component method approach to assess the flexural behaviour of connections between CHS columns and through-all double-tee profiles.

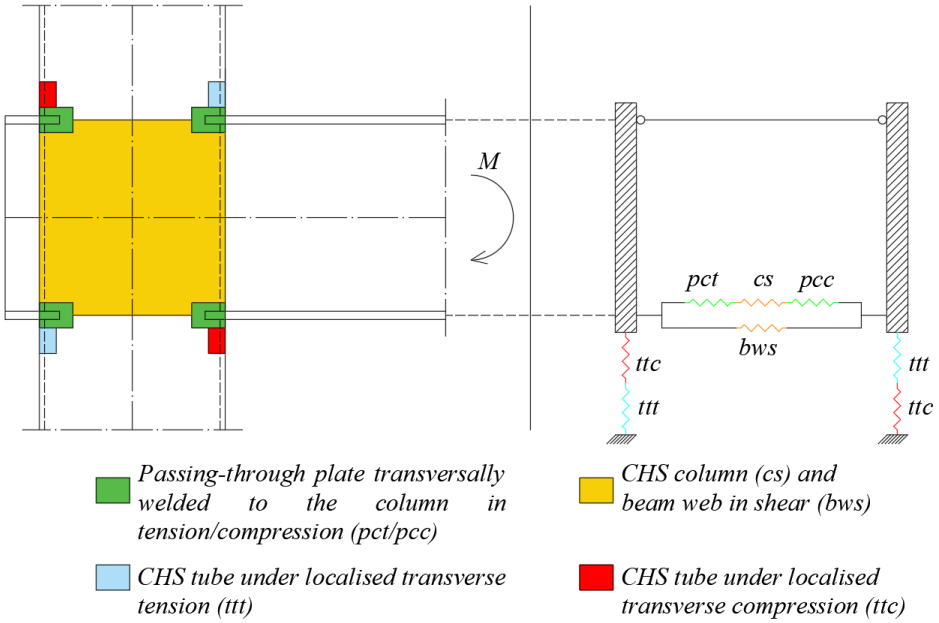

Figure 2.80 – Components constituting the connection

The mechanical model of the analysed CHS to through-all I-beam connection is reported in Figure 2.80. The plastic behaviour of the joint can be ideally defined by employing eight non-linear springs; in particular, the components *pct*, *pcc* and *cs* are in series, and these three springs are in parallel with *bws*.

Instead, the behaviour of the localised transverse actions of the plate to the tubular profile is modelled through the vertical in-series springs *ttc* and *ttt*.

The resistance of the joint depends on the weakest of its components, and for this reason, it can be assessed as:

$$M_{joint} = min\left\{\left[\min\left(F_{cs}; F_{pct/pcc}\right) + F_{bws}\right]z; \left(F_{ttt} + F_{ttc}\right)\frac{d_0}{\beta_v}\right\} \qquad (2.58)$$

Instead, each component affects the overall stiffness of the connection according to:

$$k_{joint} = \frac{1}{\dfrac{1}{\dfrac{(h_b - t_{bf})^2}{2} + \dfrac{1}{k_{pct/pcc}} + \dfrac{1}{k_{cs}}} + (h_b - t_{bf})^2 \cdot k_{bs}} + \frac{1}{2 \cdot d_0^2 \cdot k_{ttt/ttc}} \qquad (2.59)$$

The application of the previous formulations to the 30 numerically simulated CHS to through-all I-beam connections is reported in Figure 2.81, Figure 2.82, Table 2.16, Table 2.17, both in terms of resistance and stiffness.

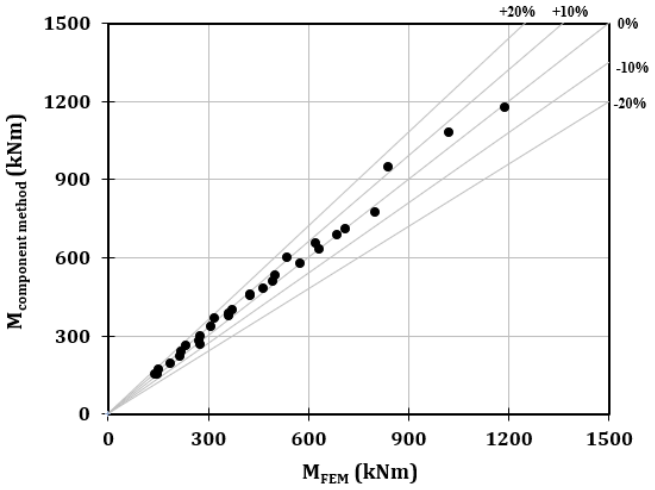

Figure 2.81 – Simulations vs predictions: strength

Table 2.16 – Validation of the component method approach: strength formulation

Test	F_{cs} (kN)	$F_{pcc/pct}$ (kN)	F_{bws} (kN)	F_{ttc} (kN)	F_{ttt} (kN)	$M_{proposal}$ (kNm)	M_{FEM} (kNm)	Proposal/FEM
1	456	427	243	354	379	154	140	1.10
2	357	356	323	343	349	170	151	1.13
3	518	388	275	343	381	153	148	1.03
4	524	455	296	407	435	195	189	1.03
5	531	555	323	475	489	238	219	1.09
6	537	664	345	522	526	262	234	1.12
7	795	761	385	639	673	365	318	1.15
8	805	894	416	698	720	400	372	1.08
9	556	365	402	387	424	222	216	1.03
10	563	406	430	426	456	266	275	0.97
11	570	461	465	465	488	300	275	1.09
12	918	871	508	737	771	483	464	1.04
13	670	370	511	407	459	280	272	1.03
14	679	408	552	445	491	333	309	1.08
15	691	444	603	483	524	383	361	1.06
16	852	526	552	535	596	374	362	1.03
17	867	572	603	582	636	454	425	1.07
18	886	631	674	630	675	507	495	1.02
19	908	518	662	546	613	456	428	1.06
20	929	563	740	591	651	530	502	1.06
21	950	620	821	637	689	579	577	1.00
22	972	678	914	684	728	631	634	0.99
23	995	757	1012	732	767	685	688	1.00
24	1064	536	846	571	655	598	535	1.12
25	1088	581	938	615	693	653	621	1.05
26	1113	625	1045	660	732	711	711	1.00
27	1140	684	1157	707	772	772	801	0.96
28	1795	1018	938	927	1064	947	841	1.13
29	1837	1096	1045	995	1123	1081	1023	1.06
30	1880	1199	1157	1065	1183	1175	1189	0.99
						Mean		1.05
						Standard deviation		0.048
						Coefficient of variation		0.046

Table 2.17 – Validation of the component method approach: stiffness formulation

Test	k_{cs} (N/mm)	k_{pct} (N/mm)	k_{bws} (N/mm)	k_{ttc} (N/mm)	$k_{proposal}$ (kNm/mrad)	k_{FEM} (kNm/mrad)	Proposal/ FEM
1	1734782	630391	554973	2420718	35.12	50.37	0.7
2	1080962	496316	586316	2022986	49.24	53.72	0.92
3	1969536	399370	627747	2132891	35.45	50.23	0.71
4	1766684	550362	599421	2463510	45.62	65.26	0.7
5	1606367	778715	586316	2802459	58.84	76.63	0.77
6	1477565	1053208	569688	3032723	72.86	71.56	1.02
7	2186417	886546	635731	3414466	81.53	112.45	0.73
8	2030814	1202974	629853	3677363	101.49	129.44	0.78
9	1683507	269698	730554	1930901	57.33	67.87	0.84
10	1548520	341745	709834	2089554	68.38	79.63	0.86
11	1438315	449882	703271	2250440	81.86	87.16	0.94
12	2080311	954480	691154	3521403	123.35	163.76	0.75
13	1842623	187539	842181	1752975	75.17	82.47	0.91
14	1711487	240711	834394	1887945	88.65	92.55	0.96
15	1564649	293816	820017	2024703	106.74	106.36	1
16	2147683	311171	834394	2273367	94.69	112.21	0.84
17	1963421	379819	820017	2438044	115.01	128.17	0.9
18	1781639	474516	813315	2604780	143.11	157.18	0.91
19	2058330	260133	900272	2129854	119.01	131.03	0.91
20	1867762	321348	892914	2275513	146.94	150.43	0.98
21	1718400	403863	891425	2422896	178.14	183.31	0.97
22	1597312	495376	901723	2571935	213.06	204.47	1.04
23	1499674	630697	915247	2722571	251.77	236.18	1.07
24	2139164	204929	1E+06	1983819	160.17	157.12	1.02
25	1968099	254435	1E+06	2112309	192.92	188.71	1.02
26	1829415	307738	1E+06	2242244	229.64	220.68	1.04
27	1717590	385492	1E+06	2373569	269.9	255.8	1.06
28	3247396	448775	1E+06	3184819	225.99	304.88	0.74
29	3018566	542793	1E+06	3380727	274.08	382.03	0.72
30	2834053	679936	1E+06	3578732	328.83	422.65	0.78
					Mean		0.89
					Standard deviation		0.121
					Coefficient of variation		0.137

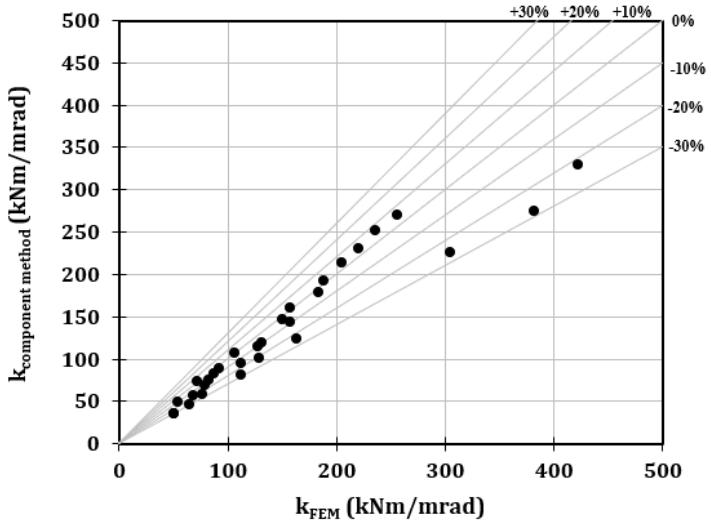

Figure 2.82 – Simulations vs predictions: stiffness

The strength formulation is more accurate than the stiffness equation since the coefficients of variations are equal to 4.6% and 13.7%, respectively.

Finally, the theoretical mechanical approach discussed above has been implemented in OpenSees according to the scheme reported in Figure 2.83. In particular, the interconnection between Matlab and OpenSees allowed conceiving a parametric geometrical configuration of the model to adapt to the geometrical properties of the 30 cases deriving from the parametric analysis. In particular, the geometrical location of the nodes has been set according to the grid reported in Figure 2.83, fixing the location of the hinge, the roller and the beam end, while all the other parameters can vary accordingly to the studied case. Furthermore, the nodal part has been modelled by using rigid elements connected employing internal hinges or non-linear spring elements.

In particular, the beam and the column have been modelled by adopting an elastic material whose mechanical properties are defined through the knowledge of the area section, the inertia and the modulus of elasticity (assumed equal to 210 GPa). Instead, all the dotted parts are rigid elements that connect each other employing internal hinges or non-linear spring elements.

All the components have been implemented using the *Steel01* uniaxial material since it requires only the basing information related to the stiffness and strength to define the behaviour of the single component. Instead, the components *pct* and *pcc* have been modelled employing the hysteretic model, whose parameters are assessed thanks to Eqs. 2.43-2.50.

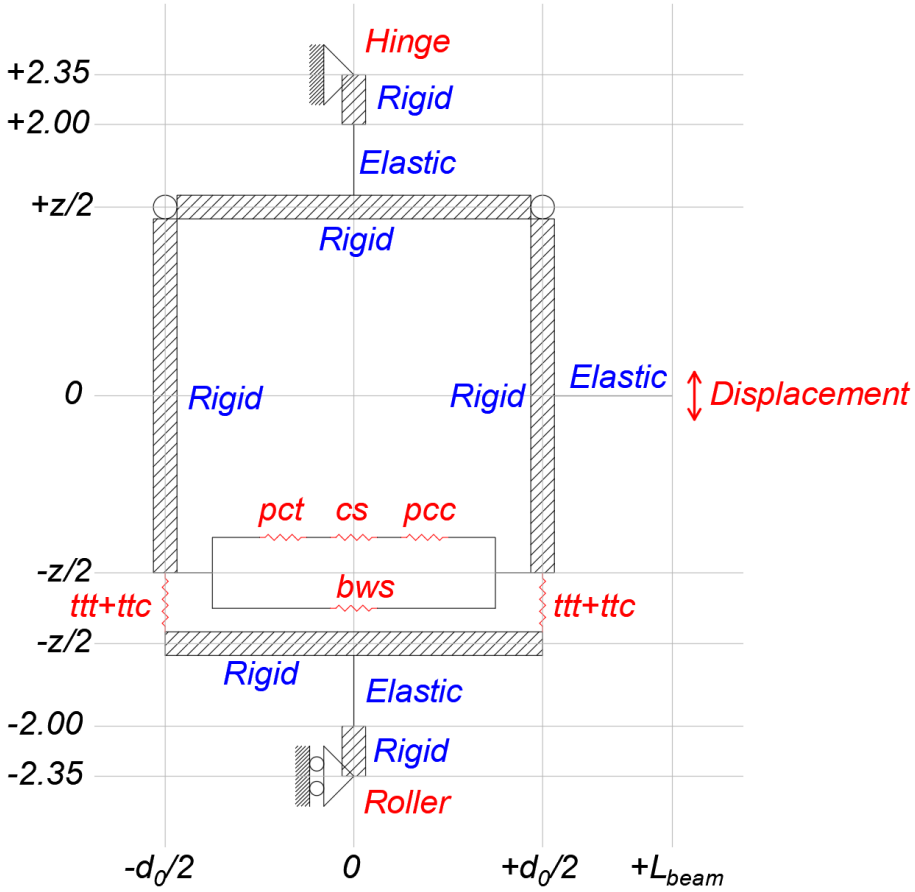

Figure 2.83 – Mechanical model implemented in OpenSees

This numerical model has been validated against the 30 cyclic analyses on CHS to through-all double-tee beam connections. In fact, it can predict both the stiffness and strength of the analysed connection typology with acceptable accuracy. Nevertheless, some approximations already remain about the strength degradation for cycles with amplitudes higher than 30 mrad, as observed in Annex A, from Figure 2.84 to Figure 2.87 and Table 2.18.

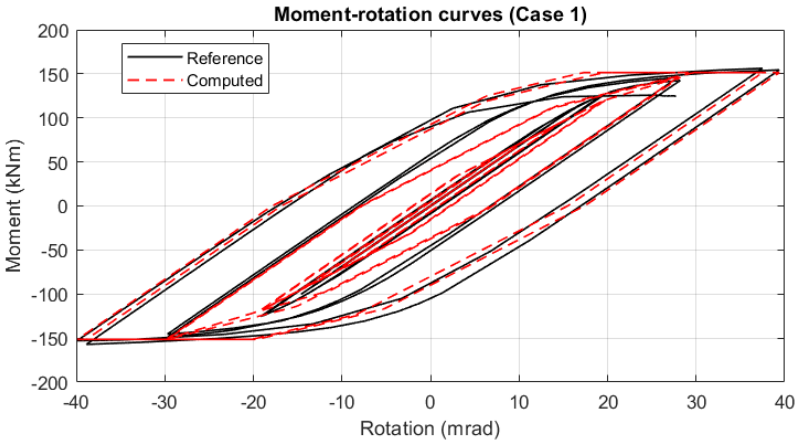

Figure 2.84 – Abaqus vs OpenSees comparison: case 1 (hysteretic curve)

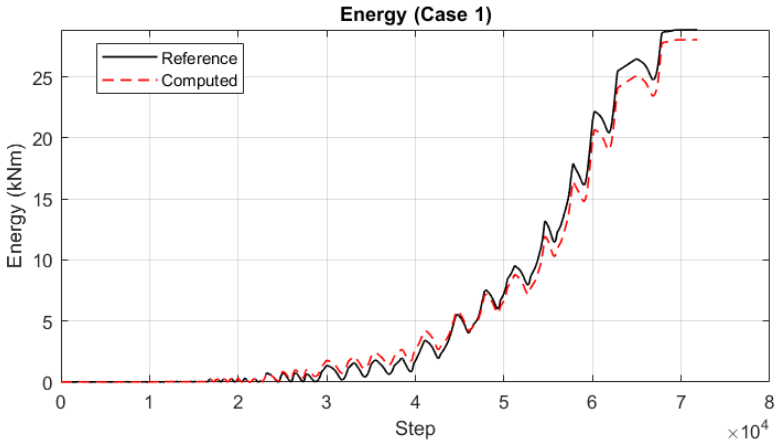

Figure 2.85 – Abaqus vs OpenSees comparison: case 1 (dissipated energy)

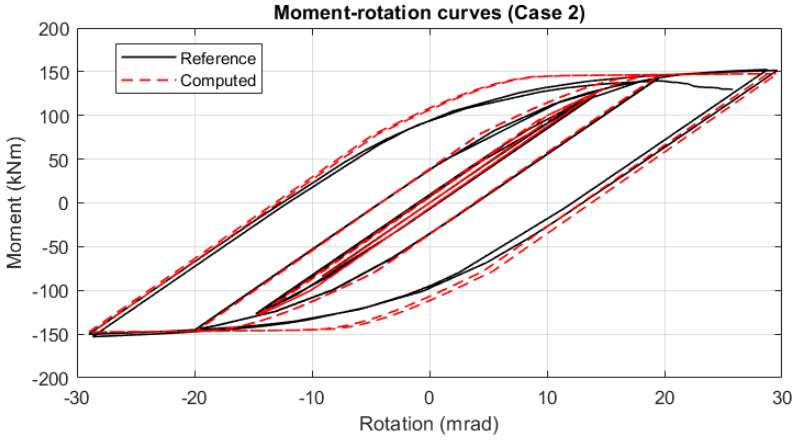

Figure 2.86 – Abaqus vs OpenSees comparison: case 2 (hysteretic curve)

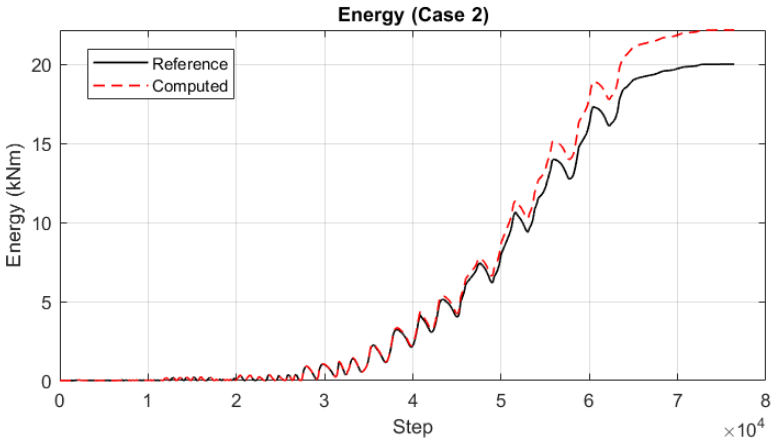

Figure 2.87 – Abaqus vs OpenSees comparison: case 2 (dissipated energy)

The outcomes reported in Table 2.18 and from Figure 2.88 to Figure 2.90 highlight that the proposed numerical model, based on the component method approach, is very accurate since the stiffness, flexural strength and energy dissipation capacity are predicted with coefficients of variation equal to 5%, 3% and 8%, respectively. It is only worth highlighting that the stiffness reported in Table 2.18 has to be intended as the stiffness of the specimens without detracting the elastic deformability of the beam and column.

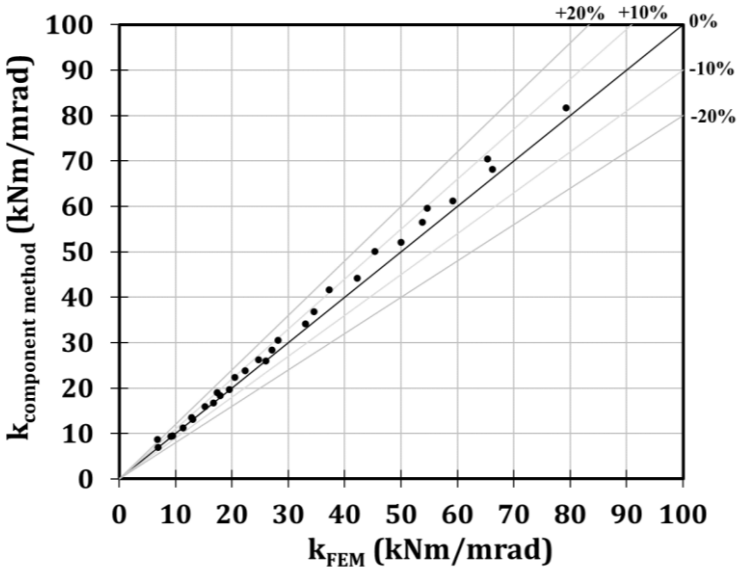

Figure 2.88 – Abaqus vs OpenSees comparison: stiffness

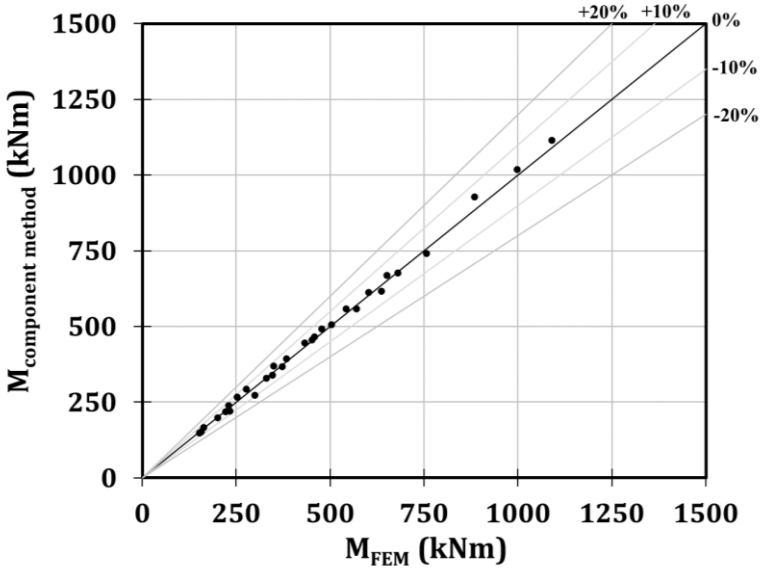

Figure 2.89 – Abaqus vs OpenSees comparison: resistance

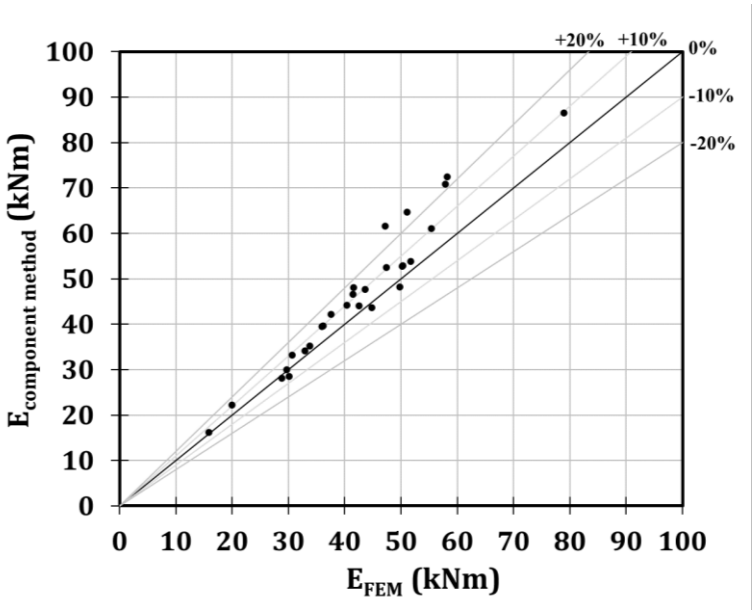

Figure 2.90 – Abaqus vs OpenSees comparison: dissipated energy

The characterization of the flexural behaviour exhibited by CHS to through-all I-beam connections is very important in the view of applying this detail with the dog-bone strategy (Figure 1.13). In fact, the RBS approach can be adopted only once the behaviour of all the nodal components has been adequately identified.

Table 2.18 – Validation of the numerical model (CAE and OS stand for Abaqus and OpenSees, respectively)

Case	Stiffness (kNm/mrad)			Strength (kNm)			Energy (kNm)		
	CAE	OS	Ratio	CAE	OS	Ratio	CAE	OS	Ratio
1	6.89	6.89	1.00	157.13	151.55	0.96	28.85	28.04	0.97
2	9.20	9.33	1.01	152.96	147.68	0.97	20.01	22.18	1.11
3	6.80	8.63	1.27	163.50	166.02	1.02	36.22	39.63	1.09
4	9.54	9.53	1.00	200.26	198.93	0.99	30.08	28.56	0.95
5	11.30	11.29	1.00	222.37	217.97	0.98	32.96	34.15	1.04
6	13.03	13.06	1.00	233.44	221.45	0.95	30.62	33.15	1.08
7	16.70	16.75	1.00	345.79	339.90	0.98	49.80	48.26	0.97
8	19.55	19.63	1.00	372.26	367.94	0.99	50.35	52.85	1.05
9	12.85	13.57	1.06	230.07	239.54	1.04	33.83	35.18	1.04
10	15.24	15.86	1.04	252.04	266.44	1.06	29.66	29.96	1.01
11	17.87	18.38	1.03	277.38	292.57	1.05	15.86	16.15	1.02
12	26.00	26.02	1.00	458.42	466.72	1.02	44.82	43.67	0.97
13	17.35	19.03	1.10	298.96	272.82	0.91	37.55	42.12	1.12
14	20.54	22.29	1.09	331.05	329.98	1.00	40.33	44.16	1.09
15	24.71	26.28	1.06	350.59	369.62	1.05	36.01	39.54	1.10
16	22.35	23.84	1.07	383.24	393.36	1.03	51.75	53.77	1.04
17	27.06	28.33	1.05	432.20	444.86	1.03	50.18	52.79	1.05
18	33.04	34.13	1.03	477.80	491.62	1.03	42.57	44.07	1.04
19	28.17	30.50	1.08	452.06	455.17	1.01	55.35	61.00	1.10
20	34.53	36.85	1.07	503.57	506.63	1.01	47.38	52.45	1.11
21	42.18	44.11	1.05	542.91	558.02	1.03	43.58	47.62	1.09
22	49.99	52.13	1.04	602.75	612.84	1.02	41.60	48.02	1.15
23	59.17	61.15	1.03	650.32	668.30	1.03	41.51	46.65	1.12
24	37.30	41.63	1.12	569.97	559.20	0.98	58.17	72.47	1.25
25	45.34	50.13	1.11	637.31	616.08	0.97	57.93	70.78	1.22
26	54.66	59.63	1.09	679.64	676.34	1.00	51.09	64.61	1.26
27	65.29	70.44	1.08	756.18	740.79	0.98	47.18	61.60	1.31
28	53.81	56.46	1.05	884.66	926.97	1.05	110.30	108.18	0.98
29	66.20	68.10	1.03	997.90	1017.7	1.02	99.30	108.00	1.09
30	79.30	81.70	1.03	1089.3	1114.1	1.02	78.90	86.50	1.10
Mean			**1.05**			**1.01**			**1.08**
Standard deviation			**0.05**			**0.03**			**0.09**
Coefficient of variation			**0.05**			**0.03**			**0.08**

2.5 Personal contribution

Chapter 2 focuses the attention on innovative beam-to-column connections. In particular, two nodal configurations have been analysed: the Reduced Beam Section (RBS) joint and the Circular-Hollow-Section (CHS) to though-all I-beam connection. For each typology, experimental, numerical and theoretical activities have been discussed.

However, investigations related to the RBS joint are part of previous studies carried out at the University of Salerno; instead, the characterization of the flexural response of CHS to through-all double-tee beam connections represents the novelty of the work and the main author's contribution. Consequently, the second joint's solution is discussed more than the RBS strategy.

2.6 References

1. Jaspart, J. P., Etude de la semi-rigidité des nœuds Poutre-Colonne et son influence sur la résistance et la stabilité des ossature en acier, PhD Thesis, University of Liège, Belgium.
2. Steenhuis, M., Jaspart, J. P., Gomes, F., Leino, T., Application of the component method to steel joints, Proceeding of the Control of the Semi-Rigid Behaviour of Civil Engineering Structural Connections Conference, 1998.
3. Tschemmernegg, F., Rubin, A., Pavlov, A., Application of the component method to composite joints, Proceeding of the Control of the Semi-Rigid Behaviour of Civil Engineering Structural Connections Conference, 1998.
4. Wald, F., Gresnigt, A. M., Weynand, K., Jaspart, J. P., Application of the component method to column bases, Proceeding of the Control of the Semi-Rigid Behaviour of Civil Engineering Structural Connections Conference, 1998.
5. da Silva, L. S., Santiago, A., Vila Real, P., Application of the Component Method to Steel Joints under Fire Loading, 10.1007/978-94-010-0950-8_37, 2000.
6. Faella, C., Piluso, V., Rizzano, G., Structural Steel Semirigid Connections, CRC Press, Boca Raton, FL, 2000.
7. Iannone, F., Latour, M., Piluso, V. and Rizzano, G., Experimental Analysis of Bolted Steel Beam-to-Column Connections: Component Identification, J. Earthq. Eng., vol. 15, no. 2, pp. 214–244, 2011.
8. Augusto, H., Simões da Silva, L., Rebelo, C., and Castro, J. M., Cyclic behaviour characterization of web panel components in bolted end-plate steel joints, J. Constr. Steel Res., vol. 133, pp. 310–333, Jun. 2017.
9. Girão Coelho, A. M., Bijlaard, F. S. K., da Silva, L. S., Experimental assessment of the ductility of extended end plate connections, Eng. Struct., 2004.
10. Swanson, J., Leon, R.T., Bolted Steel Connections: Tests on T-stub Components, ASCE, Journal of Structural Engineering, Vol.126, No.1, pp.50-56, 2000.
11. Latour, M., Piluso, V. and Rizzano, G., Cyclic modelling of bolted beam-to-column connections: Component approach, J. Earthq. Eng., vol. 15, no. 4, 2011.
12. Francavilla, A.B., Latour, M., Piluso, V., Rizzano, G., Bolted T-stubs: A refined model for flange and bolt fracture modes, Steel and Composite Structures, 20 (2), pp. 267-293, 2016.
13. ENV 1993-1-1, Eurocode 3: Design of Steel Structures. Part 1-1: General rules and rules for buildings, European Norm Voluntary, 1992.
14. CEN [2005]: EN 1993-1-8 Eurocode 3: Design of Steel Structures. Part 1-8: Design of Joints, CEN, European Committee for Standardization, 2005.
15. EUROCODE 8, "Design of structures for earthquake – part 1: General rules, seismic actions and rules for buildings", CEN, 2003.
16. Plumier, A., "New Idea for Safe Structures in Seismic Zones", Proc., Symposium of Mixed Structures Including New Materials, pp. 431-436, IABSE, Brussels, Belgium, 1990.
17. Iwankiw, R. N. and Carter, C. J., "The Dogbone: A New Idea to Chew On", Modern Steel Construct., Vol. 36. No.4, pp. 18-23, AISC, Chicago IL, 1996.
18. Chen, S. J., Yeh, C. H. and Chu, J. M., "Ductile Steel Beam-Column Connections for Seismic Resistance", J. Struct. Engrg., Vol. 122, No. 11, pp. 1292-1299, ASCE, 1996.
19. FEMA 351, (2000): "Recommended Seismic Evaluation and Upgrade Criteria for Existing Welded Steel Moment-Frame Buildings", Federal Emergency Management Agency, Washington.

20. Montuori, R., Piluso, V., "Plastic Design of Steel Frames with Dog-Bone Beam-to-Column Joints", Third International Conference on Behaviour of Steel Structures in Seismic Areas, STESSA 200, 21-24 August, Montreal, 2000.
21. ANSI/AISC, "Prequalified Connections for Special and Intermediate Steel Moment Frames for Seismic Applications", 2016.
22. Latour, M., Analisi teorico-sperimentale di collegamenti dissipativi a parziale ripristino di resistenza in strutture intelaiate in acciaio, Ph. D. Thesis, University of Salerno, 2010.
23. ANSI/AISC 341-16, Seismic Provisions for Structural Steel Buildings, American Institute for Steel Construction, Chicago, Illinois, 2016.
24. Abaqus, Analysis user's manual version 6.17, Abaqus Inc., 2017.
25. EN 10034, Structural Steel I and H sections. Tolerances on shape and dimensions, 1995.
26. CEN [2006]: EN 1993-1-5 Eurocode 3: Design of steel structures. Part 1-5: Piling, CEN European Committee for Standardization, 2006.
27. Engelhardt, M. D., Winneburger, T., Zekany, A. J., and Potyraj, T. J., "The Dogbone Connection: Part II", Modern Steel Construct., Vol. 36. No. 8, pp.46-55, AISC, 1996.
28. Iwankiw, R. N. and Carter, C. J., "The Dogbone: A New Idea to Chew On", Modern Steel Construct., Vol. 36. No.4, pp. 18-23, AISC, Chicago IL, 1996.
29. Moore, K.S., Malley, J.O., Engelhardt, M.D., "Design of reduced Beam Section (RBS) Moment Frame Connections", AISC Structural Steel Educational Council, Moraga, CA, 1999.
30. SAC Joint Venture [1997] "Interim guidelines advisory no. 1," Supplement to FEMA 267, Federal Emergency Management Agency, Washington, D.C.
31. Weynand, K., Busse, E., Jaspart, J. P., First practical implementation of the component method for joints in tubular construction, 9th International Symposium on Tubular Structures, 2001.
32. Weynand, K., Jaspart, J. P., Ly, L., Application of the component method to joints between hollow and open sections, CIDECT Final Report 5BM, Universitè de Liège, 2003.
33. Jaspart, J. P., Pietrapertosa, C., Weynand, K., Klinkhammer, R., Development of a full consistent design approach for bolted and welded joints in building frames and trusses between steel members made of hollow and/or open sections – application of the component method, CIDECT Report 5BP-4/0, Universitè de Liège, 2004.
34. Park, A. Y., Wang, Y. C., Development of component stiffness equations for bolted connections to RHS columns, Journal of Constructional Steel Research, 2011.
35. France, G. E., Buick Davison, J., Kirby, P. A., Strength and rotational stiffness of simple connections to tubular columns using flowdrill connectors, Journal of Constructional Steel Research, 50, 15-34, 1999.
36. France, G. E., Buick Davison, J., Kirby, P. A., Moment-capacity and rotational stiffness of endplate connections to concrete-filled tubular columns with flowdrilled connectors, Journal of Constructional Steel Research, 50, 35-48, 1999.
37. Garifullin, M., Bronzova, M., Jokinen, T., Heinisuo, M., Kovacic, B., Effect of fillet welds on initial rotational stiffness of welded tubular joints, Procedia Engineering 165, 1643-1650, 2016.
38. Serrano-Lopez, M. A., Lopez-Colina, C., Gonzalez, J., Lopez-Gayarre, F. L., A Simplified FE Simulation of Welded I Beam-to-RHS Column Joints, International Journal of Steel Structures, 2016.
39. Tizani, W., Al-Mughairi, A., Owen, J. S., Pitrakkos, T., Rotational stiffness of a blind-bolted connection to concrete-filled tubes using modified Hollo-bolt, Journal of Constructional Steel Research, 2013.

40. Saunders, R. J., Method and apparatus for direct laser cutting of metal stents, Advanced Cardiovascular Systems, Inc. Santa Clara, CA (US), 2002, Patent US6369355B1.
41. Zhou, Y., Liao, J., Meng, H., Liu, S., Laser micro-fabrication of endovascular stent, School of Optoelectronic Science and Engineering, South China Normal University, Guangzhou, 510631, 2005.
42. Meng, H., Liao, J., Guan, B., Zhang, Q., Zhou, Y., Fiber Laser Cutting Technology on Coronary Artery Stent, Laboratory of Photonic Information Technology, South China Normal University, Guangzhou, Guangdong, 510631, China, 2007.
43. Wang, X. and Zheng, H. (2009), High quality laser cutting of electronic printed circuit board substrates, Circuit World, Vol. 35 No. 4, pp. 46-55, 2009.
44. Buehrle, J., Bea, M., Brockmann, R., Laser Remote Process Technology on Automotive Manufacture, SAE-China, FISITA (eds) Proceedings of the FISITA 2012 World Automotive Congress. Lecture Notes in Electrical Engineering, vol 199. Springer, Berlin, Heidelberg, 2013.
45. Makino, Y., Kurobane, Y., Paul, J. C., Orita, Y., and Hiraishi, K., Ultimate capacity of gusset plate-to-tube joints under axial and in plane bending loads, Proceedings 4th International Symposium on Tubular structues, Delft, The Netherlands, pp. 424-434, 1991.
46. Makino, Y., Kurobane, Y., Ochi, K., Vegte, G., van der, and Wilmshurst, S. R., Database of test and numerical analysis results for unstiffened tubular joints, IIW Doc., XV-E-96-220, 1996.
47. AIJ, Recommendations for the design and fabrication of tubular truss structures in steel, Architectural Institute of Japan, 2002.
48. Sawada, Y., Idogaki, S. e Skeia, K., Static and fatigue tests on T-joints stiffened by an internal ring, Proceedings of the Offshore Technology Conference OTC 3422, Houston, USA, 1979.
49. Khador, M., Chan, T., Cyclic behaviour of external diaphragm joint to CHS column with built-in replaceable links, Steel Constr. 9 (4), 331–338, 2016.
50. Li, L., Wang, W., Chen, Y., Lu, Y., Experimental investigation of beam-to-tubular column moment connections under column removal scenario, Journal of Constructional Steel Research, 2013.
51. Wang, W., Chen, Y., Li, W., Bidirectional seismic performance of steel beam to circular tubular column connections with outer diaphragm, Eartq. Eng. Struct. Dyn. 40 (10), 1063-1081, 2011.
52. Quan, C., Wang, W., Chan, T. M., Khador, M., FE modelling of replaceable I-beam-to-CHS column joints under cyclic loads, Journal of Constructional Steel Research, 2017.
53. Sabbagh, A.B., Chan, T.M., Mottram, J.T., Detailing of I-beam-to-CHS column joints with external diaphragm plates for seismic actions, J. Constr. Steel Res. 88 (9), 21–33, 2013.
54. Wang, W., Chan, T.M., Shao, H., Cyclic behavior of connections equipped with NiTi shape memory alloy and steel tendons between H-shaped beam to CHS column, Eng. Struct. 88, 37–50, 2015.
55. Zhao, X. L. and Packer, J. A., Tests and design of concrete-filled elliptical hollow section stub columns, Thin-Walled Structures, Vol. 47, Np. 6/7, pp. 617-628, 2009.
56. Alostaz, Y.M., Schneider, S.P., Connections to concrete-filled steel tubes, Structural Engineering Series No. 613, University of Illinois at Urbana-Champaign, 1996.
57. Quan, C., Wang, W., Zhou, J., Cyclic behavior of stiffened joints between concrete-filled steel tubular column and steel beam with narrow outer diaphragm and partial joint penetration welds, Front. Struct. Civ. Eng. 10 (3), 333–344, 2016.

58. Li, X., Xiao, Y., Wu, Y.T., Seismic behavior of exterior connections with steel beams bolted to CFT columns, J. Constr. Steel Res. 65 (7) (2009) 1438–1446, 2009.
59. Voth, A. and Packer, J. A., Branch Plate-to-Circular Hollow Structural Section Connections. I: Experimental Investigation and Finite-Element Modeling, Journal of Structural Engineering, ASCE, August 2012.
60. Kanyilmaz, A., Castiglioni, C., Brambilla, G., Gjoka, K., Galazzi, A., Raso, S., Valli, A., Brugnolli, and M., Hojda, R., Experimental assessment of tolerances for the fabrication of laser-cut steel joints, ce/papers. 1. 776-785. 10.1002/cepa.117, 2017.
61. Kanyilmaz, A., The problematic nature of steel hollow section joint fabrication, and a remedy using laser cutting technology: a review of research, applications, opportunities, Engineering Structures, 2019.
62. Winkel, G. D. de, The Static Strength of I-beam to Circular Hollow Section, Doctoral Thesis, Delft University of Technology, 1998.
63. Voth, A., Branch Plate-to-Circular Hollow Structural Section Connections, Ph. D. Thesis, Toronto, 2010.
64. Wang, W., Fang, C., Chen, Y., Wang, M., Seismic performance of steel H-beam to SHS-column cast modular panel zone joints, Engineering Structures, 117: 145–160, 2016.
65. Wang, W., Fang, C., Quin, X., Chen, Y., Li, L., Performance of practical beam-to-SHS column connections against progressive collapse, Engineering Structures, 106: 332-347, 2016.
66. Castiglioni, C. A., Kanyilmaz, A., Salvatore, W., Morelli, F., Piscini, A., Hjiaj, M., Couchaux, M., Calado, L., Jorge Proenca, Sio, J., Raso, S., Valli, A., Brignolli, M., Hoffmeister, B., Korndorfer, J., Degee, H., Das, R., Hojda, R., Rembde, C., Galazzi, A., Mazzanti, A., EU-RFS Project LASTEICON 709807, 2016-2020, www.lasteicon.eu.
67. Togo, T., Experimental study on mechanical behavior of tubular joints, D. Eng. Thesis, Osaka University, Osaka, Japan, 1967.
68. Kurobane, Y., New developments and practices in tubular joint design, IIW Doc. XV-488-84, Kumamoto University, Kumamoto, Japan, 1981.
69. Wardenier, J., Hollow section joints, Delft University Press, Delft, The Netherlands, 1982.
70. Wardenier, J., A uniform effective width approach for the design of CHS overlap joints, Proceedings of the 5th International Conference on Advances in Steel Structures (ICASS), Singapore, Research Publishing Services, Vol. II, pp. 155-165, 2007.
71. Wardenier, J., Packer, J. A., Zhao, X. L., and van der Vegte, G. J., Hollow section in structural applications, 2nd Edition, CIDECT and Bowen met Staal, Rotterdam, The Netherlands, 2010.
72. Winkel, G. D. de, and Wardenier, J., Parametric Study on the Static Strength of Axially Loaded Multiplanar Plate to Circular Column Connections, Proceedings ISOPE Fifth International Offshore and Polar Engineering Conference, Vol. IV, The Hague, The Netherlands, 1995.
73. Winkel, G. D. de, and Wardenier, J., The Static Strength and Behaviour of Multiplanar I-beam to Tubular Column Connections loaded with In-plane Bending Moments, Proceedings of the Third International Workshop Connections in Steel Structures III, Trento, Italy, 1995.
74. Winkel, G. D. de, and Wardenier, J., Parametric Study on the Static behavior of Uniplanar I-beam-to-tubular Column Connections Loaded with In-plane Bending Moments Combined with Pre-stressed Columns, Proceedings of the Seventh Int. Symposium on Tubular Structures VII, Miskolc, Hungary, 1996.
75. Voth, A. and Packer, J. A., Circular Hollow Through Plate Connections, Steel Construction (9), 2016.

76. EN 4063, Welding and allied processes - Nomenclature of processes and reference numbers, 2011.
77. CEN [2006]: EN 1993-1-4 Eurocode 3: Design of Steel Structures. Part 1-4: General rules – Supplementary rules for stainless steel, CEN, European Committee for Standardization, 2006.
78. CEN [2005]: EN 1998-1 Eurocode 8: Design of Structures for Earthquake Resistance. Part 1: General Rules, Seismic Actions and Rules for Buildings, CEN, European Committee for Standardization, 2005.
79. Faralli, A. C., Large deformation of T-stub connection in bolted steel joints, Ph. D. Thesis, University College of London, 2019.
80. Pavlovic, M., Markovic, Z., Veljkovic, M., Budevac, D., Bolted shear connectors vs. headed studs behaviour in push-out tests, J. Constr. Steel Res., 88:134-149, 2013.
81. Wolfram Research, Inc., Mathematica, Version 5.1, Champaign, IL, 2004.
82. McKenna, F., OpenSees: A Framework for Earthquake Engineering Simulation, Computing in Science and Engineering 13, 58-66, 2011.
83. Chisari, C., Francavilla, A. B., Latour, M., Piluso, V., Rizzano G., Amadio, C., "Critical issues in parameter calibration of cyclic models for steel members", Engineering Structures, vol. 132, pp. 123-138, 2017.

CHAPTER 3 – Behaviour of resilience-oriented joints

As already discussed in Chapter 1, the last decades have been characterized by many efforts devoted to studying the behaviour of partial-strength beam-to-column connections. In this framework, Chapter 3 has been conceived to provide a short review of the behaviour exhibited by two innovative partial-strength joints studied at the University of Salerno in the last few years: the FREEDAM and the X-shaped T-stub connections. The primary purpose of such activity consists of summarizing the experimental, numerical and analytical activities that have been carried out to have a satisfactory assessment of the cyclic response of these joints.

3.1 FREE from DAMage (FREEDAM) connection

Friction connections are partial-strength joints equipped with friction dampers bolted at their lower beam flanges [1-6]. These connections can provide high local ductility and energy dissipation capacity provided that the damper stroke is selected and the damper components are designed through the application of capacity design principles at the global and local level [6-9]. Significant examples of such connections are represented by the Sliding Hinge Joint (SHJ) [10-16], developed by the research group of the University of Auckland and the FREEDAM joints recently developed within a European project [13-25] (Figure 3.1).

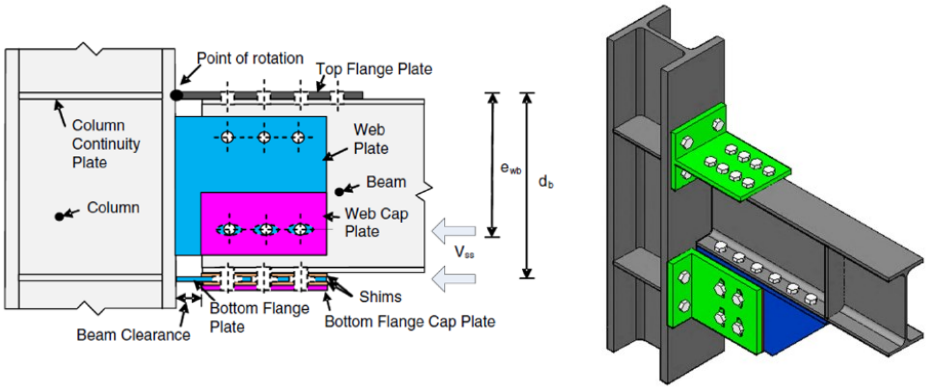

Figure 3.1 – Sliding Hinge Joint [10-16] (left) and FREEDAM connection [13-25] (right)

In these connections, a friction damper is located at the beam bottom flange of the beam end to control the joint resistance by appropriately regulating the tightening torque of pre-loadable high strength bolts and the joint ductility by adequately designing the length of the slotted holes. Moreover, the high initial stiffness, independent of the preload applied to the bolts, and the constant flexural resistance achieved at the slippage force numerically model the moment-rotation hysteretic behaviour with a rigid perfectly plastic law.

In such a way, the dissipation is not located in structural elements (e.g. beam ends or structural nodal components such as T-stubs, end-plates) but in the friction pads that can slide during the seismic event accommodating the required rotations.

During a seismic event, the FREEDAM connection is supposed to have a rigid behaviour until the achievement of the slippage force, while, afterwards, the joint starts rotating around a centre located at the stem-to-flange attachment of the upper T-stub.

The design procedure of such a kind of joint strictly relies on capacity design principles. In fact, starting from the design actions at ULS combinations, the first step consists in designing the friction dampers, which are representative of the dissipative components of the joint.

Subsequently, the attention is focused on the design of the non-dissipative components of the connection, which are sized accounting for the overstrength due to random variability of the friction pads' material properties and other structural elements. In particular, the columns are designed according to Eurocode 8 or other theoretical approaches (such as the Theory of Plastic Mechanism control) to be over-resistant than the connections and the beams.
In the last years, the European Commission has funded a research project to have a complete characterization of this innovative connection typology. The project involved the civil departments of many Italian and European universities, companies, and industries with experience in producing and designing steel in the construction market.
At the end of the project, considering the significant amount of experimental, numerical and analytical data collected in many technical reports, it is possible to state that enough information has been provided to consider the FREEDAM connection a good solution for the seismic design of steel structures.

3.1.1 Experimental activity

During the European project, many experimental tests have been carried out to characterize the friction material constituting the dampers and assess the cyclic response of beam-to-column sub-assemblies.
This paragraph briefly summarizes the main experimental results to provide only the essential information for assessing the response of the analysed connection.

3.1.1.1 Characterization of the friction pads

The main peculiarity of the FREEDAM joint consists of the possibility of dissipating the seismic input energy limiting the damages only to the friction pads and, in a very controlled way, to the T-stubs and L-stubs. Consequently, the complete restoration of the building functionality can be ensured by simply re-tightening the bolts belonging to the joints or substituting the friction shims. This aspect clarifies that the preload force of the bolts and the friction coefficient are the main parameters able to affect the response of FREEDAM connections. In this framework, many studies have been carried out at the STRENGTH laboratory of the University of Salerno to fully characterise these two aspects of the behaviour of the analysed connection typology.
A few years ago, an experimental campaign was performed to assess the behaviour of different friction materials with the main aim of defining their static and dynamic friction coefficients to propose the best solution for the FREEDAM connection.
Since the friction pad is the dissipative component, the choice of the friction material is a fundamental step without which all the other steps cannot develop.
The experimental program consisted of 63 specimens designed to comply with EN 1090-2 [26] and EN 15129 [27]. In particular, the activity was divided into two phases:

- in the first phase, the degradation and the static and kinetic friction of 13 specimens characterized by stainless steel plates with eight different materials were assessed;
- the second phase has been devoted to the characterization of the best three materials selected in the previous step.

Furthermore, the bolts' preload level and the typology of the adopted washers were not left unexplored; in fact, different levels of preloading varying between 40% and 100% of the standard preloading value were studied together with two typologies of washer: standard flat washers and Belleville disc springs. In particular, it has been observed that the Belleville washers allow the reduction of the bolt's loosening during the cyclic tests.

The internal surface of the damper is made of stainless steel, while a thermal spray process has been used to apply the materials on the friction pads. According to Bowden and Tabor, the friction coefficient (μ) of a metal interface is related to the ratio between the shear resistance of the weakest material (s_0) and the superficial hardness of the softest material (σ_0) constituting the interface. For this reason, the friction coefficient assumes a high value in the case of the high shear resistance of the weakest material and/or a low value of the superficial hardness of the softest material.

For the FREEDAM connections, the AISI 304 type stainless steel was used; it had a surface hardness of 130 HV. Five materials (ID tags M1-M5) composed of non-ferrous pure metals or metal alloys with Vickers Hardness lower than 30 were selected as soft materials. In comparison, among the remaining three hard materials (M6-M8), two were produced as powder blend and one with Electroless Nickel process from 3M Deutschland GmbH and present a superficial hardness higher than 550 HV, that in case of friction shim produced using Electroless Nickel process is between 600 and 900 HV.

The thermal spray and the Electroless Nickel Plating are the two processes used for coating the friction pads. In particular, the first process is characterized by other two categories: Electric Arc Wire and Atmospheric Plasma Spray Solutions. The materials from M1 to M5 were produced through the Electric Arc Wire process, M6 and M7 with the atmospheric Plasma and M8 with the Electroless Nickel Plating.

Complying with EN1090-2, the specimens were composed of steel plates assembled with friction shims coated with one of the eight previously discussed materials according to a layout reported in Figure 3.2. In particular, the sub-assembly is characterized by: a slotted steel plate made of 1.4301 Stainless Steel, a steel plate with traditional holes used for connecting the specimen and the testing machine, external steel plates and friction shims. In addition, M20 class 10.9 HV bolts were used.

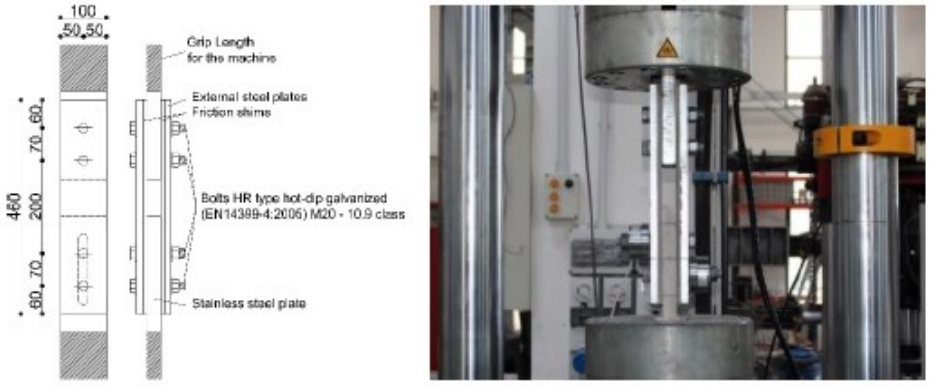

Figure 3.2 – Typical layout of a specimen (left); specimen in the testing machine (right)

The cyclic loading protocol provided by EN15129 was adopted to assess the initial slippage force and its degradation for all the specimens. The maximum slippage was defined consistently with the displacement demand of a friction damper in real applications. In particular, in the hypothesis of a friction device belonging to a FREEDAM connection with a lever arm of 600 mm and which had to accommodate a maximum rotation of 40 mrad, the maximum sliding was equal to 24 mm. Such a value was rounded to 25. The cyclic tests were performed by applying the displacements with a velocity varying between 1 mm/s and 5 mm/s. However, it is worth highlighting that during the FREEDAM project, tests with velocities of about 200 mm/s were carried out. M20 high strength bolts characterized all the specimens tightened through a torque wrench equal to $0.7A_{bolt}f_{ub}=171500\ N$.

The Schenck Hydropuls S56 universal testing machine was used to perform the tests. It is composed of a hydraulic piston with a force and a displacement capacity equal to $\pm 630\ kN$ and $\pm 125\ mm$, respectively. The acquiring data system allowed monitoring the displacement, the tightening torque, the slippage force and the bolt force. Furthermore, the bolts' preload was applied through a hand torque wrench to achieve a preload amplified with a factor equal to 1.1, as reported by EN1090-2, to consider the loosening of the preload after releasing the torque wrench. In such a way, the tightening torque applied to each bolt is about 446 Nm.
Many parameters were monitored during the tests. These data allowed to define an "effective" and an "actual" value of the friction coefficient. These factors were assessed as the ratio between the slippage force and the nominal values of the preloading forces or the bolts' forces read from the cells, respectively. The "actual" value provides a real measure of the friction coefficient, characterized by a degradation related only to the damage of the surfaces in contact; instead, the bolt loosening is assessed through donut load cells.
The present work's aim does not consist of discussing all these results. For this reason, only the primary outcomes are reported.
Typically, referring to the specimens with hard materials, the bolts lost 7% of their initial preload after the first cycle of the loading history, while the total loss at the end of the tests was about 20%. Furthermore, the degradation of the sliding force, ascribed to the degradation of the bolts' forces, was observed. In some cases (with materials M2, M3 and M5), the stick-slip phenomenon occurred due to the instability of the friction behaviour that provided the alternate and continuous sticking and slipping of the two surfaces in contact. This phenomenon was due to the high difference between the static and kinetic value of the friction coefficient.
Figure 3.3 and Figure 3.4 show the data referred to the friction coefficient and the bolt forces of the specimens with M4 material. Even though the friction coefficient is similar in the two tests, the bolt force is significantly different, inducing, as a consequence, a different hysteretic behaviour. Probably this variability is due to the production process through the arc wire spray, which is an entirely manual procedure that mainly relies on the experience of the workman. For material M4, an initial friction coefficient was observed, varying between 0.7 and 0.9.
The specimens were opened after the tests, and it was possible to observe (Figure 3.5) that the damage was concentrated on the friction shims, while the steel plates did not exhibit any damage.

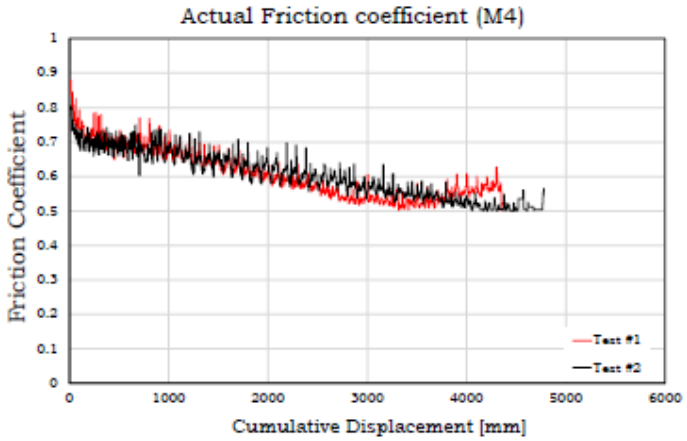

Figure 3.3 – "Actual" friction coefficient vs cumulative travel: M4

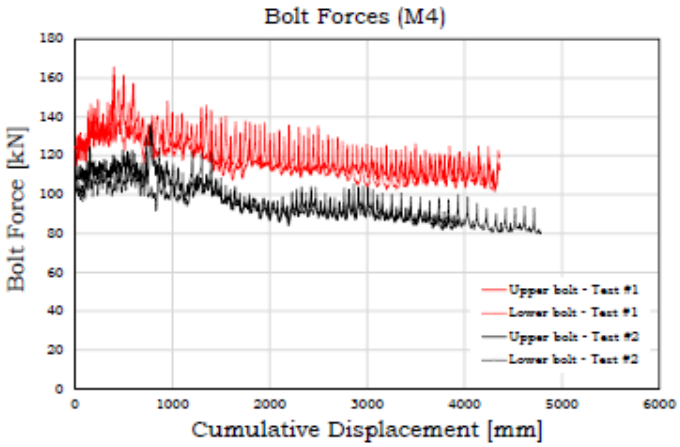

Figure 3.4 – Typical diagrams of the bolt forces

Figure 3.5 – Damage of the interfaces: M4 friction shims

The energy dissipation was not constant because of the considered value of the cumulative displacement. In fact, in Figure 3.6, the soft materials dissipate a higher amount of energy until a cumulative displacement of 1700 mm, while afterwards, the hard materials prevail.

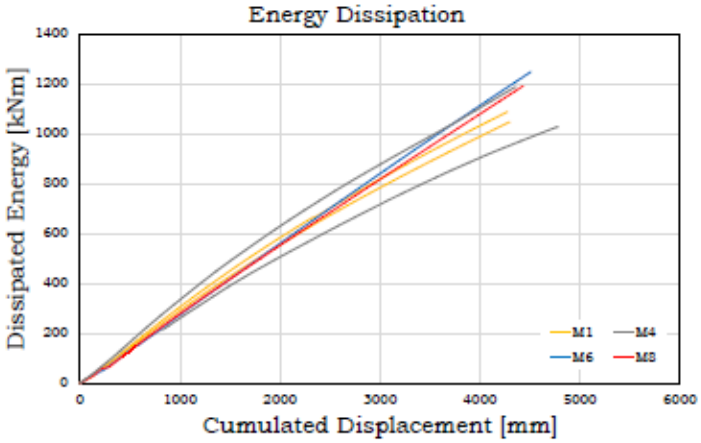

Figure 3.6 – Energy dissipation capacity

In order to select a material for the FREEDAM connection, it was helpful to refer to a target design value of the cumulative displacement based on the results of a broad set of IDAs on case study buildings.
The materials M1, M4 and M8 were considered.

During the second phase of the experimental activity, 21 tests were carried out to assess the influence of the bolts' preload and disc-springs configuration on the friction coefficient, while 30 tests were performed to evaluate the random variation of the friction coefficient.
In most of the cases, it was observed that a force-slippage behaviour characterized the tests with high initial stiffness until the achievement of the static friction coefficient that was higher than the dynamic friction coefficient obtained in the first stabilized cycle. In addition, high energy dissipation and rectangular hysteresis loops were observed (Figure 3.7).
The initial value of the friction coefficient for material M1 was between 0.67 and 0.75, for material M4 from 0.71 to 0.94, and for material M6 from 0.62 to 0.65.
A clear correlation between the friction coefficient and the bolts' force was not observed. Instead, it was noticed that the reduction of the preloading force resulted in a lower loss of the bolt's preload and lower energy degradation.

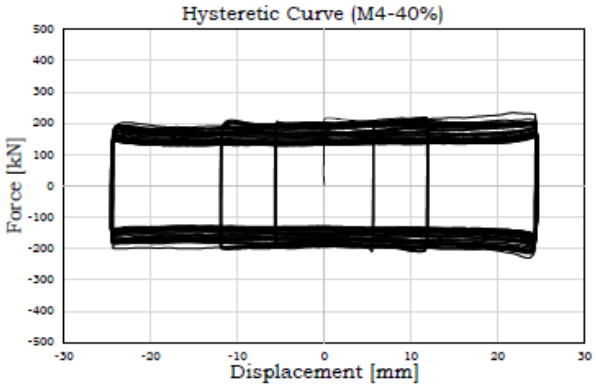

Figure 3.7 – Influence of the bolts' preload over the force-displacement hysteretic response (M4)

The conclusion was that the stick and slip phenomenon and the minimum requirements for effective damping degradation suggested limiting the preload to 60% of the proof load reported by EC3 part 1.8 [28] (Figure 3.8).

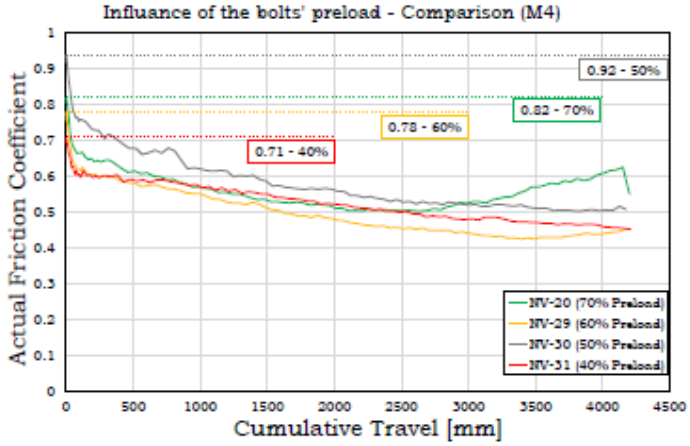

Figure 3.8 – Influence of the bolts' preload over the actual friction coefficient

According to the abovementioned considerations, the material M4 appeared to be the best solution for the FREEDAM joint.
Many other tests were performed to define a statistical range of variation of the design friction coefficients in order to know: the characteristic value of the statistic friction coefficient for SLS checks (Eq.3.1); the characteristic value of the dynamic friction coefficient to be used in the ULS

design of the dissipative components (Eq.3.2); the upper bound value of the static friction coefficient to be used, in the framework of the capacity design, for the design of the non-dissipative components of the connection and the structure (Eq.3.3).

$$\begin{cases} \mu_{eff,k} = 6.35 \cdot 10^{-5}\delta_t^2 - 6.35 \cdot 10^{-2}\delta_t + 0.69 & if\ \delta_t < 50\ mm \\ \mu_{eff,k} = 0.53 & if\ 50 < \delta_t < 400\ mm \\ \mu_{eff,k} = -1.233 \cdot 10^{-4}\delta_t + 0.579 & if\ 400 < \delta_t < 1500\ mm \\ \mu_{eff,k} = -5.32 \cdot 10^{-5}\delta_t + 0.474 & if\ 1500 < \delta_t < 4000\ mm \end{cases} \quad (3.1)$$

$$\begin{cases} \mu_{eff,ave} = 7.34 \cdot 10^{-5}\delta_t^2 - 7.34 \cdot 10^{-2}\delta_t + 0.76 & if\ \delta_t < 50\ mm \\ \mu_{eff,ave} = 0.58 & if\ 50 < \delta_t < 400\ mm \\ \mu_{eff,ave} = -9.096 \cdot 10^{-5}\delta_t + 0.616 & if\ 400 < \delta_t < 1500\ mm \\ \mu_{eff,ave} = -4.41 \cdot 10^{-5}\delta_t + 0.545 & if\ 1500 < \delta_t < 4000\ mm \end{cases} \quad (3.2)$$

$$\begin{cases} \mu_{eff,95\%} = 7.93 \cdot 10^{-5}\delta_t^2 - 7.93 \cdot 10^{-2}\delta_t + 0.84 & if\ \delta_t < 50\ mm \\ \mu_{eff,95\%} = 0.64 & if\ 50 < \delta_t < 400\ mm \\ \mu_{eff,95\%} = -7.37 \cdot 10^{-5}\delta_t + 0.669 & if\ 400 < \delta_t < 1500\ mm \\ \mu_{eff,95\%} = -3.09 \cdot 10^{-5}\delta_t + 0.604 & if\ 1500 < \delta_t < 4000\ mm \end{cases} \quad (3.3)$$

Furthermore, the influence of a particular kind of disc springs, called Belleville, was assessed. They have a cone shape and significant stiffness when subjected to elastic compression until complete flattening. These disc springs can be arranged according to two different configurations: series stack or parallel stack. In the first case, they are arranged one over the other, while in the second case, they are located face to face. In Figure 3.9, the comparison between the assembly equipped with traditional and Belleville springs is shown. It was observed that the configuration of disc springs did not influence the hysteretic response.

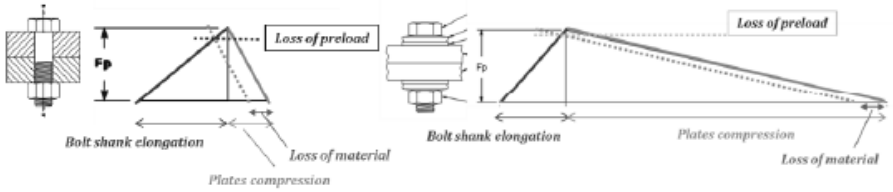

Figure 3.9 – Effect of disc springs

3.1.1.2 Tests on beam-to-column sub-assemblies

At the University of Salerno and the University of Coimbra, many experimental activities on FREEDAM joints were carried out within the framework of the homonym research project. In particular, they consisted in performing cyclic tests on external and internal beam-to-column sub-assemblies characterized both by horizontal and vertical friction dampers.

The main characteristics of the tested specimens are reported:

- FREEDAM-EX270_CYC-01 (beam IPE270 and column HEM220 in Figure 3.10), which was an external joint with the horizontal arrangement of the friction shims that were pre-stressed with M20 class 10.9 HV bolts and 6 disc-springs;
- FREEDAM-EX270_CYC-02 (beam IPE270 and column HEM220 in Figure 3.10), which was an external joint with the vertical arrangement of the friction shims that were pre-stressed with M20 class 10.9 HV bolts and 6 disc-springs;
- FREEDAM-EX270_CYC-03, which had the same configuration of FREEDAM-EX270_CYC-01, but without disc springs;
- FREEDAM-EX270_CYC-04, which had the same configuration of FREEDAM-EX270_CYC-02, but without disc springs;

- FREEDAM-IN270_CYC-01 (beam IPE270 and column HEM220 in Figure 3.11), which was an internal joint equipped with a friction device realized with a haunch and a horizontal slotted steel plate made of 1.4301 Stainless Steel, bolted to the column with mild steel angles and friction shims, all tightened with M20 class 10.9 HV bolts plus 6 disc springs;
- FREEDAM-IN270_CYC-02 (beam IPE270 and column HEM220 in Figure 3.12), which was a joint equipped with a friction device realized with a vertical rib made of stainless steel, bolted to the beam flange and the column through L-stubs and friction shims, tightened with M20 class 10.9 HV bolts plus 6 disc springs;
- FREEDAM-IN450_CYC-01 (beam IPE450 and column HEB500 in Figure 3.13), which was a joint equipped with a friction device similar to FREEDAM-IN270_CYC-01, employing in the bolted assemblies 6 disc springs;
- FREEDAM-IN450_CYC-02 (beam IPE450 and column HEB500 in Figure 3.14), which was a joint equipped with a friction device similar to FREEDAM-IN270_CYC-02, employing in the bolted assemblies 6 disc springs.

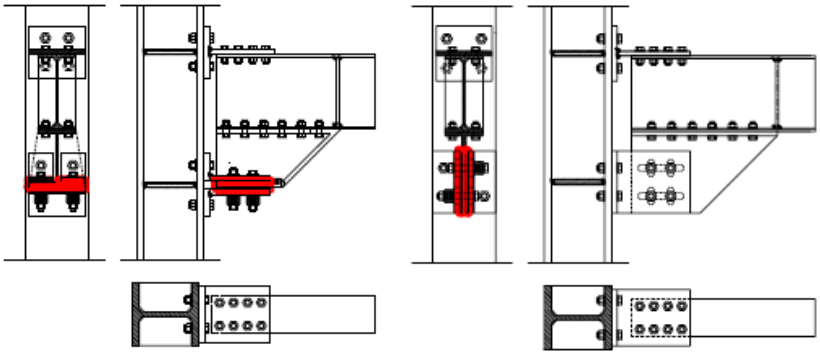

Figure 3.10 – FREEDAM-EX270_CYC-01 (left) and FREEDAM-EX270_CYC-02 (right)

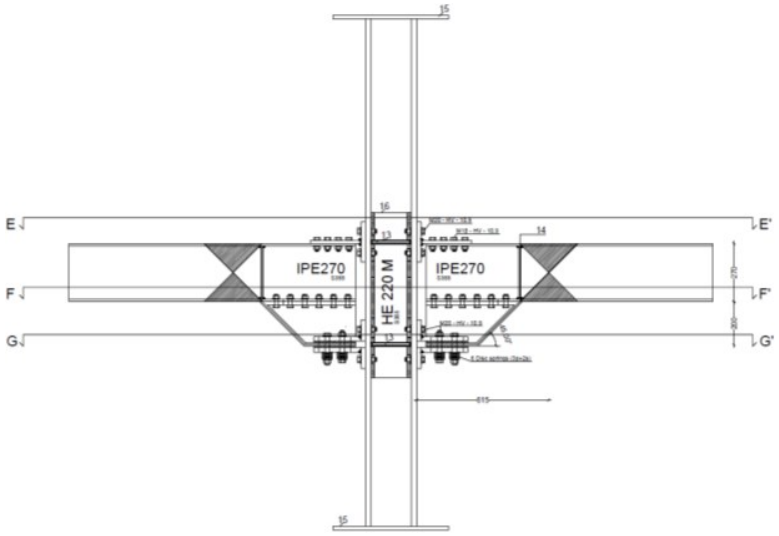

Figure 3.11 – FREEDAM-IN270_CYC-01

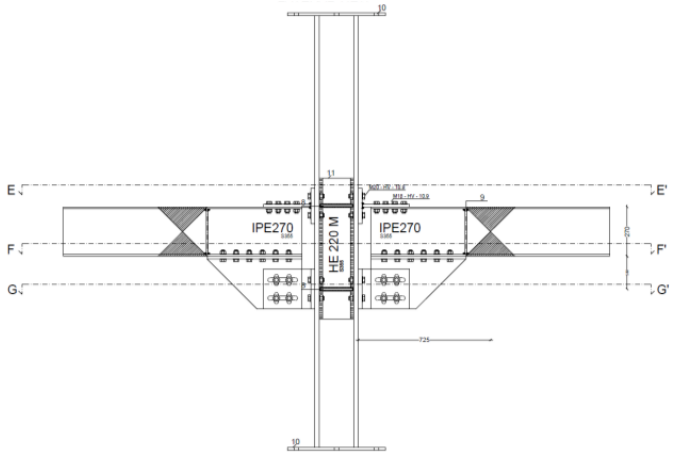

Figure 3.12 – FREEDAM-IN270_CYC-02

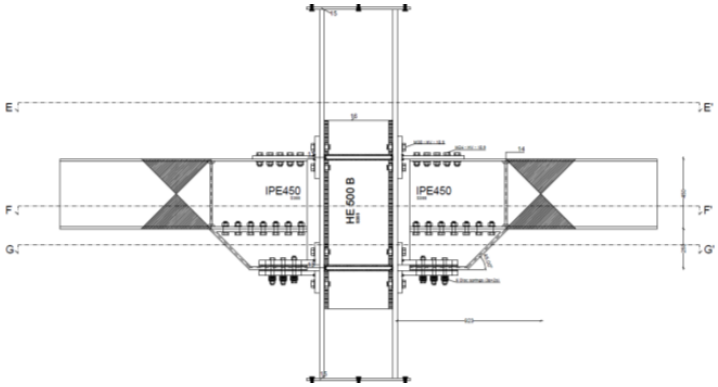

Figure 3.13 – FREEDAM-IN450_CYC-01

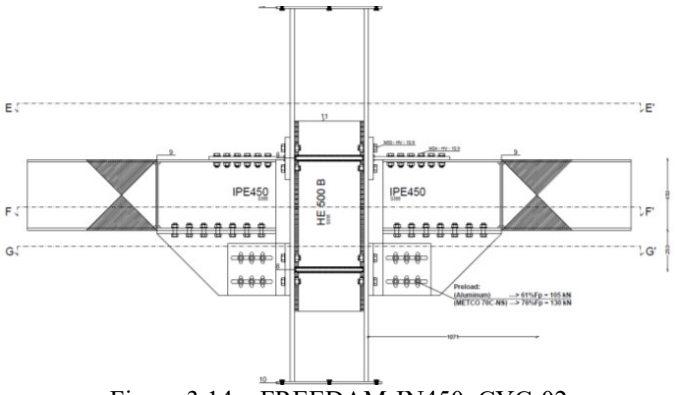

Figure 3.14 – FREEDAM-IN450_CYC-02

The experimental tests on the external connections were performed at the STRENGTH laboratory of the University of Salerno, and for this reason, the same experimental set-up adopted for the tests on CHS to through-all connections has been used. For clarity, further details are not reported, but they can be found in Chapter 2.

Instead, the tests on the internal joints were carried out at the University of Coimbra. Even though, also in this case, cyclic loading histories were applied, the experimental set-up was quite different since the column was supported only by a bottom hinge while the beam ends were vertically supported, allowing the lateral movement of the specimens, as shown in the mechanical scheme of the test layout in Figure 3.15.

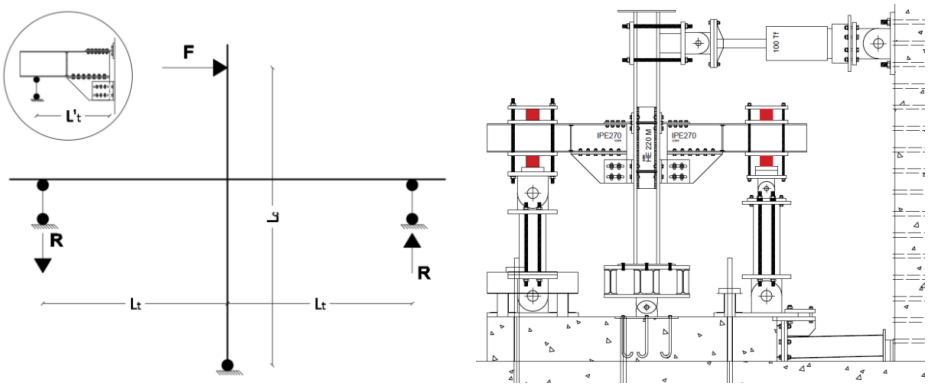

Figure 3.15 – Static scheme for the calculation of the constraint reactions in the test layout (left) and test layout (right)

The displacement history was applied to the top of the column employing a horizontal actuator with a force capacity of $\pm 900\ kN$. The constraints reactions were assessed through the equation $R = F \times L'_c/(2 \times L_t)$, while the maximum moment in the beam to column connection was defined as $M_t = R \times L'_t$. In all the cases, the length of the column was equal to 2481 mm, L_t was equal to 1125 mm and 1630 mm for the configurations with IPE270 and IPE450 beams, respectively. Instead, L'_t was equal to 1005 mm and 1380 mm for the configurations with IPE270 and IPE450 beams, respectively.

The applied loading history was defined to comply with the provision AISC 341/2010 [29], with a maximum rotation higher than the minimum required by EC8 [30] (35 mrad).

The acquiring data system was characterized by: 4 load cells (maximum capacity 500kN in compression); 15 displacement transducers - LVDT (n.4 sensors range ±25mm; n.4 sensors range ±50mm); 1 static torque transducer (nominal torque 1000Nm); 2 thermocouples; 4 annular load cells (capacity 350kN); 46 strain gauges (length 6mm, strain limit 5%).

For the sake of clarity, since the discussion of the experimental results on beam-to-column sub-assemblies belongs to the literature review and is not the topic of this thesis, only the main experimental outcomes referred to the following connections are briefly summarized:

- FREEDAM-EX270_CYC-02;
- FREEDAM-IN270_CYC-02.

The experimental evidence confirmed the connections' expected behaviour in all the cases, stressing their high energy dissipation capacity and the very limited yielding of the nodal components (T-stubs and L-stubs).

The connection FREEDAM-EX270_CYC-02 (Figure 3.16) showed the supposed rigid-plastic hysteretic response (Figure 3.17), achieving maximum bending moments equal to 185 kNm and 210 kNm in sagging and hogging, respectively. In this case, the bolt preload was set so that the sliding bending moment was equal to the plastic resistance of the beam.

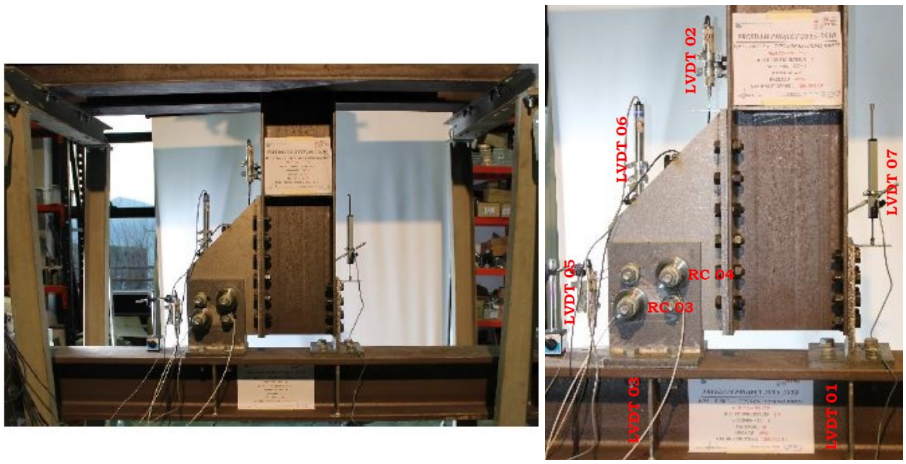

Figure 3.16 – FREEDAM-EX270_CYC-02

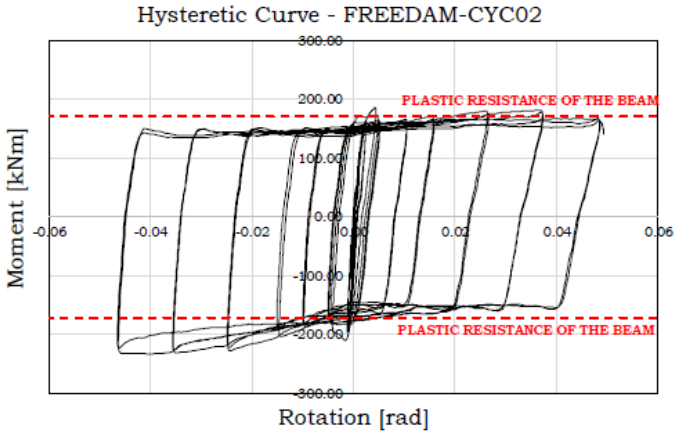

Figure 3.17 – Moment-rotation curve (specimen FREEDAM-EX270_CYC-02)

Considering the connection FREEDAM-IN270_CYC-02 (Figure 3.18), the moment-rotation hysteretic curve referred to the left column flange is shown in Figure 3.19. A rectangular shape of the hysteretic curves is observed. Furthermore, it is possible to highlight that there is no stiffness or strength degradation. The global and local behaviour of the connection was in line with the predictions. The friction dampers demonstrated to dissipate energy, avoiding any damage to the other non-dissipative components.

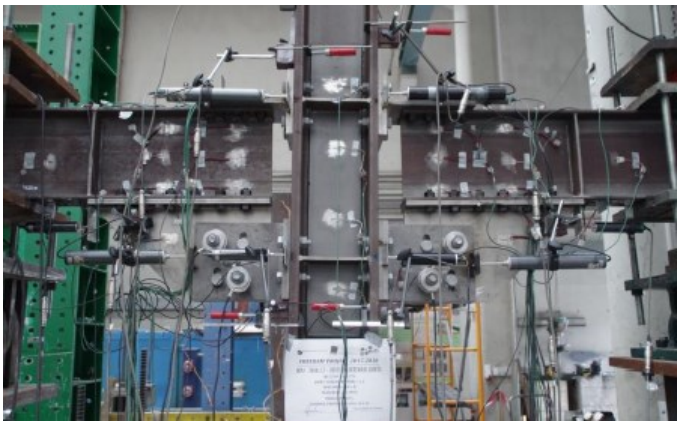

Figure 3.18 – FREEDAM-IN270_CYC-02

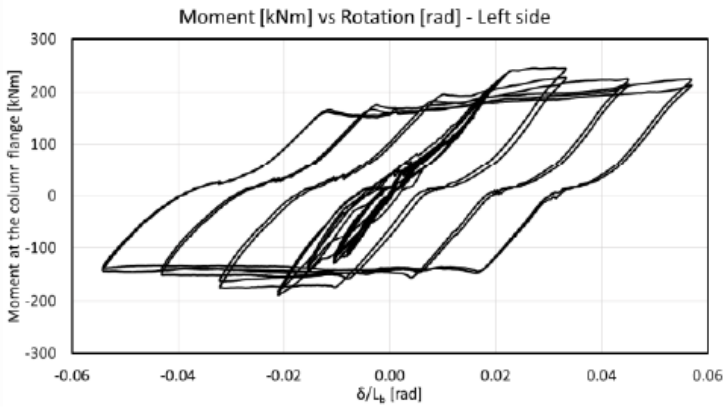

Figure 3.19 – Moment-rotation curve (specimen FREEDAM-IN270_CYC-02)

Observing the hysteretic curves (Figure 3.17 and Figure 3.19), it is possible to note that the connections behaved asymmetrically. The main reason for this asymmetry is due to the different behaviour of the damper in tension/compression due to the variation of the bolt forces.
The reduction of stiffness when the positive bending moment is close to zero is caused by local minor and negligible slidings due to the clearance of the bolted connections, which compose the experimental layout (connection between the swivels and the reaction frames, bolted supports to rigid constraints).
In the case of the tested specimen FREEDAM-IN270_CYC-02, the bolt preload was also monitored through load cells. As shown in Figure 3.20, there is a loss of preload at the beginning of the test, which increases along with the cycles.

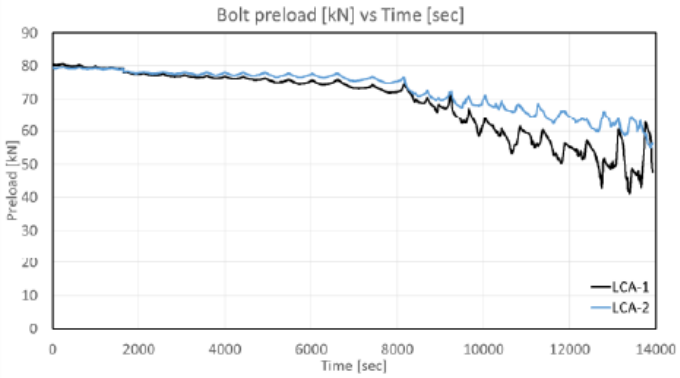

Fig. 4.48 – Bolt preload vs Time - Left side

Figure 3.20 – Bolt preload vs Time

3.1.2 Numerical activity

In order to extend the experimental results to a wide range of other cases, many Finite Element (FE) models were developed with Abaqus software and validated against the experimental results. In particular, the FE simulations were performed for all the above-listed connections experimentally tested. Also, for simplicity, no detailed data about these numerical models are reported since they can be found in the literature; nevertheless, the essential information to demonstrate the accuracy of the proposed numerical approach is briefly discussed.

In particular, consistently with the experimentally tested specimens shown in the previous paragraph, the attention is focused only on the connections FREEDAM-EX270_CYC-02 and FREEDAM-IN270_CYC-02.

The specimens' geometries have been defined by extruding the cross-sections along the longitudinal direction. The finite element type of C3D8R (an 8-node linear brick with reduced integration) was chosen for meshing all the components (Figure 3.21).

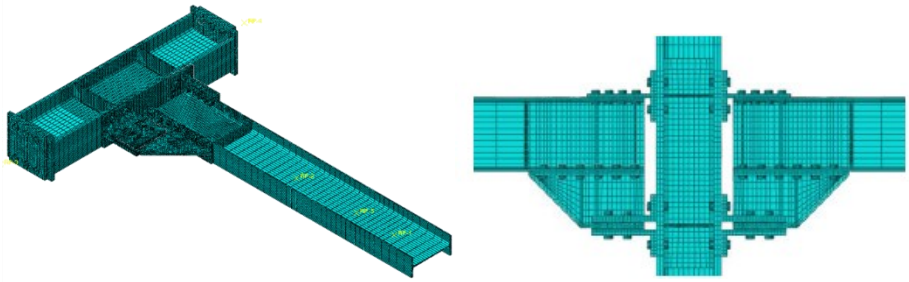

Figure 3.21 – FE models: mesh

The bolts were modelled by meshing a solid cylinder with the bolt's nominal circular gross area.

In Figure 3.22, the constitutive laws adopted to model the material properties of the structural elements and the bolts are shown.

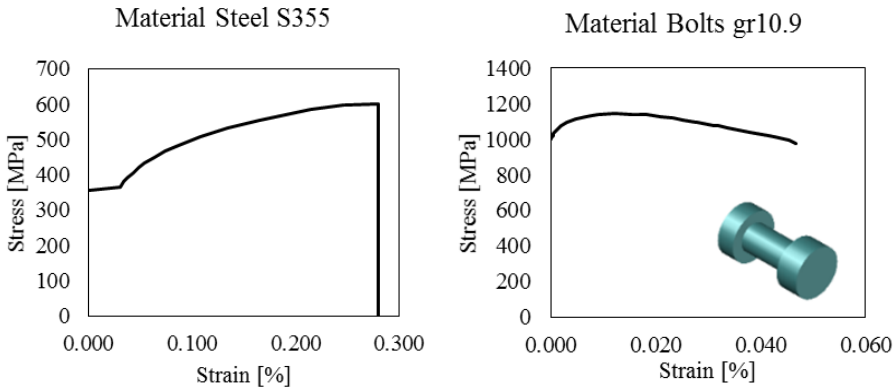

Figure 3.22 – Materials used for the structural elements (left) and the bolts (right)

The interactions between the surfaces in contact (e.g. bolt-to-plates, plate-to-plate) were modelled considering both "Normal" and "Tangential" behaviour. The former was implemented considering "Hard Contact", while the latter was modelled differently for the steel-to-steel interfaces and the friction pad-to-steel interfaces. The main difference between the two types of contacts was the definition of the friction coefficient. A constant value equal to 0.3 was considered for the steel-to-steel surfaces, while the dynamic friction coefficients obtained from lap-shear tests with the friction material considered are used for the friction damper.

The clamping of the bolts was modelled through the "Bolt load" option available in the FE software.

The boundary conditions were modelled to be representative of those adopted for both the experimental set-ups used for the tests on the external and internal joints.

In order to evaluate the fitness of the modelling assumptions, the results of numerical analyses simulating the experimental conditions were compared with the results of experimental tests performed at the University of Salerno and the University of Coimbra.

In Figure 3.23, the comparison between the experimental and numerical results referred to the specimen FREEDAM-EX270_CYC-02 are reported together with the development of the PEEQ. The numerical simulation can accurately reproduce the experimental moment-rotation hysteretic response. The figure also provides the spread of the plastic deformation at the assembly level. The limited PEEQ concentrations at the base of the Tee and L-stub's webs can be explained because the nominal S355 steel properties were used instead of the actual ones. Consistently with the experiments, no damage was observed in these regions.

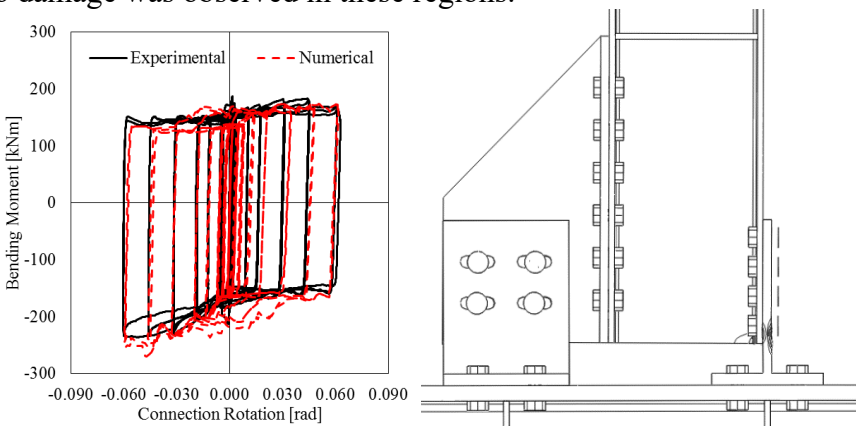

Figure 3.23 – Experimental vs FE results: FREEDAM-EX270_CYC-02

The same remarks can be attributed to the specimen FREEDAM-IN270_CYC-02, as reported in Figure 3.24 and Figure 3.25. In addition, however, some approximations of the prediction of the moment-rotation hysteretic curve were observed (Figure 3.26).

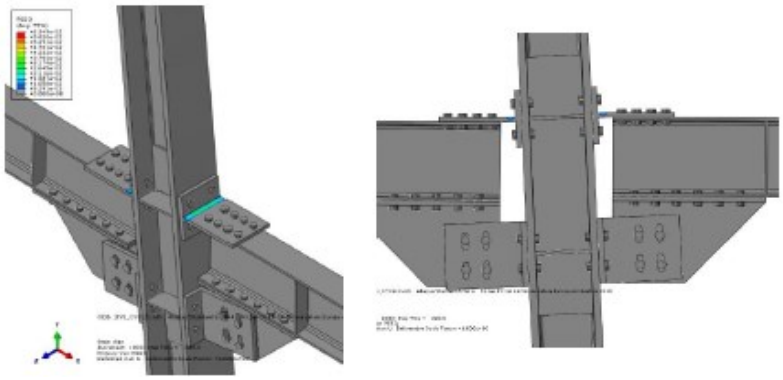

Figure 3.24 – FREEDAM-IN270_CYC-02: PEEQ

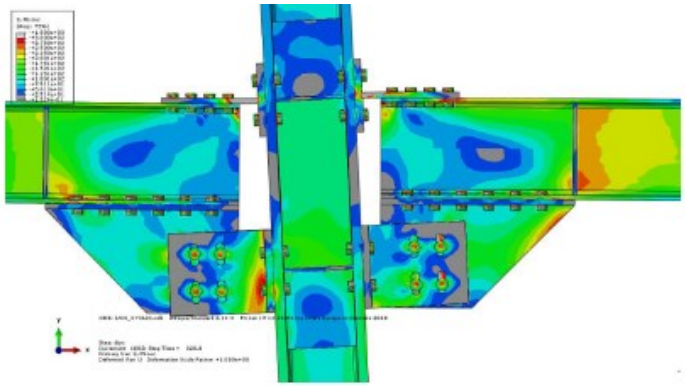

Figure 3.25 – FREEDAM-IN270_CYC-02: von Mises stress

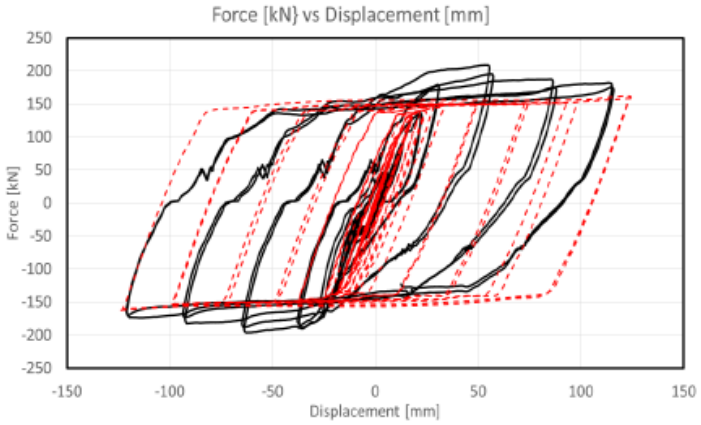

Figure 3.26 – Experimental vs FE results: FREEDAM-IN270_CYC-02

The numerical activity demonstrated that the FE models accurately predicted the response of friction connections, exhibiting an initial linear-elastic behaviour up to the activation of the sliding mechanism and subsequently a nonlinear response within the boundaries of the sliding mechanism (limited by the slotted holes). Furthermore, the FE models confirmed the high energy dissipation capacity provided by the joints. In particular, the energy was dissipated in the friction device and only up to 6% of plastic deformation was observed in the replaceable parts of the column face connection (T and L-stubs) while both beam and column remained elastic.

3.1.3 Design formulations

Within the framework of the FREEDAM project, a design procedure for the FREEDAM joints was developed according to the methodology provided by Eurocode 3 [28]. In particular, this approach strongly depends on the two capacity design principles. In fact, according to the first principle, the first step is the design of the friction damper, which is the dissipative component; instead, the second step is focused on the design of the non-dissipative components (i.e. T-stub, angles, haunch).

In this section, only the design procedure for the configuration concerning the vertical damper (Figure 3.27) is summarized. Furthermore, only the main steps will be reported, discussing in detail only those referring to the design of the dissipative component.

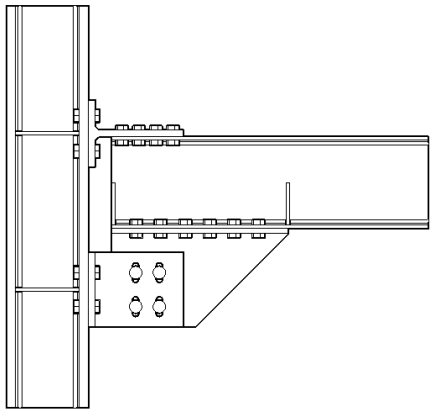

Figure 3.27 – Configuration with the vertical damper

Design of the dissipative component: the friction device

Step 1: Evaluation of the device's design actions and the tightening torque design.

This step is devoted to the design of the friction damper according to the maximum bending moment in seismic combinations $M_{Seismic,d}$ and the maximum bending moment in non-seismic combinations. The lever arm of the connection (z) is defined as the distance between the barycentre of the bolts and the stem-to-flange attachment of the upper T-stub. The design slippage force of the device is defined as follows:

$$F_{cf.Seismic,d} = \frac{M_{Seismic,d}}{z}$$
$$F_{cf.Non-seismic,d} = \frac{M_{Non-Seismic,d}}{z} \quad (3.4)$$

The slip resistance is equal to:

$$F_{slip} = \mu \cdot F_p \cdot n_b \cdot n_s \quad (3.5)$$

μ is the design value of the friction coefficient, which can assume several values depending on the considered load combination. The significant values to be used in the design are: i) $\mu_{dyn,5\%}$ that is the 5% fractile of the effective dynamic friction coefficient used to evaluate the resistance at ULS seismic load combinations; ii) $\mu_{stat,5\%}$ that is the 5% fractile of the effective static friction coefficient used to evaluate the resistance of the damper in the non-seismic load combinations both at SLS and ULS. F_p is the bolt preloading force computed according to EC3 (the proof preload equal to $F_p = 0.7 \cdot A_{res} \cdot f_{ub}$), n_b is the number of bolts, n_s is the number of the surfaces.

In order to define the minimum number of bolts required to assure the slip resistance of the friction damper, it is possible to write:

$$F_{cfSeismic,d} = \frac{\mu_{dyn,5\%} \cdot F_p \cdot n_{b,min.1} \cdot n_s}{\gamma_{M3} \cdot \gamma_{creep}}$$
$$F_{cf.Non-Seismic,d} = \frac{\mu_{stat,5\%} \cdot F_p \cdot n_{b,min.2} \cdot n_s}{\gamma_{M3} \cdot \gamma_{creep}} \quad (3.6)$$

where γ_{M3} is the partial safety factor given by Eurocode 3 Part 1-8 [28] equal to 1.10 and γ_{creep}, is a factor determined through long-term experimental tests accounting for the loss of initial preload over time. The value of this factor depends on the adopted bolt assembly. Based on the long-term tests performed, this could be conservatively assumed equal to 1.15 for assemblies including disc springs or flat washers. Starting from Eq.3.6, once the bolt diameter is fixed, the number of the minimum bolts ($n_{b,min}$) can be obtained and rounded (n_b):

$$n_{b,min} = \{n_{b,min.1};\ n_{b,min.2}\}$$
$$n_{b,min.1} = \frac{F_{cfSeismic,d} \cdot \gamma_{M3} \cdot \gamma_{creep}}{\mu_{dyn,5\%} \cdot F_p \cdot n_s}$$
$$n_{b,min.2} = \frac{F_{cf.Non-seismic,d} \cdot \gamma_{M3} \cdot \gamma_{creep}}{\mu_{stat,5\%} \cdot F_p \cdot n_s} \quad (3.7)$$

The rounded value of the number of the bolts allows for assessing a new preloading force:

$$F_{p,red.1} = \frac{F_{cf,Seismic,d}}{\mu_{dyn,5\%} \cdot n_b \cdot n_s} \qquad if\ n_{b,min} = n_{b,min.1}$$
$$F_{p,red.2} = \frac{F_{cf.Non-Seismic,d}}{\mu_{stat,5\%} \cdot n_b \cdot n_s} \qquad if\ n_{b,min} = n_{b,min.2} \quad (3.8)$$

Finally, after defining the bolt number and their torque, the design friction resistance of the damper can be re-evaluated as:

$$F_{friction,Rd.1} = \mu_{dyn,5\%} \cdot F_{p,red.1} \cdot n_b \cdot n_s$$
$$F_{friction,Rd.2} = \mu_{stat,5\%} \cdot F_{p,red.2} \cdot n_b \cdot n_s \quad (3.9)$$

The corresponding value of the design flexural friction resistance is:

$$M_{friction,Rd} = max\{M_{friction,Rd.1}; M_{friction,Rd.2}\} \quad (3.10)$$

Step 2: Design of the horizontal slots

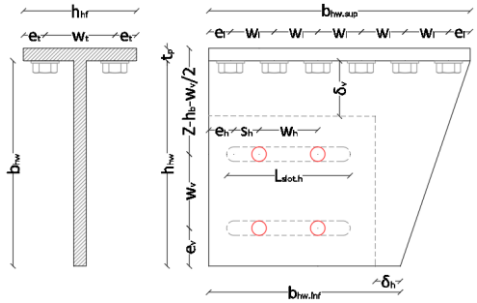

Figure 3.28 – Scheme of the haunch of the FREEDAM device with vertical damper

Concerning Figure 3.28, some geometrical parameters can be defined:

- Horizontal pitch:

$$w_h = k_{wh} \cdot d_0 \quad (3.11)$$

- Horizontal distance of the slot from the free edge:

$$e_h = k_{eh} \cdot d_0 \quad (3.12)$$

- Vertical pitch:

$$w_v = k_{wv} \cdot d_0 \quad (3.13)$$

- Vertical distance of the slot from the free edge:

$$e_v = k_{ev} \cdot d_0 \quad (3.14)$$

where d_0 is the diameter of the hole and k_{eh}, k_{ev} (whose minimum value is 1.2 according to the code requirements for bolts spacing), k_{wv}, k_{wh} (whose minimum value is 2.4 or 2.2 according to the code requirements for bolts spacing) are coefficients governing the geometry of the device.

For typical configurations, trial values of these coefficients can be suggested as follows:

$$k_{wh} = 2.5 \div 3.5; \; k_{eh} = 1.5 \div 2.5;$$
$$k_{wv} = 5 \div 6; \; k_{ev} = 2.5 \div 3.5$$

- The minimum length of the horizontal slots:

$$l_{slot,h,min} = \left(\frac{n_b}{2} - 1\right) \cdot w_h + d_0 + 2 \cdot \phi \cdot \left(z + \frac{w_v}{2}\right) \quad (3.15)$$

where ϕ is the ultimate rotation of the joint, which has been set equal to 50 mrad, which is a value 40% higher than 35 mrad, that represents the minimum value required by EC8 [30];

- Required horizontal stroke at the slotted hole level:

$$stroke_{h,D} = \phi \cdot \left(z + \frac{w_v}{2}\right) \tag{3.16}$$

- Available stroke at the slotted hole level:

$$stroke_{h,A} = \frac{l_{slot,h} - \left(\frac{n_b}{2} - 1\right) \cdot w_h - d_0}{2} \tag{3.17}$$

- Minimum horizontal displacement at the tip of the haunch:

$$\delta_{h,min} = \phi \cdot \left[e_v + \frac{w_v}{2} + z\right] \tag{3.18}$$

- The thickness of the haunch flange is taken equal to the thickness of the beam flange to satisfy the plate's check in bearing.

Design of non-dissipative components

Step 3: Calculation of the design actions for the non-dissipative components.
Applying the second principle of capacity design, the maximum bending moment at the column face $M_{cf.Cd}$ can be determined considering a proper over-strength as:

$$M_{cf,Rd} = M_{friction,Rd} \cdot \gamma_{ov} \tag{3.19}$$

where γ_{ov} is the overstrength factor accounting for the random variability of the slip resistance of the damper. For example, this factor can be assumed equal to 1.87 for aluminium friction pads. Consequently, the design resistance of the device multiplied by the overstrength factor is:

$$F_{friction,Rd} = \frac{M_{cf,Rd}}{z} \tag{3.20}$$

Finally, the design shear action is evaluated as:

$$V_{Ed} = \frac{2 \cdot M_{cf,Rd}}{(L - 2a)} + q_D \cdot \frac{(L - 2a)}{2} \tag{3.21}$$

where L is the span length, a is the half-size of the column and q_D is the span load (Figure 3.29).

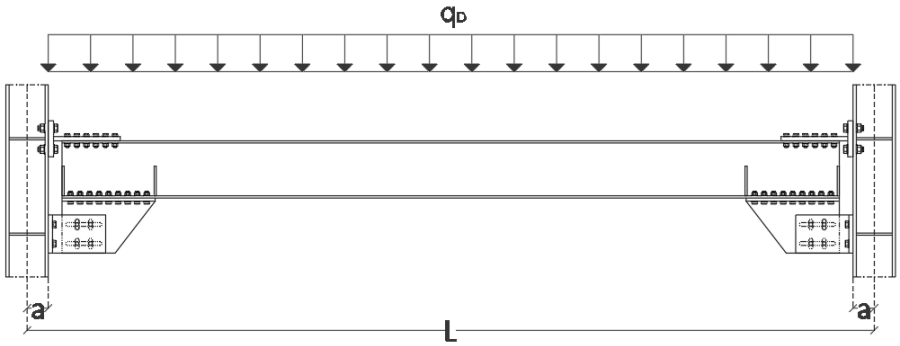

Figure 3.29 – Reference structural scheme

Step 4: Design of the T-stub.

The basic formulations adopted for the design of a T-stub are applied. However, it is worth highlighting that the size of the beam-column gap has to be determined by accommodating the joint design rotation with a typical value of 50 mrad to account for local ductility demand at ULS and execution tolerances. Additionally, the gap should be sized to provide sufficient ductility to the plastic hinge forming at the T-stub web in case of seismic events. Based on the experimental and FE analyses performed in the other tasks of the project, to meet this requirement, the gap has to be higher than $t_{T.f} + 2 \cdot t_{T.w}$. Therefore, in order to satisfy both requirements, the gap size has to be equal to:

$$gap_{min} = max\left\{t_{T.f} + 2 \cdot t_{T.w}; \phi \cdot (m_T + n_T) + t_{T.f}; \phi \cdot \left(e_v + \frac{w_v}{2} + z\right)\right\} \quad (3.22)$$

Step 5: Design and check of haunch.

Step 6: Design of the L-stub.

Step 7: Check the beam resistance

The bending moment at the column flange $M_{cf,Rd}$ could be greater than the plastic bending resistance of the beam. Therefore, it is essential to evaluate the bending moment at the potential plastic hinge location $M_{b.Ed}$ (Figure 3.30).

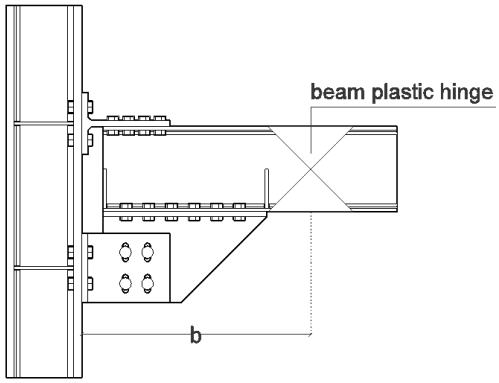

Figure 3.30 – Position of the potential beam plastic hinge

The beam, in this case, is a non-dissipative zone and has to be checked according to the following inequality:

$$M_{b.Ed} = M_{cf,Rd} \cdot \frac{L_e - b}{L_e} \leq M_{b.Rd} \quad (3.23)$$

where L_e is the shear length of the beam equal to $M_{cf,Rd}/V_{Ed}$ and b is the horizontal extension of the joint. If the inequality is not satisfied, the beam section has to be increased. It is important to underline that this check is automatically satisfied when the partial strength factor is equal to or lower than 0.534. In fact, in that case, the bending moment at the column face $M_{cf,Rd} = 0.534 \cdot 1.87 \cdot M_{b.Rd} = M_{b.Rd}$. Finally, two stiffeners must be adopted to avoid transverse buckling of the beam web unless more accurate checks are performed (Figure 3.31).

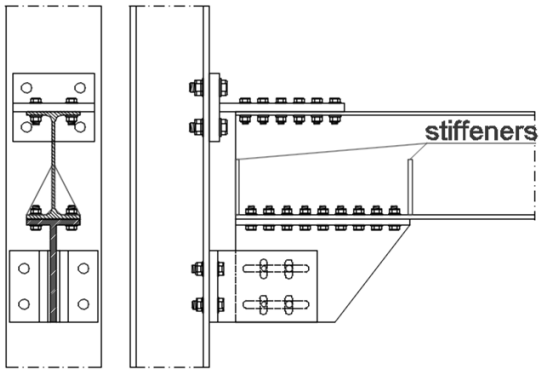

Figure 3.31 – Position of the beam web stiffeners

3.2 Dissipative T-stub connection

The joints with friction devices represent a good solution for the seismic design of steel structures; however, some of the recent research outcomes are not included yet in technical codes and provisions. Instead, much literature and proposals concerning other partial-strength bolted connections' typologies can be found [8, 30-35]. In particular, with this approach, the energy dissipation capacity can be promoted in well-defined nodal components, which can be easily substituted after the occurrence of a severe seismic event ensuring, in such a way, fast and cheap restoration of the building functionality.

The double split T-stub joint represents a good example of such a strategy. This connection typology is characterized by using a couple of T-stubs to connect the beam flanges to the column. The T-stubs, if properly designed, can act as seismic dampers with levels of ductility and energy dissipation capacity that can be easily calibrated in the design phase. With this approach, the upper and lower flanges of the beam ends are bolted to the stems of T elements which are bolted to the flange of the column (Figure 3.32).

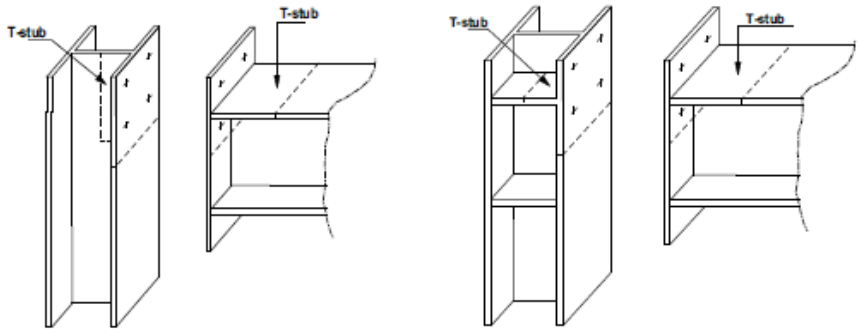

Figure 3.32 – T-stub mechanical model of an extended-end-plate connection

According to the component method approach, the bending moment at the beam end can be idealised as opposite horizontal forces, respectively stressing the T-stubs in tension and compression.

Many studies have been carried out on the classic T-stub connection; in particular, also a component method approach has been proposed by Zoetemeijer [36] starting from the knowledge of the single component (T-stub) and thoroughly investigated by many other authors [8, 9, 37, 38]. In particular, the crisis of the T-stub can occur according to three different mechanisms (Figure 3.33).

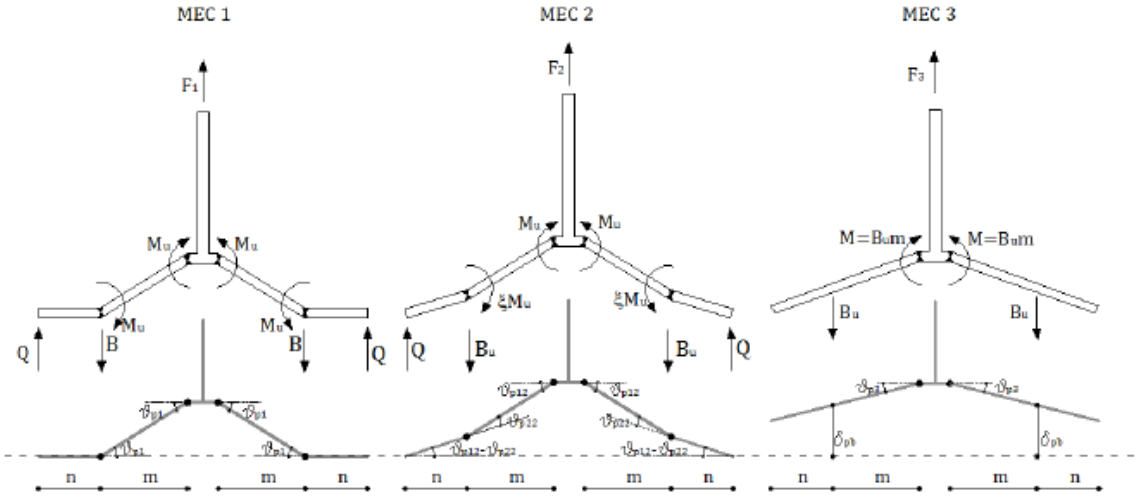

Figure 3.33 – T-stub collapse mechanisms

Details on the behaviour of the T-stub can be found in literature, and for this reason, they are not reported in this thesis. It is only worth highlighting that the most dissipative failure mechanism (type-1) is characterized by the development of four plastic hinges, two at the bolt line and two at the stem-to-flange attachment. In this case, the bending moment diagram along the flange of the T-stub is linear with equal values where the plastic hinges are located. Due to the rectangular shape of the flange, only the ends of the dissipative element can yield, confining the plastic deformation in predetermined regions inducing high curvature and strain demand.
In particular, assuming $\lambda = n/m$, the law which governs the behaviour of a T-stub can be expressed according to Figure 3.34.

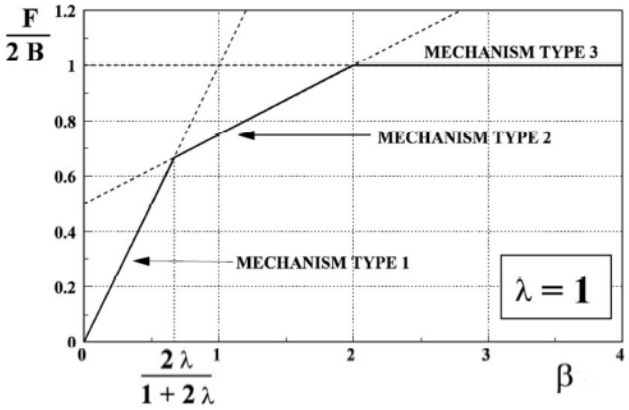

Figure 3.34 – Influence of the geometric properties on the collapse mechanism of the T.stub

It is possible to observe that the parameter $\beta = 4M_f/(2Bm)$, which depends on the geometry of the T-tub, affects the collapse behaviour according to the following rules:

- mechanism type 1 (flange collapse) if $\beta < \frac{2\lambda}{1+\lambda}$;
- mechanism type 2 (flange collapse and bolt failure) if $\frac{2\lambda}{1+\lambda} < \beta < 2$;
- mechanism type 3 (bolt failure) if $\beta > 2$.

The first mechanism is typical of T-stubs with thin flanges and strong bolts, while the third is typical of elements with thick flanges and weak bolts.

The response of the single T-stub has been widely explored, as highlighted in Chapter 1. However, Latour and Rizzano [40-42] have proposed another connection characterized by X-shaped T-stubs to enhance energy dissipation capacity.
This connection typology differs from the traditional one because the flange of the T-element is properly cut thanks to an hourglass shape so that the shape on the flange is similar to the shape of the bending moment which arises in the part of the plate between the stem and the bolts. In such a way, it is possible to ensure a uniform yielding of this part (Figure 3.35).

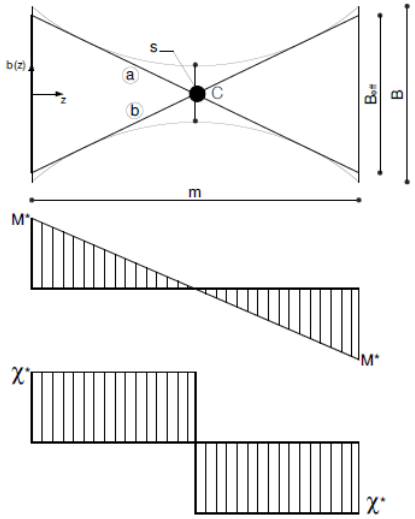

Figure 3.35 – Hourglass shape of the T-stub

This strategy is based on the behaviour of hysteretic dampers working in double curvature (ADAS in Figure 3.36).

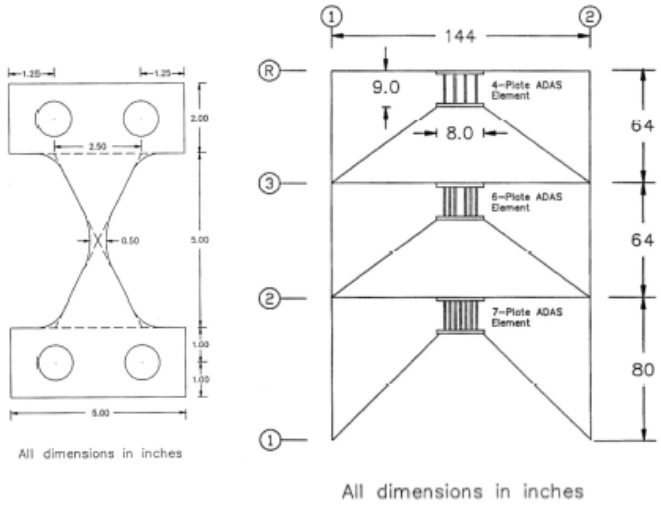

Figure 3.36 – ADAS device (left) and its application to an MRF (right)

The geometry of these devices is defined through an exponential function empirically derived by Tena-Colunga [39]:

$$\begin{cases} b(z) = Be^{-\alpha z} & per\ 0 \le z \le m/2 \\ b(z) = s \cdot e^{\alpha\left(z-\frac{m}{2}\right)} & per\ m/2 \le z \le m \end{cases}$$
$$\alpha = \frac{2}{m} ln\left(\frac{B}{s}\right) \tag{3.24}$$

In particular, s is the width of the mid-section, B is the width of the clamped section, and m is the distance between the plastic hinges.
According to Eurocode 3, it is possible to assume $m = d - 0.8r$, where d is the distance between the bolt axis and the face of the T-stub web and r is the radius of the flange-to-web attachment in the case of rolled T-stub or $r = a_c\sqrt{2}$ in the case of welded T-stub with a_c equal to the weld throat thickness.
Due to the complex geometry, simplified models assess the initial stiffness (Figure 3.37), resistance and ductility.

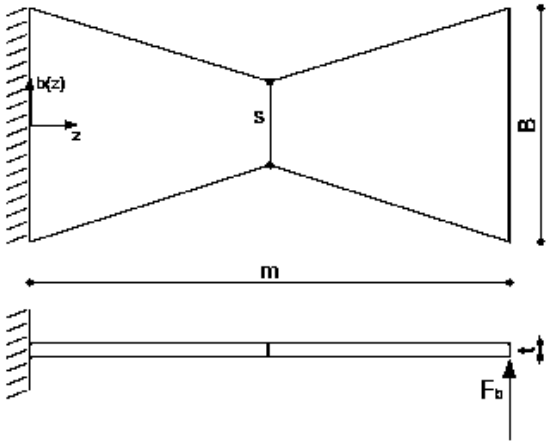

Figure 3.37 – Simplified model for the stiffness prediction

In particular, as reported in [8], the initial stiffness of the T-stub can be assessed through a mechanical approach based on an equivalent cantilever model, which leads to the formulation:

$$K_{o,HS} = \zeta \frac{EBt^3}{m^3} \tag{3.25}$$

Where:

$$\begin{cases} \zeta = \dfrac{2(B-s)}{3B} \dfrac{4(B-s)^2}{4(B-s)A_1 + 4(B-s)A_2 - 2A_3} \\ A_1 = [(B-s) + (B-2s)\ln(B/s)] \\ A_2 = [(s-B) + Bln(B/s)] \\ A_3 = [(3s-B)(B-s) + 2B(B-2s)ln(B/s)] \end{cases} \tag{3.26}$$

For $s/B = 1, \zeta = 0.5$ for the T-stub with rectangular flange; instead, for s/B ranging between 0.1 and 0.2, ζ can be assumed equal to 0.25 (Figure 3.38).

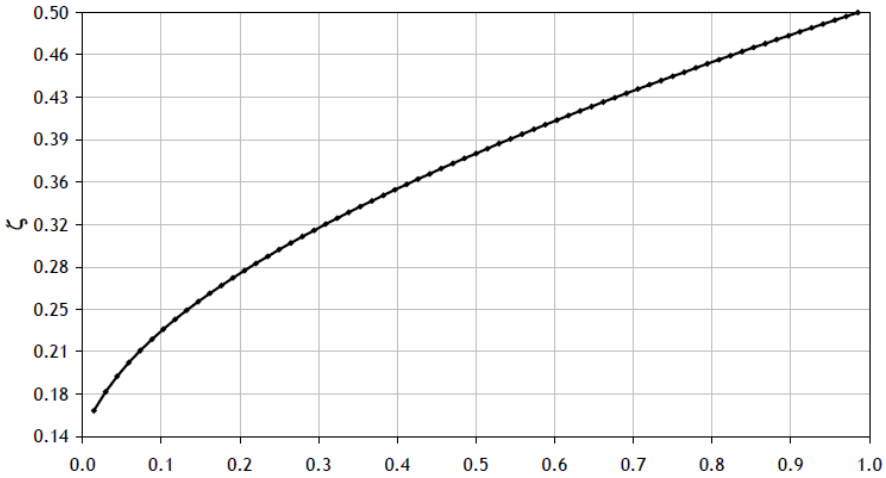

Figure 3.38 – Correlation between ζ factor and the ratio s/B

The inelastic monotonic force-displacement curve of the dissipative T-stub can be defined by increasing the bending action on the T-stub in the hypothesis that the zero-moment point is located at the centre of the distance between the bolt axis and the stem-to-flange attachment.
Also in this case, a simplified model is adopted (Figure 3.39); it allows assessing the effective width (B_{eff}) through:

$$B_1(z) = Be^{-\alpha z}$$
$$B_2(z) = B_{eff} - \frac{2B_{eff}}{m} z \tag{3.27}$$

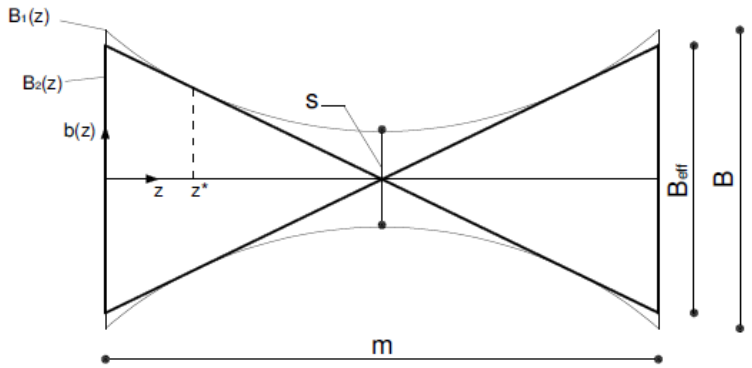

Figure 3.39 – Definition of the effective width

After mathematical formulations, which can be found in the works published by Latour and Rizzano [40-42], it is possible to define (Figure 3.40):

$$B_{eff} = B \cdot e \cdot \left(\frac{s}{B}\right) \cdot ln\left(\frac{B}{s}\right) \tag{3.28}$$

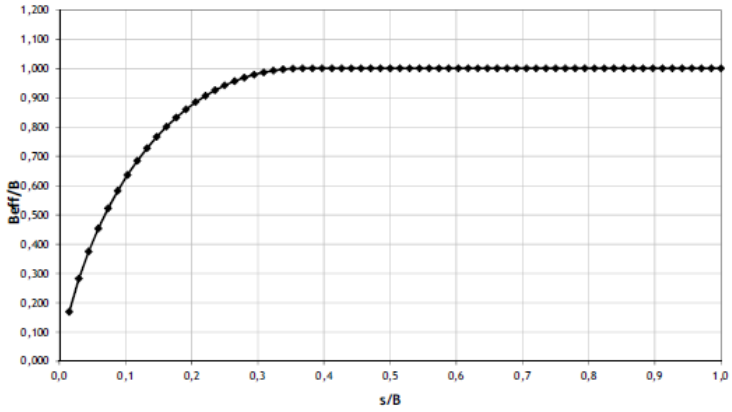

Figure 3.40 – Ratio between the effective and maximum plate width

It is clear that the effective width depends only on the width at the mid-section and the maximum width. The influence of the moment-shear interaction on the hourglass T-stubs behaviour was also investigated. It was observed (Figure 3.41) that up to values of *m/t* equal to 6, the optimum ratio between the width at mid-section and the maximum width strongly depends on *m/t*; in fact, for low values of *m/t,* shear forces provide an important influence on the flexural behaviour of the plate, and proper detailing of the plate mid-section is necessary. Conversely, for high values of plate slenderness, the bending moment becomes prevalent compared to the shear forces, and, as slenderness increases, the optimum shape becomes closer to the bi-triangular one so that the optimum ratio between minimum and maximum width becomes almost constant. Through regression analysis of the numerical data, Latour and Rizzano [40-42] obtained:

$$\begin{aligned} \left(\frac{s}{B}\right)_{optimal} &= 0{,}5634\left(\frac{m}{t}\right)^{-0{,}64} \quad if\ \frac{m}{t} \leq 6 \\ \left(\frac{s}{B}\right)_{optimal} &= 0{,}18 \qquad\qquad\qquad if\ \frac{m}{t} > 6 \end{aligned} \tag{3.29}$$

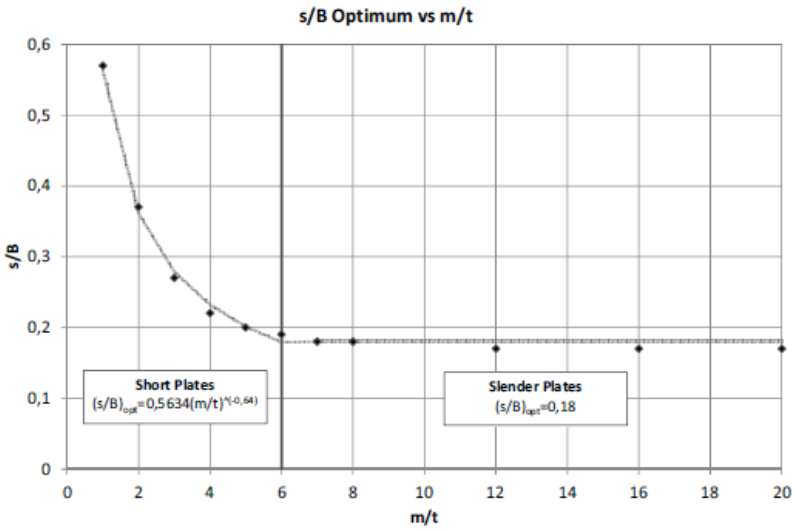

Figure 3.41 – s/B optimum vs m/t

At the University of Salerno, many research studies have been carried out on this innovative connection since experimental, numerical and analytical works have been performed. For example,

an analytical model has been proposed by Latour and Rizzano [40-43] to design the effective hourglass shape of the joint, and it has been validated against experimental results characterized by cyclic tests on a beam-to-column sub-assembly [9].
Many experimental monotonic and cyclic tests were performed in the last years on rectangular and hourglass T-stubs. In particular, 11 rectangular specimens and ten dissipative T-stubs were selected. The connections of the specimens to the rigid support were made using 18 bolts class 8.8 with a preloading level equal to 80% of the yield stress. For the structural elements, two types of steel grade were used: S275 and S355.
All the specimens experienced a tensile axial force applied to the webs under displacement control by the jaws of the Schenck Hydropuls S56 testing machine with a load capacity of 630 kN and a piston stroke of $\pm 125\ mm$. The speed adopted to perform both the monotonic and the static tests was equal to 0.01 mm/s.
All the tested specimens were modelled through the numerical software Abaqus.
Consistently with the approach applied in the case of the FREEDAM connection, only the primary experimental outcomes are reported. Further details can be found in the works by Latour and Rizzano [40-43].
The monotonic tests (Figure 3.42) showed that the experimental curves of the hourglass T-stubs were similar to the rectangular ones. In particular, it was possible to stress that the axial forces influence the monotonic behaviour since the rigid support represented a shear constraint for the bolts. During the tests, the T-stub was deformed, while the support was rigid; consequently, shear actions on the bolts arose together with the axial force in the fastened plate.

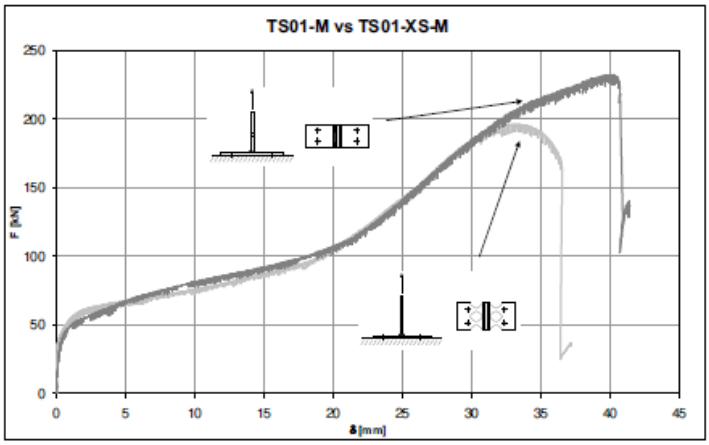

Figure 3.42 – Comparison between a rectangular and a dissipative T-stub

The experimental results were also compared with the analytical model proposed by Piluso et al. [44] for rectangular T-stubs. In Figure 3.43 and Figure 3.44, it is possible to observe that the mechanical model was very accurate for the rectangular and hourglass T-stubs. Since the mechanical model does not consider the influence of the second-order effects, the prediction accuracy is demonstrated up to the T-stub displacement corresponding to the hardening branch. However, considering that this displacement is greater than the displacement expected by the T-stubs endowed in the MRFs, this approximation is not a problem.

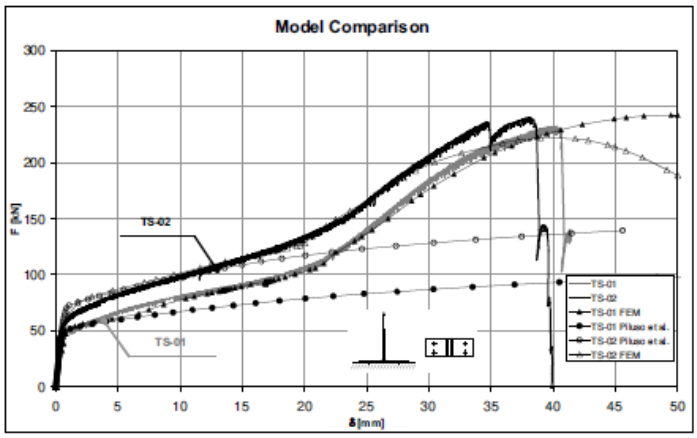

Figure 3.43 – Model comparison referred to the rectangular T-stub

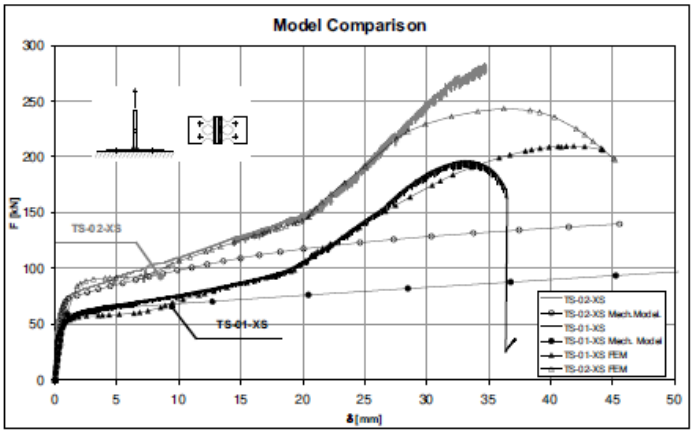

Figure 3.44 – Model comparison referred to the hourglass T-stub

Cyclic tests were also performed. In particular, in these cases, the rectangular T-stubs collapsed because of the cracking of the flanges starting from the welds and propagating along the flange width and thickness. Such a phenomenon induced a progressive deterioration of the axial strength, stiffness and energy dissipation capacity. The hourglass T-stubs showed the same failure mode characterized by the complete fracture of the flange.
During the tests, the specimens were monitored through a thermal camera, which highlighted the different spread of plasticity and, consequently, energy dissipation capacity.

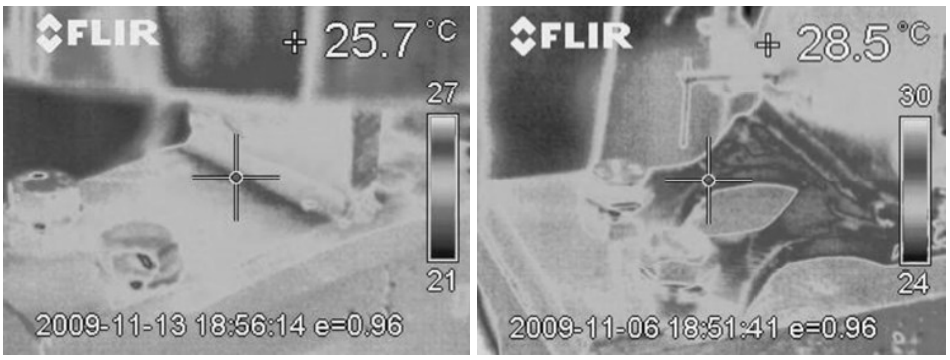

Figure 3.45 – Propagation of the heat along the flanges of the rectangular (left) and hourglass (right) T-stub

Furthermore, experimental tests on beam-to-column sub-assemblies were carried out (Figure 3.46). However, some images related to the cyclic test results are only reported for clarity (Figure 3.47 and Figure 3.48).

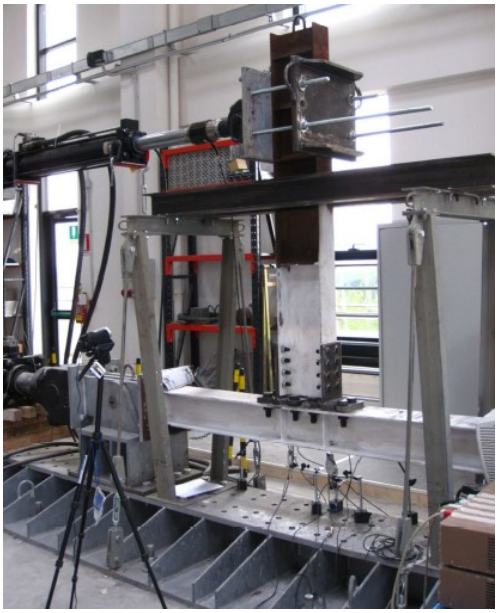

Figure 3.46 – Connection with X-shaped T-stubs

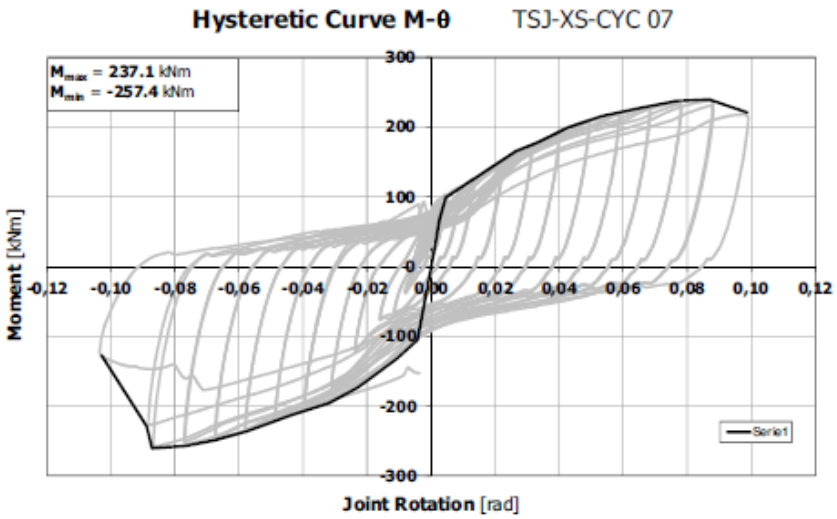

Figure 3.47 – Moment-rotation hysteretic curve

Figure 3.48 – Crack formation and propagation

The specimen members were an IPE270 beam and HEM220 column, with the same geometrical properties and displacement loading history reported with reference to the test on the RBS connection discussed in Chapter 2.
The hysteretic curve shows that even though the pinching phenomenon was not completely avoided, the connection did not exhibit strength degradation phenomena. The joint was subjected to 44 cycles reaching an ultimate rotation equal to 0.1 rad, a value higher than the limit provided by Eurocode 8 for the ultimate plastic rotation exhibited by a Ductility Class High MRF.
The only components engaged in the plastic range were the dissipative T-stubs, while the column panel and the other nodal components showed an elastic behaviour. Finally, in the 44th cycle, the collapse occurred because of the formation of a crack that started in the heat-affected zone and then propagated through the plate according to a circular-shaped pattern.

3.3 Personal contribution

Chapter 3 focuses on the behaviour of advanced resilience-oriented partial-strength beam-to-column connections that can enhance the energy dissipation capacity and limit the structural damages only to well-defined and easy to replace fuses. These joints have been studied in detail at the University of Salerno in the past years. In particular, the FREEDAM connection has been widely investigated within the framework of a homonym European research project.
Consequently, no personal contributions can be found in this chapter, but the information provided can be helpful for understanding the experimental activities discussed in Chapter 4.

3.4 References

1 Kelly, J. M., Aseismic Base Isolation: A review, Proceedings, 2nd US National Conference on Earthquake Engineering, Stanford, CA., 1979.
2 Aiken, I. D.; Clark, P. W.; Kelly, J. M., Design and Ultimate-Level Earthquake Tests of a 1/2.5 Scale Base-Isolated Reinforced-Concrete Building, Proceedings of ATC-17-1 Seminar on seismic Isolation, Passive Energy Dissipation and Active Control. San Francisco, California, 1993.
3 Yang, T. S.; Popov, E. P., Experimental and analytical studies of steel connections and energy dissipators, Berkeley: Earthquake Engineering Research Center, UCB/EERC-95/13, 1995.
4 Constantinou, M. C.; Soong, T. T.; Dargush, G. F., Passive Energy Dissipation Systems for Structural Design and Retrofit, Multidisciplinary Center for Earthquake Engineering Research, University at Buffalo, State of New York, 1998.

5 Christopoulos, C.; Filiatrault, A., Principles of Passive Supplemental Damping and Seismic Isolation, IUSS PRESS, Pavia, Italy, 2000.
6 Latour, M.; Piluso, V.; Rizzano, G., Experimental analysis of beam-to-column joints equipped with sprayed aluminium friction dampers, Journal of Constructional Steel Research, 146, pp. 33-48, 2018.
7 Steenhuis, M.; Jaspart, J. P.; Gomes, F.; & Leino, T., Application of the component method to steel joints, Proceeding of the Control of the Semi-Rigid Behaviour of Civil Engineering Structural Connections Conference, 1998.
8 Faella, C.; Piluso, V.; Rizzano, G., Structural Steel Semirigid Connections, CRC Press, Boca Raton, FL, 2000.
9 Iannone, F.; Latour, M.; Piluso, V.; Rizzano, G., Experimental Analysis of Bolted Steel Beam-to-Column Connections: Component Identification, J. Earthq. Eng., vol. 15, no. 2, pp. 214–244, 2011.
10 Pall, A. S.; Marsh, C.; Fazio P., Limited Slip Bolted Joints for Large Panel Structures, Proceedings, Symposium on Behavior of Building Systems and Building Components, Nashville, USA, 1979.
11 Marsh, C.; Pall, A. S., Friction Devices to Control Seismic Response, Proceedings Second ASCF/EMD Specialty Conference on Dynamic Response of Structures, Atlanta, U.S.A., January, pp. 809-818, 1981.
12 Pall, A. C.; Marsh, C., Response of Friction Damped Braced Frames, Journal of Structural Division, ASCE, Vol. 108, No. ST6, June, pp. 1313-1323, 1982.
13 Grigorian, C. E., and Popov, E. P., Energy dissipation with slotted bolted connections, Berkley, California, Earthquake Engineering Research Centre, 1994.
14 Butterworth, J. W.; Clifton, G. C., Performance of Hierarchical Friction Dissipating Joints in Moment Resisting Steel Frames, 12 World Conference on Earthquake Engineering, Paper N. 718, 2000.
15 MacRae, G. A.; Clifton, G. C., New Technology Applications, Recent Developments and Research Directions for Seismic Steel Structures in New Zeland, Asian Conference on Earthquake Engineering, Bangkok, Thailand, December 2010.
16 MacRae, G. A.; Clifton, G. C., Low Damage Design of Steel Structures, Steel Innovations, Workshop, Christchurch, 21-22 February 2013.
17 Yeung, S.; Zhou, H.; Khoo, H.; Clifton, G. C.; MacRae, G, Sliding shear capacities of the Asymmetric Friction Connection, NZSEE Conference, Wellington, Paper n. 27, 2013.
18 Khoo, H.; Clifton, G. C.; Macrae, G.; Ramhormozian, S., Proposed design models for the asymmetric friction connection, Earthquake Engineering and Structural Dynamics, 2014.
19 Borzouie, J.; Macrae, G.; Chase, J., Cyclic Performance of Asymmetric Friction Connections with Grade 10.9 Bolts, The Bridge and Structural Engineer, 2015.
20 Golondrino, J. C.; MacRae, G.; Chase, J.; Rodgers, G.; Clifton, G. C., Velocity effects on the behavior of asymmetrical friction connections (AFC), 8th STESSA Conference, Shanghai, China, 2015.
21 Latour, M.; Piluso V.; Rizzano G., Free from damage beam-to-column joints: Testing and design of DST connections with friction pads, Engineering Structures. 85:219-233, 2015.
22 Piluso, V., Smart Connections for Seismic-Resistant Frames: a Brief Overview, Costruzioni Metalliche, Vol. 3, 2018.

23 Latour, M., D'Aniello, M., Zimbru, M., Rizzano, G., Piluso, V., Landolfo, R., Removable friction dampers for low-damage steel beam-to-column joints, Soil Dynamics and Earthquake Engineering, 115, pp. 66-81, 2018.
24 Latour, M.; Rizzano, G., Santiago, A.; Simões da Silva, L., Experimental response of a low-yielding, self-centering, rocking column base joint with friction dampers, Soil Dynamics and Earthquake Engineering, 116, pp. 580-592, 2019.
25 Nastri, E.; D'Aniello, M.; Zimbru, M.; Streppone, S.; Landolfo, R.; Montuori, R.; Piluso, V., Seismic response of steel Moment Resisting Frames equipped with friction beam-to-column joints, Soil Dynamics and Earthquake Engineering. 119. 144-157. 10.1016/j.soildyn., 2019.
26 EN 1090-2, "Execution of steel structure and aluminium structure: Technical requirements for steel structures. Annex G: Test to determine slip factor", 2008.
27 EN 15129, "Anti-seismic devices", 2009.
28 CEN, "Eurocode 3: Design of steel structures - Part 1-8: Design of joints", 2005.
29 American Institute of Steel Construction, ANSI/AISC 341-10, AISC, 2010.
30 EUROCODE 8, "Design of structures for earthquake – part 1: General rules, seismic actions and rules for buildings", CEN, 2003.
31 Fleischman R., Hoskisson B., Modular connectors for seismic resistant steel moment frames 2000. Proceedings of Structures Congress 2000, Philadelphia, PA, May 7-10, 2000.
32 Leon R., Swanson A., Cyclic modelling of T-stub connections. Proceedings of steel structures in Seismic Areas, Canada, 2000.
33 Rizzano, G., Seismic design of steel frames with partial strength joints. Journal of earthquake engineering, vol.10, n°5, 2006.
34 Latour M., Piluso V., Rizzano G., Cyclic model of beam-to-column joints. 5th European Conference on Steel and Composite Structures, EUROSTEEL 2008, Graz, Austria. Brussels: ECCS, 3-5 September 2008.
35 Kim Y, Oh S., Ryu H., Kang C., Hysteretic behaviour of moment connections with energy absorption elements at beam bottom flanges. ICAS 2007, Oxford, 2007.
36 Zoetemeijer, P., A design method for the tension side of statically loaded bolted beam-to-column connections", Heron, Delft University, Vol. 20, n° 1, 1974.
37 Bezerra, L. M., Bonilla, J., Silva, W. A., Matias, W. T., Experimental and numerical studies of bolted T-stub steel connection with different flange thicknesses connected to a rigid base, Engineering Structures, Volume 218, 110770, ISSN 0141-0296, https://doi.org/10.1016/j.engstruct.2020.110770, 2020.
38 Bravo, M. A., Herrera, R. A., Performance under cyclic load of built-up T-stubs for Double T moment connections, Journal of Constructional Steel Research, Volume 103, Pages 117-130, ISSN 0143-974X, https://doi.org/10.1016/j.jcsr.2014.08.005, 2014.
39 Tena-Colunga A., Mathematical modelling of the ADAS energy dissipation device. Engineering Structures, Vol.19, N°10, pp 811-821, 1997.
40 Latour, M., Rizzano, G., Latour, M., Rizzano, G., Utimate Behaviour of Dissipative Tstub Connections, STESSA Conference, 2009.
41 Latour, M., Rizzano, G., Experimental Analysis and Design of X-Shaped T-stub Joints, 2011.
42 Latour, M., Rizzano, G., Design of X-shaped double split tee joints accounting for moment–shear interaction, Journal of Constructional Steel Research. 104. 10.1016/j.jcsr.2014.10.015, 2015.
43 Latour, M., Recent advances in the technologies of connection for panel structures: Design and cost analysis of different solutions with X-shaped dissipative connectors, Advances in Structural Engineering;20(3):299-315. doi:10.1177/1369433216649397, 2017.

44 Piluso, V., Faella, C., Rizzano, G., Ultimate behaviour of bolted T-stubs. Part I: Theoretical model. Journal of Structural Engineering ASCE, 127(6), pp. 686-693, 2001.

CHAPTER 4 – Large-scale tests of a mock-up with RBS and resilience-oriented joints

In the previous chapters, it has been observed that many research efforts have been devoted to the characterization of the cyclic behaviour of traditional and innovative steel beam-to-column connections, while the behaviour of the same joints when equipping real-scale structures is limited at the moment.

In this framework, an experimental program is currently ongoing at the STRENGTH (STRuctural ENGineering Test Hall) Laboratory of the University of Salerno. It consists of pseudo-dynamic tests on a large-scale one-bay two-storey steel structure equipped, alternately, with five different beam-to-column connections: RBSs (Reduced Beam Section) connections; low-damage connections (FREEDAM type), Extended End-Plate (EEP) connections, Double-Split Tee (DST) and Double-Split X-shaped Tee (DST-X) connections. The main objective of this research activity is to experimentally assess the influence on the global structural response of different typologies of beam-to-column connections characterized by the same resistance and different dissipative capacities.

In particular, this chapter is devoted to discussing the significant results concerning the execution of pseudo-dynamic tests on the structure equipped with RBS, FREEDAM and Double-split X-shaped T-stub connections. The experimental outcomes have always been complemented with numerical simulations developed through the software SeismoStruct or OpenSees to provide practical recommendations for modelling such a kind of joints in real-scale structures.

4.1 Pseudo-dynamic testing method

One of the main problems concerning seismic tests on real-scale structures or their components is how the loading conditions can be considered representative of the seismic effects due to the earthquakes.

Obviously, the execution of shaking-table tests is the best approach to evaluate the actual seismic behaviour, but this requires costly and high-tech equipment. For this reason, at the end of the 80s, the pseudo-dynamic testing method [1, 2] was developed within the framework of the U.S. - Japan Cooperative Earthquake Research Program in Japan, at the Tsukuba Building Research, and in the United States, at Berkeley, University of California, and at Ann Arbor, University of Michigan. This strategy allows assessing the seismic behaviour most reliably but through the exploitation of the same equipment adopted to perform quasi-static tests. In particular, hydraulic actuators, fixed to rigid reaction walls or frames, apply floor displacements to the analysed structure. In contrast, load cells and transducers monitor the information related to the reaction forces and the relative floor displacements.

It is worth highlighting that while the shaking table tests experimentally reproduce the seismic response of a structure through the application of the natural ground acceleration at its basement, the pseudo-dynamic method is a hybrid solution characterized by the combination of experimental techniques and numerical simulations. In fact, this strategy requires a narrow interface between numerical simulation data and experimental outcomes making these two phases cyclically dependent. For instance, in the case of tests on buildings, this numerical-experimental approach allows imposing to the structure, floor displacements assessed by solving step-by-step the equations of motion during the test. The consequence is that this quasi-static technique allows simulating inertia and viscous forces by preliminary defining the mass matrix and the damping matrix of the structure without really applying the masses to the mock-up building. For this reason,

the parameters used to set the numerical procedure can affect the experimental outcomes, and the more complex is the numerical modelling, the more time is required to solve step-by-step the equation of motion, inducing an increase in the test duration. Furthermore, unlike the shaking-table tests, the quasi-static loading history application of the pseudo-dynamic method allows the inspection of the behaviour exhibited by structural elements (e.g. connections, members, devices), making, in most cases, the interpretation of the results complex and onerous.

Given the above-reported considerations, this experimental strategy can be fully exploited to check the reliability of the analytical models to predict the non-linear behaviour both at the local (materials) and global level (structures or their components).

In particular, this strategy represents an excellent solution to assess the seismic response of structures equipped with innovative devices. In fact, the rigid decks constituting buildings allow schematizing the structures as systems with n degrees of freedom in correspondence with which the masses are assigned and the imposed displacements evaluated with the implemented calculation routine. This aspect clarifies that the pseudo-dynamic approach is very effective in the case of systems characterized by discretized masses. In contrast, the complexity of adopting such an approach tends to increase in the case of structures characterized by uniformly distributed masses, such as pylons, monuments or towers.

To perform a pseudo-dynamic test, it is necessary to define the viscous damping based on literature data, even though during the actual test, with the behaviour of the structure pushed in the plastic field, the hysteretic damping will tend to prevail over the viscous.

The quasi-static nature of the test generates a low speed of the structural deformation, inducing lower strength and stiffness than those expected during the earthquake. Such a phenomenon is known as relaxation, but it is worth highlighting that in the framework of this work, which is focused on steel structures, it can be considered insignificant.

However, in the last years, fast online testing has been proposed to solve this drawback [3, 4].

The main difference with the traditional pseudo-dynamic method is using a high-speed data acquisition system to ensure the actuators' continuous motion that does not hold between two subsequent steps. Consequently, the reaction forces are measured at each sampling period of the digital servo controller, and the motion equations are integrated at the sampling rate. According to this procedure, it is possible to extend the field of application of the pseudo-dynamic test to structures sensitive to the strain rate or equipped with isolators or dissipative devices.

The classic pseudo-dynamic technique is characterized by the alternate execution of the experimental and numerical phases. No temporal requirements must be fulfilled; instead, the fast approach requires the synchronization between the two phases imposing a maximum time step period the jobs must end. These constraints can induce convergence problems in the case of complex tested structures; for this reason, mainly to ensure the stability of the numerical simulations, it is preferable to use the explicit central differences method for the experimental part and the implicit one for the analytical part.

As already pointed out, the nature of the pseudo-dynamic method is based on a numeric-experimental approach based on solving step-by-step the dynamic equation of motion. Consequently, a model of the test sample is necessary; in the case of structures, it is possible to assume that the rigid decks to which the masses can be assigned allow defining a finite number of degrees of freedom whose main components are excited in the direction of the seismic loading.

The equations of motion to be solved can be expressed as:

$$[M]\{a_i\} + [C]\{v_i\} + \{R_i\} + \left[K_g\right]\{d_i\} = -[M][B]\{a_{gi}\} \quad (4.1)$$

where:

- $[M]$ and $[C]$ are the mass and damping matrices, respectively;
- $\{R_i\}$ is the vector that includes the reaction forces;
- $[K_g]$ is the matrix of the geometric stiffness used to compensate the loads not present on the structure during the test;
- $\{a_i\}$, $\{v_i\}$ and $\{d_i\}$ are, respectively, the vectors of accelerations, velocities and displacements of the degrees of freedom of the structure at time i;
- $\{a_{gi}\}$ is the vector of ground accelerations at time i in each direction considered;
- $[B]$ is the transformation matrix of ground acceleration; the component B_{ij} corresponds to the acceleration in correspondence with the degree of freedom i when the structure acts as a rigid body due to a unitary acceleration to the ground of component j (in the case of a flat test with a single component of horizontal ground displacement $[B]$ is a unitary vector).

After assessing the required displacements through the solution of the equations of motion, they are imposed on the structure by the actuators and the reaction forces are measured; this process is repeated recursively until the complete seismic response is evaluated.
In order to make the adopted explicit solver stable, an integration time fewer than $1/\pi$ times the most significant vibration period of the structure is required.
A conceptual scheme of the pseudo-dynamic testing method is reported in Figure 4.1.

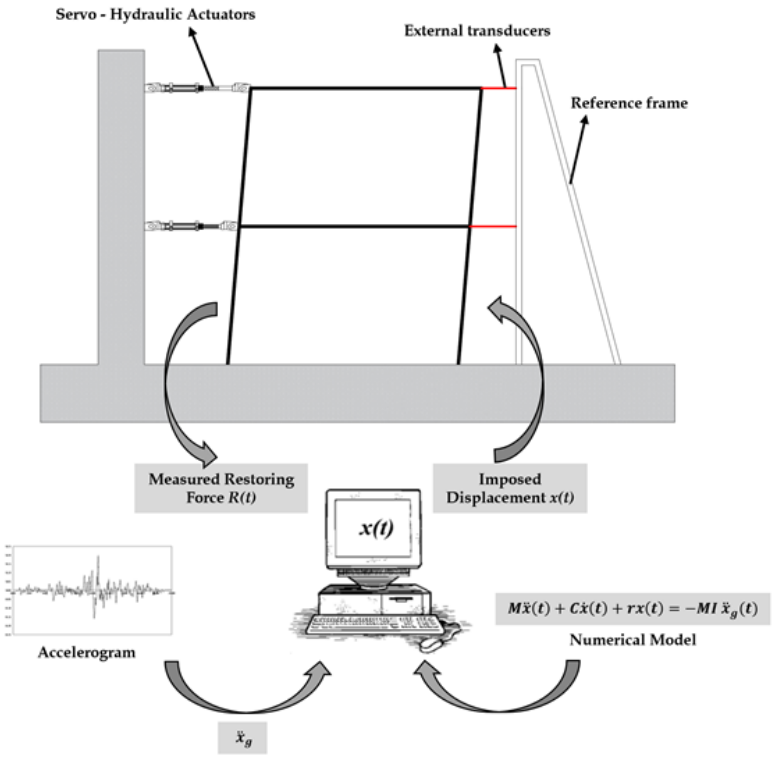

Figure 4.1 - Conceptual scheme of the pseudo-dynamic testing method

4.2 Design of the structure for the pseudo-dynamic tests

The tested mock-up represents a reference structure characterized, for each direction, by three bays with lengths equal to 4 m (Figure 4.2 and Figure 4.3). The archetype building comprises four MRFs in each direction, while the remaining bays are considered nominally pinned (Figure 4.3).

Figure 4.2 - 3D view of the reference building

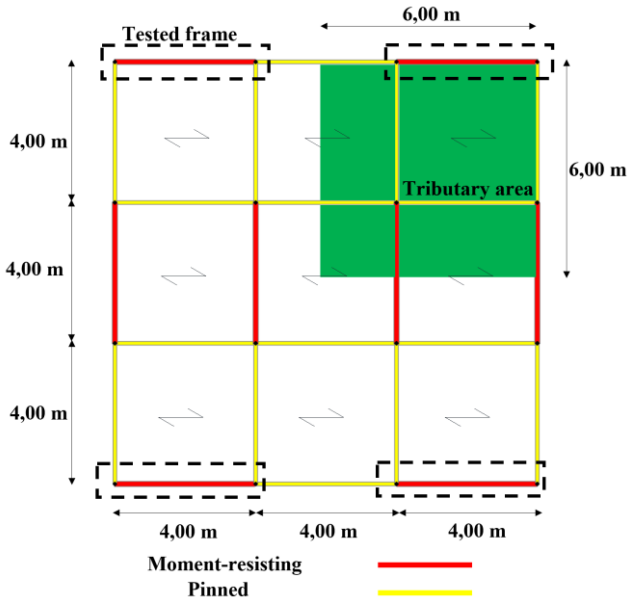

Figure 4.3 - Plan view and individuation of the tested frame

The design values of the loads are the following: i) the dead loads are equal to 3.9 kN/m^2 and 3.6 kN/m^2 at the intermediate and at the roof level, respectively; ii) the live loads are equal to 3 kN/m^2 at the first level and 0.5 kN/m^2 at the roof level. The tributary area on each MRF corresponds to 1/4 of the total floor area. The weight of the structural members and claddings has been accounted for by increasing the masses by about 10%. In particular, the masses applied on each frame equal 19 tons and 14.2 tons at the first and second level, respectively.

The tested mock-up (Figure 4.4) is made with two frames with the same MRFs belonging to the reference structure. It has been designed according to both the Theory of Plastic Mechanism Control (TPMC) [5, 6] and the Eurocode 8 [7] type-1 spectrum, with a peak ground acceleration equal to 0.35g and a type-B soil considering both serviceability and ultimate limit states requirements. The structure is designed in Ductility Class High (DCH), with a behaviour factor

equal to 6. The design interstorey drifts under service conditions have been limited to 1%, assuming, therefore, that the partition walls of the building do not interfere with the deformation of the main structure. With these design constraints, IPE 270 beams made of S275JR steel grade and HEB 200 columns made of S355JR steel grade have been selected. It is worth highlighting that the design process has been performed on the hypothesis of full-strength beam-to-column connections without accounting for the characteristics of the joints with which the structure has been equipped for the pseudo-dynamic tests.

Figure 4.4 - Lateral view of the mock-up during the assembly phase

The floors are made of HI-BOND A55 steel profiled decking, including the reinforced concrete slab, with a total height of 100 mm. The deck transfers the loads to five equally spaced IPE 140 or HEB 140 secondary beams (Figure 4.5 and Figure 4.6) connected to the slab with shear studs. The primary beams of the MRFs, instead, are IPE 270.

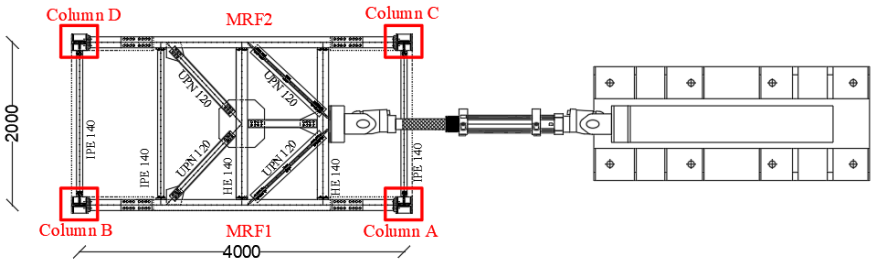

Figure 4.5 - Building mock-up: in-plane bracing

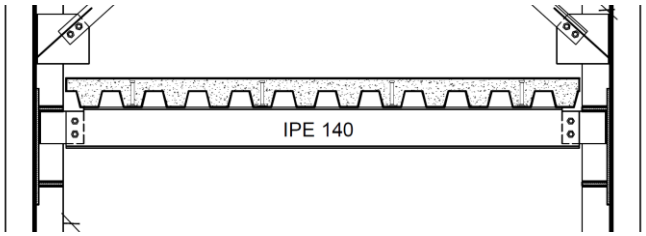

Figure 4.6 - Building mock-up: detail of the connection between the deck and the secondary beams

The slab is disconnected from the nodal regions through appropriate gaps left between the reinforced concrete slab and the columns (Figure 4.7), but it acts as a rigid diaphragm, equally distributing the forces to the frames.

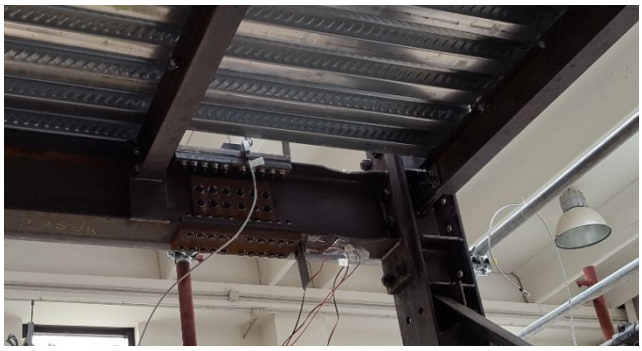

Figure 4.7 - Building mock-up: detail of the gap between the slab and the column (structure equipped with RBSs)

Rigid steel footings fastened with high-strength dywidag bars assure the connection of the mock-up to the strong floor of the laboratory. Furthermore, bracings connect the steel footings of the mock-up to the base of the reaction wall (Figure 4.8).

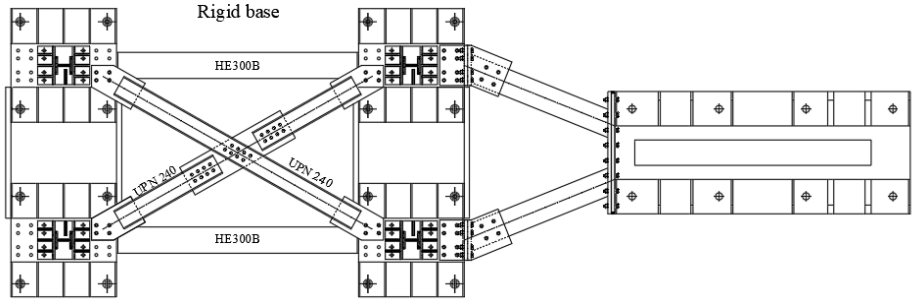

Figure 4.8 - Building mock-up: base diaphragm

4.2.1 Design of the frame according to the TPMC

The Theory of Plastic Mechanism Control (TPMC) [5, 6] has been developed to ensure the design of structures failing according to a collapse mechanism of global type. This approach is based on the kinematic theorem of plastic collapse extended to the concept of mechanism equilibrium curve considering the assumptions of a rigid-plastic behaviour of the structure and non-negligible consequences of the second-order effects:

$$\alpha_0^{(g)} - \gamma^{(g)}\delta_u \leq \alpha_{0.i_m}^{(t)} - \gamma_{i_m}^{(t)}\delta_u \qquad i_m = 1,2,3,\dots,n_s \quad t = 1,2,3 \qquad (4.2)$$

$\alpha_{0.i_m}^{(t)}$ is the kinematically admissible multiplier of horizontal forces evaluated according to the first order rigid-plastic analysis, $\gamma_{i_m}^{(t)}$ is the slope of the equilibrium curve of the mechanism (Figure 4.9), accounting for second-order effects, i_m and t are the mechanism index and the mechanism typology code, respectively. Similarly, $\alpha_0^{(g)}$ and $\gamma^{(g)}$ are the same quantities referred to the global mechanism.

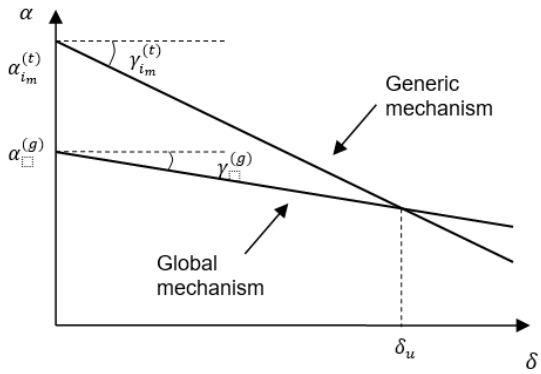

Figure 4.9 – Design condition for the failure mode control

The equilibrium curve is defined for each collapse mechanism, equating the external forces' work with the internal one induced by the plastic hinges that develop due to this mechanism. Conversely, from the traditional design approaches, in this case, the second-order effects are accounted for in the assessment of the external forces' work.

The best way to dissipate the seismic input energy is to develop a global type mechanism since it is characterized by the activation of the dissipative fuses at the beam ends and the first-floor column bases, compatibly with the local ductility supply. Instead, all the remaining non-dissipative elements behave elastically.

In particular, structures can fail according to three possible mechanisms (Figure 4.10). As already reported, the global mechanism is the best solution; it can be considered a particular case of type-2 mechanism extended to all the storeys.

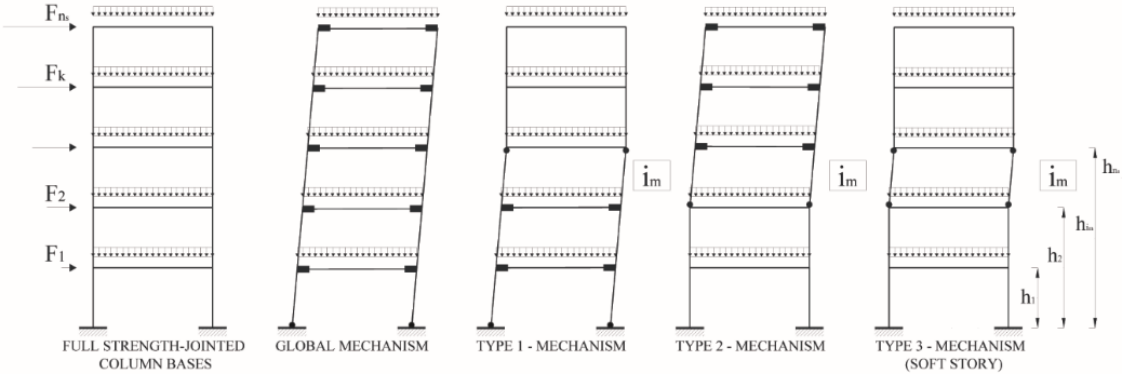

Figure 4.10 - Collapse mechanism of full-strength-jointed column bases resistant

Since many monotonic and cyclic tests have been performed on beam-to-column sub-assemblies (as reported in Chapter 2 and Chapter 3) and considering that in most of those cases, they were characterized by S275 steel grade IPE270 beams, the same profile is also adopted for the analysed mock-up.

For the global mechanism, the work of external forces due to a virtual rotation $d\vartheta$ of the plastic hinges of the column, starting from a deformed configuration (Figure 4.11) characterized by a rotation θ is:

$$W_e = \alpha \sum_{k=1}^{n_s} F_k(h_k \cdot d\vartheta) + \frac{\delta}{h_{ns}} \sum_{k=1}^{n_s} V_k(h_k \cdot d\vartheta) \qquad (4.3)$$

where:

- α is the multiplier of horizontal forces;
- F_k and h_k are, respectively, the seismic force applied to the k-th plane and the elevation of the same plane with respect to the foundation level;
- h_{ns} is the value of h_k at the level of the last floor;
- δ is the maximum horizontal displacement at the top of the structure;
- V_k is the total vertical load acting on the k-th floor.

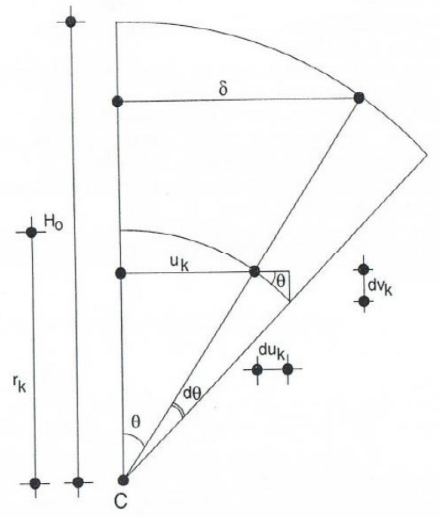

Figure 4.11 – Rigid rotation

$\alpha \sum_{k=1}^{n_s} F_k(h_k \cdot d\vartheta)$ is the external work induced by the horizontal actions, while $\frac{\delta}{h_{ns}} \sum_{k=1}^{n_s} V_k(h_k \cdot d\vartheta)$ is the work of the second-order effects.
The vector of the vertical virtual displacement is:

$$dv_k = du_k \frac{\delta}{h_{ns}} = \frac{\delta}{h_{ns}} h_k \cdot d\vartheta \tag{4.4}$$

where dv_k represents the virtual vertical displacement at the k-th floor (Figure 4.11).
The internal work is:

$$W_i = \left(\sum_{i=1}^{n_s} M_{c,i1} + 2 \sum_{k=1}^{n_s} \sum_{j=1}^{n_b} M_{b,jk} \right) \cdot d\vartheta \tag{4.5}$$

$M_{c,ik}$ is the reduced plastic moment of the i-th column of the k-th floor due to the presence of the axial force, (in the case under examination $k = 1$), while n_c, n_b, n_s are, respectively, the number of columns, beams and planes.
Equating the internal and external work results:

$$W_e = W_i \tag{4.6}$$

$$\alpha \sum_{k=1}^{n_s} F_k(h_k \cdot d\vartheta) + \frac{\delta}{h_{ns}} \sum_{k=1}^{n_s} V_k(h_k \cdot d\vartheta) = \left(\sum_{i=1}^{n_s} M_{c,i1} + 2 \sum_{k=1}^{n_s} \sum_{j=1}^{n_b} M_{b,jk} \right) \cdot d\vartheta \tag{4.7}$$

$$\alpha = \frac{\sum_{i=1}^{n_s} M_{c,i1} + 2 \sum_{k=1}^{n_s} \sum_{j=1}^{n_b} M_{b,jk}}{\sum_{k=1}^{n_s} F_k h_k} - \frac{1}{h_{ns}} \frac{\sum_{k=1}^{n_s} V_k h_k}{\sum_{k=1}^{n_s} F_k h_k} \delta \tag{4.8}$$

The equilibrium curve of the mechanism is a straight line, and it can be written as:

$$\alpha = \alpha_0 - \gamma\delta \tag{4.9}$$

Where α_0 is the cinematically permissible multiplier of the horizontal forces following a rigid-plastic analysis of the first order, and γ is the slope of the equilibrium curve of the mechanism. The formulations of α_0 and γ are reported for the different types of collapse mechanisms.

Global mechanism:

$$\alpha_0^{(g)} = \frac{\sum_{i=1}^{n_c} M_{c,i1} + 2\sum_{k=1}^{n_s}\sum_{j=1}^{n_b} M_{b,jk}}{\sum_{k=1}^{n_s} F_k h_k}$$
$$\gamma^{(g)} = \frac{1}{h_{ns}} \frac{\sum_{k=1}^{n_s} V_k h_k}{\sum_{k=1}^{n_s} F_k h_k} \tag{4.10}$$

Type-1 mechanism:

$$\alpha_{im}^{(1)} = \frac{\sum_{i=1}^{n_c} M_{c,i1} + 2\sum_{k=1}^{i_m-1}\sum_{j=1}^{n_b} M_{b,jk} + \sum_{i=1}^{n_c} M_{c,i,im}}{\sum_{k=1}^{i_m} F_k h_k + h_{im}\sum_{k=i_m+1}^{n_s} F_k}$$
$$\gamma_{im}^{(1)} = \frac{1}{h_{im}} \frac{\sum_{k=1}^{i_m} V_k h_k + h_{im}\sum_{k=i_m+1}^{n_s} F_k}{\sum_{k=1}^{i_m} F_k h_k + h_{im}\sum_{k=i_m+1}^{n_s} F_k} \tag{4.11}$$

Type-2 mechanism:

$$\alpha_{im}^{(2)} = \frac{\sum_{i=1}^{n_c} M_{c,i,im} + 2\sum_{k=i_m}^{n_s}\sum_{j=1}^{n_b} M_{b,jk}}{\sum_{k=i_m}^{n_s} F_k\,(h_k - h_{im-1})}$$
$$\gamma_{im}^{(2)} = \frac{1}{h_{ns} - h_{im-1}} \frac{\sum_{k=i_m}^{n_s} V_k\,(h_k - h_{im-1})}{\sum_{k=i_m}^{n_s} F_k\,(h_k - h_{im-1})} \tag{4.12}$$

Type-3 mechanism:

$$\alpha_1^{(3)} = \frac{2\sum_{i=1}^{n_c} M_{c,i1}}{h_1 \sum_{k=1}^{n_s} F_k} \quad for\ i = 1$$
$$\alpha_{im}^{(3)} = \frac{2\sum_{i=1}^{n_c} M_{c,i,im}}{(h_{im} - h_{im-1})\sum_{k=i_m}^{n_s} F_k} \quad for\ i > 1 \tag{4.13}$$
$$\gamma_{im}^{(3)} = \frac{1}{h_{im} - h_{im-1}} \frac{\sum_{k=i_m}^{n_s} V_k}{\sum_{k=i_m}^{n_s} F_k}$$

In the case of the global mechanism, the equilibrium curve attains its minimum slope. Therefore, according to the kinematic theorem of plastic collapse extended to the concept of the equilibrium curve of the mechanism, the design condition that must be satisfied to avoid undesired collapse mechanisms requires that the equilibrium curve corresponding to the global mechanism is located below those corresponding to the undesired mechanisms, up to a maximum top displacement δ_u compatible with the local ductility resources of the structure.

Referring to the mock-up, and assuming $\vartheta = 0.045\,rad$, since $h_{ns} = 4.80\,m$, it results: $\delta_u = 0.216\,m$.

The previous formulations have been applied to assess the slopes of the equilibrium curves both for a force distribution according to the first vibration mode (Table 4.1) and the masses (Table 4.2):

Table 4.1 – Slopes of the equilibrium curves (distribution according to the first vibration mode)

	γ_{im} (1/cm)		
i_m	**Mechanism 1**	**Mechanism 2**	**Mechanism 3**
2	0.122	0.195	0.195
1	0.275	0.122	0.275

Table 4.2 – Slopes of the equilibrium curves (distribution according to the masses)

	γ_{im} (1/cm)		
i_m	**Mechanism 1**	**Mechanism 2**	**Mechanism 3**
2	0.137	0.273	0.273
1	0.275	0.137	0.275

The sum of the plastic bending moments of the columns reduced due to the simultaneous action of the axial stress required at the first floor to prevent undesired collapse mechanisms is obtained with the following formulation:

$$\sum_{i=1}^{n_c} M_{c,i1} \geq \frac{2\sum_{k=1}^{n_s}\sum_{j=1}^{n_b} M_{b,jk} + \left(\gamma_1^{(3)} - \gamma^{(g)}\right)\delta_u \sum_{k=1}^{n_s} F_k h_k}{2\frac{\sum_{k=1}^{n_s} F_k h_k}{h_1 \sum_{k=1}^{n_s} F_k} - 1} \quad (4.14)$$

This relationship is obtained from the design condition with $i_m = 1$ and $t = 1$ or $t = 3$.

$$\alpha_0^{(g)} - \gamma^{(g)}\delta_u \leq \alpha_{im}^{(t)} - \gamma^{(t)}\delta_u \quad (4.15)$$

$$\sum_{i=1}^{n_c} M_{c,i1,1st\ vibration\ mode} = 339{,}37\ kNm \quad (4.16)$$

$$\sum_{i=1}^{n_c} M_{c,i1,masses} = 396{,}01\ kNm \quad (4.17)$$

Consequently, it is possible to assess the axial actions in the columns at collapse:

$$\sum_{i=1}^{n_c} N_{c,i,1st\ vibration\ mode} = 237{,}82\ kN \quad (4.18)$$

$$\sum_{i=1}^{n_c} N_{c,i,masses} = 237{,}82\ kN \quad (4.19)$$

The sum of the plastic moments required on the first floor is distributed between the columns proportionally to the axial force. Therefore, it is possible to design the different sections of the columns (Table 4.3).

Table 4.3 – Design of the columns sections

N_{tot} (kN)	$M_{req,c,1st\ vibration\ mode}$ (kNm)	$W_{pl,eq}$ (cm^3)	Profile	$M_{pl,column}$ (kNm)
118,91	$\frac{N_{c,i}}{\sum_{i=1}^{n_c} N_{c,i}} \sum_{i=1}^{n_c} M_{c,i1} = 169{,}68$	$\frac{M}{f_{yk}}$	HE200B	228,10
N_{tot} (kN)	$M_{req,c,masses}$ (kNm)	$W_{pl,eq}$ (cm^3)	Profile	$M_{pl,column}$ (kNm)
118,91	$\frac{N_{c,i}}{\sum_{i=1}^{n_c} N_{c,i}} \sum_{i=1}^{n_c} M_{c,i1} = 198{,}00$	$\frac{M}{f_{yk}}$	HE200B	228,10

Considering that HE200B profiles have been chosen for the column, it is possible to assess the sum of the plastic bending moments at the column bases.

$$\sum_{i=1}^{n_c} M^*_{c,i1} = 2 \cdot 228{,}10\ kNm = 456{,}21\ kNm \quad (4.20)$$

The equilibrium curve of the mechanism can be calculated using this last value, which accounts for the correct sections. Therefore, it is possible to calculate:

$$\alpha^{(g)}_{1st\ vibration\ mode} = 295{,}36 \qquad \alpha^{(g)}_{masses} = 330{,}84 \quad (4.21)$$

Type-1 mechanism:

$$\sum_{i=1}^{n_c} M^{(1)}{}_{c,i,im} \geq \left(\alpha^{(g)} + \gamma^{(1)}_{im}\delta_u\right)\left(\sum_{k=1}^{i_m} F_k h_k + h_{im} \sum_{k=i_m+1}^{n_s} F_k\right) - \sum_{i=1}^{n_c} M^*_{c,i1} - 2\sum_{k=1}^{i_m-1}\sum_{j=1}^{n_b} M_{b,jk} \quad (4.22)$$

Type-2 mechanism:

$$\sum_{i=1}^{n_c} M^{(2)}{}_{c,i,im} \geq \left(\alpha^{(g)} + \gamma^{(2)}_{im}\delta_u\right) \sum_{k=i_m}^{n_s} F_k\,(h_{im} - h_{im-1}) - 2\sum_{k=i_m}^{n_s}\sum_{j=1}^{n_b} M_{b,jk} \quad (4.23)$$

Type-3 mechanism:

$$\sum_{i=1}^{n_c} M^{(3)}{}_{c,i,im} \geq \left(\alpha^{(g)} + \gamma^{(3)}_{im}\delta_u\right)\frac{h_{im} - h_{im-1}}{2} \sum_{k=i_m}^{n_s} F_k \quad (4.24)$$

The sum of the plastic bending moments required on each floor to avoid undesired collapse mechanisms can be assessed as the maximum of the previous formulations (Table 4.4).

$$\sum_{i=1}^{n_c} M_{\ c,i,im} = max\left\{\sum_{i=1}^{n_c} M^{(1)}{}_{c,i,im}\,;\sum_{i=1}^{n_c} M^{(2)}{}_{c,i,im}\,;\sum_{i=1}^{n_c} M^{(3)}{}_{c,i,im}\right\} \quad (4.25)$$

Table 4.4 – Plastic moments of the columns

	$\sum_{i=1}^{n_c} M_{c,i,im,1st\ vibration\ mode}\ (kNm)$			
i_m	**Mechanism 1**	**Mechanism 2**	**Mechanism 3**	**Maximum**
2	343,64	86,88	215,26	343,64
1	266,91	456,21	361,56	456,21

	$\sum_{i=1}^{n_c} M_{c,i,im,masses}\ (kNm)$			
i_m	**Mechanism 1**	**Mechanism 2**	**Mechanism 3**	**Maximum**
2	343,64	1,73	172,69	343,64
1	352,06	456,21	404,13	456,21

In such a way, it is possible to check that the HEB200 with S355 steel grade can be selected as the profile of the columns (Table 4.5).

Table 4.5 – Check of the columns

Floor	**N_{tot} (kN)**	**$M_{req,c}$ (kNm)**	**$W_{pl,eq}$ (cm^3)**	**Profile**	**$M_{pl,column}$ (kNm)**
2	99,91	171,82	484,00	HEB200	228,10
1	118,91	228,10	642,55	HEB200	228,10

4.2.2 Check of the frame according to Eurocode 8

Once the structural elements have been designed according to the TPMC, the fulfilment of the Eurocode 8 requirements has been checked. Considering a type-B soil and a value of $a_g = 0.35g$, the Eurocode 8 spectrum has been defined (Figure 4.12). As already pointed out, the structure belongs to a ductility class high characterized by a behaviour factor equal to $q = 5\frac{\alpha_u}{\alpha_1} = 6$.

The base shear has been assessed through:

$$F_b = \frac{S_e \cdot m \cdot \lambda \cdot \delta}{q} \tag{4.26}$$

The parameter δ allows accounting for the accidental eccentricity (Figure 4.13):

$$\delta = 1 + 0.6\frac{x}{L_e} \tag{4.27}$$

In particular, x is the distance between the frame under examination and the centre of gravity of the masses, while L_e is the distance between the furthest seismo-resistant frames.

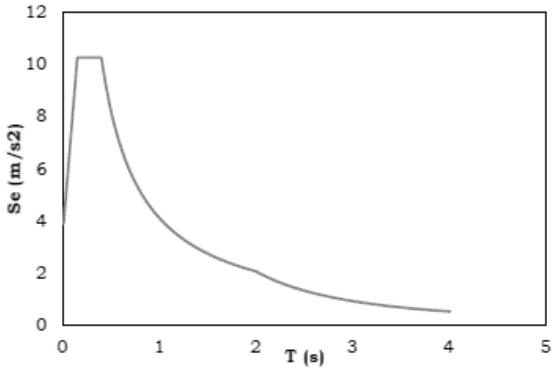

Figure 4.12 – Eurocode 8 spectrum

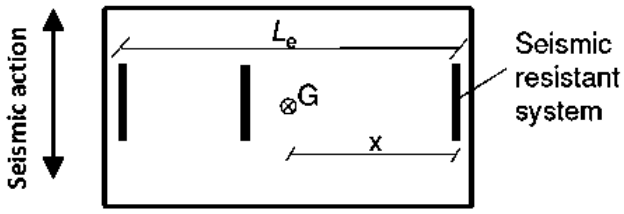

Figure 4.13 – Accidental eccentricity

According to this information, the design base shear for the single MRF equals 63 kN. Therefore, it has been distributed between the floors according to the first vibration mode and the masses.
The structural elements have already been designed in the previous paragraphs, while in the following, it is proposed to verify the satisfaction of the requests in terms of collapse and service conditions by adopting a procedure proposed by Eurocode 8 [7].
For beams, it is necessary to check:

$$\frac{M_{Ed}}{M_{pl,Rd}} \leq 1$$
$$\frac{V_{Ed}}{V_{pl,Rd}} = \frac{V_{Ed,G} + V_{Ed,M}}{V_{pl,Rd}} \leq 0.5 \quad (4.28)$$

The analysis is performed through SAP2000 software [8] to define the bending moments and shear actions used for the checks (Figure 4.14).

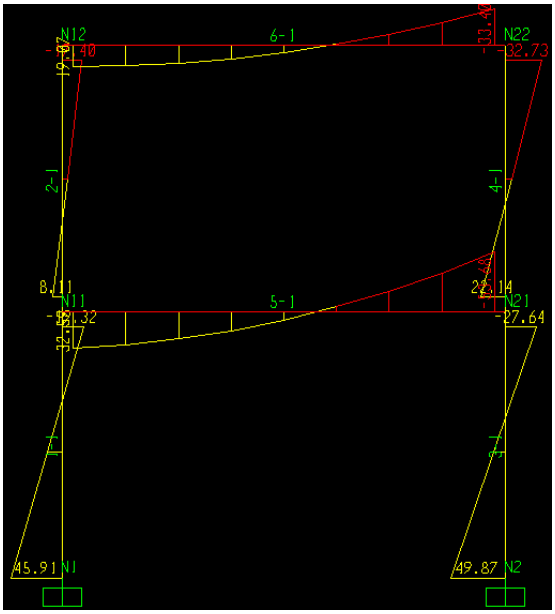

Figure 4.14 – Bending moments for the check of the beams

Instead, to check the columns (Figure 4.15), the horizontal forces applied to the floors have been amplified through the adoption of three coefficients:

- 1.10, to account for the hardening phenomenon;
- γ_{ov}, is an overstrength factor that is 1.25;
- Ω, which is the minimum value of $\Omega_i = M_{pl,Rd,i}/M_{Ed,i}$ of all the beams in which the dissipative devices are positioned; $M_{Ed,i}$ is the design value of the bending moment of the beam in

seismic conditions, while $M_{pl,Rd,i}$ is the corresponding plastic moment; in the case in question, this value is 3.20.

The resistance and stability checks are satisfied.

It is also verified that the columns are able to provide more than 30% of the flexural resistance of the connected beams.

The second-order effects have been implicitly fulfilled through the TPMC, while in the case of the Eurocode 8, the parameter ϑ has been assessed:

$$\vartheta = \frac{P \cdot d_r}{V \cdot h} \tag{4.29}$$

Where:

- P is the total gravitational load above the plane under seismic conditions;
- d_r is the relative floor displacement;
- V is the horizontal seismic action;
- h is the interstorey height.

The effects of the second order are negligible if $\vartheta \leq 0.10$; they must be taken into account with a multiplicative coefficient of the horizontal forces equal to $1/(1-\vartheta)$ if $0.10 \leq \vartheta \leq 0.20$. In any case, ϑ can not be greater than 0.30.

It is possible to observe that the effects of the second order are negligible (Table 4.6).

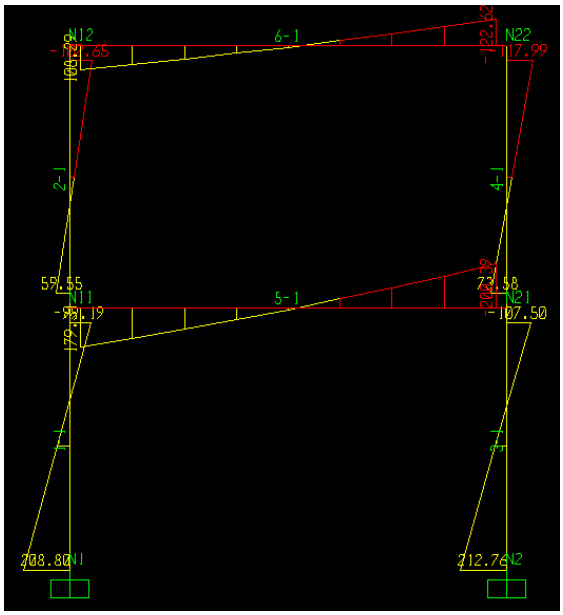

Figure 4.15 – Bending moments for the check of the columns

Table 4.6 – Check of the second-order effects

i	z (m)	P (kN)	d_r (m)	V (kN)	h (m)	θ
1	2.40	66.00	0.035826	63.02	2.40	0.01563
2	4.80	28.00	0.036192	37.74	2.40	0.01118

Finally, the serviceability check has to be satisfied by evaluating the interstorey drifts and comparing them with the values reported by the Eurocode 8 [7] to classify the type of non-structural elements that can be adopted for the structure under consideration.

The drift limits are:

- $\nu d_{rel} \leq 0{,}005 \cdot h$ for buildings that have non-structural elements of fragile material connected to the structure;
- $\nu d_{rel} \leq 0{,}075 \cdot h$ for buildings having ductile non-structural elements;
- $\nu d_{rel} \leq 0{,}010 \cdot h$ for buildings without non-structural elements or fixed non-structural elements to not interfere with structural deformations.

In the last case, the limit interstorey displacement is 24 mm. Therefore, as it is possible to see in Table 4.7, the checks are satisfied.

Table 4.7 – Serviceability limit states

i	d (m)	d_{abs} (mm)	d_{rel} (mm)	νd_{rel} (mm)	d_{lim} (mm) 3rd case	Check
1	0.005971	35.83	35.83	17.91	24.00	OK
2	0.012003	72.02	36.19	18.10	24.00	OK

4.3 Design of the connections

4.3.1 Reduced-Beam-Section connection (RBS)

It is worth underlining that the RBS connections investigated are different from those prequalified according to AISC provisions [9]. In fact, in the prequalified RBS connections, the trimming of the beam flanges according to the classical dog-bone shape is essentially conceived as a strategy to prevent the brittle failure of the welds between the beam flanges and the column flange. Therefore, AISC prequalified RBS connection is a welded connection. Conversely, the RBS connections herein analysed are extended end-plate connections whose possible low ductility failure modes are prevented by adopting the RBS strategy. However, the design rules applied for dimensioning the RBSs are the same suggested by AISC because the influence of the moment gradient along the beam length is not affected by the typology of the elements used for connecting the beam flanges to the column flange.

As already pointed out, the RBS connections equipping the MRFs are similar to the beam-to-column sub-assembly cyclically tested at the University of Salerno [10].

The design of this so-called "dog-bone" joint deals with the geometric characterization of three parameters: the distance between the reduced section zone and the end-plate (a), the length of the reduced section zone (b) and the flange reduction width (c), as shown in Figure 4.16.

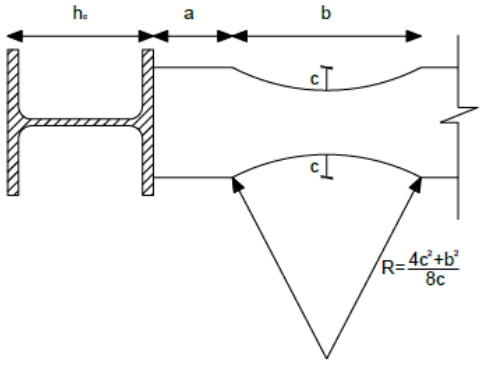

Figure 4.16 – Design parameters for RBS connections

The design procedure proposed by Moore et al. [11-13] has been adopted. According to this approach, parameters a and b should be designed to minimize the bending moment due to the

distance between the plastic hinge and the column. For this reason, they can be chosen arbitrarily in the following ranges:

$$\begin{matrix} 0{,}5b_f \leq a \leq 0{,}75b_f \\ 0{,}65d_f \leq b \leq 0{,}85d_f \end{matrix} \quad (4.30)$$

Parameter *c* controls the maximum bending moment at the RBS centerline and, consequently, the maximum flexural action at the column face. Such value should be limited to obtain a moment at the column face varying between 85% and 100% of the plastic bending moment of the beam. Furthermore, *c* should be lower than $0{,}25b_f$.

Due to the assumptions and the boundary conditions to fulfil, the proposed approach is iterative because the bending moment at the column face depends on the choice of the three abovementioned geometric parameters. In addition, the beam-column hierarchy criterion and the absence of shear mechanisms have to be checked.

Referring to the analyzed case, since an IPE270 profile has been chosen as the beam, the three parameters can range according to the following inequalities:

$$\begin{matrix} 67{,}50\ mm \leq a \leq 101{,}25\ mm \\ 168{,}87\ mm \leq b \leq 220{,}83\ mm \\ c \leq 33{,}75\ mm \end{matrix} \quad (4.31)$$

In the design phase, parameters *a* and *b* are assumed equal to 70 mm and 180 mm, respectively, while *c* has been defined according to the iterative procedure starting from the limit value of 33.75 mm until the convergence has been achieved with a value equal to 22 mm.

According to these results and considering an S275 steel grade for the beam, the plastic bending moment at the centerline of the reduced section is assessed as:

$$M_{pl,RBS} = W_{pl,RBS} f_y = \left[W_{pl,b} - 2ct_{cf}\left(d_b - t_{fb}\right)\right] f_y = 100{,}82\ kNm \quad (4.32)$$

The components belonging to the connection should remain elastic, and thus they are designed considering the dissipative zone yielded and hardened:

$$M_{RBS,E} = \gamma_{ov,rm}\gamma_{ov,sh}\gamma_{M0} W_{pl,RBS} f_y = 131{,}02\ kNm \quad (4.33)$$

Starting from the knowledge of $M_{RBS,E}$, it is necessary to calculate the bending moment at the column face to design the end-plate and the shear panel to have an elastic behaviour (Figure 4.17). For this reason, the shear force at the RBS centreline is assessed as:

$$V_{RBS,E} = \frac{M_{RBS,E}}{\left(L_b - a - \frac{b}{2}\right)} = 71{,}21\ kN \quad (4.34)$$

Where L_b is the beam length, equal to 4 m.

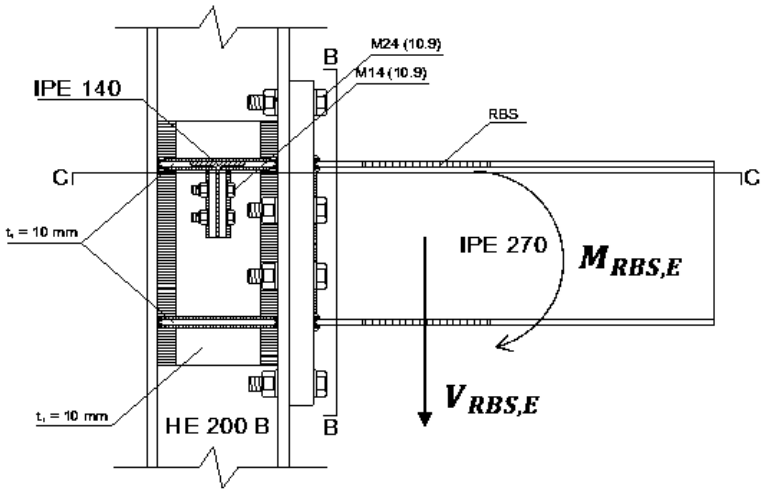

Figure 4.17 – Shear and bending moment at the RBS centerline

Neglecting the thickness of the end-plate, the moment at the column face is:

$$M_c = M_{RBS,E} + V_{RBS,E}\left(a + \frac{b}{2}\right) = 142{,}41\ kNm \qquad (4.35)$$

Considering also the random material variability, the plastic bending moment of the beam is:

$$M_{pl,b} = 149{,}91\ kNm \qquad (4.36)$$

The ratio $M_c/M_{pl,b}$ is equal to 0.95, within the above-reported limits.

Starting from the maximum shear and bending moment at the column face, it has been possible to design all the other nodal components to remain in the elastic range.

In particular, continuity plates have been designed in order to withstand an action higher than 80% of the design shear:

$$\frac{V_{Rd}}{V_{Ed}} = \frac{V_{Rd}}{\frac{0{,}8\sum M_c}{d_b - t_{bf}}} > 1 \qquad (4.37)$$

For clarity, no additional details are reported, except for the design of the end-plate. It is worth highlighting that in this case, the end-plate is not a weak element, but its design starts from the knowledge of M_c. In particular, the width of the end-plate has been fixed equal to 154 mm to define an effective width equal to 77 mm. The behaviour of the end-plate can be considered as ideally similar to that of two T-stubs. For this reason, in the hypothesis of designing a T-stub characterized by a type-1 collapse mechanism, the thickness of the end-plate can be assessed as:

$$F_{1,Rd}\left(d_b - t_{bf}\right) = M_c \qquad (4.38)$$

$$4 \cdot 2 \cdot \frac{b_{eff} t_{ep}^2}{4}\frac{f_y}{m}\left(d_b - t_{bf}\right) = M_c \qquad (4.39)$$

$$t_{ep} = \sqrt{\frac{M_c m}{2 b_{eff} f_y \left(d_b - t_{bf}\right)}} = 20{,}82\ mm \qquad (4.40)$$

$$t_{ep} \leq \sqrt{\frac{4 B_{Rd} mn}{b_{eff} f_y (m + 2n)}} = 26{,}07\ mm \qquad (4.41)$$

For this reason, it is possible to choose t_{ep} equal to $25\ mm$.

4.3.2 FREE from DAMage connection (FREEDAM)

The same design procedure reported in Chapter 3 is adopted. The connection is characterized by an IPE270 beam and a HEB200 column.

Step 1. Evaluation of the design actions for the device and design of the tightening torque.

The friction device is the first element to be designed since it is the weakest component, starting from which all the other members will be designed to have an elastic response.

In the following formulations, z is the distance between the barycenter of the bolts and the upper T-stub, where the centre of rotation is located. In the design phase, it is possible to assume $z = 440\ mm$ (Figure 4.18).

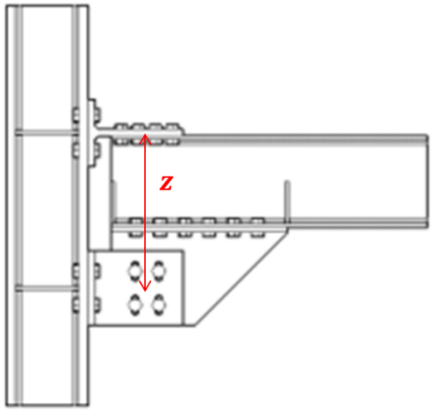

Figure 4.18 – Lever arm

The design bending moment of the connection is the same one adopted for the RBS connection and is equal to 100 kNm.

The design friction force can be assessed as:

$$F_{cf,Sd} = \frac{0.60 \cdot M_{Rd,IPE270}}{z} = 234\ kN \qquad (4.42)$$

The strict number of bolts can be derived as:

$$n_{b,min} = \frac{F_{cf,d} \cdot \gamma_{M3} \cdot \gamma_{creep}}{\mu_{dyn,5\%} \cdot F_p \cdot n_s} = \frac{234 \cdot 1.10 \cdot 1.15}{0.53 \cdot 109.90 \cdot 2} = 2.54 \qquad (4.43)$$

The number of bolts has been rounded to 4.

In such a way, the bolts preload can be defined as equal to 55.6 kN, which is about 50% of the initial value.

$$F_{p,red} = \frac{234}{0.53 \cdot 4 \cdot 2} = 55.60\ kN \qquad (4.44)$$

At this point, it is possible to recalculate the design friction resistance and the sliding bending moment of the FREEDAM connection.

$$F_{friction,Rd} = \mu_{dyn,5\%} \cdot F_{p,red} \cdot n_b \cdot n_s = 234.30\ kN$$
$$M_{friction,Rd} = 234.30\ kN \cdot 0.44\ m = 103\ kNm \qquad (4.45)$$

Step 2. Design of the slotted holes of the haunch

In Figure 4.19, the geometry of the haunch is reported.

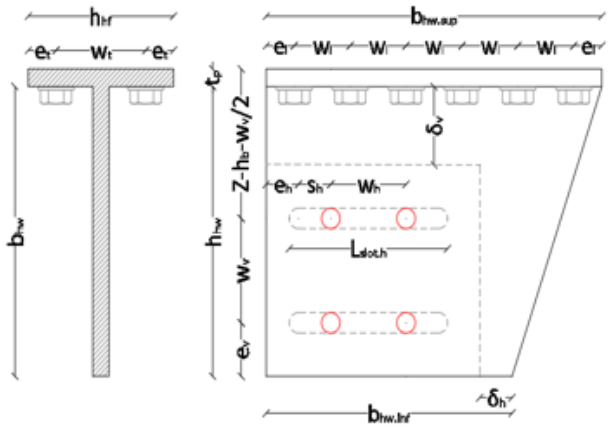

Figure 4.19 – Geometry of the haunch

Assuming $k_{wh} = 3.50$, $k_{eh} = 1.50$, $k_{wv} = 5.00$, $k_{ev} = 2.50$, the geometrical parameters can be assessed as:

$$\begin{aligned} w_h &= k_{wh} \cdot d_0 \\ e_h &= k_{eh} \cdot d_0 \\ w_v &= k_{vh} \cdot d_0 \\ e_v &= k_{ev} \cdot d_0 \end{aligned} \tag{4.46}$$

The length of the horizontal slots is fixed equal to 170 mm to assure a rotation of 50 $mrad$, which is greater than the minimum required.

$$l_{slot,h} = 170\ mm\ > l_{slot,h,min} = \\ = \left(\frac{4}{2} - 1\right) \cdot 63 + 17 + 2 \cdot 0.05 \cdot \left(440 + \frac{90}{2}\right) = 140\ mm \tag{4.47}$$

Step 3. Assessment of the design actions for the non-dissipative components

According to the second principle of capacity design, the moment acting at the column flange is evaluated by considering a coefficient of over-resistance γ_{ov} = 1.78.

$$M_{cf,Rd} = M_{friction,Rd} \cdot \gamma_{ov} = 183\ kNm \tag{4.48}$$

As a consequence, the design resistance is:

$$F_{friction,Rd} = \frac{M_{cf,Rd}}{z} = \frac{183}{0.44} = 416.91\ kN \tag{4.49}$$

In the hypothesis of a distributed load applied on the beam equal to 9.50 kN/m, a beam length of 4.00m and the height of the column, 200mm, the design shear is:

$$V_{Ed} = \frac{2 \cdot 183}{4 - 0.10} + 9.5\frac{4 - 0.10}{2} = 114.60\ kNm \tag{4.50}$$

Step 4. Design of the T-stub

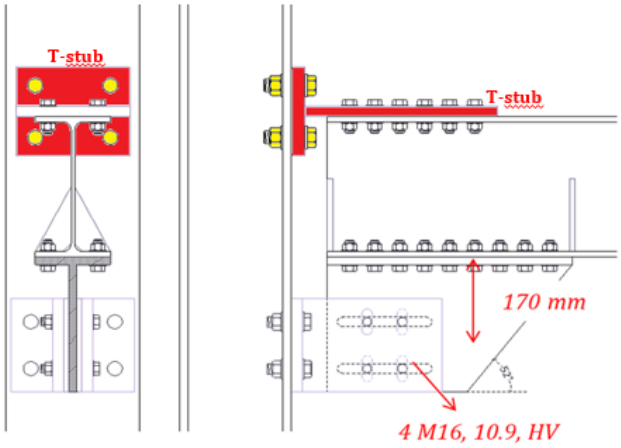

Figure 4.20 – Design of the T-stub

Both shear tension forces should be considered to design the diameter of the bolts connecting the T-stub to the column flange:

$$F_{t,Ed} = \frac{F_{friction,Rd}}{n_b} = \frac{416.91}{4} = 104.23\ kN - Tension$$
$$F_{v,Ed} = \frac{V_{Ed}}{2 \cdot n_b} = \frac{114.60}{8} = 14.32\ kN - Shear \quad (4.51)$$

According to Eurocode 3 [14], the resistant area of the bolts is:

$$A_{res,min} = max\left[\frac{\gamma_{M2}}{f_{ub}}\left(\frac{F_{v,Ed}}{\alpha_v} + \frac{F_{t,Ed}}{1.26}\right); \frac{\gamma_{M2} \cdot F_{t,Ed}}{0.9 \cdot f_{ub}}\right] = 144.76\ mm^2 \quad (4.52)$$

For this reason, M24 bolts with a resistant area equal to 353 mm^2 have been chosen.
The horizontal distance between the bolts has been set equal to 81 mm. Therefore, the width of the flange is (Figure 4.21):

$$b_T = 2e_{T,f} + w_{T,h} = 195\ mm$$
$$b_{eff} = min\{b_{eff,1}; b_{eff,2}; 0.5b_T\} = 97.5\ mm \quad (4.53)$$

The thickness of the T-stub has been set equal to 30 mm.

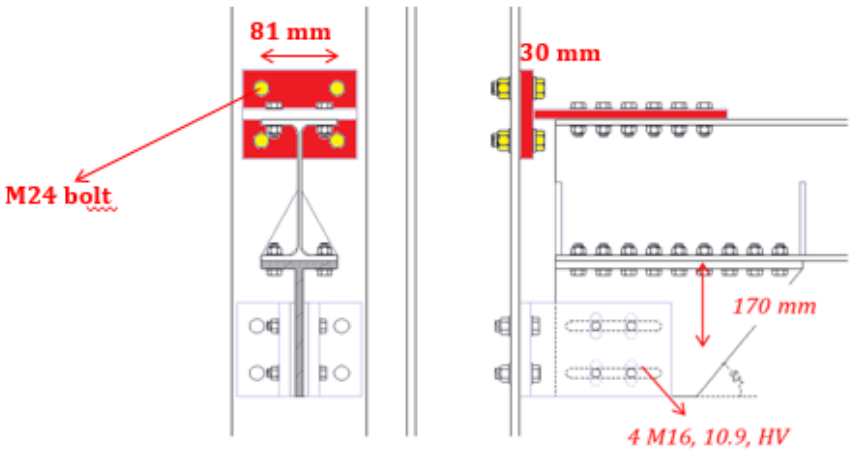

Figure 4.21 – Upper T-stub with the geometric characteristics of the flange

To avoid the interaction between shear and bending moment at the base of the T-stub:

$$t_{T-stub,w} = \frac{V_{Ed} \cdot \sqrt{3} \cdot \gamma_{M0}}{0.5 \cdot b_t \cdot f_{y,T}} = 5.73\ mm \qquad (4.54)$$

For this reason, it has been set $t_{T-stub,w}$ equal to 15 mm.

For simplicity, the width of the flange is assumed equal to the width of the web. Instead, the connection between the stem of the T-stub and the upper flange of the beam is made through M16 bolts, with a minimum number equal to 8.37 and rounded to 12.

$$n_{b,min} = \frac{F_{friction,Rd} \cdot \gamma_{M2}}{\alpha_v \cdot A_{res} \cdot f_{ub}} = 8.37 \qquad (4.55)$$

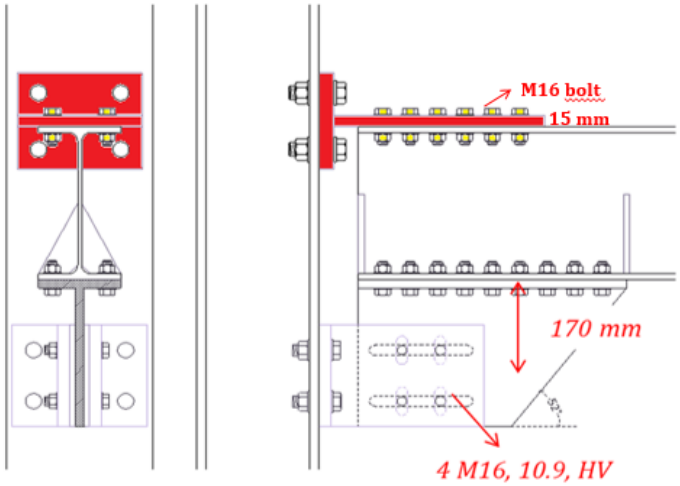

Figure 4.22 – Upper T-stub with the geometric characteristics of the stem

A proper gap has to be left between the beam and the column in order to accommodate rotations up to 50 mrad:

$$gap_{min} = max\left\{t_{T,f} + 2 \cdot t_{T,w}; \Phi \cdot (m_T + n_T) + t_{T,f}; \Phi \cdot \left(e_v + \frac{w_v}{2} + z\right)\right\} = \\ = max\{60\ mm; 34.63\ mm; 29.28\ mm\} = 60\ mm \qquad (4.56)$$

Step 5. Design of the haunch

An iterative procedure is adopted to define the geometry of the haunch flange (Figure 4.23) according to a "trial and error" procedure by fixing the number of rows of bolts, the pitch, the diameter of the bolts and the distance of the terminal rows of the bolts from the edge. Two rows of M16 bolts are adopted, with a longitudinal pitch of $2.4d_0$=45 mm and a distance from the free edge of $1.5d_0$=22.5 mm.

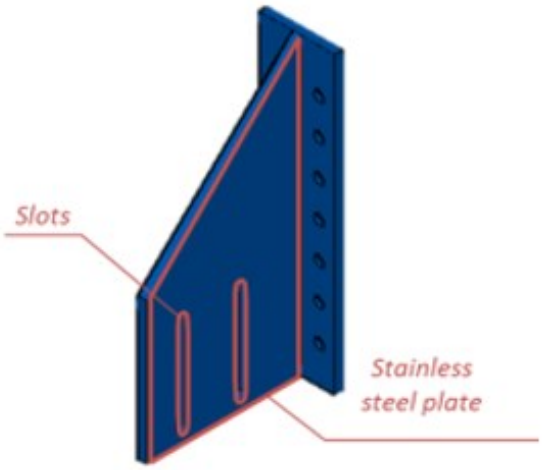

Figure 4.23 – Haunch

$$F_{t,Ed} = \frac{F_{friction,Rd} \cdot h_h}{\sum_i d_i^2} \cdot d_{max} = 43.26\ kN$$
$$F_{v,Ed} = \frac{F_{friction,Rd}}{n_{b,h}} = 29.78\ kN \quad (4.57)$$

Where:

- h_h is half-height of the haunch;
- d_i is the distance of the i-th bolt from the centre of rotation.

The web thickness is assessed as:

$$t_{hw} \geq \frac{F_{friction,Rd} \cdot \gamma_{M0}}{(h_w - 2 \cdot d_0) \cdot f_y} = 9.50\ mm \quad (4.58)$$

It is assumed t_{hw} equal to 15 mm.

Step 6. Design of the L-stubs

The same approach adopted with the T-stub is used.

$$F_{t,Ed} = \frac{F_{friction,Rd}}{n_b} = 104.23\ kN - Tension$$
$$F_{v,Ed} = \frac{F_{friction,Rd}}{2 \cdot n_b} = 14.32\ kN - Shear \quad (4.59)$$

M20 bolts are chosen to connect the L-stubs to the column flange (Figure 4.24).

$$A_{res,min} = max\left[\frac{\gamma_{M2}}{f_{ub}}\left(\frac{F_{v,Ed}}{\alpha_v} + \frac{F_{t,Ed}}{1.26}\right); \frac{\gamma_{M2} \cdot F_{t,Ed}}{0.9 \cdot f_{ub}}\right] = 144.76\ mm^2 \quad (4.60)$$

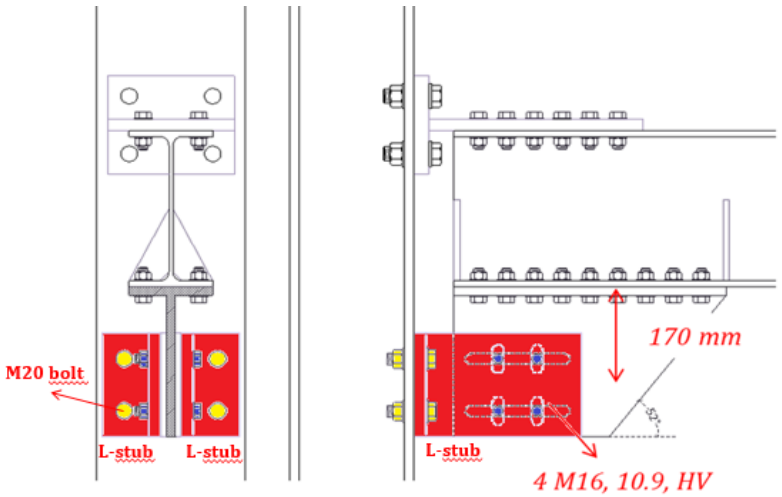

Figure 4.24 – Geometry of the L-stubs

The vertical slotted holes have to be designed:

$$stroke_{v,D} = \varphi \cdot \left(gap + e_{L,f,h} + w_{L,f,h} + stroke_{h,A}\right) = 11.67\ mm$$
$$L_{slot,v,min} = 2 \cdot stroke_{v,D} + d_0 = 41.34\ mm \rightarrow 50\ mm \quad (4.61)$$

Step 7. Check of the beam resistance

The bending moment at the column flange should be higher than the plastic resistance of the beam. Therefore it is essential to evaluate the bending moment at the presumed position of the plastic hinge $M_{b,Ed}$. The beam, in this case, is a non-dissipative zone and must be controlled by the following relation:

$$M_{b,Ed} = M_{cf,Rd}\frac{L_e - b}{L_e} = 183\frac{2.18 - 0.245}{2.18} = 162.43 \leq M_{b,Rd} \quad (4.62)$$

where b is the length of the haunch and L_e an equivalent length for shear:

$$L - 2a - \frac{M_{cf,Rd}}{V_{Ed}} = 2.18\ m \quad (4.63)$$

4.3.4 Double-split dissipative T-stub connection

Consistently with the design of the same structure with other connection typologies, the dissipative double split tee joints have been designed with a bending resistance equal to 100 kNm, with T-stubs in tension collapsing according to a type-1 mechanism. Since the design requirements are the stiffness and the resistance of the joint, the damper width and length are assumed as design parameters, while the thickness of the flange plate is assumed equal to 25 mm. Starting from the assumptions reported in Eqs. (4.64-4.65), all the geometrical details can be defined.

$$M_{j,Rd} = \frac{2\eta B_{eff} t_{ep}^2}{m} f_y\left(d_b - t_{bf}\right) = 100\ kNm \quad (4.64)$$

$$0{,}25\frac{EB_{eff} t_{ep}^3}{m^3} = S_{j,Rd} = 324.74\ kN/mm \quad (4.65)$$

In Eqs. (4.64-4.65), $M_{j,Rd}$ is the design bending moment, $S_{j,Rd}$ is the design stiffness, f_y is the material yield strength, d_b is the beam depth and t_{bf} is the thickness of the beam flange, t_{ep} is the

thickness of the T-stub, E is the modulus of elasticity, m is the distance between the plastic hinges in the flange of the T-stub, η is a parameter accounting for moment-shear interaction in the yielded part of the T-stub, B_{eff} is the effective width of the simplified X-shape.
The unknown parameters are the bolts' location and the dissipative element's thickness. However, Eqs. Eqs. (4.64-4.65) represent a system that cannot be solved in closed form because η, which accounts for the moment-shear interaction, depends on s/B and m/t (s is the shortest width of the hourglass, B is the longest width of the hourglass, m is the distance between the plastic hinges in the flange of the T-stub, i.e. the length of the hourglass, and t is the thickness of the T-stub).
For this reason, an iterative process is applied. Firstly, a random value of η is assumed, provided that it is lower than 1. In such a way, the unknown parameters are only m and B_{eff}:

$$\begin{cases} M_{j,Rd} = 2\eta \dfrac{B_{eff} t^2}{m} f_{yk}\left(h_b - t_{fb}\right) \\ 0.25 \dfrac{E B_{eff} t^3}{m^3} = S_{j,Rd} \end{cases} \tag{4.66}$$

From the solution of the system, it is possible to obtain:

$$m = \sqrt{\frac{0.25 M_{j,Rd} E t}{2\eta f_{yk}\left(h_b - t_{fb}\right) S_{j,Rd}}} \tag{4.67}$$

$$B_{eff} = \frac{S_{j,Rd} m^3}{0.25 E t^3} \tag{4.68}$$

At this point, it is possible to assess the optimal ratio s/B, according to the laws:

$$\left(\frac{s}{B}\right)_{optimal} = 0.5634 \left(\frac{m}{t}\right)^{-0.64} \quad if \ \frac{m}{t} \leq 6 \tag{4.69}$$

$$\left(\frac{s}{B}\right)_{optimal} = 0.18 \quad if \ \frac{m}{t} > 6 \tag{4.70}$$

It is possible to assess:

$$\alpha = \frac{2}{m} \cdot ln\left(\frac{B}{s}\right) \tag{4.71}$$

$$B = \frac{2 \cdot B_{eff}}{\alpha \cdot m \cdot e^{\left(1 - \alpha \frac{m}{2}\right)}} \tag{4.72}$$

Since the s/B ratio is known, it is possible to calculate the minimal width as:

$$s = \left(\frac{s}{B}\right)_{optimal} \cdot B \tag{4.73}$$

Considering an iterative approach, it is possible to define the function:

$$\eta = \frac{2 \cdot m \cdot b(z) \cdot (2 \cdot z - m)}{3 \cdot B_{eff} \cdot t^2} \left[1 - \sqrt{1 + \frac{3 \cdot t^2}{(2 \cdot z - m)^2}}\right] \tag{4.74}$$

Hereinafter, the results obtained at the end of the iterative process are summarized:

$$\begin{gathered} \eta = 0.826 \\ m = 59\ mm \\ B = 81\ mm \\ s = 26\ mm \end{gathered} \tag{4.75}$$

4.4 Definition of a set of accelerograms

The mock-up has been tested at the STRENGTH laboratory of the University of Salerno, employing the Pseudo2 software adopting an implicit algorithm with a time step equal to 0.01s. The algorithm is set to eventually reduce the time step if the equation of motion does not converge at a given time step. The mass matrix is defined starting from the loads previously introduced. Referring to the overall loads calculated for the couple of MRFs, the mass matrix can be written as:

$$\boldsymbol{M} = \begin{bmatrix} 38 & 0 \\ 0 & 28.4 \end{bmatrix} ton \tag{4.76}$$

The experimental campaign applied five accelerograms in the first and the second campaign and six seismic inputs in the third. The applied accelerograms and their spectra are reported in Table 4.8, Figure 4.25 and Figure 4.26.

The shown accelerograms have been selected so that their mean spectrum could be consistent with the type-1 spectrum provided by Eurcodoe 8 for a peak ground acceleration equal to 0.35g and a type-B soil. Before performing the pseudo-dynamic tests, a 2D SeismoStruct model of one of the MRFs of the mock-up with RBS connections was carried out. This model was exploited to perform preliminary analyses to select which accelerograms could engage the mock-up in the plastic range compatibly with the actuators' limits in terms of displacements and forces. The Imperial Valley earthquake was applied to the building as the first seismic input; even though its PGA is about 0.37g, the preliminary analyses highlighted that, due to the overstrength exhibited by the mock-up, it has been necessary to increase this value up to 1.10g. The second accelerogram, Spitak, instead, was chosen because it is characterised by one main peak with significant amplitude. The third earthquake is an artificial seismic input obtained through the SIMQKE tool by applying the same previous input parameters. Finally, the last three accelerograms are natural inputs. As already highlighted, the high overstrength exhibited by the structure required to increase the values of the peak ground accelerations for all the tests, as shown in Table 4.8.

Table 4.8 – Set of accelerograms

Station	Date	Magnitude	Fault mechanism	Natural PGA	PGA for PsD tests
Imperial Valley (USA), Agrarias	10/15/1979	6.5	Strike-Slip	0.37 g	1.10 g
Spitak (Armenia), Gukasian	12/07/1988	6.8	Thrust	0.20 g	0.80 g
Artificial, SIMQKE_GR	-	-	-	0.35 g	0.50 g
Santa Barbara (USA), Courth	08/13/1978	5.6	Strike-Slip	0.10 g	0.80 g
Coalinga (USA), Slack Canyon	05/02/1983	6.2	Thrust	0.17 g	0.80 g
Kobe (Japan), Kakogawa	01/17/1995	6.9	Strike-Slip	0.25 g	1.00 g

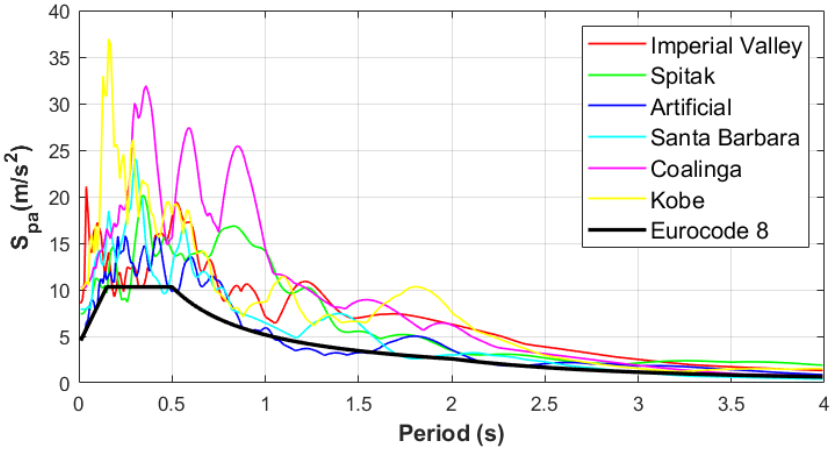

Figure 4.25 – Spectra

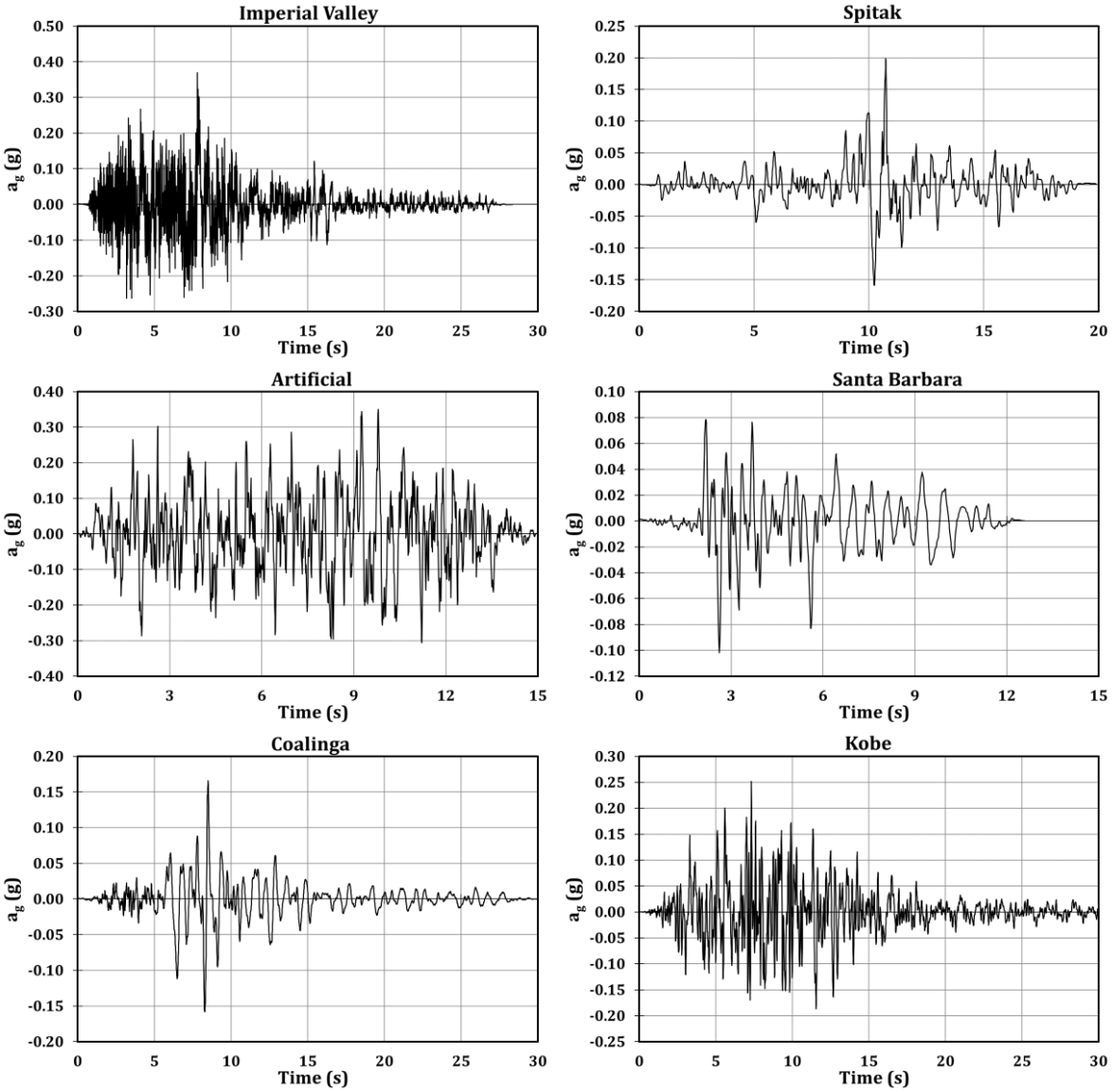

Figure 4.26 – Accelerograms

4.5 Experimental set-up

The mock-up was tested at the laboratory STRENGTH of the University of Salerno. The same mock-up has been employed to perform tests on different connection typologies. Therefore, the dissipative zones are conceived to be completely demountable. Furthermore, full-strength column splices are placed at the columns' mid-heights, and beam splices are located close to the beam ends. In this way, column bases and beam-to-column connections can be easily substituted at the end of every test (Figure 4.27) to execute other tests on the same structure with a different connection typology.

The mock-up is connected to the strong concrete floor of the laboratory through rigid steel footings fastened with high-strength Dywidag bars. The horizontal actions are applied by two actuators, which are connected to the tested structure at the floor levels. The actuators are fixed to the structure through a horizontal floor bracing fastened to the primary and secondary beams of the mock-up according to the scheme given in Figure 4.27. On the other side, the actuators are fastened to the laboratory reaction wall, constituted by a very strong and resistant steel braced frame. Initially, the base of the mock-up was disconnected from the rigid wall, and the four steel footings were not mutually connected at the foundation level. Then, the base of the frame is braced, realizing a rigid foundation diaphragm connected to the reaction wall.

The actuators employed took advantage of some preliminary time-history analyses with the FE models presented in the following sections. The actuator with higher load capacity and lower stroke (MTS 243.60-02, with load capacity equal to $648\,kN$ in tension and $1000\,kN$ in compression; piston stroke $\pm 508\,mm$) was located at the first level, while the actuator with lower capacity and more stroke (MTS 243.45-01, with a load capacity of $649\,kN$ in compression and $445\,kN$ in tension; piston stroke $\pm 1066\,mm$) was located at the top level. This choice is justified by distributing masses, higher at the first level and lower at the roof level.

Many measurement devices have been employed to monitor local and global displacements, rotations and deformations. For example, five transducers have been applied to each floor to measure the floors' global displacements. Such transducers control the floor translation in the two horizontal directions and the floor rotation (Figure 4.28 and Figure 4.29). In the considered case, transversal movements and floor rotations can be due only to geometrical imperfections resulting in accidental eccentricities.

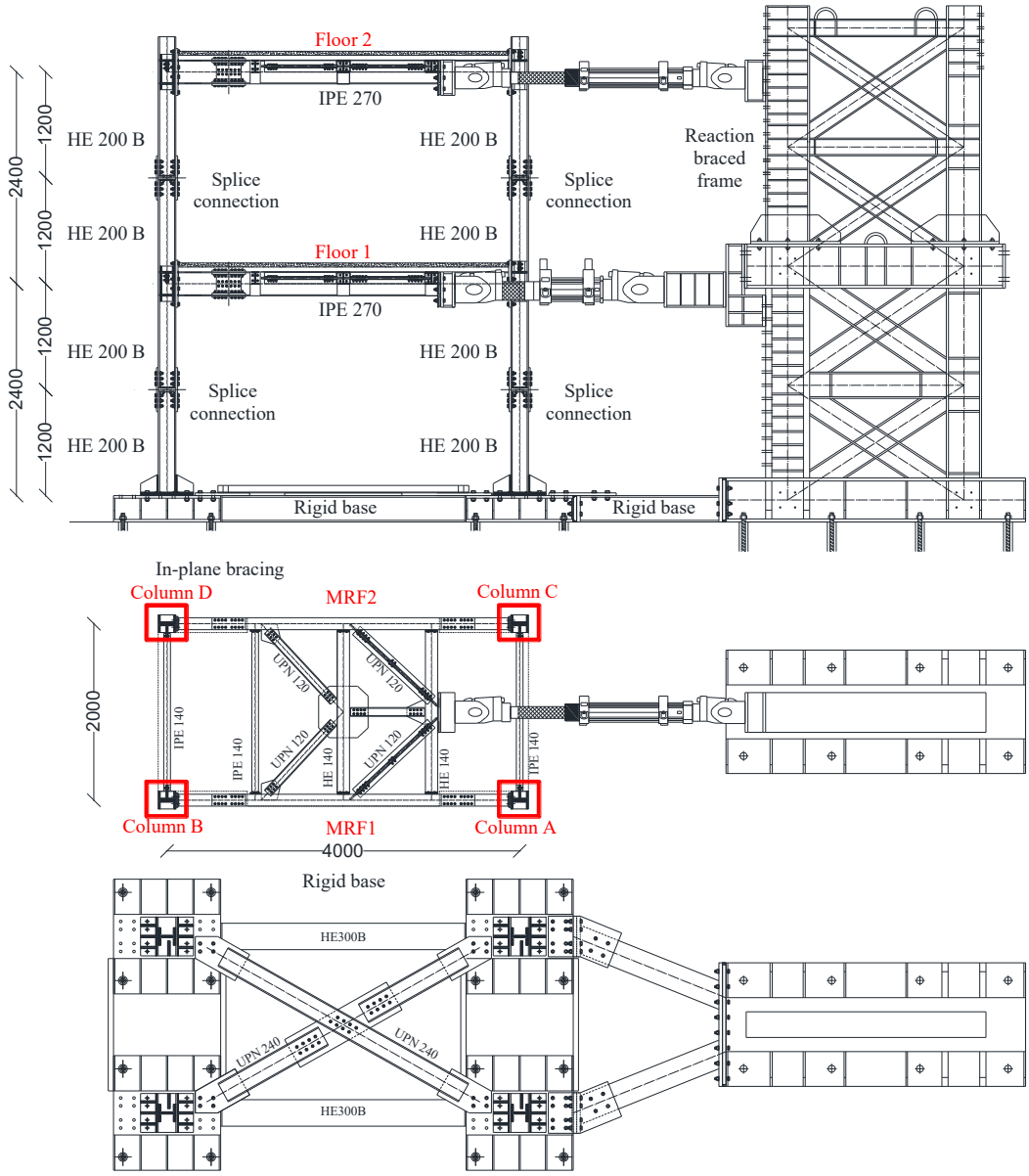

Figure 4.27 – Experimental set-up

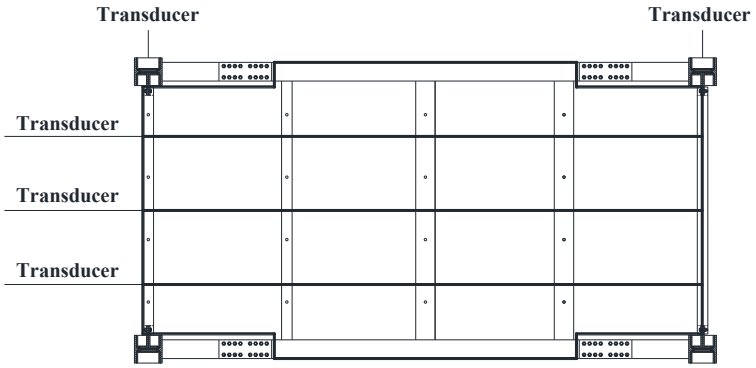

Figure 4.28 – Transducers' layout at the floor level

Figure 4.29 – Global measurement devices

Transducers and strain gauges have been used to measure the local response of the connections. In order to monitor the bending moments arising in the whole structure during the test, strain-gauges have been applied to the profile flanges in areas close to the beams and the column ends. In particular, forty-eight strain-gauges were placed at the base and the top sections of the columns of the first level and at the beam ends in sections close to the RBS zones but outside the plastic zones (Figure 4.30).

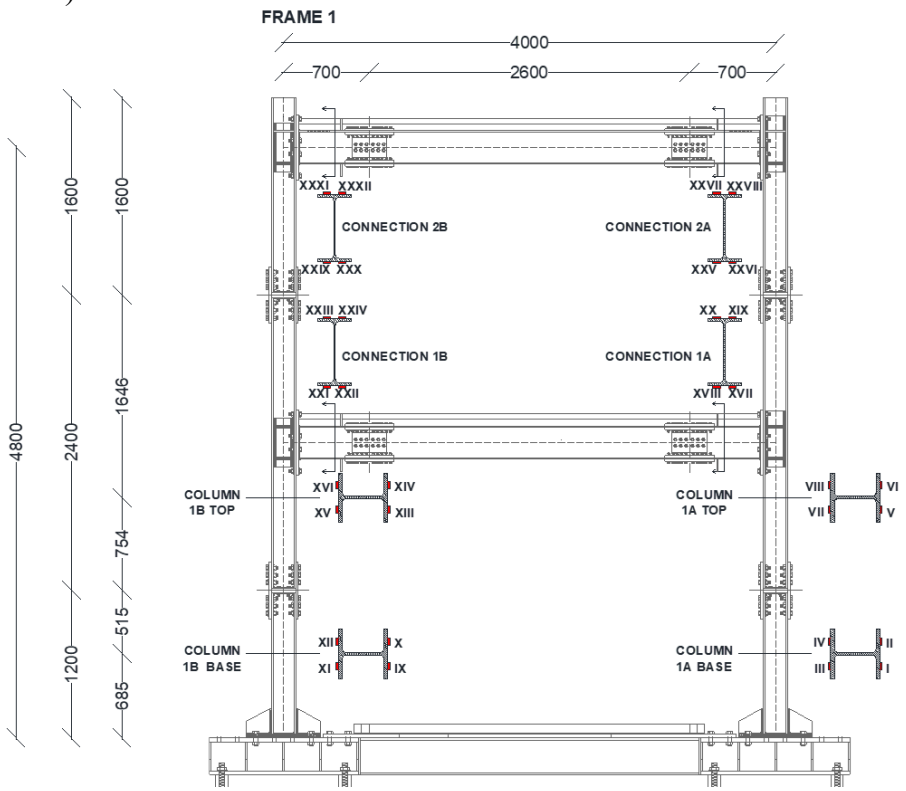

Figure 4.30 – Layout of the strain-gauges applied on MRF-1 (structure equipped with RBSs)

In the monitored sections, the strain-gauges (Figure 4.31) allow calculating the bending actions starting from the knowledge of the curvature as follows:

$$\chi = \frac{\varepsilon_u - \varepsilon_l}{h} \qquad \rightarrow \qquad M = \chi EI \tag{4.77}$$

where ε_u and ε_l represent the average values of the deformations measured by the strain-gauges located at the upper and lower flange level, respectively; h is beam or column depth, and I is the beam's or column's second moment of area.

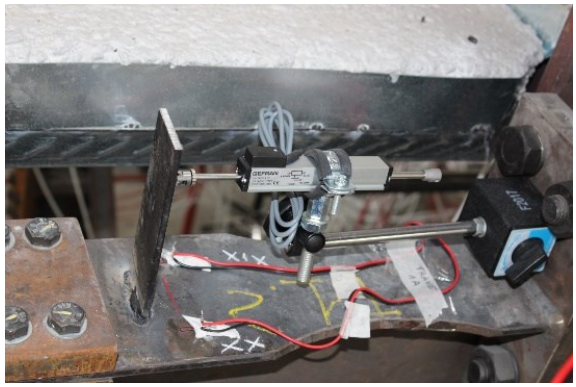

Figure 4.31 – Strain gauges on beams

In order to measure the rotations of connections, sixteen potentiometric transducers have been adopted. In addition, they have been fixed above and under the reduced flange zones to measure the elongation/shortening of the beam flanges in the reduced area (Figure 4.32). In this way, the rotations of the RBS connections can be assessed as follows:

$$\varphi = \frac{\delta_u - \delta_l}{z} \tag{4.78}$$

where δ_u and δ_l represent the displacements monitored by transducers located at the upper and lower flange level, while z is the distance between the transducers' axes.

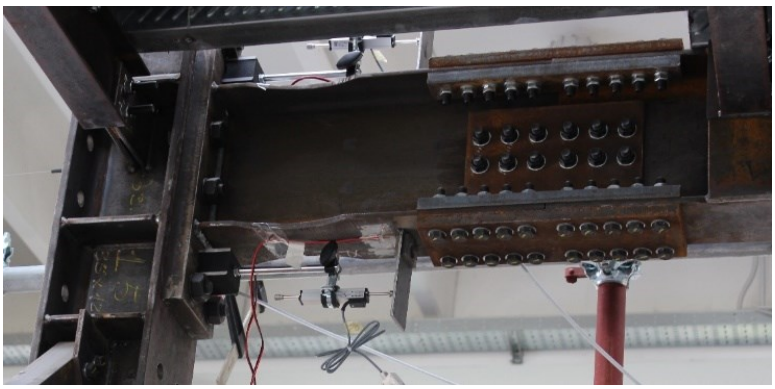

Figure 4.32 – Local transducers applied to the RBS zone

4.6 1st experimental campaign: structure equipped with RBS connections

4.6.1 Experimental results

4.6.1.1 Imperial Valley (PGA = 1.10g)

The first test consisted of applying the ground acceleration recorded by the station located at Imperial Valley (USA) in 1979. It is important to highlight that the natural peak ground acceleration was equal to 0.37g, but, in this case, an amplified PGA equal to 1.10g, about three times the real one, has been employed. This evidence is justified because the structure has been overdesigned with a factor higher than 2. This occurrence has required using a PGA, which is three times the natural value, to engage the structure in the plastic range.

In this test and those presented in the following paragraphs, the peak floor displacements and peak actuators forces occurred in the same instants (Figure 4.33). This aspect agrees with the expected response because the structure is regular, and the first vibration mode is prominent.

From Figure 4.33, it can be observed that the force values obtained from the actuator of the first level fluctuate more than the second level. This aspect is mainly due to the accuracy of the pressure cell installed in the MTS 243.60-02 actuator, which is characterized by a lower precision. In addition, while the upper actuator (MTS 243.45-01) is equipped with a strain gauge load cell, the lower actuator is equipped with a differential pressure cell.

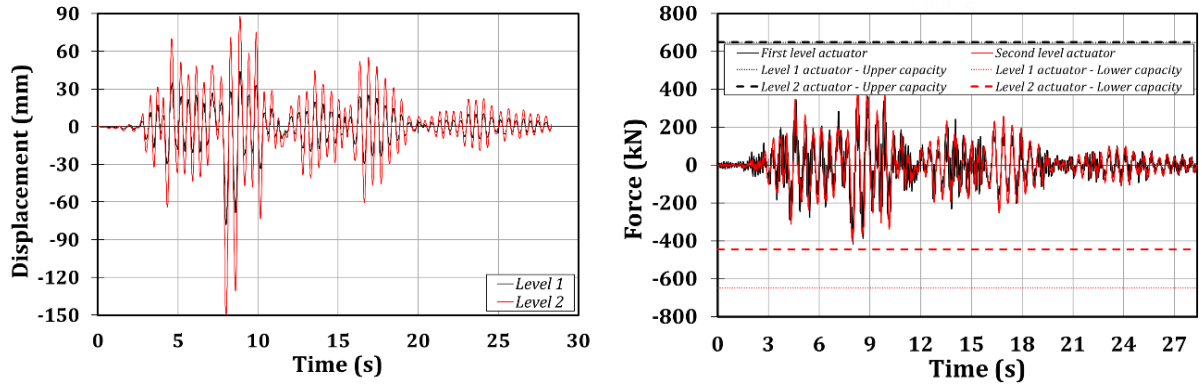

Figure 4.33 – Test 1: floor displacements (left) and reaction force (right)

The maximum base shear, peak displacements and inter-storey drifts are summarized in Table 4.9. In Test 1, the interstorey drift is about 3%, leading to a significant plastic engagement of the structural elements. In fact, the local measuring devices showed that both the RBS connections and the column bases underwent damage. The damage was more significant for the RBS connections located at the first level and lower for the RBS connections of the second storey. The observed value of the RBSs yielding force substantially agrees with the design values previously reported.

Table 4.9 – Main results related to Test 1

Imperial Valley 1.1g			Test 1
Maximum base shear (kN)	Pull		-751
	Push		667
Peak first floor displacement (mm)	Pull		-78
	Push		44
Peak roof displacement (mm)	Pull		-150
	Push		88
Maximum interstorey drift (%)	Pull	Level 1	-3.3
		Level 2	-3.0
	Push	Level 1	1.9
		Level 2	1.9

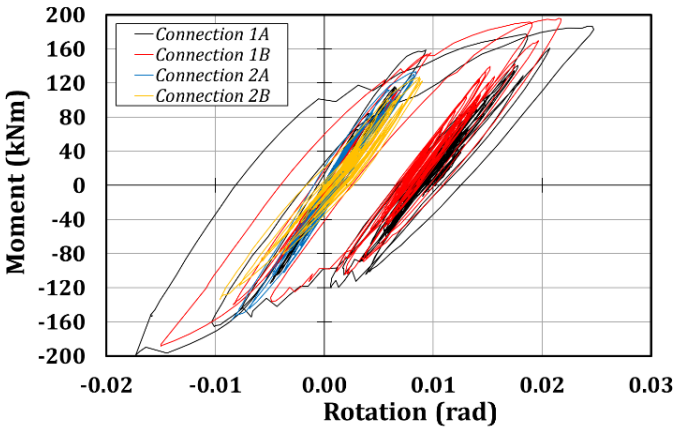

Figure 4.34 – Test 1: moment-rotation curves related to the RBS connections belonging to MRF-1

The state of damage occurring in the structure in Test 1 was due to the significant number of cycles experienced by the RBSs of the first level. This occurrence is shown by the hysteretic curves of the RBSs given in Figure 4.34. It is worth observing that the RBS connections achieved a maximum local rotation slightly lower than 30 mrad, which is very close to the EC8 requirement for beam-to-column connections in DCH MRFs (35 mrad).

4.6.1.2 Spitak (PGA = 0.80g)

The second accelerogram was very different from the previous one because it was mainly characterized by a prominent amplitude peak only, while a higher number of peaks characterized the previous one. This feature is apparent from the results (Figure 4.35): for the Spitak earthquake, there is only one main excursion in the plastic range, characterized by an inter-storey drift of about 3.6%, while in all the other instants, the structure remains practically elastic. This aspect can be clearly understood by analysing the local measurements considering, for instance, the moment-rotation response of the RBS connections (Figure 4.35). In fact, it can be noted that in Test 2, the moment-rotation response of the most stressed RBS connection is characterized by a peak rotation of about 30 mrad, with a bending moment at the RBS centreline equal to about 200 kNm.

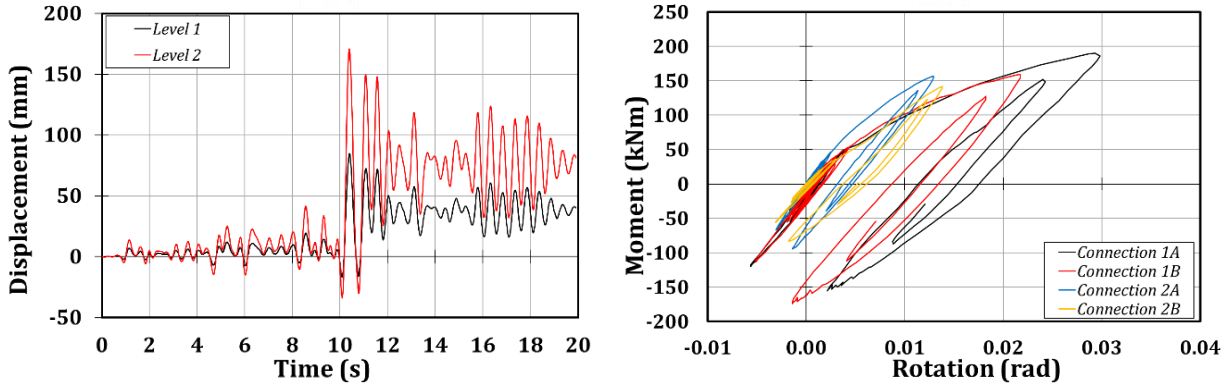

Figure 4.35 – Test 2: floor displacements (left) and moment-rotation curves related to the RBS connections belonging to MRF-1 (right)

It is helpful to observe that this value of the peak moment is far beyond the expected value of the bending moment adopted in the design phase for the check of the connection, which was determined considering the plastic zone fully yielded and strain-hardened. Consequently, the overstrength factor equal to 1.1 suggested by EC8 is largely underestimated. In fact, in this case, the ratio between the measured bending moment and the nominal value of the plastic resistance of the RBS is equal to about 1.6. This amount of overstrength, significantly exceeding the value given by the code provisions, is probably due to the reduction of the width-to-thickness ratio of the beam flanges in the RBS zone, which practically prevent local buckling, as testified by the failure mode due to the fracture of either the flange or the weld.
Additional results related to the global structural response are reported in Table 4.10.

Table 4.10 – Main results related to Test 2

Spitak 0.8g			**Test 2**
Maximum base shear (kN)	Pull		-652
	Push		670
Peak first floor displacement (mm)	Pull		-17
	Push		85
Peak roof displacement (mm)	Pull		-33.6
	Push		171
Maximum interstorey drift (%)	Pull	Level 1	-0.7
		Level 2	-0.7
	Push	Level 1	3.5
		Level 2	3.6

At the end of the test, residual deformations of about 2% were observed, leaving the structure in a deformed configuration. It is worth highlighting that the residual floor drifts are not brought back to zero at the end of each test. Consequently, a test starts from the deformed configuration achieved by the structure in the previous experiment. Such a choice relies on the need to assess how many several earthquakes the building is able to withstand before the crisis occurs. Furthermore, this choice simplifies performing numerical simulations since the time history inputs can be easily applied to the model. The preference of avoiding the recentering of the structure at the end of each test has been applied in all the experimental campaigns. Therefore, a comparison of the global and local behaviour of the mock-up equipped with the three analysed connections' typologies can be carried out.

The floor displacements are always assessed starting from the deformed initial configuration of the structure. For this reason, the displacement histories start from values equal to 0 in the first instant of the tests.

4.6.1.3 Artificial (0.50g)

During the third test, the maximum base shear was equal to 555 kN and the maximum roof displacement equal to 83 mm (Figure 4.36), leading to a maximum inter-storey drift equal to about 1.8%. In terms of moment-rotation curves (Figure 4.36), the RBS connections remained practically in the elastic range.

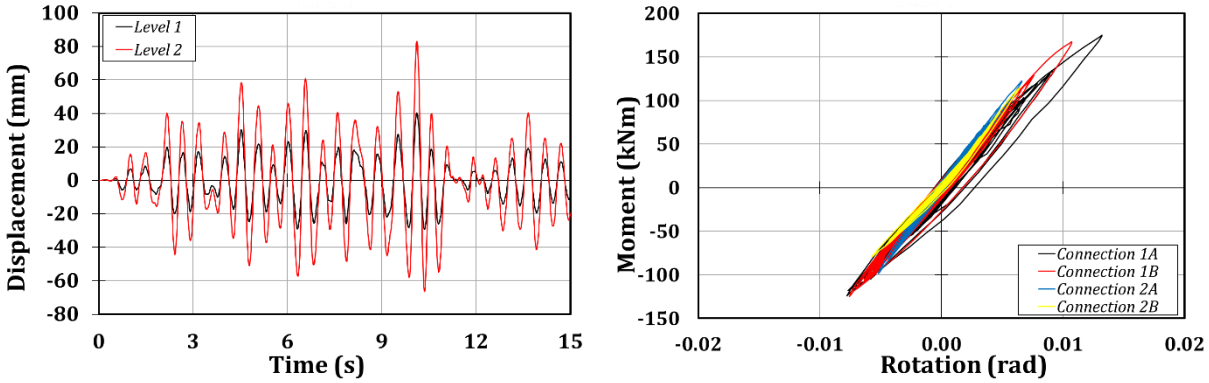

Figure 4.36 – Test 3: floor displacements (left) and moment-rotation curves related to the RBS connections belonging to MRF-1 (right)

A summary of the main test results is reported in Table 4.11.

Table 4.11 – Main results related to Test 3

Artificial 0.5g			Test 3
Maximum base shear (kN)	Pull		-444
	Push		555
Peak first floor displacement (mm)	Pull		-29
	Push		40
Peak roof displacement (mm)	Pull		-66
	Push		83
Maximum interstorey drift (%)	Pull	Level 1	-1.2
		Level 2	-1.5
	Push	Level 1	1.7
		Level 2	1.8

4.6.1.4 Santa Barbara (0.80g)

During the fourth test, the structure exhibited an elastic behaviour similar to the response observed during Test 3. Such an occurrence can be ascribed to the fact that the chosen value of PGA was not able to activate the plastic engagement of structural elements.

The maximum base shear was equal to 592 kN and the maximum roof displacement equal to about 99 mm (Figure 4.37), leading to a maximum inter-storey drift equal to about 2.2%. The RBS connections remained practically in the elastic range (Figure 4.37).

A summary of the main test results is reported in Table 4.12.

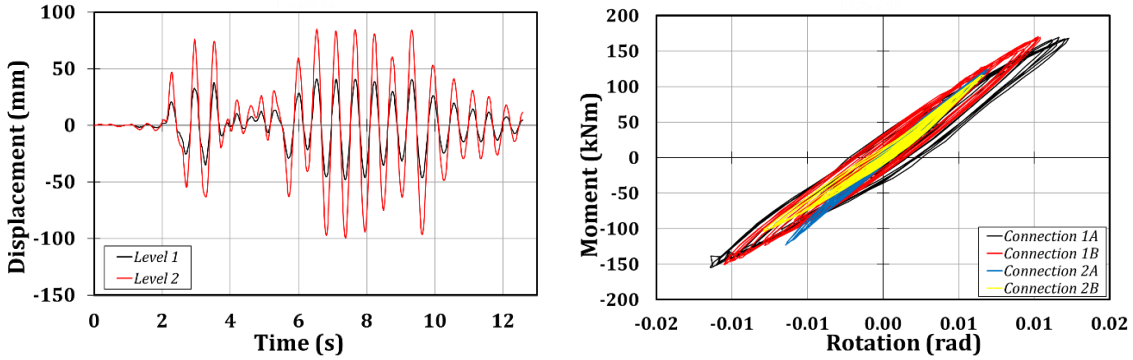

Figure 4.37 – Test 4: floor displacements (left) and moment-rotation curves related to the RBS connections belonging to MRF-1 (right)

Table 4.12 – Main results related to Test 4

Santa Barbara 0.8g			**Test 4**
Maximum base shear (kN)	Pull		-586
	Push		592
Peak first floor displacement (mm)	Pull		-48
	Push		41
Peak roof displacement (mm)	Pull		-99
	Push		85
Maximum interstorey drift (%)	Pull	Level 1	-2.0
		Level 2	-2.2
	Push	Level 1	1.7
		Level 2	1.8

4.6.1.5 Coalinga (0.80g)

The failure of the structure was achieved during Test 5 (whose main results are reported in Table 4.13, Figure 4.38). In particular, the last test was interrupted after the failure of two RBS connections located at the first storey of the building, on the two opposite frames, at the actuators' side (Figure 4.39). The failure was initiated by the local welding failure in the RBS-1A, and afterwards, RBS-1C failed due to the redistribution of the actions, which led to a torsional moment and overload of the opposite frame. The local collapse of RBS-1A was attributed to the attainment of the fatigue life of the welding and the unexpectedly high bending moment acting at the column flange level. In fact, it is worth noting that the bending moment at failure in RBS-1A was equal to 205 kNm. This value, as previously underlined, is more significant than the nominal resistance of the RBS of about 60%.

Table 4.13 – Main results related to Test 5

Coalinga 0.8g			**Test 5**
Maximum base shear (kN)	Pull		-630
	Push		612
Peak first floor displacement (mm)	Pull		-47
	Push		62
Peak roof displacement (mm)	Pull		-94
	Push		129
Maximum interstorey drift (%)	Pull	Level 1	-2.0
		Level 2	-2.0
	Push	Level 1	2.6
		Level 2	2.8

Even though the fracture of the weld connecting the beam flange to the column flange is a failure mode not expected in the case of RBS connections, it has to be considered that the loading protocol commonly adopted in the experimental analyses of the cyclic behaviour of RBS connections, typically performed on simple beam-to-column sub-assemblages, is completely different from the loading conditions occurring in the beam-to-column connections of the tested two-storey building because of the application of a series of seven earthquakes. The fracture of the welds is a consequence of the fatigue resulting from repeated earthquakes whose action overall gives rise to a high number of cycles having relatively small amplitudes. These small amplitudes cannot lead to local buckling, and only a few cycles with a large amplitude did not give rise to local buckling because of the reduction of the width-to-thickness ratio of the beam flanges in the reduced section zone.

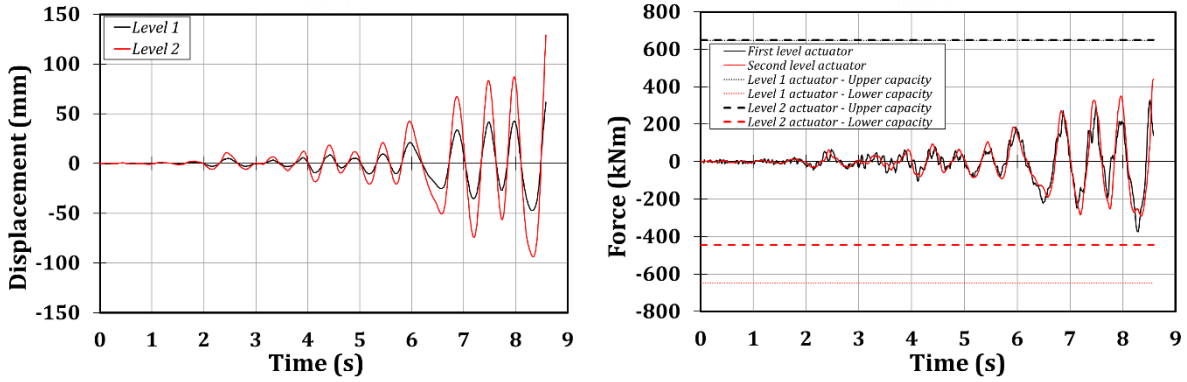

Figure 4.38 – Test 5: floor displacements (left) and reaction forces (right)

In order to check the accuracy of the welding detail, after the end of the test, a spare RBS already available in the laboratory and taken from the same product has been cut and inspected. The survey revealed that the full-penetration butt joint detail was correctly realized without significant defects (Figure 4.40).

It is worth noting that the typology of weld detail adopted complies with EC3 and EC8 regulations and complies with the indications given in the AISC Steel Design Guide [15]. In fact, beam-to-end plate welding, as recommended in the AISC Steel Design Guide, does not include access holes in the beam web to avoid the premature fracture of the beam flange due to stress concentration [16]. Therefore, as given in Figure 4.40, the beam flange was welded with 45° full-penetration butt joints, making an exception for the flange area directly above the beam web, which was welded with a partial penetration joint on the outer side and fillet welds in the roots. Since the detail complies with the code's main suggestions, the obtained result confirms that the partially brittle failure must be attributed, on the one side, to the underestimation of the overstrength factors used in the design and, on the other side, to the rules adopted to design the welding details, which probably do not consider properly the fatigue life phenomena that may occur under the effect of repeated seismic events. This outcome highlights the need for further investigations devoted to assessing the seismic response of typical welding details under seismic actions and their low-cycle fatigue life.

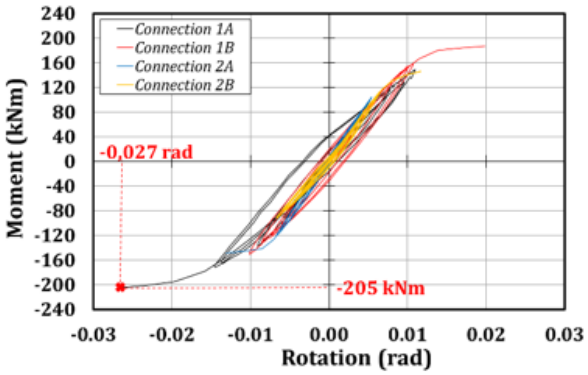

a) Test 7 – Columns A-B, 1st and 2nd storey

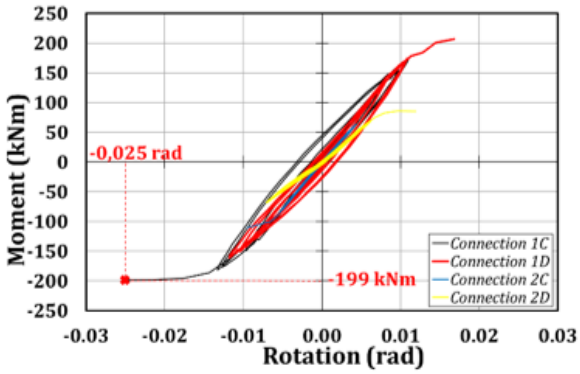

b) Test 7 – Columns C-D, 1st and 2nd storey

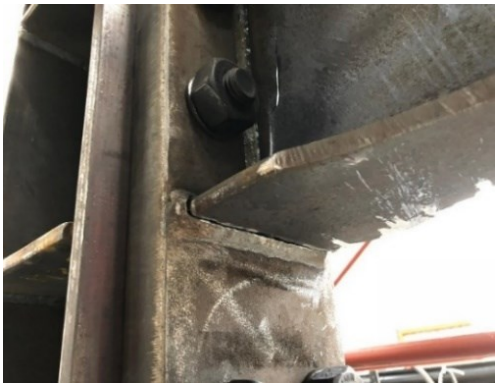

c) Failure in the welding of RBS 1A

d) Failure at the centerline of RBS 1C

Figure 4.39 – Hysteretic curves of the collapsed RBSs (top) and corresponding damage patterns (bottom)

Despite these considerations, it has to be observed that the tested RBS connections were subjected to a series of several destructive seismic events, which is a very severe condition typically not required by the current design practice. Therefore, even though the final collapse mode was not wholly satisfactory, the behaviour of the MRFs was reasonably reliable, confirming the simplicity and the large energy dissipation capacity of the RBS connections.

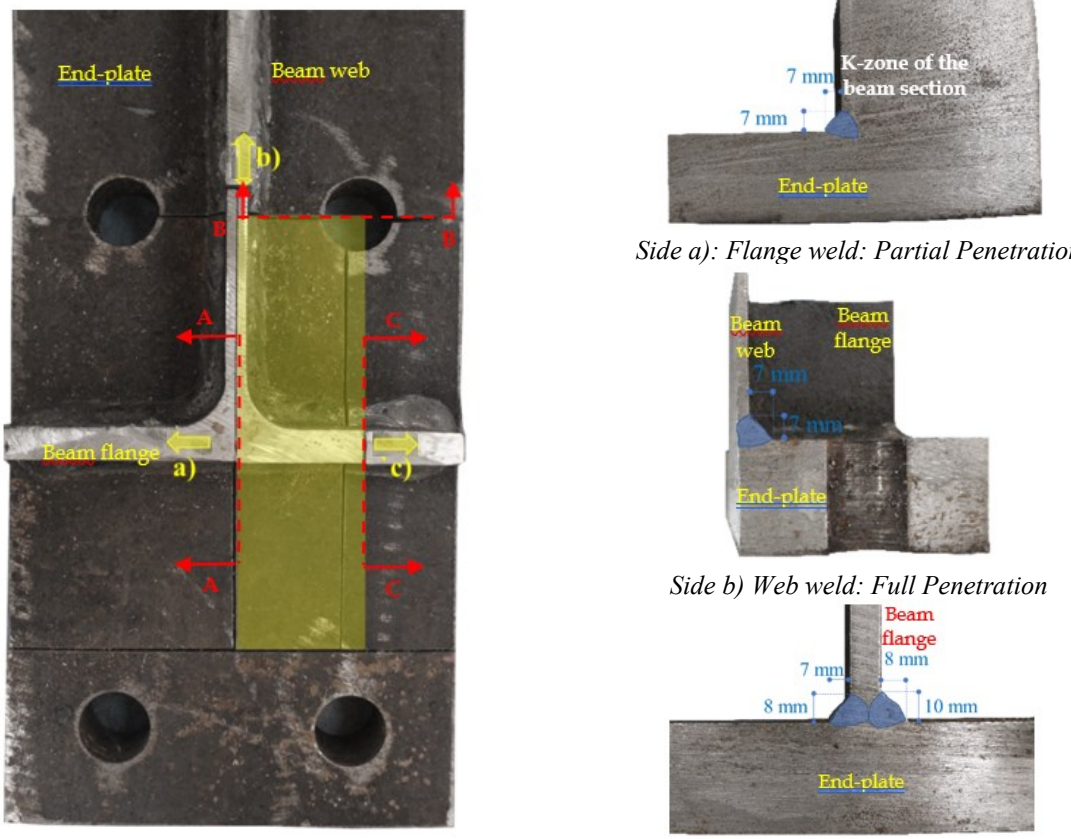

Figure 4.40 – Visual inspection of the welding detail

4.6.2 FE modelling of the tested frame

In the preliminary phase of the mock-up design, aiming to complement the test data and perform blind predictions of the seismic response, a non-linear 3D model FE of the structure (Figure 4.41) was developed with the software SeismoStruct [17]. The non-linearity of the seismic response of the structure has been modelled using a mixed lumped and distributed plasticity approach. In particular, the structural elements have been modelled with inelastic force-based elements accounting for geometric and material non-linearities with a spread plasticity approach.

Figure 4.41 – 3D model of the mock-up

The adopted finite element is characterized by five integration sections subdivided into at least 150 fibres. This subdivision is usually sufficient to accurately calculate the curvatures starting from the stress-strain material laws. Rigid links have been adopted to model the floor diaphragms, while lumped masses have been located at the centre of the spans. The structural detail of beam-to-column joints adopted in the mock-up was already tested, as reported in Chapter 2. The specimen had a connection detail with the same RBS geometry and a similar steel grade. The results of this experimental test [10] have been employed in this work to calibrate a non-linear spring, modelling the response of the RBS connections. The moment-rotation response of the RBS tested in [10] is reported in Figure 4.42, referring to the bending moment and rotations calculated at the RBS centreline. In particular, the moment-rotation behaviour of the RBS has been modelled by adopting a smooth link element [18].

This element is one of the more complete and complex hysteretic models available in current commercial software. Nevertheless, its main drawback is that it is based on many parameters, making the calibration process very complex. The calibration of these parameters employed the tool Multical [19], minimizing the scatter between the experimental and calibrated curve in energy dissipation and cyclic envelope (Figure 4.42). MultiCal is a tool for calibrating hysteretic models based on genetic algorithms.

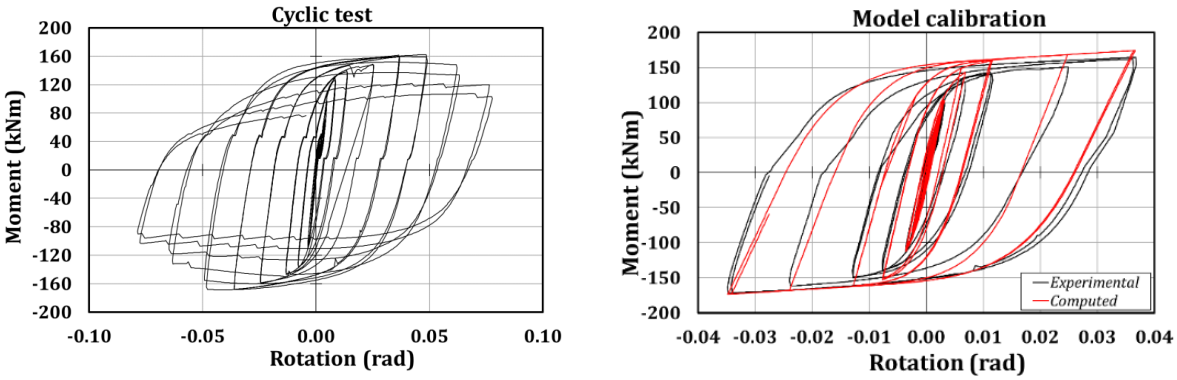

a) Cyclic response of the RBS *b) Model Calibration*

Figure 4.42 – Experimental and numerical moment-rotation response of the RBS

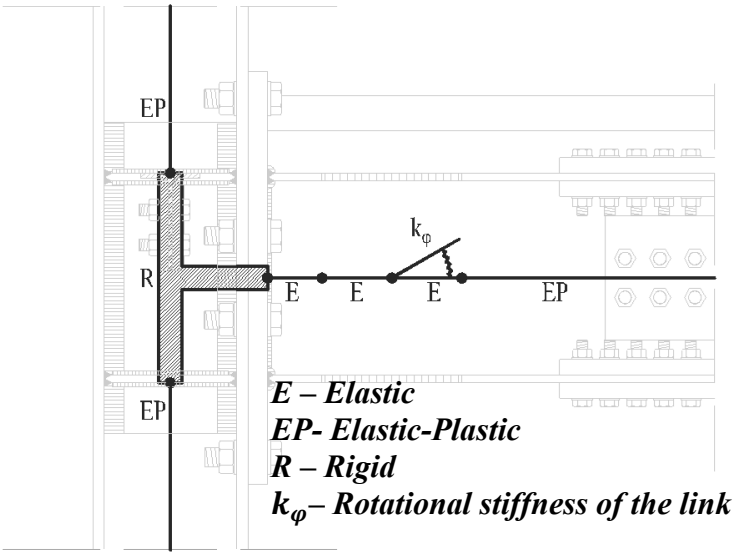

Figure 4.43 – FE model of the beam-joint system

It allows finding the best combination of parameters (Table 4.14) matching the experimental response based on the user's criteria. As far as the tests on the mock-up lead to rotation amplitudes lower than 35 mrad, the calibration procedure was applied considering the test cycles up to the amplitude of 35 mrad. This aspect is very important because the calibration of the model coefficients out of the expected range of rotations could define a set of parameters influenced by phenomena that do not occur at the design rotations. This is the case, for example, of the buckling phenomena observed in the test on the sub-assembly, which occurred only at rotations of about 50 mrad. The connection area has been modelled according to the approach described in Figure 4.43. Therefore, the stiffened portion of the panel zone has been modelled with rigid offsets, while the RBS non-linearity has been included in the previously calibrated spring. This non-linear spring is located at the RBS centreline.

Seismic loads have been applied in terms of accelerations at the base of the frame. The time-history analyses have been performed considering a time step of 0.01 s, adopting the Hilbert-Hughes-Taylor algorithm and including a damping value equal to 1% with a Rayleigh approach as already done during the pseudo-dynamic testing.

Table 4.14 – Parameters adopted to define the smooth model of link element (units in kN and m)

Curve properties	Parameter name	Value
Initial flexural stiffness	EI	41688
Cracking moment (positive)	PCP	157
Yield moment (positive)	PYP	158
Yield curvature (positive)	UYP	0.096
Ultimate curvature (positive)	UUP	0.193
Post-yield flexural stiffness (positive) as % of elastic	EI3P	0.012
Cracking moment (negative)	PCN	-157
Yield moment (negative)	PYN	-158
Yield curvature (negative)	UYN	-0.096
Ultimate curvature (negative)	UUN	-0.193
Post-yield flexural stiffness (negative) as % of elastic	EI3N	0.012
Stiffness degrading parameter	HC	4.7
Ductility-based strength decay parameter	HBD	0.006
Hysteretic energy-based strength decay parameter	HBE	0.000
Smoothness parameter for elastic-yield transition	NTRANS	1.27
Parameter for shape of unloading	ETA	0.50
Slip length parameter	HSR	0.070
Slip sharpness parameter	HSS	0.090
Parameter for mean moment level of slip	HSM	1.36
Exponent of gap-closing spring	NGAP	1
Gap closing curvature parameter	PHIGAP	1
Gap closing stiffness coefficient	STIFFGAP	1

4.6.3 Experimental versus numerical results

This section reports the main comparisons between the experimental results and the numerical model (Table 4.15, Table 4.16, and from Figure 4.44 to Figure 4.46). Compared to the five reported tests, the developed FE model seems to capture the global seismic response parameters with a sufficient degree of accuracy. In fact, the scatters between the actual and predicted peak displacements or actual and predicted peak forces do not exceed 25%, except for the Spitak accelerogram. In this specific case, the lower accuracy is probably due to the calibration procedure applied to characterise the RBSs. As explained in [19], when the accelerograms are characterized only by a few peaks, a calibration of the model parameters based only on the results of one cyclic test may lead to approximations. In fact, it was already recognized in [19] that the calibration based only on the results of one cyclic test is typically not sufficient to obtain a satisfactory prediction of the local response, especially in cases where the connection experiences only a few large amplitude cycles.

Table 4.15 – Experimental versus analytical comparison of base shear, floor displacements and interstorey drift

	Maximum base shear (kN)		*Peak first floor displacement (mm)*		*Peak roof displacement (mm)*		*Maximum interstorey drift (%)*			
Test	***Pull***	***Push***	***Pull***	***Push***	***Pull***	***Push***	***Pull (L-1)***	***Pull (L-2)***	***Push (L-1)***	***Push (L-2)***
1 - PsD	*-751*	*667*	*-79*	*44*	*-150*	*88*	*-3.27*	*-2.98*	*1.84*	*1.86*
1 - Sim.	*-656*	*601*	*-66*	*43*	*-130*	*84*	*-2.74*	*-3.02*	*1.77*	*1.97*
1 - Err. (%)	***15***	***11***	***20***	***4***	***15***	***5***	***20***	***-1***	***4***	***-5***
2 - PsD	*-652*	*670*	*-17*	*85*	*-34*	*171*	*-0.70*	*-0.72*	*3.54*	*3.61*
2 - Sim.	*-645*	*648*	*-27*	*74*	*-52*	*133*	*-1.12*	*-1.24*	*3.08*	*2.55*
2 - Err. (%)	***1***	***3***	***-37***	***15***	***-36***	***28***	***-37***	***-42***	***15***	***42***
3 - PsD	*-444*	*555*	*-29*	*40*	*-66*	*83*	*-1.22*	*-1.54*	*1.67*	*1.79*
3 - Sim.	*-477*	*563*	*-31*	*42*	*-60*	*88*	*-1.27*	*-1.52*	*1.74*	*1.97*
3 - Err. (%)	***-7***	***-1***	***-4***	***-4***	***10***	***-6***	***-4***	***2***	***-4***	***-9***
4 - PsD	*-586*	*592*	*-48*	*41*	*-99*	*85*	*-2.00*	*-2.16*	*1.71*	*1.84*
4 - Sim.	*-588*	*575*	*-47*	*44*	*-98*	*92*	*-1.95*	*-2.12*	*1.83*	*2.07*
4 - Err. (%)	***0***	***3***	***2***	***-6***	***2***	***-8***	***2***	***2***	***-6***	***-11***
5 - PsD	*-630*	*612*	*-47*	*62*	*-94*	*129*	*-1.97*	*-1.96*	*2.57*	*2.81*
5 - Sim.	*-665*	*555*	*-47*	*54*	*-81*	*117*	*-1.95*	*-1.62*	*2.26*	*2.63*
5 - Err. (%)	***-5***	***10***	***1***	***14***	***15***	***10***	***1***	***21***	***14***	*7*

For these cases, the calibration should be carried out considering at least the results of a cyclic test and the results of a monotonic test. Nevertheless, for all the other cases, the predictions of the peak floor displacements, peak forces and peak inter-storey drifts seem relatively accurate.

The accurate prediction of the global response parameters does not correspond to the same level of accuracy when test data and analytical results are compared in terms of local response parameters. While the hysteretic cycles have an overall shape similar to the experimental loops, the predictions regarding maximum/minimum rotations experienced by the RBS connections and peak moments at the RBS centreline are relatively more approximate.

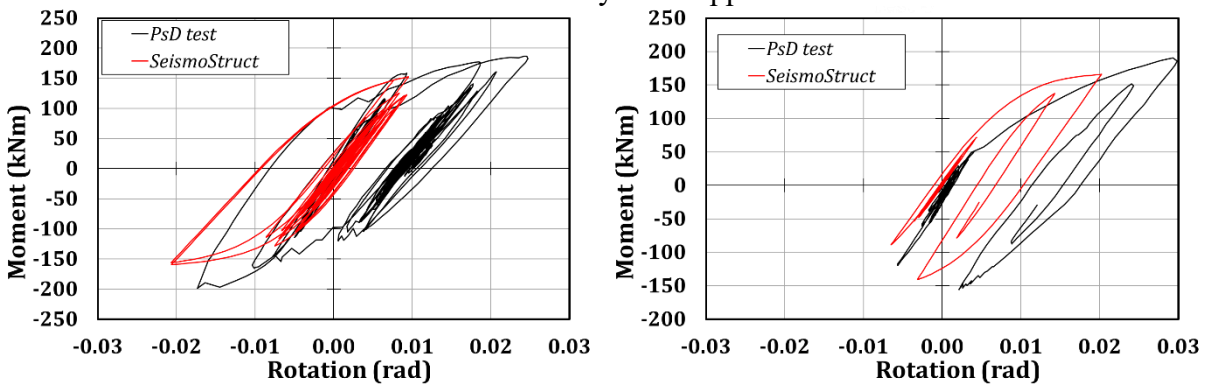

Figure 4.44 – Experimental vs numerical results - Hysteretic curves of connection 1A: Test 1 (left) and Test 2 (right)

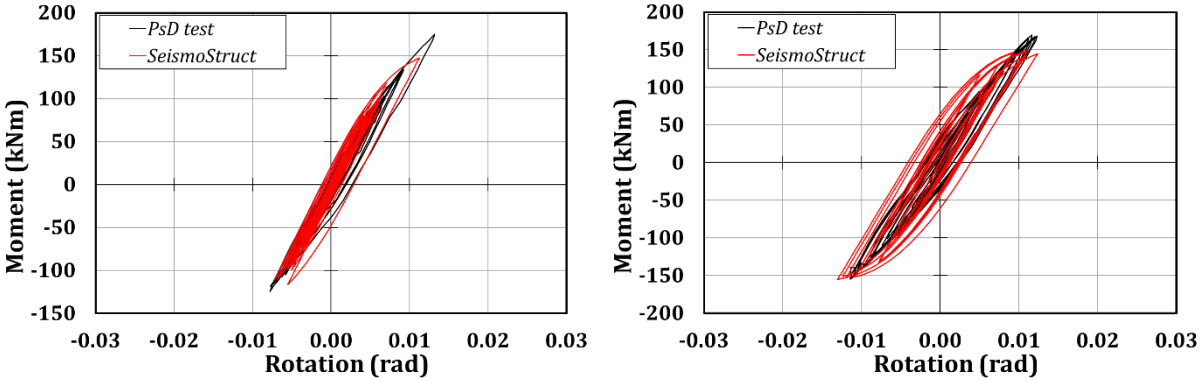

Figure 4.45 – Experimental vs numerical results - Hysteretic curves of connection 1A: Test 3 (left) and Test 4 (right)

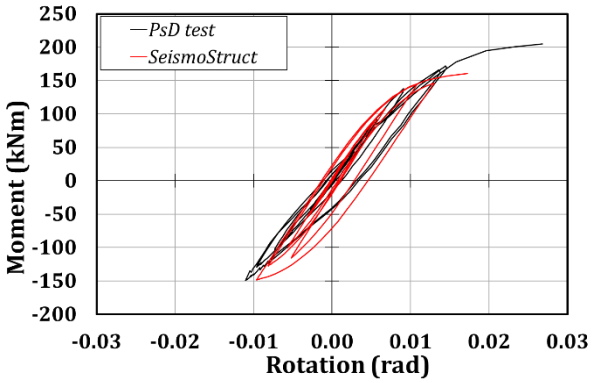

Figure 4.46 – Experimental vs numerical results - Hysteretic curves of connection 1A: Test 5

This comparison is reported in Table 4.16 for the five tests about the response of connection 1A of MRF-1. The results show that the peak rotations are predicted in many cases with low accuracy, while the peak bending moments are predicted more accurately. Consequently, even though the spring model adopted to model the moment-rotation response of the RBS connections was calibrated starting from the results of an experimental test and employing an accurate calibration procedure, the main problem of the phenomenological models is inborn in the model typology.
In fact, while in theory, such models are based on several parameters that can accurately reproduce the experimental response of any connection type, such parameters are not directly linked to the mechanical response of the modelled element. This aspect may lead to a discrepancy between the real and the simulated behaviour, which can also be significant in many cases. For example, the comparisons reported in Table 4.16 show that in terms of peak rotations, the errors vary from a minimum of 1% to a maximum of 62%, while in terms of peak moments, the errors vary from a minimum of 0% to a maximum of 31%. The range variability prediction of the peak rotations is 1% and 62% because the parameters for modelling the cyclic behaviour of the joints are calibrated against the experimental results coming from the testing of beam-to-column sub-assemblies subjected to conventional loading protocols, which can be significantly different from those occurring under earthquakes and, even more, under the occurrence of repeated earthquakes like the sequence considered in this work. The obtained results confirm the role of paramount importance played by the loading history, as already pointed out in previous works [19]. However, it is also important to point out that the scatters significantly reduce when global response parameters, such as inter-storey displacements, are concerned. This occurrence is because local inaccuracies are averaged as soon as the number of dissipative zones increases. In the case of

structures having a more significant number of storeys and bays, a further improvement in the prediction of global response parameters is expected because of the high number of dissipative zones.

Table 4.16 – Comparisons referred to connection 1A

Test	Rotation (rad)		Moment (kNm)		Energy (kNm)
	Maximum	Minimum	Maximum	Minimum	
1 – PsD	17	-25	199	-187	10
1 – Sim.	21	-10	160	-152	7
1 – Err. (%)	19	62	-20	18	-27
2 – PsD	6	-30	156	-190	4
2 – Sim.	6	-20	141	-166	3
2 – Err. (%)	15	32	-10	13	-28
3 – PsD	8	-13	124	-175	3
3 – Sim.	7	-11	117	-147	2
3 – Err. (%)	-7	15	-6	16	-18
4 – PsD	11	-12	155	-169	7
4 – Sim.	13	-12	155	-149	9
4 – Err. (%)	14	-1	0	12	40
5 – PsD	11	-27	149	-205	6
5 – Sim.	10	-17	148	-161	4
5 – Err. (%)	-13	36	0	22	-28

From the energy dissipation point of view, the scatters are also significant in many cases, as shown in Table 4.16. The trend of the energy dissipated in the RBS connections predicted by the numerical model is similar to the actual one derived from the test results. Nevertheless, a discrepancy concerning the value of the total energy dissipated occurs; the corresponding scatters range from 18% to 40%.

4.7 2nd experimental campaign: structure equipped with FREEDAM connections

4.7.1 Experimental results

4.7.1.1 Imperial Valley (PGA = 1.10g)

The first test consisted of applying the ground acceleration recorded by the station located at Imperial Valley (USA) in 1979. The same peak ground acceleration of the first experimental campaign was applied. Unfortunately, because of technical problems that occurred with the external transducers during this test, no data about the local response of the connections are available. Therefore, it is only possible to discuss the floor displacements and the forces recorded by the actuators as depicted in Figure 4.47.

The displacements at the first and second floors achieved peak values equal to 73 and 104 mm, respectively, and the maximum base shear was equal to 537 kN. Therefore, it is possible to observe that the peak floor displacements and the peak reaction forces recorded by the actuators occurred at the same instants. This occurrence was expected because the structure is regular, characterized by the prominence of the first vibration mode. Furthermore, since the analysed FREEDAM connections are not endowed with components able to ensure the self-centring capability, it is reasonable that residual displacements are observed at the end of the test. In particular, the residual

drifts are about 15 mm and 29 mm at the first and second level, respectively, which correspond to inter-storey drifts of 0.63% at Level 1 and 0.58% at Level 2 (Figure 4.48). Therefore, it is possible to see that these values exceed the permissible residual deformation equal to 0.5%, suggested in [20].

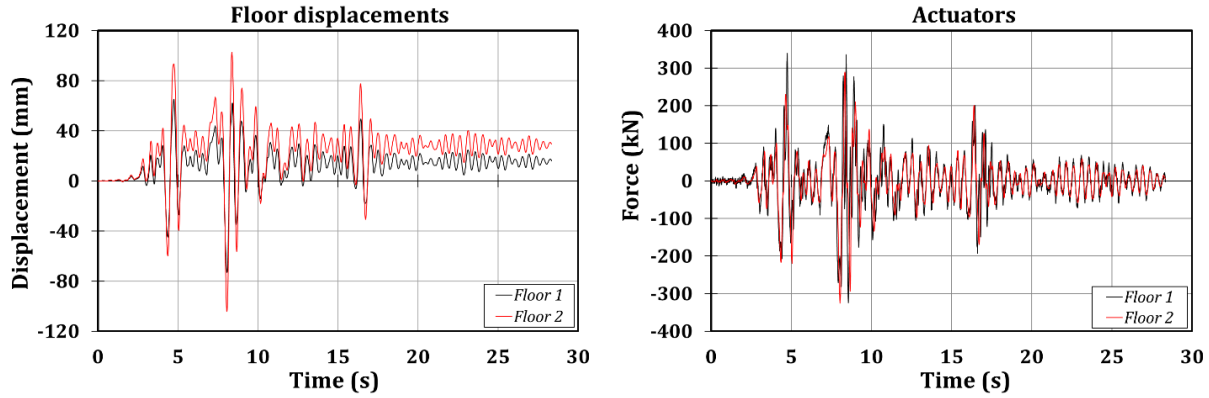

Figure 4.47 – Test 1: floor displacements (left) and reaction forces (right)

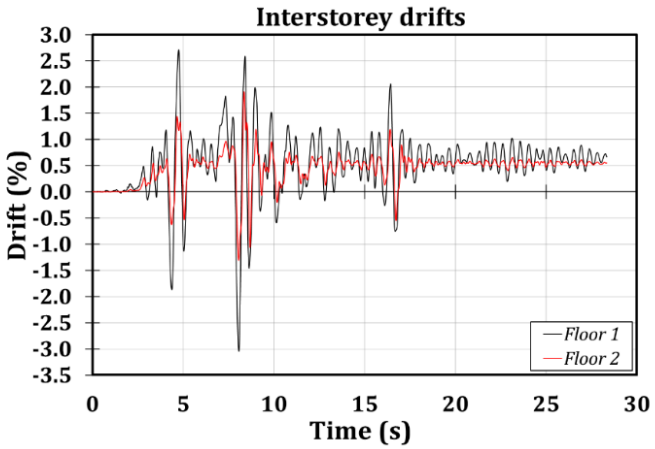

Figure 4.48 – Test 1: interstorey drifts

During this test, some of the friction dampers were subjected to slippage. In Table 4.17, it is possible to note that the maximum inter-storey drifts achieved 3% and 1.8% at the first and second floors, well beyond the nominal elastic limit of the structure equal to about the 1% as assumed in the design phase.

Table 4.17 – Main results related to Test 1

Imperial Valley 1.1g			Test 1
Maximum base shear (kN)	Pull		-537
	Push		477
Peak first floor displacement (mm)	Pull		-73
	Push		65
Peak roof displacement (mm)	Pull		-104
	Push		103
Maximum inter-storey drift (%)	Pull	Level 1	-3.0
		Level 2	-1.3
	Push	Level 1	2.7
		Level 2	1.8

4.7.1.2 Spitak (PGA = 0.80g)

The mock-up building has been subjected to the Spitak earthquake. In this case, the experimental data referred to the behaviour exhibited by the connections are available. It is worth highlighting that this accelerogram has a relevant feature: its time history is characterized by only one peak of significant amplitude, while many significant peaks characterize all the other accelerograms. This aspect is reflected in the results: the mock-up experienced only one main excursion in the plastic range, as is evident in Figure 4.49, where the results in terms of floor displacements and actuators' reaction forces have been reported.

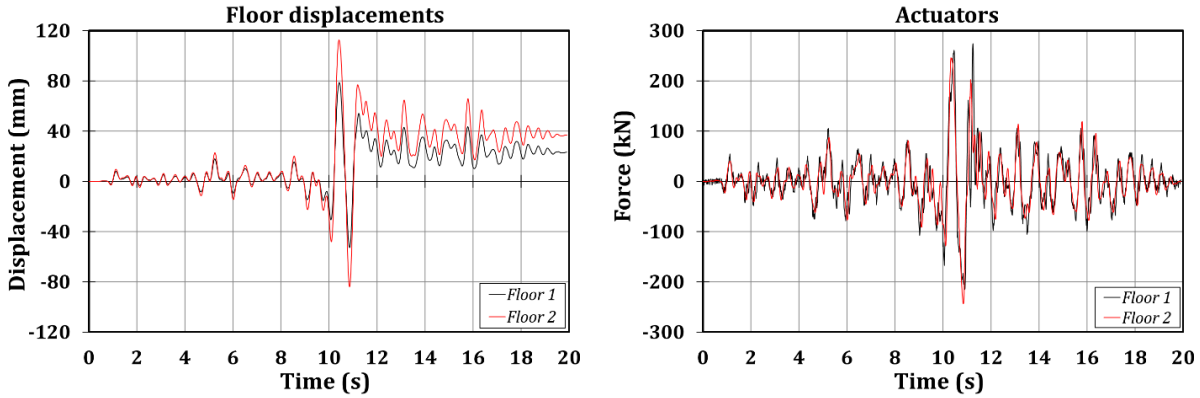

Figure 4.49 – Test 2: floor displacements (left) and reaction forces (right)

In Table 4.18, a summary of the overall seismic response of the structure is reported. Even though a maximum reduction of about 15% in terms of base shear has been observed, in comparison with

Test 1, it is possible to mention a slightly larger peak roof displacement (112 mm *vs* 104 mm) and a maximum inter-storey drift equal to 3.3% at the first level (Figure 4.50).

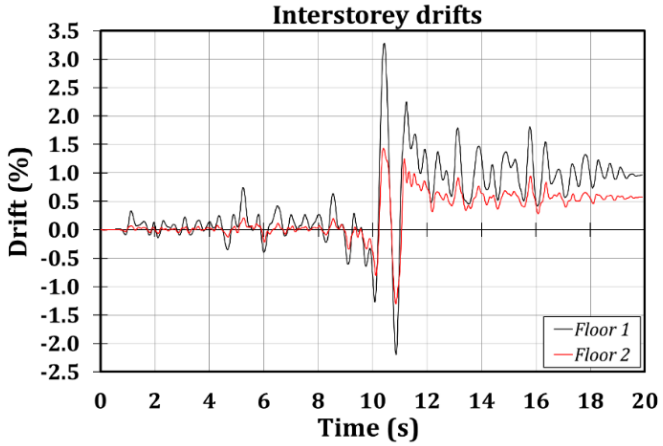

Figure 4.50 – Test 2: interstorey drifts

Table 4.18 – Main results related to Test 2

Spitak 0.8g			Test 2
Maximum base shear (kN)	Pull		-447
	Push		470
Peak first floor displacement (mm)	Pull		-53
	Push		79
Peak roof displacement (mm)	Pull		-84
	Push		112
Maximum inter-storey drift (%)	Pull	Level 1	-2.2
		Level 2	-1.3
	Push	Level 1	3.3
		Level 2	1.4

Moreover, the maximum inter-storey drifts are very low at the second level. However, higher residual inter-storey drifts were observed at the end of this test: 0.96% and 0.57% at the first and second floors, respectively. The reason for such higher residual drift is due to the activation of the friction devices occurring only around the instant of the peak of the accelerogram: the friction pads slipped mainly in one direction, leaving, in such a way, large residual floor displacements.

The local response in terms of hysteretic moment-rotation curves is reported in Figure 4.51. From this figure, it is possible to observe that wide and stable hysteretic rectangular-shaped moment-rotation curves were obtained, as expected. Nevertheless, it is possible to remark the asymmetric behaviour of the connections since the absolute values of the maximum and minimum bending moments are around 80 kNm and 120 kNm, respectively. This occurrence agrees with the asymmetry of the connection's behaviour already pointed out by the experimental tests on simple beam-to-column joint sub-assemblages [21]. Considering that the Spitak accelerogram is characterized by one prominent peak, it was expected, and it has been experimentally confirmed, that the friction devices exhibit only one slipping excursion corresponding to the achievement of the PGA. The maximum rotation experienced by the connections was achieved by connection 1A, and its value is about 17 mrad. The other connections achieved reduced rotations. In particular, as

expected, the connection rotations achieved values of about 0.007 and 0.002 rad at the second level.

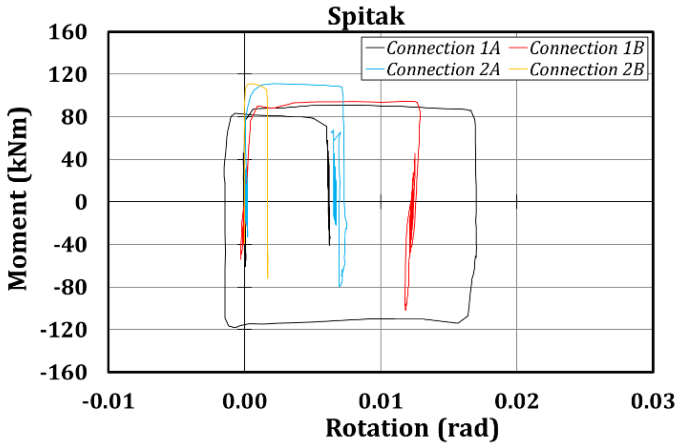

Figure 4.51 – Test 2: moment-rotation curves related to the FREEDAM connections belonging to MRF-1

The deformed configuration of a connection belonging to the first floor is shown in Figure 4.52. It is possible to observe that the friction pad is not located at the end of the test at the initial position (highlighted with red dotted lines). Consequently, the friction pad is still in the deformed configuration achieved at the peak instant. Except for the friction pads and the yielding of the first-floor column bases, no structural damages have been observed in other structural elements.

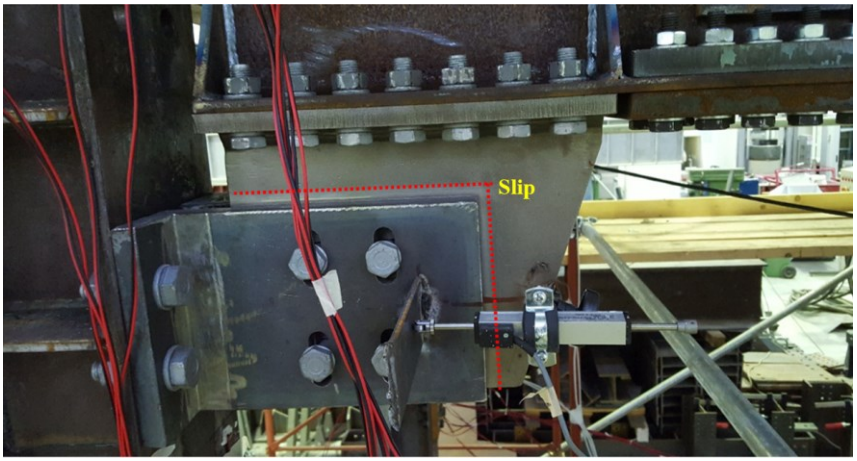

Figure 4.52 – FREEDAM connection (Test 2)

4.7.1.3 Artificial record (PGA = 0.50g)

The third accelerogram has been artificially created by the SIMQKE tool to match the adopted design spectrum. This choice aimed to investigate the effects of an earthquake with many acceleration peaks. In this case, a peak ground acceleration (PGA) equal to 0.50g has been chosen. The MRFs remained almost elastic with this accelerogram without additional residual displacements (Figure 4.53, Figure 4.54 and Table 4.19). For both the floors, the residual inter-storey drifts are equal to 0.1%. The local measurements in this test also suggest a low plastic engagement of the structure as only connection 1A was slightly engaged in the plastic range, experiencing a rotation of only 4 mrad (Figure 4.55).

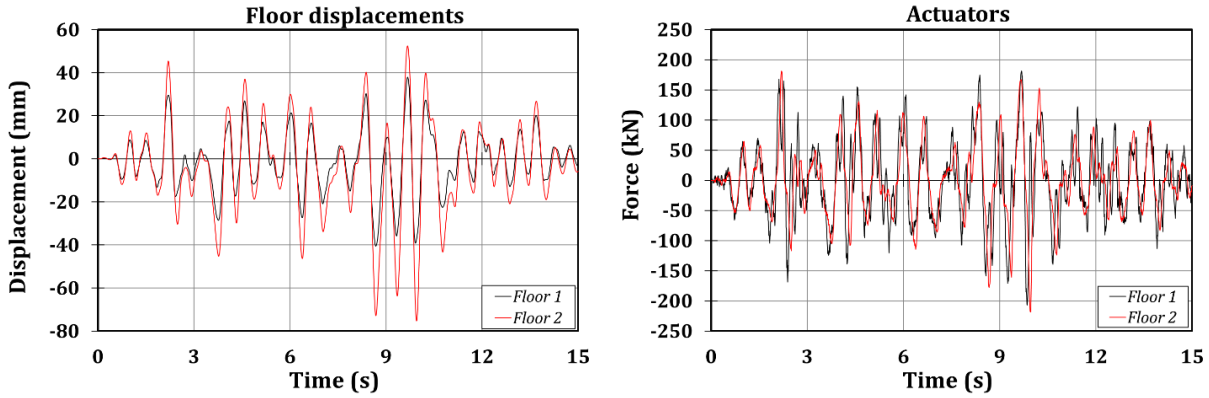

Figure 4.53 – Test 3: floor displacements (left) and reaction forces (right)

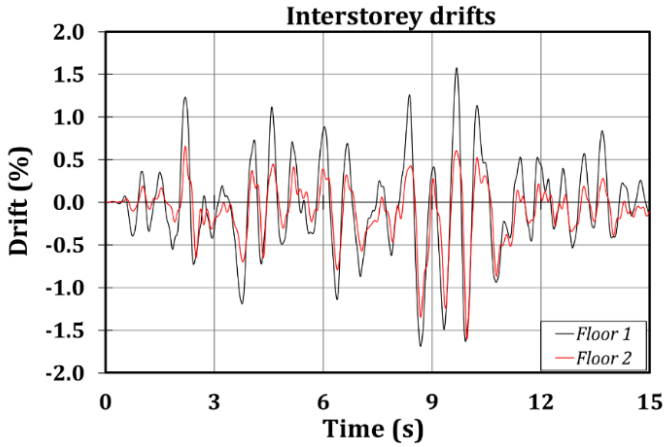

Figure 4.54 – Test 3: interstorey drifts

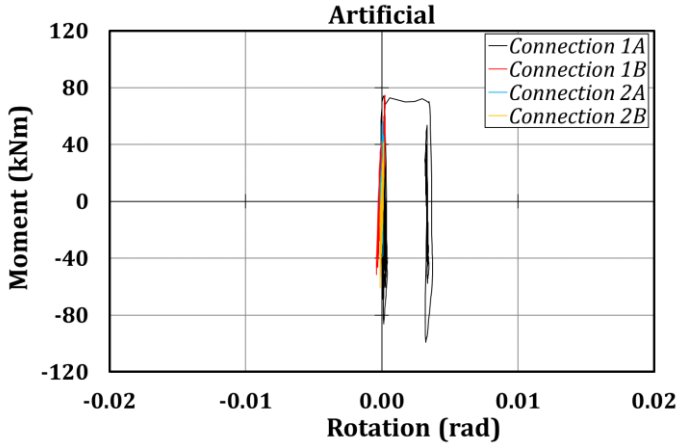

Figure 4.55 – Test 3: Test 3: moment-rotation curves related to FREEDAM connections belonging to MRF-1

Table 4.19 – Main results related to Test 3

Artificial 0.5g			Test 3
Maximum base shear (kN)	Pull		-272
	Push		347
Peak first floor displacement (mm)	Pull		-41
	Push		38
Peak roof displacement (mm)	Pull		-75
	Push		52
Maximum inter-storey drift (%)	Pull	Level 1	-1.7
		Level 2	-1.6
	Push	Level 1	1.6
		Level 2	0.6

4.7.1.4 Santa Barbara (PGA = 0.80g)

The fourth test consisted in applying the ground acceleration recorded by the station located in Santa Barbara (USA) in 1978. Even though peaks with relevant amplitude characterize the time history, the adopted peak ground acceleration (0.80g) enabled only a moderate sliding of the friction devices. The overall behaviour is not far from the features highlighted for Test 3: the floor displacements did not exceed 60 and 90 mm at the first and the second floor, respectively, inducing a maximum inter-storey drift equal to 2.3% at the first level (Figure 4.56, Figure 4.57, Table 4.20). Residual drifts of 0.17% and 0.01% have been observed on the first and second floors. Similarly to Test 3, only connection 1A was activated. Its maximum rotation was equal to 4.6 mrad (Figure 4.58).

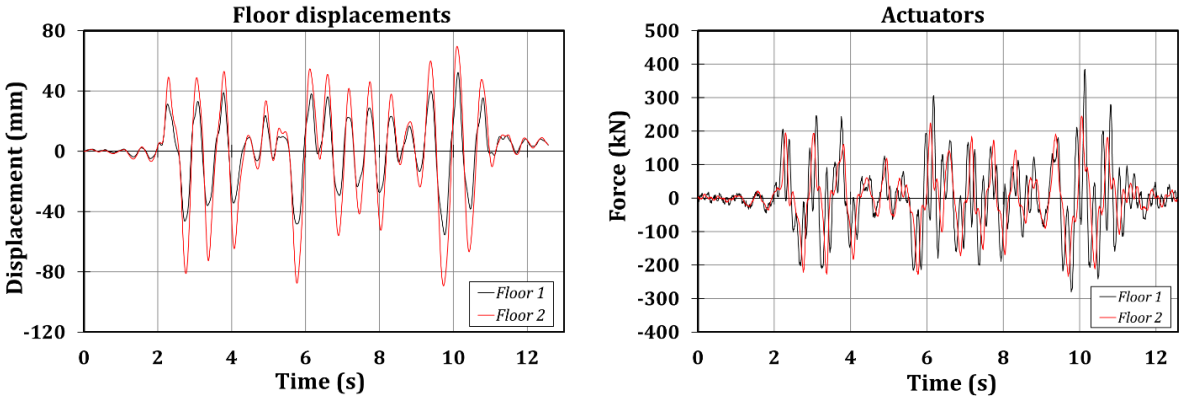

Figure 4.56 – Test 4: floor displacements (left) and reaction forces (right)

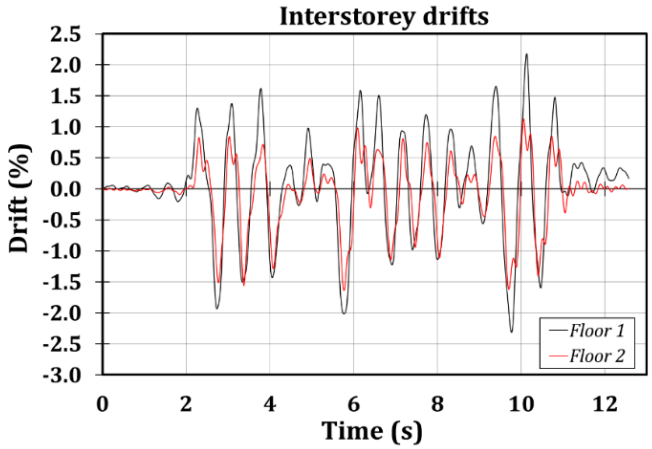

Figure 4.57 – Test 4: interstorey drifts

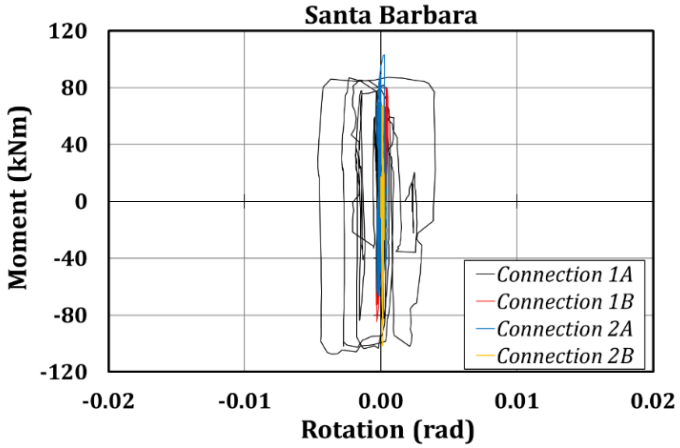

Figure 4.58 – Test 4: moment-rotation curves related to FREEDAM connections belonging to MRF-1

Table 4.20 – Main results related to Test 4

Santa Barbara 0.8g			Test 4
Maximum base shear (kN)	Pull		-388
	Push		483
Peak first floor displacement (mm)	Pull		-56
	Push		52
Peak roof displacement (mm)	Pull		-89
	Push		70
Maximum inter-storey drift (%)	Pull	Level 1	-2.3
		Level 2	-1.6
	Push	Level 1	2.2
		Level 2	1.1

4.7.1.5 Coalinga (PGA = 0.80g)

During the last test, a higher energy dissipation occurred. This test has not been completed due to a technical problem (loss of control), giving rise to significant damage to an element connecting the mock-up and the actuator located on the first floor. This drawback happened at 8.58 seconds. In Figure 4.59, the displacement histories and the forces experienced by the actuators during Test 5 are reported. The maximum floor displacement (Table 4.21) at the roof level is equal to 112 mm (the same value experienced by the structure in Test 2), inducing a maximum interstorey drift of 3% (Figure 4.60). The hysteretic curves (Figure 4.61) are characterized by asymmetry in terms of positive and negative bending moments. Moreover, it is possible to observe that the peak moments decreased as the number of cycles increased because of the reduction of the tightening torque of pre-loadable high-strength bolts caused by the consumption of friction pads.

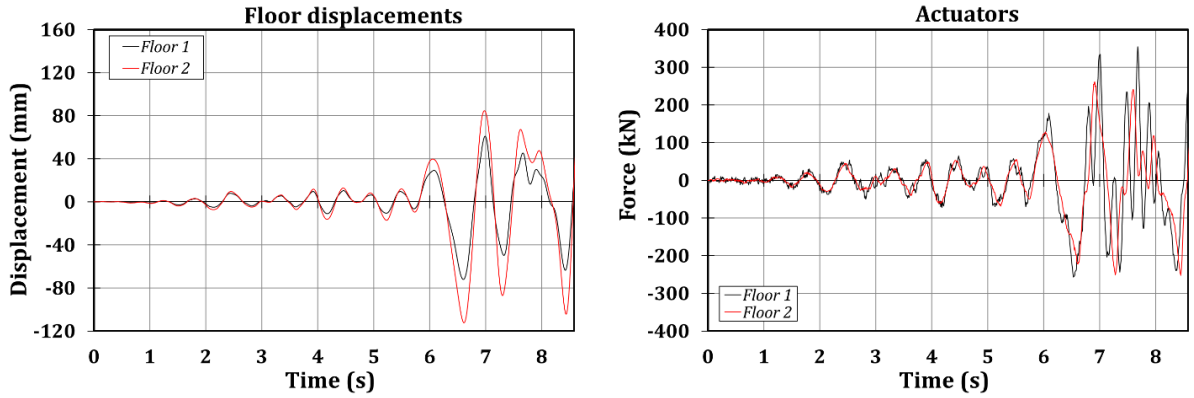

Figure 4.59 – Test 5: floor displacements (left) and reaction forces (right)

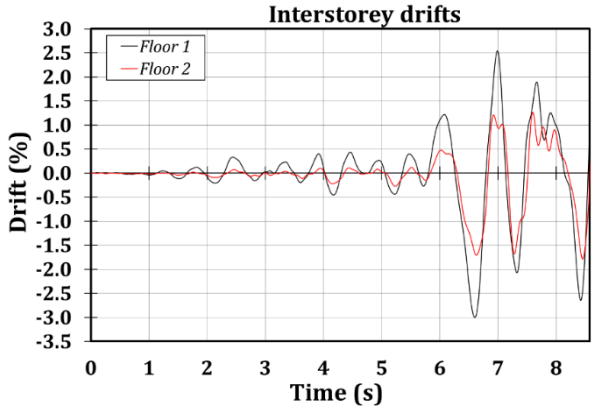

Figure 4.60 – Test 5: interstorey drifts

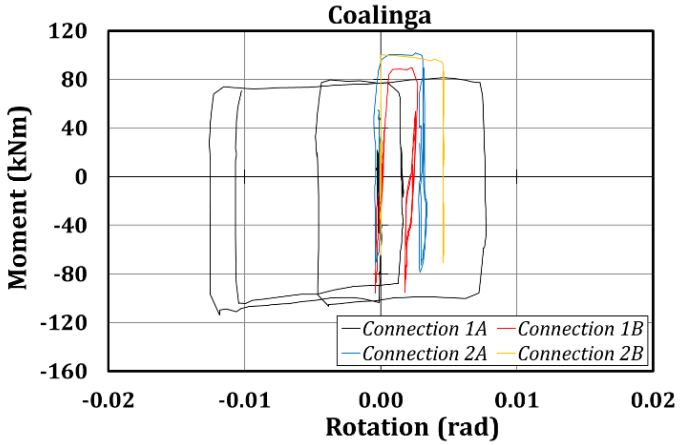

Figure 4.61 – Test 5: moment-rotation curves related to FREEDAM connections belonging to MRF-1

Table 4.21 – Main results related to Test 5

Coalinga 0.8g (partial)			Test 5
Maximum base shear (kN)	Pull		-439
	Push		495
Peak first floor displacement (mm)	Pull		-72
	Push		61
Peak roof displacement (mm)	Pull		-112
	Push		85
Maximum inter-storey drift (%)	Pull	Level 1	-3.0
		Level 2	-1.7
	Push	Level 1	2.5
		Level 2	1.2

It is worth highlighting that since the columns have been designed to comply with the buckling and serviceability checks imposed by Eurocode 8, the structure exhibits a noticeable overstrength. This reason justifies the high values of PGAs selected to perform the tests. Furthermore, accounting for the limited displacement and force capacities provided by the actuators, a maximum joints' rotation equal to 17 mrad has been observed.

Finally, it is worth underlining that the beam-to-column joints exhibited no damage (Figure 4.62 and Figure 4.63), confirming the behaviour exhibited by beam-to-column joint sub-assemblies during experimental tests under cyclic loading conditions [21]. They can be referred to as low-damage connections because only minor yielding occurred in the stem of the bolted T-stub close to the centre of rotation. Similar minor yielding occurred in the angles connecting the friction damper to the column flange (Figure 4.62 and Figure 4.63).

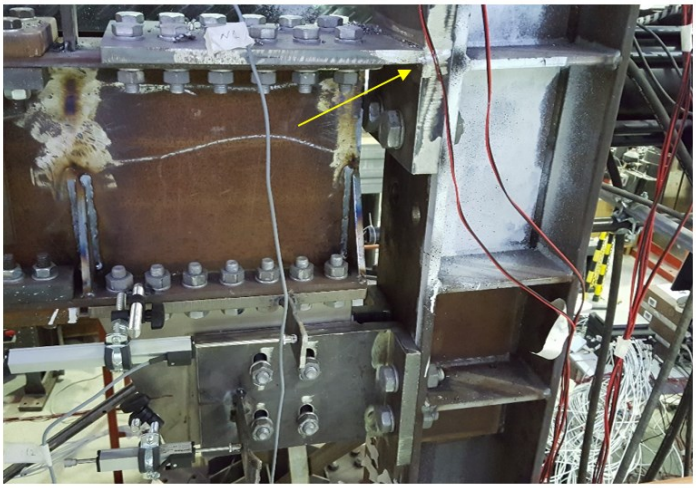

Figure 4.62 – Test 5: Connection 1A at the end of the experimental campaign

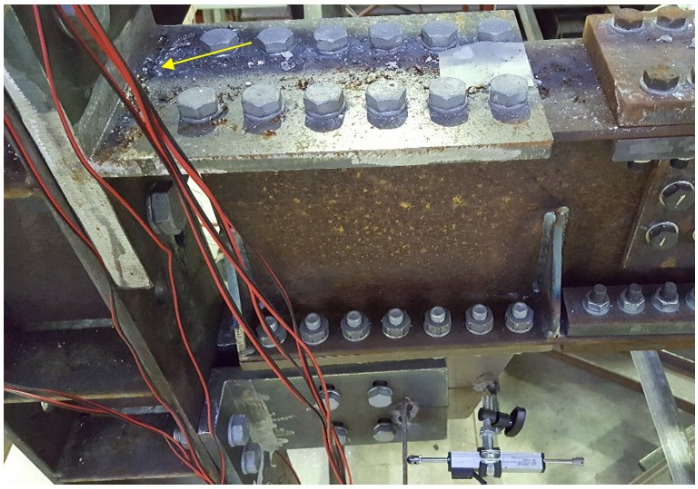

Figure 4.63 – Test 5: Connection 1B at the end of the experimental campaign

Instead, the energy dissipation is concentrated in the friction pads, as is clear also from Figure 4.64, where scratches due to the sliding of the friction pads are highlighted, confirming that the connection slid, as expected.

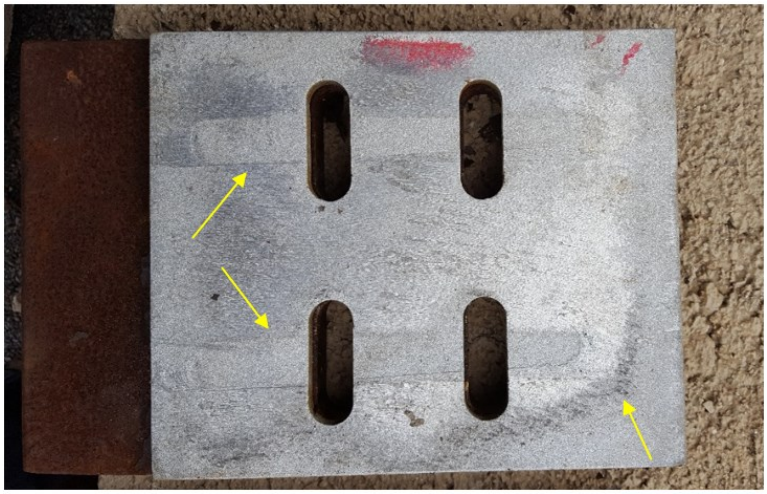

Figure 4.64 – Test 5: Friction pad belonging to connection 1A at the end of the experimental campaign

During the tests, the yielding of the column bases was observed (Figure 4.65). This occurrence could be physically recognized by the yield lines appearing on the surface of the column during the tests.

Figure 4.65 – Test 5: Yielding of the column bases

Conversely, the same building equipped with extended end-plate connection with RBS subjected to the same earthquake sequence exhibited, at the end of the seismic sequence, the failure of the connection because of the fracture of the beam flanges in the reduced beam section zone and, for some joints, because of the fracture of the welds connecting the beam to the end-plate.

4.7.2 FE modelling of the tested frame

A non-linear 2D model of the structure was developed with the software OpenSees [22] (Figure 4.66) to achieve a twofold purpose: 1) the FE model was initially developed to perform blind predictions of the seismic response of the building; 2) the FE results were aimed to check the design of the testing setup and equipment by predicting the reaction forces to be applied and verifying their compatibility with the capacities of the actuation system.

The strategy adopted for the FE modelling has been based on a mixed lumped and distributed plasticity approach. In particular, the beams and the columns have been modelled with inelastic force-based elements (*forceBeamColumn element* in OpenSees) to account for the geometric and material non-linearities with a spread plasticity approach. Each element has been characterized by five integration sections subdivided into at least 120 fibres to ensure a good accuracy for assessing curvatures and internal actions starting from the knowledge of the material properties. In addition, lumped masses have been located 65 mm below the centre of the spans to model the points of application of the inertia forces by the actuators in the testing setup (Figure 4.66).

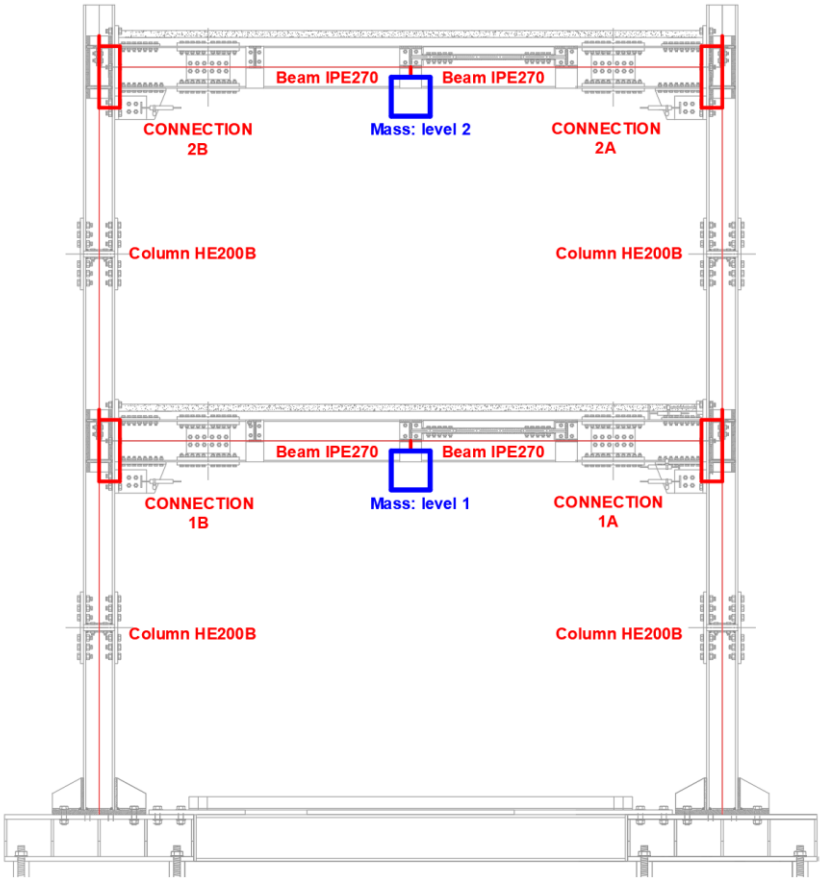

Figure 4.66 – FE model of the structure

Besides aiming to investigate the best modelling of the connections, two different modelling approaches have been conceived.

The first strategy consists of lumping plasticity into a *zeroLength element* located at the beam end, providing the moment-rotation hysteretic response of the joint (Figure 4.67) as reported in [23].

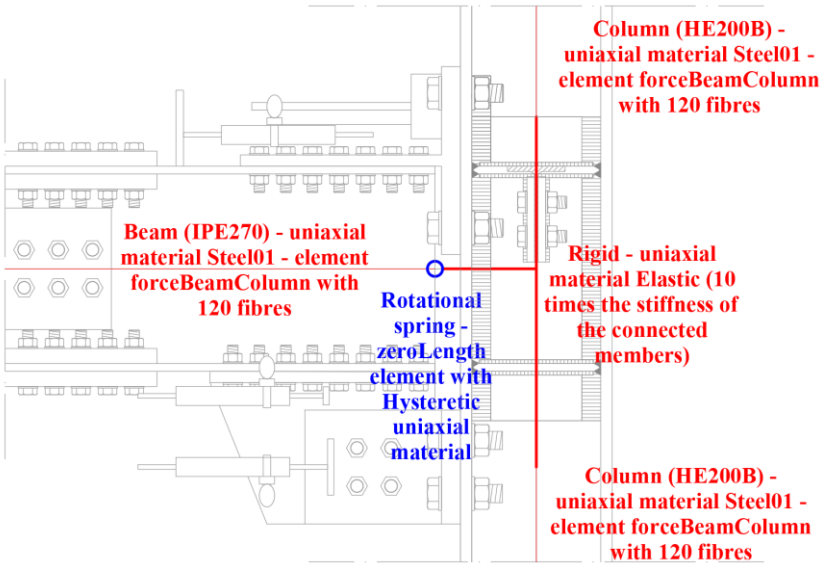

Figure 4.67 – FE model of the beam-to-column connection (initial model)

Such an approach has been adopted for the preliminary blind prediction of the seismic response of the structure [23]. Nevertheless, a new and more refined mechanical modelling of the FREEDAM joints has been performed due to the large scatter. From now on, only this refined and more accurate model is reported (Figure 4.68).

The model includes a hinge located at the level of the upper beam flange where the T-stub fixing the centre of rotation is located. Therefore, the model is consistent with the physical location of the centre of rotation. Besides, a *zeroLength element* endowed with a translational inelastic force-displacement law is placed at the centreline of the friction damper (Figure 4.68).

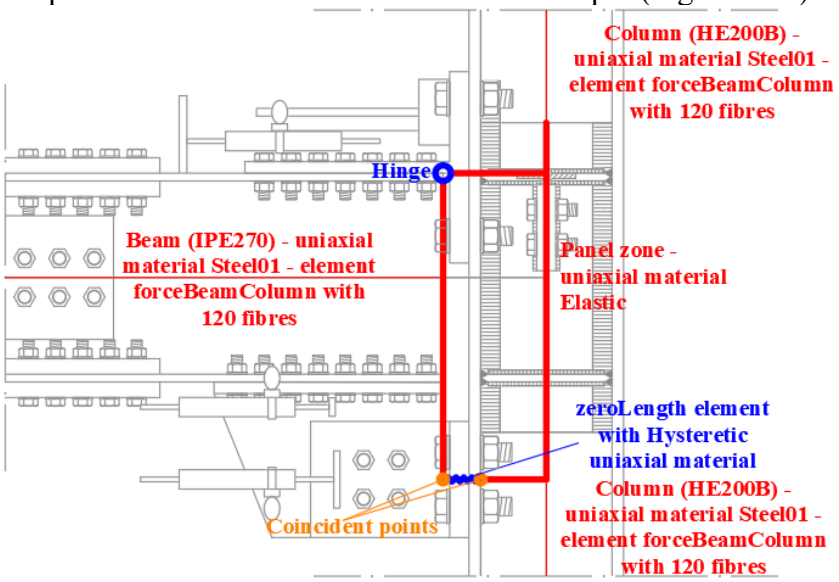

Figure 4.68 – FE model of the beam-to-column connection (refined model)

In particular, the force-displacement law of the translational spring has been provided using the *uniaxialmaterial Hysteretic* element, whose input parameters are depicted in Figure 4.69; these parameters include the coordinates of six points to model the non-linear behaviour of the connection. Moreover, it is possible to model also an unloading stiffness with a ductility-dependent

degradation according to a factor given by $\mu^{-\beta}$. The connection is assumed to be rigid according to Eurocode 3 part 1.8 [14]; therefore, the initial stiffness has been assumed equal to 25 times the flexural stiffness of the beam.
The hysteretic model of OpenSees has been chosen to simulate the rigid-plastic behaviour associated with the sliding of the friction pads. However, this model is not conceived to account for the local deformation demands of the connected members. Instead, beams and columns' possible local deformations are modelled through inelastic force-based elements.

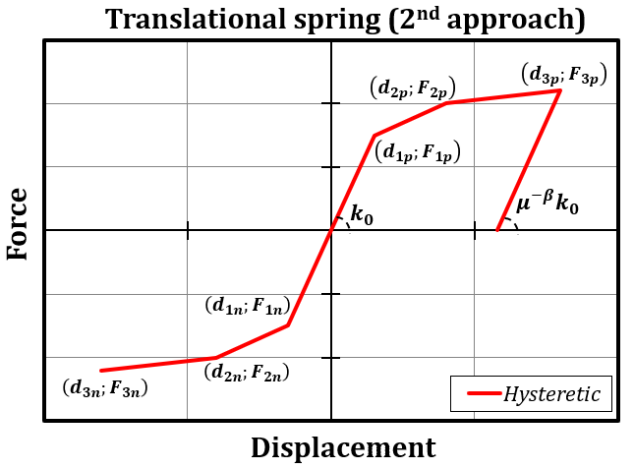

Figure 4.69 – Uniaxial Hysteretic material: parameters

A symmetric trilinear force-displacement law has been adopted for the analysed case, assuming the yielding force equal to the sliding force of the friction devices ($F_{cf,Sd} = 234\ kN$), and a negligible post-elastic hardening. The displacement at which yield occurs has been fixed so that the two proposed modelling approaches of the low-damage connections have the same initial flexural stiffness. For clarity, the coordinates of the points have been reported in Table 4.22, while the β factor has been fixed equal to zero so that the degrading unloading stiffness is equal to the initial stiffness since the expected behaviour of the connection is rigid-plastic.
The friction connection is conceived to concentrate the energy dissipation in the friction devices, while all the other nodal components have been designed to have an elastic behaviour. Consequently, the panel zone has not been explicitly modelled as given in Figure 4.68.

Table 4.22 – Uniaxial Hysteretic material: parameters

Point	d (mm)	F (kN)
3n	-170.00	-236.00
2n	-10.00	-235.00
1n	-0.02	-234.00
	0.00	0.00
1p	0.02	234.00
2p	10.00	235.00
3p	170.00	236.00

Accelerations at the structure's base have been applied to assign the input ground motion. The adopted time-history analyses are characterized by a time step equal to 0.01 s. The equation of motion has been solved using the Newmark algorithm setting a damping value equal to 1% in all the tests, with a Rayleigh approach as done during the pseudo-dynamic testing. As better described

in the next paragraph, this modelling approach allows predicting the global structural response rather accurately, while the local response of the connections is predicted with a lower level of accuracy.
Because of technical limits with the equipment available in the laboratory, it has not been possible to account for the effect of the gravity loads and gravity frames in the experimental work. For this reason, to ensure consistency between the numerical and physical outcomes, these loads have not been modelled in the OpenSees software. Furthermore, as already specified, the masses are numerically simulated, and for such a reason, the adopted approach accounts consistently for the hypothesized distribution of the masses.
Constraints among the nodes intersecting the connections have been applied to simulate the rigid floor diaphragms.

4.7.3 Experimental versus numerical results

This section is devoted to the comparison between the experimental and numerical results. Primarily, it is possible to highlight that the numerical model can predict the overall building seismic response with a rather satisfactory accuracy since the scatters in terms of peak floor displacements and base shear are lower than 25%, as is clear in Table 4.23, Figure 4.70 and Figure 4.71. Moreover, the displacements of the time histories are in phase, confirming the proper prediction of the natural vibration period of the structure.

Table 4.23 – Experimental versus numerical comparison of actuators' forces and floor displacements (PsD tests vs OpenSees)

Test	Base shear (kN)	Peak floor displacement (mm)	
		(L-1)	(L-2)
1 – PsD	537	73	104
1 - OS	480	58	119
1 - Err. (%)	**-11**	**-21**	**14**
2 - PsD	483	79	112
2 - OS	448	59	133
2 - Err. (%)	**-7**	**-25**	**18**
3 - PsD	381	41	75
3 - OS	443	36	92
3 - Err. (%)	**16**	**-12**	**22**
4 - PsD	502	56	89
4 - OS	437	43	103
4 - Err. (%)	**-13**	**-23**	**15**
5 - PsD	499	72	112
5 - OS	494	58	126
5 - Err. (%)	**-1**	**-20**	**12**

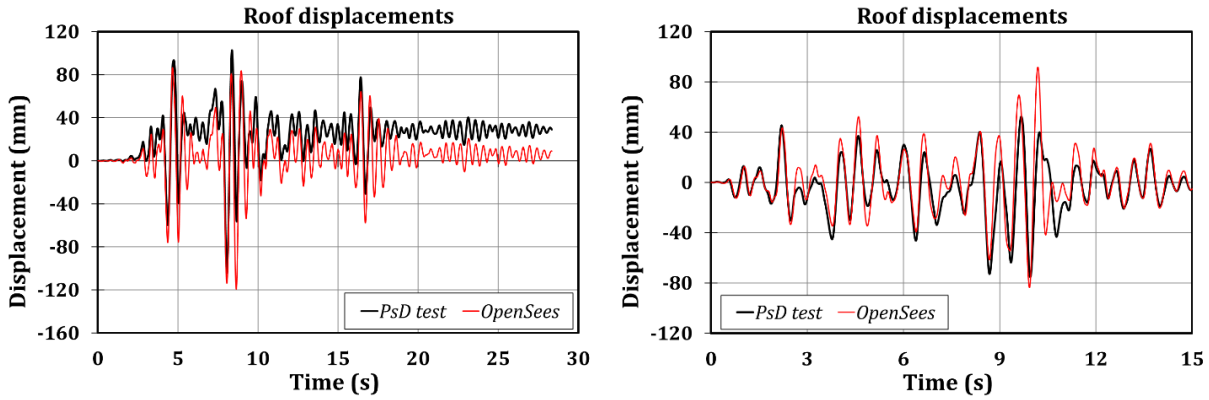

Figure 4.70 – Roof displacements: Test 1 (left) and Test 3 (right)

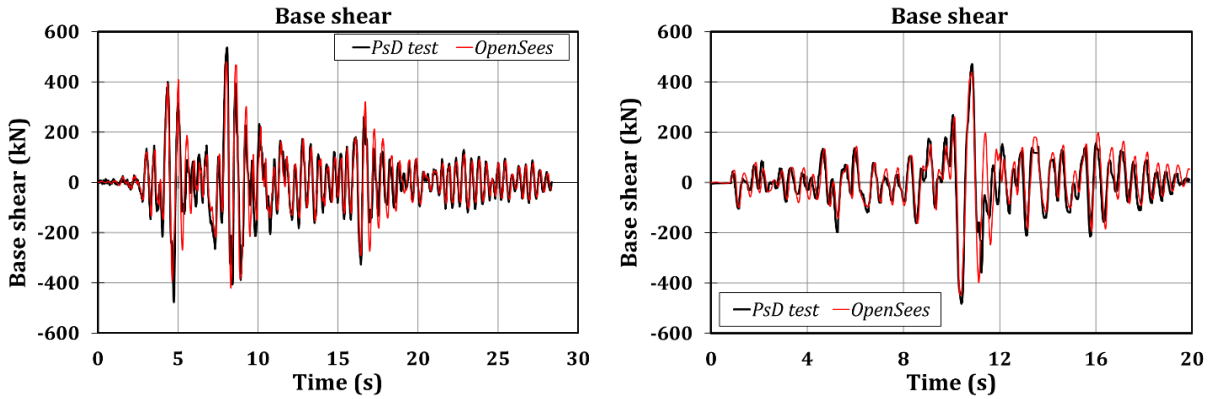

Figure 4.71 – Base shear: Test 2

On the contrary, the local behaviour of the friction devices is predicted with some approximations. In Table 4.24 and Figure 4.72, the comparison between experimental results and numerical simulations is presented, referring to the bending moments and the rotations experienced by connection 1A. The maximum scatters in bending moments vary between -14 and +28%. It is possible to highlight that the scatters between experimental and numerical results are not negligible, testifying the difficulties in predicting the non-linear seismic response of structures due to many sources of uncertainties. In particular, a relevant influence is undoubtedly due to the random variability of the friction coefficient of the dampers and preloading of the bolts, both affecting the slippage resistance of the friction dampers and the time corresponding to their slippage under the seismic action.

Table 4.24 – Experimental versus numerical comparison of connection 1A (PsD tests vs OpenSees)

Test	Rotation (mrad)	Moment (kNm)		Energy (kNm)
		Negative	Positive	
2 - PsD	17.03	118.36	90.98	4.14
2 - OS	10.52	103.50	103.93	2.15
2 - Err. (%)	**-38**	**-13**	**14**	**-48**
3 - PsD	3.74	99.24	74.11	0.34
3 - OS	0.65	85.63	103.53	0.07
3 - Err. (%)	**-83**	**-14**	**40**	**-81**
4 - PsD	4.61	107.55	87.42	2.64
4 - OS	2.53	103.60	98.49	0.26
4 - Err. (%)	**-45**	**-4**	**13**	**-90**
5 - PsD	12.58	113.82	81.36	5.69
5 - OS	7.42	103.80	103.74	1.98
5 - Err. (%)	**-41**	**-9**	**28**	**-65**

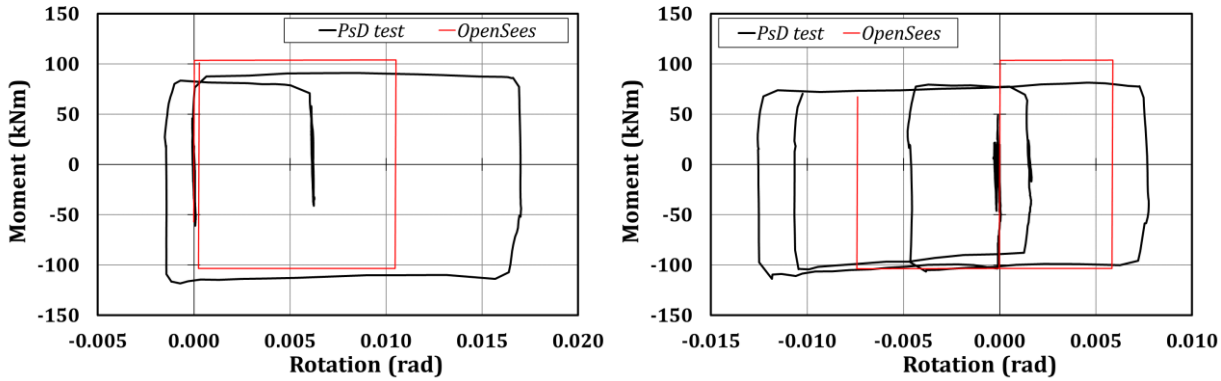

Figure 4.72 – Hysteretic curves (connection 1A): Test 2 (left) and Test 5 (right)

4.8 3rd experimental campaign: structure equipped with X-shaped T-stub connections

4.8.1 Experimental results

4.8.1.1 Imperial Valley (PGA = 1.10g)

The seismic event recorded at Imperial Valley (USA) in 1979 was applied as the first earthquake of the experimental campaign.

The structural floor displacements and the forces recorded by the actuators are reported in Figure 4.73 and Figure 4.74. The peak values of the floor displacements are equal to 68 and 166 mm at the first and the second storey, respectively. Furthermore, consistently with the hypothesis that the structure is regular and the first vibration mode is the prominent one, Figure 4.73 allows highlighting that the peak floor displacements and actuators' forces occur at the same instants.

Residual floor displacements equal to 13 and 28 mm at the first and second storey have been observed. This occurrence is because the proposed detail of beam-to-column connection does not ensure the self-centring capacity of the structure.

Table 4.25 summarizes the main results related to the global behaviour of the structure, while in Figure 4.75, the moment-rotation hysteretic curves of the connections are shown. It is clear that the connections at the first level exhibited a relevant excursion in the plastic range achieving rotations up to 15-20 mrad. Instead, connection 2A remains in the elastic range, while the non-conventional shape of the hysteretic curve related to connection 2B is related to the acquiring data system; however, for clarity, the moment-rotation response is reported.

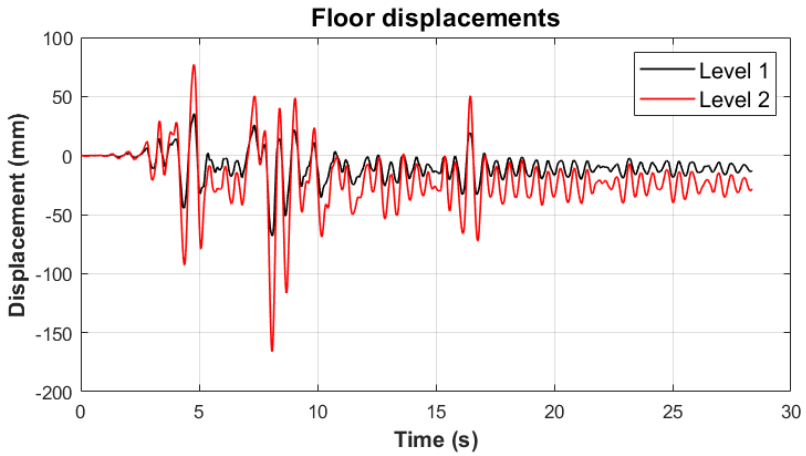

Figure 4.73 – Test 1: floor displacements

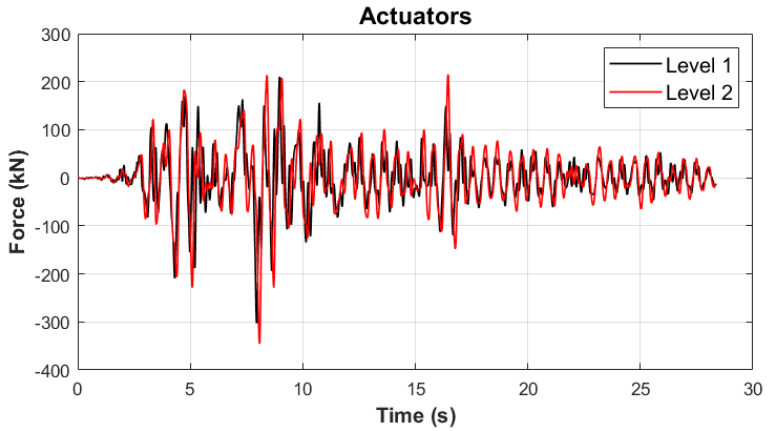

Figure 4.74 – Test 1: reaction forces

Table 4.25 – Main results related to Test 1

Imperial Valley 1.1g			Test 1
Maximum base shear (kN)	Pull		-427
	Push		345
Peak first floor displacement (mm)	Pull		-68
	Push		35
Peak roof displacement (mm)	Pull		-166
	Push		77
Maximum inter-storey drift (%)	Pull	Level 1	-2.8
		Level 2	-4.1
	Push	Level 1	1.5
		Level 2	1.7

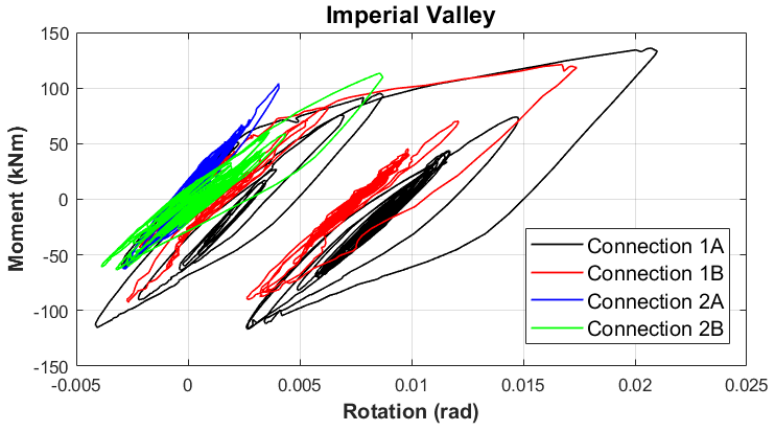

Figure 4.75 – Test 1: moment-rotation curves related to the X-shaped T-stub connections belonging to MRF-1

4.8.1.2 Spitak (PGA = 0.80g)

The Spitak earthquake was applied to the mock-up during the second test. It is characterized by only one peak of significant amplitude. This feature affects the results because the structure exhibits only one main excursion in the plastic range, clearly observing the floor displacements and actuators' forces reported in Figure 4.76 and Figure 4.77.

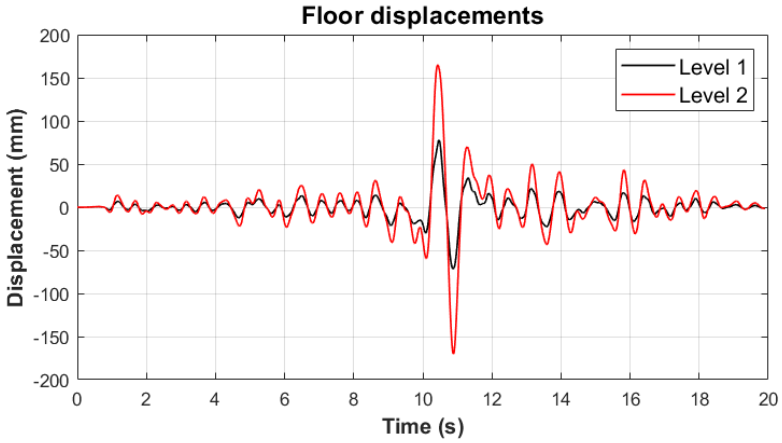

Figure 4.76 – Test 2: floor displacements

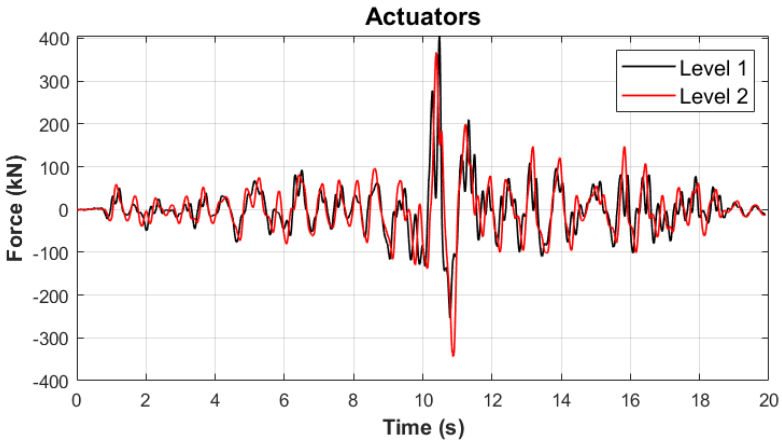

Figure 4.77 – Test 2: reaction forces

Table 4.26 summarizes the main information about the global structural response exhibited by the mock-up during the second test. It is possible to observe that the maximum peak roof displacement is similar to the corresponding parameter recorded during the first test (170 vs 166 mm), inducing a maximum interstorey drift equal to 4%. Instead, it is worth noting that the maximum base shear has increased by about 30% (from 427 kN in Test 1 to 572 kN in Test 2). The moment-rotation hysteretic curves exhibited by the X-shaped T-stub connections are reported in Figure 4.78. Since the seismic input is characterized by one relevant peak, the beam-to-column connections exhibit only one main excursion in the plastic range achieving bending moments higher than 150 kNm and rotations of about 15 mrad. Even in this case, the peak rotations and bending moments are achieved concerning the connections located at the first level, while the joints at the second floor have an elastic behaviour achieving rotations slightly higher than 5 mrad. The hysteretic curves highlight the symmetric behaviour.

Table 4.26 – Main results related to Test 2

Spitak 0.8g			Test 2
Maximum base shear (kN)	Pull		-489
	Push		572
Peak first floor displacement (mm)	Pull		-71
	Push		78
Peak roof displacement (mm)	Pull		-170
	Push		165
Maximum inter-storey drift (%)	Pull	Level 1	-3.0
		Level 2	-4.1
	Push	Level 1	3.2
		Level 2	4.0

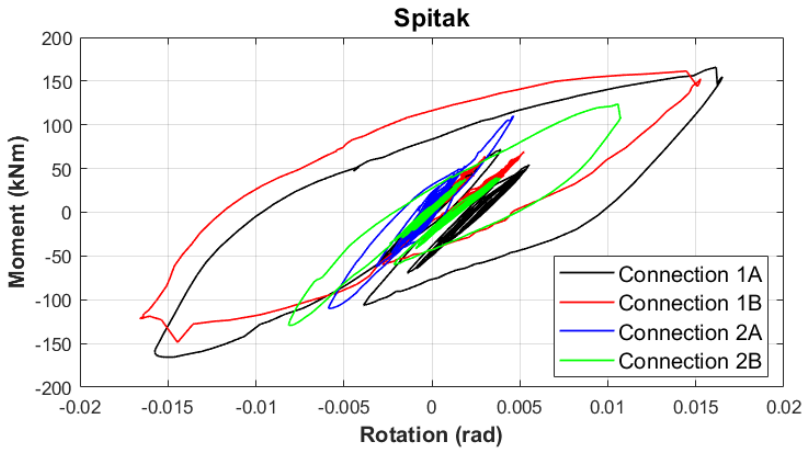

Figure 4.78 – Test 2: moment-rotation curves related to the X-shaped T-stub connections belonging to MRF-1

4.8.1.3 Artificial record (PGA = 0.50g)

The third test has been carried out by adopting an accelerogram which has been artificially created to match the design spectrum thanks to the SIMQKE tool. This choice is justified by assessing the behaviour of the structure when subjected to a seismic input characterized by a high number of peaks. The peak ground acceleration (PGA) selected for this test equals 0.50g.

The main remark related to this test is that the structure had an elastic behaviour, as is evident in Figure 4.79, Figure 4.80 and Table 4.27. In fact, the maximum base shear is about half of the base shear exhibited in the previous tests, and the connections do not show excursion in the plastic range since they achieve bending moments below 100 kNm and rotations of about 6 mrad (Figure 4.81) consistently with the corresponding parameters observed in the previous experimental campaigns.

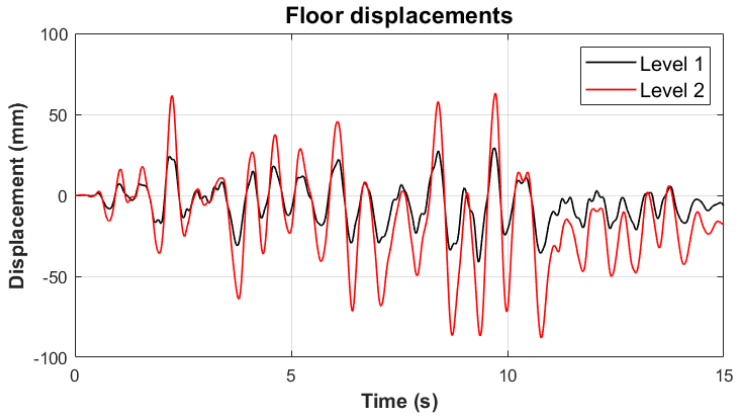

Figure 4.79 – Test 3: floor displacements

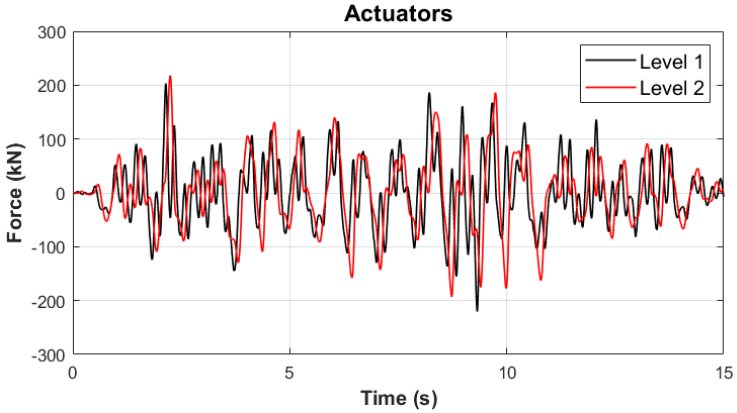

Figure 4.80 – Test 3: reaction forces

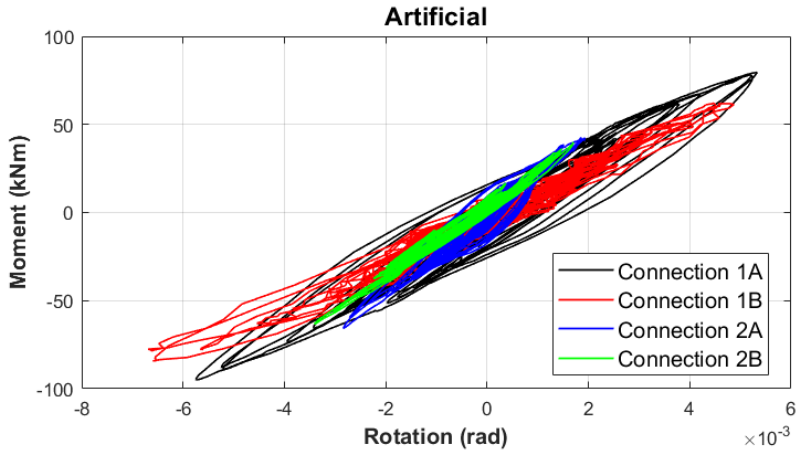

Figure 4.81 – Test 3: moment-rotation curves related to the X-shaped T-stub connections belonging to MRF-1

Table 4.27 – Main results related to Test 3

Artificial 0.5g			Test 3
Maximum base shear (kN)	Pull		-297
	Push		289
Peak first floor displacement (mm)	Pull		-41
	Push		29
Peak roof displacement (mm)	Pull		-88
	Push		63
Maximum inter-storey drift (%)	Pull	Level 1	-1.7
		Level 2	-2.3
	Push	Level 1	1.2
		Level 2	1.6

4.8.1.4 Santa Barbara (PGA = 0.80g)

The seismic event in Santa Barbara (USA) in 1978 was adopted to perform the fourth test. Many peaks with relevant amplitude characterize the accelerogram, but the chosen PGA (equal to 0.80g) does not induce a considerable plasticization. Such an occurrence allows stating that the global structural behaviour is very similar to the features underlined for Test 3: the floor displacements are about 50 and 110 mm at first and the second storey, respectively, making a maximum interstorey drift equal to 3% (Figure 4.82, Figure 4.83 and Table 4.28). At the end of the test, the residual displacements are about 5 and 12 mm at the first and the second floor, respectively, corresponding to a maximum residual drift equal to 0.3%, below the limit [20] for compliance with the serviceability requirements. In Figure 4.84, the moment-rotation hysteretic curves are reported. As in Test 3, all the connections exhibited an elastic behaviour even though reaching slightly higher values of bending moments and rotations values.

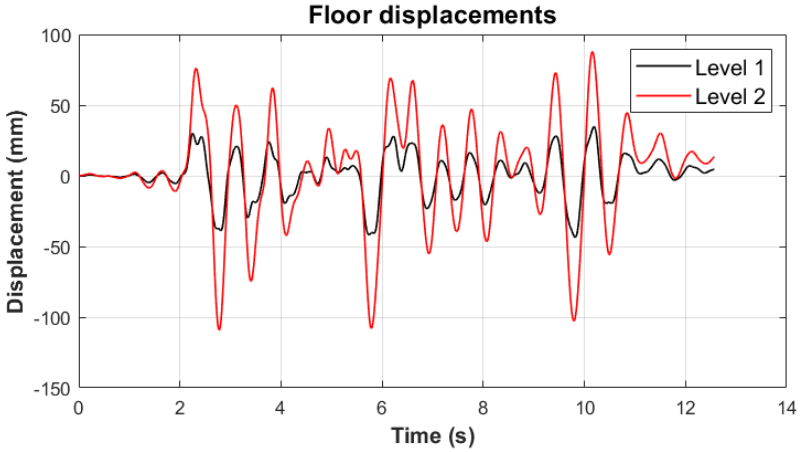

Figure 4.82 – Test 4: floor displacements

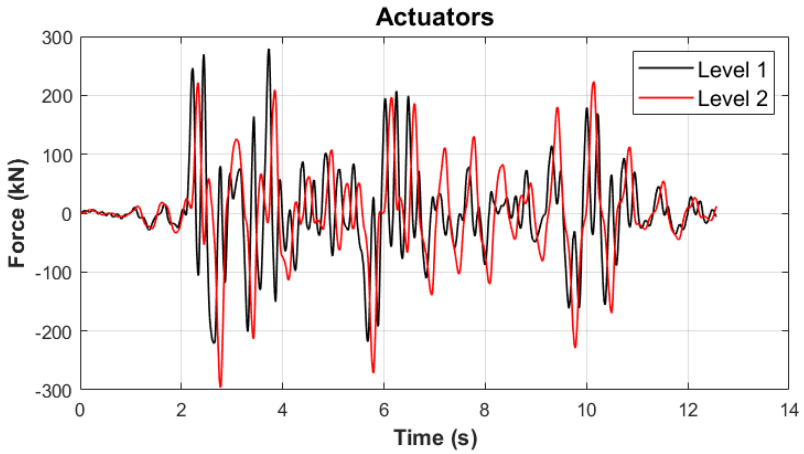

Figure 4.83 – Test 4: reaction forces

Table 4.28 – Main results related to Test 4

Santa Barbara 0.8g			Test 4
Maximum base shear (kN)	Pull		-303
	Push		281
Peak first floor displacement (mm)	Pull		-44
	Push		35
Peak roof displacement (mm)	Pull		-109
	Push		88
Maximum inter-storey drift (%)	Pull	Level 1	-1.8
		Level 2	-3.0
	Push	Level 1	1.5
		Level 2	2.3

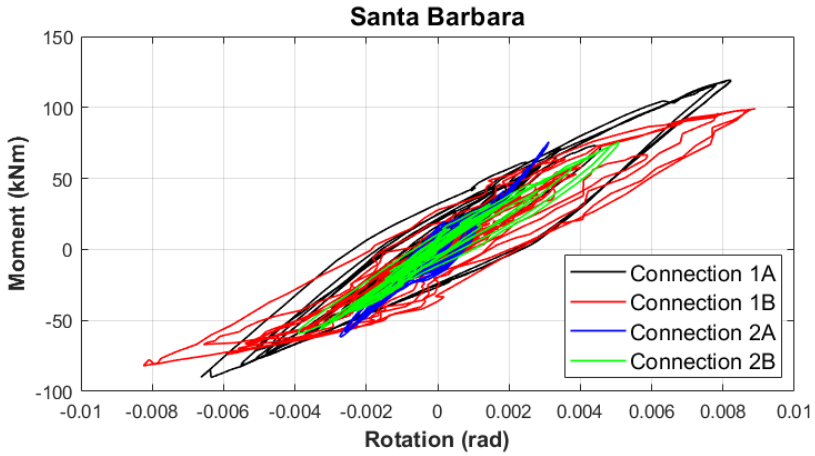

Figure 4.84 – Test 4: moment-rotation curves related to the X-shaped T-stub connections belonging to MRF-1

4.8.1.5 Coalinga (PGA = 0.80g)

The adoption of the Coalinga earthquake represented the last test in both the two previous experimental campaigns with the structure equipped with RBS and FREEDAM connections because of the brittle fracture of the joint and technical issues, respectively. Instead, in the present experimental campaign, this test was performed entirely. In Figure 4.85, Figure 4.86 and Table

4.29, the main results about the overall structural behaviour are reported. It is possible to observe that the very high values of the floor displacements (84 and 187 mm at the first and the second storey, respectively) and the maximum base shear (566 kN) are similar to the corresponding values observed in Test 2. Referring to the moment-rotation hysteretic curves, it is worth noting (Figure 4.87) that many cycles characterized by relevant amplitude have been carried out.

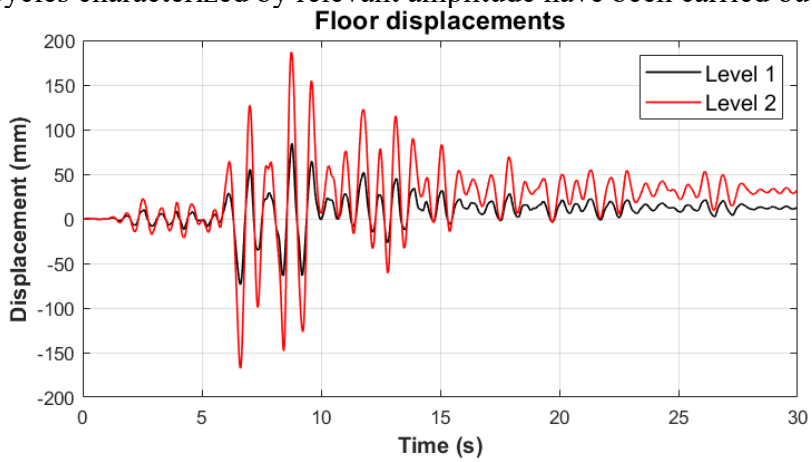

Figure 4.85 – Test 5: floor displacements

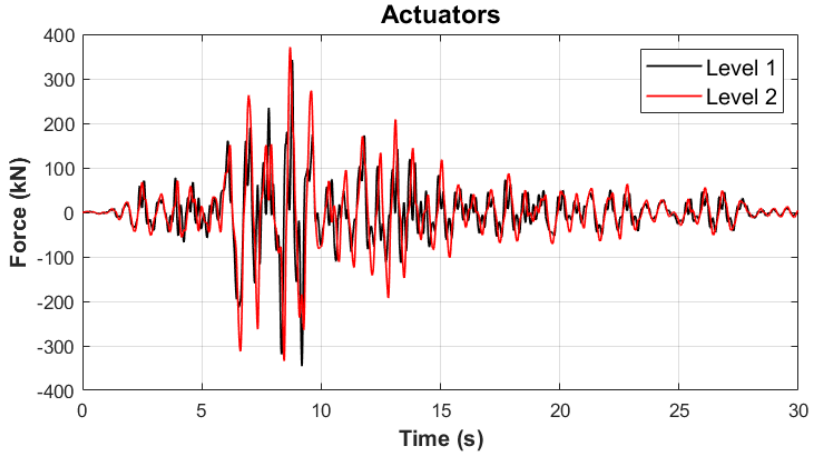

Figure 4.86 – Test 5: reaction forces

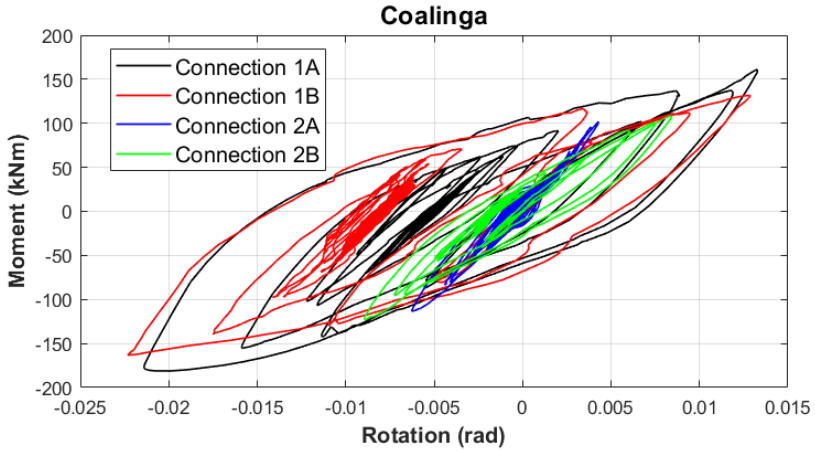

Figure 4.87 – Test 5: moment-rotation curves related to the X-shaped T-stub connections belonging to MRF-1

Table 4.29 – Main results related to Test 5

Coalinga 0.8g			Test 5
Maximum base shear (kN)	Pull		-533
	Push		566
Peak first floor displacement (mm)	Pull		-74
	Push		84
Peak roof displacement (mm)	Pull		-168
	Push		187
Maximum inter-storey drift (%)	Pull	Level 1	-3.1
		Level 2	-3.9
	Push	Level 1	3.5
		Level 2	4.5

4.8.1.6 Kobe (PGA = 1.00g)

The seismic event of Kobe, which occurred in 1995, represents a turning point in the seismic design of steel moment-resisting frames (MRFs). For this reason, Test 6 has been performed, choosing the Kobe earthquake with a peak ground acceleration equal to 1.00 g. As in the previous tests, the main outcomes related to the global structural response of the mock-up are summarized in Table 4.30, Figure 4.88 and Figure 4.89. A maximum roof displacement of 116 mm has been recorded, while the maximum base shear is 356 kN, quite far from the analogous parameter observed in Test 2 and Test 5. This occurrence is because the adopted PGA is far from the required value to induce the structure's more relevant plastic engagement. In fact, at the beginning of each test, the structure is in a deformed configuration characterized by residual displacements; the limited stroke of the transducers in the deformed structural configuration has induced the choice of the adopted PGA. However, a limited plasticization can be observed in Figure 4.90, where the maximum rotation of the connections achieves values slightly below 10 mrad.

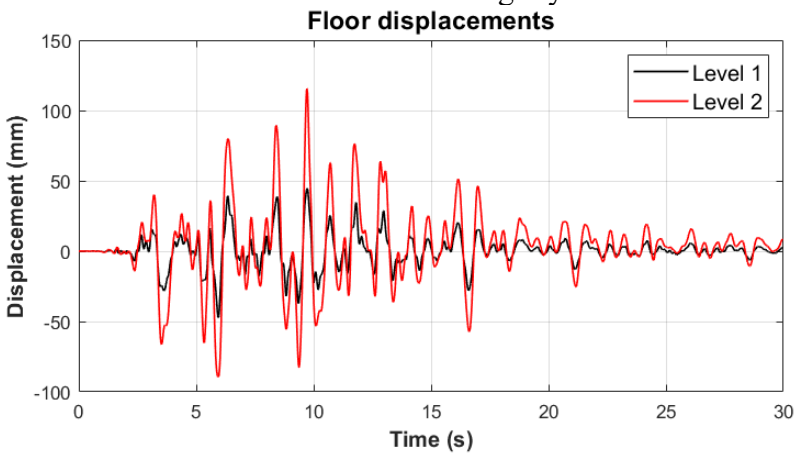

Figure 4.88 – Test 6: floor displacements

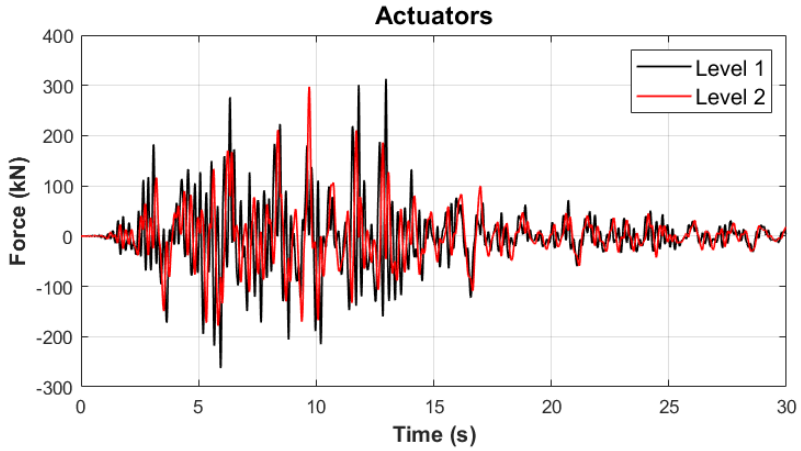

Figure 4.89 – Test 6: reaction forces

Table 4.30 – Main results related to Test 6

Kobe 1.0g			Test 6
Maximum base shear (kN)	Pull		-344
	Push		356
Peak first floor displacement (mm)	Pull		-47
	Push		45
Peak roof displacement (mm)	Pull		-89
	Push		116
Maximum inter-storey drift (%)	Pull	Level 1	-2.0
		Level 2	-2.1
	Push	Level 1	1.9
		Level 2	3.0

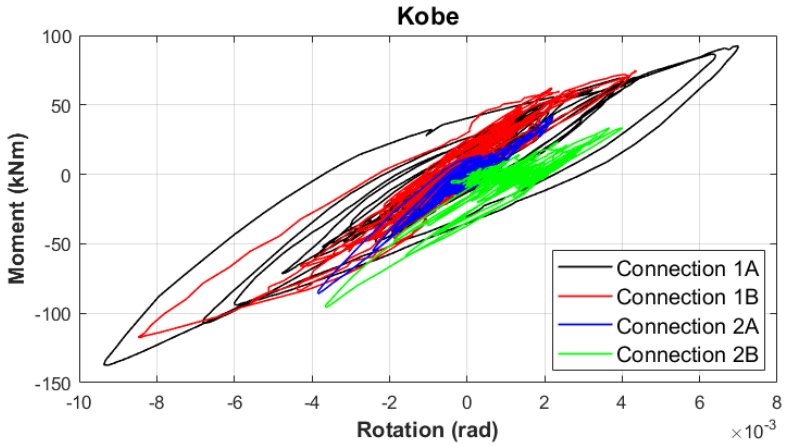

Figure 4.90 – Test 6: moment-rotation curves related to the X-shaped T-stub connections belonging to MRF-1

The deformed configurations of the structure and one T-stub are shown at the peak of the earthquake in Figure 4.91 and Figure 4.92. Instead, in Figure 4.93, the deformed configurations of two T-stubs are reported at the end of this test. Figure 4.93 highlights that only the connections located at the first storey have been engaged in the plastic range, while the lack of damages and

deformations of the T-stubs located at the second storey prove that they have exhibited an elastic response.

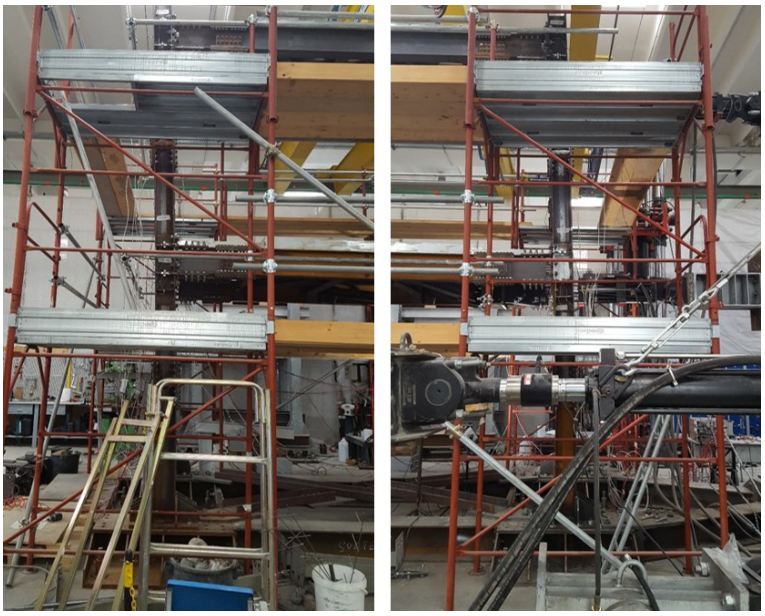

Figure 4.91 – Deformed configurations of two columns at the peak displacement occurred in Test 6

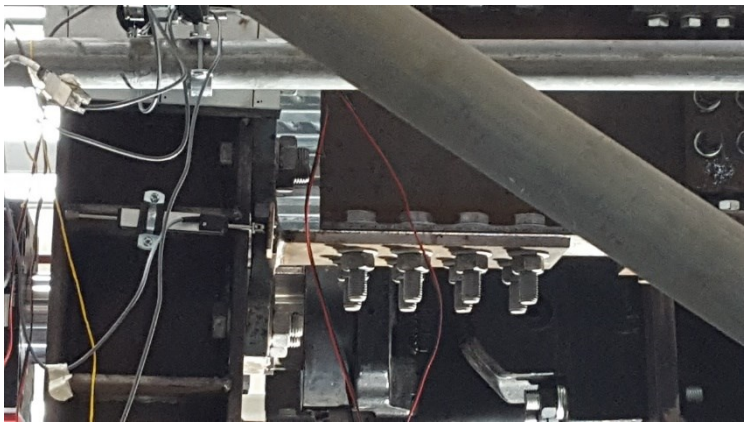

Figure 4.92 – Deformed configurations of a T-stub during Test 6

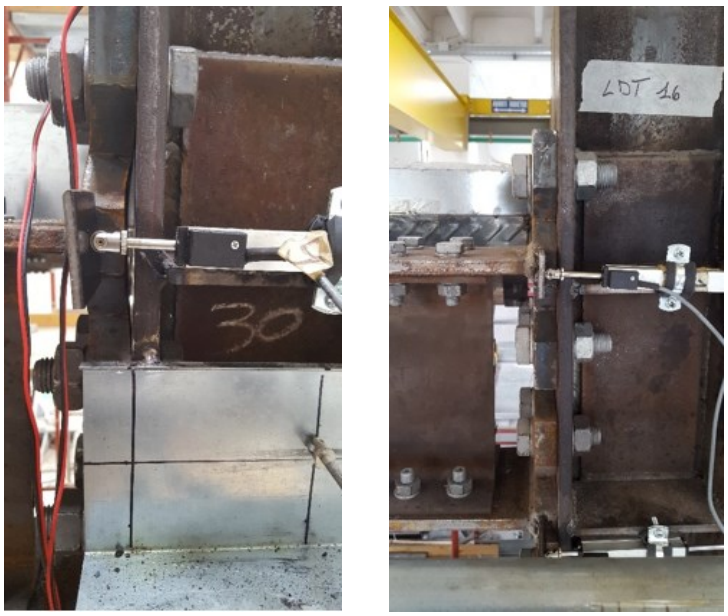

Figure 4.93 – Deformed configuration of a T-stub belonging to the first level (left) and undamaged T-stub belonging to the second level (right) at the end of Test 6

4.8.1.7 Coalinga (partial with PGA = 0.80g)

After the Kobe earthquake, it was chosen to apply the Coalinga seismic input again with the same PGA equal to 0.80g since it allows the highest engagement of the structure in the plastic range. Unfortunately, the arisen damage in the T-stubs due to the many previous tests experienced by the structure induced higher structural deformability, which did not allow the end of the test because the maximum stroke of the actuator located at the first level was achieved at 6.62 s of the accelerogram. This occurrence is evident in Figure 4.94, Figure 4.95 and Figure 4.96, where the floor displacements, the actuators' forces and the moment-rotation hysteretic curves are shown. The interruption of the test occurred around the first peak of relevant amplitude. At this time, the maximum roof displacement is equal to 214 mm, the base shear is 517 kN, and the maximum rotation of the connections is equal to 20 mrad (Table 4.31).

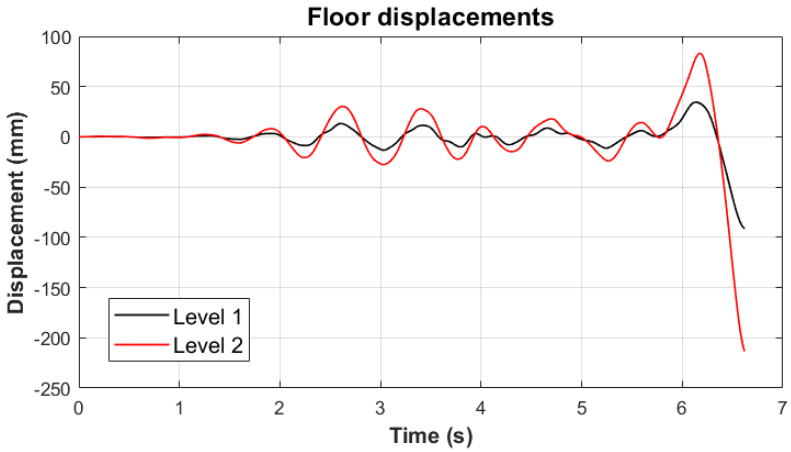

Figure 4.94 – Test 7: floor displacements

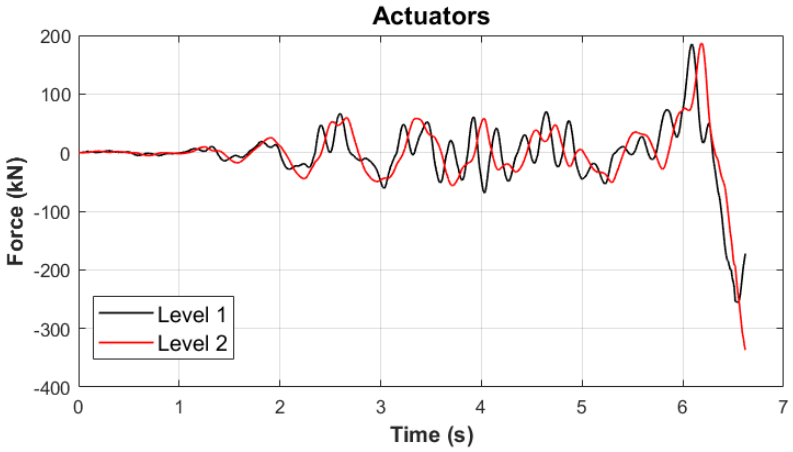

Figure 4.95 – Test 7: reaction forces

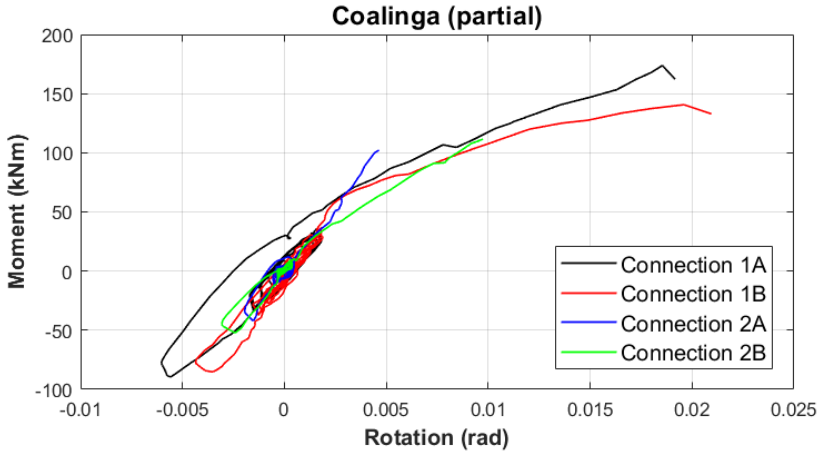

Figure 4.96 – Test 7: moment-rotation curves related to the X-shaped T-stub connections belonging to MRF-1

Table 4.31 – Main results related to Test 7

Coalinga 0.8g (partial)			**Test 7**
Maximum base shear (kN)	Pull		-517
	Push		271
Peak first floor displacement (mm)	Pull		-91
	Push		35
Peak roof displacement (mm)	Pull		-214
	Push		83
Maximum inter-storey drift (%)	Pull	Level 1	-3.8
		Level 2	-5.1
	Push	Level 1	1.4
		Level 2	2.1

Similarly to Test 6, in Figure 4.97 and Figure 4.98, the photos of two T-stubs are shown at the end of Test 7.

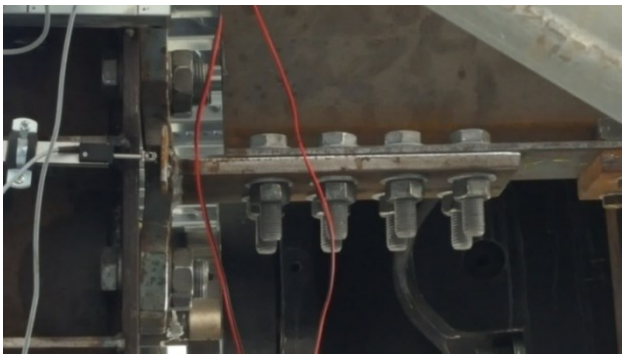

Figure 4.97 – Deformed configuration of a T-stub belonging to the first level at the end of Test 7

Figure 4.98 – Undamaged T-stub belonging to the second level at the end of Test 7

The structure has been subjected to many earthquakes. For this reason, the connections have dissipated the seismic input energy through damage in the flanges of the X-shaped T-stubs and at the column bases (Figure 4.99).

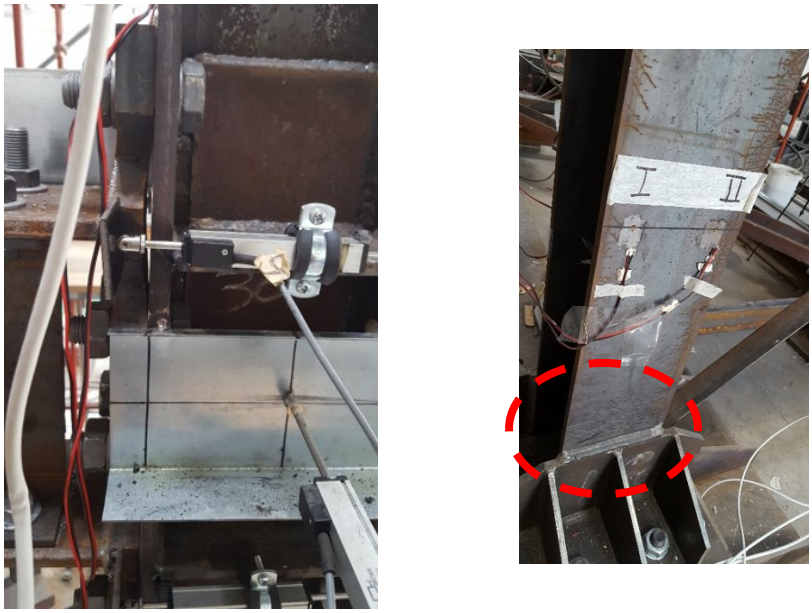

a) *b)*

Figure 4.99 – Damaged T-stub (a) and column base (b) at the end of the experimental campaign

Minor damages also occurred in some parts of the columns due to the local actions transmitted by the nodal components (Figure 4.100).

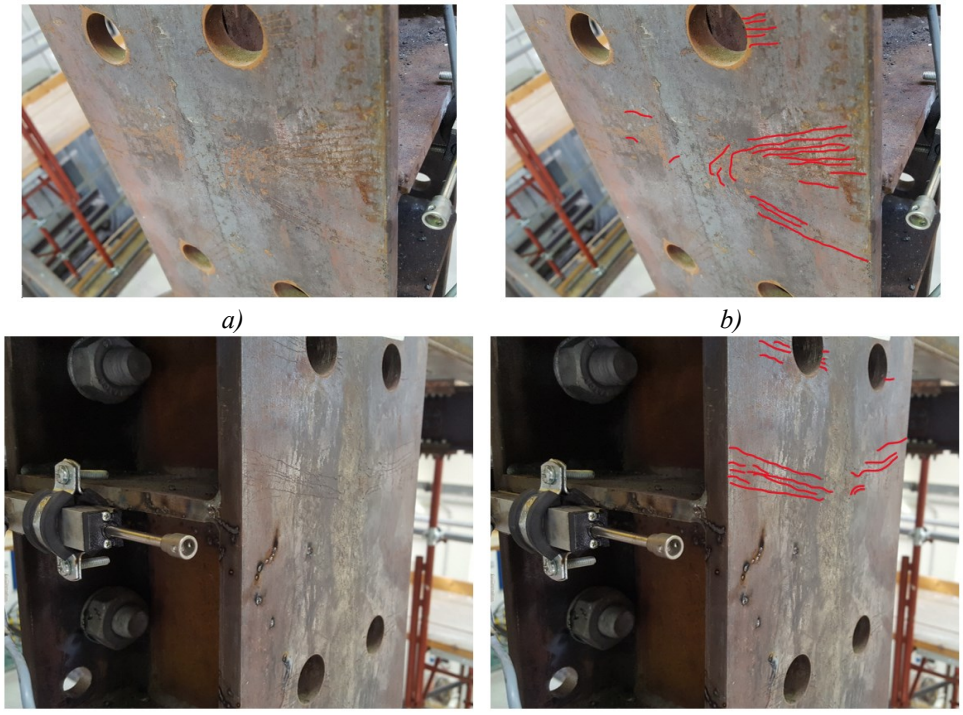

a) *b)*

c) *d)*

Figure 4.100 – Minor damages in other structural elements

This experimental campaign has shown that the proposed connections accommodate high rotations without inducing relevant damages to structural elements, except for the dissipative Tee elements, which can be easily substituted at the end of a severe seismic event. Differently from the two previous experimental campaigns, interrupted for the brittle fracture of the joints or technical issues, in this case, the end of the experimental campaign has been achieved by the stiffness degradation exhibited by the connections in the last test and which has induced such high structural deformability that the required displacements exceed the piston stroke of the actuators.

4.8.2 FE modelling of the tested frame

A simplified non-linear 2D Finite Element (FE) model of the structure (Figure 4.101) has been developed with the OpenSees software [22] to complement the test data.

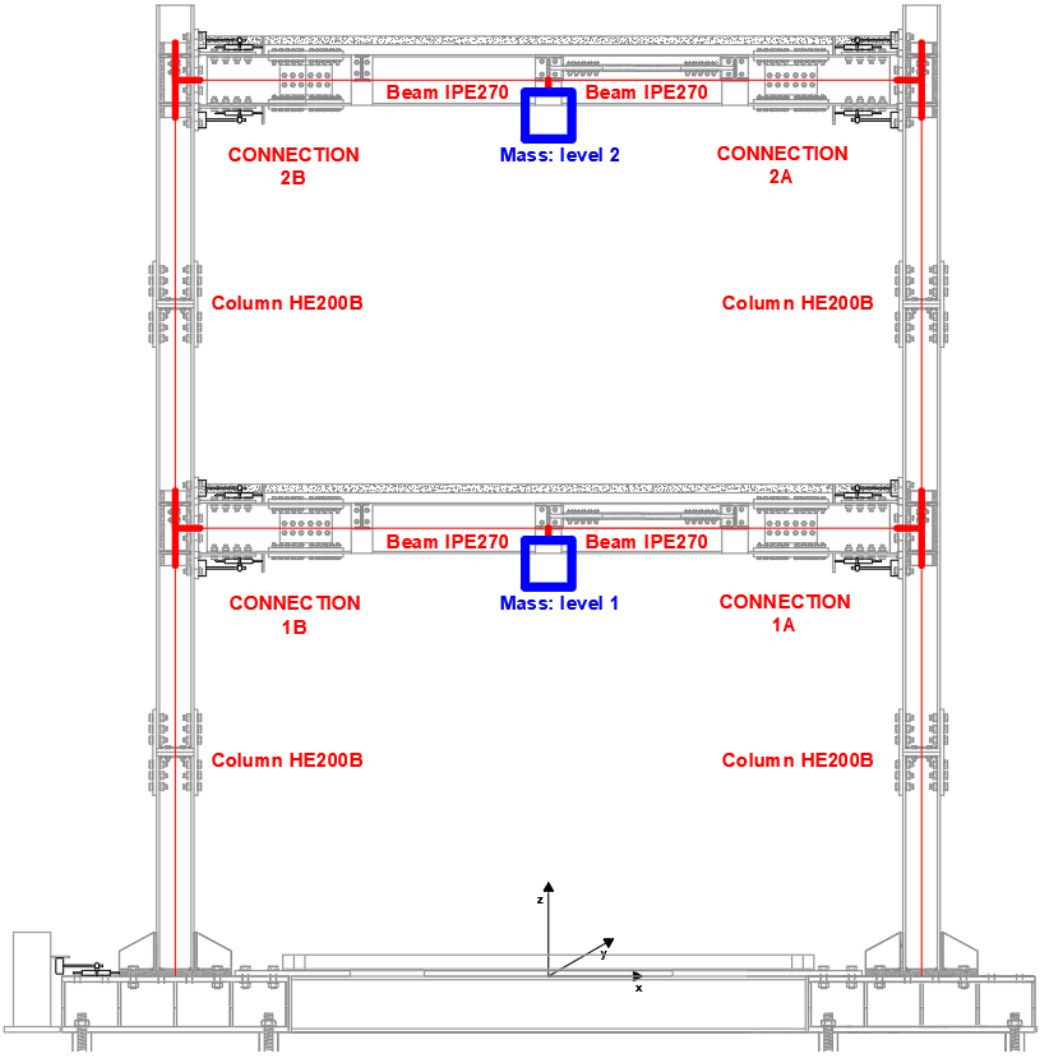

Figure 4.101 – FE model of the structure

The non-linearity has been embedded in the model employing a mixed lumped and distributed plasticity approach. Inelastic force-based elements (*forceBeamColumn element* in OpenSees), characterized by five integration sections, have been used to model the beams and the columns embedding the geometric and material nonlinearities in the model. Each section has been subdivided into 120 fibres to reliably assess the curvatures and internal actions. Rigid links have been used to model the diaphragmatic behaviour of the deck. Lumped masses have been placed at the physical locations where the actuators are connected to the mock-up (i.e. 65 mm below the centre of the spans).

Finally, the behaviour of the X-shaped T-stub connections has been accounted for through a rotational non-linear spring element (Figure 4.102), whose parameters have been calibrated against the response of an analogous and isolated beam-to-column sub-assembly [24-27] tested a few years ago at the University of Salerno.

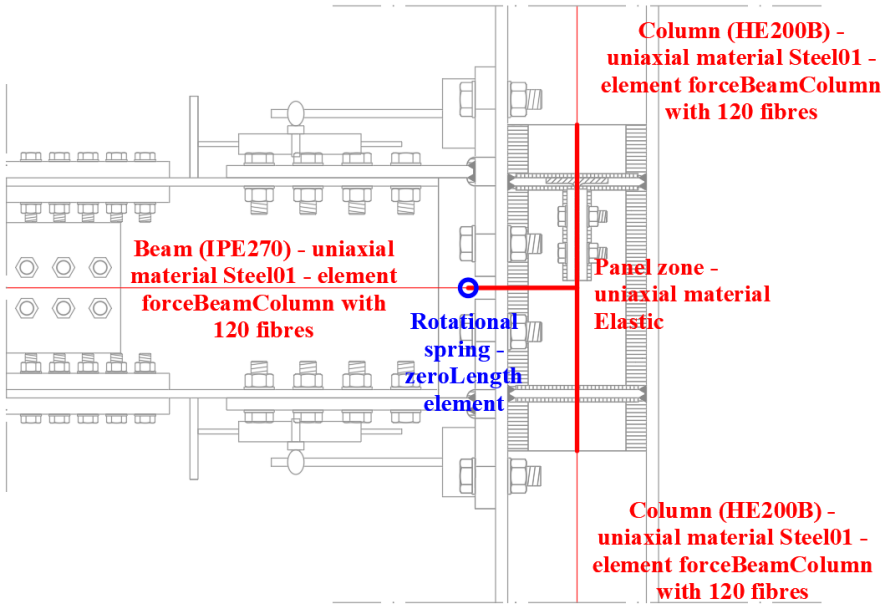

Figure 4.102 – FE model of the beam-to-column connection (initial model)

In particular, the considered isolated specimen had the same geometric and material properties of the connections with which the structure has been equipped, and it was subjected to a cyclic test complying with [24-27]. The moment-rotation response of the dissipative connection is reported in Figure 4.103a, while the corresponding calibration adopting the *pinching4* model is shown in Figure 4.103b. In particular, the *pinching4* model requires 38 parameters to be fully defined; for this reason, the MultiCal [19] tool has been exploited to perform the calibration. In fact, this software is based on adopting a Genetic-Algorithm to obtain a multi-objective optimization. It is only worth highlighting that the calibration has not been carried out in the rotation range experienced by the sub-assembly during the cyclic test (between $-0.12\ rad$ rad and $+0.12\ rad$), because these rotations are not consistent with the expected rotations that the connections belonging to the structure can experience. For this reason, the calibration has concerned the range $\pm 0.06\ rad$. The values of the parameters of the *pinching4* model are reported in Table 4.32.

Table 4.32 – Parameters adopted to define the pinching4 model of the link element (units in N, m, rad)

String:		
uniaxialMaterial Pinching4 $matTag $ePf1 $ePd1 $ePf2 $ePd2 $ePf3 $ePd3 $ePf4 $ePd4 <$eNf1 $eNd1 $eNf2 $eNd2 $eNf3 $eNd3 $eNf4 $eNd4> $rDispP $rForceP $uForceP <$rDispN $rForceN $uForceN > $gK1 $gK2 $gK3 $gK4 $gKLim $gD1 $gD2 $gD3 $gD4 $gDLim $gF1 $gF2 $gF3 $gF4 $gFLim $gE $dmgType		
Parameters	**Properties**	**Values**
$ePf1 $ePf2 $ePf3 $ePf4	floating point values defining force points on the positive response envelope	184517.26 256922.76 380712.82 441440.02
$ePd1 $ePd2 $ePd3 $ePd4	floating point values defining deformation points on the positive response envelope	0.00823 0.05350 0.09524 0.14228
$eNf1 $eNf2 $eNf3 $eNf4	floating point values defining force points on the negative response envelope	-184517.26 -256922.76 -380712.82 -441440.02
$eNd1 $eNd2 $eNd3 $eNd4	floating point values defining deformation points on the negative response envelope	-0.00823 -0.05350 -0.09524 -0.14228
$rDispP	floating-point value defining the ratio of the deformation at which reloading occurs to the maximum historic deformation demand	0.1
$fForceP	floating-point value defining the ratio of the force at which reloading begins to force corresponding to the maximum historic deformation demand	0.45
$uForceP	floating-point value defining the ratio of strength developed upon unloading from negative load to the maximum strength developed under monotonic loading	7.53E-16
$rDispN	floating-point value defining the ratio of the deformation at which reloading occurs to the minimum historic deformation demand	0.1
$fForceN	floating point value defining the ratio of the force at which reloading begins to force corresponding to the minimum historic deformation demand	0.45
$uForceN	floating point value defining the ratio of strength developed upon unloading from negative load to the minimum strength developed under monotonic loading	7.53E-16
$gK1 $gK2 $gK3 $gK4 $gKLim	floating point values controlling cyclic degradation model for unloading stiffness degradation	0.23 0.65 0.44 0.76 0
$gD1 $gD2 $gD3 $gD4 $gDLim	floating point values controlling cyclic degradation model for reloading stiffness degradation	0 1.38 0.6 0.63 1.2
$gF1 $gF2 $gF3 $gF4 $gFLim	floating point values controlling cyclic degradation model for strength degradation	0.57 0.1 0.51 0.72 0.18
$gE	floating point value used to define maximum energy dissipation under cyclic loading. Total energy dissipation capacity is defined as this factor multiplied by the energy dissipated under monotonic loading.	14.71
$dmgType	string to indicate type of damage (option: "cycle", "energy")	"energy"

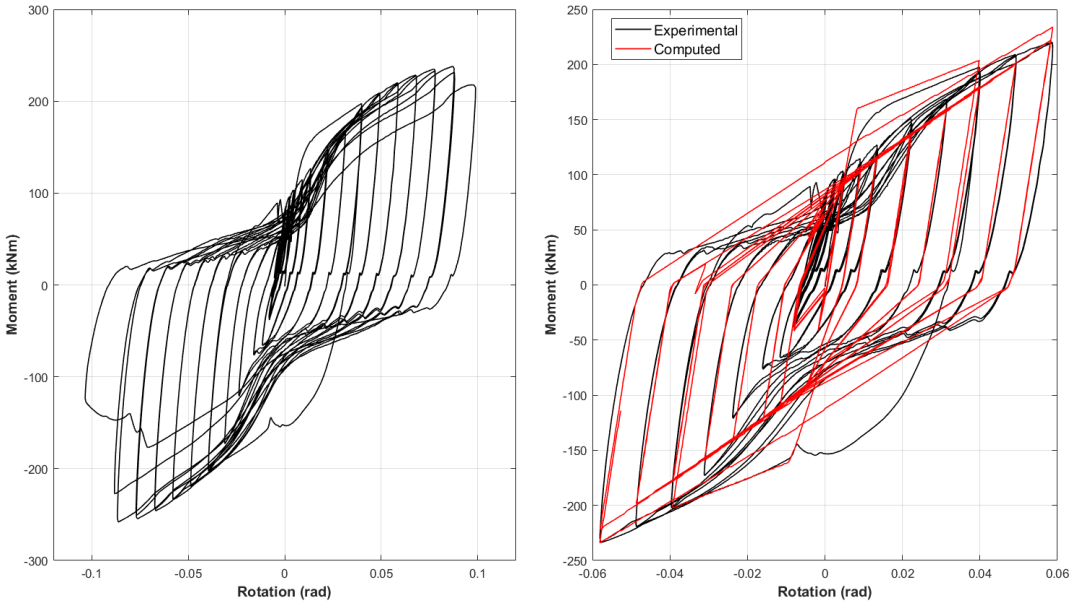

Figure 4.103 – Experimental and numerical moment-rotation response of the dissipative connection: cyclic response (left) and model calibration (right)

4.8.3 Experimental versus numerical results

This paragraph is devoted to the comparison of the experimental and numerical outcomes. In most cases, the global structural response is captured with adequate precision, mainly referring to the structure's tests in the plastic range (tests 1, 2, 5, 6). Instead, especially in Test 3 and Test 4, higher scatters have been observed when the structure has behaved elastically. These occurrences are ascribed to the spring elements, which exhibit, after the first yielding, a stiffness very different from that one experienced in the real tests. The main results are summarized in Table 4.33 and from Figure 4.104 to Figure 4.107.

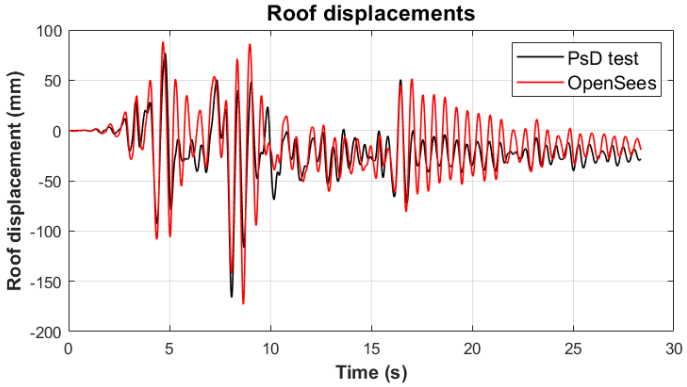

Figure 4.104 – Roof displacements: Test 1

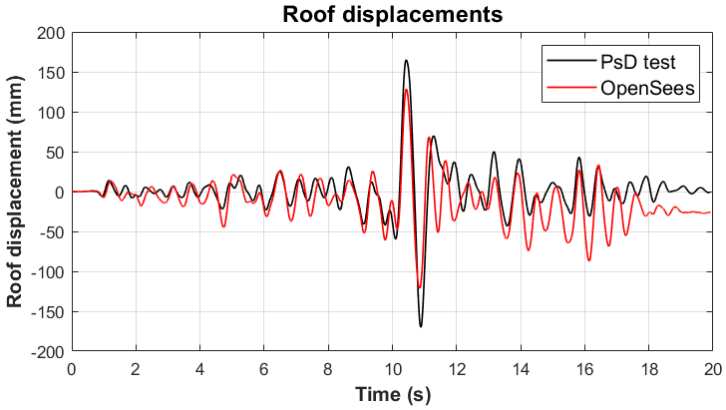

Figure 4.105 – Roof displacements: Test 2

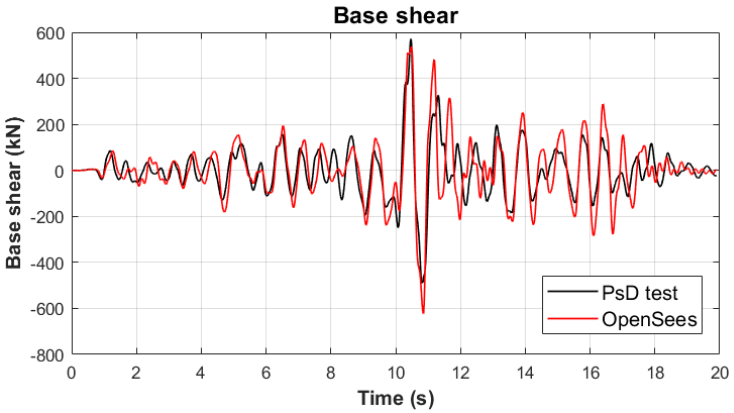

Figure 4.106 – Base shear: Test 7

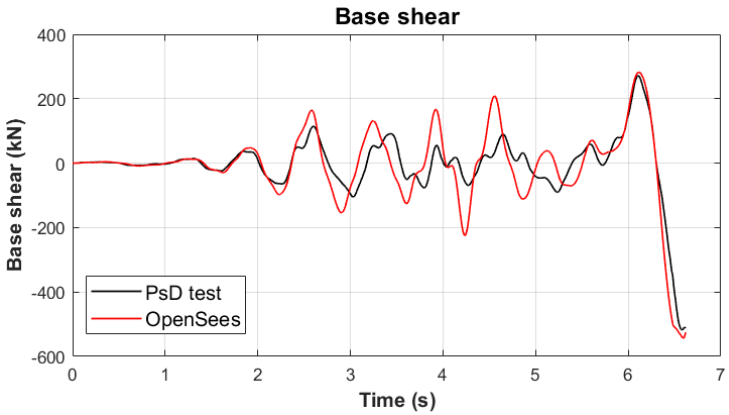

Figure 4.107 – Base shear: Test 7

Table 4.33 – Experimental versus numerical comparison of actuators' forces and floor displacements (PsD tests vs OpenSees)

Test	Base shear (kN)	Peak floor displacement (mm)	
		(L-1)	(L-2)
1 – PsD	427	68	166
1 - OS	577	72	173
1 - Err. (%)	**35**	**6**	**4**
2 - PsD	572	78	170
2 - OS	623	68	128
2 - Err. (%)	**9**	**-12**	**-25**
3 - PsD	297	41	88
3 - OS	523	54	128
3 - Err. (%)	**76**	**30**	**46**
4 - PsD	303	44	109
4 - OS	510	56	136
4 - Err. (%)	**68**	**28**	**24**
5 - PsD	566	84	187
5 - OS	678	100	187
5 - Err. (%)	**20**	**18**	**0**
6 - PsD	356	47	116
6 - OS	545	54	125
6 - Err. (%)	**53**	**14**	**9**
7 - PsD	517	91	214
7 - OS	543	58	126
7 - Err. (%)	**5**	**-37**	**-41**

Instead, the local response of the connections is simulated with some approximations, as is shown in Table 4.34, Figure 4.108 and Figure 4.109.

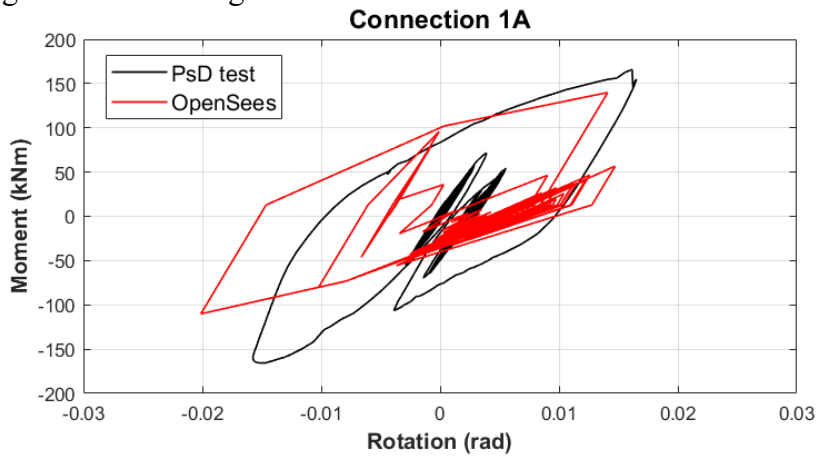

Figure 4.108 – Hysteretic curves (connection 1A): Test 2

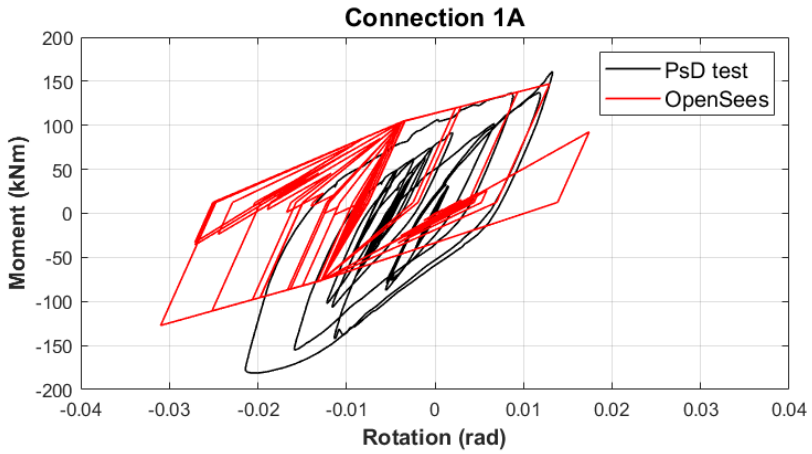

Figure 4.109 – Hysteretic curves (connection 1A): Test 5

Table 4.34 - Experimental versus numerical comparison of connection 1A (PsD tests vs OpenSees)

Test	Rotation (mrad)	Moment (kNm)
1 - PsD	21.0	136.0
1 - OS	28.9	135.6
1 - Err. (%)	**37.6**	**-0.3**
2 - PsD	16.5	165.9
2 - OS	20.1	139.9
2 - Err. (%)	**21.9**	**-15.6**
3 - PsD	5.7	95.0
3 - OS	22.5	136.8
3 - Err. (%)	**290.9**	**44.0**
4 - PsD	8.2	119.2
4 - OS	23.2	135.7
4 - Err. (%)	**182.0**	**13.8**
5 - PsD	21.4	181.2
5 - OS	31.0	147.1
5 - Err. (%)	**44.7**	**-18.8**
6 - PsD	9.4	137.3
6 - OS	20.4	141.3
6 - Err. (%)	**117.2**	**2.9**
7 - PsD	19.2	173.8
7 - OS	20.9	98.0
7 - Err. (%)	**9.0**	**-43.6**

4.9 Comparison among the results of the three experimental campaigns

This paragraph compares the experimental results observed in the three experimental campaigns. This comparison can be achieved since the three campaigns have been carried out using the same seismic inputs, material and modal properties.

As reported in the previous paragraphs, not all the accelerograms could engage the structure in the plastic range. Such an occurrence can be ascribed to the overstrength exhibited by the mock-up

and the limits of the available experimental set-up, which did not allow the increase of the PGAs. In particular, the Artificial and Santa Barbara ground motions caused the elastic response of the mock-up in all three campaigns. Instead, the seismic inputs of Imperial Valley, Spitak and Coalinga were able to engage the structure in the plastic range activating the dissipative fuses both at the beam-to-column joints and at the column bases.
As already pointed out, this paragraph intends to summarize the main differences observed by comparing the structural response of the mock-up equipped with the three analysed connections' typologies.
In particular, from Figure 4.110 to Figure 4.144, some graphs in terms of roof displacements, base shear, moment-rotation and dissipated energy of connections 1A and overall energy dissipated by the joints only, the column bases only and both of them are reported.

4.9.1 Test 1

Concerning Test 1, it is clear also that the three connections' typologies do not ensure the self-centring of the structure. However, it is worth highlighting that high base shear is observed for the structure equipped with RBS joints, while the mock-up with the remaining beam-to-column joints exhibits lower base shear values of about 30%.
Because of technical issues related to the acquiring data system, no data about the local response of FREEDAM connections is available. For this reason, the moment-rotation hysteretic curves and energy dissipation capacity related to Test 1 cannot be discussed in detail.

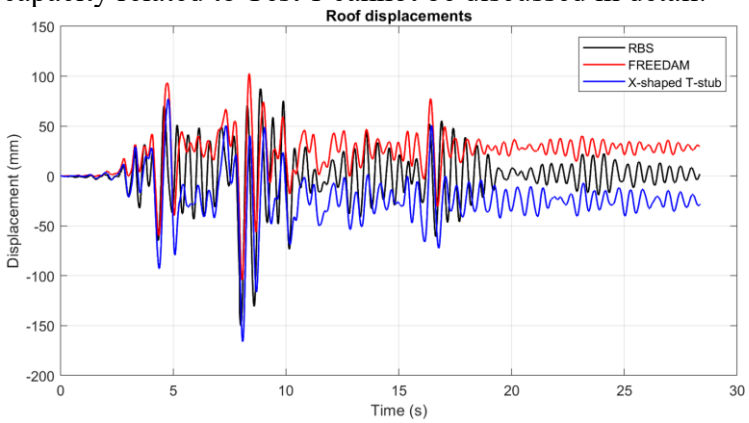

Figure 4.110 – Test 1: roof displacements

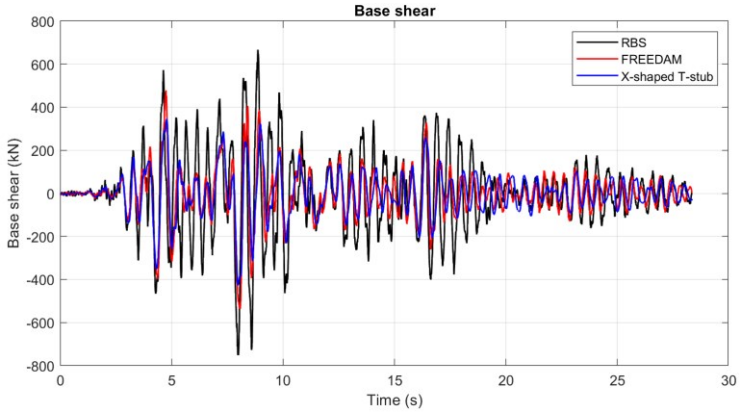

Figure 4.111 – Test 1: base shear

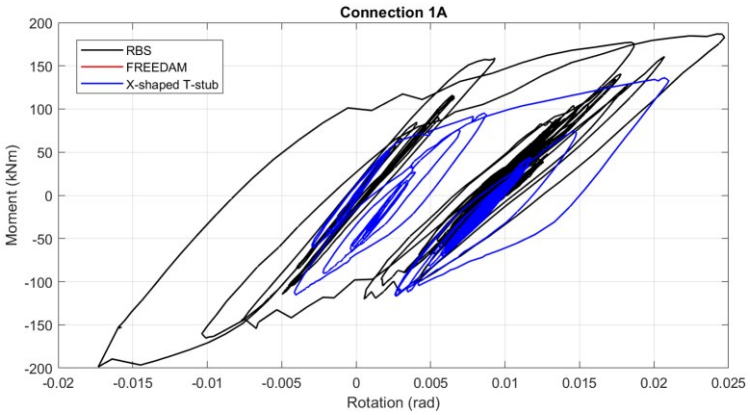

Figure 4.112 – Test 1: hysteretic curves referred to connection 1A

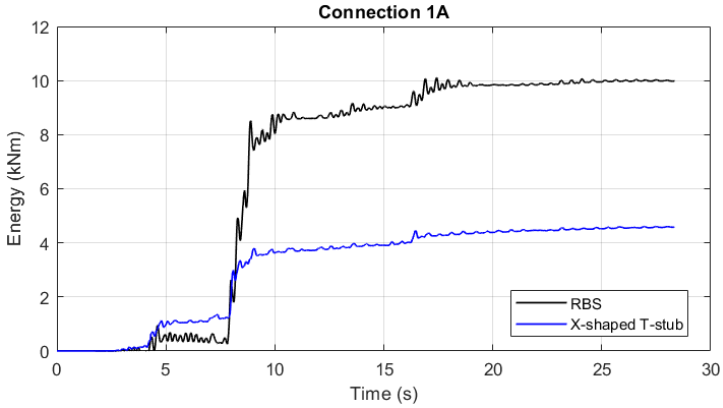

Figure 4.113 – Test 1: dissipated energy referred to connection 1A

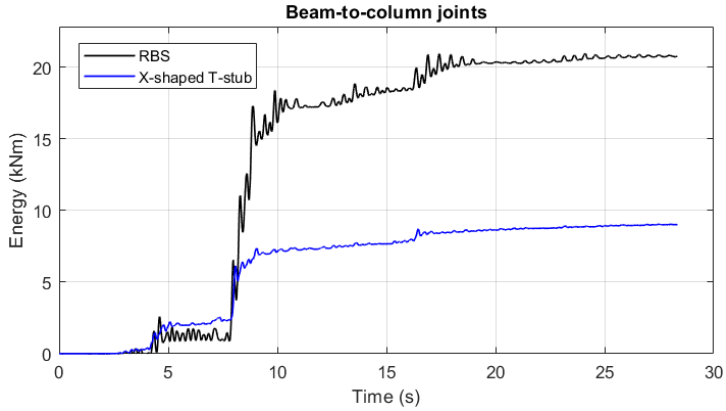

Figure 4.114 – Test 1: energy dissipated by the joints of one MRF

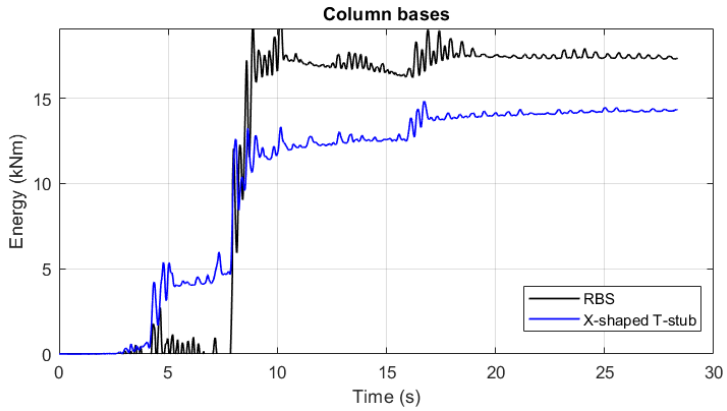

Figure 4.115 – Test 1: energy dissipated by the column bases of one MRF

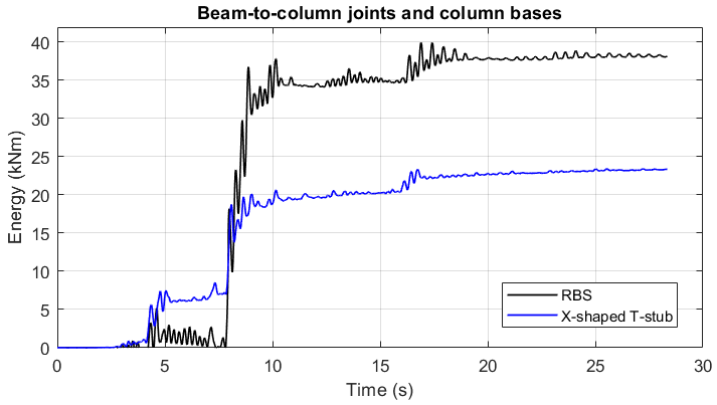

Figure 4.116 – Test 1: energy dissipated by the joints and column bases of one MRF

4.9.2 Test 2

The same considerations concerning Test 2 (Spitak with a PGA equal to 0.8g) can be made. However, in this case, consistently with the previous outcomes, the higher deformability exhibited by the mock-up equipped with X-shaped T-stub connections is also evident. Furthermore, since this accelerogram is characterized by one peak with significant amplitude, the MRF with X-shaped T-stub joints is able to dissipate higher energy than the other two connections' typologies, both at the level of the beam-to-column joints and the column bases.

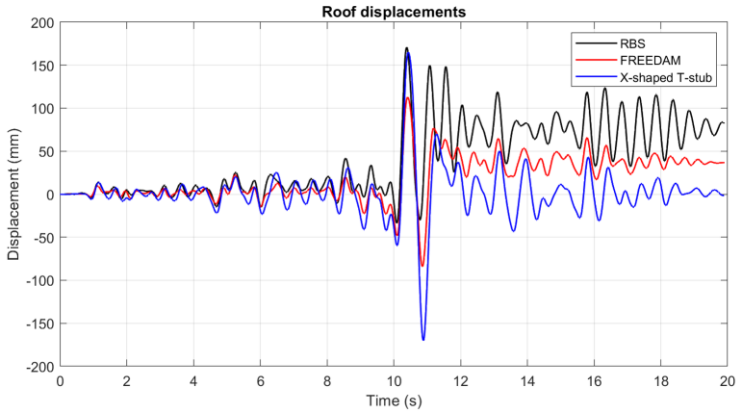

Figure 4.117 – Test 2: roof displacements

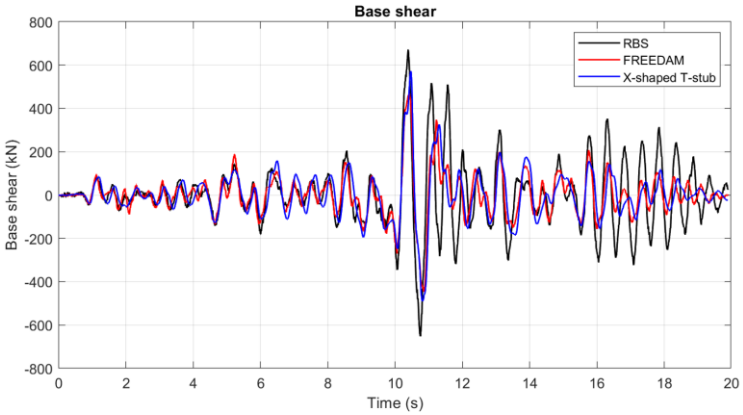

Figure 4.118 – Test 2: base shear

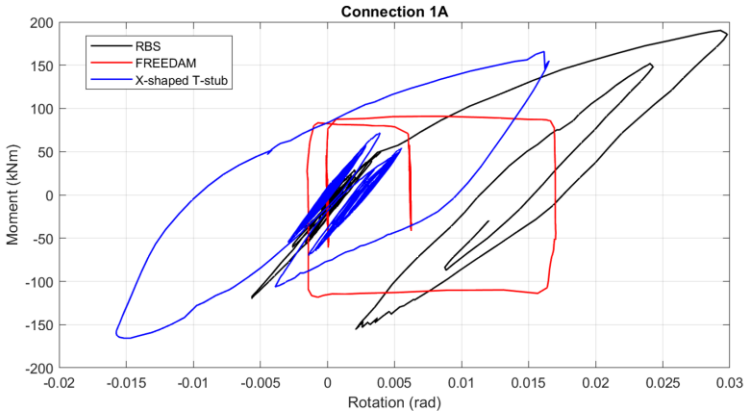

Figure 4.119 – Test 2: hysteretic curves referred to connection 1A

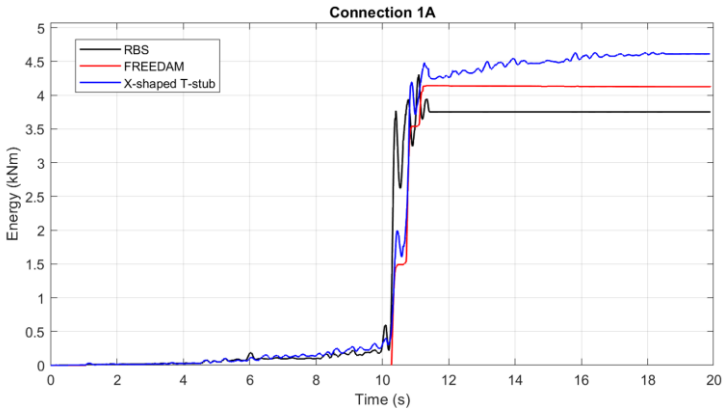

Figure 4.120 – Test 2: dissipated energy referred to connection 1A

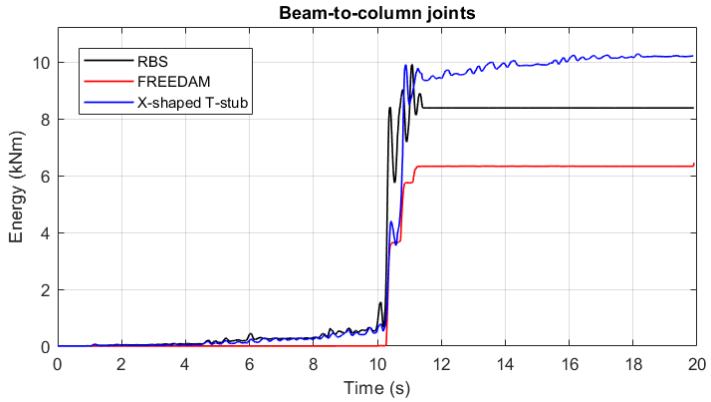

Figure 4.121 – Test 2: energy dissipated by the joints of one MRF

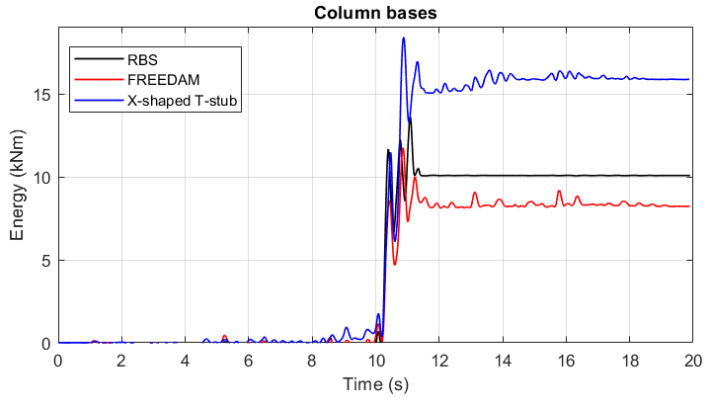

Figure 4.122 – Test 2: energy dissipated by the column bases of one MRF

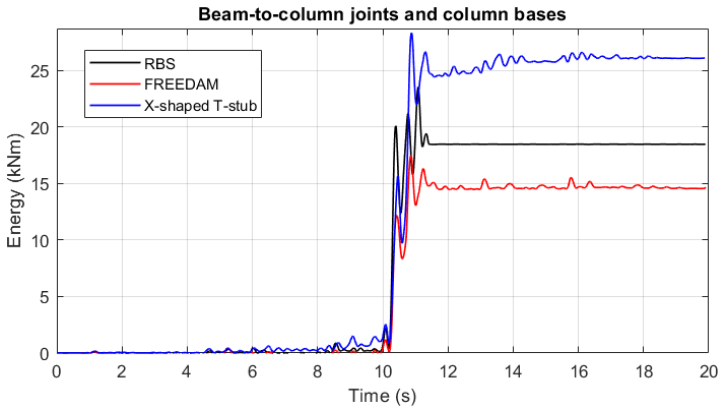

Figure 4.123 – Test 2: energy dissipated by the joints and column bases of one MRF

4.9.3 Test 3

During Test 3, the structure exhibited an elastic behaviour, as shown from Figure 4.124 to Figure 4.130. The excursion in the plastic range is minimal in the three experimental campaigns.

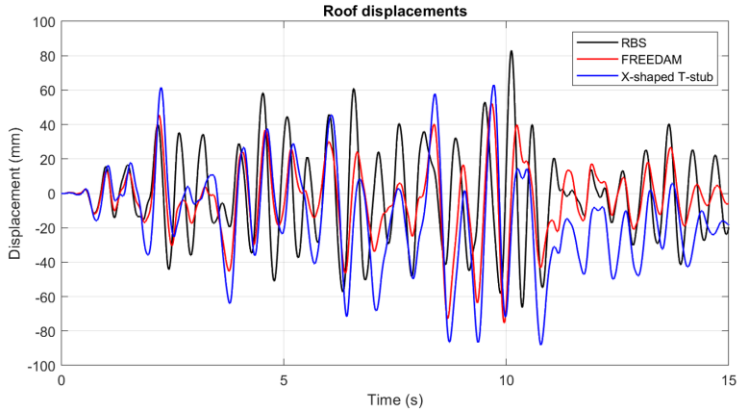

Figure 4.124 – Test 3: roof displacements

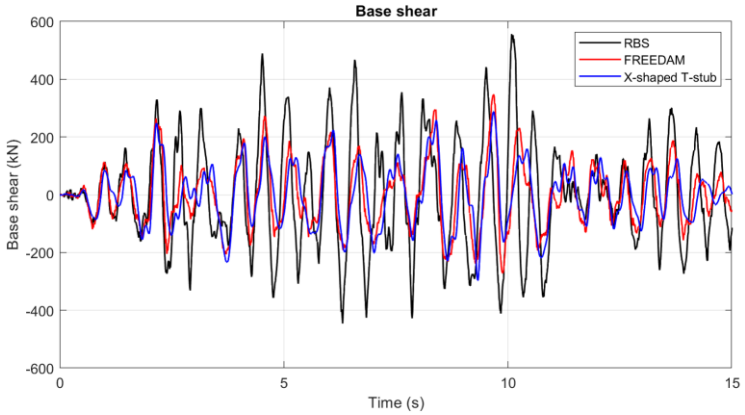

Figure 4.125 – Test 3: base shear

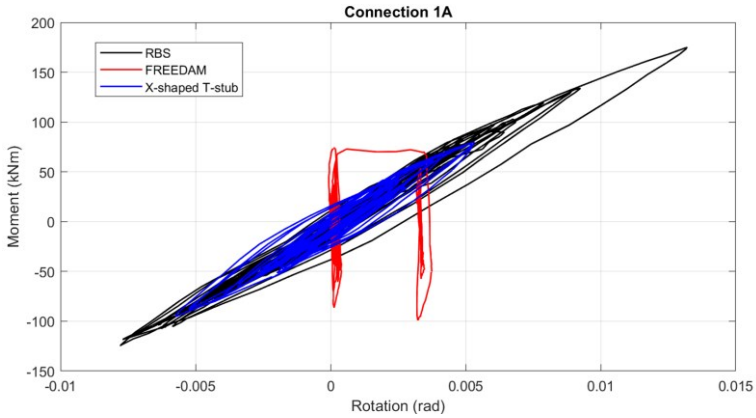

Figure 4.126 – Test 3: hysteretic curves referred to connection 1A

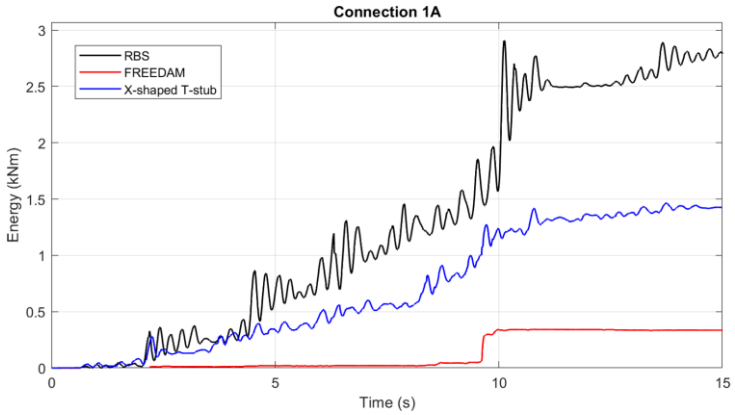

Figure 4.127 – Test 3: dissipated energy referred to connection 1A

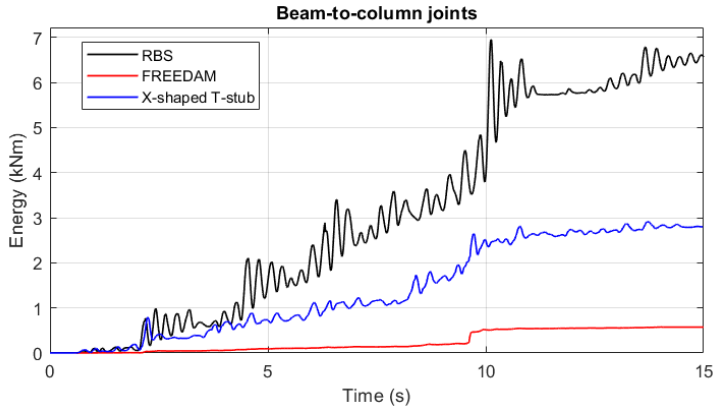

Figure 4.128 – Test 3: energy dissipated by the joints of one MRF

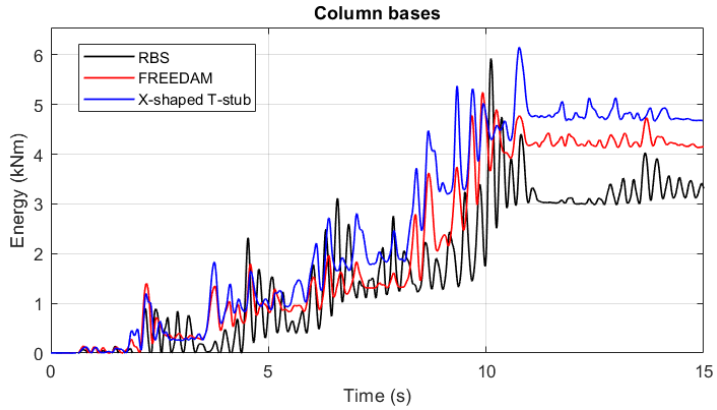

Figure 4.129 – Test 3: energy dissipated by the column bases of one MRF

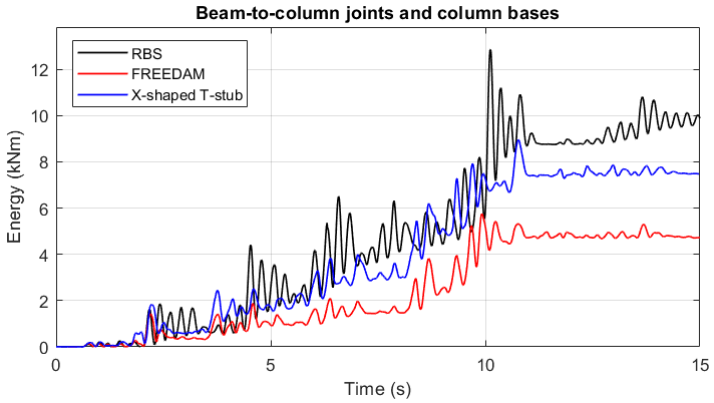

Figure 4.130 – Test 3: energy dissipated by the joints and column bases of one MRF

4.9.4 Test 4

The same considerations are valid for the results relating to Test 4 because the mock-up exhibited an elastic behaviour (see from Figure 4.131 to Figure 4.137).

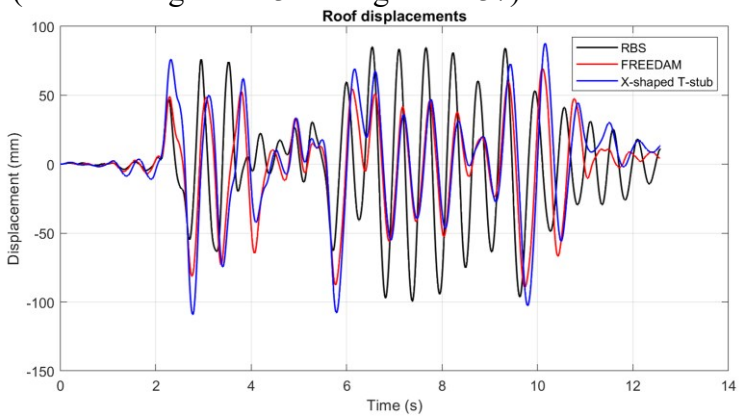

Figure 4.131 – Test 4: roof displacements

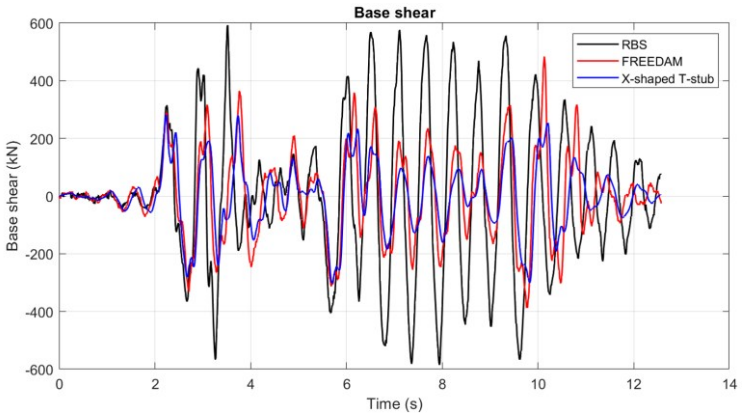

Figure 4.132 – Test 4: base shear

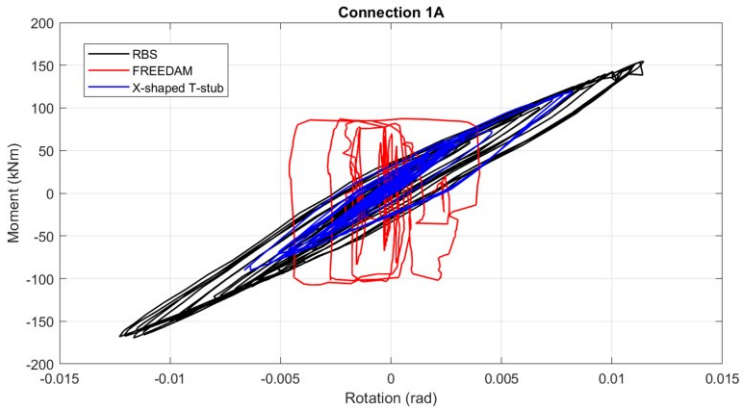

Figure 4.133 – Test 4: hysteretic curves referred to connection 1A

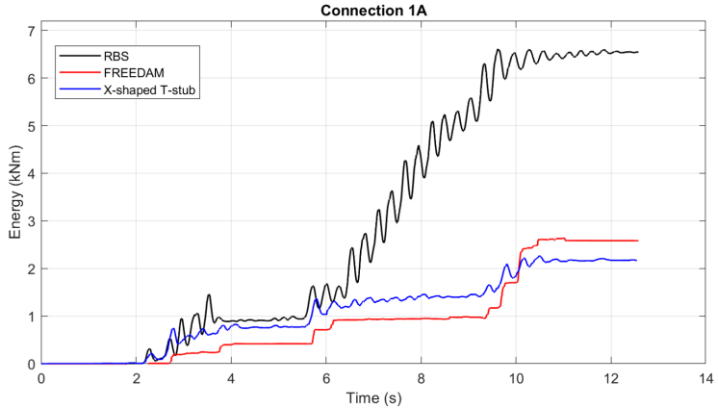

Figure 4.134 – Test 4: dissipated energy referred to connection 1A

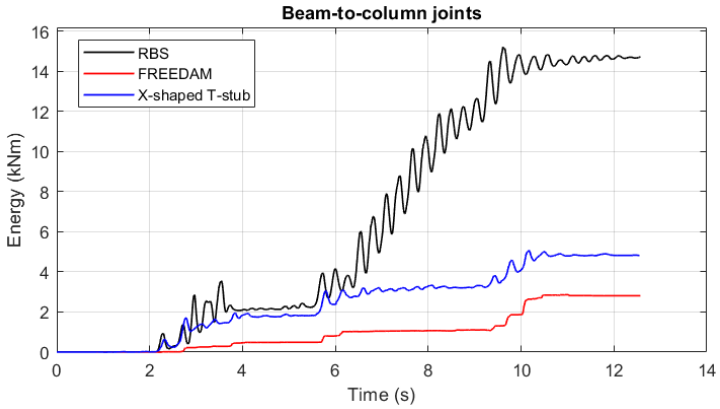

Figure 4.135 – Test 4: energy dissipated by the joints of one MRF

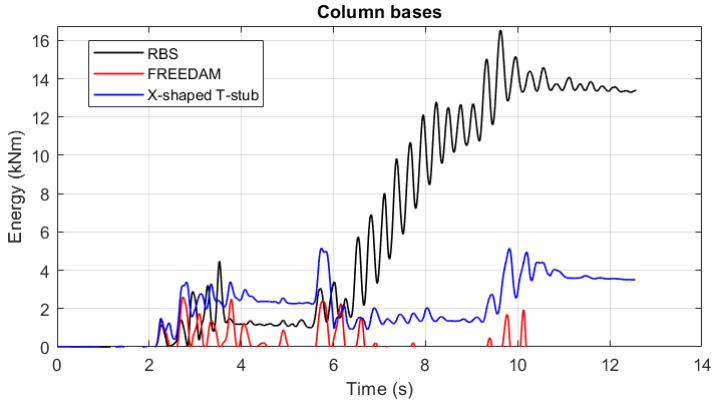

Figure 4.136 – Test 4: energy dissipated by the column bases of one MRF

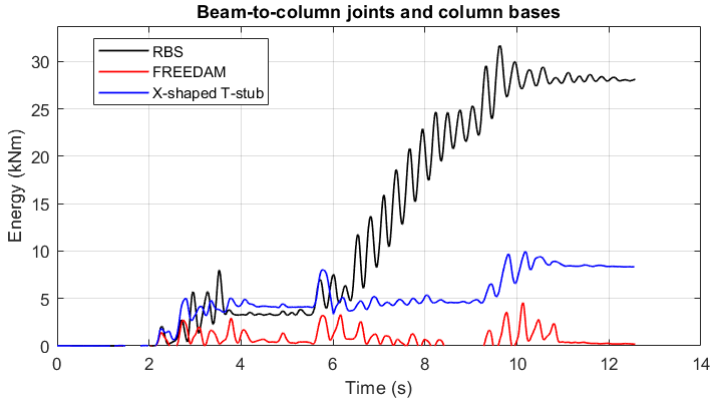

Figure 4.137 – Test 4: energy dissipated by the joints and column bases of one MRF

4.9.5 Test 5

Instead, Test 5 is meaningful because it represents the test in which the RBSs failed, while the structure with FREEDAM and dissipative double-split joints did not reach the collapse. Furthermore, the roof displacements curves show that generally, the mock-up exhibited higher deformability starting from the RBS to the X-shaped T-stub typologies.

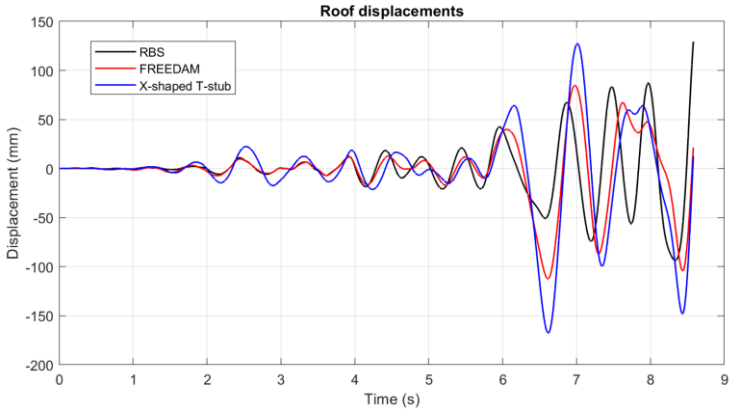

Figure 4.138 – Test 5: roof displacements

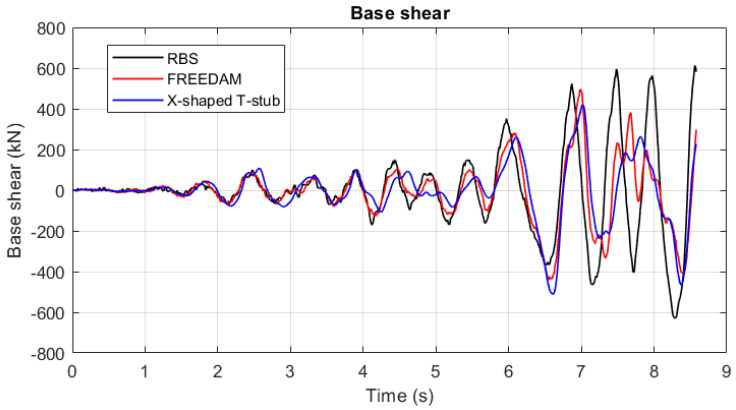

Figure 4.139 – Test 5: base shear

At the local response, generally, the FREEDAM connections exhibit very stable rectangular-shaped moment-rotation hysteretic curves even though no high rotations are achieved. Instead, the RBS and X-shaped T-stub show a similar response. Observing the overall energy dissipated by one MRF (Figure 4.144), similarly to Test 2, it is clear that the solution with the dissipative T-stubs can ensure high dissipation capacity at the global level while FREEDAM joints are activated more efficiently.

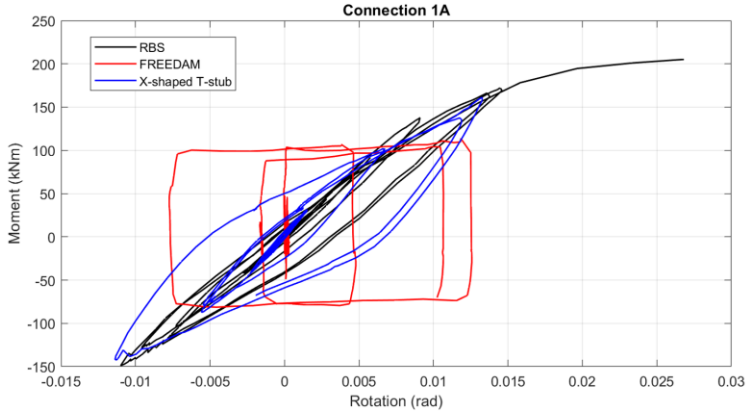

Figure 4.140 – Test 5: hysteretic curves referred to connection 1A

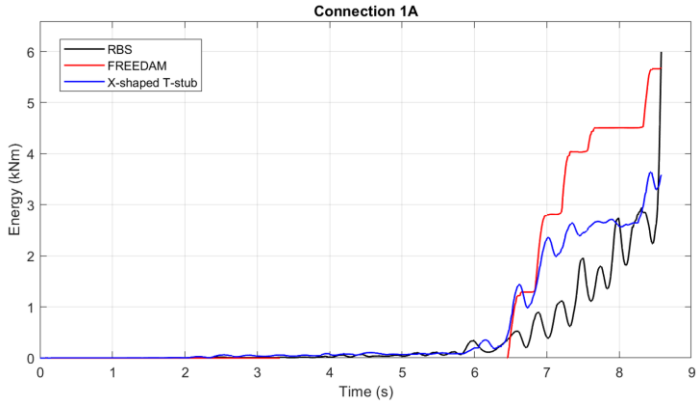

Figure 4.141 – Test 5: dissipated energy referred to connection 1A

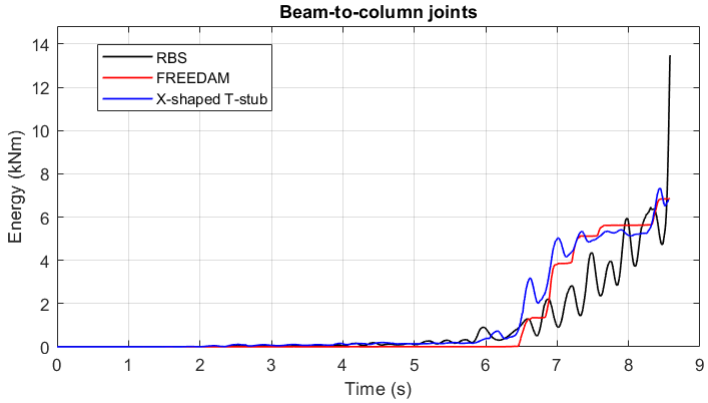

Figure 4.142 – Test 5: energy dissipated by the joints of one MRF

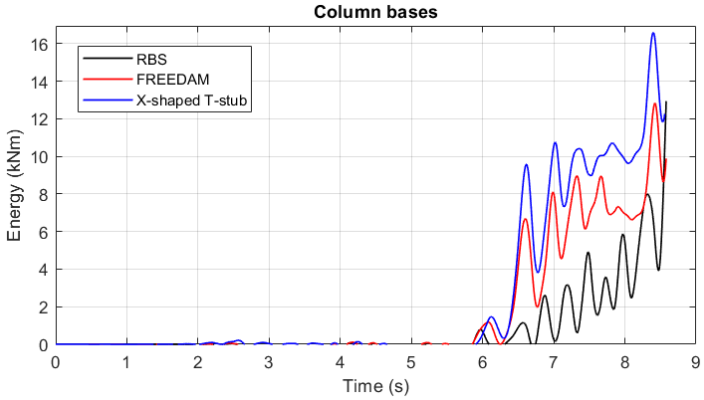

Figure 4.143 – Test 5: energy dissipated by the column bases of one MRF

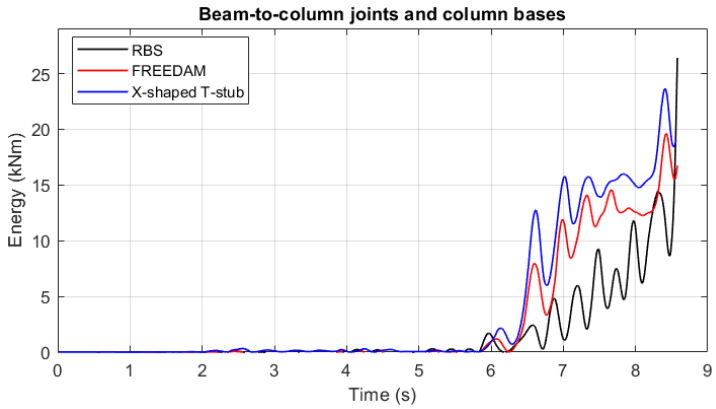

Figure 4.144 – Test 5: energy dissipated by the joints and column bases of one MRF

In Table 4.35 and from Figure 4.145 to Figure 4.147, some results comparing the primary global outcomes are reported. Generally, the results highlight that the mock-up exhibits more deformability and lower base shear from the first (RBS) to the third (X-shaped T-stub) solution. This aspect is justified in the case of FREEDAM connections because of the fixed maximum bending moments transferred by the joints to the columns; however, this occurrence is observed in the T-stub solution.

Table 4.35 – Comparison among the results of the experimental campaigns in terms of base shear, roof displacements and maximum interstorey drifts

		RBS	FREEDAM	X-shaped T-stub
Test 1	Base shear (kN)	751	537	427
	Roof displacement (mm)	150	104	166
	Maximum drift (%)	3.3	3	4.1
Test 2	Base shear (kN)	670	470	572
	Roof displacement (mm)	171	112	170
	Maximum drift (%)	3.6	3.3	4.1
Test 3	Base shear (kN)	555	347	297
	Roof displacement (mm)	83	75	88
	Maximum drift (%)	1.8	1.7	2.3
Test 4	Base shear (kN)	592	483	303
	Roof displacement (mm)	99	89	109
	Maximum drift (%)	2.2	2.3	3
Test 5	Base shear (kN)	630	495	566
	Roof displacement (mm)	129	112	187
	Maximum drift (%)	2.8	3	4.5

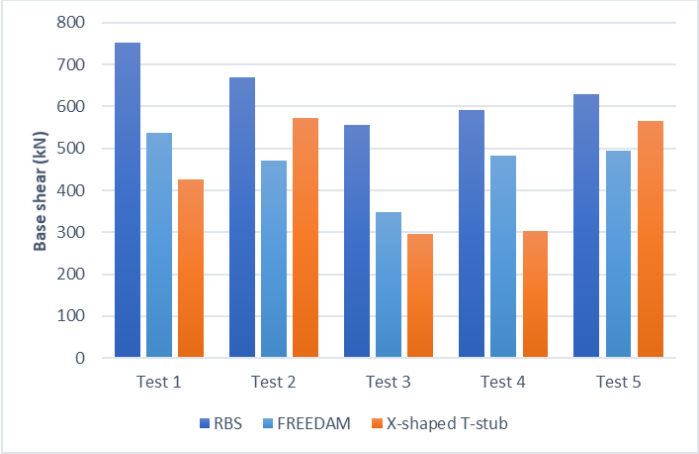

Figure 4.145 – Comparison of the results of the experimental campaigns: base shear

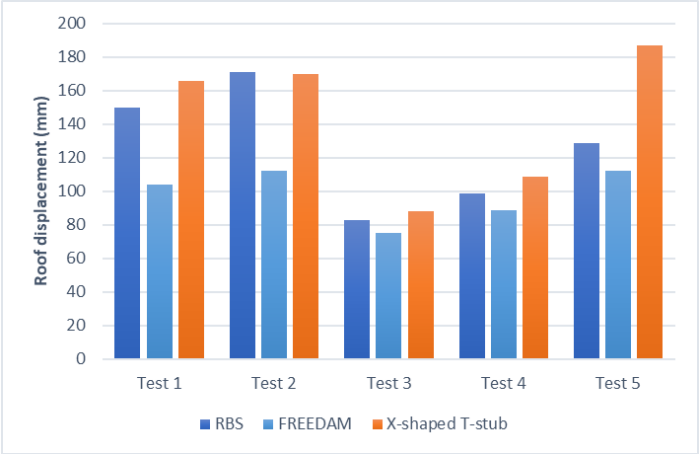

Figure 4.146 – Comparison among the results of the experimental campaigns: roof displacements

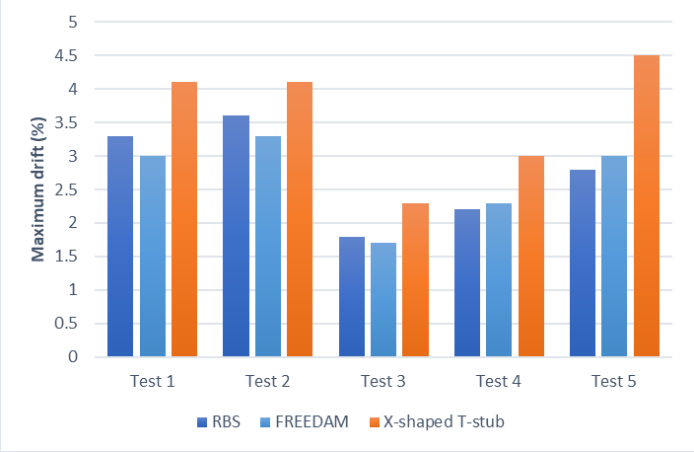

Figure 4.147 – Comparison among the results of the experimental campaigns: maximum interstorey drifts

In Table 4.36 and from Figure 4.148 to Figure 4.150, the local response of the connections 1A is reported. Referring only to the case in which the structure is plastically engaged, it is clear that the energy dissipation capacity is quite similar.

Table 4.36 – Comparison among the results of the experimental campaigns in terms of rotation, bending moment and energy (connection 1A)

		RBS	FREEDAM	X-shaped T-stub
Test 1	Rotation (mrad)	25	-	21
	Moment (kNm)	199	-	136
	Energy (kNm)	10	-	5
Test 2	Rotation (mrad)	30	17	16.5
	Moment (kNm)	190	118	166
	Energy (kNm)	4	4	5
Test 3	Rotation (mrad)	13	4	5.7
	Moment (kNm)	175	99	95
	Energy (kNm)	3	0.3	1
Test 4	Rotation (mrad)	13	5	8.2
	Moment (kNm)	169	108	119
	Energy (kNm)	7	3	2
Test 5	Rotation (mrad)	27	13	21.4
	Moment (kNm)	205	114	181
	Energy (kNm)	6	6	4

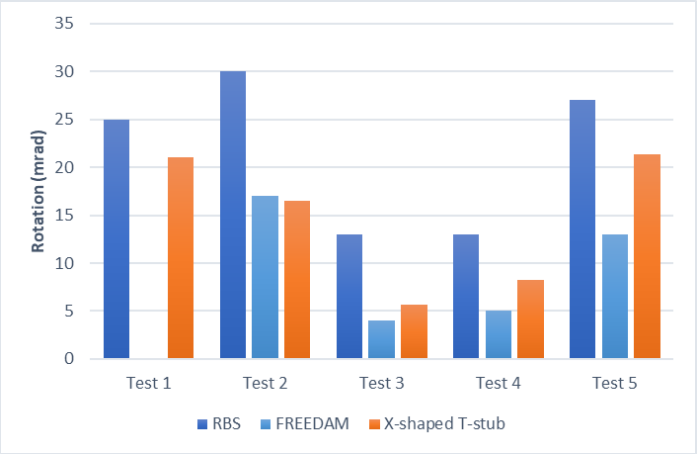

Figure 4.148 – Comparison among the results of the experimental campaigns: rotation (connection 1A)

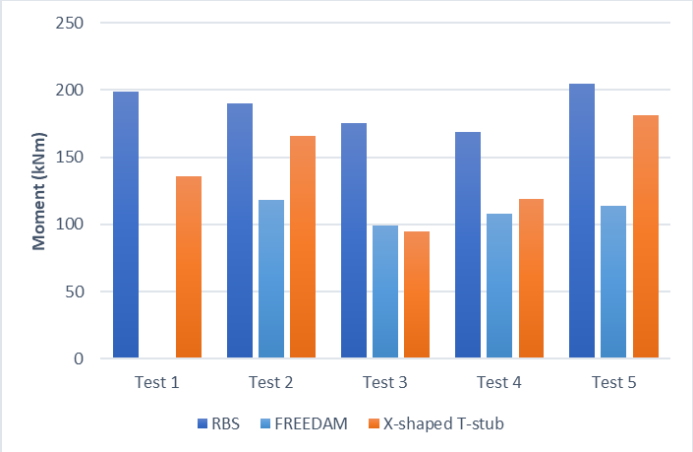

Figure 4.149 – Comparison among the results of the experimental campaigns: moment (connection 1A)

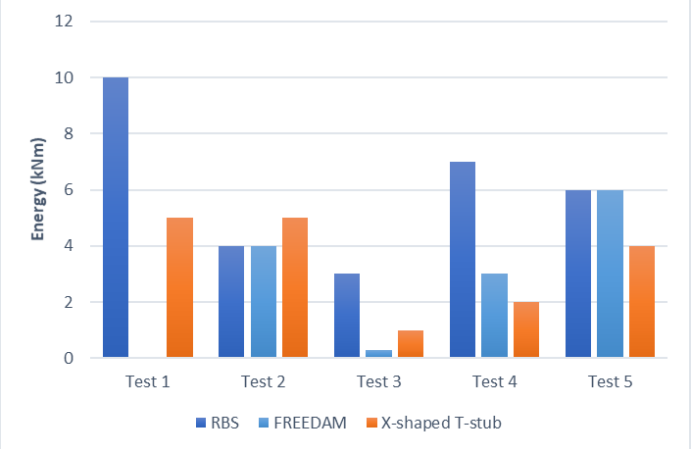

Figure 4.150 – Comparison of the results of the experimental campaigns: dissipated energy (connection 1A)

Finally, the comparison among the energy dissipated by the connections and the column bases in all the tests is reported in Table 4.37 and from Figure 4.151 to Figure 4.153. The results show that the joints and column bases generally dissipate the same energy.

Table 4.37 – Energy dissipation capacity related to one MRF

		RBS	FREEDAM	X-shaped T-stub
Test 1	Joints (kNm)	20.8	-	9
	Column bases (kNm)	17.4	-	13.3
	All (kNm)	38.2	-	22.3
Test 2	Joints (kNm)	8.4	6.3	10.22
	Column bases (kNm)	10.1	8.3	15.9
	All (kNm)	18.5	14.6	26.12
Test 3	Joints (kNm)	6.6	0.6	2.8
	Column bases (kNm)	3.4	4.1	4.7
	All (kNm)	10	4.7	7.5
Test 4	Joints (kNm)	14.7	2.8	4.8
	Column bases (kNm)	13.4	0	3.5
	All (kNm)	28.1	2.8	8.3
Test 5	Joints (kNm)	13.5	8.9	8.9
	Column bases (kNm)	12.9	9.9	12.3
	All (kNm)	26.4	18.8	21.2

However, in the case of the accelerogram with one prominent peak, the X-shaped T-stub connections dissipate higher energy than the other solutions; instead, with seismic inputs characterized by many peaks, the RBS solution has been shown to prevail, while the energy dissipation capacity of the remaining two connections is quite similar.

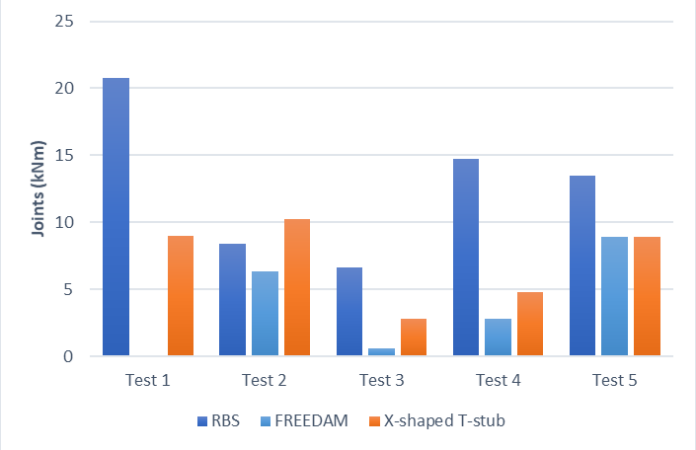

Figure 4.151 – Comparison among the results of the experimental campaigns: energy dissipated by the joints

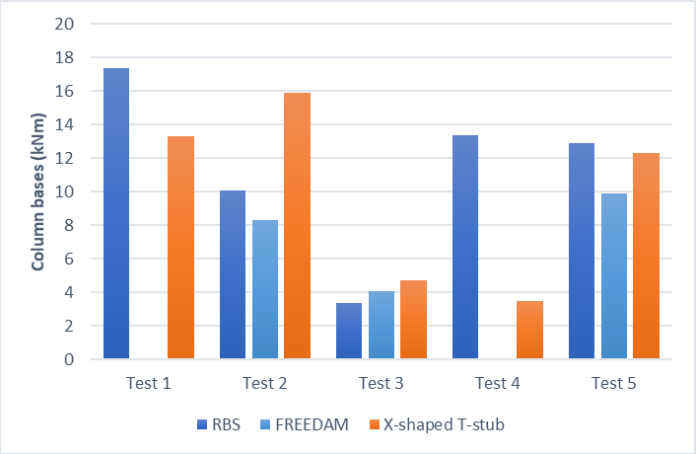

Figure 4.152 – Comparison among the results of the experimental campaigns: energy dissipated by the column bases

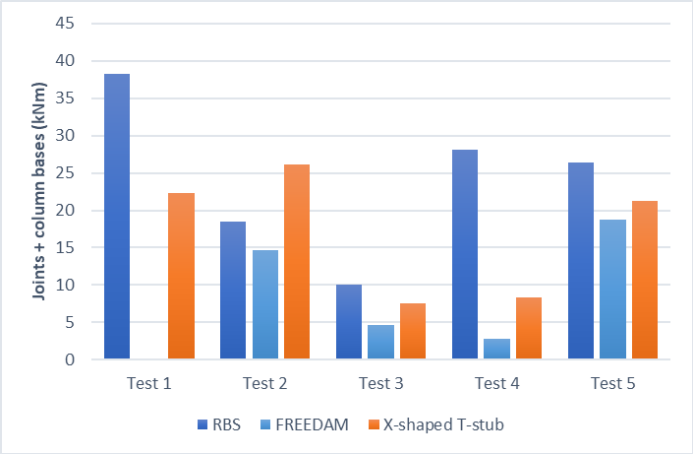

Figure 4.153 – Comparison among the results of the experimental campaigns: energy dissipated by the joints and column bases

4.10 Refined numerical model concerning the structure subjected to the 1st experimental campaign

The results discussed in paragraphs 4.6-4.8 highlight the limits of the phenomenological models currently adopted for the design of structures in predicting the behaviour of the local information. For this reason, one of the two MRFs equipped with RBS connections constituting the mock-up has been modelled through the software Abaqus.

This section's main aim consists of evaluating how a more refined model can improve the predictive results.

4.10.1 FE modelling

The geometry of the elements has been defined by extruding the profiles' sections and proper cuts to create the reduced beam section (Figure 4.154).

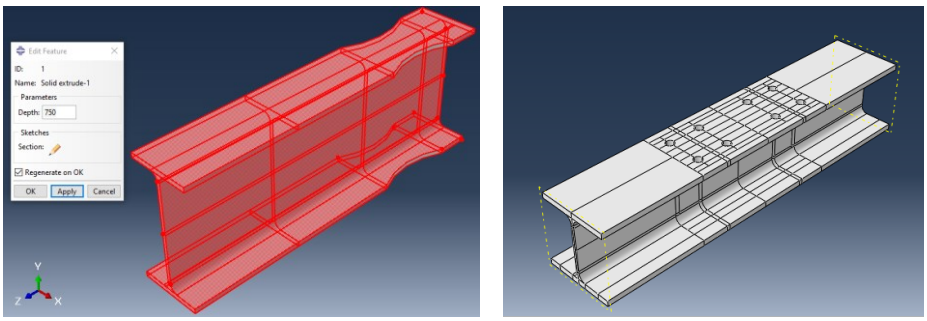

Figure 4.154 – Solid elements: RBS (left) and column (right)

The beams and columns have been modelled as solid 3D elements only in those parts close to the connections, while all the remaining parts are wire elements (Figure 4.155). The software allows assigning the geometrical properties of the cross-sections of these elements through the use of double-tee profile settings (Figure 4.156).

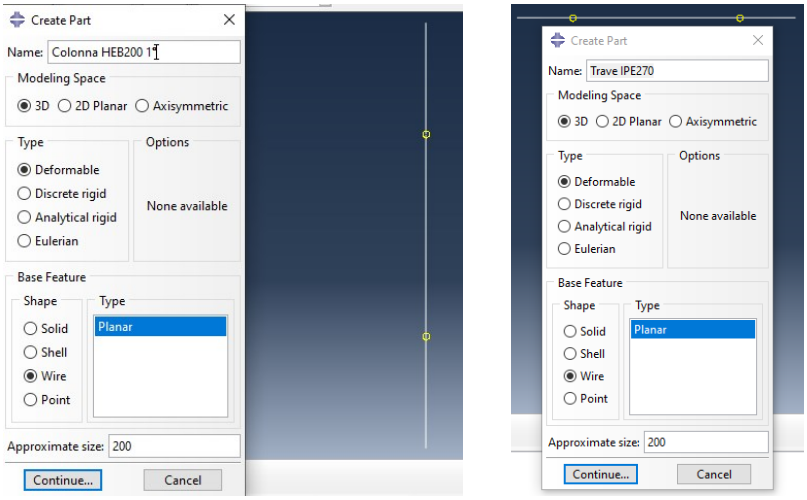

Figure 4.155 – Wire elements: column (left) and beam (right)

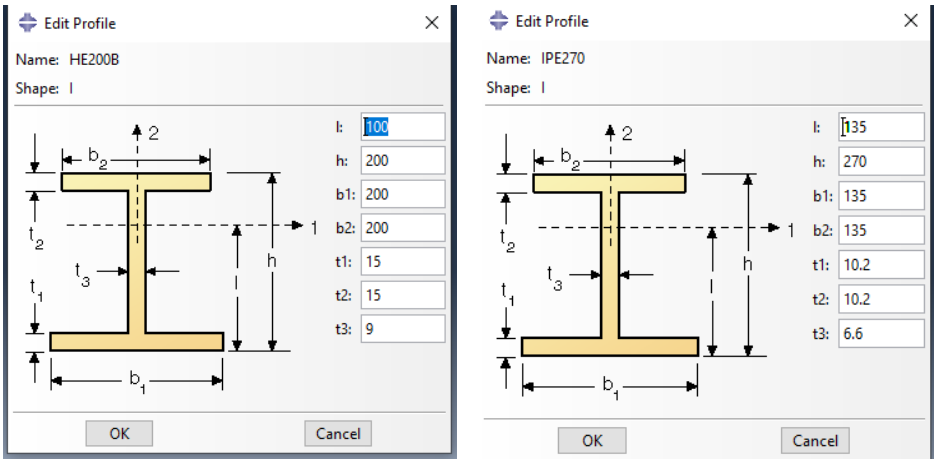

Figure 4.156 – Profiles of the wire elements: column (left) and beam (right)

The connection between the wire and solid elements has been created by employing the Coupling constraint (Figure 4.157).

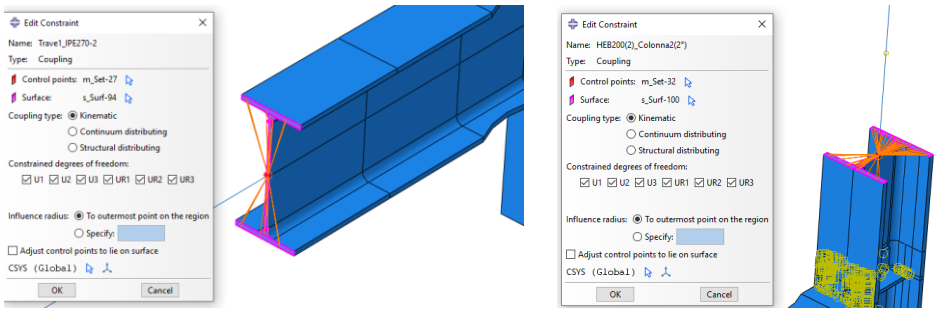

Figure 4.157 – Coupling constraints

The material properties assigned to the structural elements have been defined consistently with the results of the coupon tests obtained from the beams and columns tested with the pseudo-dynamic approach (Figure 4.158 and Figure 4.159) with a kinematic hardening rule.

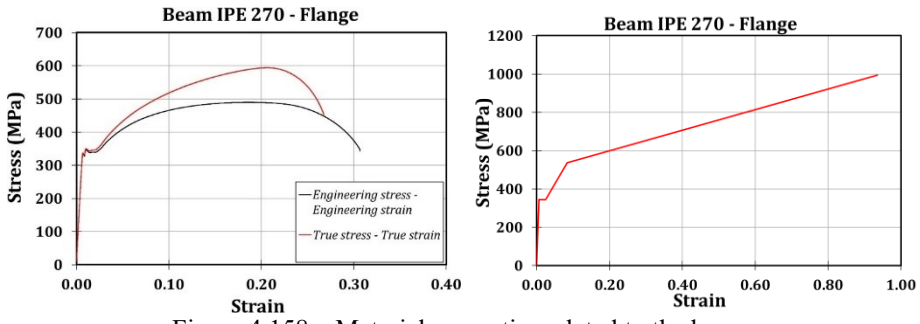

Figure 4.158 – Material properties related to the beams

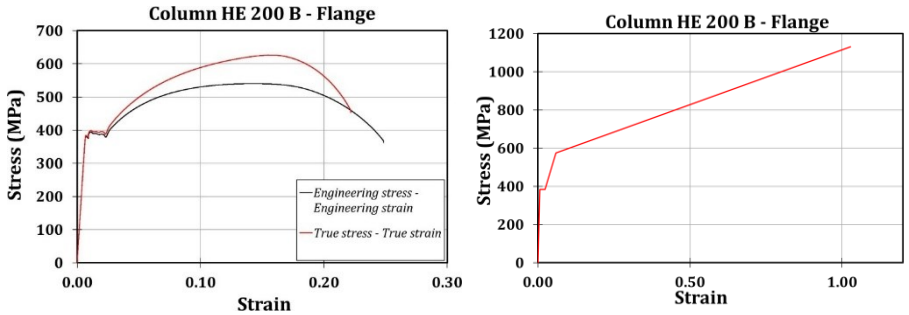

Figure 4.159 – Material properties related to the columns

All the elements have been adequately assembled (Figure 4.160).

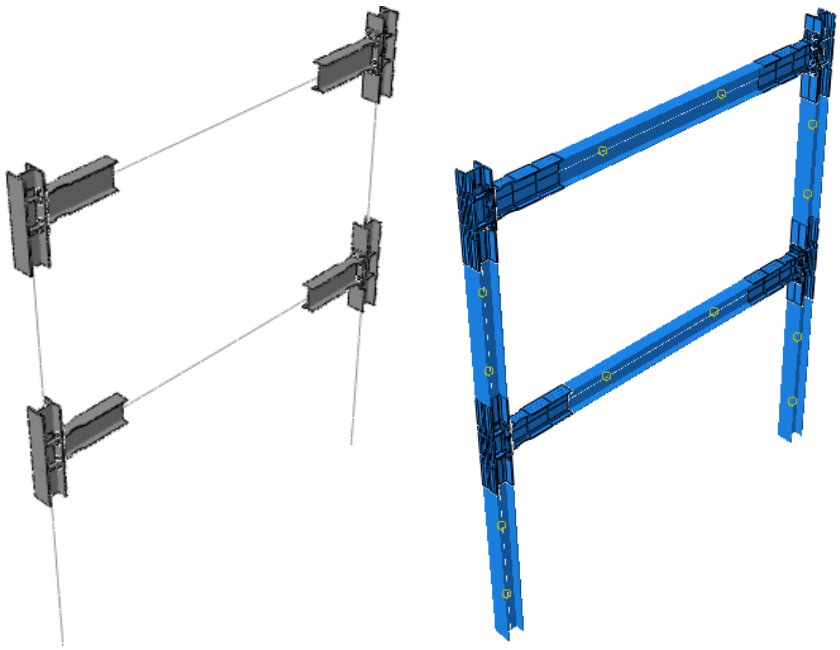

Figure 4.160 – Assembly of the frame with wire elements (left) and the solid counterpart (right)

The bolts' load has been assigned through concentrated forces in a static step prior to the definition of the analyses (Figure 4.161). The column bases have been constrained thanks to fixed supports, while the lateral-torsional effects on the frame have been prevented by employing constraints able to prevent the out-of-plane rotations of the structure (Figure 4.161).

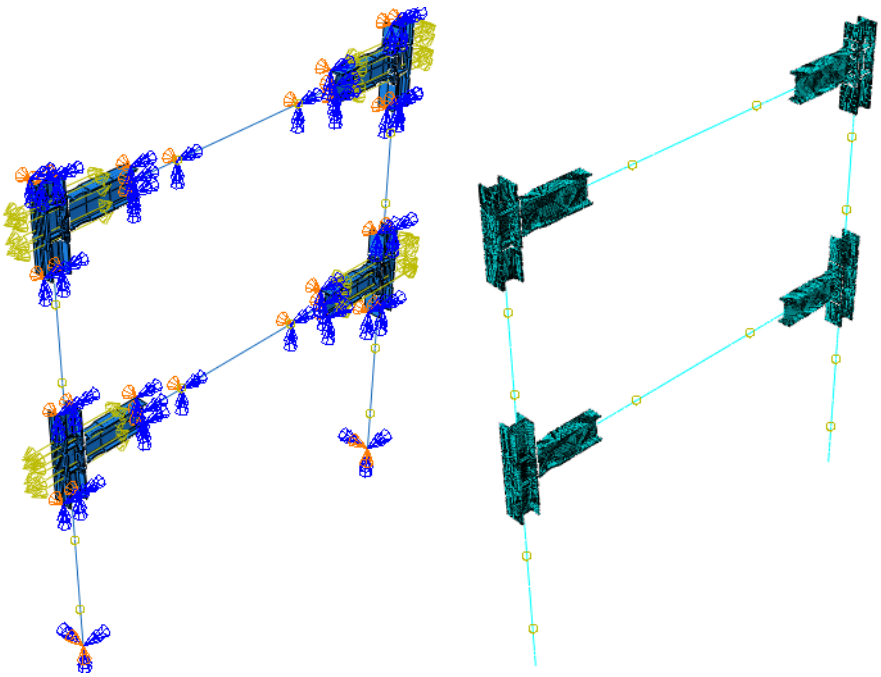

Figure 4.161 – FE model (left) and mesh size (right)

C3D8-type (8-node linear brick) elements have been used to mesh the solid members with a mesh size equal to 10 mm (Figure 4.161).

4.10.2 Static analysis

In particular, static analysis has been performed applying to the analysed structure the same floor displacements registered by the transducers during Test 1 (Imperial Valley). This section aims to understand if a refined model is able to predict in a more accurate way the local response exhibited by the structural elements.

In Figure 4.162 and Figure 4.163, the von Mises stresses and the PEEQ strains are shown in the last step of the accelerogram. It is worth noting that the FE analysis highlights plastic deformation at the flanges-to-end-plates attachments and the RBSs' centrelines, justifying the fatigue collapses that have been observed with the application of the Coalinga seismic input.

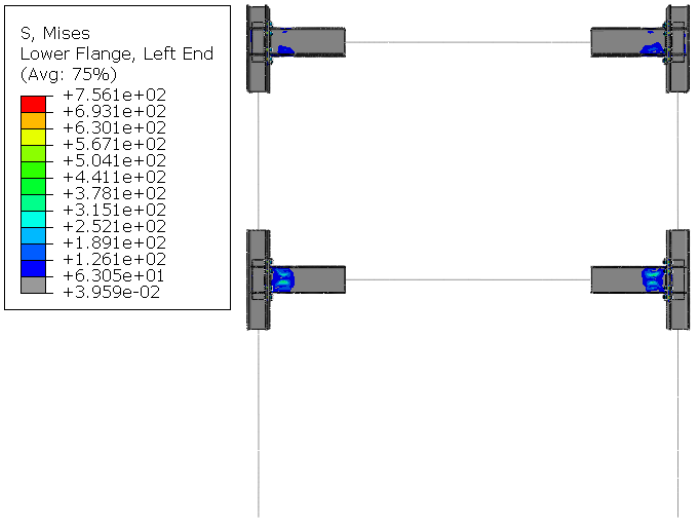

Figure 4.162 – Von Mises stresses

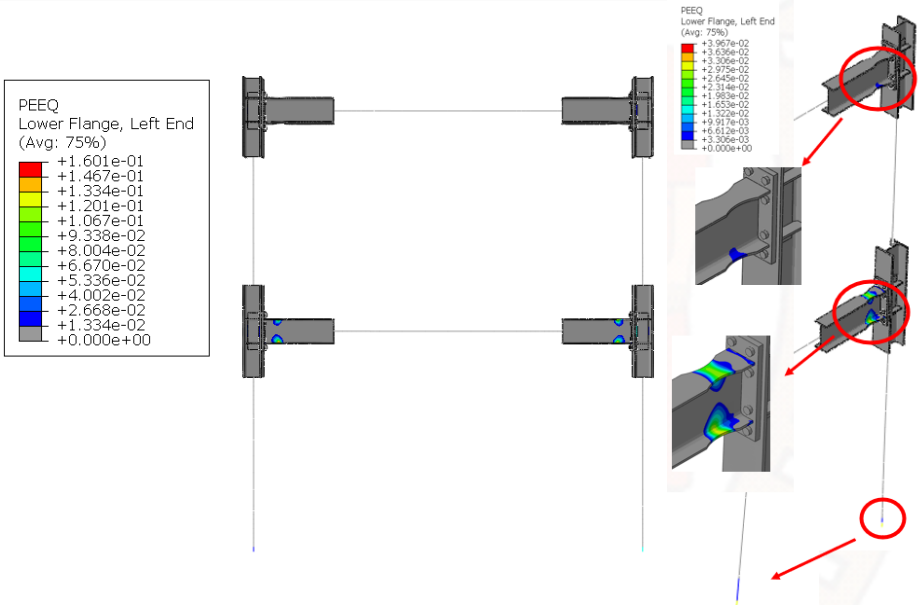

Figure 4.163 – PEEQ

From Figure 4.164 to Figure 4.167, the local response of the RBS connections is reported and compared to the experimental results and the outcomes provided by the numerical model developed in SeismoStruct.

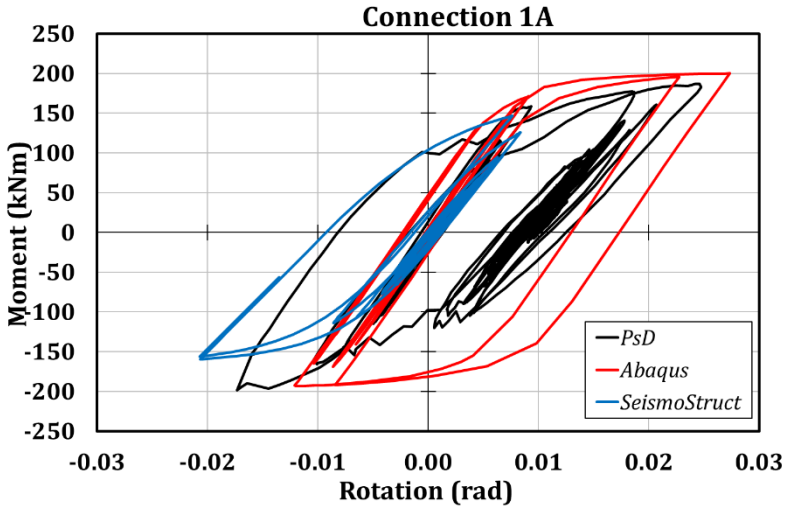

Figure 4.164 – Connection 1A: comparison among the PsD, Abaqus and SeismoStruct outcomes for Test 1

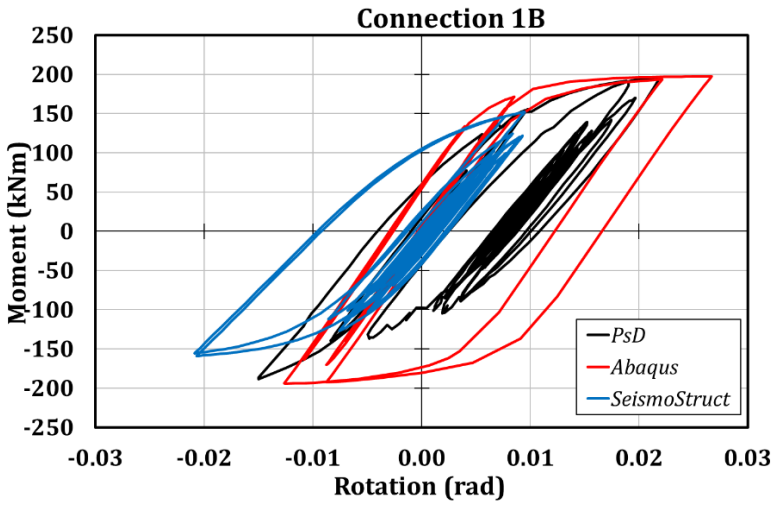

Figure 4.165 – Connection 1B: comparison among the PsD, Abaqus and SeismoStruct outcomes for Test 1

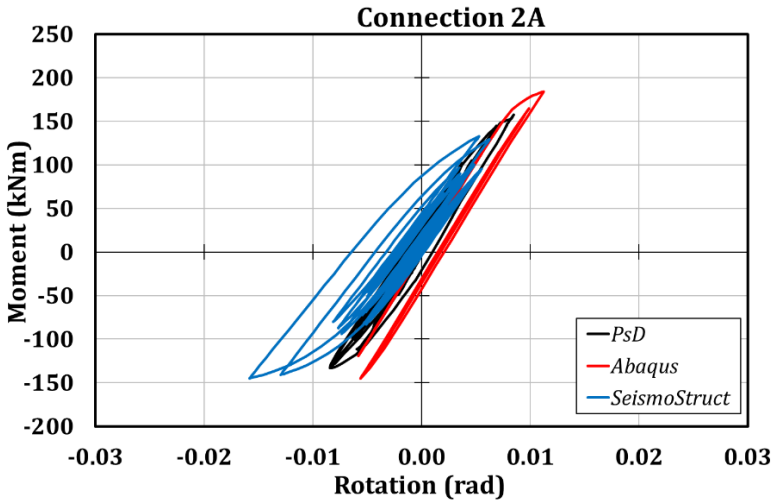

Figure 4.166 – Connection 2A: comparison among the PsD, Abaqus and SeismoStruct outcomes for Test 1

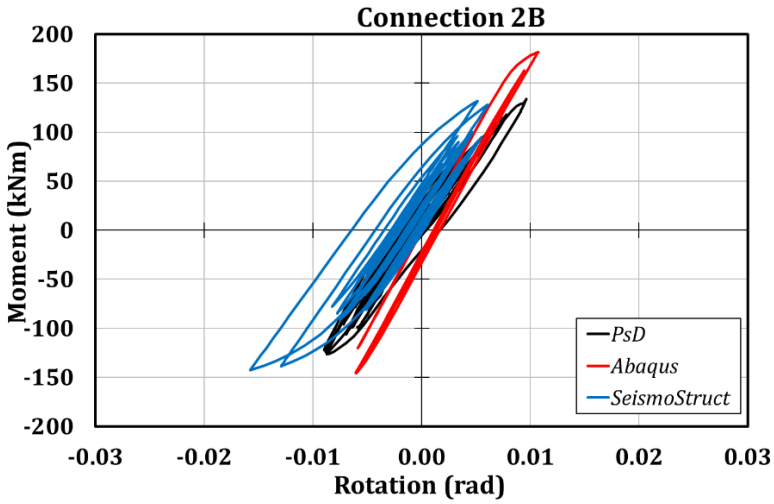

Figure 4.167 – Connection 2B: comparison among the PsD, Abaqus and SeismoStruct outcomes for Test 1

As also highlighted in Table 4.38, it is possible to conclude that the more refined model is able to evaluate with higher accuracy the stiffness and the resistance of the connections than the simplified approach developed with the phenomenological models of SeismoStruct.
However, in order to have more substantial proof of such a conclusion, it is necessary to perform a time-history analysis, which at the moment is incompatible with the computational capability provided by the hardware used to achieve the results presented in this work.

Table 4.38 – Main results related to the local behaviour of the connections

	Connection 1A			Connection 1B		
	PsD	**SeismoStruct**	**Abaqus**	**PsD**	**SeismoStruct**	**Abaqus**
Rotation (mrad)	24.72	20.68	27.36	21.72	20.89	26.69
Moment (kNm)	198.79	159.63	199.94	195.89	159.14	197.52
Energy (kNm)	9.99	7.21	11.59	7.71	7.12	11.31

	Connection 2A			Connection 2B		
	PsD	**SeismoStruct**	**Abaqus**	**PsD**	**SeismoStruct**	**Abaqus**
Rotation (mrad)	8.45	15.83	11.21	9.61	15.78	10.73
Moment (kNm)	157.47	144.97	183.81	133.75	142.69	181.65
Energy (kNm)	1.59	2.69	0.53	1.48	2.57	0.44

4.11 Personal contribution

Chapter 4 represents the novelty of the present work since it deals with the pseudo-dynamic testing of a large-scale steel structure equipped with three of the connections described in Chapter 2 and Chapter 3.
The author contributed in:

- defining the experimental set-up;
- participating in the experimental campaigns;
- post-processing the experimental data;
- providing numerical models of the tested structure through the software SeismoStruct, OpenSees and Abaqus;
- comparing the structural behaviour exhibited by the mock-up with the three analysed joints.

4.12 References

1. Mahin S.A., Shing P.B., “Pseudo-dynamic method for seismic testing”, Journal Structural Engineering, Vol. 111, pp. 1482-1503, 1985.
2. Takanashi K., Nakashima M., “Japanese activities on online testing”, Journal of Engineering Mechanics, Vol. 113, pp. 1014-1032, 1987.
3. Pegon, P., Molina, F. J. and Magonette, G., “Continuous pseudo-dynamic testing at ELSA” in Hybrid Simulation; Theory, Implementation and Applications, ed. Saouma V.E. and Sivaselvan M. V. (Taylor & Francis/Balkema) 79-88, 2008.

4. Molina, F., Magonette, G., Pegon, P., Negro, P., Viera, A., "Pseudo-Dynamic Testing. Evolution of the Method and the Testing Facilities", 2010.
5. Longo A., Nastri E., Piluso V., "Theory of plastic mechanism control: State-of-the-art", Open Construction and Building Technology Journal, Volume 8, Pages 262-278, 2014.
6. Montuori, R., Nastri, E., Piluso, V., "Advances in Theory of Plastic Mechanism Control: Closed Form Solution for Mr-Frames", Earthquake Engineering and Structural Dynamics, 2015.
7. CEN. Eurocode 8: "Design of structures for earthquake resistance - Part 1: General rules, seismic actions and rules for buildings", 2005.
8. CSI, "SAP2000 Integrated Software for Structural Analysis and Design," Computers and Structures Inc., Berkeley, California.
9. ANSI/AISC, "Prequalified Connections for Special and Intermediate Steel Moment Frames for Seismic Applications", 2016.
10. Iannone, F., Latour, M., Piluso, V. and Rizzano, G., "Experimental Analysis of Bolted Steel Beam-to-Column Connections: Component Identification," J. Earthq. Eng., vol. 15, no. 2, pp. 214–244, 2011.
11. Engelhardt, M. D., Winneburger, T., Zekany, A. J., and Potyraj, T. J., "The Dogbone Connection: Part II", Modern Steel Construct., Vol. 36. No. 8, pp.46-55, AISC, 1996.
12. Iwankiw, R. N. and Carter, C. J., "The Dogbone: A New Idea to Chew On", Modern Steel Construct., Vol. 36. No.4, pp. 18-23, AISC, Chicago IL, 1996.
13. Moore, K.S., Malley, J.O., Engelhardt, M.D., "Design of reduced Beam Section (RBS) Moment Frame Connections", AISC Structural Steel Educational Council, Moraga, CA, 1999.
14. CEN, "Eurocode 3: Design of steel structures - Part 1-8: Design of joints", 2005.
15. AISC Steel Design Guide, Murray, T. M., Summer, E. A., "Extended End-Plate Moment Connections. Seismic and Wind Applications", 2003.
16. Meng., R. L., "Design of moment end-plate connections for seismic loading", Ph. D. Thesis, College of Architecture and Urban Studies, The Virginia Polytechnic Institute and State University, USA, 1996.
17. SeismoSoft (2016). "SeismoStruct 2016 – A computer program for static and dynamic analysis of framed structures".
18. Sivaselvan, MV; Reinhorn, "HYSTERETIC MODELS FOR DETERIORATING INELASTIC STRUCTURES," J. Eng. Mech., vol. 126, no. June, pp. 633–640, 2000.
19. Chisari, C., Francavilla, A. B., Latour, M., Piluso, V., Rizzano G., Amadio, C., "Critical issues in parameter calibration of cyclic models for steel members", Engineering Structures, vol. 132, pp. 123-138, 2017.
20. McCormick, J., Aburano, H., Ikenaga, M., Nakashima, M.; Permissible Residual Deformation Levels for Building Structures Considering both Safety and Human Elements, The 14th World Conference on Earthquake Engineering, October 12-17, Beijing, China: China Earthquake Administration Ministry of Construction; 2008.
21. Francavilla, A.B.; Latour, M.; Piluso, V.; Rizzano, G.; Design criteria for beam-to-column connections equipped with friction devices, Journal of Constructional Steel Research, 172 (2020) 106240.
22. McKenna, F., OpenSees: A Framework for Earthquake Engineering Simulation, Computing in Science and Engineering 13, 58-66, 2011.

23. Di Benedetto, S., Francavilla, A.B., Latour, M., Ferrante Cavallaro, G., Piluso, V., Rizzano, G.; Seismic Behavior of Moment-Resisting Frames with Conventional and Innovative Connections, Symmetry, https://doi.org/10.3390/sym1212209, 2020.
24. Latour, M., Rizzano, G., Latour, M., Rizzano, G., Utimate Behaviour of Dissipative Tstub Connections, STESSA Conference, 2009.
25. Latour, M., Rizzano, G., Experimental Analysis and Design of X-Shaped T-stub Joints, 2011.
26. Latour, M., Rizzano, G., Design of X-shaped double split tee joints accounting for moment–shear interaction, Journal of Constructional Steel Research. 104. 10.1016/j.jcsr.2014.10.015, 2015.
27. Latour, M., Recent advances in the technologies of connection for panel structures: Design and cost analysis of different solutions with X-shaped dissipative connectors, Advances in Structural Engineering;20(3):299-315. doi:10.1177/1369433216649397, 2017.

CHAPTER 5 – Hybrid testing method with the substructuring technique

The previous chapters have investigated the static and dynamic behaviour of traditional and innovative steel beam-to-column connections. In particular, preliminary studies concerning CHS to through-all I-beam joints have been discussed, and the component method approach has been applied to define the cyclic response of such a kind of connection. This research activity has been developed to make this connection available to be adopted with traditional and well-known solutions like the dog-bone strategy. Instead, the investigations carried out in the last years on the static behaviour of RBS, FREEDAM and X-shaped T-stub joints have been reported. Furthermore, the dynamic response of these joints connecting double-tee profiles has been examined employing pseudo-dynamic tests on a large-scale steel structure equipped, alternately, with these connections' typologies. The three experimental campaigns have been performed because the mock-up has been conceived to be demountable so that the damaged connections and the column bases could be substituted at the end of the tests. However, this feature cannot fit with the connection characterized by the circular hollow section column.

For this reason, the dynamic behaviour of this connection typology could be performed by adopting the hybrid simulation with dynamic substructuring technique (HSDS) that is not conceptually far from the pseudo-dynamic method.

For clarity, in Figure 5.1 the MRF with CHS columns and dog-bone connections intended to be analysed is reported. It is characterized by one bay and two storeys and has the same geometrical properties as the mock-up tested with the pseudo-dynamic tests. This choice ensures the comparison between the results of the pseudo-dynamic and hybrid simulation with dynamic substructure tests allowing the possibility to assess the behaviour of two structures characterized by identical beams, dog-bones, masses, and differing only in the columns' profiles.

The columns should be adequately selected fulfilling the design procedures already applied in Chapter 4. In particular, S355 steel grade circular hollow section columns characterized by an external diameter of 323.9 mm and thickness of 6.3 mm are expected to be selected. In fact, complying with the Theory of Plastic Mechanism Control, this profile has the same plastic bending resistance as the HEB200 sections adopted for the mock-up subjected to the pseudo-dynamic tests. Therefore, the beams will be S275 steel grade IPE270 profiles. Since the HEB200 and CHS323.9/6.3 have the same bending resistance but differ in the inertia modulus (the tubular profile has inertia higher by about 40% than the double-tee solution), it is expected that the structure with tubular columns is stiffer than the other solution. Instead, it is interesting to assess how the connections' dissipative behaviour changes.

However, a more detailed design of the structural elements and the dog-bone will be carried out.

In Figure 5.1 the analysed frame comprises two parts highlighted with different colours: black for those structural components intended to be numerically simulated; red for the physical substructure.

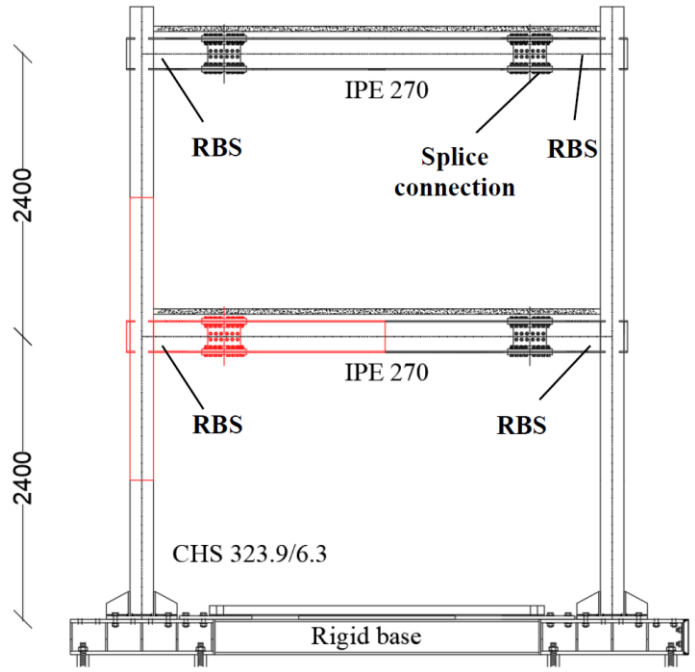

Figure 5.1 – Frame intended to be analysed: numerical substructure in black and physical substructure in red

The physical substructure will be tested according to the experimental layout shown in Figure 5.2, in which the specimen is subjected to a 90° rotation for compatibility issues. For clarity, it is worth highlighting that the physical substructure is characterized by a column with a length of 2400 mm (which corresponds to the interstorey height) and a beam with a length equal to 2000 mm (which corresponds to the half span of the bay). These geometric properties have been selected so that the beam and the column ends of the physical substructure are representative of those sections of the analysed frame in seismic conditions where the bending moments intersect the columns' axes. This occurrence allows using a roller and a hinge at the column ends and a hinge at the beam end to apply the required forces or displacements through the actuators. In particular, the actuator connected to the CHS profile can transmit only the axial load to the column; instead, the actuator applied to the beam end can apply the displacement history. In Figure 5.2 only a schematic representation of the experimental layout is reported; a more detailed design will be carried out in the future.

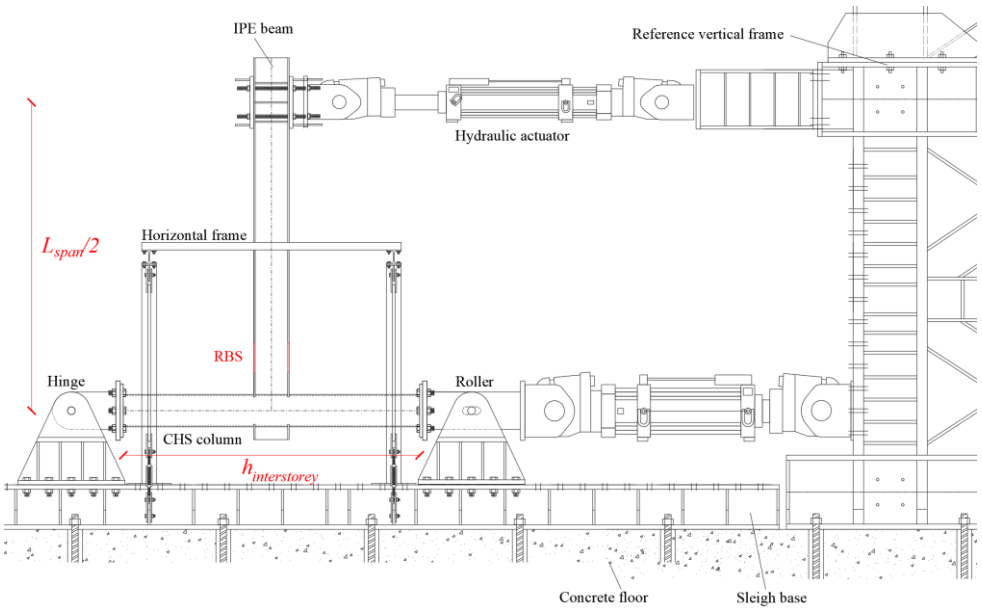

Figure 5.2 – Experimental layout of the physical substructure

Instead, the numerical substructure will be modelled through Simulink software; in particular, the structural members will be modelled thanks to elastic elements, while the nonlinear behaviour will be achieved through the component approach studied in Chapter 2 for the CHS to I-beam connection and a rotational spring to model the reduced section of the beam. It is worth highlighting that the above-studied relationships will be appropriately calibrated through the Bouc-Wen model complying with Eqs. 2.36-2.57, and thanks to the MultiCal tool to calibrate the RBS. The detail concerning the numerical modelling of the connection is shown in Figure 5.3.

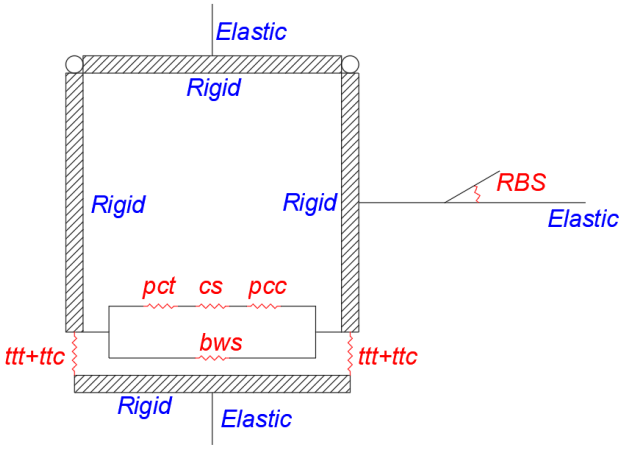

Figure 5.3 – Detail of the connection in the numerical substructure (CHS to through I-beam + RBS)

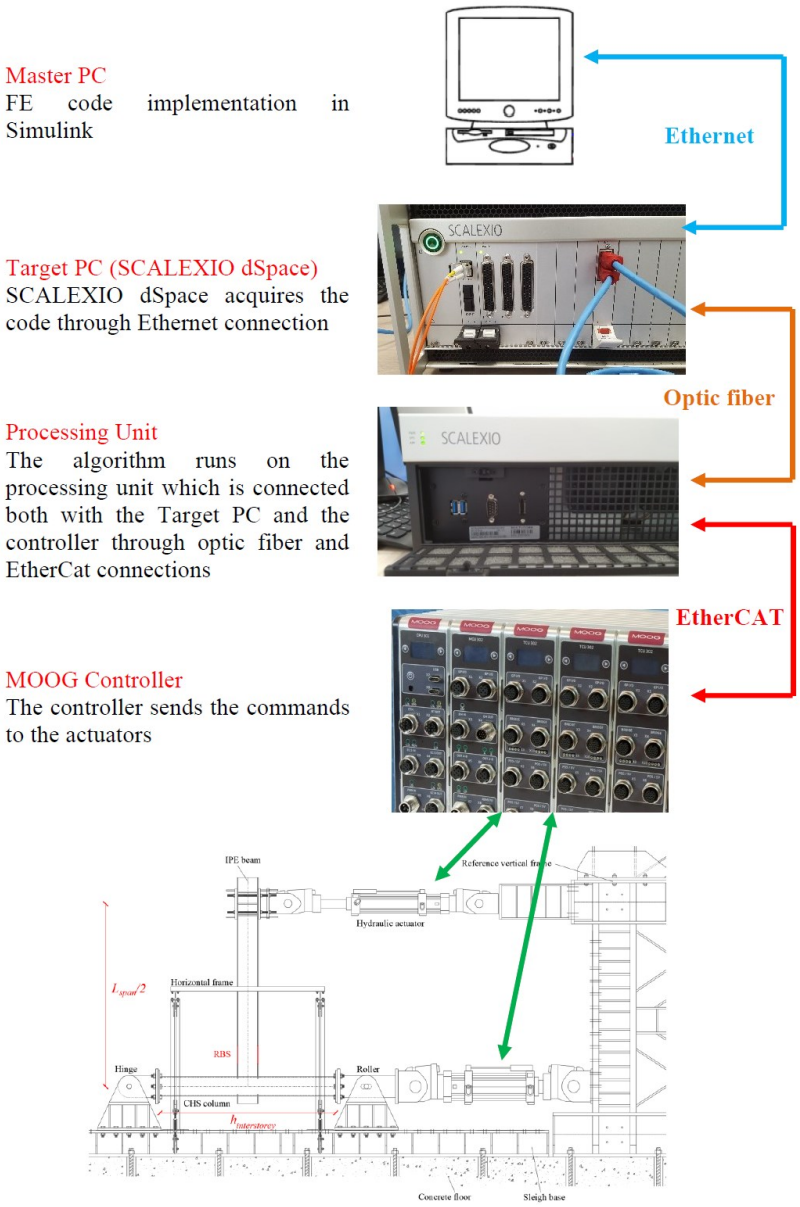

Figure 5.4 – Main components and connectivity of the hybrid simulation system

The main components and connectivity of the hybrid simulation system are shown in Figure 5.4. A Windows-based Master PC runs the Matlab-Simulink environment in which the numerical substructure is modelled and the solver algorithm is implemented. Simulink allows executing a C-code, which is loaded in the ControlDesk of the SCALEXIO dSpace simulator through an Ethernet connection. SCALEXIO dSpace plays the role of Target PC, which is connected to a processing unit through an optic fiber. An E3-1275v3 processor characterizes the processing unit with a 3.5 GHz clock, 4 cores and a RAM of 4 GB. It enhances the speed in solving the implemented algorithm and transfers to the MOOG controller the displacements/loads intended to be applied to the specimen. EtherCAT cables ensure a fast interaction between the controller and the processing unit. Then the controller transfers/recorders the displacements/loads from/to the actuators.

Since, at the moment, the STRENGTH laboratory of the University of Salerno does not own the hardware and software to perform these kinds of tests, the present chapter briefly discusses this testing strategy since it could be an interesting future application to the case study reported above. The following paragraphs do not provide any novelty in this research branch, but they can represent the first steps for future investigations.

5.1 Hybrid simulation with dynamic substructuring technique

The hybrid simulation with dynamic substructuring (HSDS) technique is a procedure to characterize the dynamic response of a system whose components are in part physically tested (physical substructure or PS) and in part numerically simulated (numerical substructure or NS) [1]. In fact, at the same time, the implemented code procedure is able to solve the NS and accounts for the response of the PS so that compatibility between the two systems can be ensured. In particular, the code advances solving the equations of motion step by step through a compatible time integrator and interaction between NS and PS. For clarity, the testing procedure consists of imposing the numerically assessed displacements to the specimen through the actuators to a well-discretized number of degrees of freedom, which in most cases represent the floors' locations. Obviously, the success of this strategy depends both on the tested components and on their interface with the numerical part [2]. In fact, the interface problem is essential, and it can be solved only if the kinematic and static equilibria are fulfilled. Furthermore, because of the imposed displacements, reaction forces are measured by the load cells of the actuators and are used for the solution of the equation of motion, ensuring the advancement of the integration loop [1].

This approach appears as a very interesting solution when peculiar devices have to be tested as part of very geometrically complex structures, provided that the numerical substructure does not endow several distributed nonlinearities. However, another issue is related to the interface between the numerical and the physical substructures; in fact, usually, the physical substructure is characterized by some degrees of freedom located in such a way to make the interface compatibility more difficult. In order to overcome such a problem, when the analyzed structure (NS and PS) is representative of the frame of a classic building, usually the adoption of the pins is at the beams or columns sections where the interface degrees of freedom are located. In fact, the pins simplify the interface between NS and PS by excluding the control of rotations and bending moments at the boundaries.

To perform the HSDS procedure, the interface between NS and PS must be ensured both by the load cells and transducers of the actuators and the implemented numerical code by fulfilling these requirements: i) kinematic compatibility; ii) force balance.

Besides the interface problem, another relevant aspect is the time integration employed to solve the numerical simulation and apply and register the experimental response. The recent advances in servohydraulic control systems allow performing the tests by adopting sampling times of about 1 ms or below. This topic can lead to another aspect related to the parallel advancement of NS and PS. In fact, the current codes allow solving the step-by-step equations of motions at a different sample rate of the PS. This aspect can be a benefit because it can provide much time to the NS to find the solution in a defined instant; nevertheless, it is clear that a synchronization of the two time-integration processes is essential. For this reason, parallel partitioned time integration algorithms represent an interesting strategy to solve this issue. In fact, without any assumptions, they ensure the displacement histories' continuous application, avoiding hold interruptions.

Among the different suggested implementations, the Finite Element Tearing and Interconnecting (FETI) method, proposed in 1991 by Farhat and Roux [3, 4], represents a promising solution referring to the cases of quasi-static mechanical problems. In order to endure the coupling between

the analyzed substructures, Lagrange multipliers are considered continuity conditions at the interface nodes.

Gravouil [5] proposed the multi-time-step coupling GC method, which demonstrated to be unconditionally stable in coupling Newmark schemes with different time steps in different subdomains, provided that the subdomains satisfied their stability requirements. However, because of this approach's lack of concurrency, Pegon and Magonette [6, 7] implemented an advanced parallel partitioned algorithm (PM method). This algorithm is based on the GC method, but the numerical and physical subdomains run in parallel, fulfilling the simultaneity and continuity requirements. The main benefits provided by this strategy have been deeply studied by Bonelli [8]. The PM method has been subjected to many enhancements [9-13]. For instance, Bursi et al. [13] extended the application of this approach through the introduction of the Generalized-α method, which has the main benefit of controlling the damping feature that allows for filtering out spurious high-frequency components but preserving low-frequency components. In addition, Prakash and Hjelmstad [9] proposed the PH method, a staggered approach characterized by the lack of the calculation of the interface reactions in the time step.

In 2012 Bursi et al. [13] proposed two procedures (Linearly Stable Real-Time or LSRT-2, and Parallel LSRT-2 or PLSRT-2) for the parallel implementation of partitioned schemes. These strategies explicitly solve the interface problem through Lagrange multipliers and proceed to the solution in all the subdomains.

5.2 Partitioned generalized-α (PG-α) time integration algorithm

In order to effectively apply the HSDS technique, Abbiati et al. [14] have proposed the partitioned generalized-α (PG-α) method. This solver allows solving the system of equations of motion in the state-space form:

$$\boldsymbol{M}\dot{\boldsymbol{Y}} + \boldsymbol{R}(\boldsymbol{Y}) = \boldsymbol{F}(t) \tag{5.1}$$

In particular:

$$\boldsymbol{Y} = \begin{bmatrix} \boldsymbol{u} \\ \boldsymbol{v} \\ \boldsymbol{s} \end{bmatrix} \tag{5.2}$$

$$\boldsymbol{M} = \begin{bmatrix} \boldsymbol{I} & \boldsymbol{0} & \boldsymbol{0} \\ \boldsymbol{0} & \boldsymbol{m} & \boldsymbol{0} \\ \boldsymbol{0} & \boldsymbol{0} & \boldsymbol{I} \end{bmatrix} \tag{5.3}$$

$$\boldsymbol{R} = \begin{bmatrix} -\boldsymbol{v} \\ \boldsymbol{r}(\boldsymbol{u}, \boldsymbol{v}, \boldsymbol{s}) \\ \boldsymbol{g}(\boldsymbol{u}, \boldsymbol{v}, \boldsymbol{s}) \end{bmatrix} \tag{5.4}$$

$$\boldsymbol{F}(t) = \begin{bmatrix} \boldsymbol{0} \\ \boldsymbol{f}(t) \\ \boldsymbol{0} \end{bmatrix} \tag{5.5}$$

For clarity, $\boldsymbol{u}$, $\boldsymbol{v}$ and $\boldsymbol{s}$ represent, respectively, the displacement, velocity and additional state vectors. In particular, $\boldsymbol{s}$ is strictly related to the nonlinearities that the system can be composed of. Instead, $\boldsymbol{r}(\boldsymbol{u}, \boldsymbol{v}, \boldsymbol{s})$ and $\boldsymbol{g}(\boldsymbol{u}, \boldsymbol{v}, \boldsymbol{s})$ represent, respectively, the vector associated with the non-linear restoring force and the non-linear function modelling the evolution of the state vector $\boldsymbol{s}$. $\boldsymbol{m}$ is the mass matrix, $\boldsymbol{f}(t)$ is the time-dependent external load, while $\boldsymbol{I}$ and $\boldsymbol{0}$ are, respectively, the identity and zero matrices.

Referring to the case of linear systems, Eqs. 5.1-5.5 simplify in:

$$\boldsymbol{M}\dot{\boldsymbol{Y}} + \boldsymbol{K}\boldsymbol{Y} = \boldsymbol{F}(t) \tag{5.6}$$

$$\boldsymbol{Y} = \begin{bmatrix} \boldsymbol{u} \\ \boldsymbol{v} \end{bmatrix} \tag{5.7}$$

$$\boldsymbol{M} = \begin{bmatrix} \boldsymbol{I} & \boldsymbol{0} \\ \boldsymbol{0} & \boldsymbol{m} \end{bmatrix} \tag{5.8}$$

$$\boldsymbol{K} = \begin{bmatrix} \boldsymbol{0} & -\boldsymbol{I} \\ \boldsymbol{k} & \boldsymbol{c} \end{bmatrix} \tag{5.9}$$

$$\boldsymbol{F}(t) = \begin{bmatrix} \boldsymbol{0} \\ \boldsymbol{f}(t) \end{bmatrix} \tag{5.10}$$

$\boldsymbol{k}$ and $\boldsymbol{c}$ represent the stiffness and damping matrices, respectively.

Before describing the partitioned algorithm, the original monolithic G-α algorithm (MG-α) proposed by Jansen et al. [15] is briefly reported. This solver allows integrating the equations of motion between subsequent time steps (Eq. 5.11): from t_n to t_{n+1}.

$$\boldsymbol{M}\dot{\boldsymbol{Y}}_{\boldsymbol{n+\alpha_m}} + \boldsymbol{R}\left(\boldsymbol{Y}_{\boldsymbol{n+\alpha_f}}\right) = \boldsymbol{F}_{\boldsymbol{n+\alpha_f}} \tag{5.11}$$

In particular:

$$\dot{\boldsymbol{Y}}_{\boldsymbol{n+\alpha_m}} = (1-\alpha_m)\dot{\boldsymbol{Y}}_{\boldsymbol{n}} + \alpha_m\dot{\boldsymbol{Y}}_{\boldsymbol{n+1}} \tag{5.12}$$

$$\boldsymbol{Y}_{\boldsymbol{n+\alpha_f}} = \left(\boldsymbol{1}-\boldsymbol{\alpha}_f\right)\dot{\boldsymbol{Y}}_{\boldsymbol{n}} + \boldsymbol{\alpha}_f\boldsymbol{Y}_{\boldsymbol{n+1}} \tag{5.13}$$

$$\boldsymbol{Y}_{\boldsymbol{n+1}} = \boldsymbol{Y}_{\boldsymbol{n}} + \dot{\boldsymbol{Y}}_{\boldsymbol{n}}(1-\gamma)\Delta t + \dot{\boldsymbol{Y}}_{\boldsymbol{n+1}}\gamma\Delta t \tag{5.14}$$

α_m, α_f and γ are parameters defining the algorithm setting and depend on the infinity spectral radius ρ_∞:

$$\alpha_m = \frac{3-\rho_\infty}{2(1+\rho_\infty)} \tag{5.15}$$

$$\alpha_f = \frac{1}{1+\rho_\infty} \tag{5.16}$$

$$\gamma = \frac{1}{2} + \alpha_m - \alpha_f \tag{5.17}$$

If $\rho_\infty = 0$, the proposed solver does not consider those components of the systems characterized by higher frequencies than the sampling frequency; instead, if $\rho_\infty = 1$, the G-α method simplifies in the trapezoidal rule.

Brüls and Arnolds [16] adopted the following equation:

$$(1-\alpha_m)\boldsymbol{V}_{\boldsymbol{n}} + \alpha_m\boldsymbol{V}_{\boldsymbol{n+1}} = \left(\boldsymbol{1}-\boldsymbol{\alpha}_f\right)\dot{\boldsymbol{Y}}_{\boldsymbol{n}} + \boldsymbol{\alpha}_f\boldsymbol{Y}_{\boldsymbol{n+1}} + \boldsymbol{o}(\Delta t^2) \tag{5.18}$$

In such a way, it is possible to write:

$$\boldsymbol{M}\dot{\boldsymbol{Y}}_{\boldsymbol{n+1}} + \boldsymbol{R}(\boldsymbol{Y}_{\boldsymbol{n+1}}) = \boldsymbol{F}_{\boldsymbol{n+1}} \tag{5.19}$$

with

$$\boldsymbol{Y}_{\boldsymbol{n+1}} = \boldsymbol{Y}_{\boldsymbol{n}} + \boldsymbol{V}_{\boldsymbol{n}}(1-\gamma)\Delta t + \boldsymbol{V}_{\boldsymbol{n+1}}\gamma\Delta t \tag{5.20}$$

$$\boldsymbol{V}_{\boldsymbol{n+1}} = \dot{\boldsymbol{Y}}_{\boldsymbol{n}}\frac{1-\alpha_m}{\alpha_f} - \boldsymbol{V}_{\boldsymbol{n}}\frac{1-\alpha_m}{\alpha_m} + \dot{\boldsymbol{Y}}_{\boldsymbol{n+1}}\frac{\alpha_f}{\alpha_m} \tag{5.21}$$

Starting from the previs equations, it is possible to derive a predictor-corrector procedure within the integration time step $\Delta t = t_{n+1} - t_n$.

Firstly, the state predictor $[\widetilde{\boldsymbol{Y}}_{\boldsymbol{n+1}}, \widetilde{\boldsymbol{V}}_{\boldsymbol{n+1}}]$ at the time step t_{n+1} is assessed:

$$\widetilde{\boldsymbol{Y}}_{\boldsymbol{n+1}} = \boldsymbol{Y}_{\boldsymbol{n}} + \dot{\boldsymbol{Y}}_{\boldsymbol{n}}\gamma\Delta t\frac{1-\alpha_f}{\alpha_m} + \boldsymbol{V}_{\boldsymbol{n}}\Delta t\frac{\alpha_m-\gamma}{\alpha_m} \tag{5.22}$$

$$\widetilde{\boldsymbol{V}}_{\boldsymbol{n+1}} = \dot{\boldsymbol{Y}}_{\boldsymbol{n}}\frac{1-\alpha_f}{\alpha_m} - \boldsymbol{V}_{\boldsymbol{n}}\frac{1-\alpha_m}{\alpha_m} \tag{5.23}$$

Then, $\dot{\boldsymbol{Y}}_{\boldsymbol{n+1}}$ can be calculated:

$$\dot{\boldsymbol{Y}}_{\boldsymbol{n+1}} = \boldsymbol{D}^{-1}\left(\boldsymbol{F}_{\boldsymbol{n+1}} - \boldsymbol{R}\left(\widetilde{\boldsymbol{Y}}_{\boldsymbol{n+1}}\right)\right) \tag{5.24}$$

Considering that the matrix $\boldsymbol{D} = \boldsymbol{M} + \nabla_{Y_0}\boldsymbol{R}\gamma\Delta t\,\alpha_f/\alpha_m$ is evaluated at the beginning of the analysis starting from the knowledge of the mass matrix ($\boldsymbol{M}$) and the Jacobian ($\nabla_{Y_0}\boldsymbol{R}$) of the generalized restoring force vector at zero state.
In this way, the state at t_{n+1} can be defined:

$$\boldsymbol{Y_{n+1}} = \tilde{\boldsymbol{Y}}_{\boldsymbol{n+1}} + \dot{\boldsymbol{Y}}_{\boldsymbol{n+1}}\gamma\Delta t\,\alpha_f/\alpha_m \tag{5.25}$$

$$\boldsymbol{V_{n+1}} = \tilde{\boldsymbol{V}}_{\boldsymbol{n+1}} + \dot{\boldsymbol{Y}}_{\boldsymbol{n+1}}\,\alpha_f/\alpha_m \tag{5.26}$$

The main formulations necessary for implementing the partitioned G-α time integration algorithm are reported. This solver has been conceived to avoid load relaxation of the PS in the case of large time steps adopted in the classic approaches. In particular, in this case, the partitioned time integration algorithm can coordinate the PS and NS subdomains that run through monolithic processes at different time steps, compatibly with the frequency of the acquiring data system and the computational capacity of the hardware/software. In this way, the actuators can move without holding ramps, and the following system of equations is solved:

$$\begin{cases} \boldsymbol{M^N\dot{Y}^N_{n+1}} + \boldsymbol{R^N}\left(\boldsymbol{Y^N_{n+1}}\right) = \boldsymbol{L^N\Lambda_{n+1}} + \boldsymbol{F^N_{n+1}} \\ \boldsymbol{M^P\dot{Y}^P_{n+j/ss}} + \boldsymbol{R^P}\left(\boldsymbol{Y^P_{n+j/ss}}\right) = \boldsymbol{L^P\Lambda_{n+j/ss}} + \boldsymbol{F^P_{n+j/ss}} \end{cases} \tag{5.27}$$

$$\boldsymbol{G^N\dot{Y}^N_{n+1}} + \boldsymbol{G^P\dot{Y}^P_{n+1}} = \boldsymbol{0} \tag{5.28}$$

$\boldsymbol{G}$ and $\boldsymbol{L}$ are Boolean matrices to localize the interface forces and define the compatibility equations, while $\boldsymbol{\Lambda_{n+1}}$ and $\boldsymbol{\Lambda_{n+j/ss}}$ represent the Lagrange multipliers to link the physical and numerical substructures.
The task sequence of the PG-α method, as conceived by Abbiati et al. [14], is reported in Figure 5.5. This image highlights that the PS and NS integration processes run in parallel even though an assembly procedure has to ensure the coupling of the two subdomains at each time step of NS.

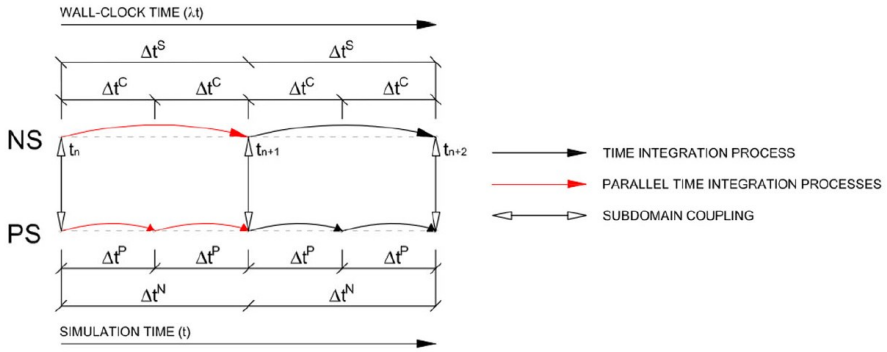

Figure 5.5 – Task sequence of the PG-α method [14]

Figure 5.5 shows that different time steps, Δt^N and Δt^P, are used for NS and PS. Usually, Δt^N is equal to 1 ms. Δt^S is the maximum solving time to compute the NS response, while Δt^C is the actuator controller time step. Instead, *ss* is a subcycling parameter used to discretize the numerical solver.
The procedure to implement the partitioned G-α time integration algorithm is reported.
The first step consists in initializing the coupled solution:

$$\boldsymbol{V_0} = \dot{\boldsymbol{Y}}_{\boldsymbol{0}} = \boldsymbol{M^{-1}}\left(\boldsymbol{F_0} - \boldsymbol{R}(\boldsymbol{Y_0})\right) \tag{5.29}$$

The interface force field represented by the Lagrange multipliers can be defined according to one of these two equations:

$$\boldsymbol{\Lambda_0} = \boldsymbol{L^{N^T}}\left(\boldsymbol{M^N\dot{Y}^N_0} + \boldsymbol{R^N}\left(\boldsymbol{Y^N_0}\right) - \boldsymbol{F^N_0}\right) \tag{5.30}$$

$$\boldsymbol{\Lambda_0} = \boldsymbol{L^{P^T}}\left(\boldsymbol{M^P}\dot{\boldsymbol{Y}}_{\boldsymbol{0}}^{\boldsymbol{P}} + \boldsymbol{R^P}\left(\boldsymbol{Y_0^P}\right) - \boldsymbol{F_0^P}\right) \quad (5.31)$$

Usually, the procedure starts with zero initial conditions to skip Eqs. 5.29-5.31.

The code must be implemented using a time integration loop over n from 0 to N, where N represents the algorithm's maximum number of time steps. The free state predictor $[\widetilde{\boldsymbol{Y}}_{\boldsymbol{n+1}}^{\boldsymbol{N,free}}, \widetilde{\boldsymbol{V}}_{\boldsymbol{n+1}}^{\boldsymbol{N,free}}]$ at the time step t_{n+1} is assessed:

$$\widetilde{\boldsymbol{Y}}_{\boldsymbol{n+1}}^{\boldsymbol{N,free}} = \boldsymbol{Y_{n+1}^N} + \dot{\boldsymbol{Y}}_{\boldsymbol{n}}^{\boldsymbol{N}}\gamma\Delta t^N\frac{1-\alpha_f}{\alpha_m} + \boldsymbol{V_n^N}\Delta t^N\frac{\alpha_m-\gamma}{\alpha_m} \quad (5.32)$$

$$\widetilde{\boldsymbol{V}}_{\boldsymbol{n+1}}^{\boldsymbol{N,free}} = \dot{\boldsymbol{Y}}_{\boldsymbol{n}}^{\boldsymbol{N}}\frac{1-\alpha_f}{\alpha_m} - \boldsymbol{V_n^N}\frac{1-\alpha_m}{\alpha_m} \quad (5.33)$$

Thus, the state rate $\dot{\boldsymbol{Y}}_{\boldsymbol{n+1}}^{\boldsymbol{N,free}}$ can be assessed.

$$\dot{\boldsymbol{Y}}_{\boldsymbol{n+1}}^{\boldsymbol{N,free}} = \boldsymbol{D^{N^{-1}}}\left(\boldsymbol{F_{n+1}^{N,free}} - \boldsymbol{R^N}\left(\widetilde{\boldsymbol{Y}}_{\boldsymbol{n+1}}^{\boldsymbol{N,free}}\right)\right) \quad (5.34)$$

where $\boldsymbol{D^N} = \boldsymbol{M^N} + \nabla_{Y_0^N}\boldsymbol{R^N}\gamma\Delta t\,\alpha_f/\alpha_m$ is calculated at the first step of the procedure.

The free state $[\boldsymbol{Y}_{\boldsymbol{n+1}}^{\boldsymbol{N,free}}, \boldsymbol{V}_{\boldsymbol{n+1}}^{\boldsymbol{N,free}}]$ at the time step t_{n+1} can be calculated:

$$\boldsymbol{Y}_{\boldsymbol{n+1}}^{\boldsymbol{N,free}} = \widetilde{\boldsymbol{Y}}_{\boldsymbol{n+1}}^{\boldsymbol{N,free}} + \dot{\boldsymbol{Y}}_{\boldsymbol{n+1}}^{\boldsymbol{N,free}}\gamma\Delta t^N\,\alpha_f/\alpha_m \quad (5.35)$$

$$\boldsymbol{V}_{\boldsymbol{n+1}}^{\boldsymbol{N,free}} = \widetilde{\boldsymbol{V}}_{\boldsymbol{n+1}}^{\boldsymbol{N,free}} + \dot{\boldsymbol{Y}}_{\boldsymbol{n+1}}^{\boldsymbol{N,free}}\,\alpha_f/\alpha_m \quad (5.36)$$

The subsequent step calculates the PS free solution through a subcycling loop from 1 to *ss*. The free state predictor $[\widetilde{\boldsymbol{Y}}_{\boldsymbol{n+j/ss}}^{\boldsymbol{P,free}}, \widetilde{\boldsymbol{V}}_{\boldsymbol{n+j/ss}}^{\boldsymbol{P,free}}]$ is assessed at the time $t_{n+j/ss}$.

$$\widetilde{\boldsymbol{Y}}_{\boldsymbol{n+j/ss}}^{\boldsymbol{P,free}} = \boldsymbol{Y}_{\boldsymbol{n+(j-1)/ss}}^{\boldsymbol{P}} + \dot{\boldsymbol{Y}}_{\boldsymbol{n+(j-1)/ss}}^{\boldsymbol{P}}\gamma\Delta t^P\frac{1-\alpha_f}{\alpha_m} + \boldsymbol{V}_{\boldsymbol{n+(j-1)/ss}}^{\boldsymbol{P}}\Delta t^P\frac{\alpha_m-\gamma}{\alpha_m} \quad (5.37)$$

$$\widetilde{\boldsymbol{V}}_{\boldsymbol{n+j/ss}}^{\boldsymbol{P,free}} = \dot{\boldsymbol{Y}}_{\boldsymbol{n+(j-1)/ss}}^{\boldsymbol{P}}\frac{1-\alpha_f}{\alpha_m} - \boldsymbol{V}_{\boldsymbol{n+(j-1)/ss}}^{\boldsymbol{P}}\frac{1-\alpha_m}{\alpha_m} \quad (5.38)$$

Thus, the state rate $\dot{\boldsymbol{Y}}_{\boldsymbol{n+j/ss}}^{\boldsymbol{P,free}}$ can be assessed.

$$\dot{\boldsymbol{Y}}_{\boldsymbol{n+j/ss}}^{\boldsymbol{P,free}} = \boldsymbol{D^{P^{-1}}}\left(\boldsymbol{F_{n+j/ss}^{P,free}} - \boldsymbol{R^P}\left(\widetilde{\boldsymbol{Y}}_{\boldsymbol{n+\frac{j}{ss}}}^{\boldsymbol{P,free}}\right) + \boldsymbol{L^P\Lambda_n}\left(1-\frac{j}{ss}\right)\right) \quad (5.39)$$

$\widetilde{\boldsymbol{Y}}_{\boldsymbol{n+\frac{j}{ss}}}^{\boldsymbol{P,free}}$ is a vector composed of $\left[\widetilde{\boldsymbol{u}}_{\boldsymbol{n+\frac{j}{ss}}}^{\boldsymbol{P,free}}, \widetilde{\boldsymbol{v}}_{\boldsymbol{n+\frac{j}{ss}}}^{\boldsymbol{P,free}}\right]$ which represent the displacements and velocities imposed by the actuators on the physical substructure. Furthermore, $\boldsymbol{R^P} = \left[-\widetilde{\boldsymbol{v}}_{\boldsymbol{n+\frac{j}{ss}}}^{\boldsymbol{P,free}}; \tilde{\boldsymbol{r}}_{\boldsymbol{n+\frac{j}{ss}}}^{\boldsymbol{P,free}}\right]$ and $\boldsymbol{D^P} = \boldsymbol{M^P} + \boldsymbol{K^P}\gamma\Delta t^P\,\alpha_f/\alpha_m$.

The free state $[\boldsymbol{Y}_{\boldsymbol{n+j/ss}}^{\boldsymbol{P,free}}, \boldsymbol{V}_{\boldsymbol{n+j/ss}}^{\boldsymbol{P,free}}]$ at the time step $t_{n+j/ss}$ can be calculated:

$$\boldsymbol{Y}_{\boldsymbol{n+j/ss}}^{\boldsymbol{P,free}} = \widetilde{\boldsymbol{Y}}_{\boldsymbol{n+j/ss}}^{\boldsymbol{P,free}} + \dot{\boldsymbol{Y}}_{\boldsymbol{n+j/ss}}^{\boldsymbol{P,free}}\gamma\Delta t^P\,\alpha_f/\alpha_m \quad (5.40)$$

$$\boldsymbol{V}_{\boldsymbol{n+j/ss}}^{\boldsymbol{P,free}} = \widetilde{\boldsymbol{V}}_{\boldsymbol{n+j/ss}}^{\boldsymbol{P,free}} + \dot{\boldsymbol{Y}}_{\boldsymbol{n+j/ss}}^{\boldsymbol{P,free}}\,\alpha_f/\alpha_m \quad (5.41)$$

The procedure stays in this loop until *j*=*ss*.

Starting from the knowledge of the free solutions of both NS and PS, it is possible to calculate the link solutions expressed as linear functions of interface Lagrange multipliers obtained by decoupling the subdomains equations at zero states. Considering:

$$\mathbb{Y}_{n+1}^{P,free} = \begin{bmatrix}\boldsymbol{Y}_{\boldsymbol{n+1}}^{\boldsymbol{P,free}}\\ \dot{\boldsymbol{Y}}_{\boldsymbol{n+1}}^{\boldsymbol{P,free}}\\ \boldsymbol{V}_{\boldsymbol{n+1}}^{\boldsymbol{P,free}}\end{bmatrix}, \qquad \mathbb{Y}_{n+1}^{N,free} = \begin{bmatrix}\boldsymbol{Y}_{\boldsymbol{n+1}}^{\boldsymbol{N,free}}\\ \dot{\boldsymbol{Y}}_{\boldsymbol{n+1}}^{\boldsymbol{N,free}}\\ \boldsymbol{V}_{\boldsymbol{n+1}}^{\boldsymbol{N,free}}\end{bmatrix} \quad (5.42)$$

$$\mathbb{Y}_{n+1}^{P,link} = \begin{bmatrix} \boldsymbol{Y_{n+1}^{P,link}} \\ \boldsymbol{\dot{Y}_{n+1}^{P,link}} \\ \boldsymbol{V_{n+1}^{P,link}} \end{bmatrix}, \qquad \mathbb{Y}_{n+1}^{N,link} = \begin{bmatrix} \boldsymbol{Y_{n+1}^{N,link}} \\ \boldsymbol{\dot{Y}_{n+1}^{N,link}} \\ \boldsymbol{V_{n+1}^{N,link}} \end{bmatrix} \tag{5.43}$$

It is possible to condense the solving equations in:

$$\begin{bmatrix} \mathbb{Y}_{n+1/ss}^{P,link} \\ \mathbb{Y}_{n+2/ss}^{P,link} \\ \dots \\ \mathbb{Y}_{n+1}^{P,link} \end{bmatrix} = \begin{bmatrix} \mathbb{M}^P & & & \\ \mathbb{N}^P & \mathbb{M}^P & & \\ & \mathbb{N}^P & \dots & \\ & & \dots & \mathbb{M}^P \end{bmatrix}^{-1} \begin{bmatrix} \frac{1}{ss}\mathbb{L}^P \\ \frac{2}{ss}\mathbb{L}^P \\ \dots \\ \mathbb{L}^P \end{bmatrix} \boldsymbol{\Lambda_{n+1}} = \begin{bmatrix} \mathbb{Q}_{1/ss}^P \\ \mathbb{Q}_{2/ss}^P \\ \dots \\ \mathbb{Q}^P \end{bmatrix} \boldsymbol{\Lambda_{n+1}} \tag{5.44}$$

$$\mathbb{Y}_{n+1}^{N,link} = \mathbb{M}^{N^{-1}} \mathbb{L}^N \boldsymbol{\Lambda_{n+1}} = \mathbb{Q}^N \boldsymbol{\Lambda_{n+1}} \tag{5.45}$$

In particular, $\mathbb{L}^{N^T} = [\boldsymbol{L^{N^T}}\ \mathbf{0}\ \ \mathbf{0}]$ and $\mathbb{L}^{P^T} = [\boldsymbol{L^{P^T}}\ \mathbf{0}\ \ \mathbf{0}]$ are Boolean matrices to localize the interface forces on state-space equations.

$$\mathbb{Y}_{n+1}^{P,link} = \mathbb{Q}^{\boldsymbol{P}} \boldsymbol{\Lambda_{n+1}} \tag{5.46}$$

$$\mathbb{Y}_{n+1}^{N,link} = \mathbb{Q}^{\boldsymbol{N}} \boldsymbol{\Lambda_{n+1}} \tag{5.47}$$

$$\mathbb{Y}_{n+1}^{P} = \mathbb{Y}_{n+1}^{P,free} + \mathbb{Y}_{n+1}^{P,link} \tag{5.48}$$

$$\mathbb{Y}_{n+1}^{N} = \mathbb{Y}_{n+1}^{N,free} + \mathbb{Y}_{n+1}^{N,link} \tag{5.49}$$

The compatibility equation can be written to define the interface Lagrange multipliers:

$$\mathbb{G}^N \mathbb{Y}_{n+1}^N + \mathbb{G}^P \mathbb{Y}_{n+1}^P = \mathbf{0} \tag{5.50}$$

where $\mathbb{G}^N = [\mathbf{0}\ \ \boldsymbol{L^N}\ \ \mathbf{0}]$ and $\mathbb{G}^P = [\mathbf{0}\ \ \boldsymbol{L^P}\ \mathbf{0}]$ are Boolean matrices to localize the interface degrees of freedom on state vectors.

The interface Lagrange multiplier vector is defined as:

$$\boldsymbol{\Lambda_{n+1}} = -\mathbb{H}^{-1}\left(\mathbb{G}^N \mathbb{Y}_{n+1}^{N,free} + \mathbb{G}^P \mathbb{Y}_{n+1}^{P,free}\right) \tag{5.51}$$

where the so-called Steklov-Poincaré operator is:

$$\mathbb{H} = \mathbb{G}^N \mathbb{Q}^{\boldsymbol{N}} + \mathbb{G}^P \mathbb{Q}^{\boldsymbol{P}} \tag{5.52}$$

5.3 Application of the partitioned generalized-α (PG-α) time integration algorithm

This section is devoted to applying the partitioned generalized-α (PG-α) time integration algorithm to a straightforward system to show the accuracy of the implemented code. The reference system used for this analysis is the same described by Abbiati et al. [14] and reported in Figure 5.6. It consists of three masses connected to each other and the fixed supports through elastic springs. The system is divided into two substructures, namely PS and NS, which stand for the physical and numerical subdomain, respectively, as shown in Figure 5.6. In particular, the substructures have been defined so that two parts (m_1 and m_2) of one lumped mass belong to the two different subdomains.

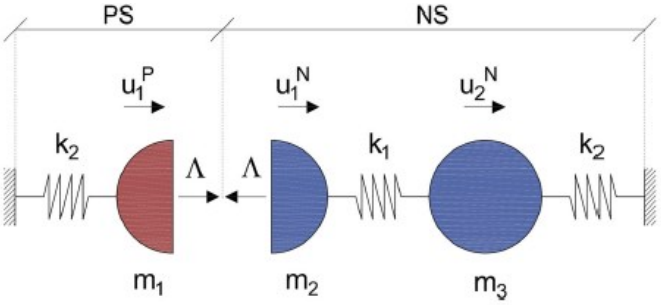

Figure 5.6 – Analysed configuration [14]

It is assumed that $m_1 = m_2 = 4000\ kg$, $m_3 = 9000\ kg$, $k_1 = 400\ kN/m$ and $k_2 = 500\ kN/m$. The system is subjected to a horizontal seismic input of Imperial Valley (the same accelerogram used in Chapter 4 to perform the pseudo-dynamic tests) with a PGA equal to 1.00g and in the hypothesis of zero viscous damping. According to these assumptions, the state vectors and Boolean matrices can be written as:

$$\boldsymbol{Y^P} = \begin{bmatrix} u_1^P \\ v_1^P \end{bmatrix}, \quad \boldsymbol{L^P} = \begin{bmatrix} 0 \\ 1 \end{bmatrix}, \quad \boldsymbol{G^P} = [1 \quad 0]$$

$$\boldsymbol{Y^N} = \begin{bmatrix} u_1^N \\ u_2^N \\ v_1^N \\ v_2^N \end{bmatrix}, \quad \boldsymbol{L^N} = \begin{bmatrix} 0 \\ 0 \\ -1 \\ 0 \end{bmatrix}, \quad \boldsymbol{G^N} = [-1 \quad 0 \quad 0 \quad 0]$$

Referring to the analyzed case, a code of the partitioned-α time integration algorithm has been implemented in Matlab 2018b [17]. For the sake of clarity, the code is reported:

```
clear
clc

dof_N=2;
dof_P=1;

m1=4000;
m2=4000;
m3=9000;

k1=400000;
k2=500000;

m_N=[m2 0;0 m3];
m_P=[m1];
c_N=zeros(dof_N);
c_P=zeros(dof_P);
k_N=[k1 -k1;-k1 k1+k2];
k_P=[k2];

rho=1;
alpham=(3-rho)/2/(1+rho);
alphaf=1/(1+rho);
gamma=1/2+alpham-alphaf;

I_N=eye(dof_N);
M_N=[I_N zeros(dof_N);zeros(dof_N) m_N];
K_N=[zeros(dof_N) -I_N;k_N c_N];
L_N=[0; 0; -1; 0];
G_N=[-1 0 0 0];

I_P=eye(dof_P);
M_P=[I_P zeros(dof_P);zeros(dof_P) m_P];
K_P=[zeros(dof_P) -I_P;k_P c_P];
L_P=[0; 1];
G_P=[1 0];

seismic_input=xlsread('imperialvalley.xlsx',1,'b1:b2836')*9.81*0.37;
```

```
dt=0.01;
parts=50;
for a=1:size(seismic_input)-1
    pre=seismic_input(a);
    post=seismic_input(a+1);
    for j=0:parts
        input(1+(a-1)*parts+j)=pre+(post-pre)/parts*j;
    end
end
input=input';

dt=dt/parts;
ss=10;
lambda=0;

Ydot_N=zeros(2*dof_N,1);
Y_N=zeros(2*dof_N,1);
V_N=zeros(2*dof_N,1);
collY_N=[];
D_N=M_N;

Ydot_P=zeros(2*dof_P,1);
Y_P=zeros(2*dof_P,1);
V_P=zeros(2*dof_P,1);
collY_P=[];
D_P=M_P+K_P*gamma*dt/ss*alphaf/alpham;

for a=2:size(input,1)
    fprintf('The analysis is running (%.2f/100)\n',a/(size(input,1)-1)*100)
    f_N=-m_N*ones(dof_N,1)*input(a);
    F_N=[zeros(dof_N,1); f_N];
    Ytilde_N=Y_N+Ydot_N*gamma*dt*(1-alphaf)/alpham+V_N*dt*(alpham-gamma)/alpham;
    Vtilde_N=Ydot_N*(1-alphaf)/alpham-V_N*(1-alpham)/alpham;
    Ydot_N=inv(D_N)*(F_N-K_N*Ytilde_N);
    Y_N=Ytilde_N+Ydot_N*gamma*dt*alphaf/alpham;
    V_N=Vtilde_N+Ydot_N*alphaf/alpham;

    for b=1:ss
        Ytilde_P=Y_P+Ydot_P*gamma*dt/ss*(1-alphaf)/alpham+V_P*dt/ss*(alpham-
gamma)/alpham;
        Vtilde_P=Ydot_P*(1-alphaf)/alpham-V_P*(1-alpham)/alpham;
        f_P=-m_P*ones(dof_P,1)*(input(a-1)+(input(a)-input(a-1))/ss*b);
        F_P=[zeros(dof_P,1); f_P];
        Ydot_P=inv(D_P)*(F_P-K_P*Ytilde_P+L_P*lambda*(1-b/ss));
        Y_P=Ytilde_P+Ydot_P*gamma*dt/ss*alphaf/alpham;
        V_P=Vtilde_P+Ydot_P*alphaf/alpham;
    end

    MM_P=[K_P M_P zeros(size(M_P));
    eye(size(M_P)) zeros(size(M_P)) -gamma*dt*eye(size(M_P));
    zeros(size(M_P)) -alphaf*eye(size(M_P)) alpham*eye(size(M_P))];

    MM_N=[K_N M_N zeros(size(M_N));
    eye(size(M_N)) zeros(size(M_N)) -gamma*dt*eye(size(M_N));
```

```
    zeros(size(M_N)) -alphaf*eye(size(M_N)) alpham*eye(size(M_N))];

    LL_P=[L_P; zeros(2*dof_P,1); zeros(2*dof_P,1)];
    LL_N=[L_N; zeros(2*dof_N,1); zeros(2*dof_N,1)];

    Q_P=inv(MM_P)*LL_P;
    Q_N=inv(MM_N)*LL_N;

    GG_N=[zeros(1,2*dof_N) G_N zeros(1,2*dof_N)];
    GG_P=[zeros(1,2*dof_P) G_P zeros(1,2*dof_P)];

    YY_P_free=[Y_P; Ydot_P; V_P];
    YY_N_free=[Y_N; Ydot_N; V_N];
    HH=GG_N*Q_N+GG_P*Q_P;
    lambda=-inv(HH)*(GG_N*YY_N_free+GG_P*YY_P_free);

    YY_P_link=Q_P*lambda;
    YY_N_link=Q_N*lambda;

    YY_P=YY_P_free+YY_P_link;
    YY_N=YY_N_free+YY_N_link;

    Y_P=YY_P(1:size(Y_P),:);
    Ydot_P=YY_P(1+size(Y_P):2*size(Y_P),:);
    V_P=YY_P(1+2*size(Y_P):3*size(Y_P),:);
    collY_P=[collY_P Y_P];

    Y_N=YY_N(1:size(Y_N),:);
    Ydot_N=YY_N(1+size(Y_N):2*size(Y_N),:);
    V_N=YY_N(1+2*size(Y_N):3*size(Y_N),:);
    collY_N=[collY_N Y_N];
end

comparison12=xlsread('Displacements_model_for_partitioned.xlsx',1,'b1:b2836')*1000;
comparison3=xlsread('Displacements_model_for_partitioned.xlsx',1,'c1:c2836')*1000;

figure('WindowState','maximized','Color',[1 1 1]);
subplot(2,1,1);
plot([0.01/parts:0.01/parts:28.35],collY_N(1,:)*1000,'k')
hold on
plot([0:0.01:28.35],comparison12,'b')
legend('Matlab (Partitioned G-alpha algorithm)','SeismoStruct')
title('Displacements (m1 and m2)')
xlabel('Time (s)')
ylabel('Displacement (mm)')
grid on
savefig('Partitioned_figure')
hold off
subplot(2,1,2);
plot([0.01/parts:0.01/parts:28.35],collY_N(2,:)*1000,'k')
hold on
plot([0:0.01:28.35],comparison3,'b')
legend('Matlab (Partitioned G-alpha algorithm)','SeismoStruct')
title('Displacements (m3)')
xlabel('Time (s)')
ylabel('Displacement (mm)')
```

```
grid on
savefig('Partitioned_figure')
hold off
```

Furthermore, to demonstrate the obtained results' reliability, the same model reported in Figure 5.6 has been implemented in SeismoStruct software [18]. Finally, the method's accuracy is shown in Figure 5.7, where the displacements provided by the implemented code concerning masses m_1 and m_2 are compared to the numerical counterparts obtained by SeismoStruct.

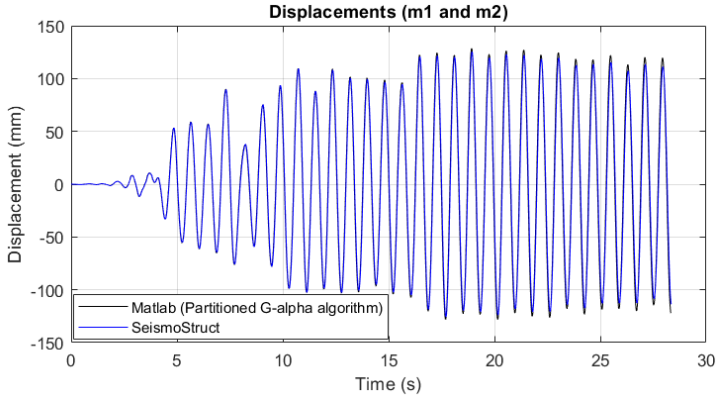

Figure 5.7 – Comparison between the PG-α method and the monolithic configuration developed in SeismoStruct [18]

This section has not been discussed in detail, and only a straightforward example has been reported. However, this aspect demonstrates that starting from this approach, it is possible to develop a more complex procedure that can allow performing hybrid tests with a dynamic substructuring technique. In fact, in the forthcoming years, the University of Salerno will equip with advanced hardware and software to reach this aim.

5.4 Condensation methods

In many structural dynamics applications, it is particularly appropriate to work with reduced dynamic models, i.e. built with a limited number of degrees of freedom compared to those used for static models.

The general idea of a dynamic reduction technique can be expressed from the mathematical point of view; considering a large-scale system, it is possible to reduce it to a minor number *r* (retained) of degrees of freedom, truncating the residual *t* (truncated). The relationship between the retained and truncated degrees of freedom is expressed by:

$$\boldsymbol{x} = \begin{bmatrix} \boldsymbol{x_r} \\ \boldsymbol{x_t} \end{bmatrix} = \boldsymbol{T}\boldsymbol{x_r} \tag{5.53}$$

$\boldsymbol{x}$ represents the vector of the degrees of freedom of the system, while $\boldsymbol{x_r}$ and $\boldsymbol{x_t}$ are, respectively, the vectors related to the retained and truncated degrees of freedom. Instead, $\boldsymbol{T}$ is the transformation matrix, which is appropriately formulated consistently with the considered condensation method.

The reduction techniques were initially developed to reduce the number of equations of a generic complex dynamic system, allowing a faster resolution than the algebraic system. However, with the passing years, their use has expanded, as demonstrated by their application in dynamic substructuring, a technique that allows considering the whole structure subdivided into a certain number of substructures. In such a way, the analysis is carried out at the level of each substructure, requiring lower computational efforts and the coupling among the various components.

This paragraph briefly describes the most commonly used condensation methods.

5.4.1 Guyan static condensation

The Guyan static condensation represents the most typical reduction technique. However, for the sake of simplicity, considering the equations of motion neglecting the damping contribution, it is possible to write:

$$\boldsymbol{M}\ddot{\boldsymbol{x}} + \boldsymbol{K}\boldsymbol{x} = \boldsymbol{F}(t) \tag{5.54}$$

where $\boldsymbol{M}$ and $\boldsymbol{K}$ are, respectively, the mass and stiffness matrices, which can be appropriately re-written so that the retained and truncated degrees of freedom can be considered:

$$\begin{bmatrix} \boldsymbol{M_{rr}} & \boldsymbol{M_{rt}} \\ \boldsymbol{M_{tr}} & \boldsymbol{M_{tt}} \end{bmatrix} \begin{Bmatrix} \ddot{\boldsymbol{x}}_r \\ \ddot{\boldsymbol{x}}_t \end{Bmatrix} + \begin{bmatrix} \boldsymbol{K_{rr}} & \boldsymbol{K_{rt}} \\ \boldsymbol{K_{tr}} & \boldsymbol{K_{tt}} \end{bmatrix} \begin{Bmatrix} \boldsymbol{x}_r \\ \boldsymbol{x}_t \end{Bmatrix} = \begin{Bmatrix} \boldsymbol{F}_r \\ \boldsymbol{0} \end{Bmatrix} \tag{5.55}$$

Neglecting the inertial terms of the truncated nodes, which is a valid approximation operating with low frequencies, from the second equation of Eq. 5.55, it is possible to obtain:

$$\boldsymbol{K_{tr}x_r} + \boldsymbol{K_{tt}x_t} = \boldsymbol{0} \tag{5.56}$$

$$\boldsymbol{x_t} = -\boldsymbol{K_{tt}^{-1}K_{tr}x_r} \tag{5.57}$$

$$\boldsymbol{x} = \begin{bmatrix} \boldsymbol{x_r} \\ \boldsymbol{x_t} \end{bmatrix} = \begin{bmatrix} \boldsymbol{I} \\ -\boldsymbol{K_{tt}^{-1}K_{tr}} \end{bmatrix} \boldsymbol{x_r} = \boldsymbol{T_s x_r} \tag{5.58}$$

$$\boldsymbol{T_s} = \begin{bmatrix} \boldsymbol{I} \\ -\boldsymbol{K_{tt}^{-1}K_{tr}} \end{bmatrix} \tag{5.59}$$

Starting from the knowledge of $\boldsymbol{T_s}$, the equations of motions can be appropriately modified so that:

$$\widetilde{\boldsymbol{M}}\ddot{\boldsymbol{x}}_r + \widetilde{\boldsymbol{C}}\dot{\boldsymbol{x}}_r + \widetilde{\boldsymbol{K}}\boldsymbol{x}_r = \widetilde{\boldsymbol{F}} \tag{5.60}$$

where:

$$\widetilde{\boldsymbol{M}} = \boldsymbol{T_s^T M T_s} \tag{5.61}$$

$$\widetilde{\boldsymbol{C}} = \boldsymbol{T_s^T C T_s} \tag{5.62}$$

$$\widetilde{\boldsymbol{K}} = \boldsymbol{T_s^T K T_s} \tag{5.63}$$

$$\widetilde{\boldsymbol{F}} = \boldsymbol{T_s^T F} \tag{5.64}$$

According to this approach, it is assumed that all the movements are related to the principal retained nodes *r*; this means that they are "dragged behind" by the movement of the latter but without having their inertia. Consequently, dynamic modes have a static trend (as if inertia is, by hypothesis, null). It is also possible to note that the reduced system frequencies are always higher than those of the original system.

5.4.2 Dynamic condensation

Dynamic condensation is an extension of Guyan static condensation since the transformation matrix of the Guyan reduction is modified to include the terms of inertia relative to a given frequency ω_n:

$$\boldsymbol{T_d} = \begin{bmatrix} \boldsymbol{I} \\ -(\boldsymbol{K_{tt}} - \omega_n \boldsymbol{M_{tt}})^{-1}(\boldsymbol{K_{tr}} - \omega_n \boldsymbol{M_{tr}}) \end{bmatrix} \tag{5.65}$$

The transformation matrix $\boldsymbol{T_d}$ affects the equations of motion similarly to $\boldsymbol{T_s}$.

5.4.3 System Equivalent Reduction Expansion Process (SEREP)

This method aims to reduce the dimension of the system reported in Eq.5.54 so that it can include *p* modes and *m* degrees of freedom necessary to describe the system. The number of the retained coordinates should be equal to the number of considered modes. Starting from Eq.5.55, the solution $\boldsymbol{x}(t)$ can be written as a linear combination of the vibration modes:

$$\boldsymbol{x}(t) = \begin{bmatrix} \boldsymbol{x_r} \\ \boldsymbol{x_t} \end{bmatrix} = \begin{bmatrix} \boldsymbol{\Phi_{rr}} & \boldsymbol{\Phi_{rt}} \\ \boldsymbol{\Phi_{tr}} & \boldsymbol{\Phi_{tt}} \end{bmatrix} \begin{bmatrix} \boldsymbol{r_r} \\ \boldsymbol{r_t} \end{bmatrix} = [\boldsymbol{\Phi_{ar}} \quad \boldsymbol{\Phi_{at}}] \begin{bmatrix} \boldsymbol{r_r} \\ \boldsymbol{r_t} \end{bmatrix} \tag{5.66}$$

In such a way, it is possible to obtain:

$$\boldsymbol{I} \cdot \ddot{\boldsymbol{r}} + \boldsymbol{\lambda} \cdot \boldsymbol{r} = \boldsymbol{\Phi}^T \cdot \boldsymbol{F} \tag{5.67}$$

$$\begin{bmatrix} \boldsymbol{\Phi_{ar}^T} \\ \boldsymbol{\Phi_{at}^T} \end{bmatrix} \cdot \begin{bmatrix} \boldsymbol{M_{rr}} & \boldsymbol{M_{rt}} \\ \boldsymbol{M_{tr}} & \boldsymbol{M_{tt}} \end{bmatrix} \cdot [\boldsymbol{\Phi_{ar}} \quad \boldsymbol{\Phi_{at}}] = \begin{bmatrix} \boldsymbol{I_r} & \boldsymbol{0} \\ \boldsymbol{0} & \boldsymbol{I_t} \end{bmatrix} = \boldsymbol{I} \tag{5.68}$$

$$\begin{bmatrix} \boldsymbol{\Phi_{ar}^T} \\ \boldsymbol{\Phi_{at}^T} \end{bmatrix} \cdot \begin{bmatrix} \boldsymbol{K_{rr}} & \boldsymbol{K_{rt}} \\ \boldsymbol{K_{tr}} & \boldsymbol{K_{tt}} \end{bmatrix} \cdot [\boldsymbol{\Phi_{ar}} \quad \boldsymbol{\Phi_{at}}] = \begin{bmatrix} \boldsymbol{\lambda_r} & \boldsymbol{0} \\ \boldsymbol{0} & \boldsymbol{\lambda_t} \end{bmatrix} = \boldsymbol{\lambda} \tag{5.69}$$

Truncating the vector of the modal coordinates (i.e. assuming $\boldsymbol{r_t} = \boldsymbol{0}$):

$$\boldsymbol{I_r} \cdot \ddot{\boldsymbol{r}}_r + \boldsymbol{\lambda_r} \cdot \boldsymbol{r_r} = \boldsymbol{\Phi_{ar}^T} \cdot \boldsymbol{F_r}(t) \tag{5.70}$$

Considering that $\boldsymbol{x_r} = \boldsymbol{\Phi_{rr}} \boldsymbol{r_r}$, it is possible to obtain:

$$\boldsymbol{\Phi_{rr}^{-1}} \boldsymbol{\Phi_{ar}^T} \boldsymbol{M} \boldsymbol{\Phi_{ar}} \boldsymbol{\Phi_{rr}^{-1}} \ddot{\boldsymbol{x}}_r + \boldsymbol{\Phi_{rr}^{-1}} \boldsymbol{\Phi_{ar}^T} \boldsymbol{K} \boldsymbol{\Phi_{ar}} \boldsymbol{\Phi_{rr}^{-1}} \boldsymbol{x_r} = \boldsymbol{\Phi_{rr}^{-1}} \boldsymbol{\Phi_{ar}^T} \boldsymbol{F_r}(t) \tag{5.71}$$

In such a way, the transformation matrix can be defined as:

$$\boldsymbol{T_{SEREP}} = \boldsymbol{\Phi_{ar}} \boldsymbol{\Phi_{rr}^{-1}} = \begin{bmatrix} \boldsymbol{\Phi_{rr}} \\ \boldsymbol{\Phi_{tr}} \end{bmatrix} \boldsymbol{\Phi_{rr}^{-1}} = \begin{bmatrix} \boldsymbol{I} \\ \boldsymbol{\Phi_{tr}} \boldsymbol{\Phi_{rr}^{-1}} \end{bmatrix} \tag{5.72}$$

Through Eq.5.72, it is possible to define the terms of the equations of motion Eq.5.54. It is worth highlighting that this approach changes the system coordinates from the geometric to the modal coordinates.

5.4.4 Craig-Bampton method

According to this approach, the Guyan condensation method is appropriately enhanced by adding the modes calculated by simultaneously imposing a constraint on all the coupling nodes, *C*. in such a way, new generalized degrees of freedom are defined to express the new coordinates according to the new modal base (Component Mode Synthesis). Referring to the physical substructure only, as the first step, it is required to rearrange the system of equations partitioning the displacement vector between coupling (*c*) and internal (*i*) degrees of freedom.

$$\boldsymbol{x}(t) = \begin{bmatrix} \boldsymbol{x_c} \\ \boldsymbol{x_i} \end{bmatrix} \tag{5.73}$$

$$\begin{bmatrix} \boldsymbol{M_{cc}} & \boldsymbol{M_{ci}} \\ \boldsymbol{M_{ic}} & \boldsymbol{M_{ii}} \end{bmatrix} \begin{Bmatrix} \ddot{\boldsymbol{x}}_c \\ \ddot{\boldsymbol{x}}_i \end{Bmatrix} + \begin{bmatrix} \boldsymbol{K_{cc}} & \boldsymbol{K_{ci}} \\ \boldsymbol{K_{ic}} & \boldsymbol{K_{ii}} \end{bmatrix} \begin{Bmatrix} \boldsymbol{x_c} \\ \boldsymbol{x_i} \end{Bmatrix} = \begin{Bmatrix} \boldsymbol{F_c} \\ \boldsymbol{F_i} \end{Bmatrix} \tag{5.74}$$

For simplicity, the damping has not been considered in Eq.5.74.

With this method, the finite element model of the substructure is transformed from a complete physical set of coordinates to a hybrid set of physical coordinates, represented by coupling and modal nodes. Such a set of modal coordinates Q_L is truncated only to a few low-frequency modes called q_m. This hybrid set of Craig Bampton coordinates is related to the physical coordinates of the entire structure employing the following equation:

$$\begin{Bmatrix} \ddot{\boldsymbol{x}}_c \\ \ddot{\boldsymbol{x}}_i \end{Bmatrix} = \begin{bmatrix} \boldsymbol{I} & \boldsymbol{0} \\ \boldsymbol{\Phi_c} & \boldsymbol{\Phi_i} \end{bmatrix} \begin{Bmatrix} \boldsymbol{x_c} \\ \boldsymbol{q_m} \end{Bmatrix} = \boldsymbol{T_{CB}} \begin{Bmatrix} \boldsymbol{x_c} \\ \boldsymbol{q_m} \end{Bmatrix} \quad with\, m < L \tag{5.75}$$

The first part of the transformation matrix is dimensionless, while the second part, which multiplies some generalized modal coordinates, has the dimension of a length.

For the calculation of the static modes ($\boldsymbol{\Phi_c}$), all the degrees of freedom on the contour are fixed so that the static case can be written as:

$$\boldsymbol{K_{ic}} \boldsymbol{x_c} + \boldsymbol{K_{ii}} \boldsymbol{x_i} = \boldsymbol{0} \tag{5.76}$$

Instead, $\boldsymbol{\Phi_i}$ represents a set of eigenvectors calculated on the PS fixed at the coupling nodes. Therefore, it is interesting to note that the first equation is simple equality for the coupling nodes,

and thus the displacement is given only by a static contribution. Conversely, for internal nodes (second set of equations of Eq.5.75), the displacement is expressed as the linear combination of static and dynamic modes of the PS.
Starting from the knowledge of the transformation matrix, it is possible to write:

$$\begin{bmatrix} \boldsymbol{M_{BB}} & \boldsymbol{M_{Bq}} \\ \boldsymbol{M_{qB}} & \boldsymbol{M_{qq}} \end{bmatrix} \begin{Bmatrix} \ddot{\boldsymbol{x}}_{\boldsymbol{c}} \\ \ddot{\boldsymbol{q}}_{\boldsymbol{m}} \end{Bmatrix} + \begin{bmatrix} \boldsymbol{K_{BB}} & \boldsymbol{0} \\ \boldsymbol{0} & \boldsymbol{K_{qq}} \end{bmatrix} \begin{Bmatrix} \boldsymbol{x_c} \\ \boldsymbol{q_m} \end{Bmatrix} = \begin{Bmatrix} \boldsymbol{F_c} + \boldsymbol{\Phi_c F_i} \\ \boldsymbol{\Phi_i F_i} \end{Bmatrix} \qquad (5.77)$$

This technique's main drawback is that more equations are necessary to represent the reduced model than the physical degrees of freedom. Nevertheless, the most important benefit is that a few vibration modes are necessary to predict the dynamic behaviour of the substructure correctly.

5.5 Personal contribution

Chapter 5 does not deal with any novelty because it simply summarises some algorithms which are used to perform hybrid tests with dynamic substructuring techniques. This chapter is the result of a period study spent by the author at the University of Trento, during which the pseudo-dynamic and hybrid testing techniques have been examined. Moreover, the implementation proposed in this section can be an interesting starting point for performing hybrid tests in the future also at the University of Salerno.

5.6 References

1. Bursi, O. S., Gonzalez-Buelga, A., Vulcan, L., Neild, S. A., Wagg, D. J., Novel coupling Rosenbrock-based algorithms for real-time dynamic substructure testing. Earthquake Engineering & Structural Dynamics, 37(3):339–360, 2008. ISSN 00988847. doi: 10.1002/eqe.757. URL http://doi.wiley.com/10.1002/eqe. 757.
2. De Klerk, D., Rixen, D. J., Voormeeren. S. N., General Framework for Dynamic Substructuring: History, Review and Classification of Techniques. AIAA Journal, 46(5):1169–1181, May 2008. ISSN 0001-1452. doi: 10.2514/1.33274. URL http://arc.aiaa.org/doi/abs/10.2514/1.33274.
3. Farhat, C., Roux, F. X., A method of finite element tearing and interconnecting and its parallel solution algorithm. International Journal for Numerical Methods in Engineering, 32(6):1205–1227, 1991. ISSN 1097-0207. doi: 10.1002/nme.1620320604. URL http://dx.doi.org/10.1002/nme.1620320604.
4. Farhat, C., Chen, P. S., Mandel, J., A scalable lagrange multiplier based domain decomposition method for time-dependent problems. International Journal for Numerical Methods in Engineering, 38(22):3831–3853, 1995. ISSN 1097-0207. doi: 10.1002/nme.1620382207. URL http://dx.doi.org/10. 1002/nme.1620382207.
5. Gravouil, A. Combescure, A., A numerical scheme to couple subdomains with different time-steps for predominantly linear transient analysis. 191:1129– 1157, 2002. URL http://www.sciencedirect.com/science/article/pii/ S0045782501001906.
6. Pegon, P., Magonette, G., Continuous psd testing with non-linear substructuring: Presentation of a stable parallel inter-field procedure - tr 1.02.167. Technical report, European Laboratory for Structural Assessment (ELSA), Joint Research Centre of Ispra (VA), Italy, 2002.
7. Pegon, P., Magonette, G., Continuous psd testing with non-linear substructuring: Using the operator splitting technique to avoid iterative procedures - tr spi.05.30. Technical report, European Laboratory for Structural Assessment (ELSA), Joint Research Centre of Ispra (VA), Italy, 2005.

8. Bonelli, A., Bursi, O. S., He, L., Magonette, G., Pegon, P., Convergence analysis of a parallel interfield method for heterogeneous simulations with dynamic substructuring. International journal for numerical methods in engineering, 75(7):800–825, 2008. URL http://onlinelibrary.wiley.com/doi/10.1002/nme.2285.
9. Prakash, A., Hjelmstad. K. D., A FETI-based multi-time-step coupling method for Newmark schemes in structural dynamics. International Journal for Numerical Methods in Engineering, 61(13):2183–2204, December 2004. ISSN 0029-5981. doi: 10.1002/nme.1136. URL http://doi.wiley.com/10.1002/nme.1136.
10. Nakshatrala, K. B., Hjelmstad, K. D., Tortorelli, D. A., A feti-based domain decomposition technique for time-dependent first-order systems based on a dae approach. International Journal for Numerical Methods in Engineering, 75(12):1385–1415, 2008. ISSN 1097-0207. doi: 10.1002/nme.2303. URL http://dx.doi.org/10.1002/nme.2303.
11. He, L., Bonelli, A., Pegon, P., Bursi, OS, Novel generalized-α methods for interfiled parallel integration of heterogeneous structural dynamic systems. Journal of Computational and Applied Mathematics, 234(7):2250–2258, August 2010. ISSN 03770427. doi: 10.1016/j.cam.2009.08.082. URL http://linkinghub.elsevier.com/retrieve/pii/S0377042709005615.
12. Mahjoubi, N., Methode generale de couplage de schema dintegration multiechelles en temps en dynamique des structures. PhD thesis, Institut National des Sciences Appliqu´ees de Lyon, 2010.
13. Bursi, O. S., Wang, Z., Jia, C., Wu, B., Monolithic and partitioned time integration methods for real-time heterogeneous simulations. Computational Mechanics, 2012. ISSN 0178-7675. doi: 10.1007/s00466-012-0800-0. URL http://link.springer.com/10.1007/s00466-012-0800-0.
14. Abbiati, G., Lanese, I., Cazzador, E., Bursi, O. S., Pavese, A., A computational framework for fast-time hybrid simulation based on partitioned time integration and state-space modeling. Structural Control and Health Monitoring. 26. 10.1002/stc.2419, 2019.
15. Jansen, K. E., Whiting, C. H., Hulbert, G.M., A generalized-α method for integrating the filtered Navier–Stokes equations with a stabilized finite element method. *Comput Methods Appl Mech Eng*.;190(3–4):305-319, 2000.
16. Brüls O, Arnold M. The generalized-α scheme as a linear multistep integrator: toward a general mechatronic simulator. *J Comput Nonlinear Dyn*.;3(4):41007, 2008.
17. MATLAB, R2018b. Natick, Massachusetts: The MathWorks Inc.; 2018.
18. SeismoSoft (2016). “SeismoStruct 2016 – A computer program for static and dynamic analysis of framed structures”.

Chapter 6 - Conclusions

The seismic events of Northridge (1994) and Kobe (1995) represent a turning point in the seismic design of steel structures. In fact, after the occurrence of those earthquakes, much more attention was devoted by researchers to the characterization of the seismic response of beam-to-column connections. These efforts were well-reflected by the several joints' typologies conceived, studied and standardized during the last 30 years. To arrive at this standardization, design formulations, numerical models and a relevant number of experimental investigations have been necessary. In most cases, these activities concerned beam-to-column sub-assemblies whose mechanical properties related to stiffness, resistance, ductility and energy dissipation capacity were defined according to monotonic or cyclic displacement loading histories.

This PhD thesis's main aim consisted in investigating the seismic behaviour of some innovative steel beam-to-column connections through experimental, numerical and analytical activities.

In particular, the attention has been focused on four typologies: Reduced Beam Section (RBS) connections, circular-hollow-section to through-all double-tee profiles with RBS, FREE from DAMage (FREEDAM) connections, dissipative double-split-tee joints.

Specifically, the seismic response of RBS, FREEDAM and X-shaped T-stub joints was investigated through pseudo-dynamic tests carried out on a two-storey steel building mock-up composed of two equal frames extracted from a more complex reference structure. The MRFs have been equipped alternately with the abovementioned three connections. Furthermore, the mock-up has been tested by adopting the pseudo-dynamic method, considering a sequence of five accelerograms.

The results of the experimental campaign have been complemented with FE simulations carried out with the SeismoStruct, Abaqus and OpenSees software. As a result, the following conclusions can be drawn regarding the obtained test results and experimental/numerical comparisons.

- The seismic response of the tested MRFs with RBSs has proved to be satisfactory, even though the failure of the structure at the end of the tests was due either to the fracture of the beam flange or the fracture of the welding detail of a beam-to-column connection. In fact, the structure was subjected to several destructive seismic events and, before failing, was able to dissipate a large amount of energy. The maximum rotation occurring in the RBS connections was slightly less than 3% and, therefore, in agreement with the benchmark value suggested by Eurocode 8 for the high ductility class, equal to 0.035 rad. The tests showed that, even though capacity design principles were adopted in design, the current values of the overstrength factors suggested by EC8 cannot avoid the possibility of failure in the welds due to damage accumulation phenomena. In the case of RBS connections, this is probably due to the reduction of the width-to-thickness ratio of the beam flange in the RBS zone, which practically prevented the occurrence of local buckling with the contemporaneous increase of the strain-hardening exhibited by the RBS zone.
- The FREEDAM joints did not undergo damage, except minor yielding in agreement with previous experimental tests on beam-to-column joints sub-assemblies. Furthermore, the only components which needed to be substituted at the end of the campaign were the friction pads, which dissipated most of the seismic input energy, and the column bases. As expected, the moment-rotation hysteretic curves of the friction joints had a rectangular shape and were characterized only by a slight degradation of the flexural resistance. During the tests, the correspondence between the design value of the sliding resistance of the

connections and the obtained values was verified with some unavoidable scatters due to the normal variability of the dampers' behavioural properties.

- In agreement with the expectations, the structure with X-shaped T-stub joints underwent damage and energy dissipation only in the connections and column bases. In particular, the connections exhibited a ductile behaviour avoiding any brittle fractures.
- For all the connections' typologies, the comparisons with the experimental results have shown that the applied mixed distributed and concentrated plasticity approach based on the adoption of phenomenological spring models can capture the global seismic response of the structure accurately. However, it predicts the local response parameters with lower accuracy, such as the peak moments and rotations. This occurrence highlights that even when proper modelling of the connections is used with refined mechanical models, scatters are not negligible because of epistemic uncertainties. Notwithstanding, the adoption of simplified numerical tools may be satisfactory for design assessment, but it does not provide a reliable representation of the local response of beam-to-column joints. In order to have an accurate prediction of the local response, more refined and computationally complex models have to be defined.

This work has also focused on the possibility of exploiting connections characterized by circular hollow section (CHS) columns. In particular, the connections between CHS columns and through-all double-tee profiles have been investigated.

- The component method approach for the static characterization of the behaviour exhibited by CHS to through-all I-beam connections has been proposed. In particular, all the nodal components have been identified and studied by employing experimental, numerical and analytical activities. In particular, the Togo ring model theory has adequately been modified to fit this approach to define the strength formulation of the passing-through plate transversally welded to the column in tension/compression component. Referring to this component and the whole beam-to-column sub-assembly, experimental tests and numerical simulations have been carried out by applying monotonic and cyclic loading histories. Furthermore, in order to enhance the range of geometrical configurations, also parametric analyses have been carried out. Finally, after the characterization of all the components, the whole component method approach has been implemented in OpenSees and validated against 30 cyclically loaded Abaqus models showing a high accuracy of the proposed approach.
- Since double-tee profiles characterize the mock-up used for the pseudo-dynamic tests, preliminary algorithms have been studied to implement a code procedure able to perform hybrid tests with the dynamic substructuring technique to investigate the seismic behaviour of CHS to through-all I-beam joints.

ANNEX A

A1. CHS to through-all I-beam connections: monotonic simulations

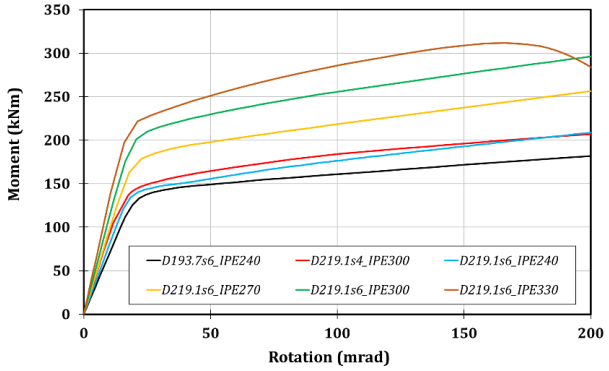

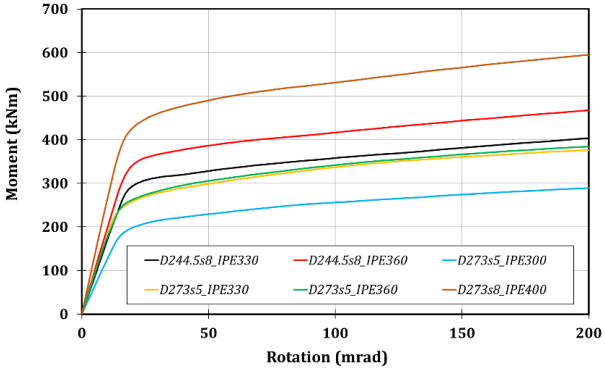

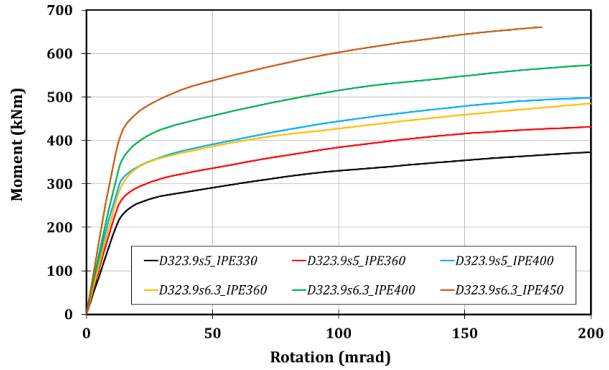

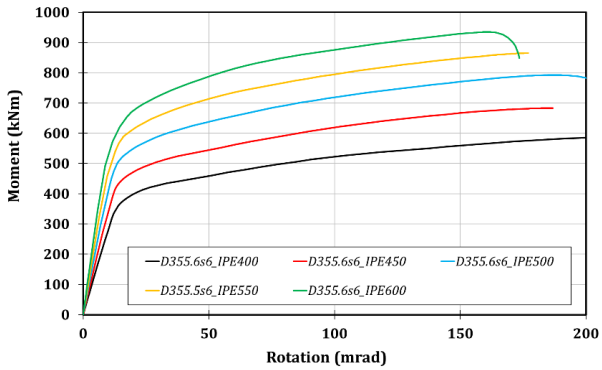

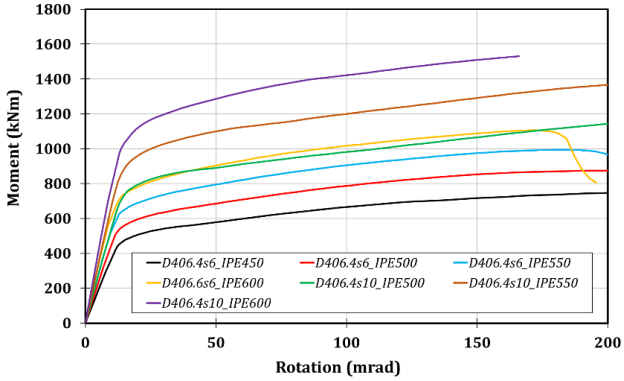

A2. CHS to through-all plate connections: monotonic simulations

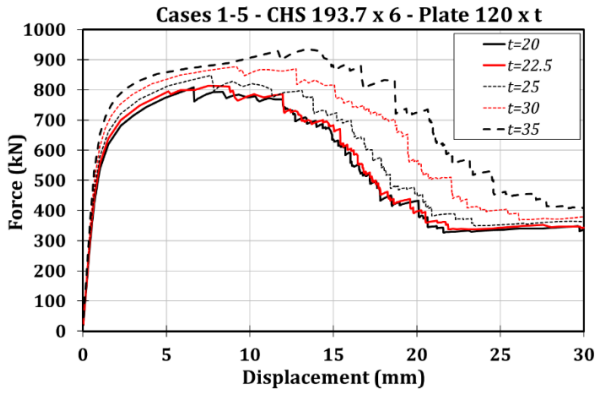

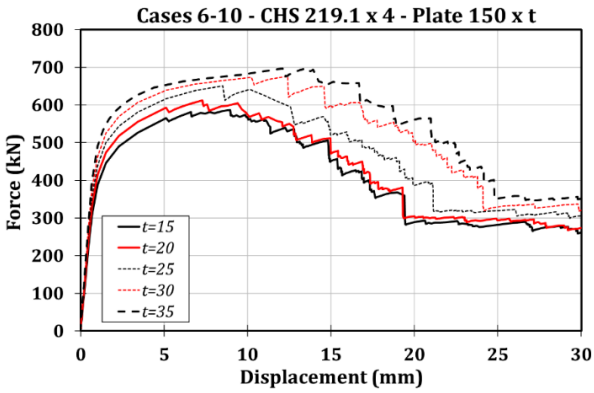

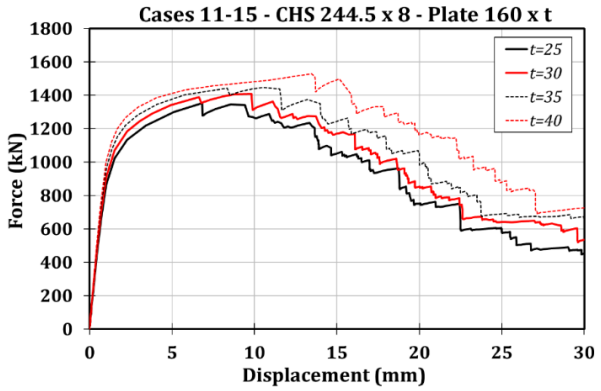

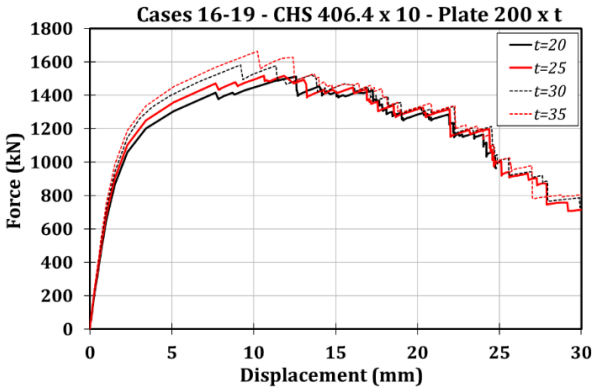

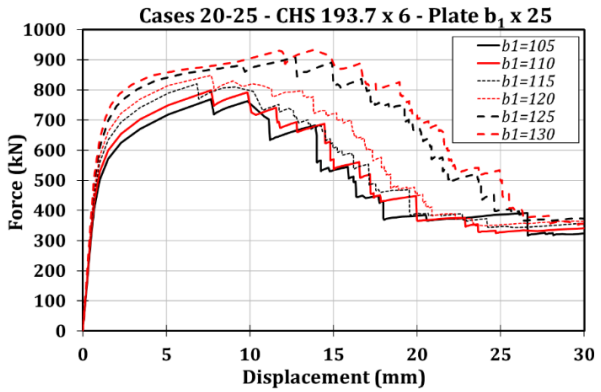

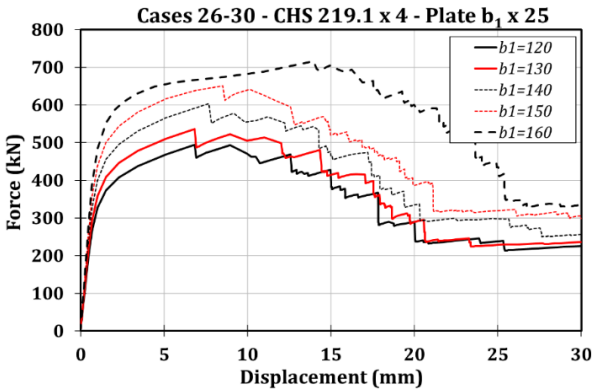

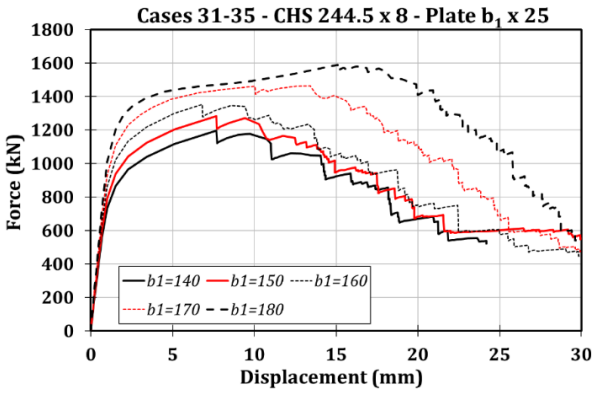
Cases 31-35 - CHS 244.5 x 8 - Plate b1 x 25
Force (kN)
Displacement (mm)
b1=140
b1=150
b1=160
b1=170
b1=180

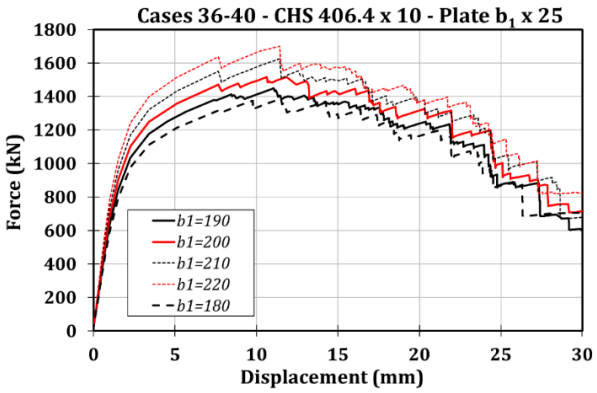
Cases 36-40 - CHS 406.4 x 10 - Plate b1 x 25
Force (kN)
Displacement (mm)
b1=190
b1=200
b1=210
b1=220
b1=180

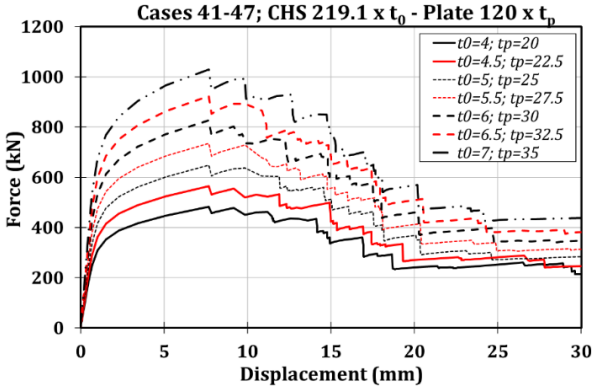
Cases 41-47; CHS 219.1 x t0 - Plate 120 x tp
Force (kN)
Displacement (mm)
t0=4; tp=20
t0=4.5; tp=22.5
t0=5; tp=25
t0=5.5; tp=27.5
t0=6; tp=30
t0=6.5; tp=32.5
t0=7; tp=35

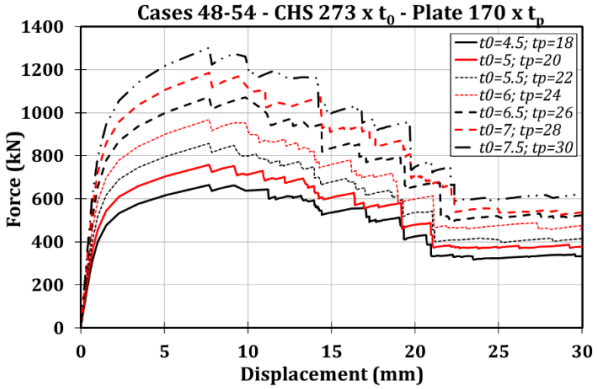
Cases 48-54 - CHS 273 x t0 - Plate 170 x tp
Force (kN)
Displacement (mm)
t0=4.5; tp=18
t0=5; tp=20
t0=5.5; tp=22
t0=6; tp=24
t0=6.5; tp=26
t0=7; tp=28
t0=7.5; tp=30

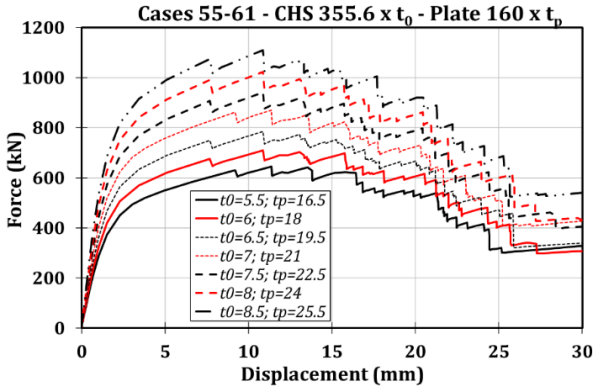
Cases 55-61 - CHS 355.6 x t0 - Plate 160 x tp
Force (kN)
Displacement (mm)
t0=5.5; tp=16.5
t0=6; tp=18
t0=6.5; tp=19.5
t0=7; tp=21
t0=7.5; tp=22.5
t0=8; tp=24
t0=8.5; tp=25.5

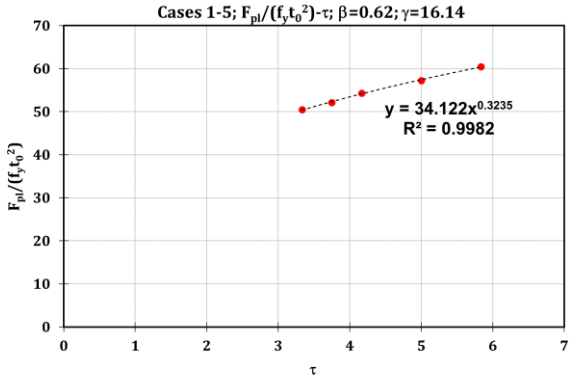
Cases 1-5; $F_{pl}/(f_y t_0^2)$-τ; β=0.62; γ=16.14
y = 34.122x^0.3235
R² = 0.9982
$F_{pl}/(f_y t_0^2)$
τ

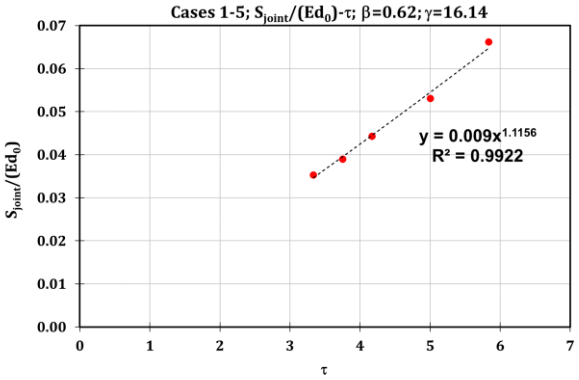
Cases 1-5; $S_{joint}/(Ed_0)$-τ; β=0.62; γ=16.14
y = 0.009x^1.1156
R² = 0.9922
$S_{joint}/(Ed_0)$
τ

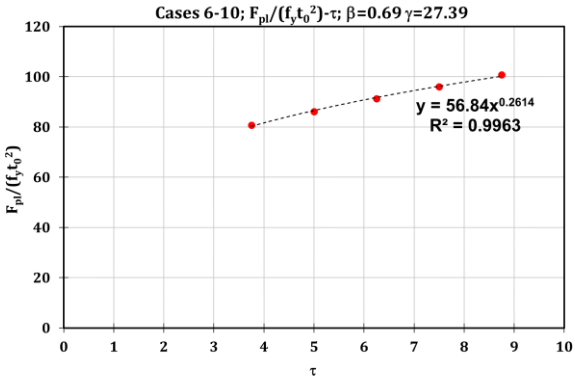
Cases 6-10; $F_{pl}/(f_y t_0^2)$-τ; β=0.69 γ=27.39
y = 56.84x^0.2614
R² = 0.9963
$F_{pl}/(f_y t_0^2)$
τ

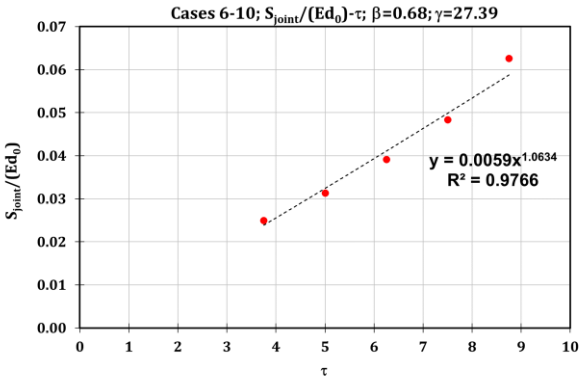
Cases 6-10; $S_{joint}/(Ed_0)$-τ; β=0.68; γ=27.39
y = 0.0059x^1.0634
R² = 0.9766
$S_{joint}/(Ed_0)$
τ

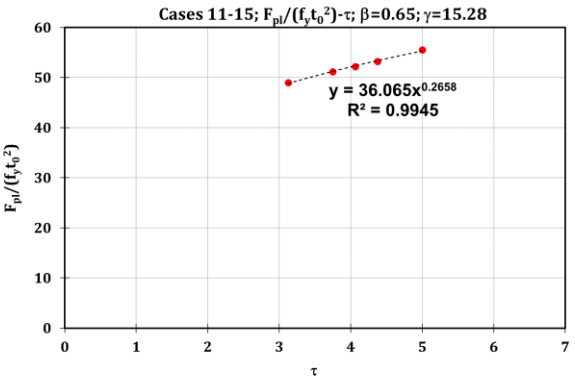
Cases 11-15; $F_{pl}/(f_y t_0^2)$-τ; β=0.65; γ=15.28
y = 36.065x^0.2658
R² = 0.9945
$F_{pl}/(f_y t_0^2)$
τ

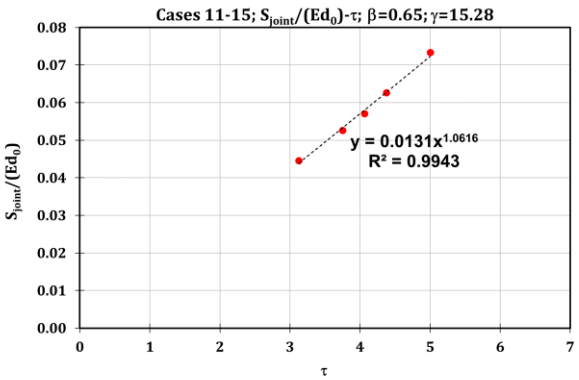
Cases 11-15; $S_{joint}/(Ed_0)$-τ; β=0.65; γ=15.28
y = 0.0131x^1.0616
R² = 0.9943
$S_{joint}/(Ed_0)$
τ

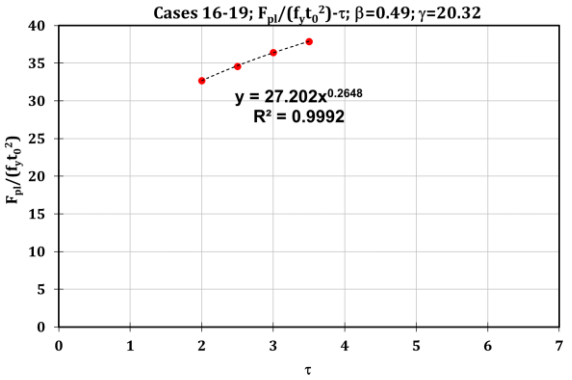
Cases 16-19; $F_{pl}/(f_y t_0^2)$-τ; β=0.49; γ=20.32
y = 27.202x^0.2648
R² = 0.9992
$F_{pl}/(f_y t_0^2)$
τ

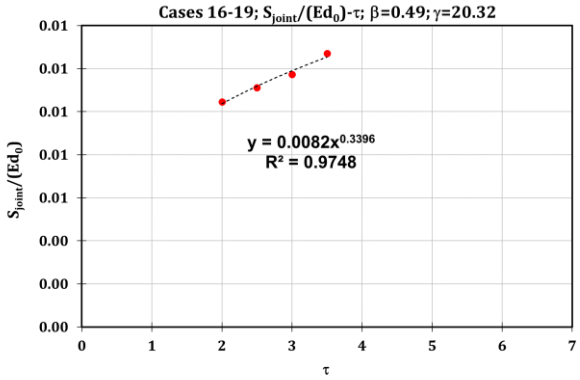
Cases 16-19; $S_{joint}/(Ed_0)$-τ; β=0.49; γ=20.32
y = 0.0082x^0.3396
R² = 0.9748
$S_{joint}/(Ed_0)$
τ

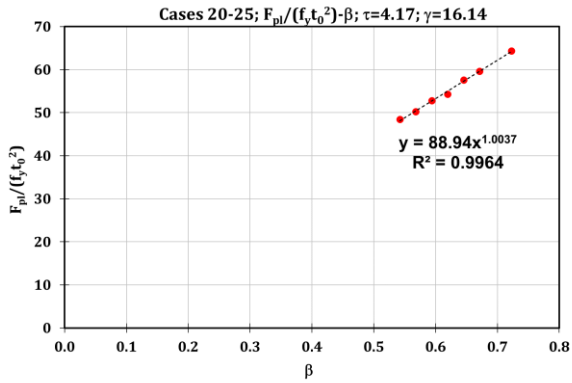
Cases 20-25; $F_{pl}/(f_y t_0^2)$-β; τ=4.17; γ=16.14
y = 88.94x^1.0037
R² = 0.9964
$F_{pl}/(f_y t_0^2)$
β

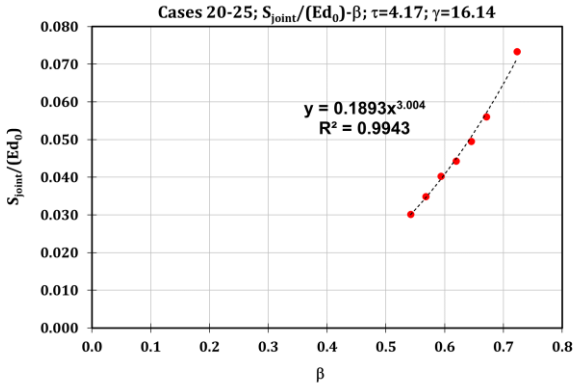
Cases 20-25; $S_{joint}/(Ed_0)$-β; τ=4.17; γ=16.14
y = 0.1893x^3.004
R² = 0.9943
$S_{joint}/(Ed_0)$
β

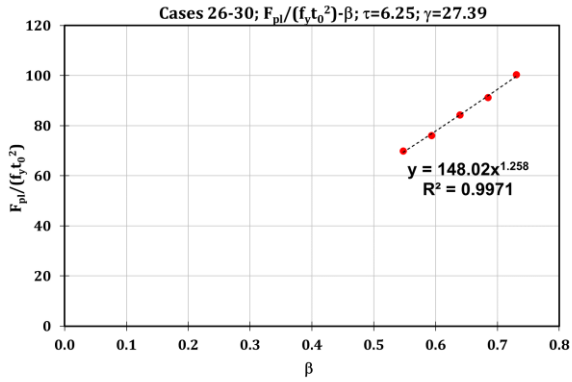
Cases 26-30; $F_{pl}/(f_y t_0^2)$-β; τ=6.25; γ=27.39
y = 148.02x^1.258
R² = 0.9971
$F_{pl}/(f_y t_0^2)$
β

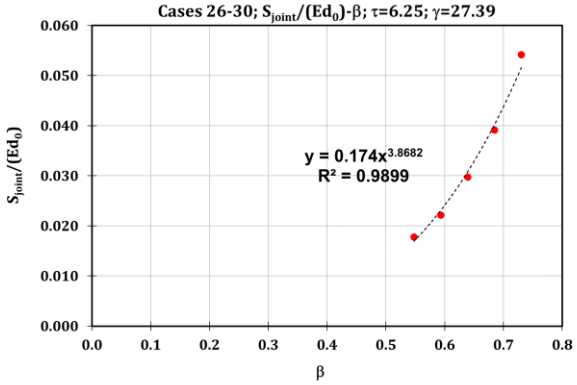
Cases 26-30; $S_{joint}/(Ed_0)$-β; τ=6.25; γ=27.39
y = 0.174x^3.8682
R² = 0.9899
$S_{joint}/(Ed_0)$
β

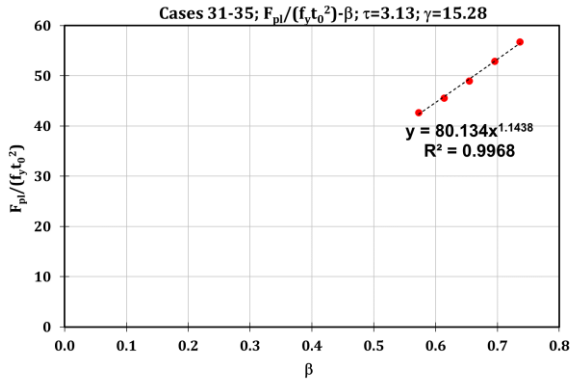
Cases 31-35; $F_{pl}/(f_y t_0^2)$-β; τ=3.13; γ=15.28
y = 80.134x^1.1438
R² = 0.9968
$F_{pl}/(f_y t_0^2)$
β

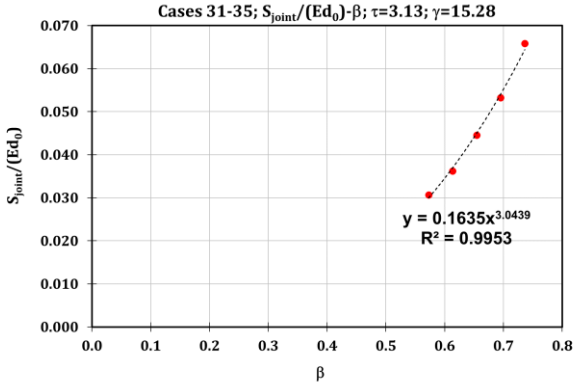
Cases 31-35; $S_{joint}/(Ed_0)$-β; τ=3.13; γ=15.28
y = 0.1635x^3.0439
R² = 0.9953
$S_{joint}/(Ed_0)$
β

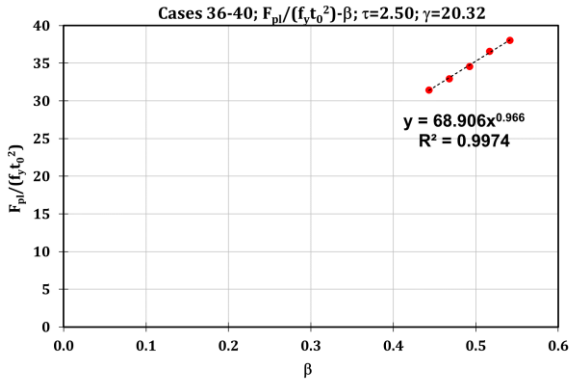
Cases 36-40; $F_{pl}/(f_y t_0^2)$-β; τ=2.50; γ=20.32
$F_{pl}/(f_y t_0^2)$
β
y = 68.906x^0.966
R² = 0.9974

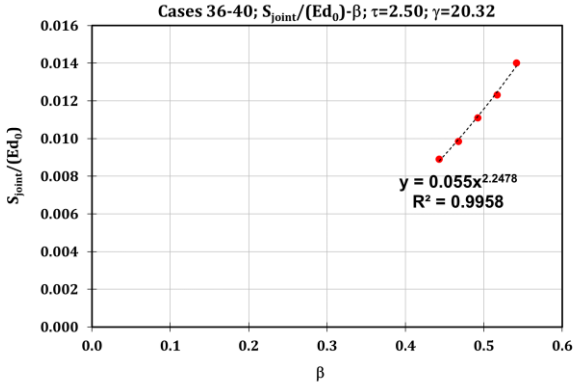
Cases 36-40; $S_{joint}/(Ed_0)$-β; τ=2.50; γ=20.32
$S_{joint}/(Ed_0)$
β
y = 0.055x^2.2478
R² = 0.9958

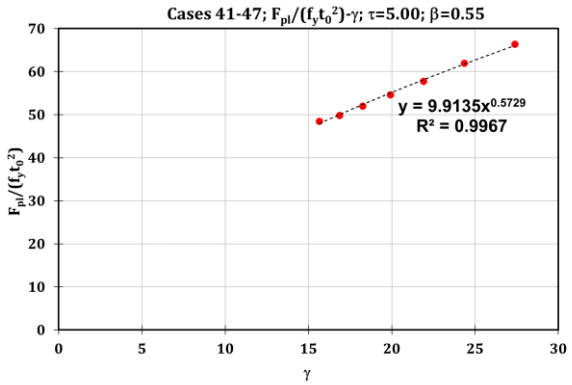
Cases 41-47; $F_{pl}/(f_y t_0^2)$-γ; τ=5.00; β=0.55
$F_{pl}/(f_y t_0^2)$
γ
y = 9.9135x^0.5729
R² = 0.9967

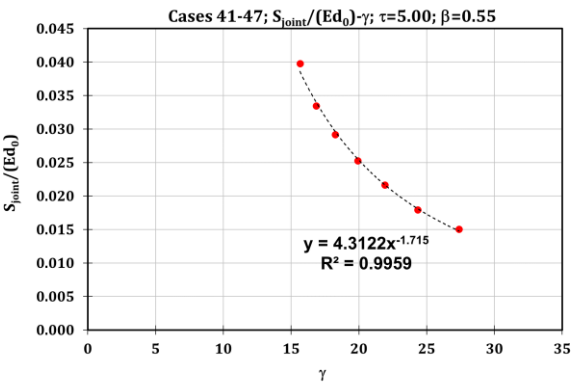
Cases 41-47; $S_{joint}/(Ed_0)$-γ; τ=5.00; β=0.55
$S_{joint}/(Ed_0)$
γ
y = 4.3122x^-1.715
R² = 0.9959

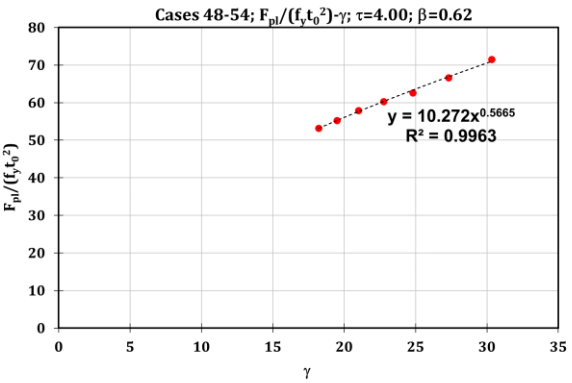
Cases 48-54; $F_{pl}/(f_y t_0^2)$-γ; τ=4.00; β=0.62
$F_{pl}/(f_y t_0^2)$
γ
y = 10.272x^0.5665
R² = 0.9963

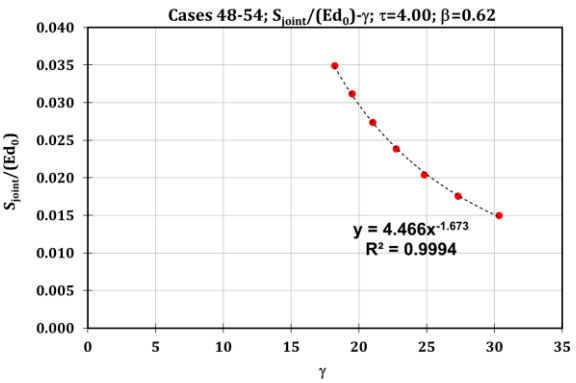
Cases 48-54; $S_{joint}/(Ed_0)$-γ; τ=4.00; β=0.62
$S_{joint}/(Ed_0)$
γ
y = 4.466x^-1.673
R² = 0.9994

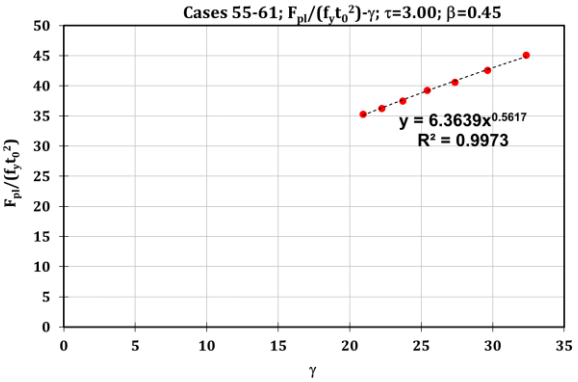
Cases 55-61; $F_{pl}/(f_y t_0^2)$-γ; τ=3.00; β=0.45
$F_{pl}/(f_y t_0^2)$
γ
y = 6.3639x^0.5617
R² = 0.9973

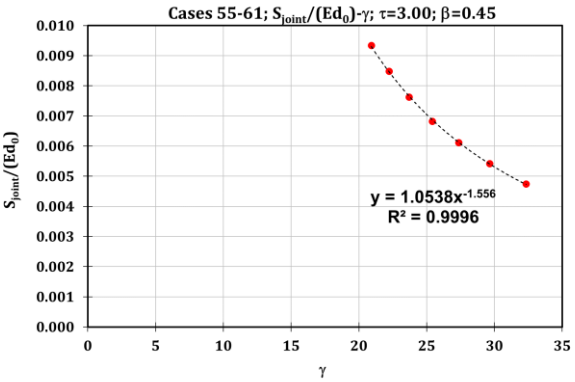
Cases 55-61; $S_{joint}/(Ed_0)$-γ; τ=3.00; β=0.45
$S_{joint}/(Ed_0)$
γ
y = 1.0538x^-1.556
R² = 0.9996

A3. CHS to through-all plate connections: cyclic simulations

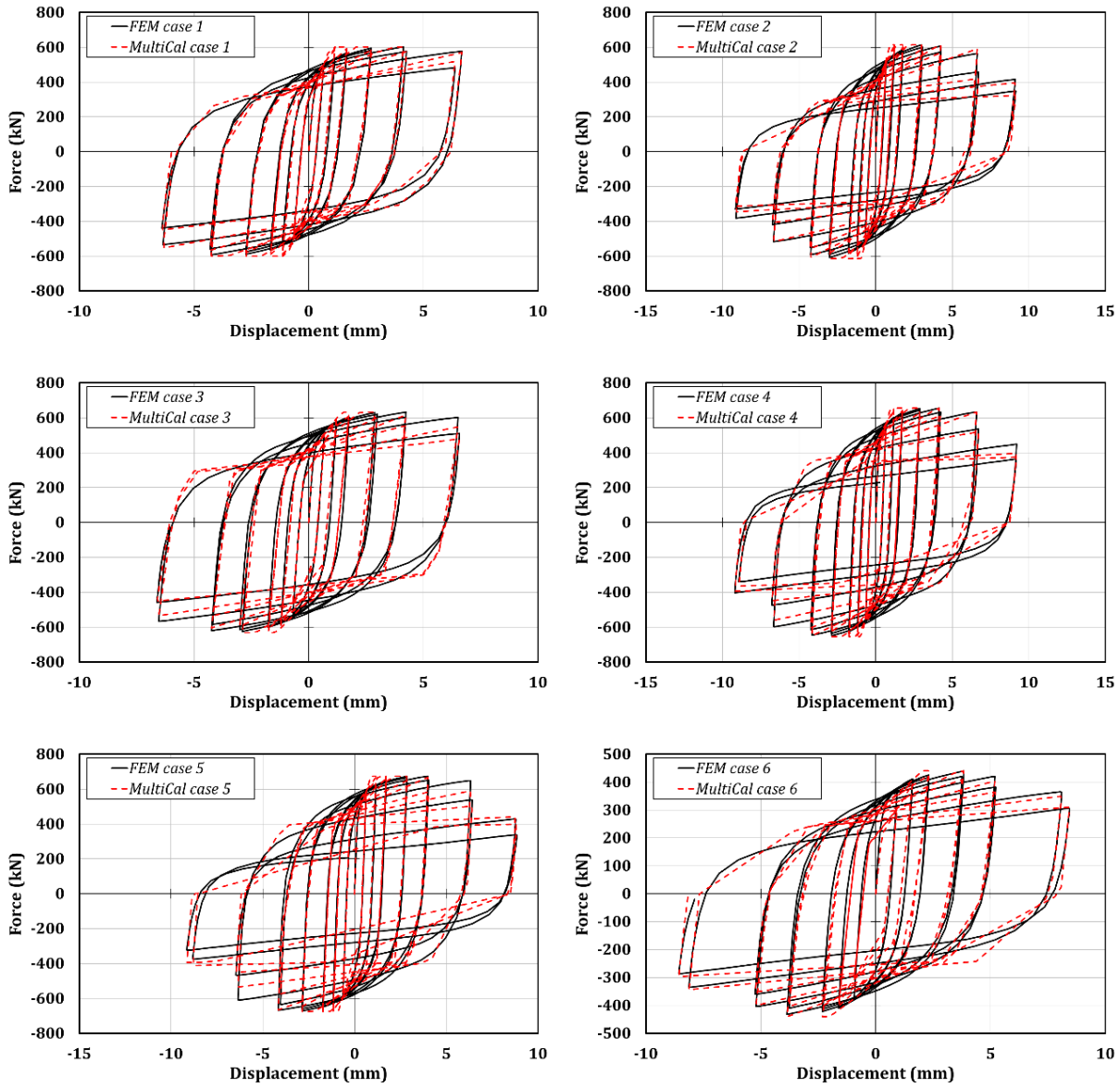

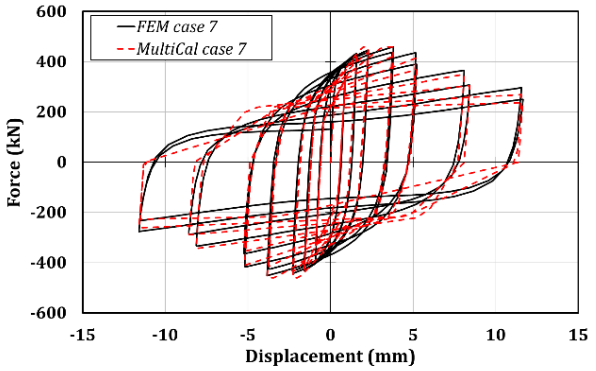
FEM case 7
MultiCal case 7
Force (kN)
Displacement (mm)

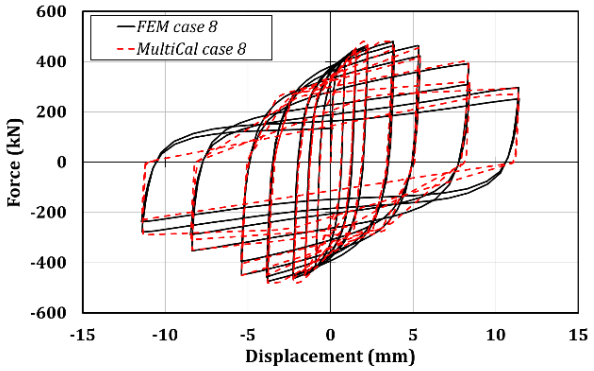
FEM case 8
MultiCal case 8
Force (kN)
Displacement (mm)

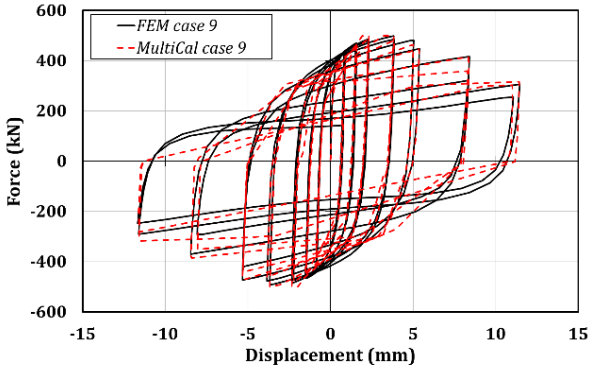
FEM case 9
MultiCal case 9
Force (kN)
Displacement (mm)

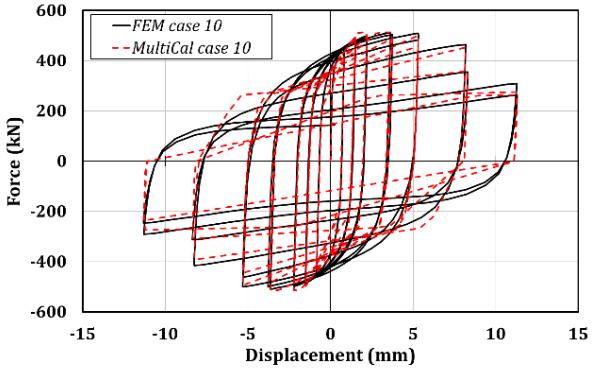
FEM case 10
MultiCal case 10
Force (kN)
Displacement (mm)

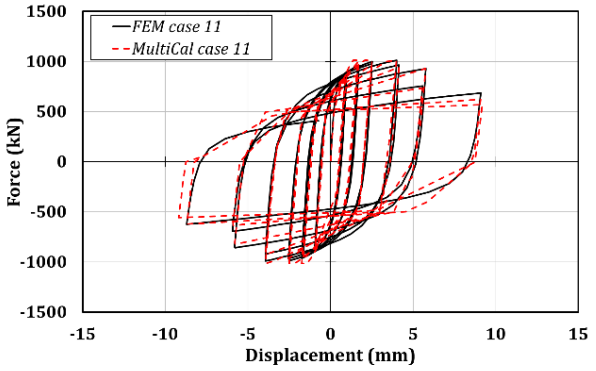
FEM case 11
MultiCal case 11
Force (kN)
Displacement (mm)

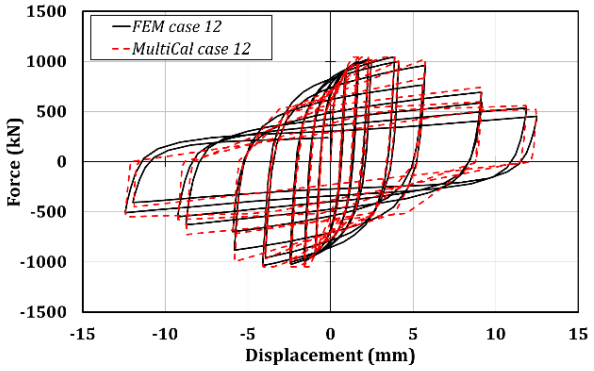
FEM case 12
MultiCal case 12
Force (kN)
Displacement (mm)

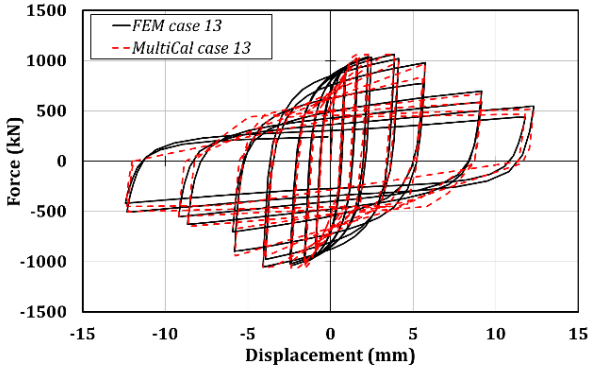
FEM case 13
MultiCal case 13
Force (kN)
Displacement (mm)

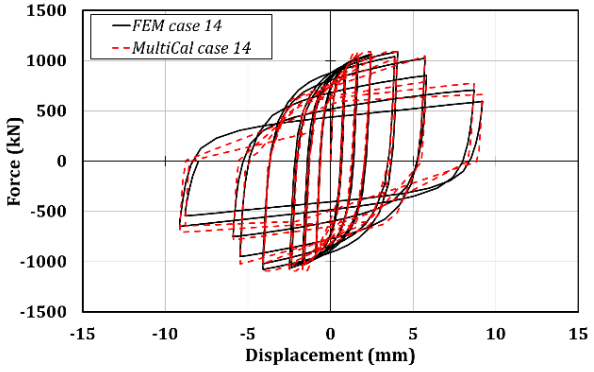
FEM case 14
MultiCal case 14
Force (kN)
Displacement (mm)

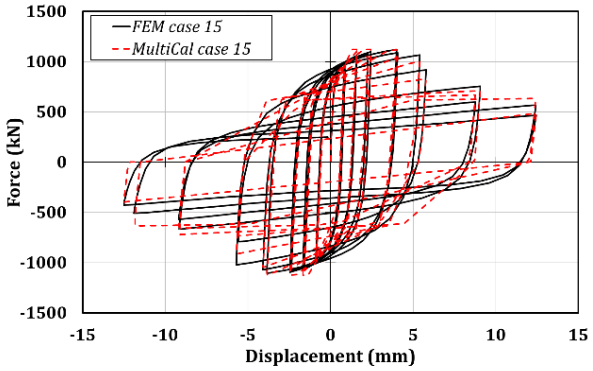
FEM case 15
MultiCal case 15
Force (kN)
Displacement (mm)

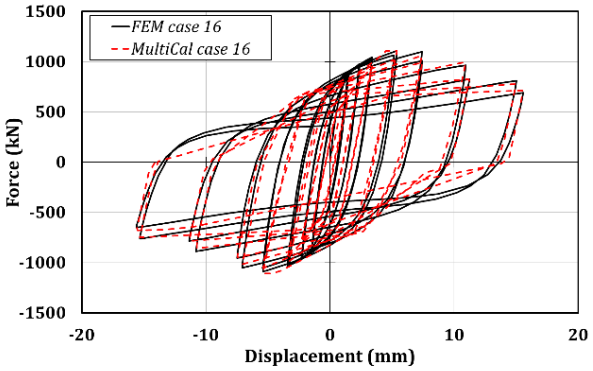
FEM case 16
MultiCal case 16
Force (kN)
Displacement (mm)

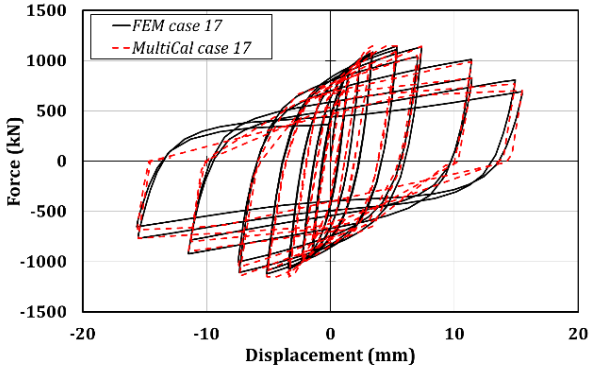
FEM case 17
MultiCal case 17
Force (kN)
Displacement (mm)

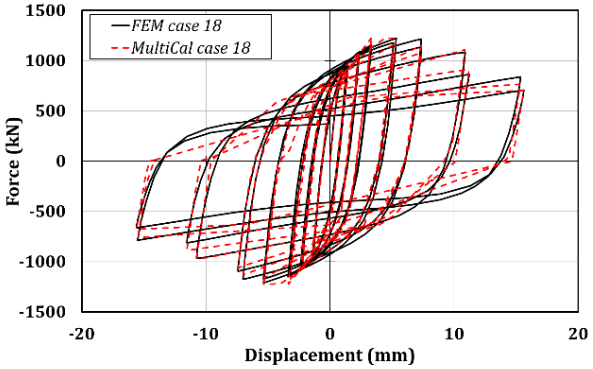
FEM case 18
MultiCal case 18
Force (kN)
Displacement (mm)

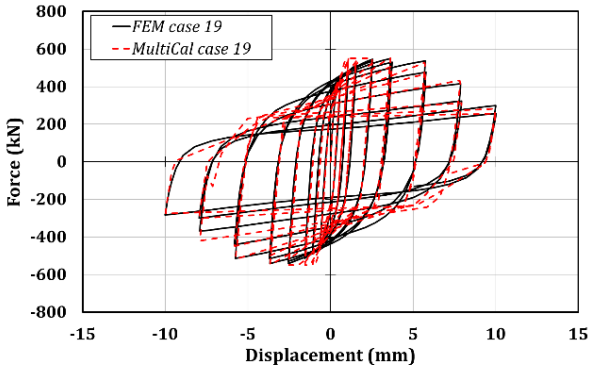
FEM case 19
MultiCal case 19
Force (kN)
Displacement (mm)

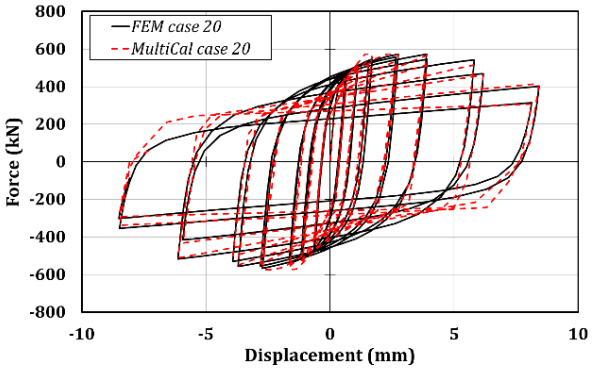
FEM case 20
MultiCal case 20
Force (kN)
Displacement (mm)

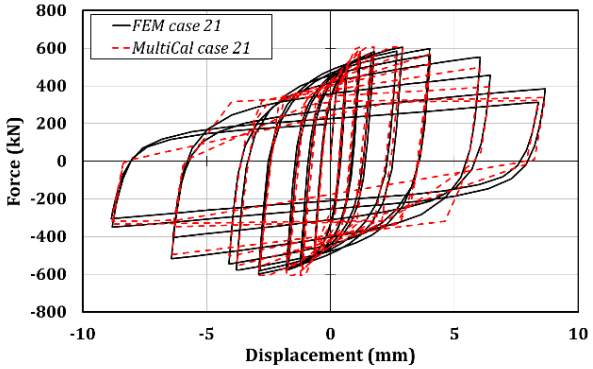
FEM case 21
MultiCal case 21
Force (kN)
Displacement (mm)

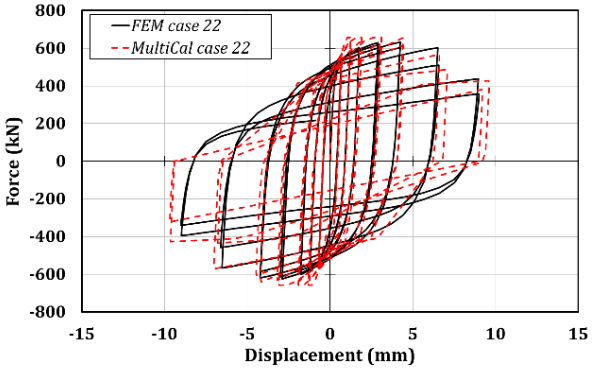
FEM case 22
MultiCal case 22
Force (kN)
Displacement (mm)

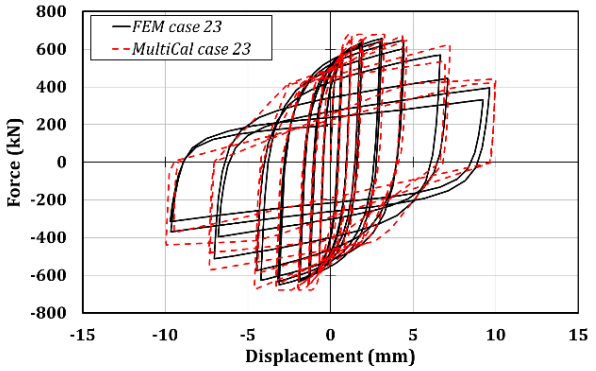
FEM case 23
MultiCal case 23
Force (kN)
Displacement (mm)

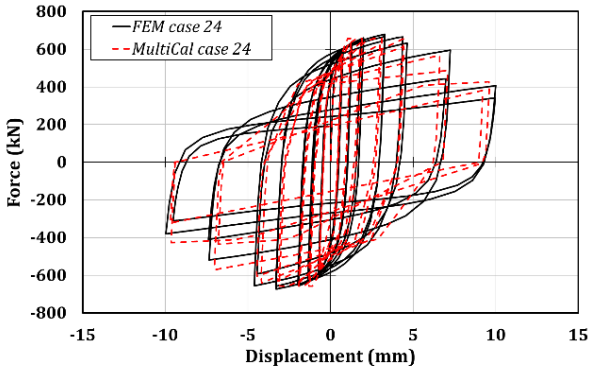
FEM case 24
MultiCal case 24
Force (kN)
Displacement (mm)

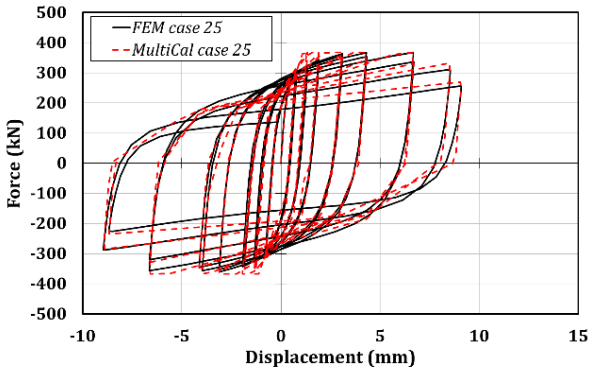
FEM case 25
MultiCal case 25
Force (kN)
Displacement (mm)

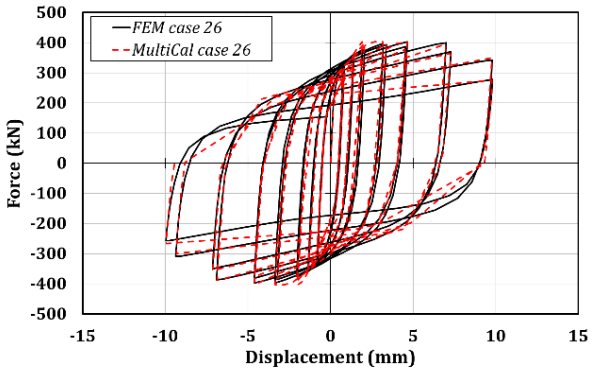
FEM case 26
MultiCal case 26
Force (kN)
Displacement (mm)

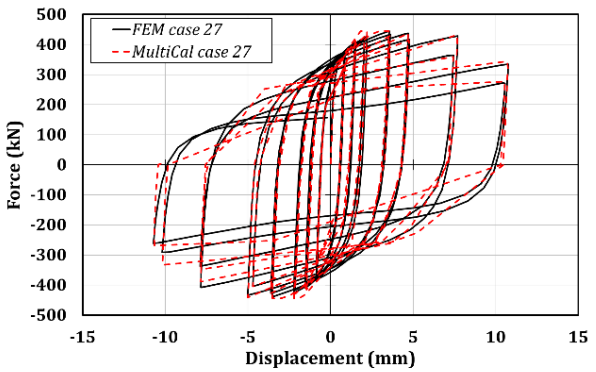
FEM case 27
MultiCal case 27
Force (kN)
Displacement (mm)

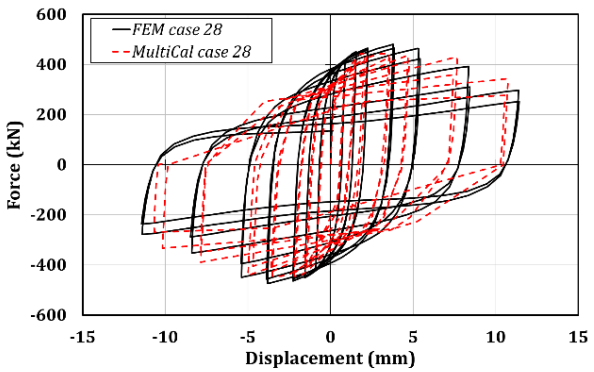
FEM case 28
MultiCal case 28
Force (kN)
Displacement (mm)

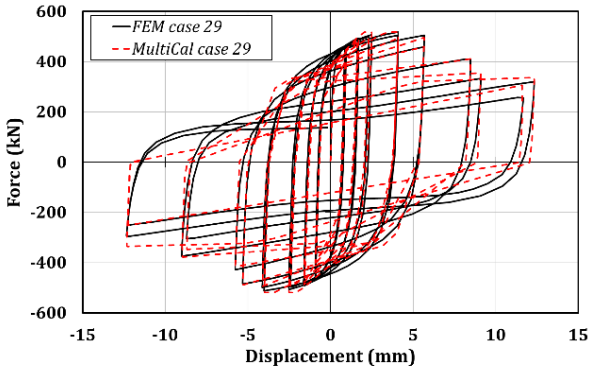
FEM case 29
MultiCal case 29
Force (kN)
Displacement (mm)

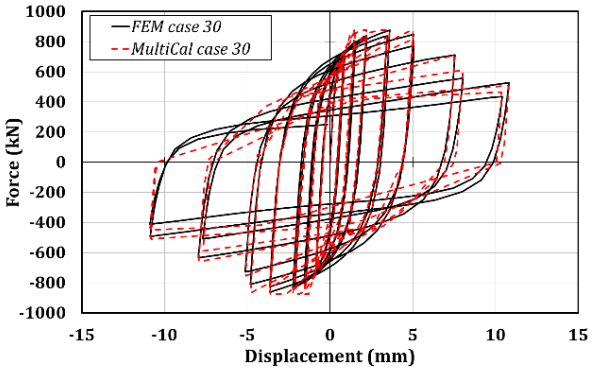
FEM case 30
MultiCal case 30
Force (kN)
Displacement (mm)

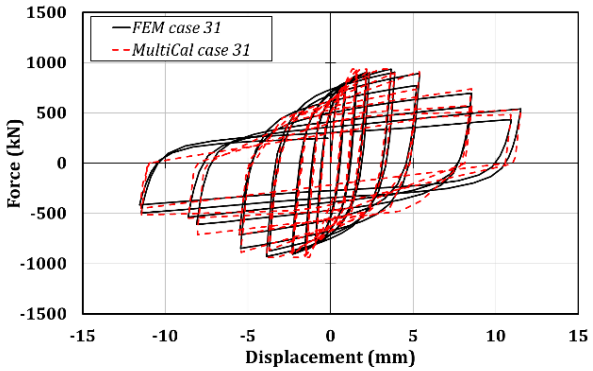
FEM case 31
MultiCal case 31
Force (kN)
Displacement (mm)

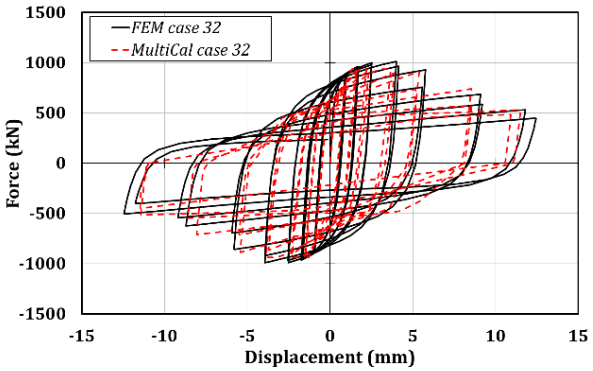
FEM case 32
MultiCal case 32
Force (kN)
Displacement (mm)

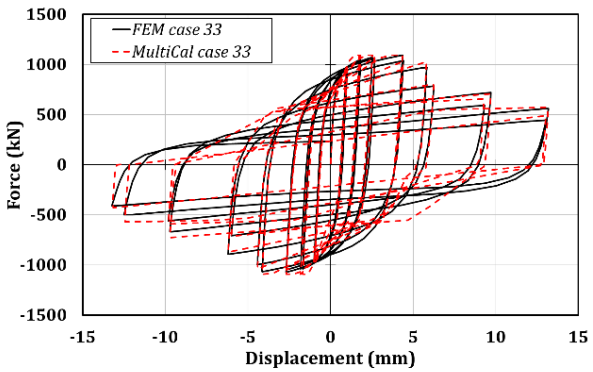
FEM case 33
MultiCal case 33
Force (kN)
Displacement (mm)

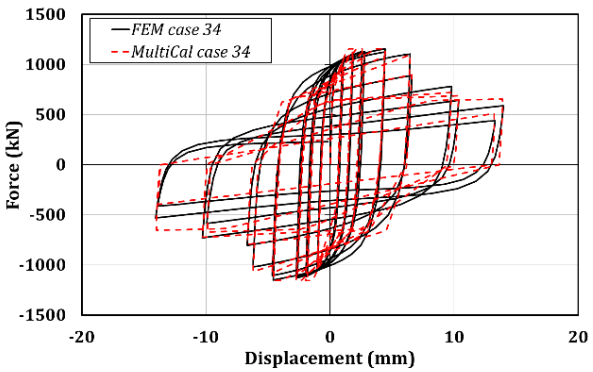
FEM case 34
MultiCal case 34
Force (kN)
Displacement (mm)

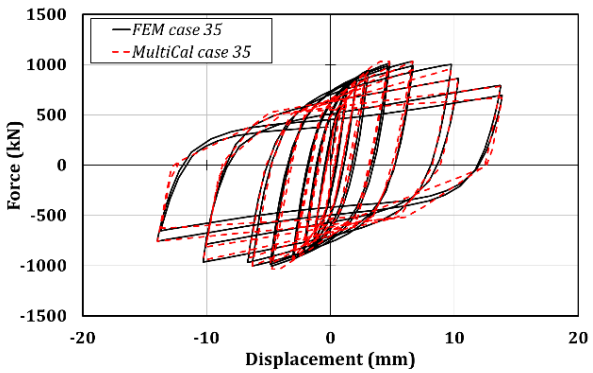
FEM case 35
MultiCal case 35
Force (kN)
Displacement (mm)

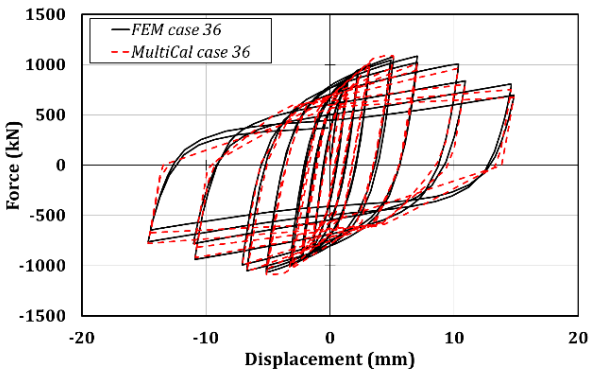
FEM case 36
MultiCal case 36
Force (kN)
Displacement (mm)

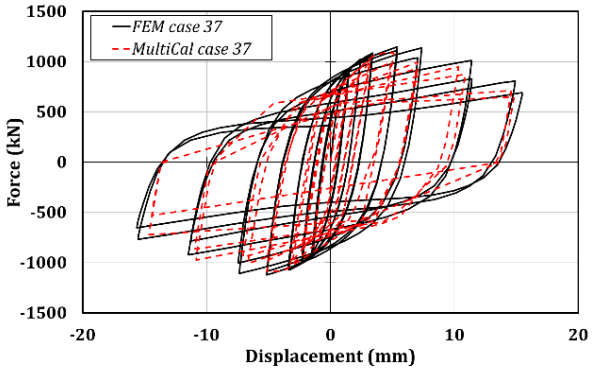
FEM case 37
MultiCal case 37
Force (kN)
Displacement (mm)

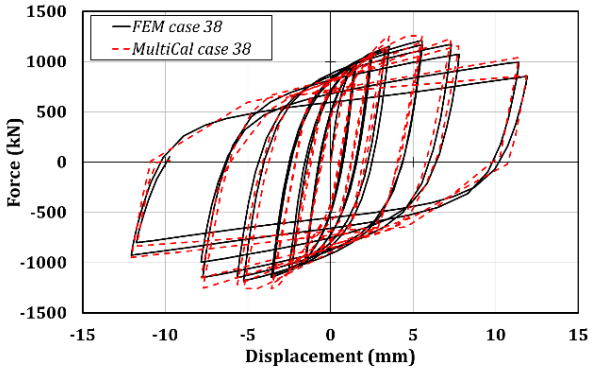
FEM case 38
MultiCal case 38
Force (kN)
Displacement (mm)

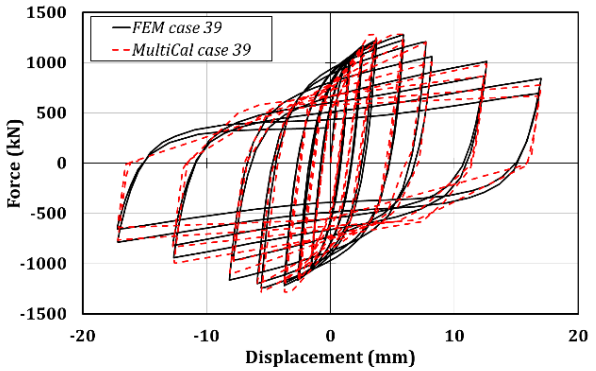
FEM case 39
MultiCal case 39
Force (kN)
Displacement (mm)

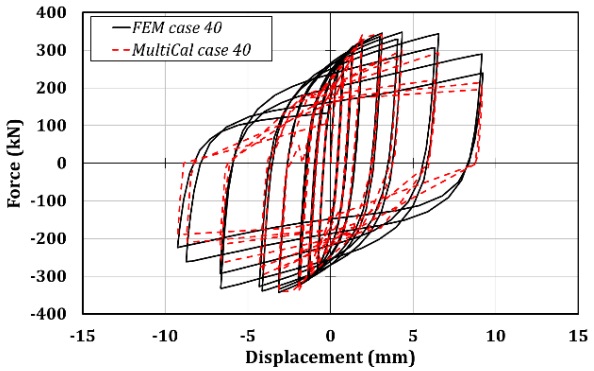
FEM case 40
MultiCal case 40
Force (kN)
Displacement (mm)

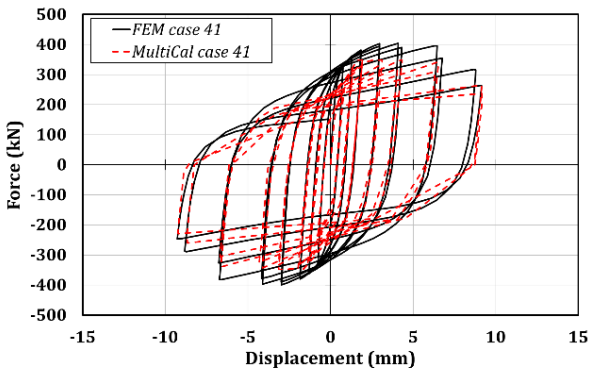
FEM case 41
MultiCal case 41
Force (kN)
Displacement (mm)

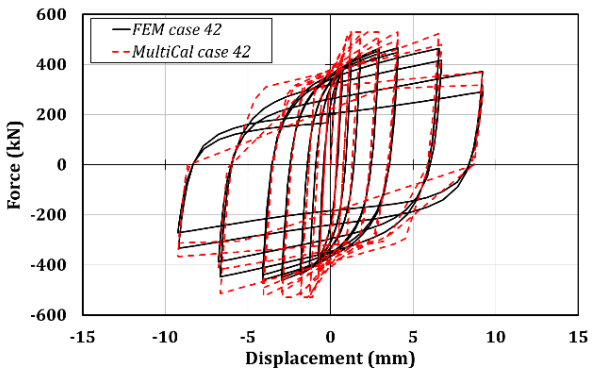
FEM case 42
MultiCal case 42
Force (kN)
Displacement (mm)

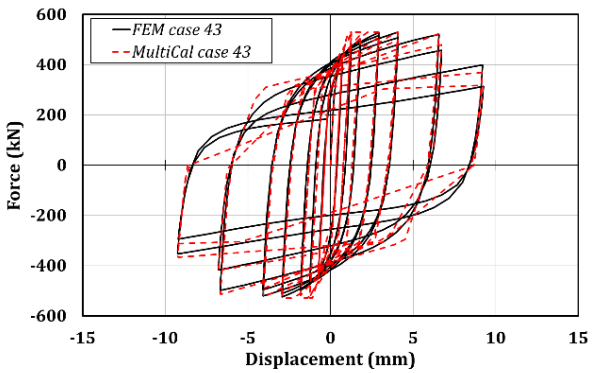
FEM case 43
MultiCal case 43
Force (kN)
Displacement (mm)

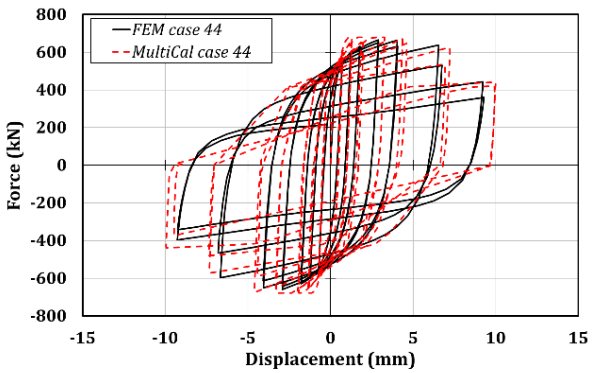
FEM case 44
MultiCal case 44
Force (kN)
Displacement (mm)

A4. CHS to through-all plate connections: CHS tube under localised transverse compression (ttc)

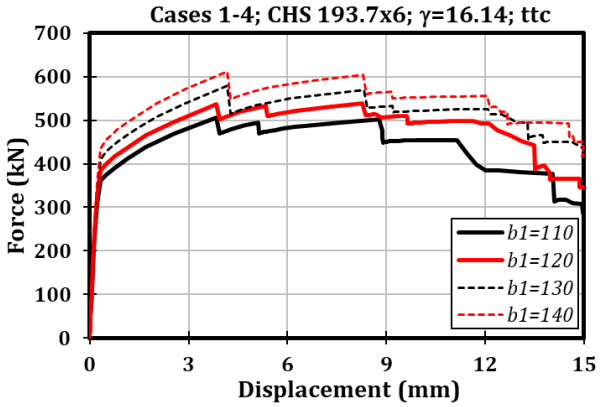

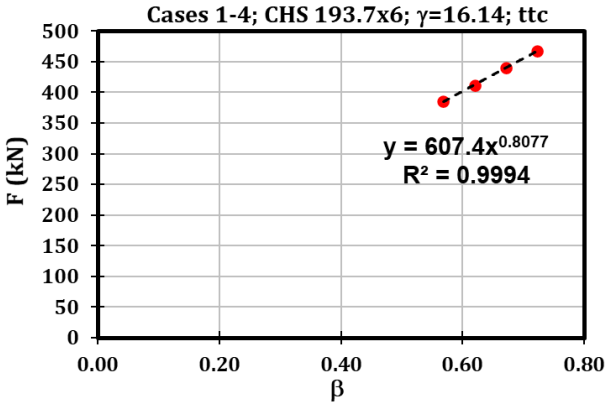

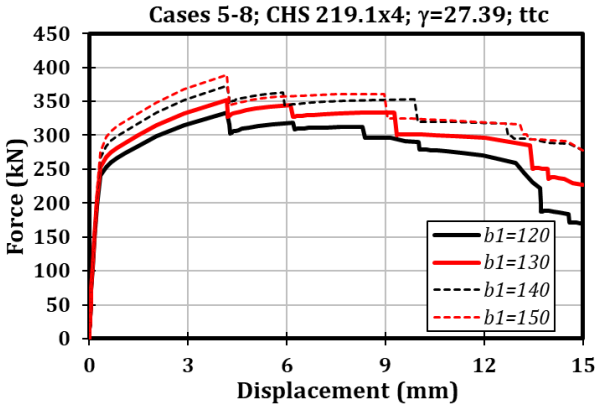

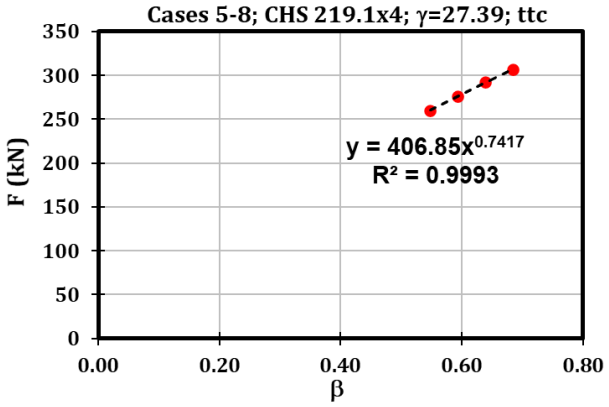

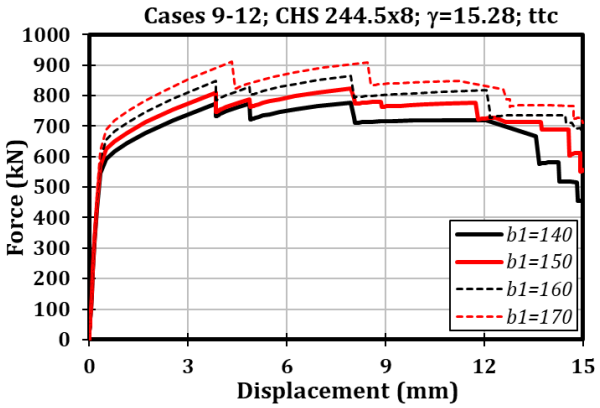

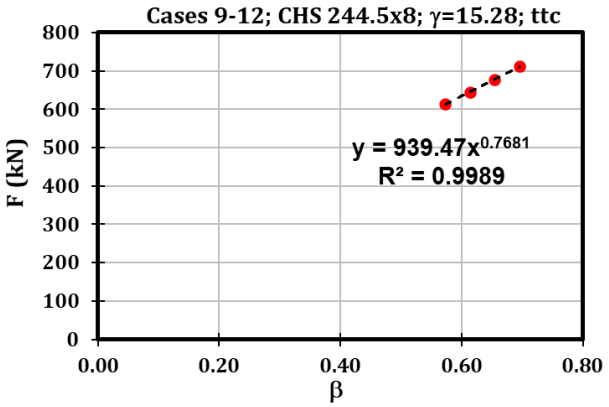

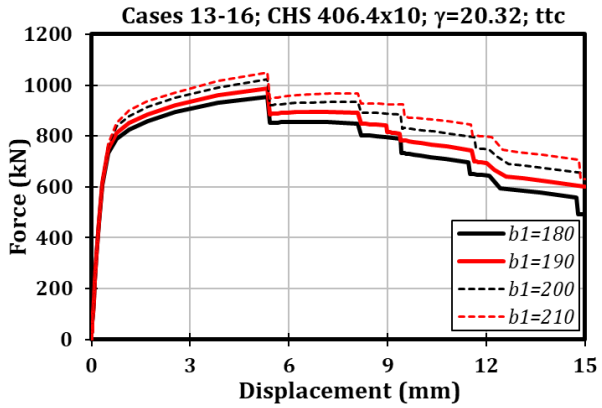
Cases 13-16; CHS 406.4x10; γ=20.32; ttc
Force (kN)
Displacement (mm)
b1=180
b1=190
b1=200
b1=210

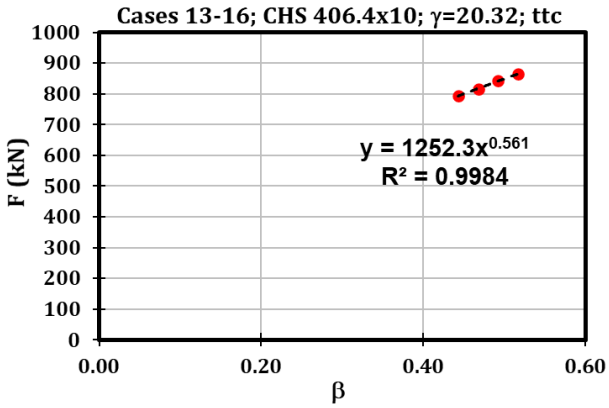
Cases 13-16; CHS 406.4x10; γ=20.32; ttc
F (kN)
β
y = 1252.3x^0.561
R² = 0.9984

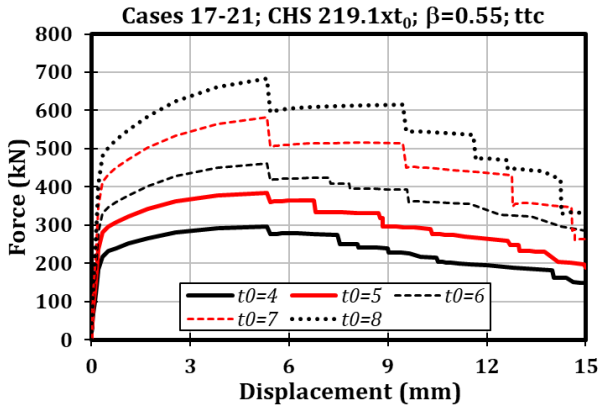
Cases 17-21; CHS 219.1xt0; β=0.55; ttc
Force (kN)
Displacement (mm)
t0=4
t0=5
t0=6
t0=7
t0=8

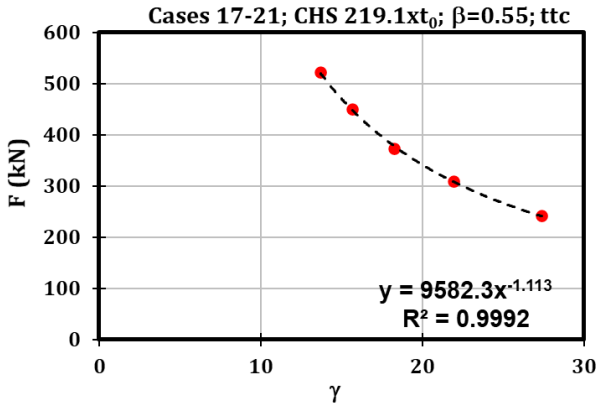
Cases 17-21; CHS 219.1xt0; β=0.55; ttc
F (kN)
γ
y = 9582.3x^-1.113
R² = 0.9992

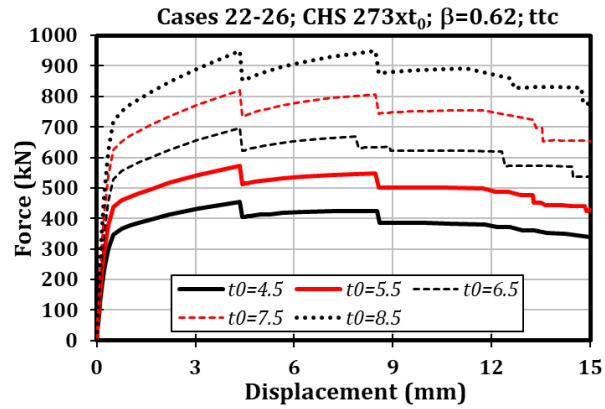
Cases 22-26; CHS 273xt0; β=0.62; ttc
Force (kN)
Displacement (mm)
t0=4.5
t0=5.5
t0=6.5
t0=7.5
t0=8.5

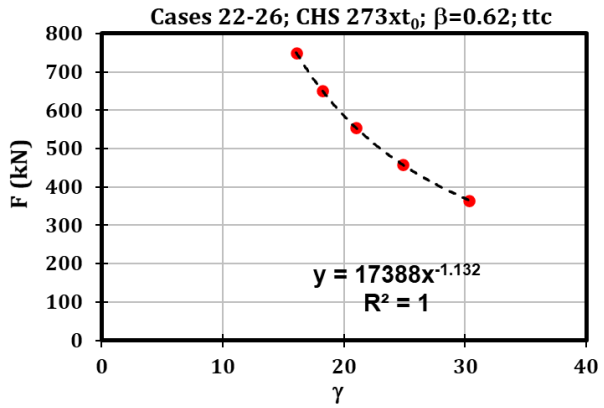
Cases 22-26; CHS 273xt0; β=0.62; ttc
F (kN)
γ
y = 17388x^-1.132
R² = 1

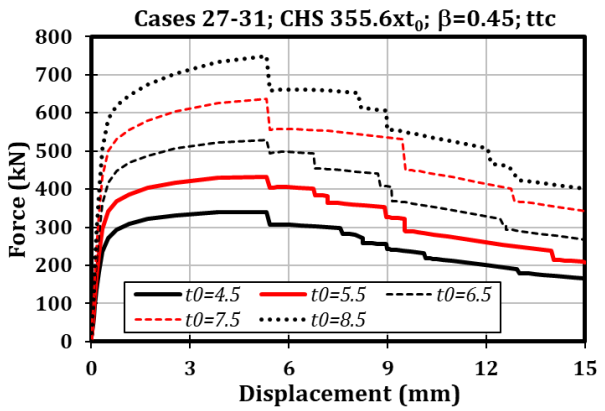
Cases 27-31; CHS 355.6xt0; β=0.45; ttc
Force (kN)
Displacement (mm)
t0=4.5
t0=5.5
t0=6.5
t0=7.5
t0=8.5

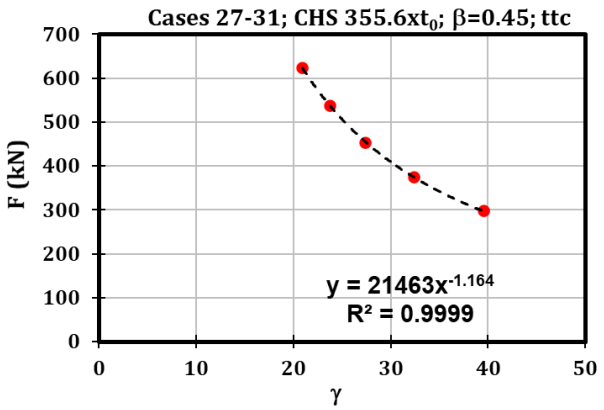
Cases 27-31; CHS 355.6xt0; β=0.45; ttc
F (kN)
γ
y = 21463x^-1.164
R² = 0.9999

A5. CHS to through-all plate connections: CHS tube under localised transverse compression (ttt)

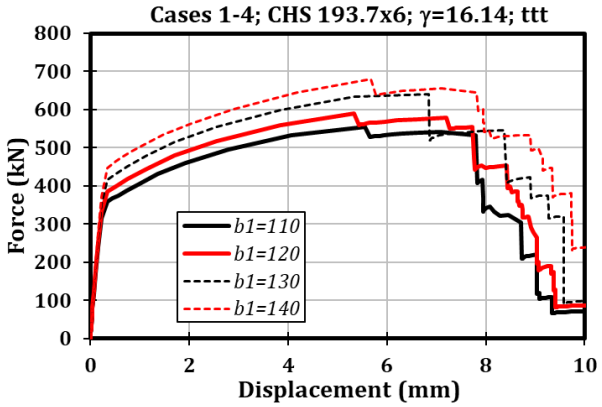

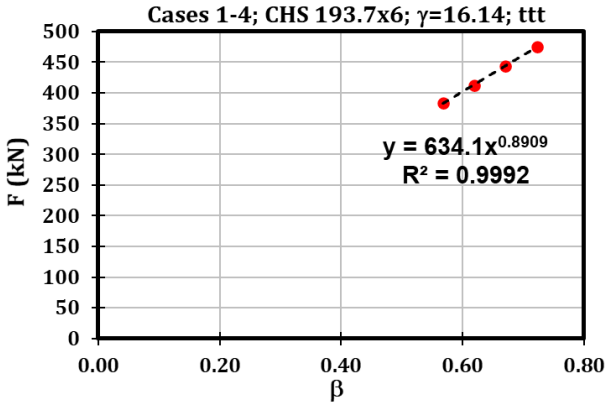

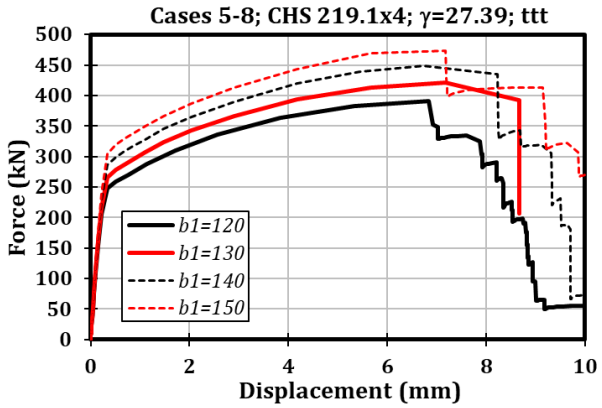

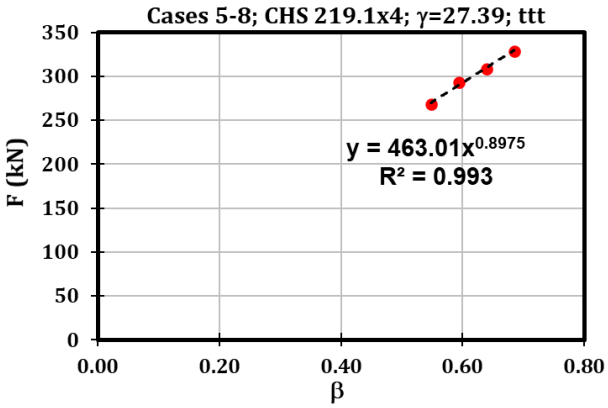

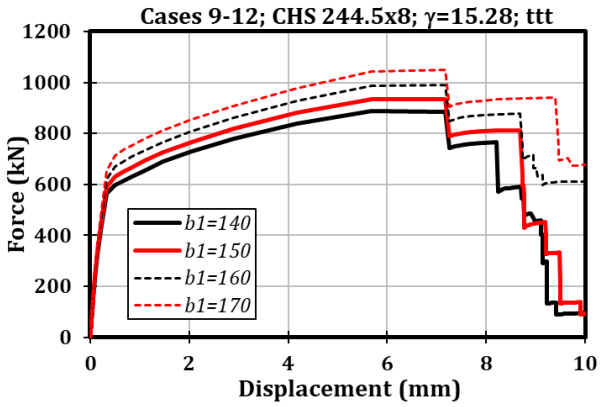

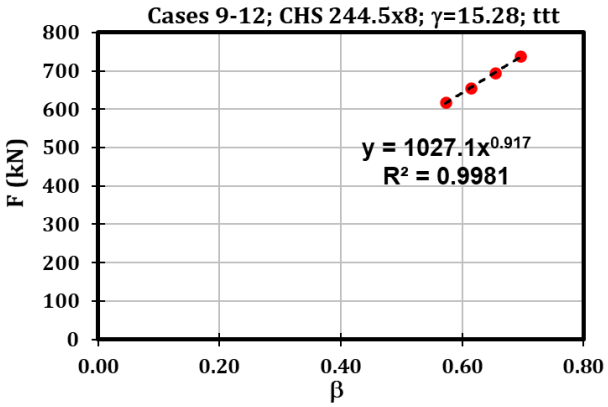

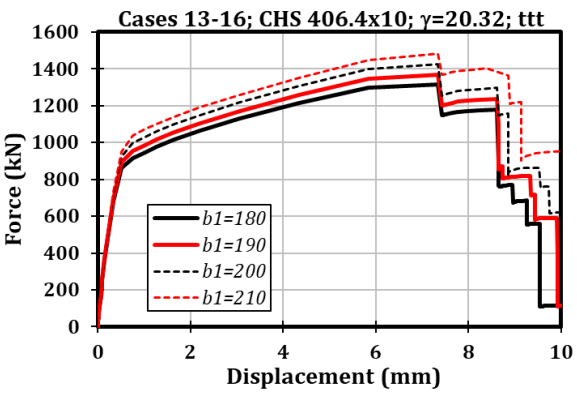
Cases 13-16; CHS 406.4x10; γ=20.32; ttt
Force (kN)
Displacement (mm)
b1=180
b1=190
b1=200
b1=210

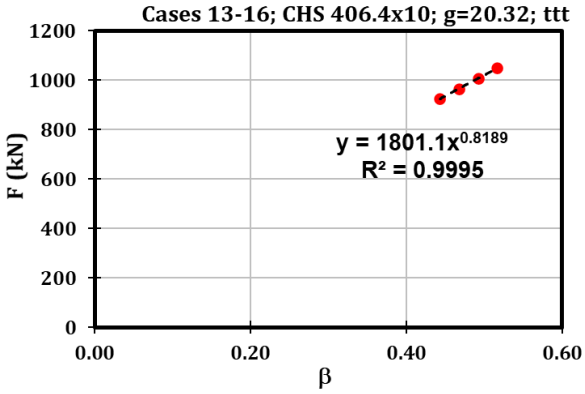
Cases 13-16; CHS 406.4x10; g=20.32; ttt
F (kN)
β
y = 1801.1x^0.8189
R² = 0.9995

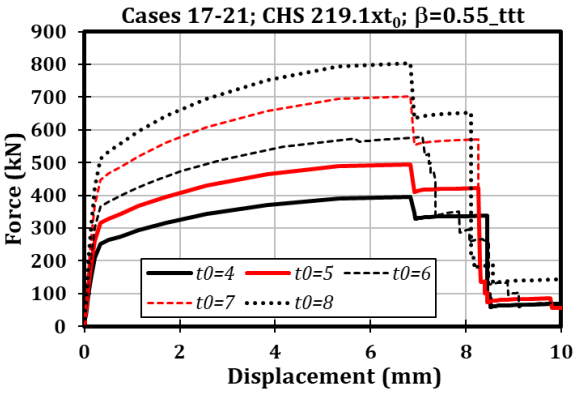
Cases 17-21; CHS 219.1xt0; β=0.55_ttt
Force (kN)
Displacement (mm)
t0=4
t0=5
t0=6
t0=7
t0=8

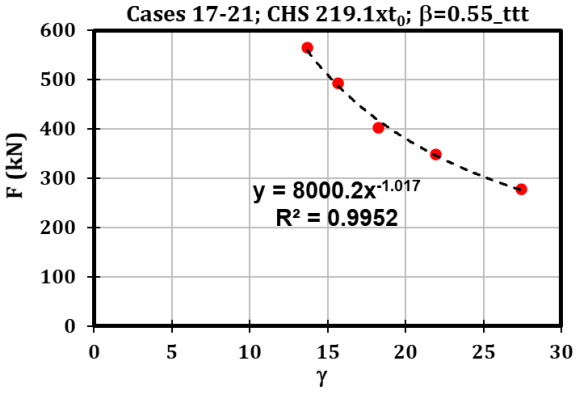
Cases 17-21; CHS 219.1xt0; β=0.55_ttt
F (kN)
γ
y = 8000.2x^-1.017
R² = 0.9952

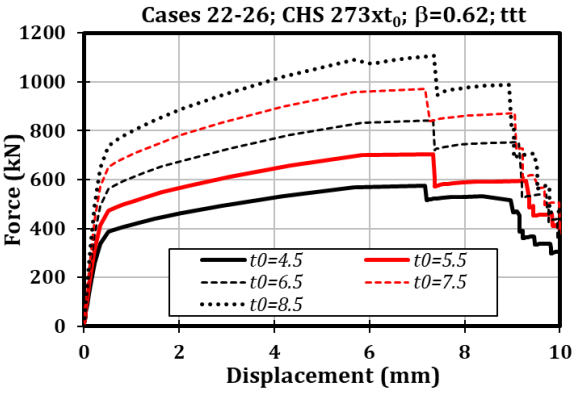
Cases 22-26; CHS 273xt0; β=0.62; ttt
Force (kN)
Displacement (mm)
t0=4.5
t0=5.5
t0=6.5
t0=7.5
t0=8.5

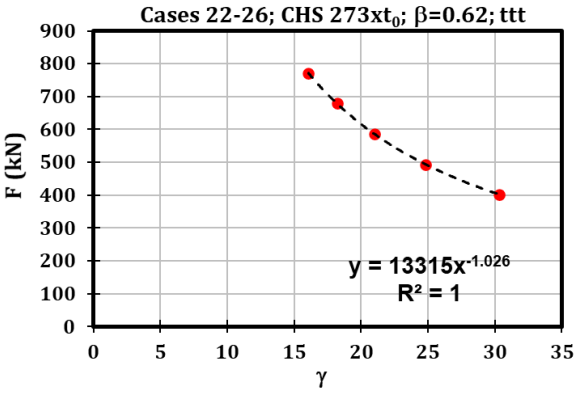
Cases 22-26; CHS 273xt0; β=0.62; ttt
F (kN)
γ
y = 13315x^-1.026
R² = 1

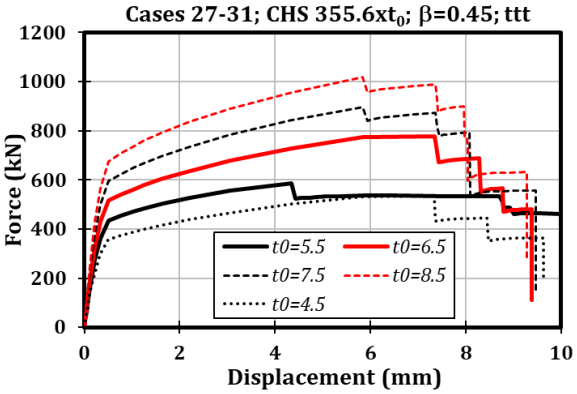
Cases 27-31; CHS 355.6xt0; β=0.45; ttt
Force (kN)
Displacement (mm)
t0=5.5
t0=6.5
t0=7.5
t0=8.5
t0=4.5

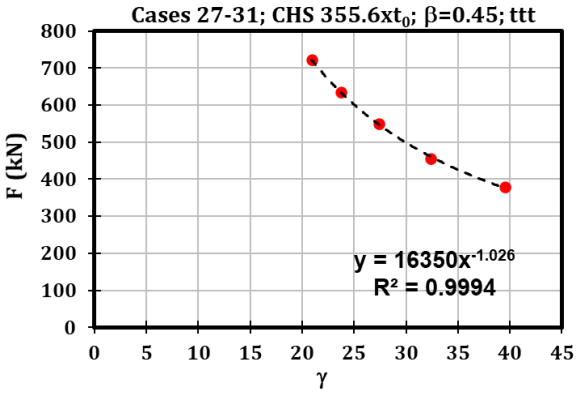
Cases 27-31; CHS 355.6xt0; β=0.45; ttt
F (kN)
γ
y = 16350x^-1.026
R² = 0.9994

A6. CHS to through-all I-beam connections: cyclic FE simulations vs component method approach

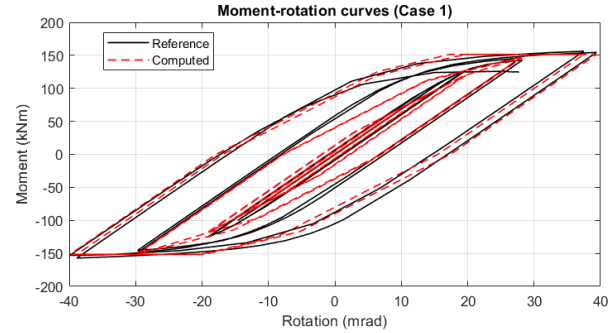

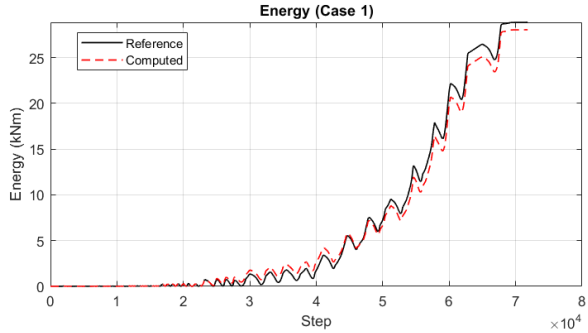

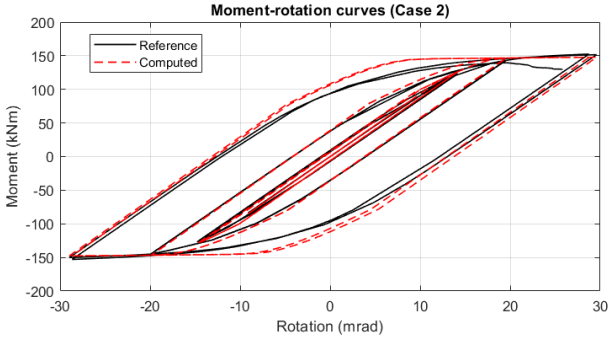

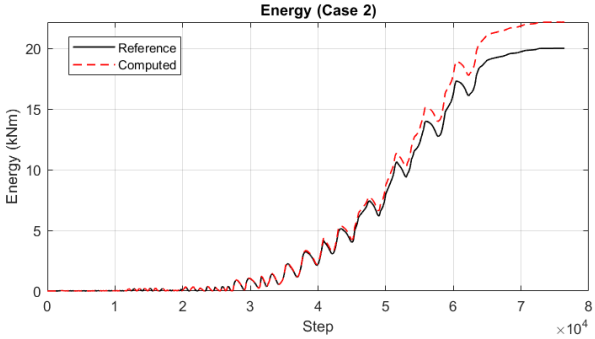

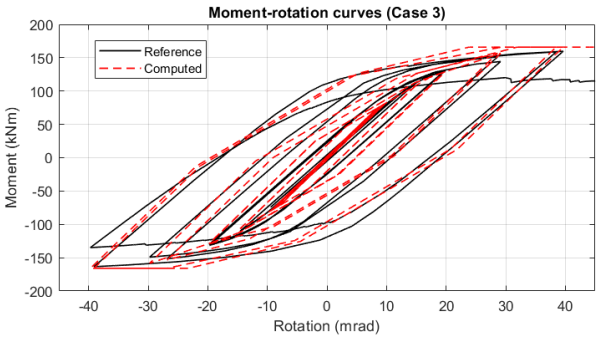

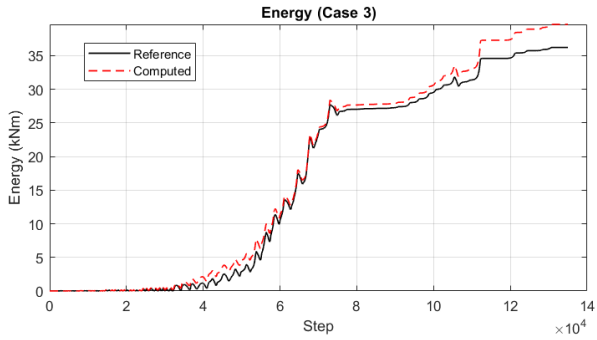

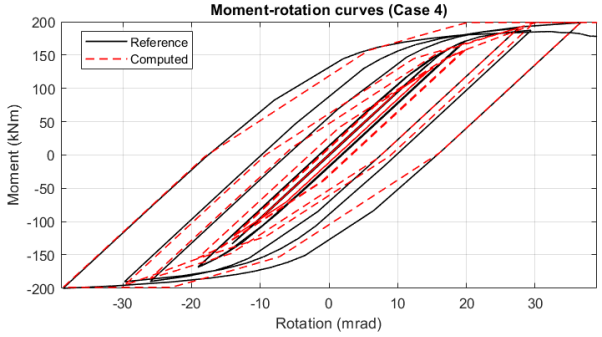
Moment-rotation curves (Case 4)
Reference
Computed
Moment (kNm)
Rotation (mrad)

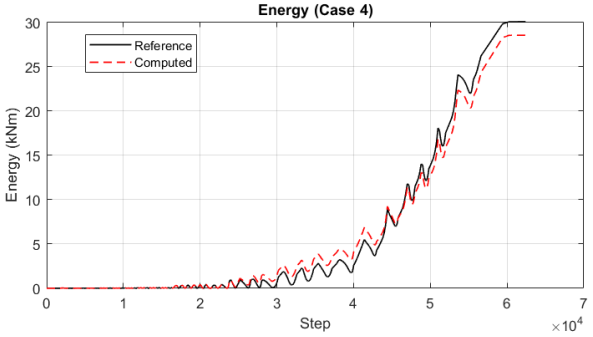
Energy (Case 4)
Reference
Computed
Energy (kNm)
Step
×10^4

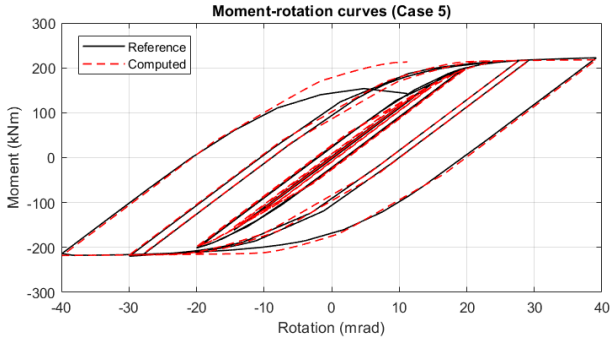
Moment-rotation curves (Case 5)
Reference
Computed
Moment (kNm)
Rotation (mrad)

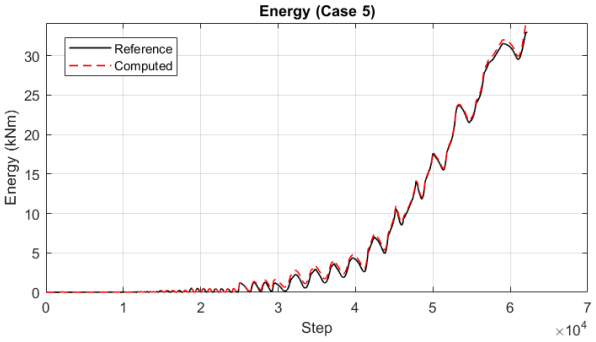
Energy (Case 5)
Reference
Computed
Energy (kNm)
Step
×10^4

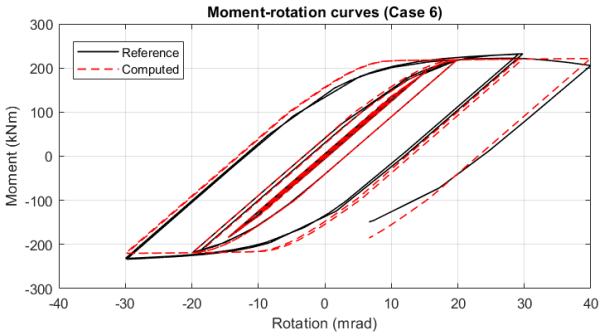
Moment-rotation curves (Case 6)
Reference
Computed
Moment (kNm)
Rotation (mrad)

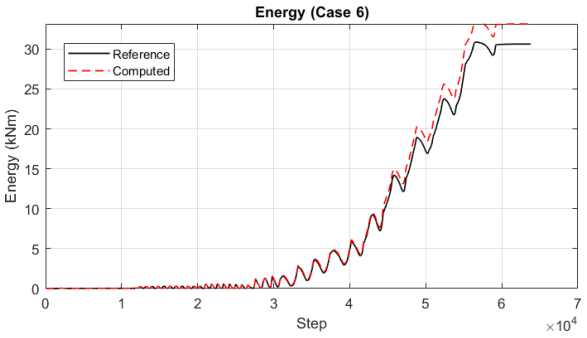
Energy (Case 6)
Reference
Computed
Energy (kNm)
Step
×10^4

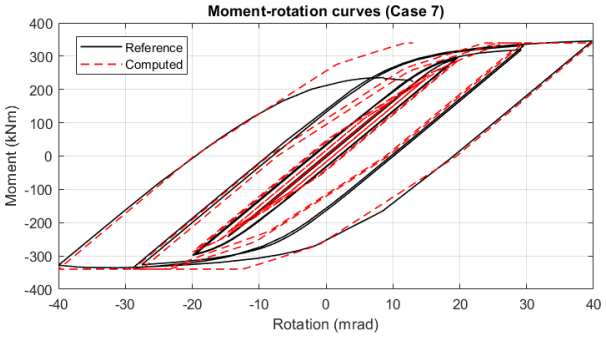
Moment-rotation curves (Case 7)
Reference
Computed
Moment (kNm)
Rotation (mrad)

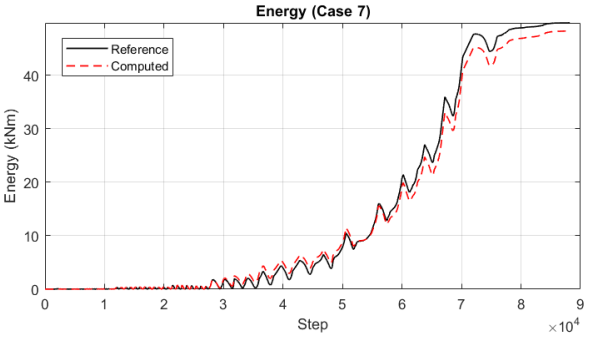
Energy (Case 7)
Reference
Computed
Energy (kNm)
Step
×10^4

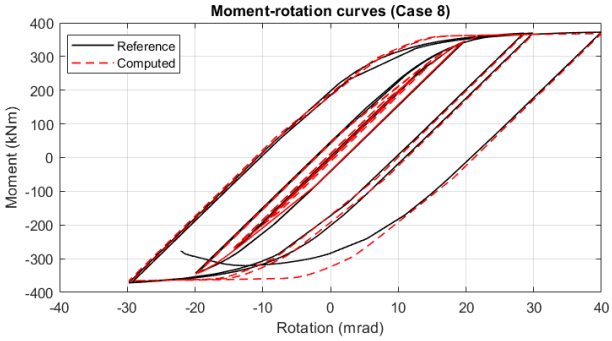
Moment-rotation curves (Case 8)
Reference
Computed
Moment (kNm)
Rotation (mrad)

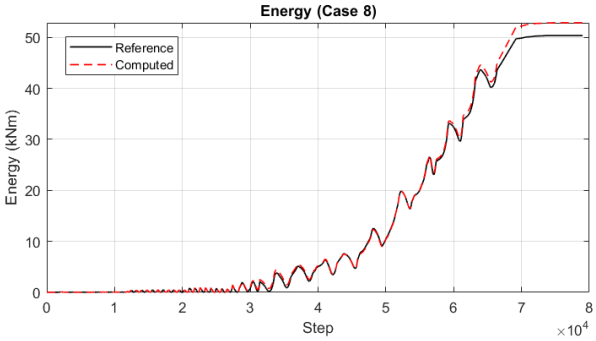
Energy (Case 8)
Reference
Computed
Energy (kNm)
Step
×10^4

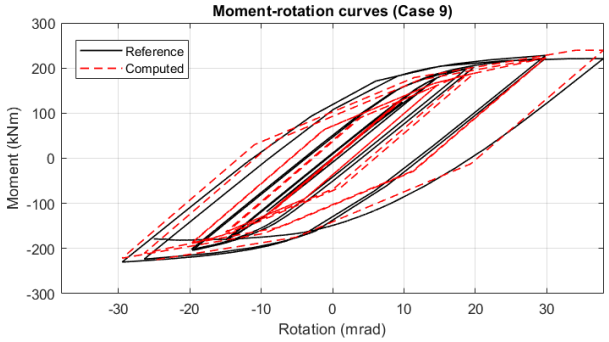
Moment-rotation curves (Case 9)
Reference
Computed
Moment (kNm)
Rotation (mrad)

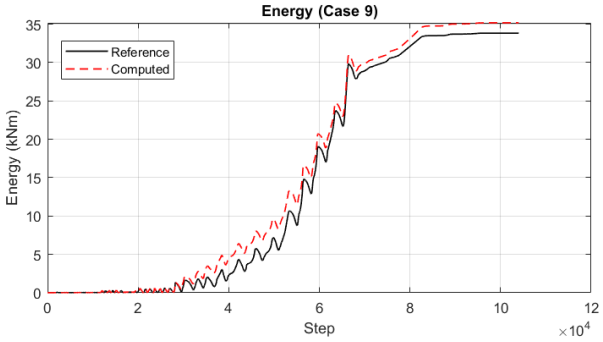
Energy (Case 9)
Reference
Computed
Energy (kNm)
Step
×10^4

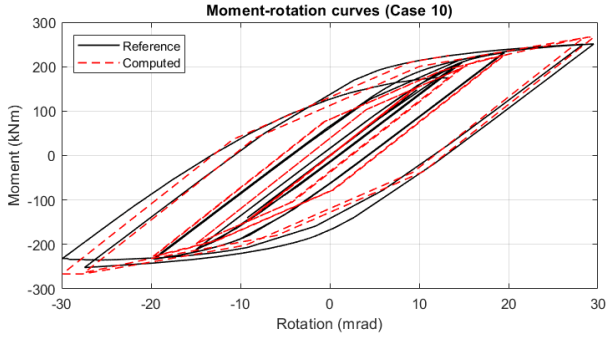
Moment-rotation curves (Case 10)
Reference
Computed
Moment (kNm)
Rotation (mrad)

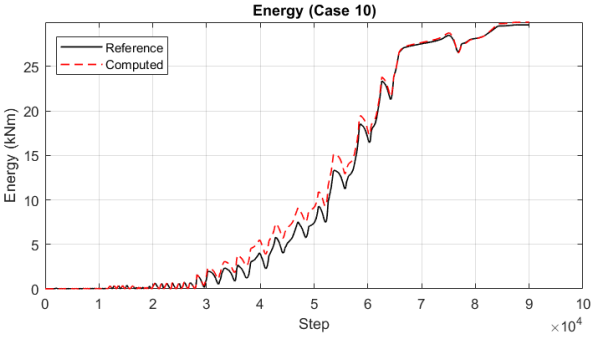
Energy (Case 10)
Reference
Computed
Energy (kNm)
Step
×10^4

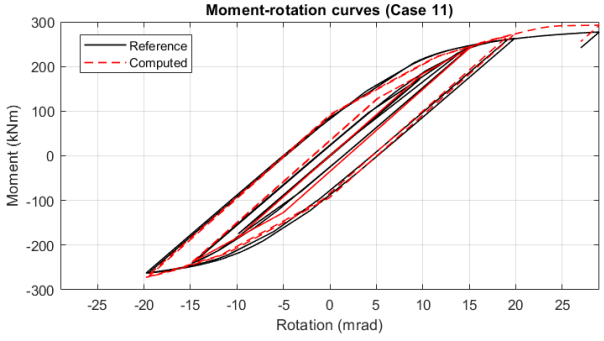
Moment-rotation curves (Case 11)
Reference
Computed
Moment (kNm)
Rotation (mrad)

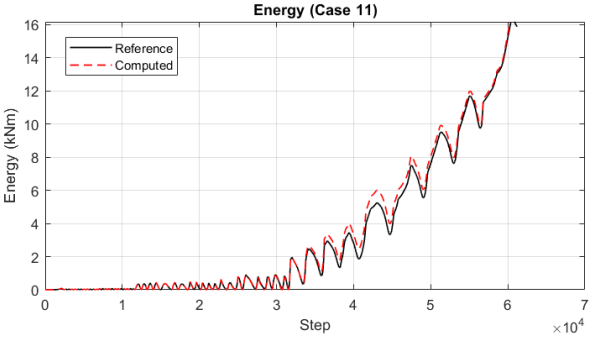
Energy (Case 11)
Reference
Computed
Energy (kNm)
Step
×10^4

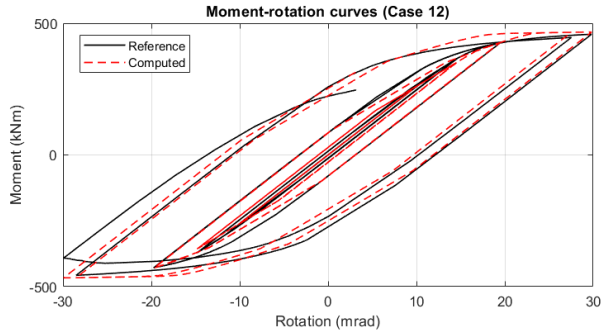
Moment-rotation curves (Case 12)
Reference
Computed
Moment (kNm)
Rotation (mrad)

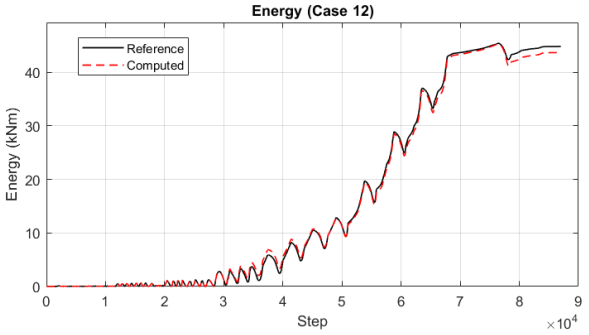
Energy (Case 12)
Reference
Computed
Energy (kNm)
Step
×10^4

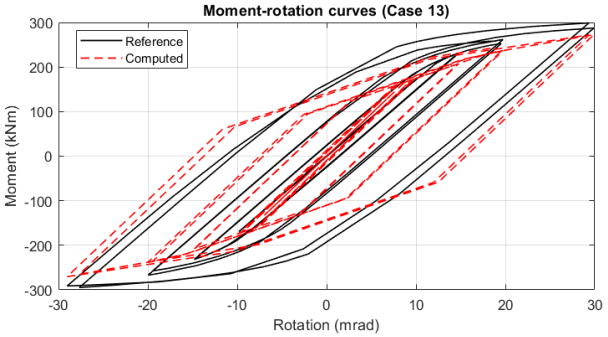
Moment-rotation curves (Case 13)
Reference
Computed
Moment (kNm)
Rotation (mrad)

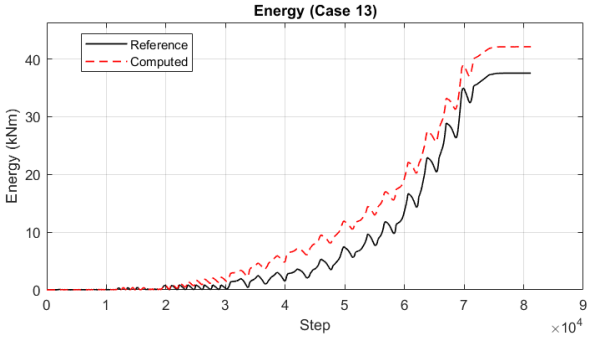
Energy (Case 13)
Reference
Computed
Energy (kNm)
Step
×10^4

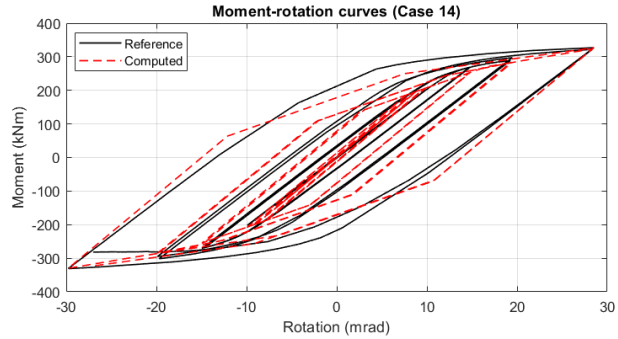
Moment-rotation curves (Case 14)
Reference
Computed
Moment (kNm)
Rotation (mrad)

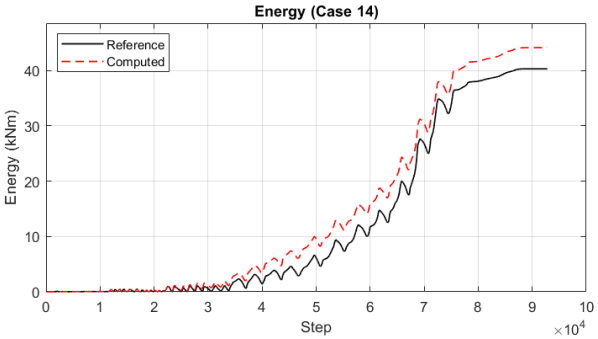
Energy (Case 14)
Reference
Computed
Energy (kNm)
Step
×10^4

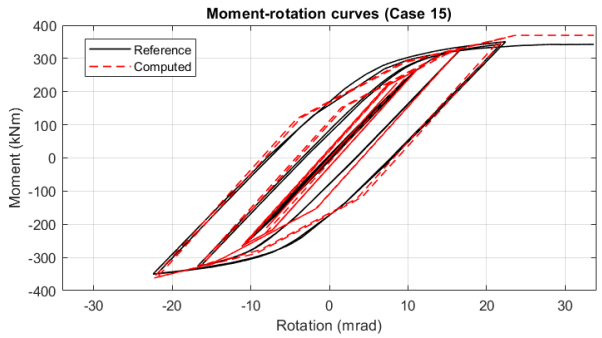
Moment-rotation curves (Case 15)
Reference
Computed
Moment (kNm)
Rotation (mrad)

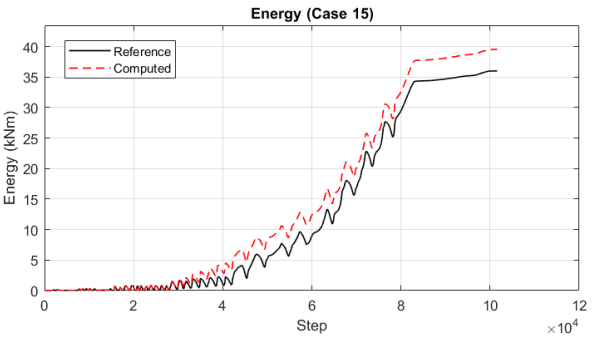
Energy (Case 15)
Reference
Computed
Energy (kNm)
Step
×10^4

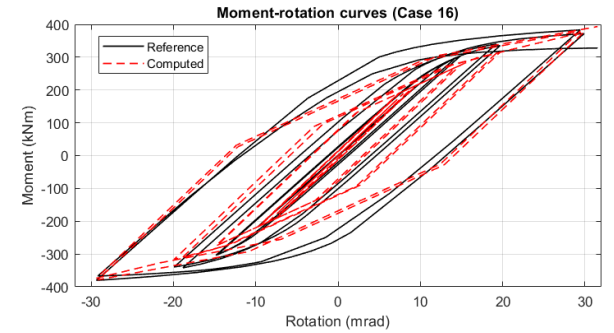
Moment-rotation curves (Case 16)
Reference
Computed
Moment (kNm)
Rotation (mrad)

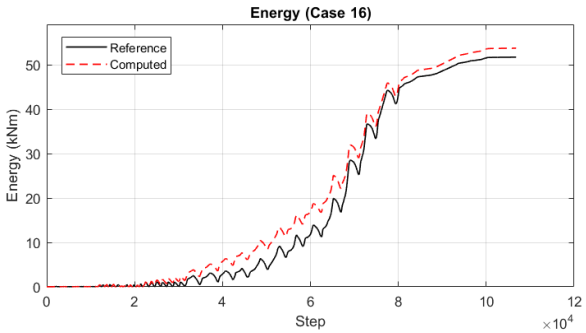
Energy (Case 16)
Reference
Computed
Energy (kNm)
Step
×10^4

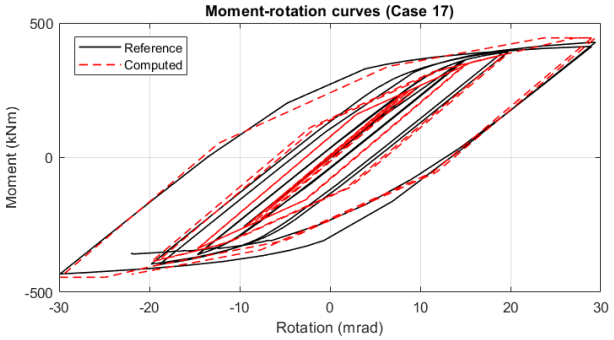
Moment-rotation curves (Case 17)
Reference
Computed
Moment (kNm)
Rotation (mrad)

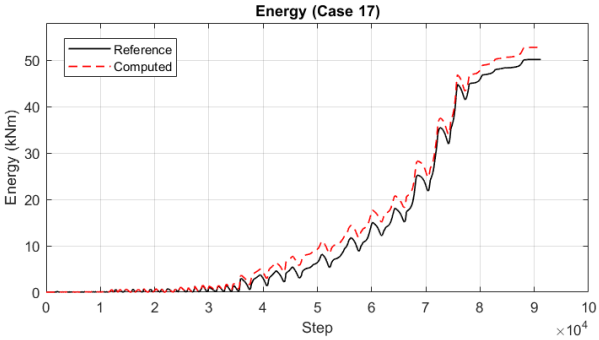
Energy (Case 17)
Reference
Computed
Energy (kNm)
Step
×10^4

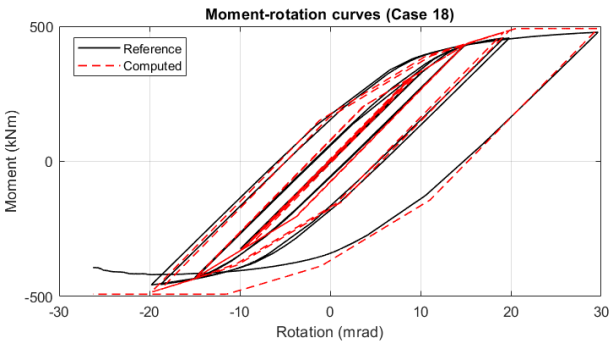
Moment-rotation curves (Case 18)
Reference
Computed
Moment (kNm)
Rotation (mrad)

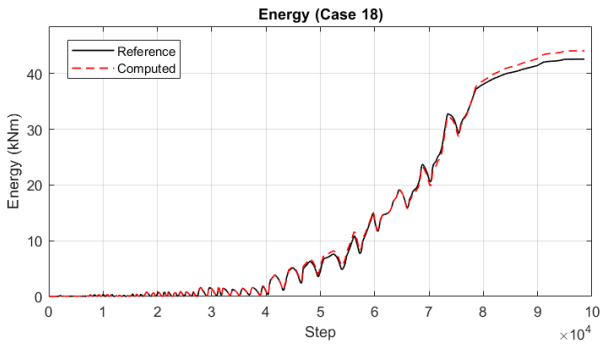
Energy (Case 18)
Reference
Computed
Energy (kNm)
Step
×10^4

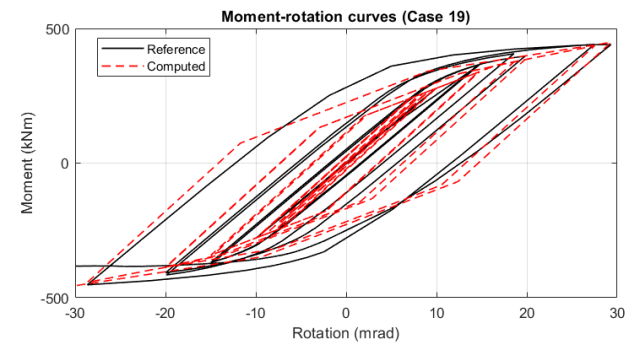
Moment-rotation curves (Case 19)
Reference
Computed
Moment (kNm)
Rotation (mrad)

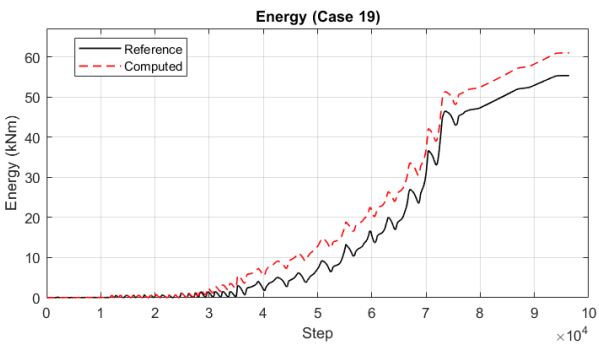
Energy (Case 19)
Reference
Computed
Energy (kNm)
Step
×10^4

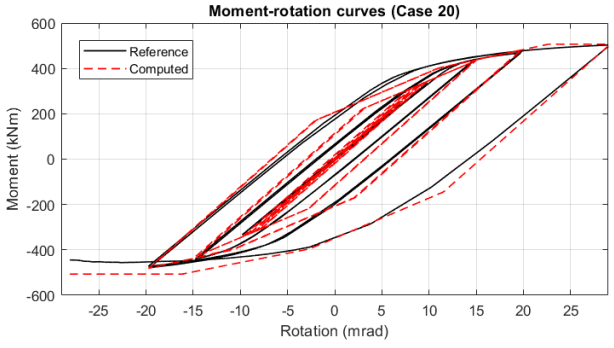
Moment-rotation curves (Case 20)
Reference
Computed
Moment (kNm)
Rotation (mrad)

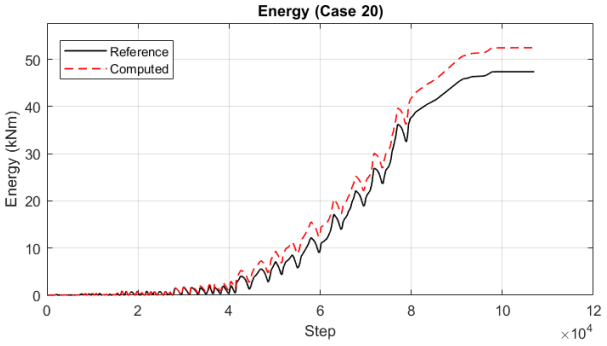
Energy (Case 20)
Reference
Computed
Energy (kNm)
Step
×10^4

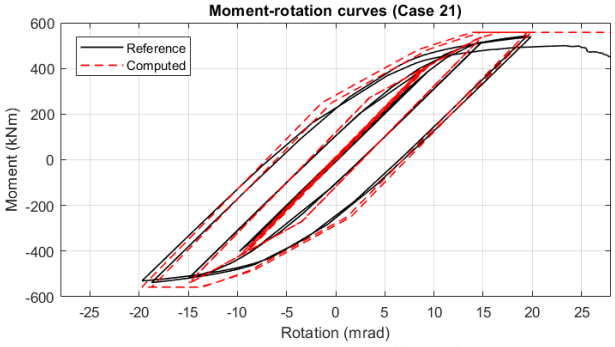
Moment-rotation curves (Case 21)
Reference
Computed
Moment (kNm)
Rotation (mrad)

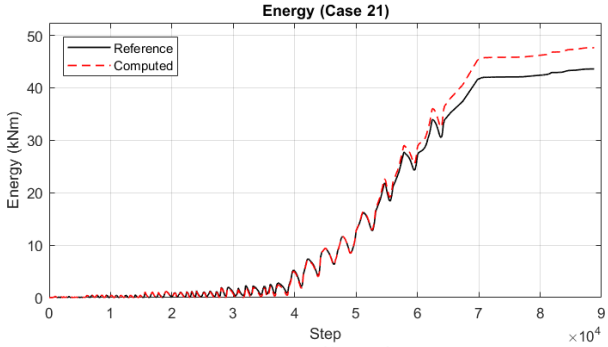
Energy (Case 21)
Reference
Computed
Energy (kNm)
Step
×10^4

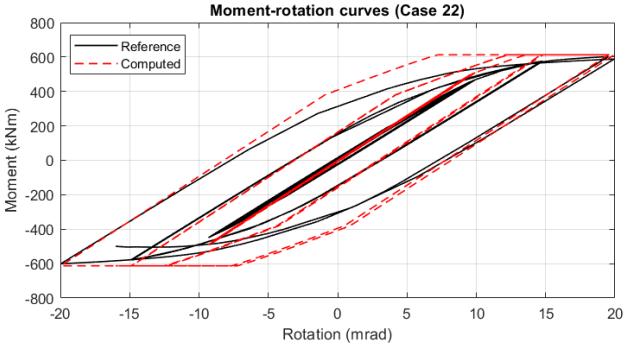
Moment-rotation curves (Case 22)
Reference
Computed
Moment (kNm)
Rotation (mrad)

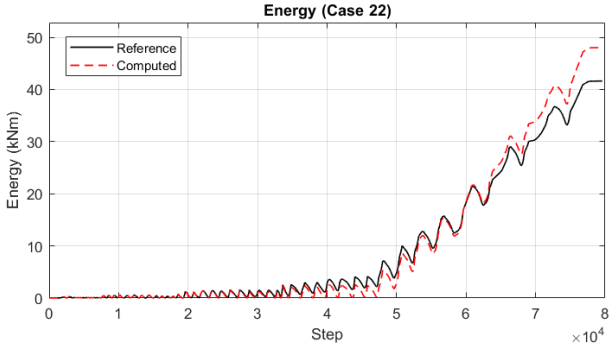
Energy (Case 22)
Reference
Computed
Energy (kNm)
Step
×10^4

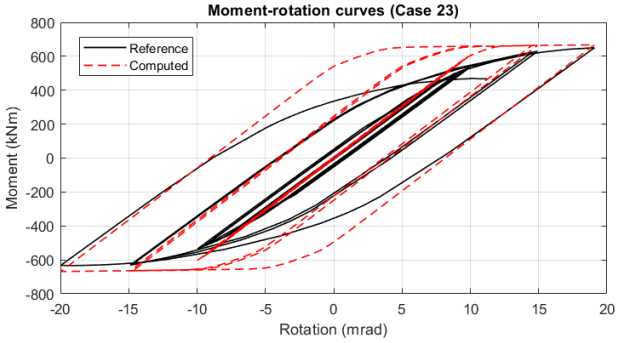
Moment-rotation curves (Case 23)
Reference
Computed
Moment (kNm)
Rotation (mrad)

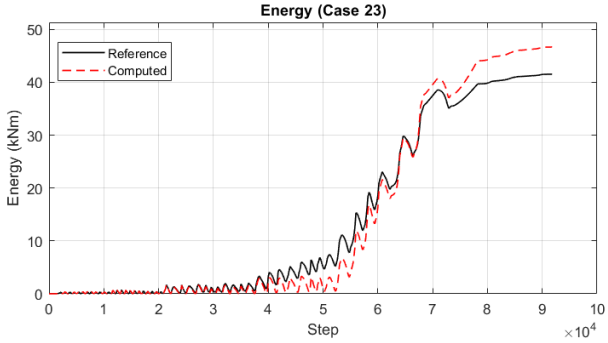
Energy (Case 23)
Reference
Computed
Energy (kNm)
Step
×10^4

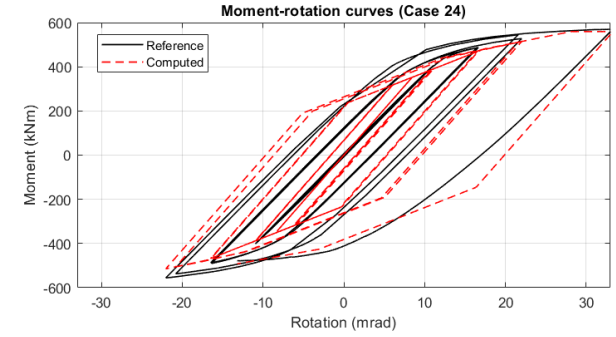
Moment-rotation curves (Case 24)
Reference
Computed
Moment (kNm)
Rotation (mrad)

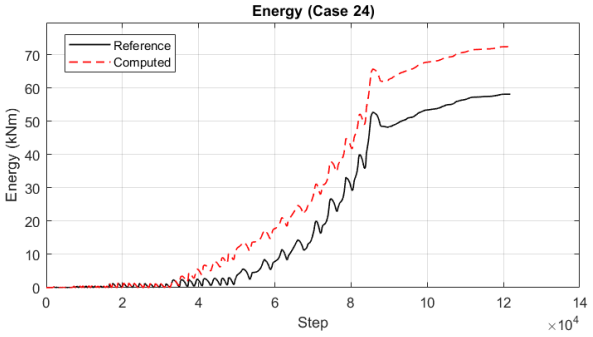
Energy (Case 24)
Reference
Computed
Energy (kNm)
Step
×10^4

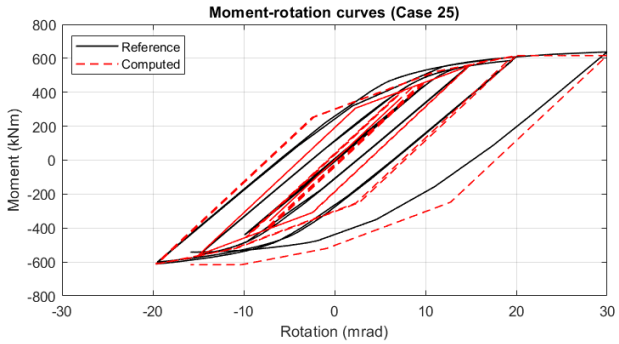
Moment-rotation curves (Case 25)
Reference
Computed
Moment (kNm)
Rotation (mrad)

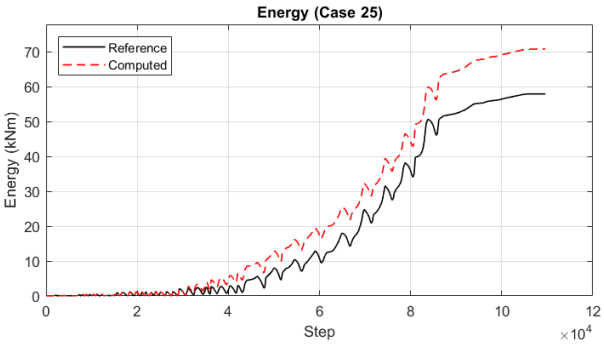
Energy (Case 25)
Reference
Computed
Energy (kNm)
Step
×10^4

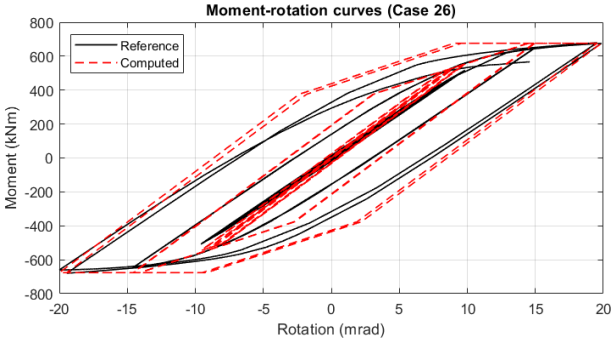
Moment-rotation curves (Case 26)
Reference
Computed
Moment (kNm)
Rotation (mrad)

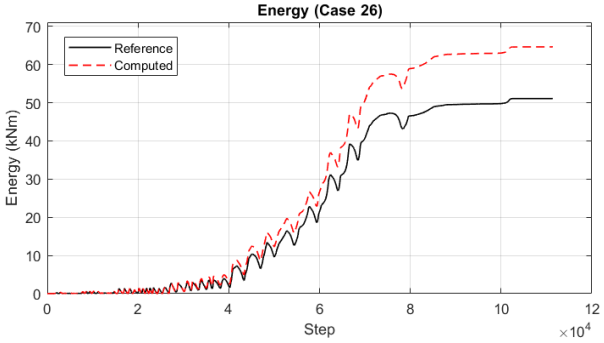
Energy (Case 26)
Reference
Computed
Energy (kNm)
Step
×10^4

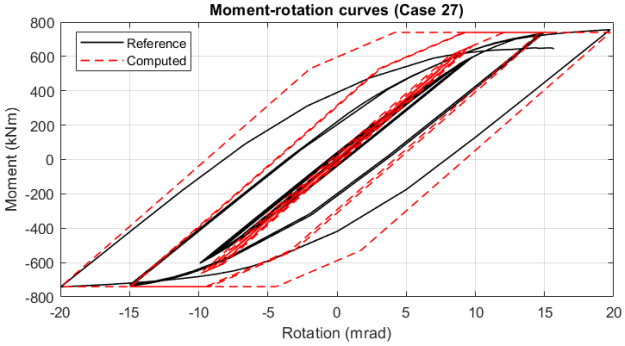
Moment-rotation curves (Case 27)
Reference
Computed
Moment (kNm)
Rotation (mrad)

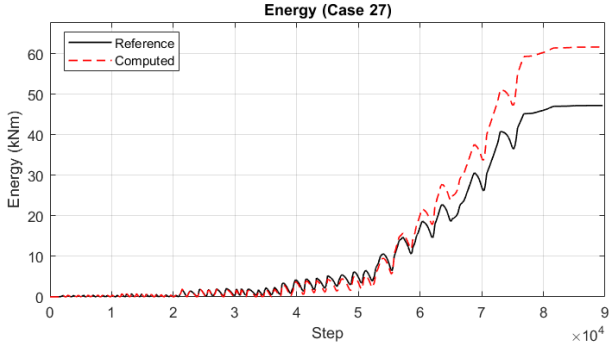
Energy (Case 27)
Reference
Computed
Energy (kNm)
Step
×10^4

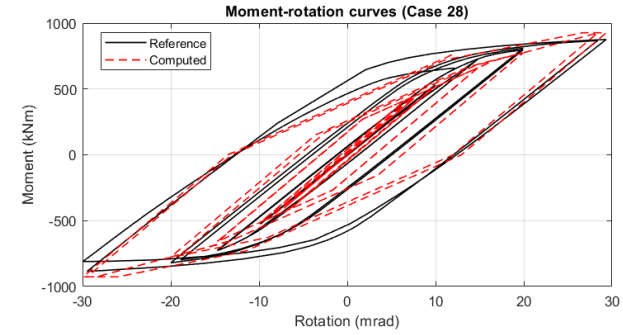
Moment-rotation curves (Case 28)
Reference
Computed
Moment (kNm)
Rotation (mrad)

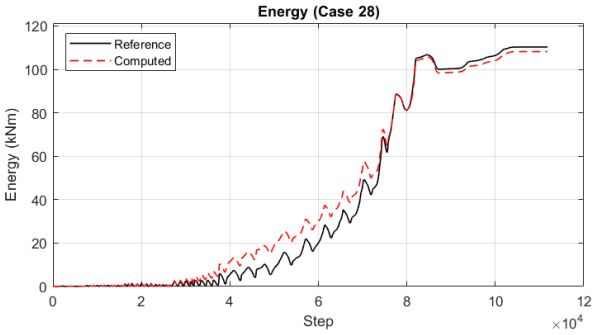
Energy (Case 28)
Reference
Computed
Energy (kNm)
Step
×10^4

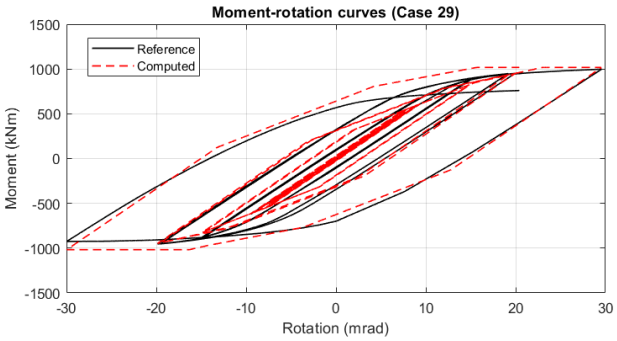
Moment-rotation curves (Case 29)
Reference
Computed
Moment (kNm)
Rotation (mrad)

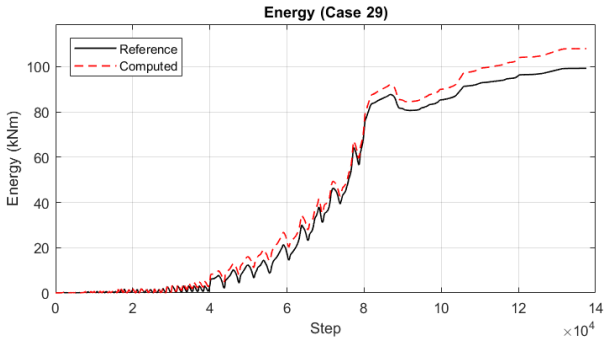
Energy (Case 29)
Reference
Computed
Energy (kNm)
Step
×10^4

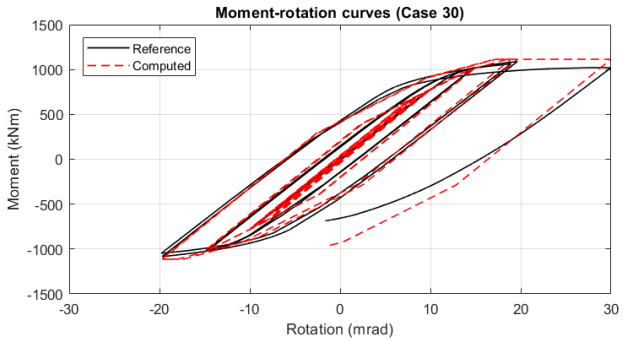
Moment-rotation curves (Case 30)
Reference
Computed
Moment (kNm)
Rotation (mrad)

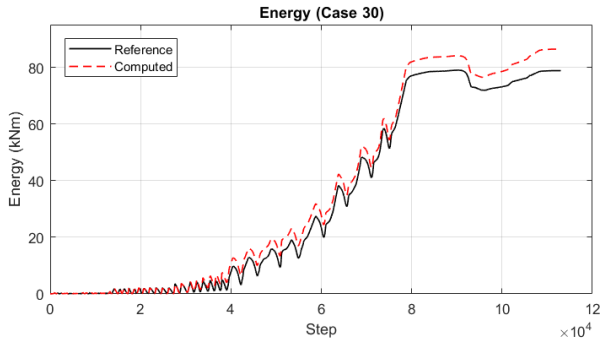
Energy (Case 30)
Reference
Computed
Energy (kNm)
Step
×10^4

A7. Closed-form solution of the stiffness formulation

In paragraph 2.4.4.1.2, the model to predict the stiffness of the analysed component has been discussed. However, for clarity, the analytical formulations that have led to the proposed design equation are reported.

The stiffness formulation derives from the mechanical model shown in Figure A.1: guided supports have been considered at the plate to column attachments, while an external roller has been placed in the middle of the studied arch. This hyperstatic scheme has been solved by employing the virtual work principle to assess the reactions at its restrains (R_A, R_B, R_C, M_A, M_C).

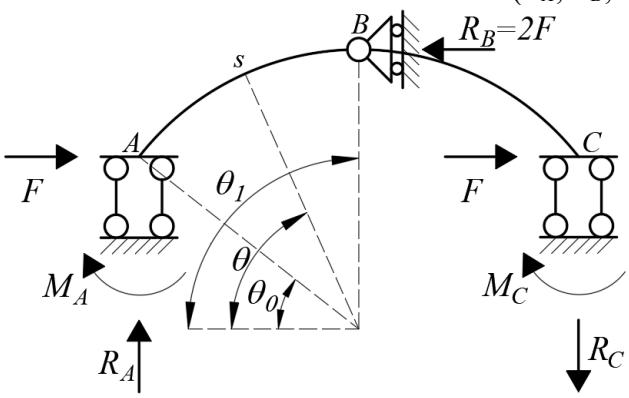

Figure A.1 - The 2D scheme to assess the stiffness of the analysed component

The bending reaction at support A is assumed as the hyperstatic unknown parameter, leading to the schemes S_0' and S_1' (Figure A.2 and Figure A.3).

Solution of the scheme S_0'

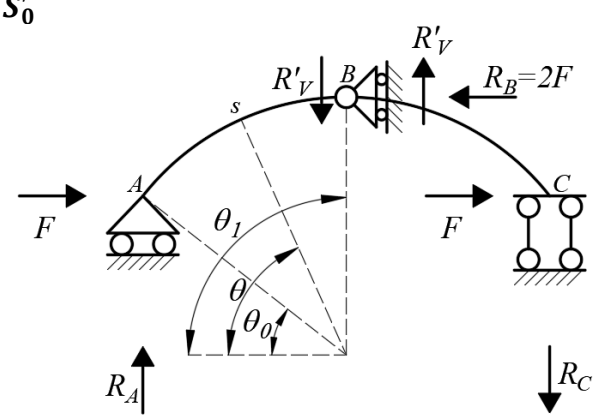

Figure A.2 – S0' scheme with reaction forces

For the translational equilibrium, it is possible to observe that:

$$R_B = 2F \tag{A.1}$$

$$R_A = R'_V \tag{A.2}$$

$$R_C = R'_V \tag{A.3}$$

Instead, the rotational equilibrium around A:

$$F\left(\frac{d_0}{2} - \frac{d_0}{2}\sin\vartheta_0\right) - R'_V\frac{d_0}{2}\sin\left(\frac{\pi}{2} - \vartheta_0\right) = 0 \;\rightarrow\; R'_V = \frac{F\,(1-\sin\vartheta_0)}{\cos\vartheta_0} \tag{A.4}$$

For this reason, the bending moment and the axial and shear forces vary along the arch according to Eq.A5-Eq.A10.

$$M_{s,(AB)}^{0} = -F\frac{d_0}{2}(\sin\vartheta - \sin\vartheta_0) + F\frac{d_0}{2}\frac{(1-\sin\vartheta_0)}{\cos\vartheta_0}(\cos\vartheta_0 - \cos\vartheta) \quad \text{(A.5)}$$

$$T_{s,(AB)}^{0} = F\frac{(1-\sin\vartheta_0)}{\cos\vartheta_0}\sin\vartheta - F\cos\vartheta \quad \text{(A.6)}$$

$$N_{s,(AB)}^{0} = -F\frac{(1-\sin\vartheta_0)}{\cos\vartheta_0}\cos\vartheta - F\sin\vartheta \quad \text{(A.7)}$$

$$M_{s,(BC)}^{0} = -F\frac{d_0}{2}(\sin\vartheta - \sin\vartheta_0) + F\frac{d_0}{2}\frac{(1-\sin\vartheta_0)}{\cos\vartheta_0}(\cos\vartheta_0 - \cos\vartheta) - 2F\left(\frac{d_0}{2} - \frac{d_0}{2}\sin\vartheta\right) \quad \text{(A.8)}$$

$$T_{s,(BC)}^{0} = F\frac{(1-\sin\vartheta_0)}{\cos\vartheta_0}\sin\vartheta - F\cos\vartheta + 2F\cos\vartheta \quad \text{(A.9)}$$

$$N_{s,(BC)}^{0} = -F\frac{(1-\sin\vartheta_0)}{\cos\vartheta_0}\cos\vartheta - F\sin\vartheta + 2F\sin\vartheta \quad \text{(A.10)}$$

ion of the scheme S_1'

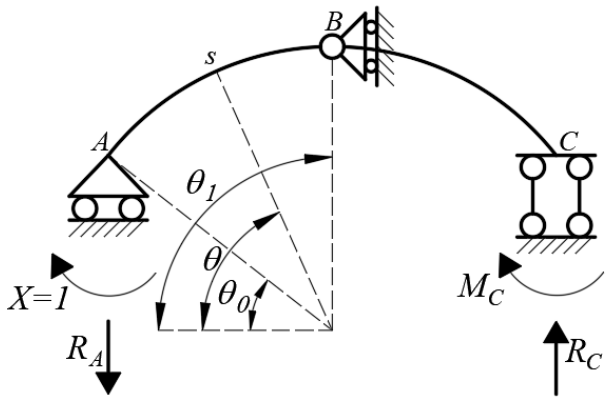

Figure A.3 – S1' scheme with reaction forces

In this case, the hyperstatic unknown has been set equal to 1. Consequently, the reaction forces are assessed as reported in Eq.A11.

$$R_A = R_C = \frac{2\cdot 1}{d_0\cos\vartheta_0} \quad \text{(A.11)}$$

The bending moment, shear, and axial diagrams are evaluated for both the arches AB and BC according to Eq.A12-Eq.A14:

$$M_s^1 = 1 - \frac{2\cdot 1}{d_0\cos\vartheta_0}\frac{d_0}{2}(\cos\vartheta_0 - \cos\vartheta) \quad \text{(A.12)}$$

$$T_s^1 = -\frac{2\cdot 1\cdot\sin\vartheta}{d_0\ \cos\vartheta_0} \quad \text{(A.13)}$$

$$N_s^1 = \frac{2\cdot 1\cdot\ \cos\vartheta}{d_0\ \cos\vartheta_0} \quad \text{(A.14)}$$

The virtual work principle is applied in Eq.A15:

$$\int_C M^1\,\theta^s\,dz + \int_C T^1\,\gamma^s\,dz + \int_C N^1\,\varepsilon^s\,dz = 0 \quad \text{(A.15)}$$

Where:

$$\theta^s = \frac{M^s}{EI};\ \gamma^s = \frac{T^s\chi}{GA};\ \varepsilon^s = \frac{N^s}{EA}$$

$$M^s = M^0 + X\,M^1;\; T^s = T^0 + X\,T^1;\; N^s = N^0 + X\,N^1$$

By making all the parameters explicit, it results:

$$\begin{aligned}
&\frac{d_0}{2\,E\,I}\int_{\vartheta_0}^{\frac{\pi}{2}}\left[1-\frac{2\cdot 1}{d_0\cos\vartheta_0}\frac{d_0}{2}(\cos\vartheta_0-\cos\vartheta)\right]\left\{\left[-F\frac{d_0}{2}(\sin\vartheta-\sin\vartheta_0)+F\frac{d_0}{2}\frac{(1-\sin\vartheta_0)}{\cos\vartheta_0}(\cos\vartheta_0-\cos\vartheta)\right]\right.\\
&\qquad\left.+X\left[1-\frac{2\cdot 1}{d_0\cos\vartheta_0}\frac{d_0}{2}(\cos\vartheta_0-\cos\vartheta)\right]\right\}d\vartheta\\
&\qquad+\frac{d_0}{2\,E\,I}\int_{\frac{\pi}{2}}^{\pi-\vartheta_0}\left[1\right.\\
&\qquad\left.-\frac{2\cdot 1}{d_0\cos\vartheta_0}\frac{d_0}{2}(\cos\vartheta_0-\cos\vartheta)\right]\left\{\left[-F\frac{d_0}{2}(\sin\vartheta-\sin\vartheta_0)\right.\right.\\
&\qquad\left.+F\frac{d_0}{2}\frac{(1-\sin\vartheta_0)}{\cos\vartheta_0}(\cos\vartheta_0-\cos\vartheta)-2F\left(\frac{d_0}{2}-\frac{d_0}{2}\sin\vartheta\right)\right]\\
&\qquad\left.+X\left[1-\frac{2\cdot 1}{d_0\cos\vartheta_0}\frac{d_0}{2}(\cos\vartheta_0-\cos\vartheta)\right]\right\}d\vartheta\\
&\qquad+\frac{d_0\,\chi}{2\,G\,A}\int_{\vartheta_0}^{\frac{\pi}{2}}\left[-\frac{2\cdot 1\cdot\sin\vartheta}{d_0\,\cos\vartheta_0}\right]\left\{\left[F\frac{(1-\sin\vartheta_0)}{\cos\vartheta_0}\sin\vartheta-F\cos\vartheta\right]+X\left[-\frac{2\cdot 1\cdot\sin\vartheta}{d_0\,\cos\vartheta_0}\right]\right\}d\vartheta\\
&\qquad+\frac{d_0\,\chi}{2\,G\,A}\int_{\frac{\pi}{2}}^{\pi-\vartheta_0}\left[-\frac{2\cdot 1\cdot\sin\vartheta}{d_0\,\cos\vartheta_0}\right]\left\{\left[F\frac{(1-\sin\vartheta_0)}{\cos\vartheta_0}\sin\vartheta-F\cos\vartheta+2F\cos\vartheta\right]\right.\\
&\qquad\left.+X\left[-\frac{2\cdot 1\cdot\sin\vartheta}{d_0\,\cos\vartheta_0}\right]\right\}d\vartheta\\
&\qquad+\frac{d_0}{2\,E\,A}\int_{\vartheta_0}^{\frac{\pi}{2}}\left[\frac{2\cdot 1\cdot\cos\vartheta}{d_0\,\cos\vartheta_0}\right]\left\{\left[-F\frac{(1-\sin\vartheta_0)}{\cos\vartheta_0}\cos\vartheta-F\sin\vartheta\right]+X\left[\frac{2\cdot 1\cdot\cos\vartheta}{d_0\,\cos\vartheta_0}\right]\right\}d\vartheta\\
&\qquad+\frac{d_0}{2\,E\,A}\int_{\frac{\pi}{2}}^{\pi-\vartheta_0}\left[\frac{2\cdot 1\cdot\cos\vartheta}{d_0\,\cos\vartheta_0}\right]\left\{\left[-F\frac{(1-\sin\vartheta_0)}{\cos\vartheta_0}\cos\vartheta-F\sin\vartheta+2F\sin\vartheta\right]\right.\\
&\qquad\left.+X\left[\frac{2\cdot 1\cdot\cos\vartheta}{d_0\,\cos\vartheta_0}\right]\right\}d\vartheta=0
\end{aligned}\tag{A.16}$$

As a consequence:

$$\begin{aligned}
&\frac{d_0}{2\,E\,I\,\cos\vartheta_0}\left\{F\frac{d_0}{2}\left[\frac{\sin\vartheta_0{}^2}{2}-\frac{\sin(\pi-\vartheta_0)^2}{2}+\sin\vartheta_0\left(-\sin\vartheta_0+\sin(\pi-\vartheta_0)\right)-\sin\vartheta_0+\sin(\pi-\vartheta_0)+\frac{\vartheta_0}{2\,\cos\vartheta_0}+\frac{\sin\vartheta_0}{2}-\frac{\pi-\vartheta_0}{2\,\cos\vartheta_0}\right.\right.\\
&\qquad-\frac{\sin(\pi-\vartheta_0)\,cos\,(\pi-\vartheta_0)}{2\,\cos\vartheta_0}+\sin\vartheta_0{}^2-\sin\vartheta_0 sin(\pi-\vartheta_0)-\frac{\sin\vartheta_0}{2\,\cos\vartheta_0}\vartheta_0-\frac{\sin\vartheta_0{}^2}{2}+\frac{\pi-\vartheta_0}{2\,\cos\vartheta_0}sin\,\vartheta_0\\
&\qquad\left.+\frac{\sin(\pi-\vartheta_0)\,cos\,(\pi-\vartheta_0)sin\,\vartheta_0}{2\,\cos\vartheta_0}\right]+X\left[-\frac{\vartheta_0}{2\,\cos\vartheta_0}-\frac{sin\,\vartheta_0}{2}+\frac{\pi-\vartheta_0}{2\,\cos\vartheta_0}+\frac{\sin(\pi-\vartheta_0)\,cos\,(\pi-\vartheta_0)}{2\,\cos\vartheta_0}\right]\\
&\qquad\left.+F\,d_0\left[-sin\,(\pi-\vartheta_0)+\,sin\,\frac{\pi}{2}+\frac{sin\,(\pi-\vartheta_0)^2}{2}-\frac{sin\,\frac{\pi^2}{2}}{2}\right]\right\}\\
&\qquad+\frac{\chi}{G\,A\,\cos\vartheta_0}\left\{-\frac{F}{\cos\vartheta_0}(1-\sin\vartheta_0)\left[\frac{\pi-\vartheta_0}{2}-\frac{\sin(\pi-\vartheta_0)\,\cos(\pi-\vartheta_0)}{2}-\frac{\vartheta_0}{2}+\frac{\sin\vartheta_0\,\cos\vartheta_0}{2}\right]\right.\\
&\qquad+F\left[\frac{sin\,(\pi-\vartheta_0)^2-sin\,\vartheta_0{}^2}{2}\right]+\frac{2\,X}{d_0\cos\vartheta_0}\left[\frac{\pi-\vartheta_0}{2}-\frac{\sin(\pi-\vartheta_0)\,\cos(\pi-\vartheta_0)}{2}-\frac{\vartheta_0}{2}+\frac{\sin\vartheta_0\,\cos\vartheta_0}{2}\right]\\
&\qquad\left.-2\,F\left[\frac{sin\,(\pi-\vartheta_0)^2-sin\,\frac{\pi^2}{2}}{2}\right]\right\}\\
&\qquad+\frac{1}{E\,A\,\cos\vartheta_0}\left\{-\frac{F}{\cos\vartheta_0}(1-\sin\vartheta_0)\left[\frac{\pi-\vartheta_0}{2}+\frac{\sin(\pi-\vartheta_0)\,\cos(\pi-\vartheta_0)}{2}-\frac{\vartheta_0}{2}-\frac{\sin\vartheta_0\,\cos\vartheta_0}{2}\right]\right.\\
&\qquad-F\left[\frac{sin\,(\pi-\vartheta_0)^2-sin\,\vartheta_0{}^2}{2}\right]+\frac{2\,X}{d_0\cos\vartheta_0}\left[\frac{\pi-\vartheta_0}{2}+\frac{\sin(\pi-\vartheta_0)\,\cos(\pi-\vartheta_0)}{2}-\frac{\vartheta_0}{2}-\frac{\sin\vartheta_0\,\cos\vartheta_0}{2}\right]\\
&\qquad\left.+2\,F\left[\frac{sin\,(\pi-\vartheta_0)^2-sin\,\frac{\pi^2}{2}}{2}\right]\right\}=0
\end{aligned}\tag{A.17}$$

Assuming:

$$a = F\frac{d_0}{2}\left[\frac{sin\,\vartheta_0{}^2}{2} - \frac{sin\,(\pi-\vartheta_0)^2}{2} + sin\,\vartheta_0\big(-sin\,\vartheta_0 + sin\,(\pi-\vartheta_0)\big) - sin\,\vartheta_0 + sin\,(\pi-\vartheta_0)\right.$$
$$+\frac{\vartheta_0}{2\,\cos\vartheta_0} + \frac{sin\,\vartheta_0}{2} - \frac{\pi-\vartheta_0}{2\,\cos\vartheta_0} - \frac{sin\,(\pi-\vartheta_0)\,cos\,(\pi-\vartheta_0)}{2\,\cos\vartheta_0} + sin\,\vartheta_0{}^2$$
$$-sin\,\vartheta_0 sin\,(\pi-\vartheta_0) - \frac{sin\,\vartheta_0}{2\,\cos\vartheta_0}\vartheta_0 - \frac{sin\,\vartheta_0{}^2}{2} + \frac{\pi-\vartheta_0}{2\,\cos\vartheta_0}sin\,\vartheta_0 \tag{A.18}$$
$$\left.+\frac{sin\,(\pi-\vartheta_0)\,cos\,(\pi-\vartheta_0)sin\,\vartheta_0}{2\,\cos\vartheta_0}\right]$$

$$b = \left[-\frac{\vartheta_0}{2\,\cos\vartheta_0} - \frac{sin\,\vartheta_0}{2} + \frac{\pi-\vartheta_0}{2\,\cos\vartheta_0} + \frac{sin\,(\pi-\vartheta_0)\,cos\,(\pi-\vartheta_0)}{2\,\cos\vartheta_0}\right] \tag{A.19}$$

$$c = F\,d_0\left[-sin\,(\pi-\vartheta_0) + sin\,\frac{\pi}{2} + \frac{sin\,(\pi-\vartheta_0)^2}{2} - \frac{sin\,\frac{\pi^2}{2}}{2}\right] \tag{A.20}$$

$$d = -\frac{F}{\cos\vartheta_0}(1-\sin\vartheta_0)\left[\frac{\pi-\vartheta_0}{2} - \frac{\sin(\pi-\vartheta_0)\,\cos(\pi-\vartheta_0)}{2} - \frac{\vartheta_0}{2} + \frac{\sin\vartheta_0\,\cos\vartheta_0}{2}\right]$$
$$+F\left[\frac{sin\,(\pi-\vartheta_0)^2 - sin\,\vartheta_0{}^2}{2}\right] \tag{A.21}$$

$$e = \frac{2}{d_0\cos\vartheta_0}\left[\frac{\pi-\vartheta_0}{2} - \frac{\sin(\pi-\vartheta_0)\,\cos(\pi-\vartheta_0)}{2} - \frac{\vartheta_0}{2} + \frac{\sin\vartheta_0\,\cos\vartheta_0}{2}\right] \tag{A.22}$$

$$f = -2\,F\left[\frac{sin(\pi-\vartheta_0)^2 - sin\,\frac{\pi^2}{2}}{2}\right] \tag{A.23}$$

$$g = -\frac{F}{\cos\vartheta_0}(1-\sin\vartheta_0)\left[\frac{\pi-\vartheta_0}{2} + \frac{\sin(\pi-\vartheta_0)\,\cos(\pi-\vartheta_0)}{2} - \frac{\vartheta_0}{2} - \frac{\sin\vartheta_0\,\cos\vartheta_0}{2}\right]$$
$$-F\left[\frac{sin(\pi-\vartheta_0)^2 - sin\,\vartheta_0{}^2}{2}\right] \tag{A.24}$$

$$h = \frac{2}{d_0\cos\vartheta_0}\left[\frac{\pi-\vartheta_0}{2} + \frac{\sin(\pi-\vartheta_0)\,\cos(\pi-\vartheta_0)}{2} - \frac{\vartheta_0}{2} - \frac{\sin\vartheta_0\,\cos\vartheta_0}{2}\right] \tag{A.25}$$

$$i = 2\,F\left[\frac{sin\,(\pi-\vartheta_0)^2 - sin\,\frac{\pi^2}{2}}{2}\right] \tag{A.26}$$

Considering the above assumptions (Eq.A18-Eq.A26), Eq. A.17 can be written as:

$$\frac{d_0}{2\,E\,I\,\cos\vartheta_0}(a + b\,X + c) + \frac{\chi}{G\,A\,\cos\vartheta_0}(d + e\,X + f) + \frac{1}{E\,A\,\cos\vartheta_0}(g + h\,X + i) = 0 \tag{A.27}$$

The hyperstatic unknown X can be evaluated according to Eq.A28.

$$X = -\frac{a + c + d + f + g + i}{b + e + h} \tag{A.28}$$

The knowledge of X allows the assessment of the reaction forces Eq.A29-Eq.A31:

$$R_A = R_A^0 + X\,R_A^1 = \frac{F\,(1-\sin\vartheta_0)}{\cos\vartheta_0} - \frac{2\,X}{d_0\cos\vartheta_0} \tag{A.29}$$

$$R_C = R_C^0 + X\,R_C^1 = -\frac{F\,(1-\sin\vartheta_0)}{\cos\vartheta_0} + \frac{2\,X}{d_0\cos\vartheta_0} \tag{A.30}$$

$$M_C = M_C^0 + X\,M_C^1 = X \tag{A.31}$$

Once the reaction forces are known, Clapeyron's theorem (Figure A.4) can be applied to define the stiffness of the studied component. It is worth highlighting that, because of the symmetry of the analysed scheme, the virtual work principle is applied only to the arch AB.

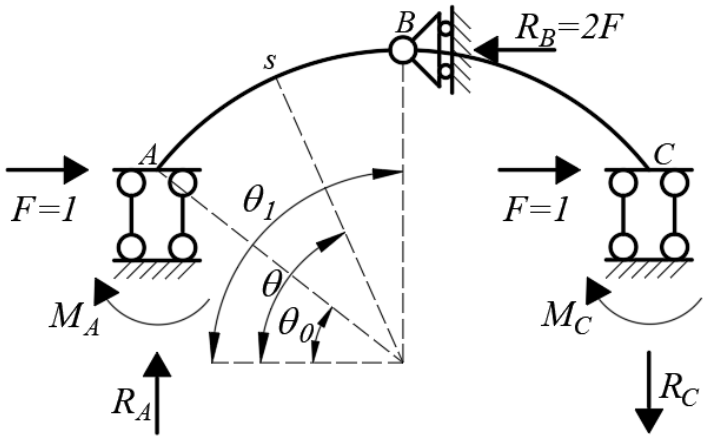

Figure A.4 – Scheme considered for the application of Clapeyron's theorem

As a consequence, the bending moment, shear, and axial forces along with the arch AB can be expressed as reported in Eq.A32-Eq.A34:

$$M_{s,(AB)} = M_A - F\frac{d_0}{2}(\sin\vartheta - \sin\vartheta_0) + R_A\frac{d_0}{2}(\cos\vartheta_0 - \cos\vartheta) \tag{A.32}$$

$$T_{s,(AB)} = F\frac{(1-\sin\vartheta_0)}{\cos\vartheta_0}\sin\vartheta - F\cos\vartheta \tag{A.33}$$

$$N_{s,(AB)} = -F\frac{(1-\sin\vartheta_0)}{\cos\vartheta_0}\cos\vartheta - F\sin\vartheta \tag{A.34}$$

The acting forces F are assumed equal to 1, and Clapeyron's theorem can be applied.

$$1\cdot\delta_A = \int_C M^s\,\theta^s\,dz + \int_C T^s\,\gamma^s\,dz + \int_C N^s\,\varepsilon^s\,dz \tag{A.35}$$

$$\begin{aligned}\delta_A = \frac{d_0}{2\,E\,I}\int_{\vartheta_0}^{\frac{\pi}{2}} &[M_A - F\frac{d_0}{2}(\sin\vartheta - \sin\vartheta_0) + R_A\frac{d_0}{2}(\cos\vartheta_0 - \cos\vartheta)]^2 d\vartheta \\ &+ \frac{d_0\,\chi}{2\,G\,A}\int_{\vartheta_0}^{\frac{\pi}{2}}[F\frac{(1-\sin\vartheta_0)}{\cos\vartheta_0}\sin\vartheta - F\cos\vartheta]^2 d\vartheta \\ &+ \frac{d_0}{2\,E\,A}\int_{\vartheta_0}^{\frac{\pi}{2}}[-F\frac{(1-\sin\vartheta_0)}{\cos\vartheta_0}\cos\vartheta - F\sin\vartheta]^2 d\vartheta\end{aligned} \tag{A.36}$$

Assuming:

$$\alpha = X + F\frac{d_0}{2}\sin\vartheta + R_A\frac{d_0}{2}\cos\vartheta_0 \tag{A.37}$$

$$\beta = F\frac{d_0}{2} \tag{A.38}$$

$$\gamma = R_A\frac{d_0}{2} \tag{A.39}$$

$$\eta = F\frac{(1-\sin\vartheta_0)}{\cos\vartheta_0} \tag{A.40}$$

It is possible to obtain:

$$\delta_A = \frac{d_0}{2\,E\,I}\int_{\vartheta_0}^{\frac{\pi}{2}} \alpha^2 + \beta^2 sin\,\vartheta^2 + \gamma^2 cos\,\vartheta^2 - 2\alpha\beta sin\,\vartheta - 2\alpha\gamma cos\,\theta + 2\beta\gamma sen\vartheta cos\vartheta\,d\vartheta + \frac{d_0\,\chi}{2\,G\,A}\int_{\vartheta_0}^{\frac{\pi}{2}} \eta^2 sin\,\vartheta^2 + F^2 cos\,\vartheta^2 - 2\eta F sen\,\vartheta cos\vartheta\,d\vartheta + \frac{d_0}{2\,E\,A}\int_{\vartheta_0}^{\frac{\pi}{2}} \eta^2 cos\,\vartheta^2 + F^2 sin\,\vartheta^2 + 2\eta F sen\,\vartheta cos\vartheta d\vartheta \tag{A.41}$$

$$\delta_A = \frac{d_0}{2\,E\,I}\left\{\alpha^2[\vartheta]_{\vartheta_0}^{\frac{\pi}{2}} + \beta^2\left[\frac{\vartheta}{2} - \frac{\sin\vartheta\ \cos\vartheta}{2}\right]_{\vartheta_0}^{\frac{\pi}{2}} + \gamma^2\left[\frac{\vartheta}{2} + \frac{\sin\vartheta\ \cos\vartheta}{2}\right]_{\vartheta_0}^{\frac{\pi}{2}} - 2\alpha\beta[-\cos\vartheta]_{\vartheta_0}^{\frac{\pi}{2}} - 2\alpha\gamma[\sin\vartheta]_{\vartheta_0}^{\frac{\pi}{2}} + 2\beta\gamma\left[\frac{\sin\vartheta^2}{2}\right]_{\vartheta_0}^{\frac{\pi}{2}}\right\} + \frac{d_0\,\chi}{2\,G\,A}\left\{\eta^2\left[\frac{\vartheta}{2} - \frac{\sin\vartheta\ \cos\vartheta}{2}\right]_{\vartheta_0}^{\frac{\pi}{2}} + F^2\left[\frac{\vartheta}{2} + \frac{\sin\vartheta\ \cos\vartheta}{2}\right]_{\vartheta_0}^{\frac{\pi}{2}} - 2\eta F\left[\frac{\sin\vartheta^2}{2}\right]_{\vartheta_0}^{\frac{\pi}{2}}\right\} + \frac{d_0}{2\,E\,A}\left\{\eta^2\left[\frac{\vartheta}{2} + \frac{\sin\vartheta\ \cos\vartheta}{2}\right]_{\vartheta_0}^{\frac{\pi}{2}} + F^2\left[\frac{\vartheta}{2} - \frac{\sin\vartheta\ \cos\vartheta}{2}\right]_{\vartheta_0}^{\frac{\pi}{2}} + 2\eta F\left[\frac{\sin\vartheta^2}{2}\right]_{\vartheta_0}^{\frac{\pi}{2}}\right\} \tag{A.42}$$

$$\delta_A = \frac{d_0}{2\,E\,I}\left\{\alpha^2\left(\frac{\pi}{2} - \vartheta_0\right) + \beta^2\left[\frac{\pi/2}{2} - \frac{\sin(\pi/2)\ \cos(\pi/2)}{2} - \frac{\vartheta_0}{2} + \frac{\sin\vartheta_0\ \cos\vartheta_0}{2}\right] + \gamma^2\left[\frac{\pi/2}{2} + \frac{\sin(\pi/2)\ \cos(\pi/2)}{2} - \frac{\vartheta_0}{2} - \frac{\sin\vartheta_0\ \cos\vartheta_0}{2}\right] - 2\alpha\beta[-\cos(\pi/2) + \cos\vartheta_0] - 2\alpha\gamma[\sin(\pi/2) - \sin\vartheta_0] + 2\beta\gamma\frac{\sin(\pi/2)^2 - \sin{\vartheta_0}^2}{2}\right\} + \frac{d_0\,\chi}{2\,G\,A}\left\{\eta^2\left[\frac{\pi/2}{2} - \frac{\sin(\pi/2)\ \cos(\pi/2)}{2} - \frac{\vartheta_0}{2} + \frac{\sin\vartheta_0\ \cos\vartheta_0}{2}\right] + F^2\left[\frac{\pi/2}{2} + \frac{\sin(\pi/2)\ \cos(\pi/2)}{2} - \frac{\vartheta_0}{2} - \frac{\sin\vartheta_0\ \cos\vartheta_0}{2}\right] - 2\eta F\frac{\sin(\pi/2)^2 - \sin{\vartheta_0}^2}{2}\right\} + \frac{d_0}{2\,E\,A}\left\{\eta^2\left[\frac{\pi/2}{2} + \frac{\sin(\pi/2)\ \cos(\pi/2)}{2} - \frac{\vartheta_0}{2} - \frac{\sin\vartheta_0\ \cos\vartheta_0}{2}\right] + F^2\left[\frac{\pi/2}{2} - \frac{\sin(\pi/2)\ \cos(\pi/2)}{2} - \frac{\vartheta_0}{2} + \frac{\sin\vartheta_0\ \cos\vartheta_0}{2}\right] + 2\eta F\frac{\sin(\pi/2)^2 - \sin{\vartheta_0}^2}{2}\right\} \tag{A.43}$$

Starting from the knowledge of the displacement δ_A (Eq.A43) due to a unitary force *F*, which is representative of the deformability of the arch, and considering the symmetry of the assumed mechanical scheme, the analytical formulation for the stiffness prediction can be written as Eq.A44:

$$k_{2D} = 4\frac{F}{\delta_A} \tag{A.44}$$

This analysed scheme refers to a unitary width; for this reason, all the mechanical properties have been assessed with Eq.A45-Eq.A50.

$$I = \frac{b \cdot {t_0}^3}{12} = \frac{1 \cdot {t_0}^3}{12} \quad \text{(A.45)}$$

$$A = b \cdot t_0 = 1 \cdot t_0 \quad \text{(A.46)}$$

$$\chi = 1.2 \quad \text{(A.47)}$$

$$E = 210{\cdot}000\ MPa \quad \text{(A.48)}$$

$$G = \frac{E}{2(1+\upsilon)} \quad \text{(A.49)}$$

$$Poisson's\ coefficient = \upsilon = 0.3 \quad \text{(A.50)}$$

As it is clear from the previous equations, the closed-form formulation is too complex for practical application. For this reason, starting from the 61 numerical simulations on the beam-to-plate connections, a simplified equivalent formulation has been derived.

It was verified that a formulation that can interpret rather faithfully the analytical results deriving from the resolution of Eq.A35 could be written in the following form (Eq.A51):

$$k_{2D} = EB_{eff} \frac{c_2 \gamma^{c_3}}{\beta^{c_1} - 1} \quad \text{(A.51)}$$

where k_{2D} is the stiffness of a tube with unitary width, and c_1, c_2, and c_3 are regression parameters calibrated on the closed-form solution of the previous equations. The ratio between the calibrated formulation and the analytical solution applied to all the analysed cases has shown a mean value equal to 1.04 and a coefficient of variation equal to 6.1%. In Figure A.5 and Figure A.6 it is possible to observe the variation laws of the parameters β and γ against the stiffness.

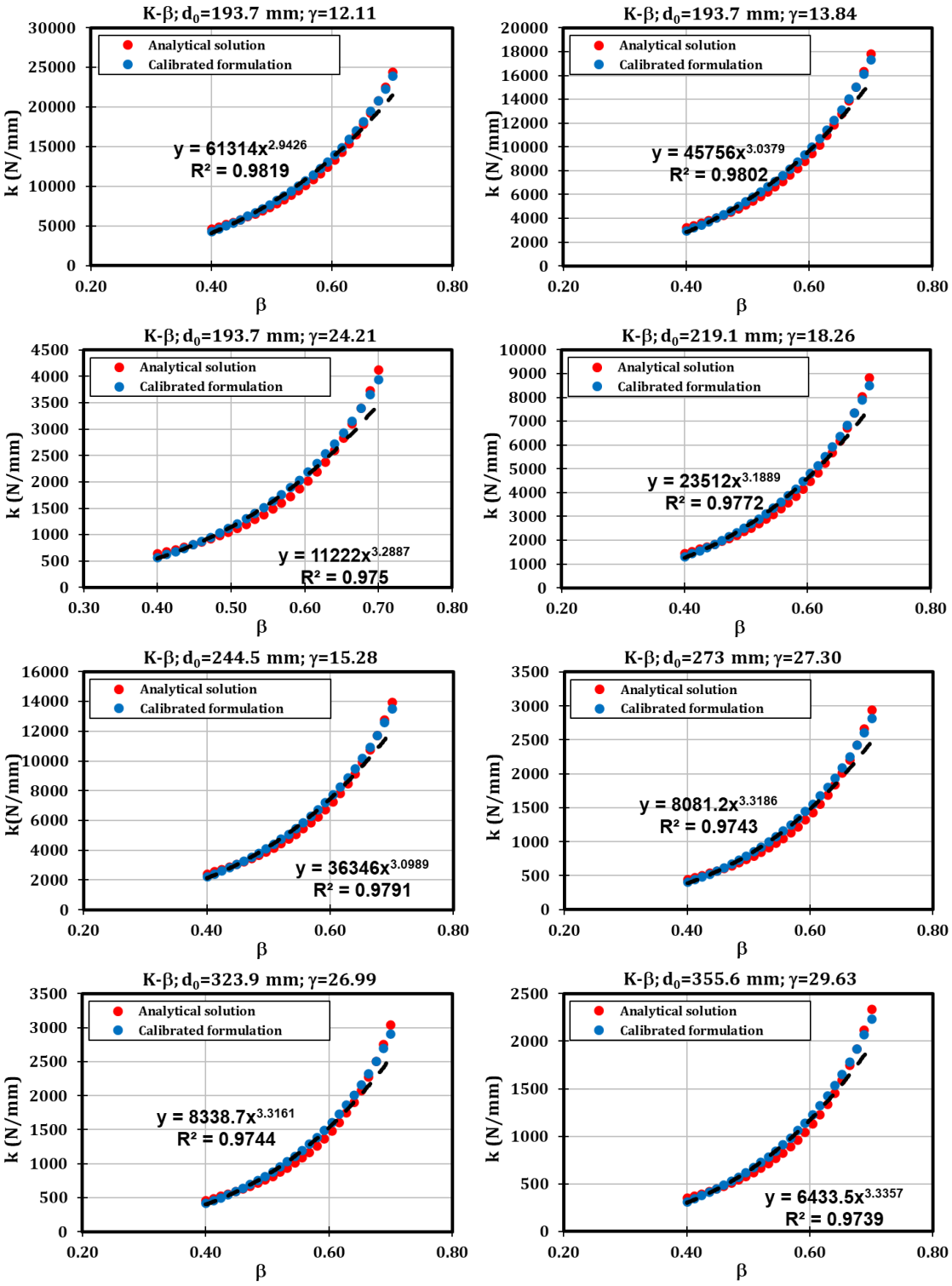

Figure A.5 – Accuracy of the calibrated formulation

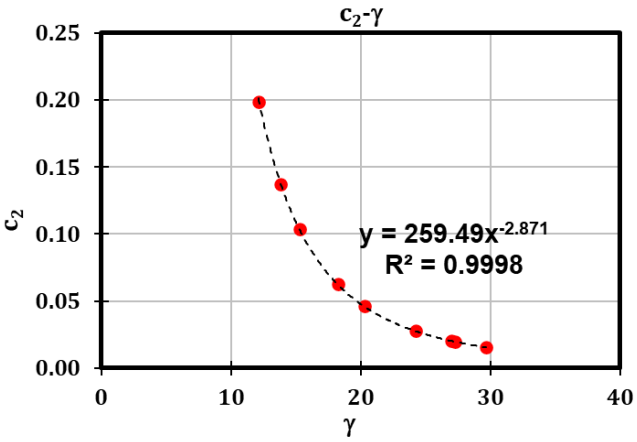

Figure A.6 – c1-γ law

Similarly to the strength model, the final equation for the stiffness prediction (Eq.A51) has been defined by evaluating an appropriate value of the effective width for stiffness calculation as a function of the three non-dimensional parameters β, γ, τ (Eq.A52):

$$k_{3D} = 9.6 \frac{\beta^{-1.17} \gamma^{-2.42} \tau^{1.31}}{\beta^{-2.61} - 1} E d_0 \tag{A.52}$$

ANNEX B

B1. Main details and location of the measurement devices

B1.1 Structure with RBS connections

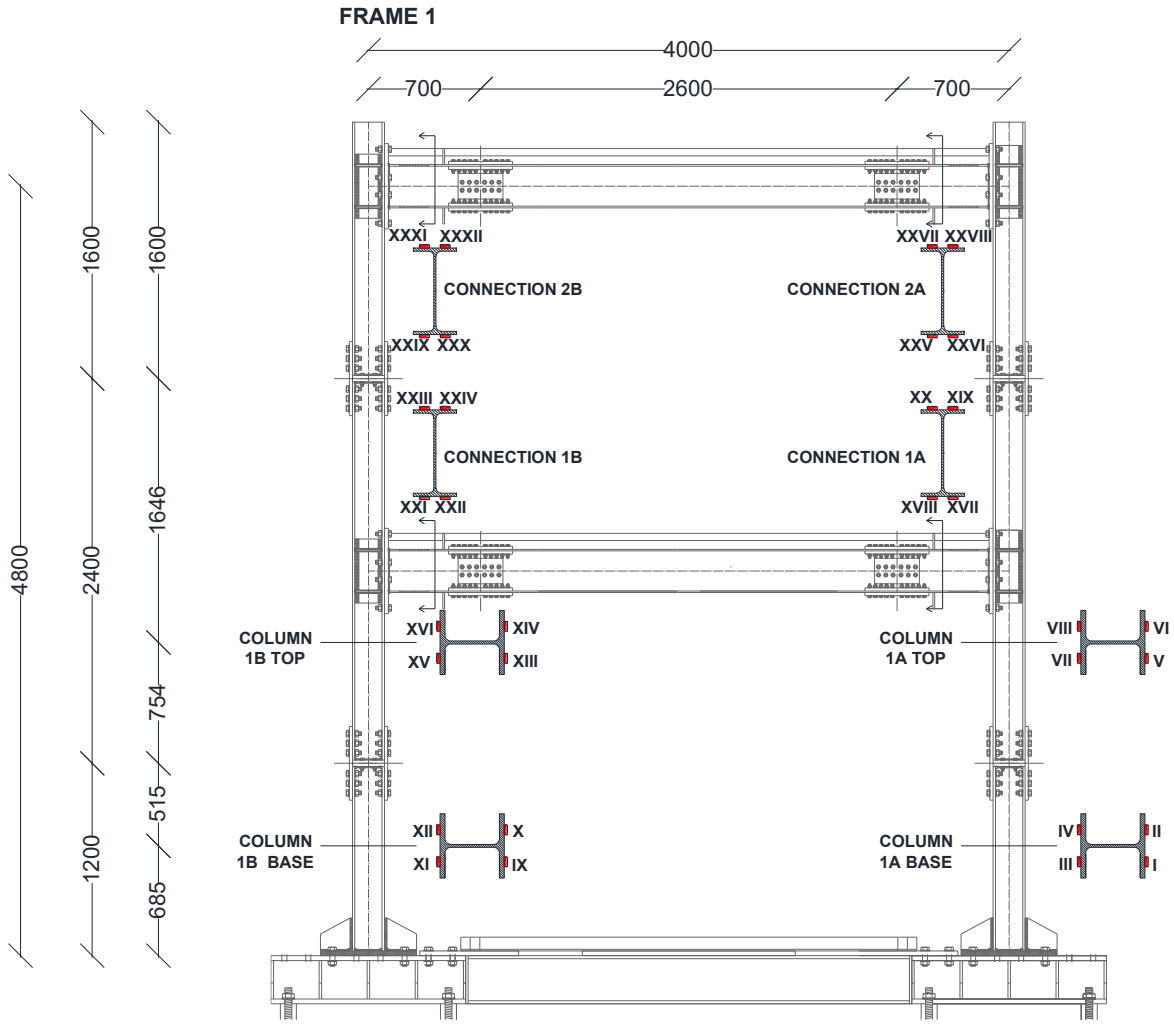

Figure B.7 – Location of strain gauges on MRF-1

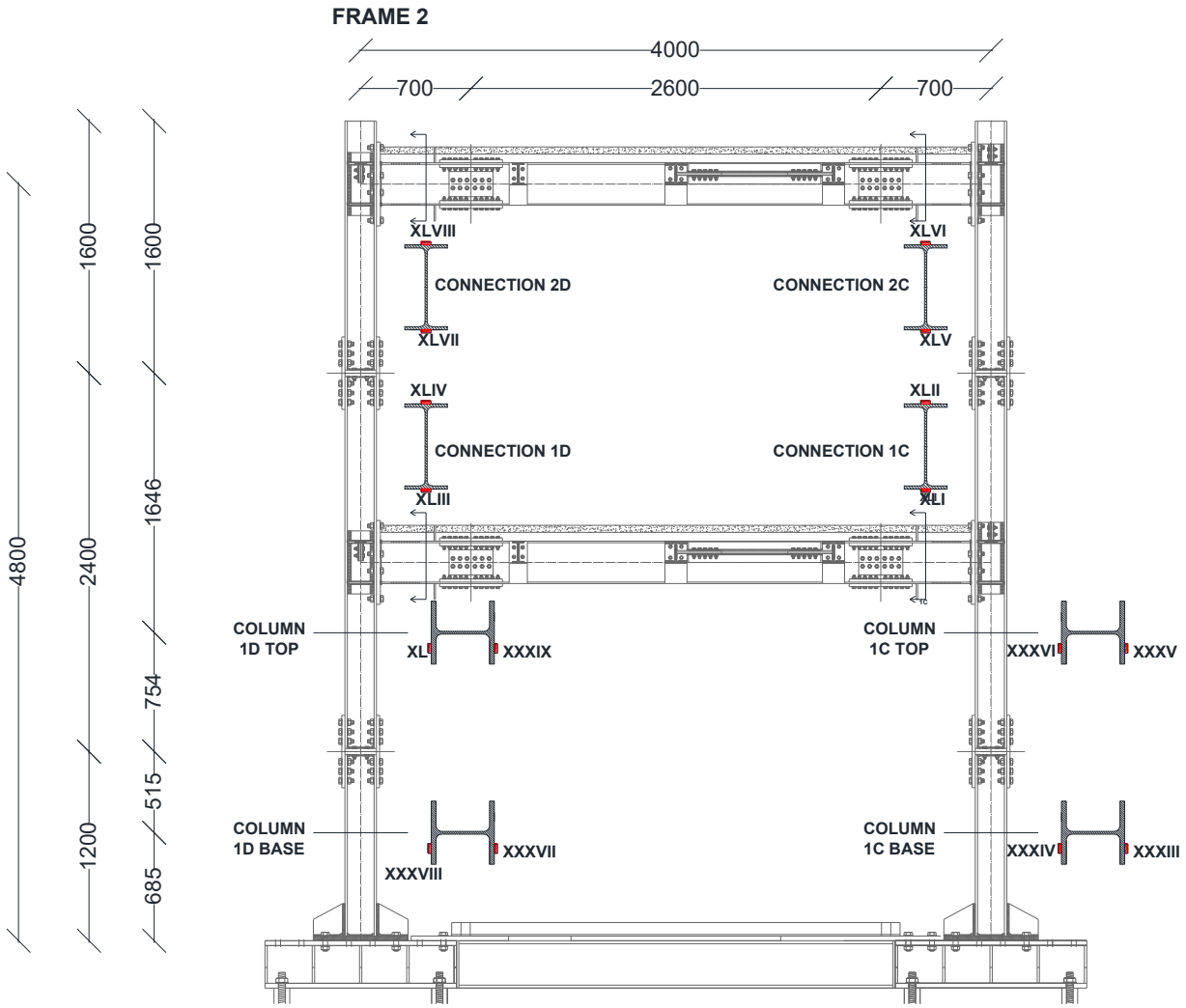

Figure B.8 - Location of strain gauges on MRF-2

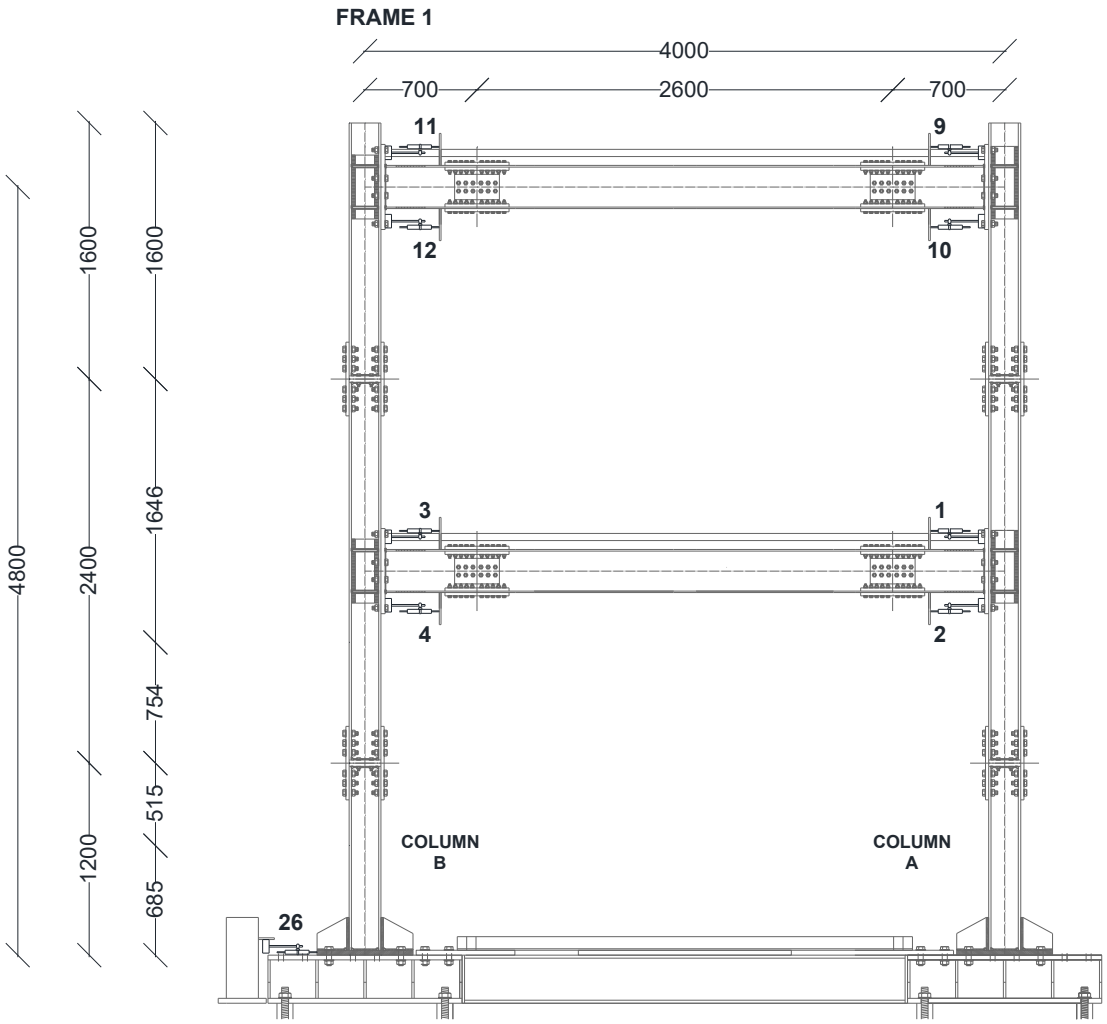

Figure B.9 - Location of potentiometric transducers on MRF-1

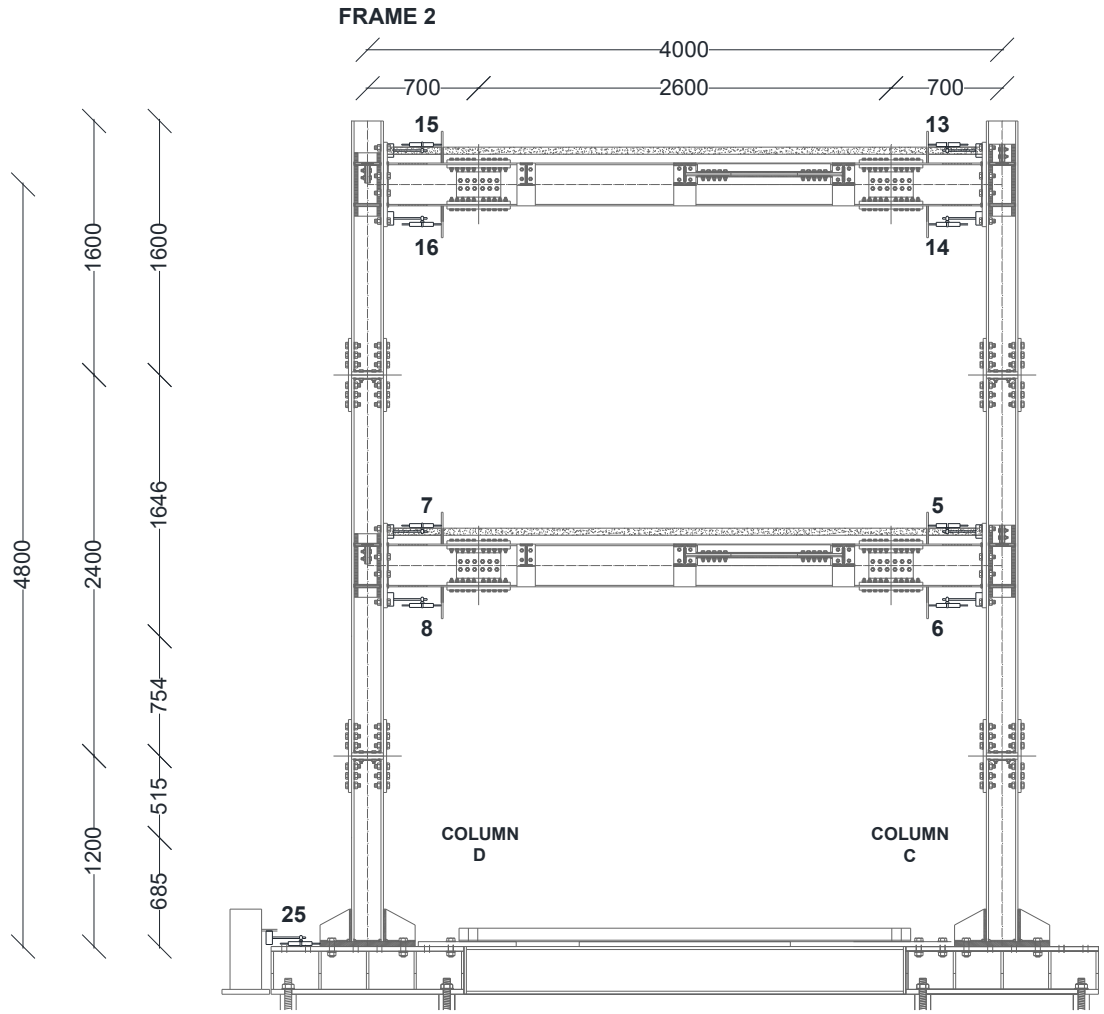

Figure B.10 - Location of potentiometric transducers on MRF-2

B1.2 Structure with FREEDAM connections

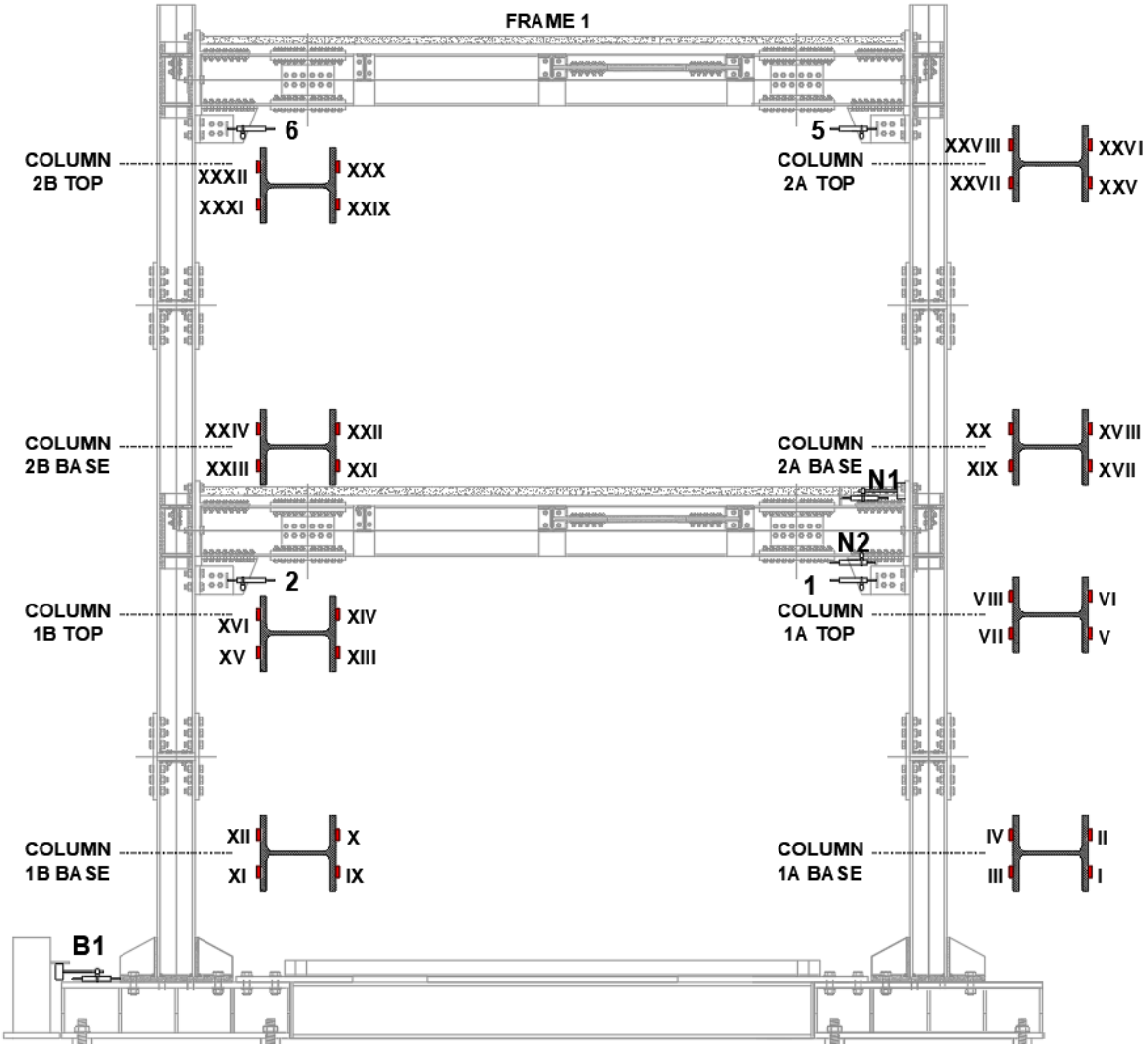

Figure B.11 – Location of strain gauges and transducers on MRF-1

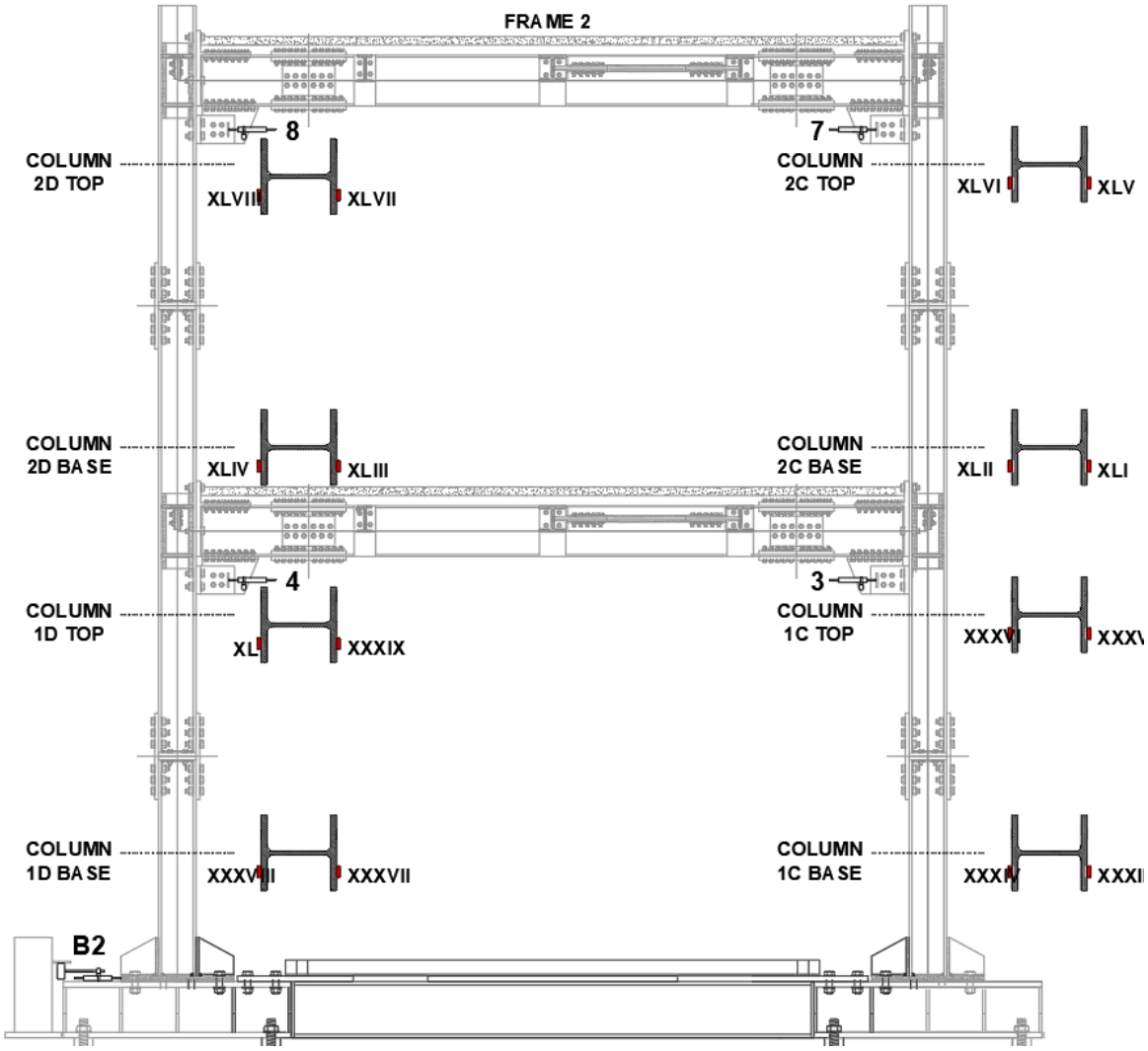

Figure B.12 - Location of strain gauges and transducers on MRF-2

B1.3 Structure with X-shaped T-stub connections

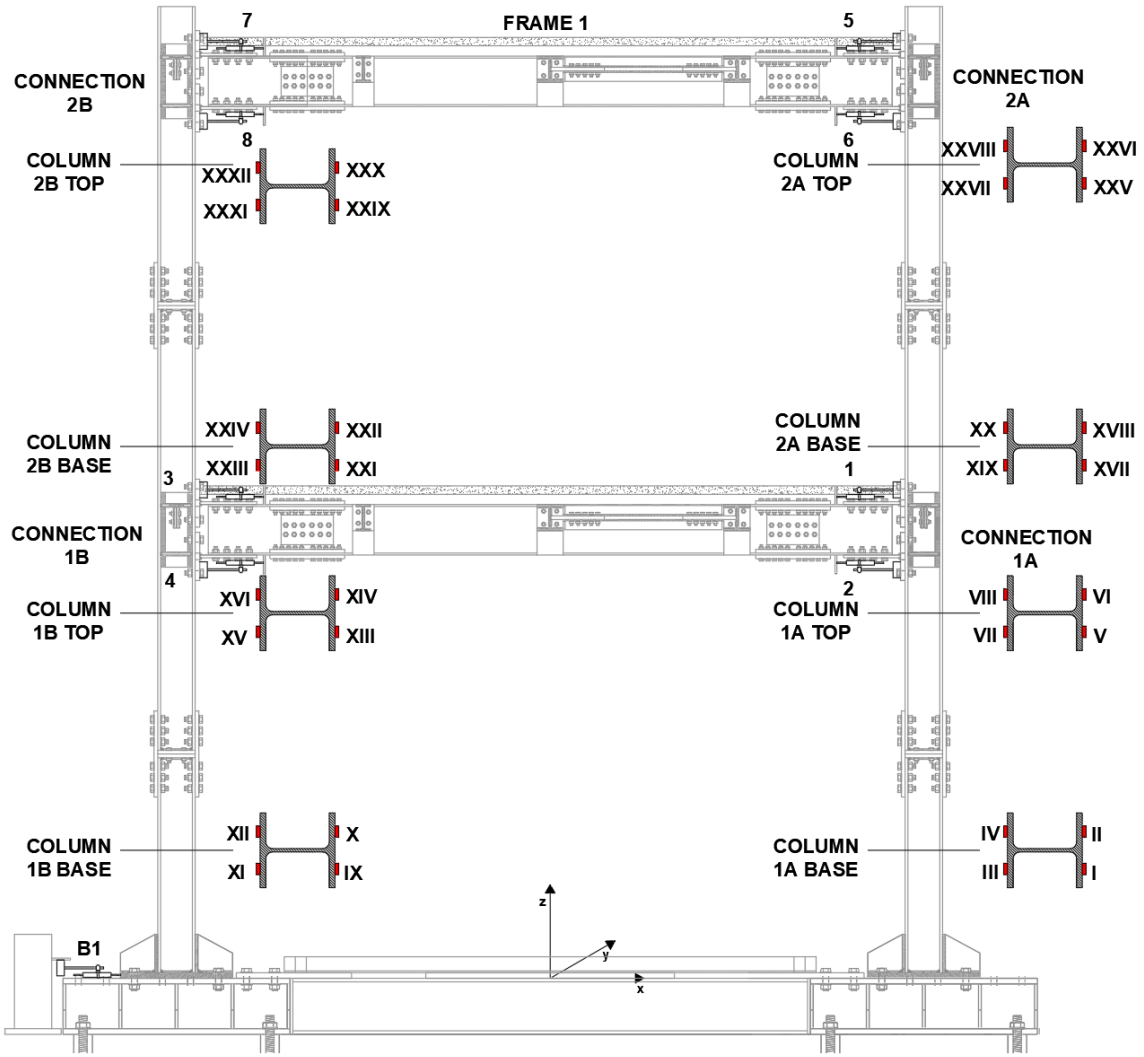

Figure B.13 – Location of strain gauges and transducers on MRF-1

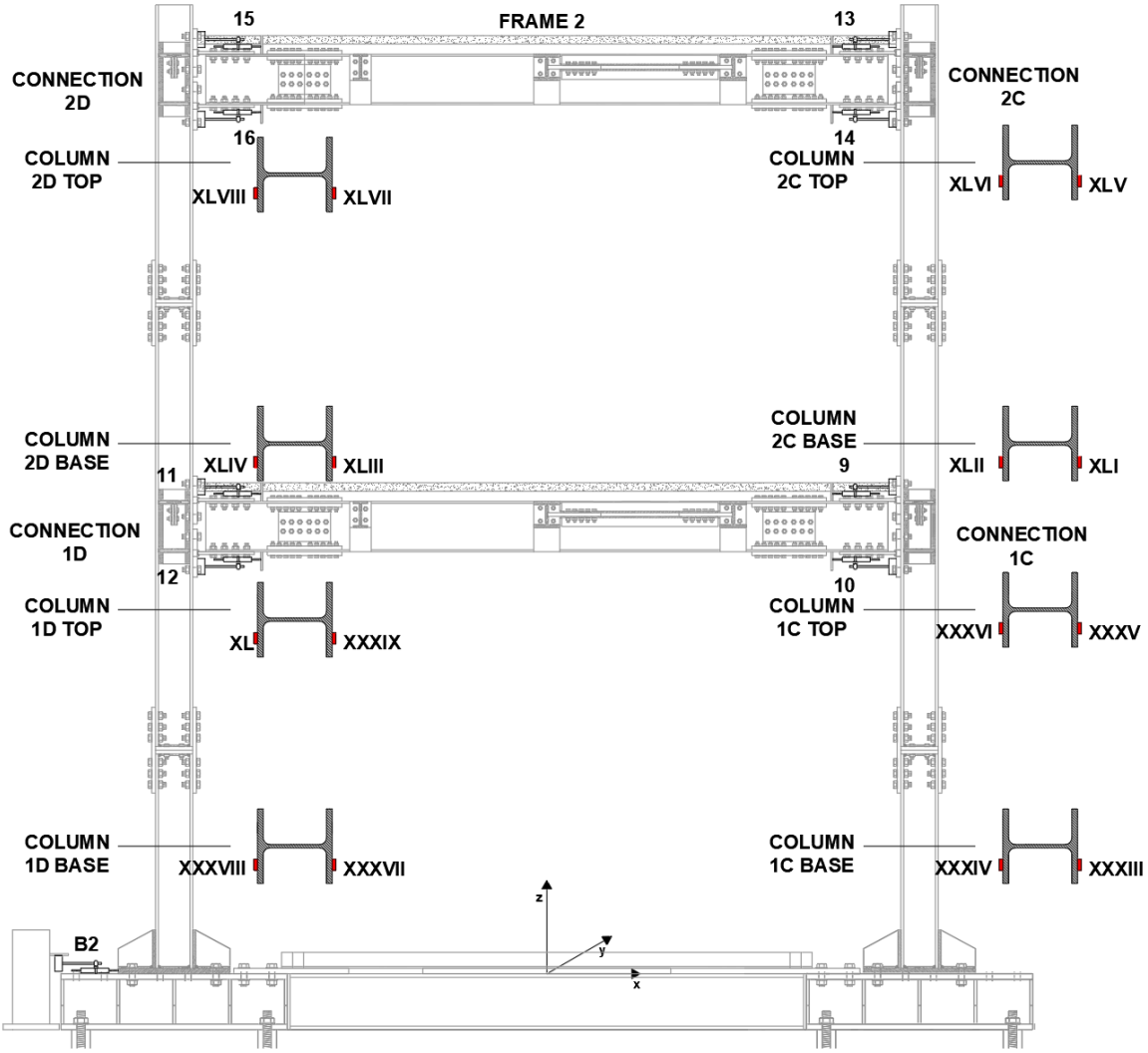

Figure B.14 - Location of strain gauges and transducers on MRF-2

B1.4 Details

Beam splice

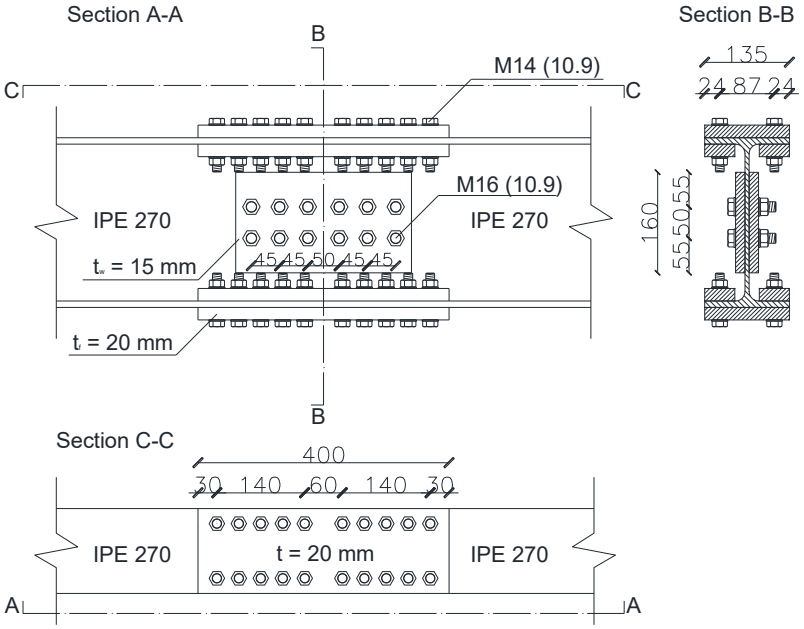

Figure B.15 – Detail of the beam splice

Column splice

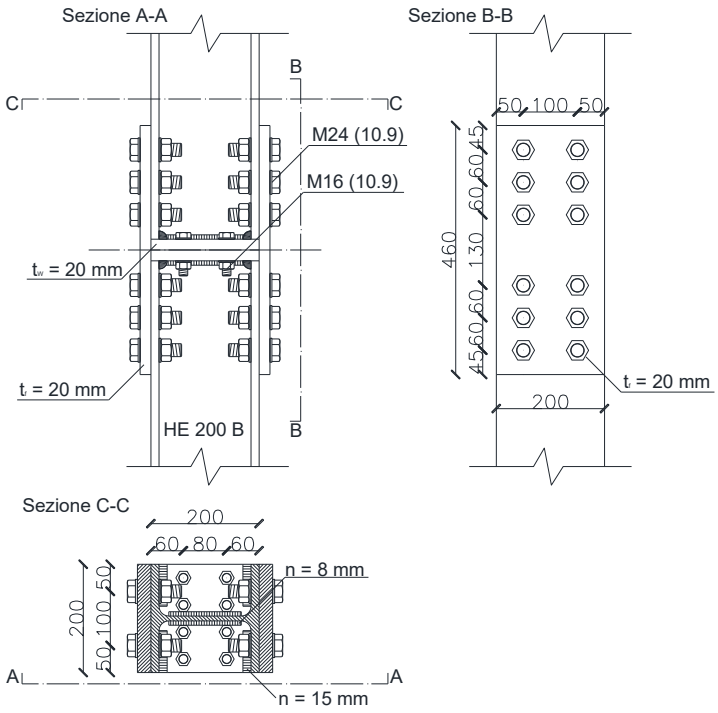

Figure B.16 – Detail of the column splice

Column base

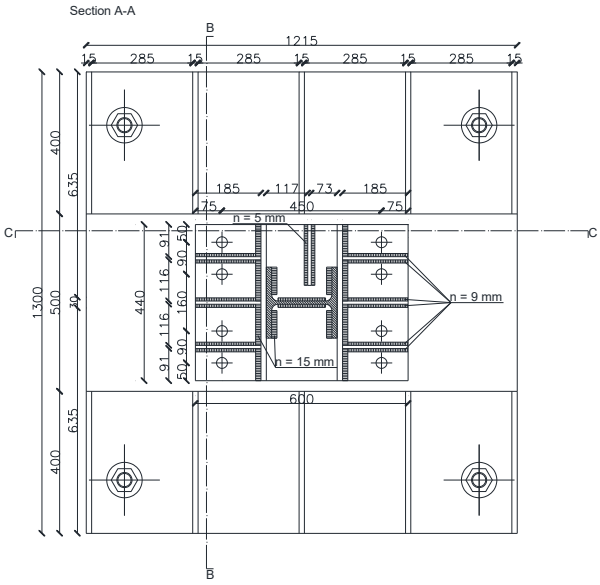

Figure B.17 – Plan view of the column base

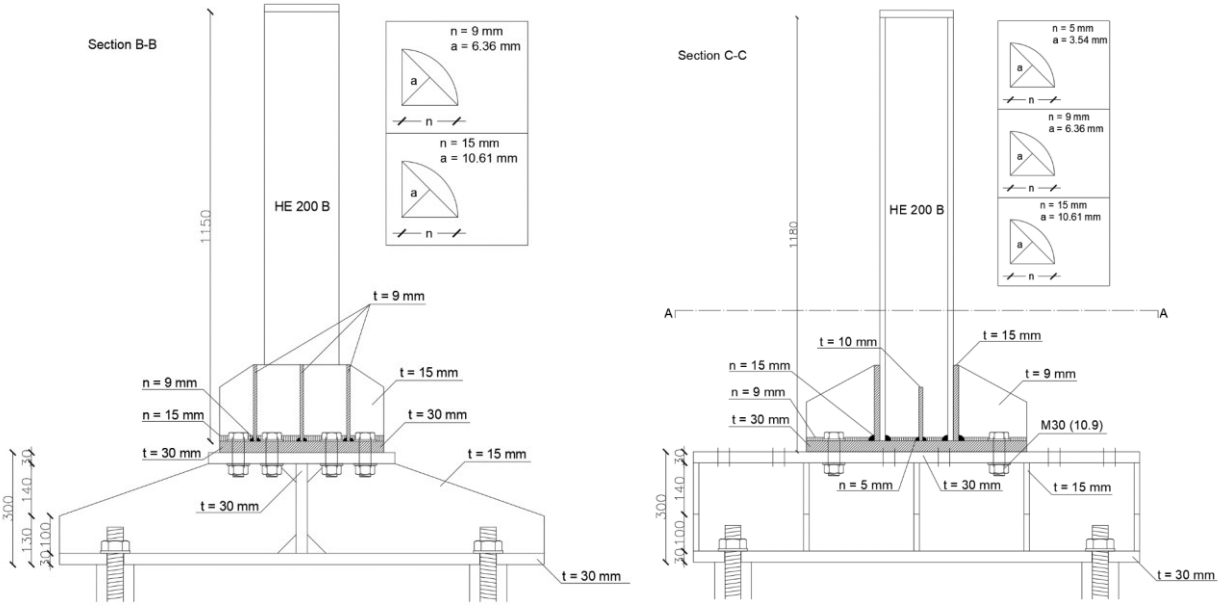

Figure B.18 – Side views of the column base

B2. Materials properties

B2.1 Beam IPE 270

Table B.2 – Initial and final geometry of the coupons

Initial geometry

b [mm]	*t [mm]*	*L_c [mm]*	*L_0 [mm]*	*A_0 [mm^2]*
29.2	10.1	103.5	100	294.92

Final geometry

b [mm]	*t [mm]*	*$L_{c,u}$ [mm]*	*L_u [mm]*	*A_f [mm^2]*
19.4	6.2	134.8	120	120.28

Z [%]	*ε_u*
59.22%	89.69%

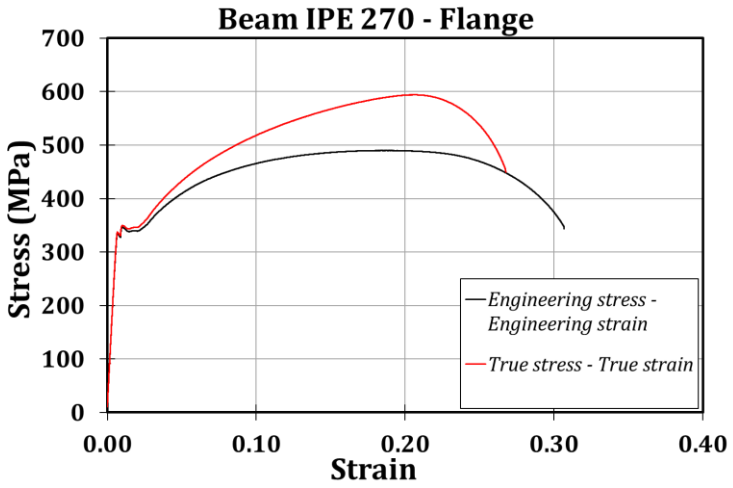

Figure B.19 – Stress-strain curves

B2.2 Column HE 200 B

Table B.3 – Initial and final geometry of the coupons

Initial geometry

b [mm]	*t [mm]*	*L_c [mm]*	*L_0 [mm]*	*A_0 [mm^2]*
26.2	14.5	117	110	379.9

Final geometry

b [mm]	*t [mm]*	*$L_{c,u}$ [mm]*	*L_u [mm]*	*A_f [mm^2]*
17	8	131	106	136

Z [%]	*ε_u*
64.20%	102.73%

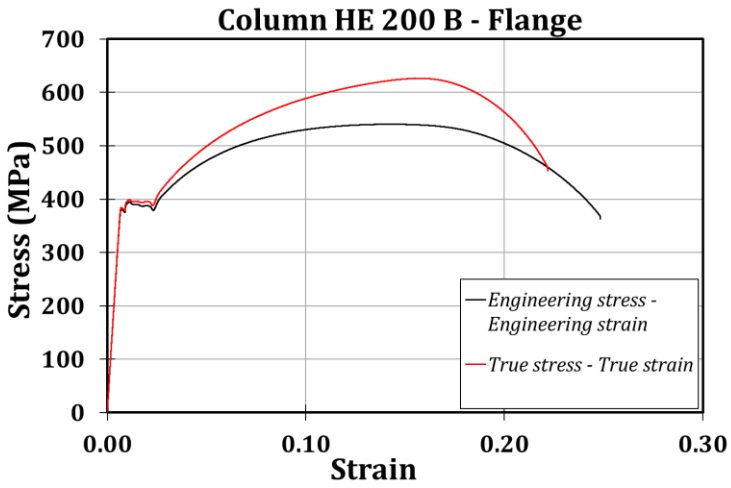

Figure B.20 – Stress-strain curves

B3. Main results and comparisons with the analytical models

B3.1 Structure with RBS connections

B3.1.1 Test 1 – Imperial Valley 1.1g

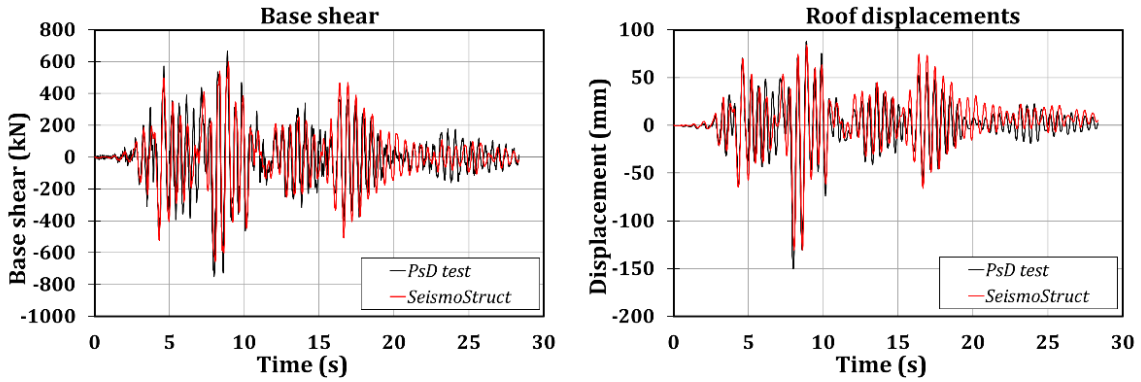

Figure B.21 – Base shear and roof displacement curves

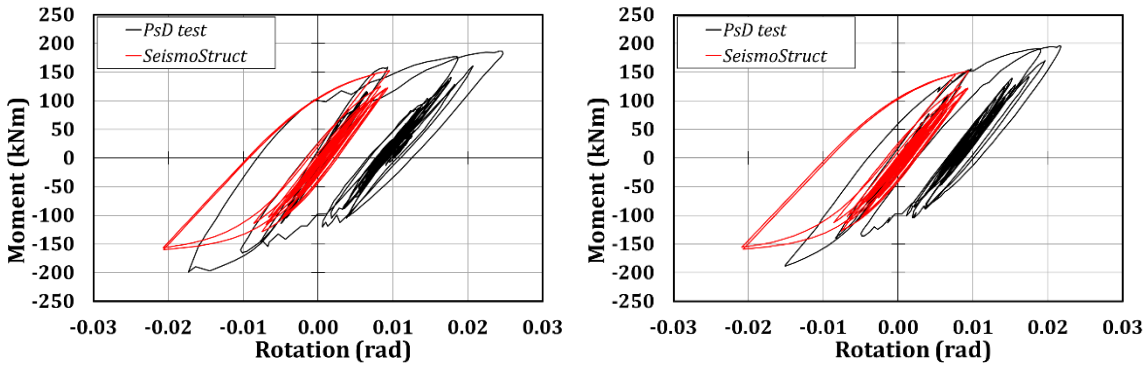

Figure B.22 – Hysteretic curves; connections 1A (left) and 1B (right)

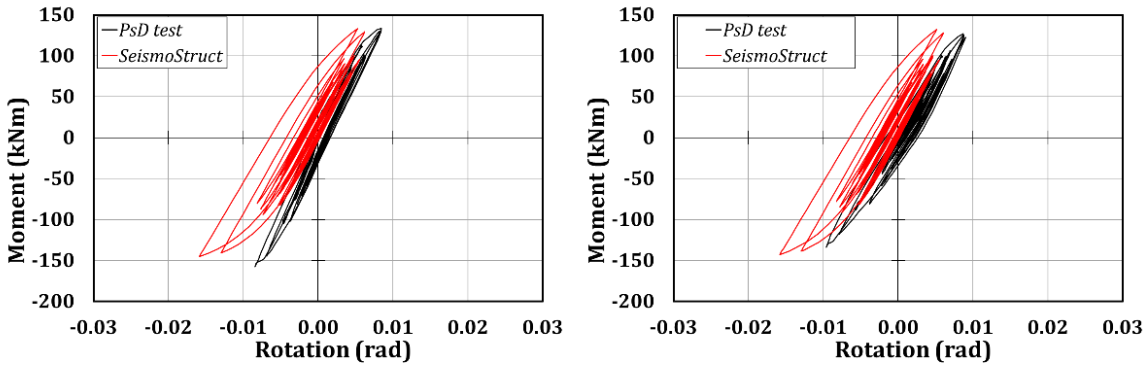

Figure B.23 – Hysteretic curves; connections 2A (left) and 2B (right)

B3.1.2 Test 2 – Spitak 0.8g

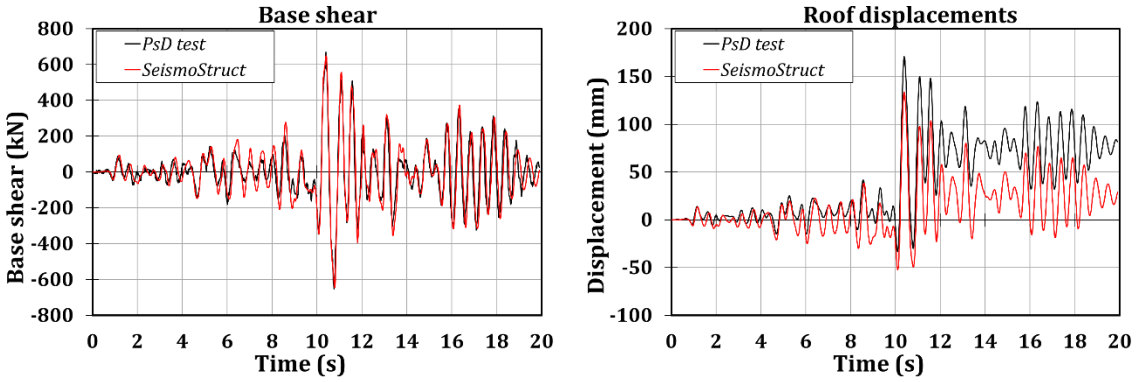

Figure B.24 – Base shear and roof displacement curves

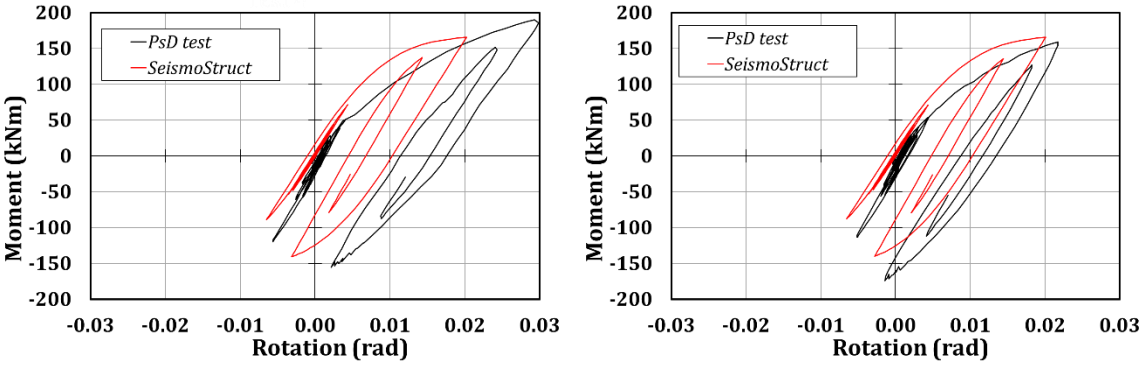

Figure B.25 – Hysteretic curves; connections 1A (left) and 1B (right)

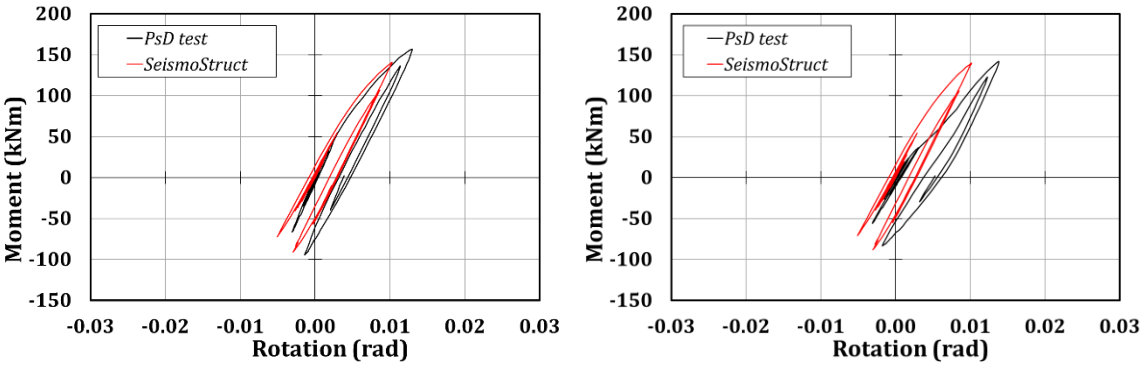

Figure B.26 – Hysteretic curves; connections 2A (left) and 2B (right)

B3.1.3 Test 3 – Artificial 0.5g

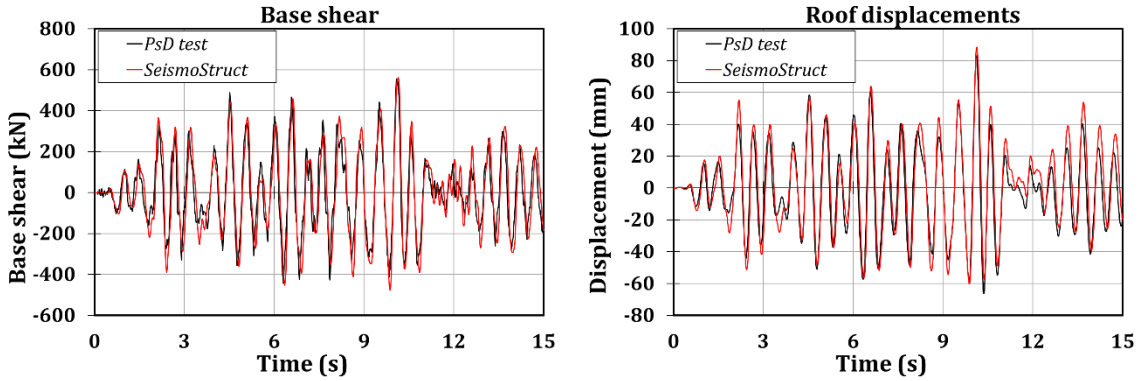

Figure B.27 – Base shear and roof displacement curves

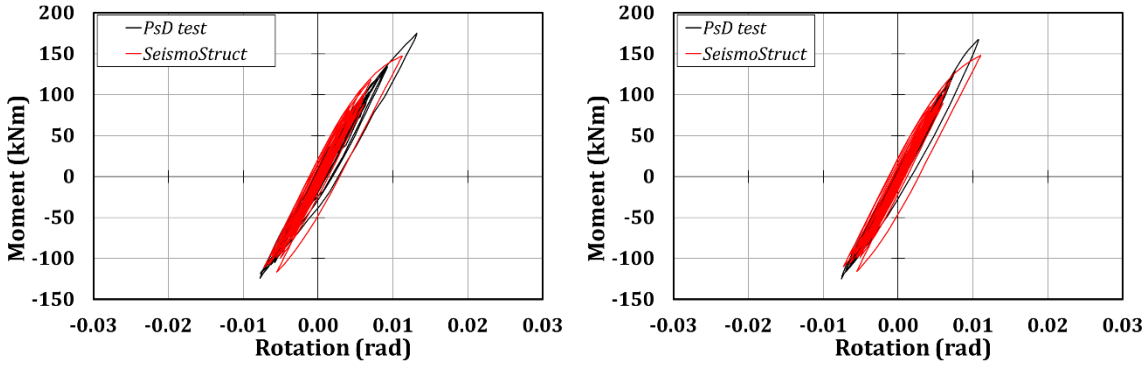

Figure B.28 – Hysteretic curves; connections 1A (left) and 1B (right)

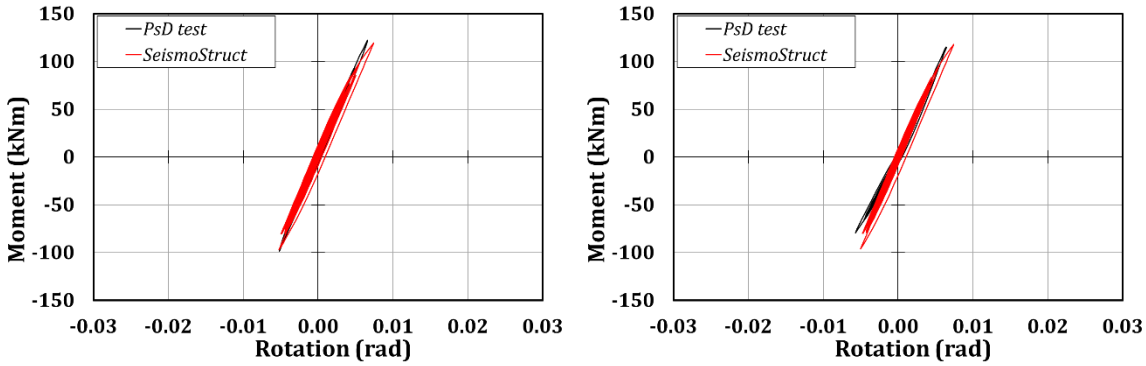

Figure B.29 – Hysteretic curves; connections 2A (left) and 2B (right)

B3.1.4 Test 4 – Santa Barbara 0.8g

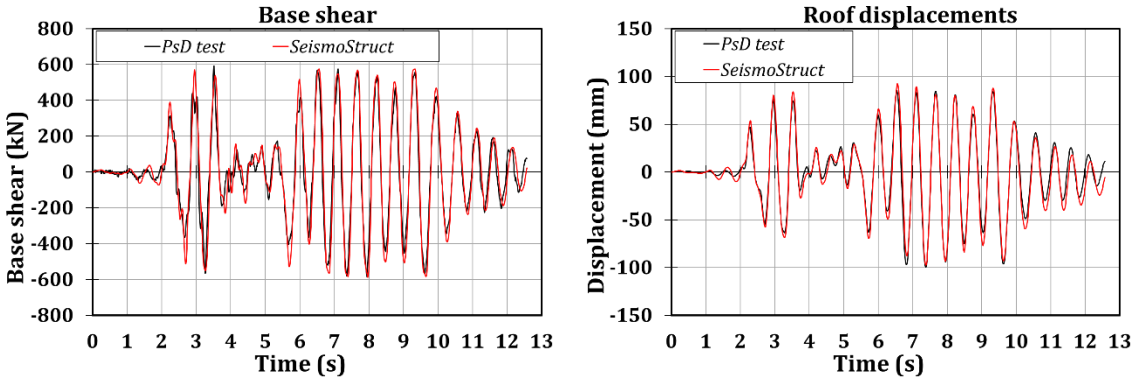

Figure B.30 – Base shear and roof displacement curves

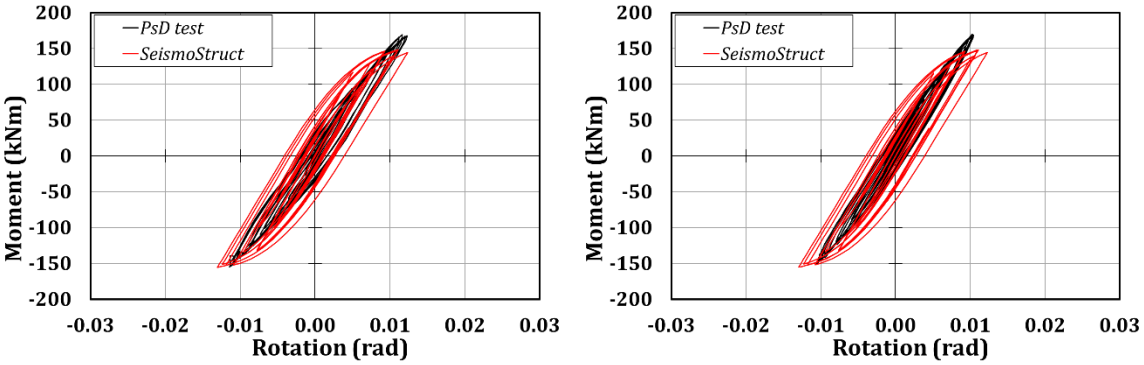

Figure B.31 – Hysteretic curves; connections 1A (left) and 1B (right)

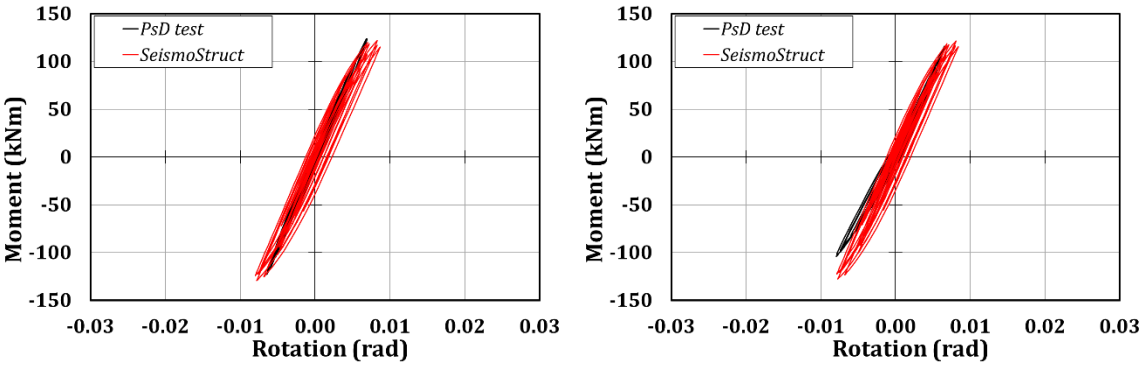

Figure B.32 – Hysteretic curves; connections 2A (left) and 2B (right)

B3.1.5 Test 5 – Coalinga 0.8g

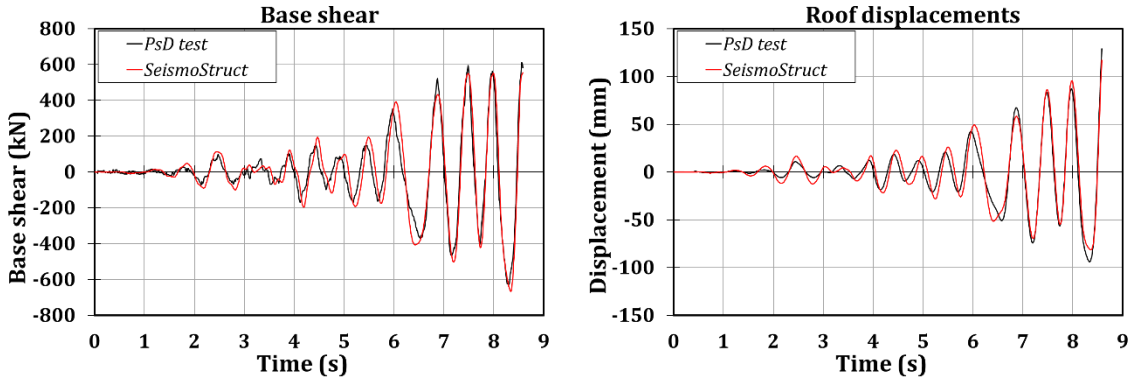

Figure B.33 – Base shear and roof displacement curves

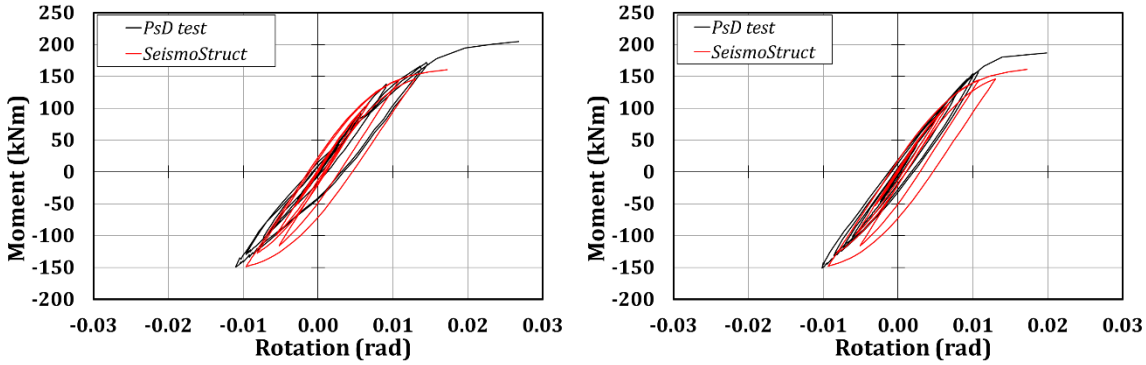

Figure B.34 – Hysteretic curves; connections 1A (left) and 1B (right)

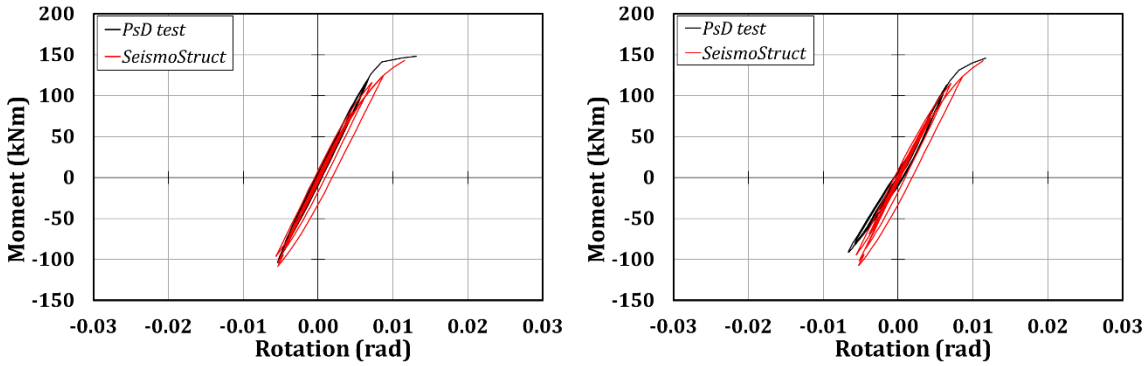

Figure B.35 – Hysteretic curves; connections 2A (left) and 2B (right)

B3.2 Structure with FREEDAM connections

B3.2.1 Test 1 – Imperial Valley 1.1g

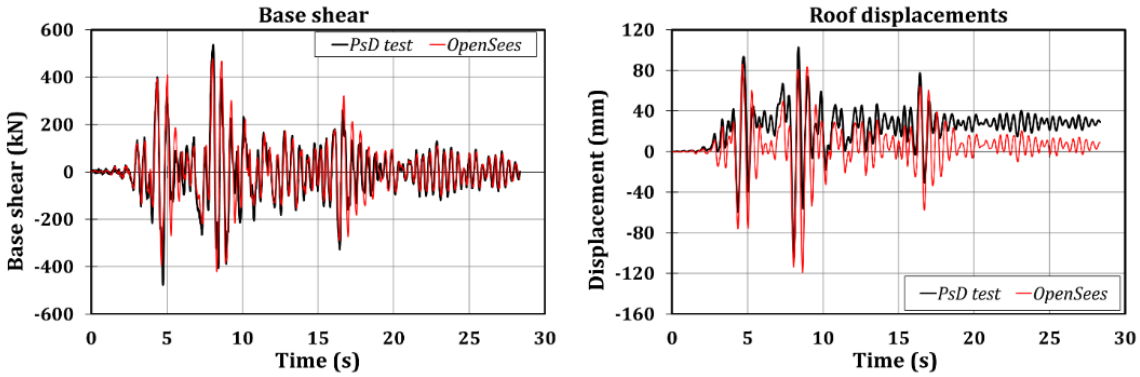

Figure B.36 – Base shear (left) and roof displacement (right) curves

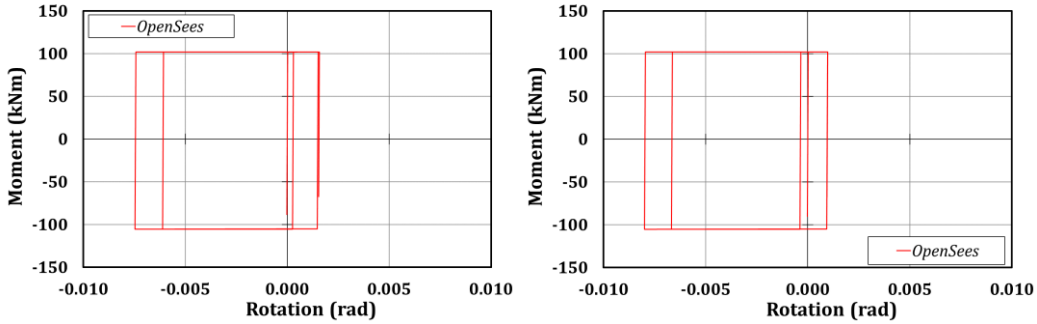

Figure B.37 – Hysteretic curves: connection 1A (left) and 1B (right)

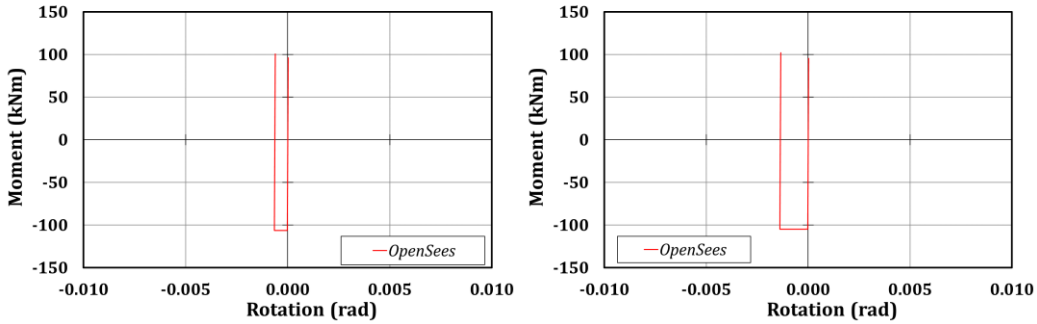

Figure B.38 – Hysteretic curves: connection 2A (left) and 2B (right)

B3.2.2 Test 2 – Spitak 0.8g

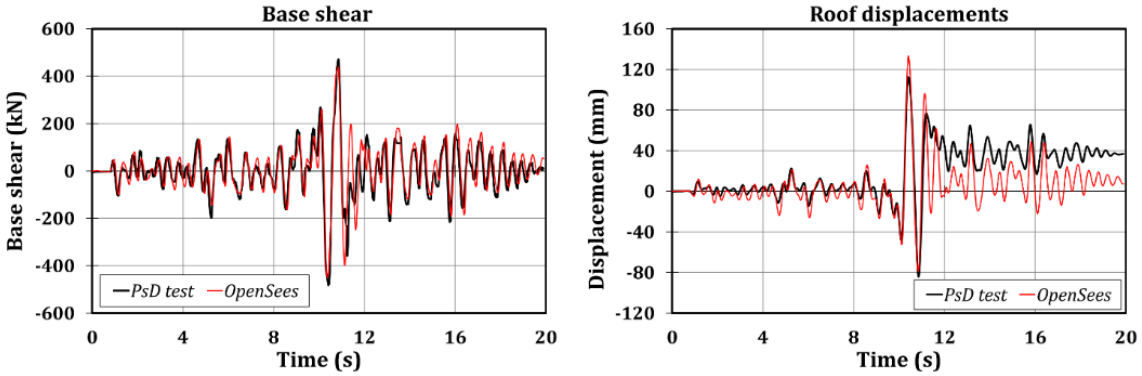

Figure B.39 – Base shear (left) and roof displacement (right) curves

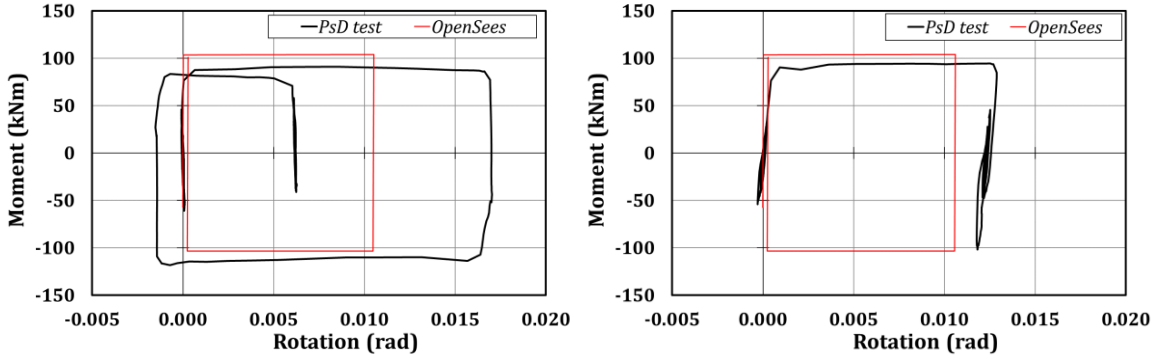

Figure B.40 – Hysteretic curves: connection 1A (left) and 1B (right)

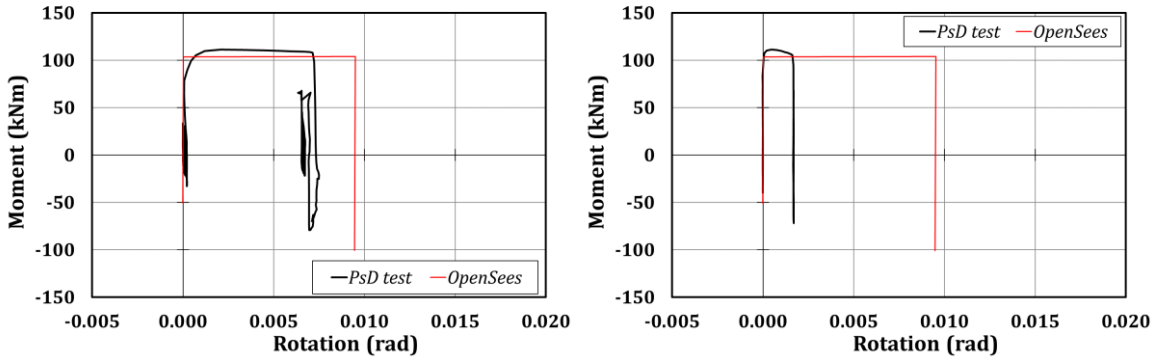

Figure B.41 – Hysteretic curves: connection 2A (left) and 2B (right)

B3.2.3 Test 3 – Artificial 0.5g

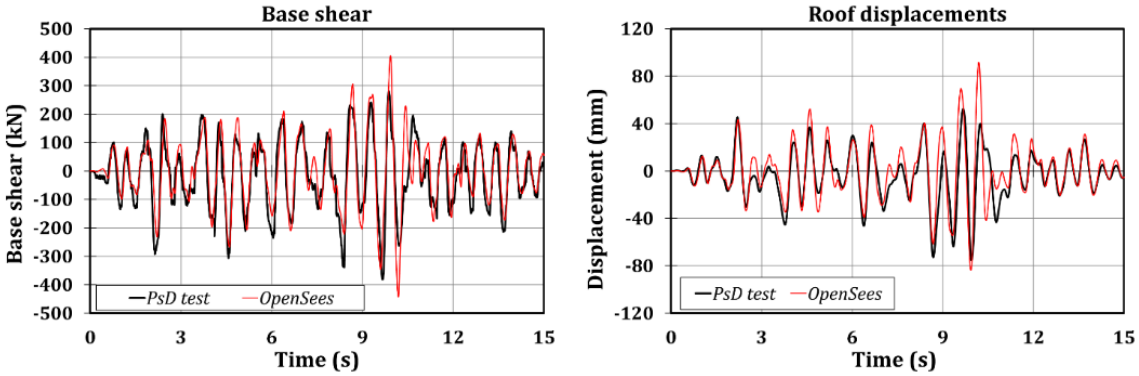

Figure B.42 – Base shear (left) and roof displacement (right) curves

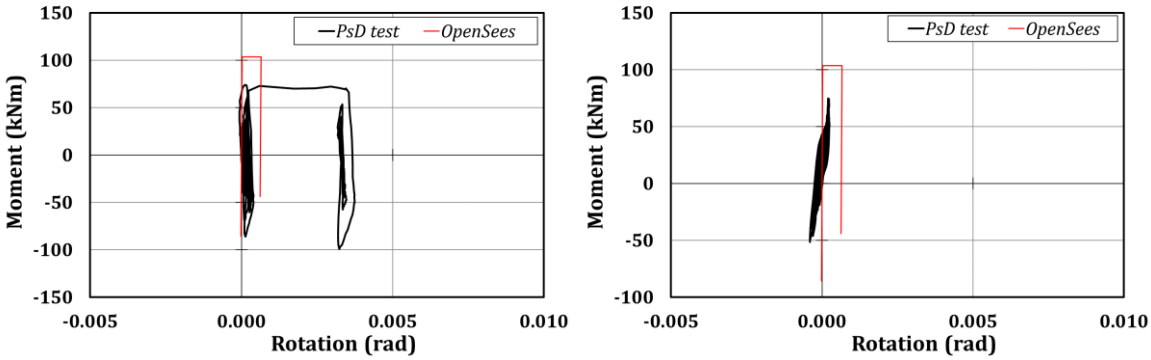

Figure B.43 – Hysteretic curves: connection 1A (left) and 1B (right)

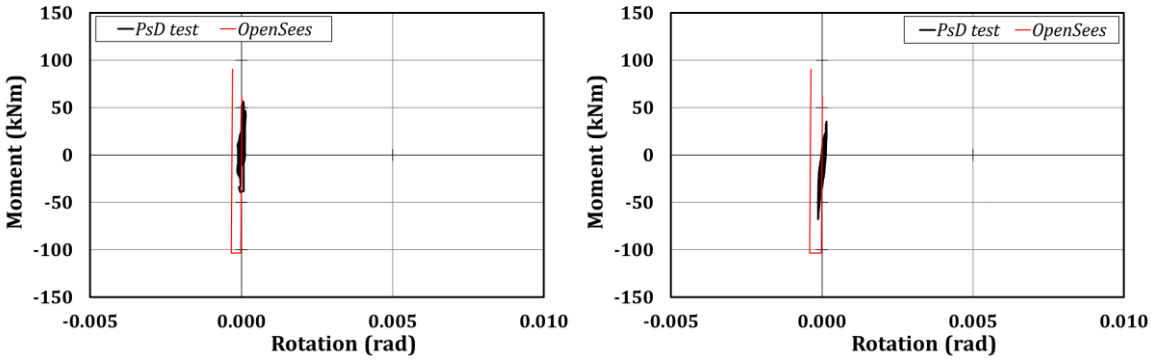

Figure B.44 – Hysteretic curves: connection 2A (left) and 2B (right)

B3.2.4 Test 4 – Santa Barbara 0.8g

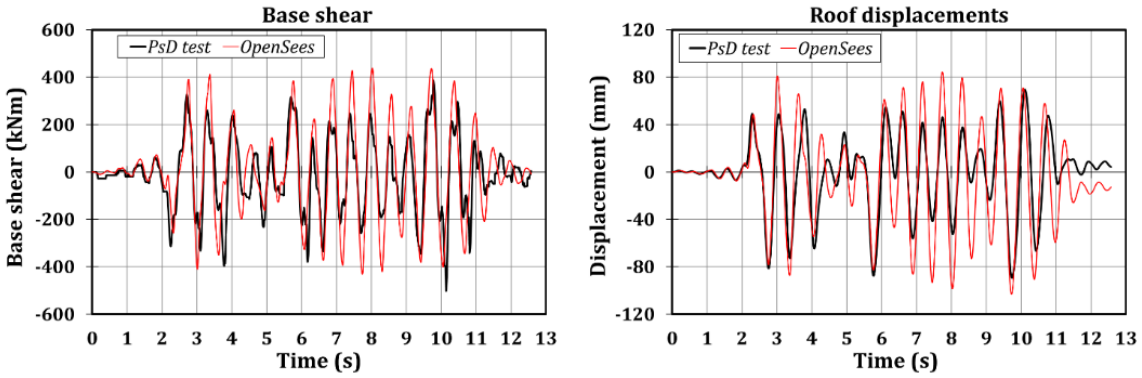

Figure B.45 – Base shear (left) and roof displacement (right) curves

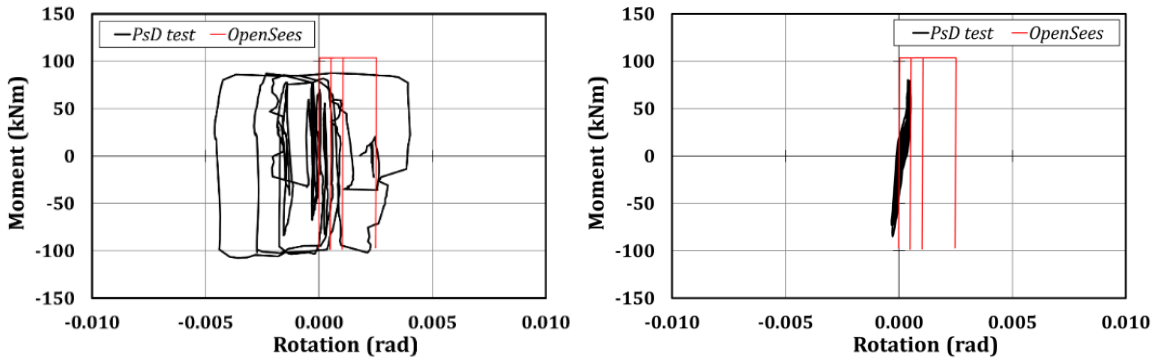

Figure B.46 – Hysteretic curves: connection 1A (left) and 1B (right)

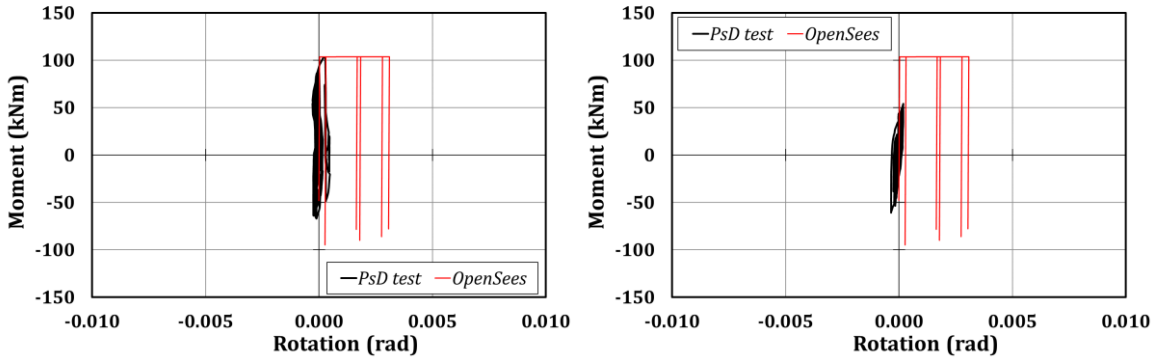

Figure B.47 – Hysteretic curves: connection 2A (left) and 2B (right)

B3.2.5 Test 5 – Coalinga 0.8g

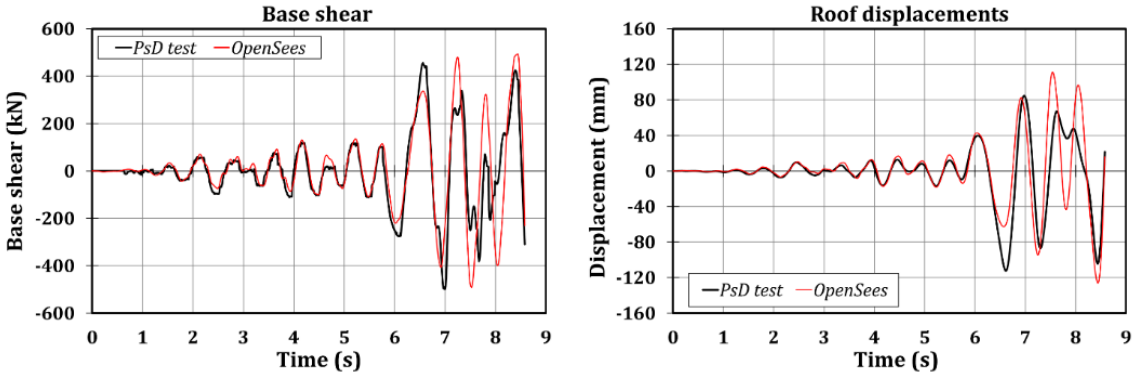

Figure B.48 – Base shear (left) and roof displacement (right) curves

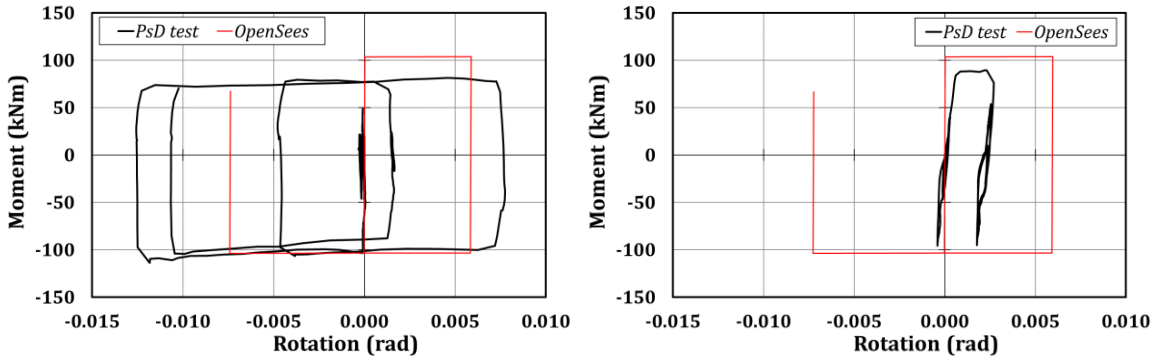

Figure B.49 – Hysteretic curves: connection 1A (left) and 1B (right)

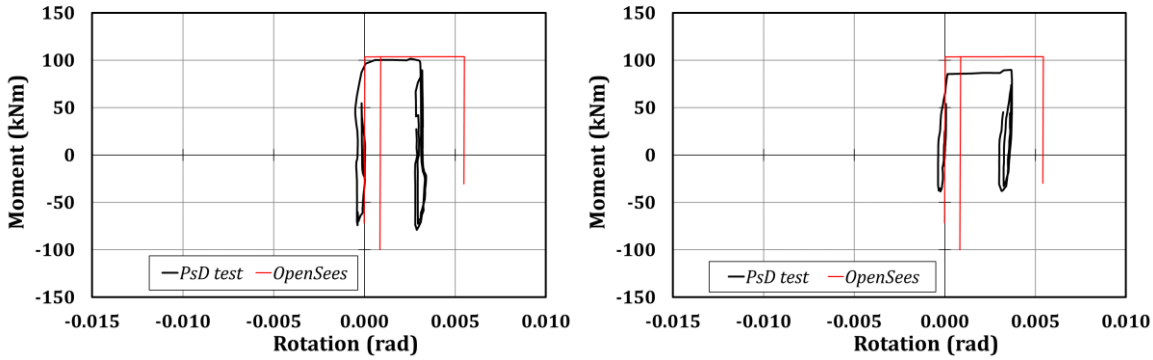

Figure B.50 – Hysteretic curves: connection 2A (left) and 2B (right)

B3.3 Structure with X-shaped T-stub connections

B3.3.1 Test 1 – Imperial Valley 1.1g

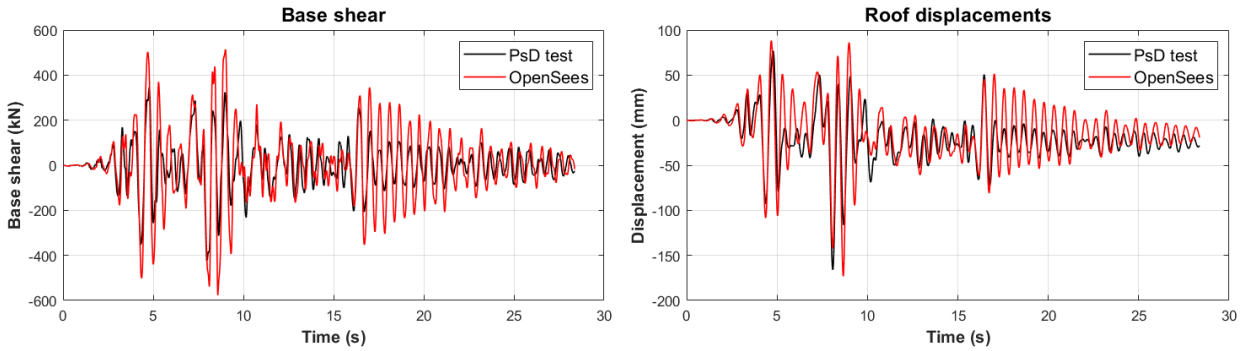

Figure B.51 – Base shear (left) and roof displacement (right) curves

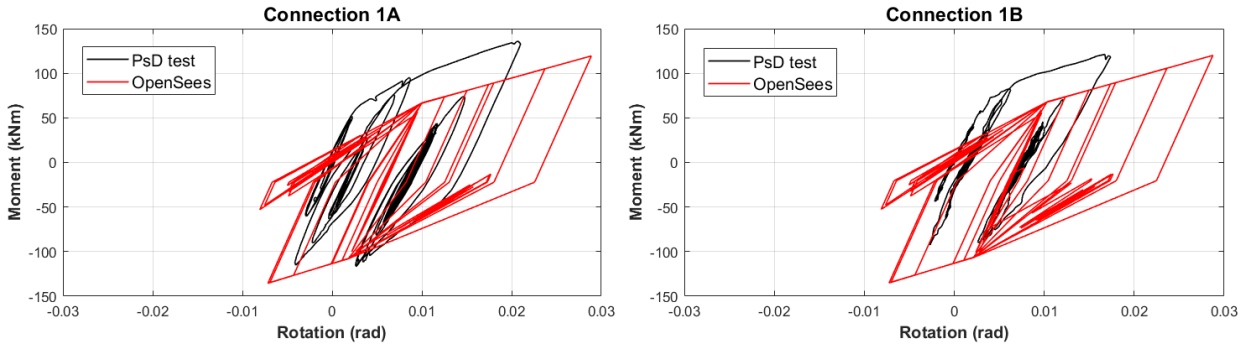

Figure B.52 – Hysteretic curves: connections 1A (left) and 1B (right)

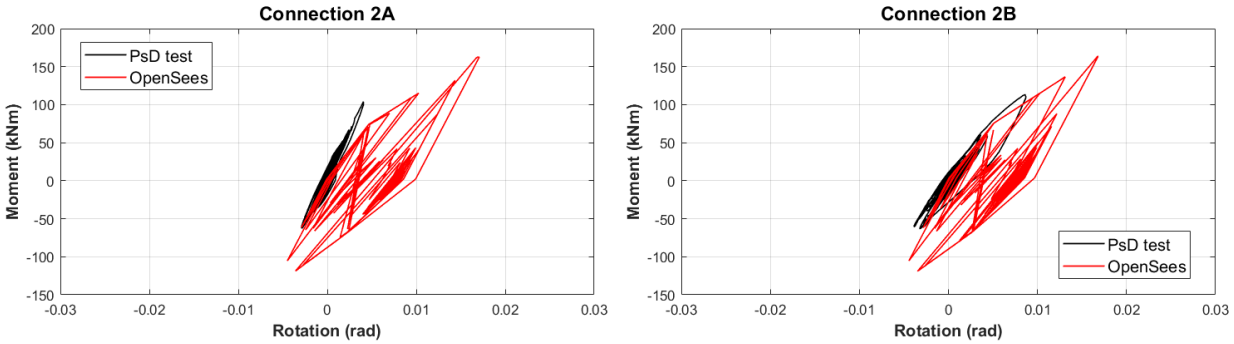

Figure B.53 – Hysteretic curves: connections 2A (left) and 2B (right)

B3.3.2 Test 2 – Spitak 0.8g

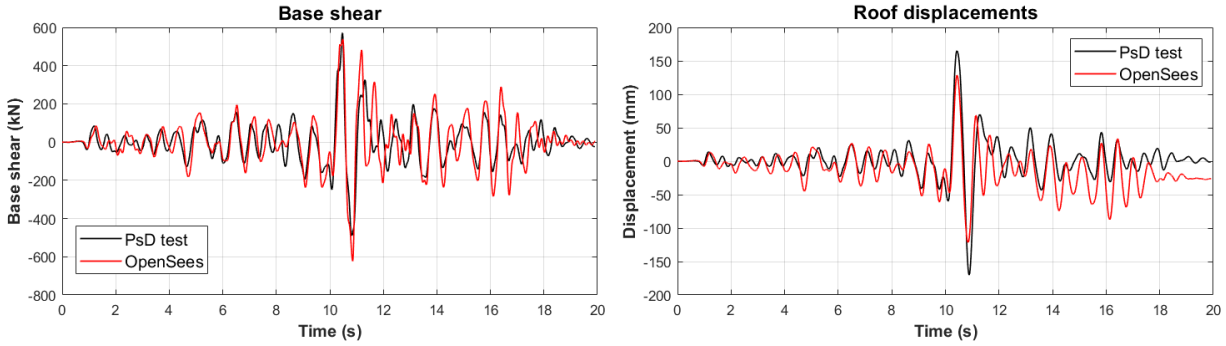

Figure B.54 – Base shear (left) and roof displacement (right) curves

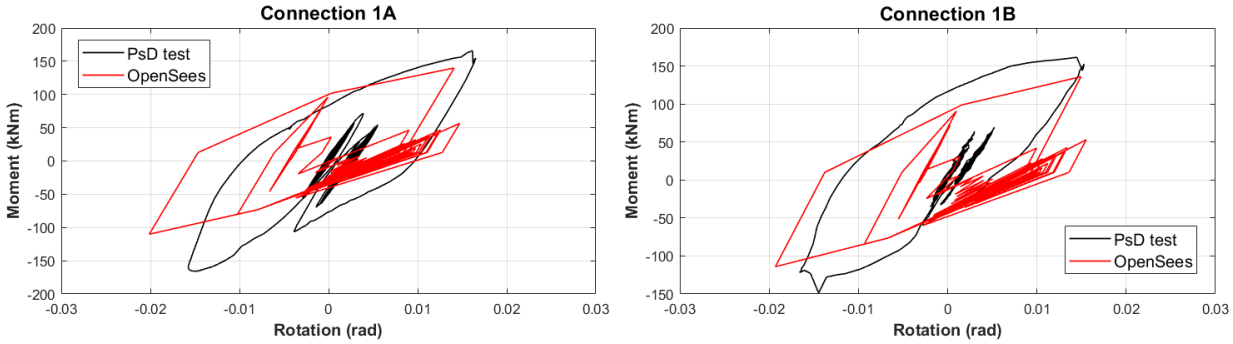

Figure B.55 – Hysteretic curves: connections 1A (left) and 1B (right)

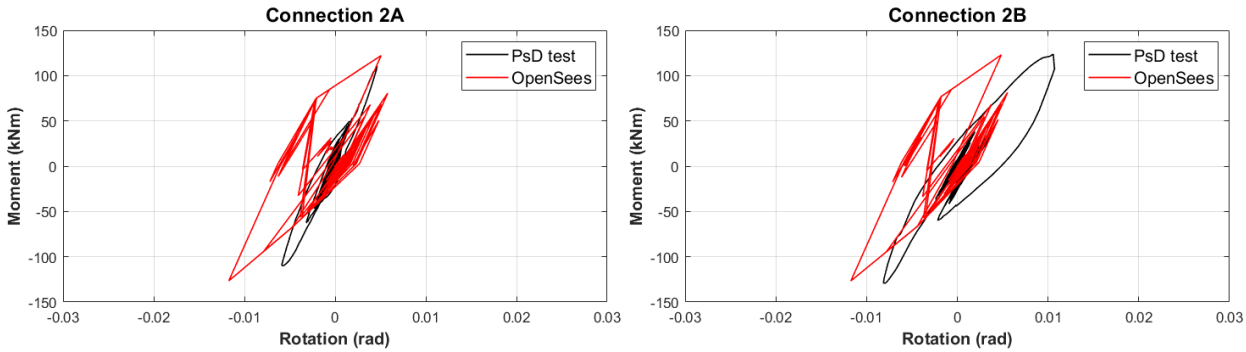

Figure B.56 – Hysteretic curves: connections 2A (left) and 2B (right)

B3.3.3 Test 3 – Artificial 0.5g

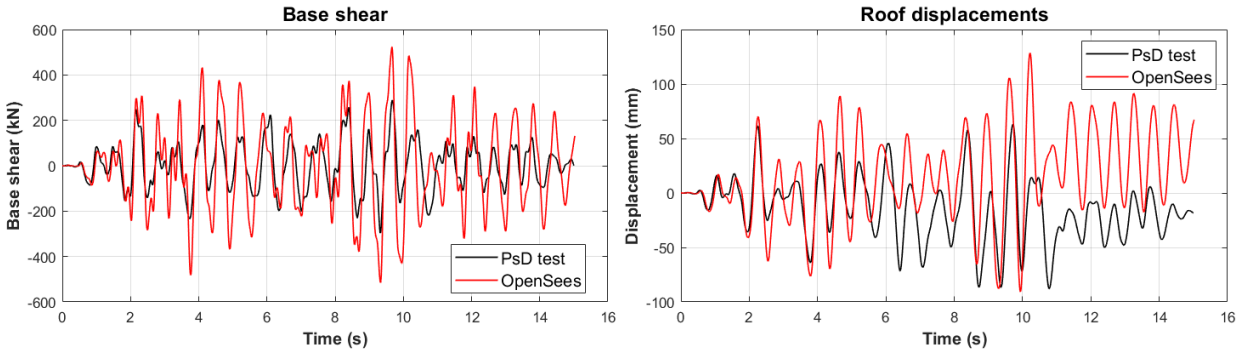

Figure B.57 – Base shear (left) and roof displacement (right) curves

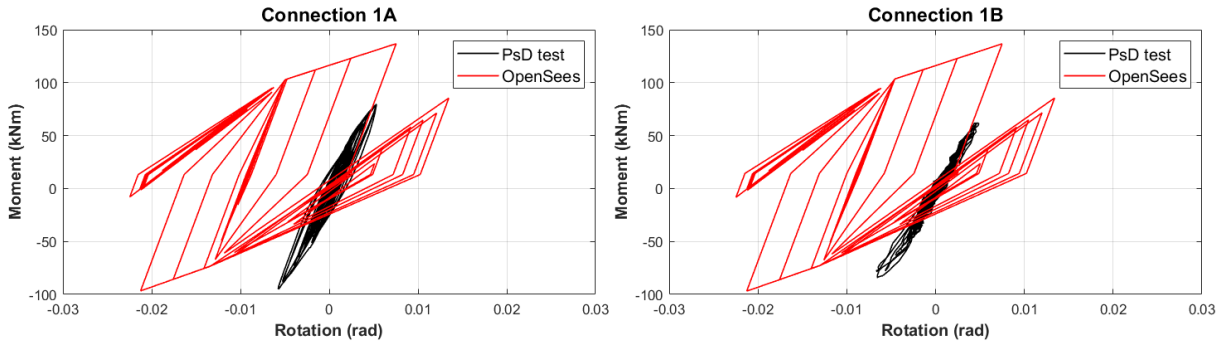

Figure B.58 – Hysteretic curves: connections 1A (left) and 1B (right)

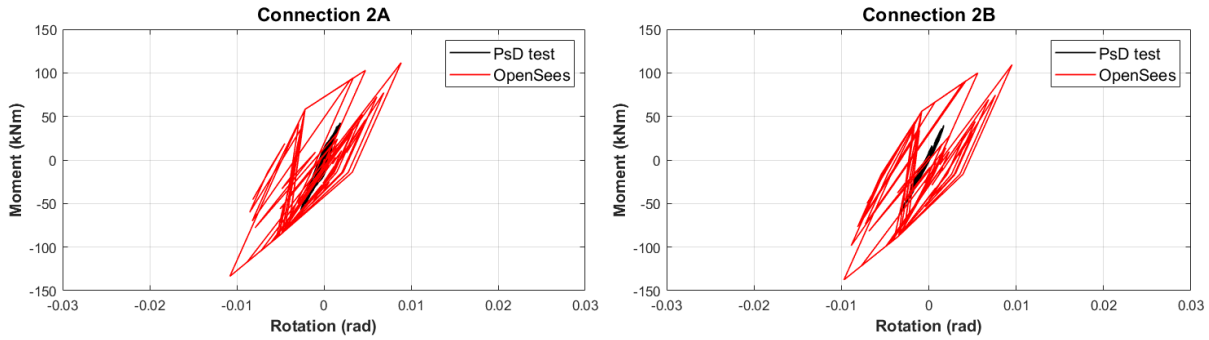

Figure B.59 – Hysteretic curves: connections 2A (left) and 2B (right)

B3.3.4 Test 4 – Santa Barbara 0.8g

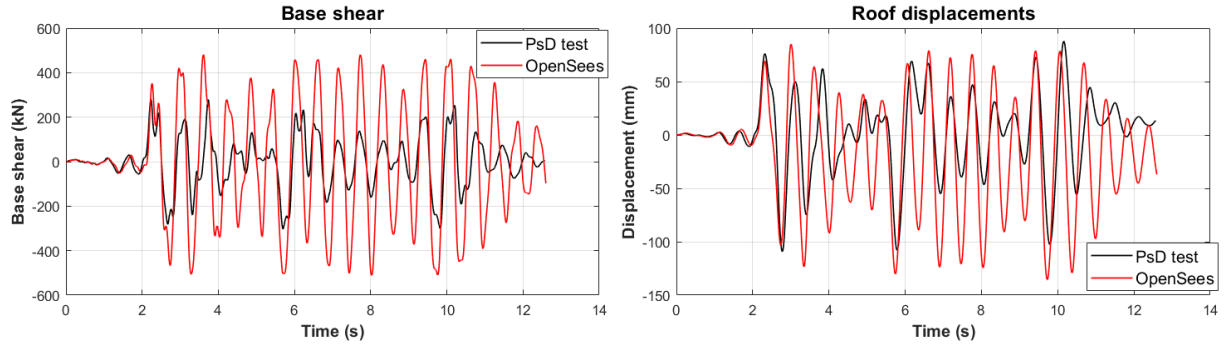

Figure B.60 – Base shear (left) and roof displacement (right) curves

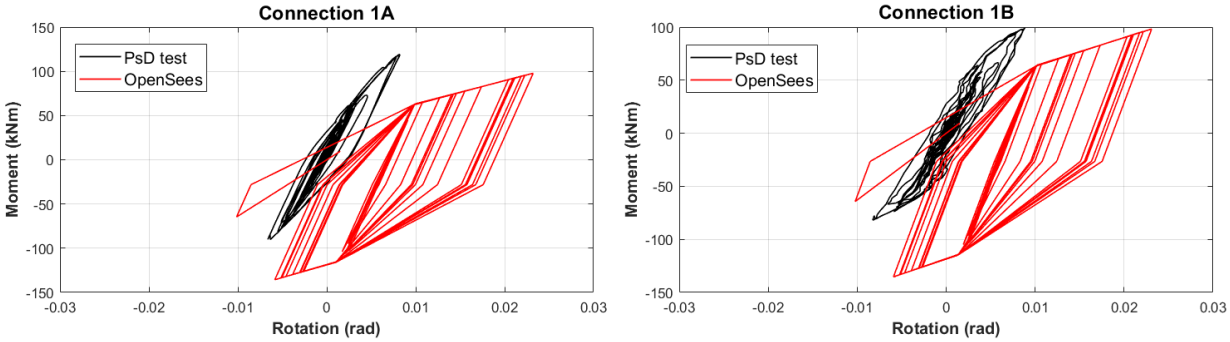

Figure B.61 – Hysteretic curves: connections 1A (left) and 1B (right)

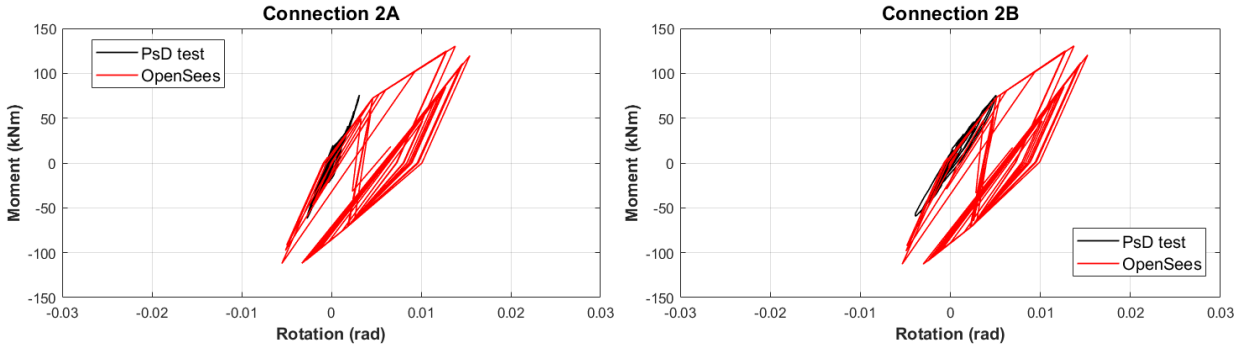

Figure B.62 – Hysteretic curves: connections 2A (left) and 2B (right)

B3.3.5 Test 5 – Coalinga 0.8g

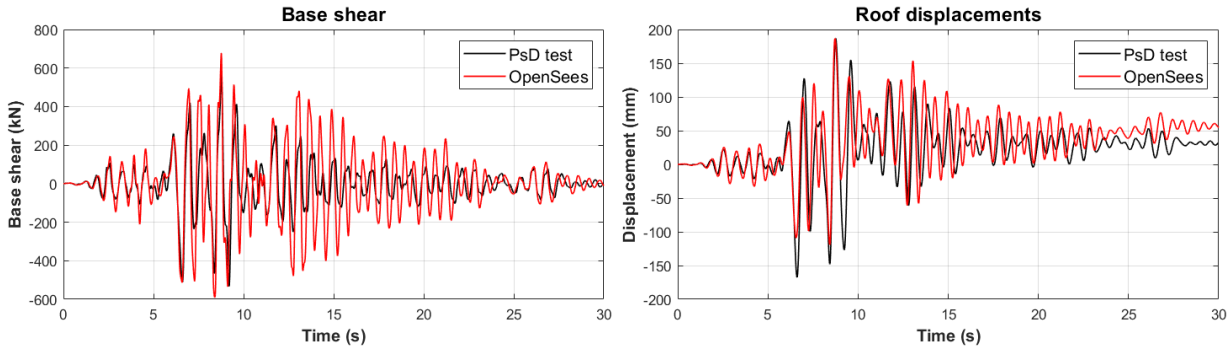

Figure B.63 – Base shear (left) and roof displacement (right) curves

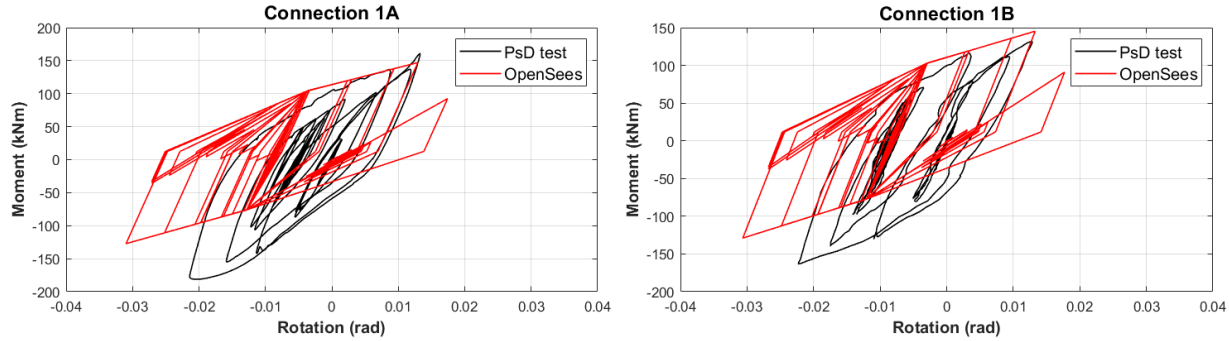

Figure B.64 – Hysteretic curves: connections 1A (left) and 1B (right)

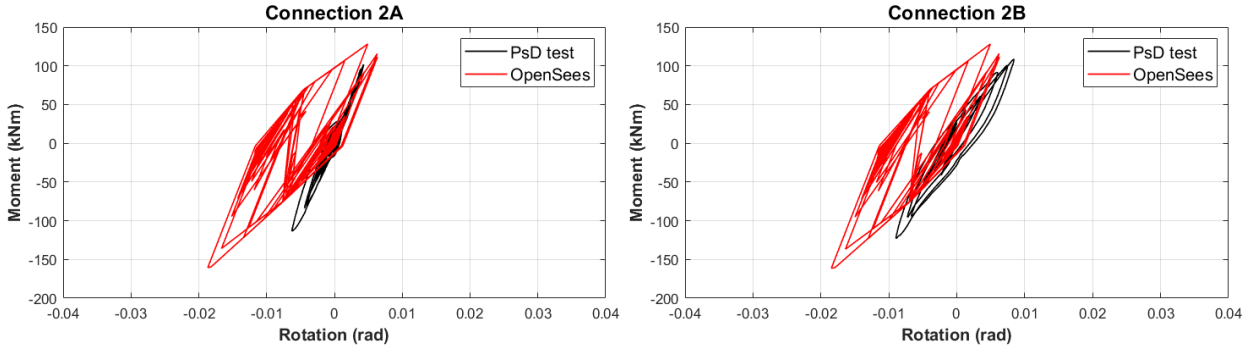

Figure B.65 – Hysteretic curves: connections 2A (left) and 2B (right)

B3.3.6 Test 6 – Kobe 1.0g

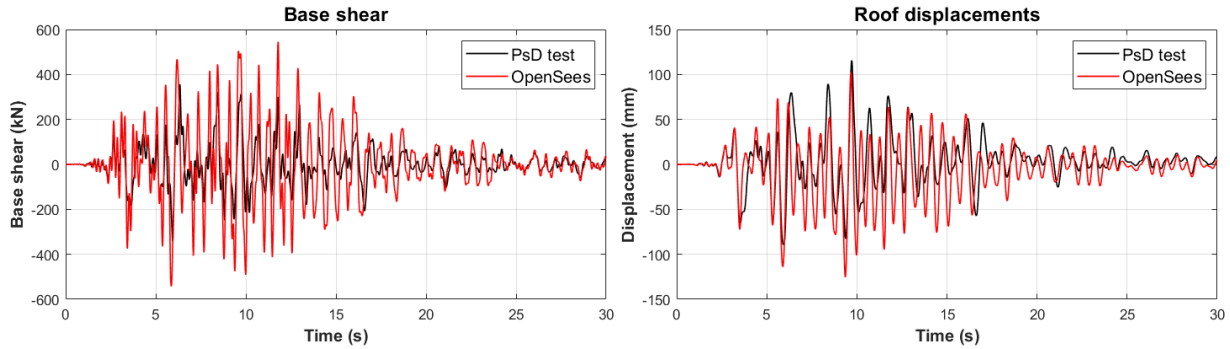

Figure B.66 – Base shear (left) and roof displacement (right) curves

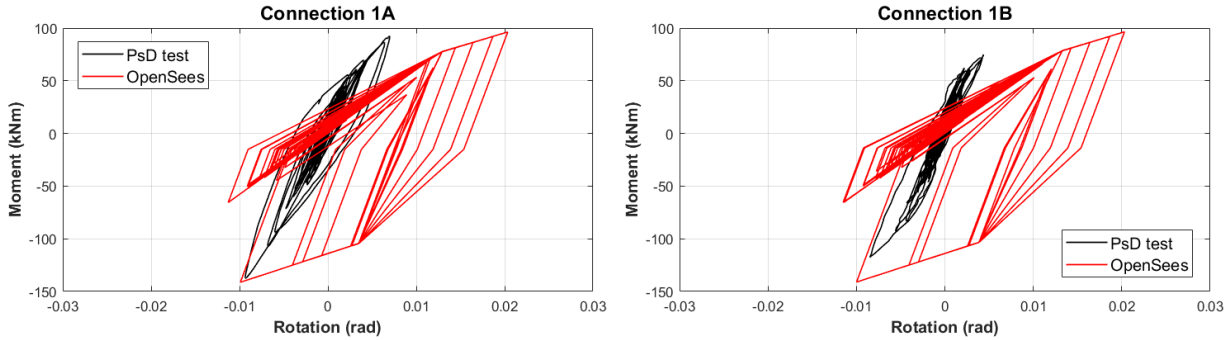

Figure B.67 – Hysteretic curves: connections 1A (left) and 1B (right)

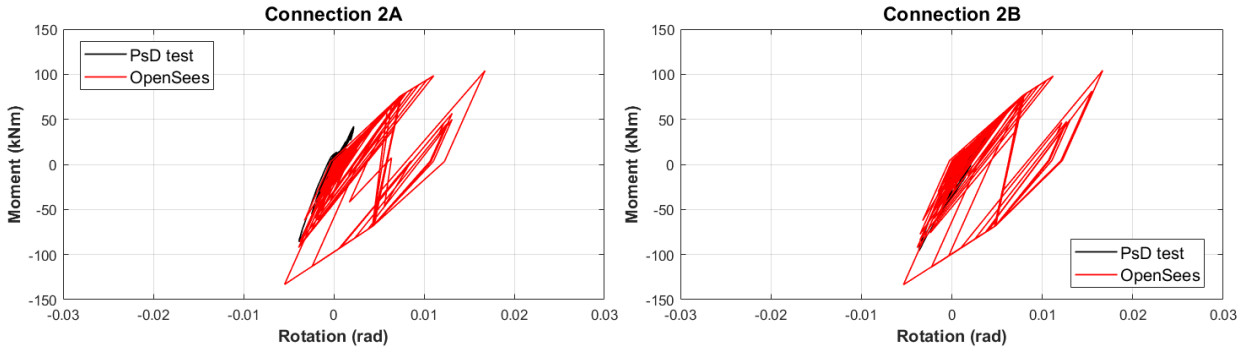

Figure B.68 – Hysteretic curves: connections 2A (left) and 2B (right)

B3.3.7 Test 7 – Coalinga 0.8g

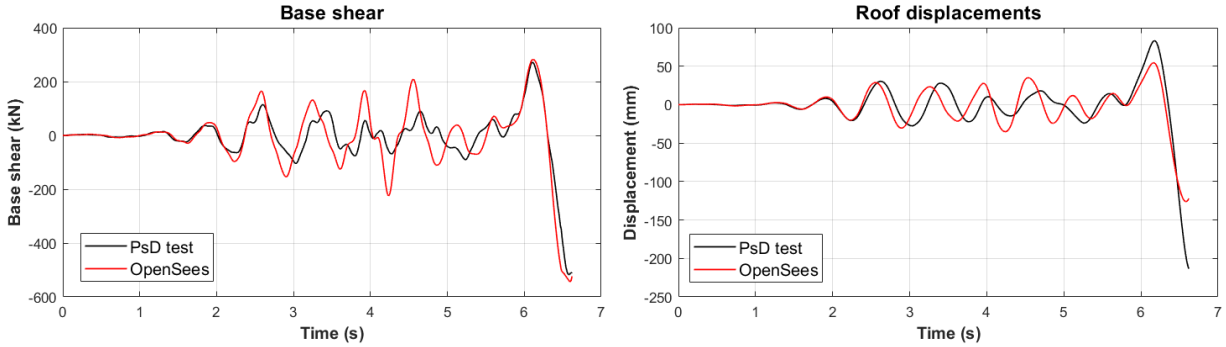

Figure B.69 – Base shear (left) and roof displacement (right) curves

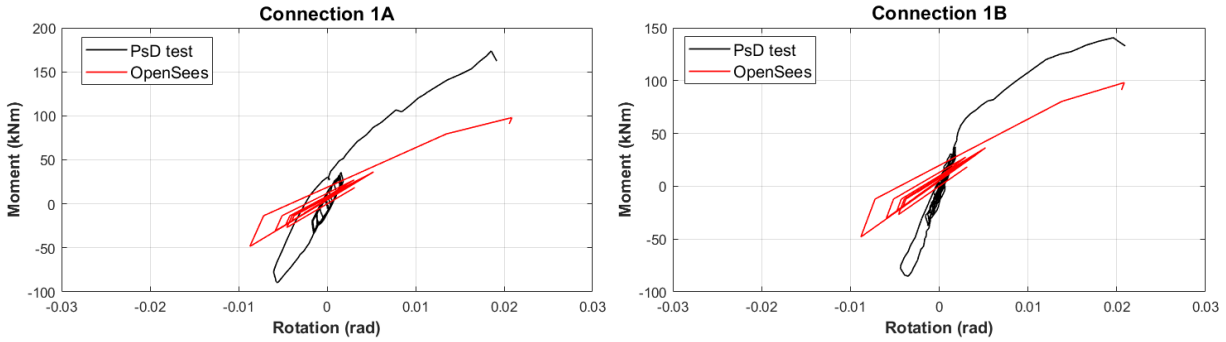

Figure B.70 – Hysteretic curves: connections 1A (left) and 1B (right)

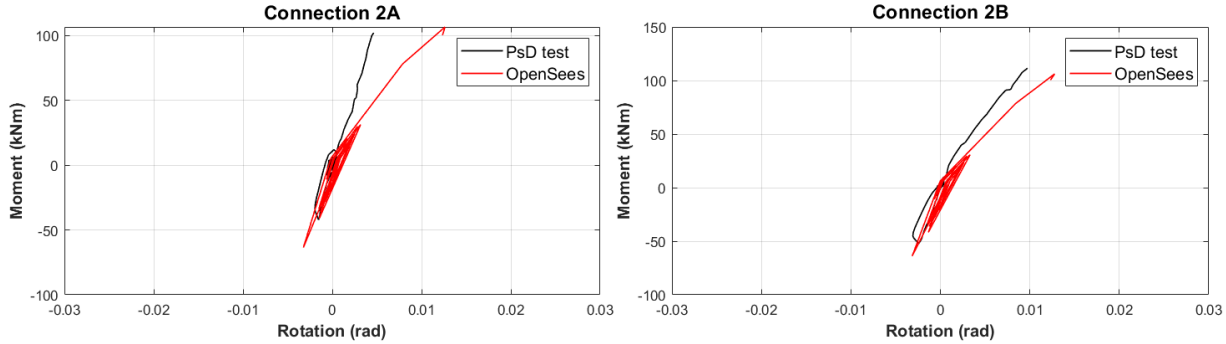

Figure B.71 – Hysteretic curves: connections 2A (left) and 2B (right)